DESIGN AND ANALYSIS OF CONCENTRICALLY BRACED STEEL FRAMES UNDER SEISMIC LOADING

by

Alan D. Hunt
B.A., B.A.I., P.G. Dip. Stat., MIEI

A thesis submitted to the University of Dublin, Trinity College in partial satisfaction for the degree of Doctor of Philosophy

September 2013

DEPARTMENT OF CIVIL, STRUCTURAL & ENVIRONMENTAL ENGINEERING
UNIVERSITY OF DUBLIN
TRINITY COLLEGE
DUBLIN

Declaration

The author hereby declares that this thesis has not been submitted as an exercise for a degree at this or any other university. Except where reference has been given in the text, it is entirely the author's own work.

The author agrees to deposit this thesis in the University's open access institutional repository or allow the library to do so on the author's behalf, subject to Irish Copyright Legislation and Trinity College Library conditions of use and acknowledgement.

Abstract

The lateral resistance of many steel framed structures is provided by diagonal brace members and their connections to the frame. Although concentrically braced frames (CBFs) are common throughout international design guidance, their behaviour is still not fully understood. Conventional seismic design of gusset plate connections utilises a clearance zone that permits out-of-plane brace deformation but results in large and stiff gusset plates that do not buckle or yield along the axis of the brace member. Recent design proposals suggest using an elliptical clearance zone and reducing all gusset plate dimensions to permit yielding in the gusset plate after brace buckling and yielding. This strength hierarchy can result in improved brace member and global frame ductility.

The purpose of this thesis is to investigate specific aspects of brace behaviour including: brace section size and slenderness; gusset plate geometrical design and connectivity of the brace to the frame. Furthermore, empirical models for the ductility capacity of hollow section bracing members and recent proposals for improved detailing of gusset plate connections are validated under realistic dynamic earthquake loading.

The seismic performance of CBFs with diagonal brace-gusset members is investigated experimentally and numerically. An experimental programme comprising six pseudo-static cyclic tests and twelve shake table tests is undertaken investigating a consistent set of structural properties. Finite element models of the test frames are developed and correlative post-test simulations using pushover and time-history analysis are performed using the OpenSees seismic analysis software

The pseudo-static tests provide information on frame stiffness, brace buckling and yield capacities, gusset plate deformation zones, the influence of gusset plate geometry and brace ductility. Test results show a strong influence of the brace-gusset-frame connection type. Gusset plates connected to both beam and column flanges display larger frame stiffness and larger hysteresis loops compared to gusset plates connected to the beam flange only. Larger drift capacity is observed with the newly proposed gusset designs, but the brace cross section slenderness is dominant at large width-to-thickness ratios.

As part of the BRACED project, shake table tests are performed to investigate the ultimate behaviour of similar brace-gusset members and connections under dynamic low cycle fatigue conditions; identify active yield mechanisms and failure modes in different brace member/connection configurations; and to provide experimental data on the earthquake response

of European CBFs. These shake table experiments investigate a full-scale model single-storey CBF designed to Eurocode 8. Twelve separate experiments are performed on the AZALEE seismic testing facility at CEA Saclay. Each experiment examines the response of the test frame and brace-gusset plate specimens to table excitations scaled to produce elastic response, brace buckling/yielding and brace fracture. The outputs of the research programme represent a unique set of data on the ultimate earthquake response of CBFs with realistic brace members and connections. The principal experimental outcomes include measurements of elastic frame stiffness and its evolution with brace damage, measurements of the displacement ductility capacity of the brace specimens; an evaluation of the influence of brace connection configuration and gusset plate detailing on frame stiffness, damping and ductility; and observations on the contributions of brace and connection yielding to the overall inelastic deformation of CBFs.

Prior to developing complete numerical simulation models of full CBFs in OpenSees, a tiered hierarchical approach was used with fundamental modelling aspects investigated first, progressing to model optimisation using advanced models with greater detail. A parametric study that examined different aspects of the available OpenSees modelling techniques was followed by a correlation study which demonstrated the capabilities and limitations of the OpenSees physical theory model using the data from a series of singe member cyclic loading experiments. The numerical modelling procedures were then implemented for the CBF test structure and correlated against the results from the cyclic loading CBF tests. Finally, a reference model is presented and further modelling techniques are discussed in relation to its application to the shake table tests. The numerical modelling is shown to have validated a methodology of modelling this class of structure in OpenSees, while the research project as a whole supports an assessment of Eurocode 8 design guidance for CBFs.

Acknowledgements

My work was carried out in the Department of Civil, Structural and Environmental Engineering in Trinity College Dublin and at the Laboratoire d'Etudes de Mécanique Sismique (EMSI) at CEA Saclay, France. I am very grateful for the financial support of the Postgraduate Research Studentship fund for the past three years. The support of the European Union Seventh Framework Programme [FP7/2007-2013] under grant agreement n° 227887 [SERIES] is also gratefully acknowledged. The 'Transnational Access' provided by the SERIES programme enabled the BRACED team to perform the extensive shake table testing programme at CEA Saclay. I also wish to thank Dr Jamie Goggins for his permission to reproduce his findings for the purpose of this study.

I would sincerely like to thank Prof. Brian Broderick for all his help, encouraging ideas and for all the time and effort he put into the BRACED project (including all the travelling and the enormous amount of design experimental and analytical work leading up to it!).

I am indebted to the technical staff in the department, in particular to Dave McAuley, Dr Kevin Ryan and to the chief Chris O'Donovan. Without all of your advice and great patience I would not have finished with a thesis as good as this!

I would like to acknowledge all those who contributed in the lead up to and during the BRACED project at CEA Saclay. In particular, the design advice from Jack English, Drs Jamie Goggins, Primoz Može and Franc Sinur and the incredible patience of Gerard O'Reilly and Dr Suhaib Salawdeh with the help in getting the knack of OpenSees, is greatly appreciated. I would also like to thank the CEA technical staff - Philippe Mongabure, Stéphane Poupin and Michele Le Corre.

The informal support and encouragement of my housemates and friends throughout the years has been indispensible. It started off in the rough auld days in Leinster Square and progressed from there, with Alan D, Jim, Simon, Sean, Greg, Tiernan, Martin, Beccy and of course Rockin Robin. Thanks to all the postgraduates that have made these years fly by! Without Will, Andy G., John, Ronnie, Simon, Dan and Lucy and many others, these years would have been nowhere near as great. Also, thanks to Lucy for the great craic on that spontaneous trip to Japan! I would like to particularly thank Greg for proof reading this thesis.

My parents, brother and sister have been a constant source of support – emotional and of course financial – during my postgraduate years, and this work would not have existed without them. This thesis is dedicated to you; Stephen, Mary, Zoë and Hugh.

Table of Contents

Principal Notation

List of nomenclature used in this thesis.

Latin upper case letters

A	Area; elongation ratio
A_e	Effective area
A_g	Gross area
B	Bolt force
C	Damping matrix
C_d	Deflection coefficient factor
C_u	Compressive resistance
$C_u{}'$	Post buckling compressive capacity
CA	Connection type (Section 3.4)
CB	Connection type (Section 3.4)
CBF	Concentrically braced frame
D	Diameter
D_s	Storey drift
DI	Damage index
D_u	Maximum inelastic drift
E	Young's modulus; energy
E_d	Energy dissipated
E_t	Tangent modulus
E_{tot}	Total energy dissipated
E_{10}	Energy dissipated at end of 10th loading cycle
EBF	Eccentrically braced frame
EC	Elliptical clearance method for gusset plate design
F	Force
F_b	Base shear force
F_c	Conservative force
F_{el}	Elastic seismic force in SDOF system
F_{nc}	Non-conservative force
F_y	Yield force; yield stress for design (AISI, 2007)
F_{ya}	Average yield stress for cross section (AISI, 2007)
F_u	Ultimate force
I	Second moment of area
K	Stiffness matrix; effective length factor
K_e	Secant stiffness
K_i	Initial stiffness
L	Length
L_{avg}	Average plate buckling length
L_{bu}	Location of buckle/fracture along brace tube length
L_{cr}	Critical buckling length
L_e	Extensometer gauge length
L_{fg}	Gusset plate free length
L_o	Coupon original gauge length
L_T	Total length
L_u	Final gauge length
M	Mass matrix; bending moment
M_W	Moment magnitude
MRF	Moment resisting frame
$N_{b,Rd}$	Design buckling capacity
N_{cr}	Critical elastic force
N_f	Number cycles to fracture
$N_{pl,Rd}$	Design plastic capacity

P	Web force	S_u	Minimum cross section area after fracture
PGA	Peak ground acceleration	SLC	Standard linear clearance method for gusset plate design
Q	Prying force in T-stub	T_1	Period of first mode of vibration
R	Response modification coefficient; Reduction factor	T_B, T_C, T_D	Transition periods for elastic response spectrum
R_{eH}	Upper yield strength	T_e	Effective period
R_m	Tensile strength	T_n	Natural period
R_n	Yield mechanism resistance	UHS	Uniform hazard spectrum
$R_{p,0.2}$	0.2% plastic proof strength	V_e	Elastic design base shear force
$R_{t,0.5}$	0.5% total proof strength	V_s	Design base shear force
R_y	Ratio of expected yield strength to minimum specified yield	Z	Cross section area percentage reduction
$S_d(T)$	Design Spectrum	2%/50	Earthquake record scaled to UHS with 2% in 50 years probability of exceedence
S_e	Elastic spectral acceleration	10%/50	Earthquake record scaled to UHS with 10% in 50 years probability of exceedence
S_o	Coupon cross section area	50%/50	Earthquake record scaled to UHS with 50% in 50 years probability of exceedence

Latin lower case letters

a	Acceleration	f_y	Yield strength
a_g	Ground acceleration	f_{ya}	Average cross section yield strength
b	Width	f_u	Ultimate strength
b_e	Effective width	g	Acceleration due to gravity
b_o	Original width	i	Radius of gyration
b_{ww}	Whitmore Width	k	Stiffness
c	Damping coefficient	l_h	Horizontal plate length
d	Depth	l_v	Vertical plate length
$\dot{e}$	Strain rate	m	Mass; slope of Coffin-Manson log-log curve
e_y	Yield displacement	m_e	Effective mass
f_n	Natural frequency	n	Number; node

t	Thickness	v_c	Crosshead separation rate
t_p	Plate thickness	q	Behaviour factor

Greek upper case letters

Δ	Lateral deformation; interstorey drift	Δ_y	Member yield displacement
Δ_d	Structural displacement	Ω_0	System overstrength factor
Δ_u	Member ultimate displacement		

Greek lower case letters

β	Balance factor	θ	Rotation angle
β_{ww}	Balance factor based on Whitmore width	λ	Slenderness; Modal participation correction factor
γ_{ovr}	Overstrength factor	λ_1	Slenderness value to determine the relative slenderness
δ_y	Structural yield displacement	$\bar{\bar{\lambda}}$	Non-dimensional slenderness
δ_{max}	Maximum structural displacement	$\bar{\bar{\lambda}}_{Rd}$	'Design' non-dimensional slenderness from nominal strengths
ε	Strain	$\bar{\bar{\lambda}}_{meas}$	'Measured' non-dimensional slenderness from measured strengths
ε'_f	Fatigue ductility coefficient	μ_Δ	Displacement ductility
ε_p	Plastic strain	ξ	Structural damping ratio
ε_y	Yield strain	ξ_{eq}	Equivalent viscous damping
ε_0	Strain for failure after one cycle	ω_n	Natural frequency

1 Introduction

1.1 Earthquakes and Structural Design

It is commonly known that earthquakes affect the lives of millions of people in all parts of the world. Amongst factors such as social upheaval and long-term economic costs, loss of life is the primary concern in relation to earthquake events. The scale of such casualties varies significantly with each seismic event. Magnitude (M_W), location and time-period have all heavily influenced the number of deaths in the significant earthquakes of the past century. Since commencing this research work in 2009, more recent devastating earthquake events have occurred: 2009 Sumatra earthquake in Indonesia ($M_W = 7.9$); 2010 Haiti earthquake ($M_W = 7.0$); 2011 Christchurch earthquake ($M_W = 6.3$) and 2011 Tōhoku earthquake off the coast of Japan ($M_W = 9.0$). These seismic events are remembered for causing hundreds of thousands of deaths and billions of dollars in economic costs.

An earthquake is the sudden release of energy in the earth's crust that creates seismic waves. The primary source of this accumulation and release of energy is tectonic activity. Tectonics is an aspect of geology related to the structure and deformations of the earth's crust, particularly the theory of plate tectonics. Seismic waves are complex ground vibrations that propagate from an energy source and interact with each other. As a result, there is typically large variability in the seismic wave characteristics (peak, period, duration) at different locations for the same earthquake event. Seismic waves are typically classified as body waves and surface waves. Body waves are further characterised as primary or P-waves and shear or S-waves with surface waves characterised as Love waves and Rayleigh waves (Figure 1.1(a)). P-waves are compression waves and as they travel the fastest, are felt first. They are generally of small amplitude and high frequency content. S-waves arrive shortly after and have very strong ground motion content. These waves typically cause the most damage with surface waves following afterwards.

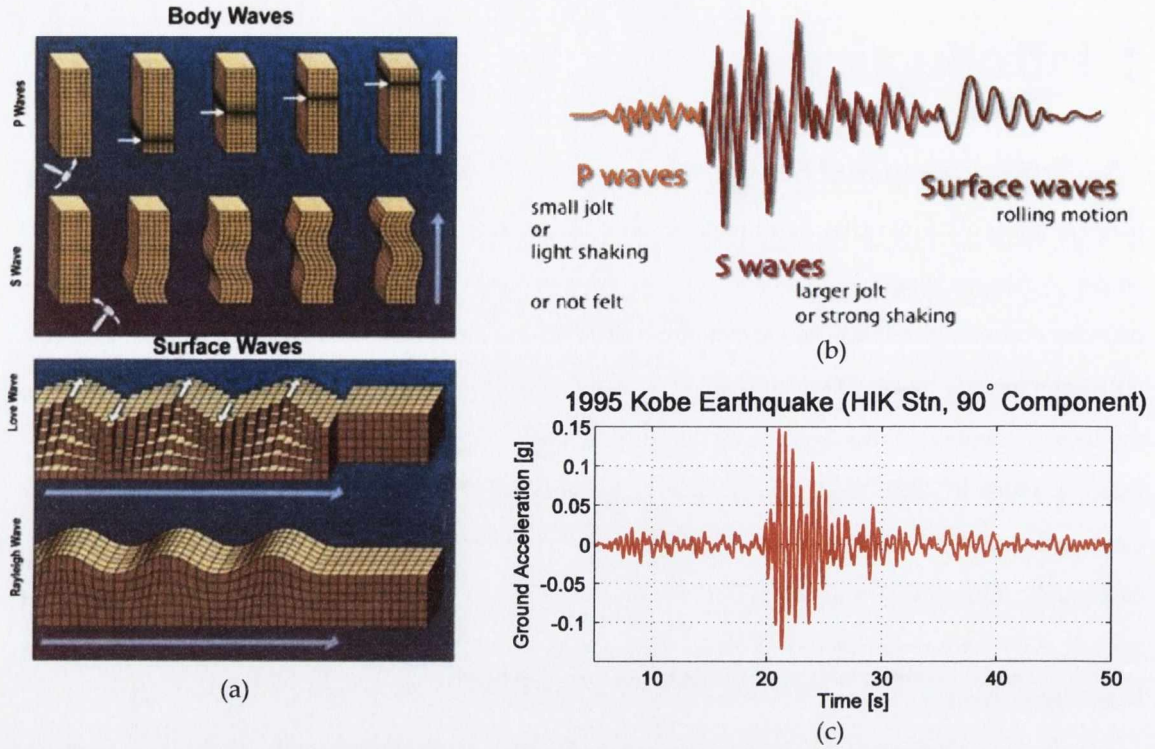

Figure 1.1 – Diagram showing (a) seismic wave characterisation for body and surface waves (USGS, 2013) (b) identification of wave characteristics in acceleration data (USGS, 2013) and (c) accelerogram showing acceleration time-history from 1995 Kobe earthquake ($M_W = 6.8$) in Japan.

There are various parties involved in the reduction of earthquake risks such as geologists, engineers, architects and government agencies. In particular, the structural engineering community can directly influence the impact of earthquakes and their subsequent consequences. A proper understanding of structural dynamics and design can reduce the loss of life in any earthquake either through structural collapse or secondary damage caused by falling debris or subsequent fire. Furthermore, sufficient structural design can ensure continued operation and function of the built environment (especially critical structures such as hospitals and power facilities).

During an earthquake, seismic waves induce ground motion which causes structures to move horizontally and vertically. Most of this is horizontal motion and is typically measured as a ground acceleration, a_g. The response of a structure is composed of inertial forces F which (in accordance with Newton's second law) are the product of the structural mass m, and the structural response acceleration a: $F = m \times a$. The inertial forces are typically conceptualised as static lateral forces applied to the side of a structure. The structural acceleration is largely determined by the individual earthquake event and local site conditions. The mass is a function of the size, shape and layout of a building. Earthquakes are time-variant events and the mass and stiffness of a structure control its dynamic behaviour. More flexible structures have a lower natural frequency of vibration and higher natural period of vibration. The opposite is true for stiffer structures. Through careful

design procedures, lateral forces are transferred down through the structure to the foundation. The methods for sustaining these lateral forces are fundamental for reducing the risk associated with earthquakes and are discussed in the following section.

1.2 Statement of Problem

Common construction methods for steel framed buildings include concentrically braced frames (CBFs) and moment-resisting frames (MRFs). CBFS consist of diagonal brace members for lateral resistance. Some of the earliest braced frame structural systems were used for support against wind loading. Particularly after the 1940 Imperial Valley earthquake, it was noted that some braced structures demonstrated better seismic performance as shown in the photograph in Figure 1.2(a). MRFs are based on the idea of using beam-column connection stiffness for lateral resistance. MRFs were employed in Olive View Hospital in California, however, unbalanced stiffness distribution lead to soft-storey formation and resulting collapse after the 1971 San Fernando earthquake (Figure 1.2(b)).

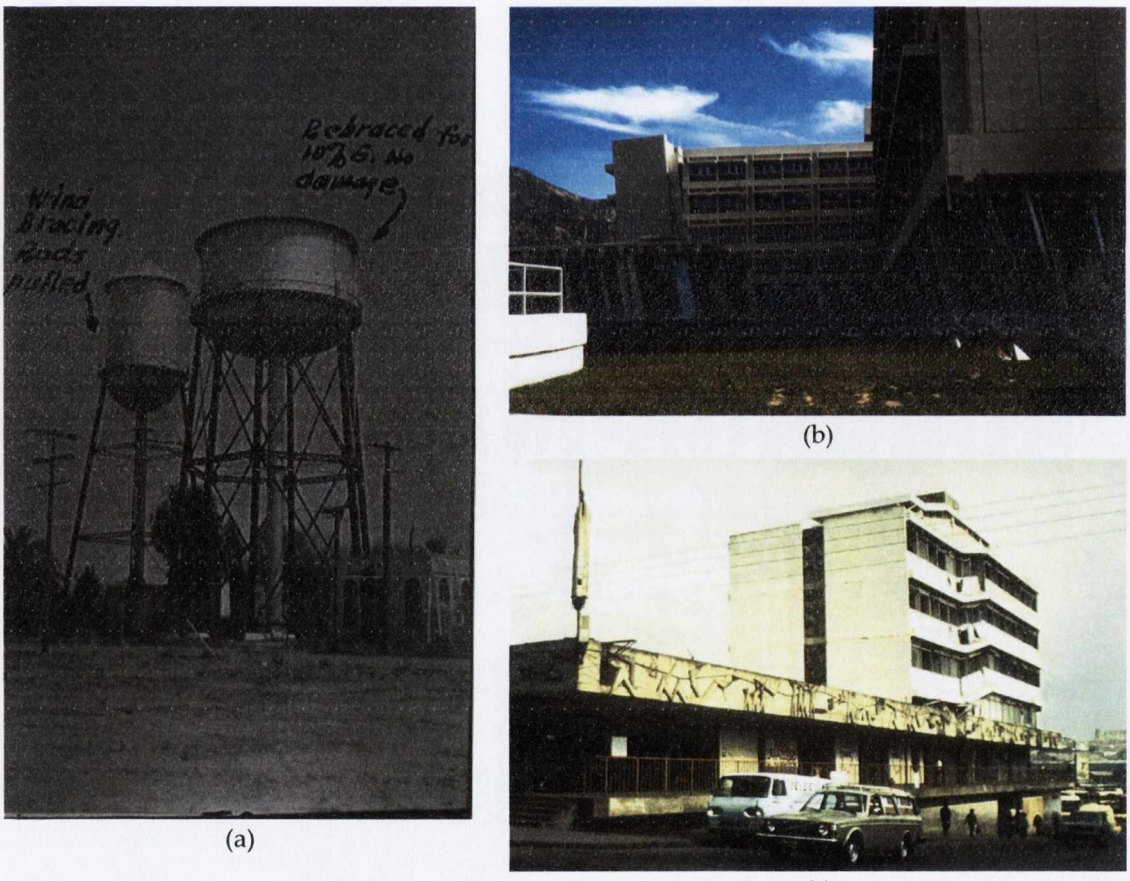

(a)

(b)

(c)

Figure 1.2 – (a) Water towers with diagonal bracing in El Centro, California after 1940 Imperial Valley earthquake (NISEE, 2011). Tank on left was braced for wind loading only and suffered considerable damage; tank on right had been braced for a 10% lateral force before earthquake. (b) Olive View Hospital, California after 1971 San Fernando earthquake (Godden, 1997); large interstorey drift due to soft storey formation at the first storey level. (c) Hotel Terminal, Guatemala City; damaged due to torsional failure of second storey during 1976 Guatemala earthquake.

Prior to the 1994 Northridge earthquake and 1995 Hanshin/Awaji (Kobe) earthquakes, MRFs were particularly prevalent in steel construction. After the earthquake events, it was found that many of the moment-resisting connections did not perform as expected and some buildings sustained significant damage, without any immediate signs of collapse (Mahin, 1998). These connection types suffered from brittle fracture of welded joints. This unexpected behaviour prompted significant investigation of design theory and drove a shift in long-term trends towards CBF usage.

Fracture is an undesirable phenomenon that occurs in structures and can reduce ductility under seismic loading. As illustrated in the general load-displacement curve in Figure 1.3, displacement ductility is the ability of a material, member or structure to undergo deformation after initial yield (F_y) without any significant reduction in strength. To quantify displacement ductility μ_Δ, it can be expressed as the ratio of ultimate displacement Δ_u to yield displacement Δ_y. If fracture can be delayed, displacement ductility can be extended and can result in greater structural energy dissipation.

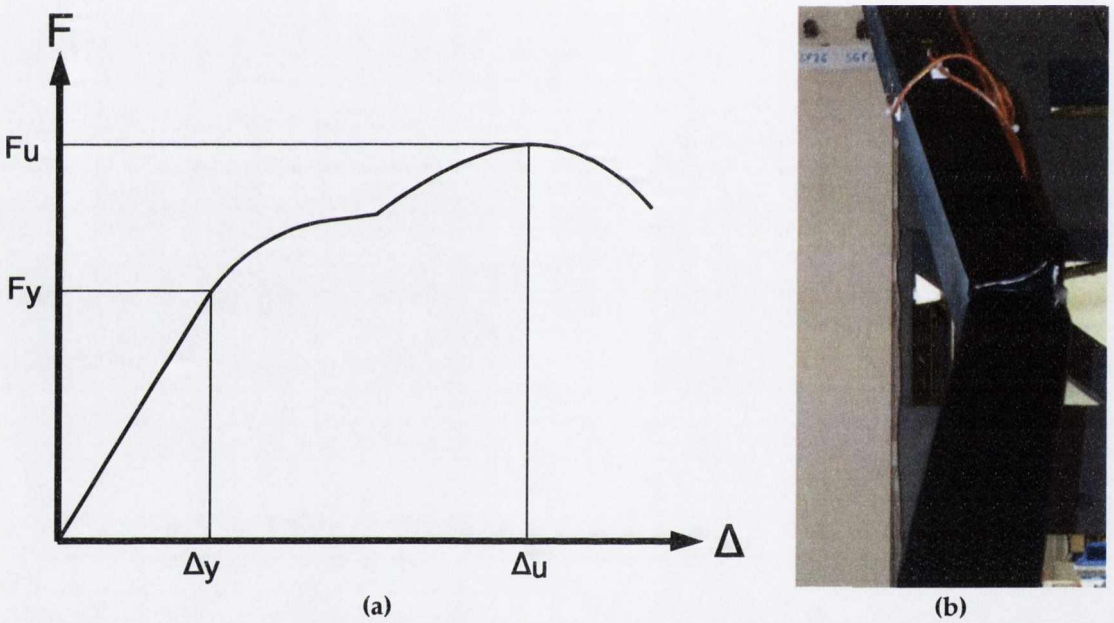

Figure 1.3 – (a) General force-displacement plot of structural member.(b) Photograph of brace with fracture developed into tearing of section.

Considerable effort in recent years by Tremblay et al. (2003), Goggins et al. (2006), Nip et al. (2010) and others has helped advance understanding and assessment of the displacement ductility concept particularly in relation to brace members. Predictive models have been developed that account for brace parameters and have shown reasonable accuracy. However, improvement is needed to consider brace boundary conditions and performance under dynamic loading conditions.

Existing design methods focus significant plastic strain formation in certain brace members especially in the compression loading range. This causes local buckling around the brace mid span and large lateral deformations of the brace at this region. Large strains associated with local buckling can lead to fracture development under low cycle fatigue conditions. In a CBF, braces are connected to the beam and column members using gusset plates. Gusset plates are sized to permit the development of a plastic hinge that allows lateral displacement of the brace member under compression. Recent improvements have been suggested by Lehman et al. (2008), the provide alternative methodologies for gusset plate plastic hinge design. The concentration of plastic strains under seismic loading is reduced using the balanced design concept. In this way, in addition to the plastic hinge mechanism, tensile yielding of the gusset plate is permitted. This has shown improvements in structural performance parameters such as drift ratio but additional experimentation is required particularly under seismic loading conditions. This has been employed in the context of American design practice, where brace members tend to be larger due to design code stipulations. In a European design context, there is a requirement for applying these concepts with more slender braces.

An expansive volume of research has taken place to date on the numerical modelling of braced frames. Little research exists investigating the seismic response of alternative design methods and correlation with realistic results. In light of the above, the research presented herein aims to investigate the seismic behaviour of different brace member and connection designs through experimental testing. In conjunction, numerical models are developed and a number of modelling options are correlated with the experimental results.

1.3 Research Objectives

The overall aim of this work is to improve upon existing understanding of, and numerical modelling methods for, steel CBFs subjected to seismic loading; and to assess the implications for design methods and guidance. This is achieved by addressing several distinct objectives:

- A large body of research has generated theoretical and empirical formulae to predict key brace performance parameters. This study shall examine the validity of these predictive formulae under realistic dynamic response conditions using pseudo-static and shake table testing of model CBFs.
- More recent research has shown that standard practice with respect to brace connection design can be improved by using alternative geometrical details. This study shall assess the influence of different gusset-plate characteristics on the dynamic response of CBFs subjected to earthquake ground motion. Conventional and recently-proposed design methods shall be qualitatively and quantitatively compared.

- Finite element software has been used to model the global response of braced frames and the local response of brace members and brace connections. In this work, OpenSees modelling techniques proposed for this form of structure will be investigated, and the software's ability to model the earthquake response of CBFs will be validated through correlation with test results.
- Based on this validation and parametric analysis, any identified improvements to the existing modelling techniques shall be represented as recommendations for future modelling studies.

1.4 Organisation of Thesis

This section describes the overall layout of the thesis document. A summary of each chapter is provided so that the natural progression of each chapter and the rationale behind the structure of the document as a whole is explained.

Chapter 2

This chapter comprises a review of previous work on design philosophies and methodologies for steel CBFs. The general behaviour of brace members under inelastic cyclic loading is explained, followed by a discussion of the recent research literature on brace ductility. A brief discussion of structural damping is also included.

Chapter 3

A review specific to brace member connection design is presented. Current design procedures are surveyed alongside alternative proposed procedures. This elucidates the rationale behind the brace specimen selection and design used for experimental testing in subsequent chapters.

Chapter 4

The open-source finite element software used in this study is described. The stiffness and flexibility methods are reviewed and are examined for their suitability for this project. A parameter study on inelastic brace member response is presented which considers important modelling parameters that have been highlighted in existing literature. Progressing from this parameter study, a general model for brace members is discussed, particularly in relation to modelling fracture due to fatigue. The general brace model is then correlated with monotonic cyclic loading tests. Finally, techniques available for modelling the whole CBF are discussed and the general brace model is employed.

Chapter 5

This chapter details the preparation and underlying design of an experimental programme of cyclic tests on a model CBF. This includes the design of the experimental specimens, measurement of material properties, and cold-formed cross-section strength considerations. Also included is an overview of the cyclic testing procedure and the test control system and instrumentation used during the cyclic experimental programme.

Chapter 6

Primary observations from the cyclic experimental programme are presented followed by detailed results from direct measurements obtained in each test. An analysis of these results draws some preliminary conclusions concerning the investigated experimental parameters. This information helps guide the dynamic shake table experiments in later chapters.

Chapter 7

Finite element models of the test structure and specimens from the previous cyclic tests are demonstrated. This leads to a comparison of model output with the experimental test measurements. The aim of this chapter is to investigate the model's ability to capture the observed response of the cyclic test specimens. These models will then be further developed for application to dynamic testing, as discussed in Chapter 10.

Chapter 8

The background to the BRACED project and the shake table tests completed are described in this chapter. The aims of the project are set out, the test frame outlined and the design of the brace-gusset plate specimens explained. Details of the instrumentation equipment and its locations on the test frame and specimens are presented as these become key references for interpreting the experimental results in the subsequent chapter. The testing regime employed in the shake table tests is also outlined.

Chapter 9

The results from the BRACED project tests are presented showing the actual measured brace areas and directly recorded test data for both types of tests performed using the selected specimens. Secondly, an analysis of this data discusses and compares behaviour and performance parameters.

Chapter 10

Using the previously developed finite element models from Chapter 7, the responses of the test frame in each experiment are modelled. First, different modelling options are presented then correlations between the experimental results and the response obtained using a general reference

model are shown. Based on this correlation study, alternative methods are described to offer potential improvements to future model development.

Chapter 11

This chapter summarises the work completed within this research project. Following this a series of conclusions and recommendations for future work are outlined.

2 Background: Seismic Behaviour and Design of Tubular Bracing Members in CBFs

2.1 Introduction

Having being initially developed to provide lateral stability and to resist lateral wind loads in the elastic range, braced building frames have seen increased refinement and adaptation over the past number of decades to ensure good earthquake resistance through nonlinear behaviour. Braced building frames generally consist of members that span diagonally in an orthogonal frame. The diagonal members are normally connected using gusset plate connections forming an efficient system for resisting lateral loads induced by both earthquakes and wind. Typical structural frame types are described in Eurocode 8 (CEN, 2004a) under three main classifications of frames as shown in Figure 2.1. These are concentrically braced frames (CBFs), eccentrically braced frames (EBFs) and moment resisting frames (MRFs).

In CBFs the axes of the brace members are coincident with the intersection of the beam and column members. Although the behaviour of CBFs is often analysed similar to that of a vertical cantilevered truss, the assumption that the frame members resist pure axial loads is a simplification. Large gusset plate connections at the brace ends can create a semi-rigid, moment-resisting connection resulting in significant bending moments and eventual inelastic deformation within the connected beams and columns (Roeder and Lehman, 2008). In Eurocode 8, the classification of CBFs is subdivided into Diagonal Frames and V-Frames.

EBFs are defined as frames where brace axes are non-coincident with beam and column intersections. They do not possess the same extensive deployment across seismic regions as that of CBFs. Their design minimises buckling in the braces and encourages inelastic rotations in the beams, known as links, to promote stable nonlinear frame behaviour. EBFs offer the combined advantage of high elastic stiffness and large inelastic energy dissipation capacity (O'Malley and Popov, 1984).

MRFs feature stiff frames of beams, columns and connections with flexural behaviour. At an MRF connection, if the angle between the beam and column remains constant, then the connection is designated fully restrained. Energy is dissipated when the yield load of either the beam or column is reached. Partially restrained connections permit a change in the angle of intersection and

therefore allow yielding of connection elementts. Steel MRFs have long been recognised as a highly suitable structural system for use in regions of high seismicity. However, unanticipated brittle fracture of connections during the 1994 Northridge and the 1995 Hanshin/Awaji (Kobe) earthquakes contradicted the expectations of many structural engineers who anticipated that such systems would undergo large plastic deformation (Mahin, 1998). In particular, after the Northridge earthquake, Mahin outlines that brittle fractures usually occurred without damage to architectural finishes and cladding and was only observable in buildings under construction at the time. These observations resulted in a reduction in confidence in the seismic performance of MRFs, amendments to the design procedures for MRFs and a more frequent implementation of CBFs for seismic design. This in turn has prompted a reassessment of the large body of research on CBFs (see Section 2.3) motivated in part by the relatively larger stiffness and reduced interstorey drifts offered by this frame type.

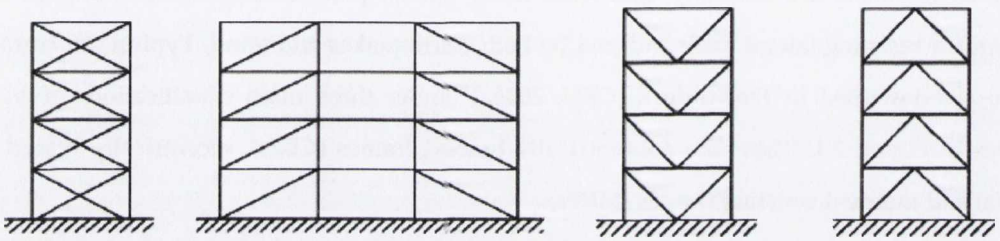

Concentric Diagonal Bracing Concentric V-Bracing

(a) Concentrically Braced Frame (CBF)

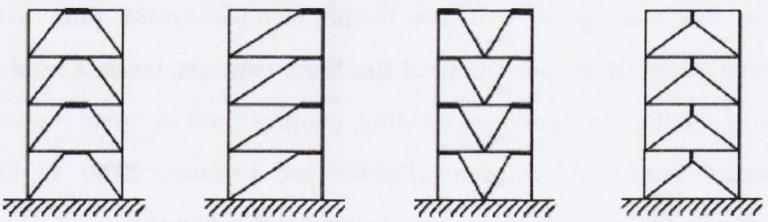

(b) Eccentrically Braced Frames (EBF)

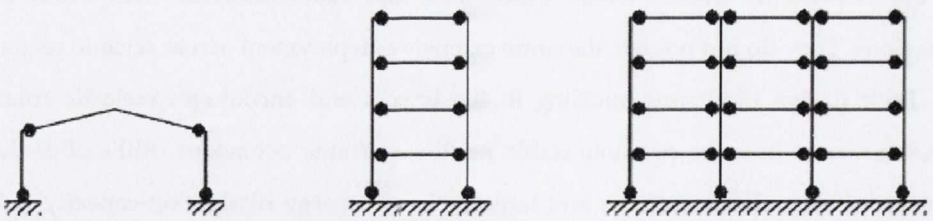

(c) Moment Resisting Frames (MRF)

Figure 2.1 – Structural frame types as classified by Eurocode 8 (CEN, 2004a).

2.2 Seismic Design of Braced Steel Frames

Since the 1970s, a large body of research has been carried out on the seismic design and performance of braced frames, for example Hjelmstad and Popov (1984), O'Malley and Popov

(1984), Khatib et al. (1988), Tremblay et al. (2003), Goggins (2004), Broderick et al. (2005) and Uriz and Mahin (2008). Internationally, seismic design guidelines have been developed based on this body of research. For example, European seismic design codes are contained in Eurocode 8 (CEN, 2004a) and in Canada the Canadian Standards Association expresses seismic design requirements in 'Design of Steel Structures' (CSA, 2009). In the United States several seismic building codes are currently in use throughout different regions, but the International Building Code (IBC, 2009) is extensively-used, making reference to the American Institute of Steel Construction (AISC) Specification for Structural Steel Buildings (AISC, 2005b). The design regulations used by the International Building Code are primarily based on the recommendations of the American Society of Civil Engineers (ASCE) entitled 'Minimum Design Loads for Buildings and Other Structures' (ASCE, 2010) which in turn is partly based on the provisions of the AISC guidelines 'Seismic Provisions for Structural Steel Buildings' (AISC, 2010).

In these seismic design guidelines, there generally exists an implied, tiered design philosophy with specific performance based design criteria. During small, frequent earthquakes a structure is designed to remain elastic and provide adequate stiffness and strength to ensure no structural damage occurs (damage-limitation requirement). However, during large infrequent seismic events significant inelastic deformation is expected to allow for energy dissipation and structural ductility whilst preventing structural collapse (no-collapse requirement). In design codes these damage states are typically linked with different levels of seismic activity.

Eurocode 8 (CEN, 2004a) meets this two-tiered design philosophy through limit state design. The former, small earthquake requirements are addressed through by deformation-based limit states, while the compliance criteria for the no-collapse requirement are specified as a force-based ultimate limit state. The design seismicity level with this limit state has a probability of exceedence of 10% in 50 years approximately corresponding to an average return period of 475 years. To meet the latter, large earthquake requirements, no-collapse criteria adopt force-based ultimate limit states. The design seismicity level with this limit state has a probability of exceedence of 2% in 50 years approximately corresponding to an average return period of 2500 years.

Two design approaches are discussed in the following sub-sections with emphasis on CBF design. Force-Based Design has been traditionally utilised across many designs codes. However, an emerging method known as Displacement-Based Design has been proposed by Priestley et al. (2007).

2.2.1 Force-Based Seismic Design

Eurocode 8 (CEN, 2004a) describes the compliance criteria for the no-collapse requirement as a force-based ultimate limit state. This prescribes an ultimate lateral strength to a structure to resist

the applied lateral forces representative of ground motions. This is against the physical reality, whereby a dynamic earthquake action imposed on a structure is composed of a total energy input and a demand to tolerate certain displacements and deformations (Fardis et al., 2005). Termed differently, it is deformations and not forces that cause structural failure. The use of the forced-based method can be linked to the traditional analysis of structures undergoing a static equilibrium of forces e.g. gravity and wind actions.

For practical purposes, the no-collapse requirement allows for inelastic deformations and thus structural members do not have to be designed for a wholly elastic structural response (which would be prohibitively impractical and expensive). Therefore, the no-collapse requirement encompasses design for energy dissipation and ductility of specific structural members.

This is implemented in Eurocode 8 through two different design concepts according to three structural ductility classes. Structural ductility is grouped according to the availability of member ductility: low ductility (DCL), medium ductility (DCM) and high ductility (DCH). The first design concept specifies that the expected response of DCL structures fulfils both damage-limitation and no-collapse requirements while remaining substantially elastic. The second concept takes into account the capability of the DCM and DCH structures to resist seismic forces through inelastic deformation.

Seismic design codes specify different types of linear analysis for the design of structures and for an evaluation of their seismic performance. Generally, a designer can choose between a linear static analysis or a linear dynamic analysis. In Eurocode 8 (CEN, 2004a) and ASCE-7 (2010) a linear static analysis is known as 'lateral force method of analysis' and a linear dynamic analysis is known as the 'modal response spectrum analysis'. The lateral force method may be used for buildings meeting criteria described below and the modal response spectrum is applicable to all types of buildings.

Both of these linear-elastic methods utilise a design response spectrum to account for the capacity of a structure to dissipate energy through inelastic and ductile behaviour and a typical viscous damping ratio $\xi = 0.05$. The design response spectrum is simply a single-degree-of-freedom (SDOF) response spectrum reduced with respect to the elastic response spectrum (Figure 2.2). In practice, this is carried out by reducing the horizontal and vertical elastic response spectra using a behaviour factor q which can be expressed as

$$q = \frac{F_{el}}{F_y} \qquad 2.1$$

where F_{el} is the peak seismic force that would develop in an SDOF system with a linear-elastic response and F_y is the yield force of the SDOF system. At this point, it is worthy to note that a linear analysis performed in this way does not imply that the structure will perform elastically, it is merely a method adopted to reduce the complexity of force-based seismic design. For DCL structures mentioned above, the behaviour factor is limited to 1.5. This value accounts for overstrength design of the structure and ensures the response is elastic. For DCM and DCH structures, behaviour factor limits larger than 1.5 are permitted depending on the structural type.

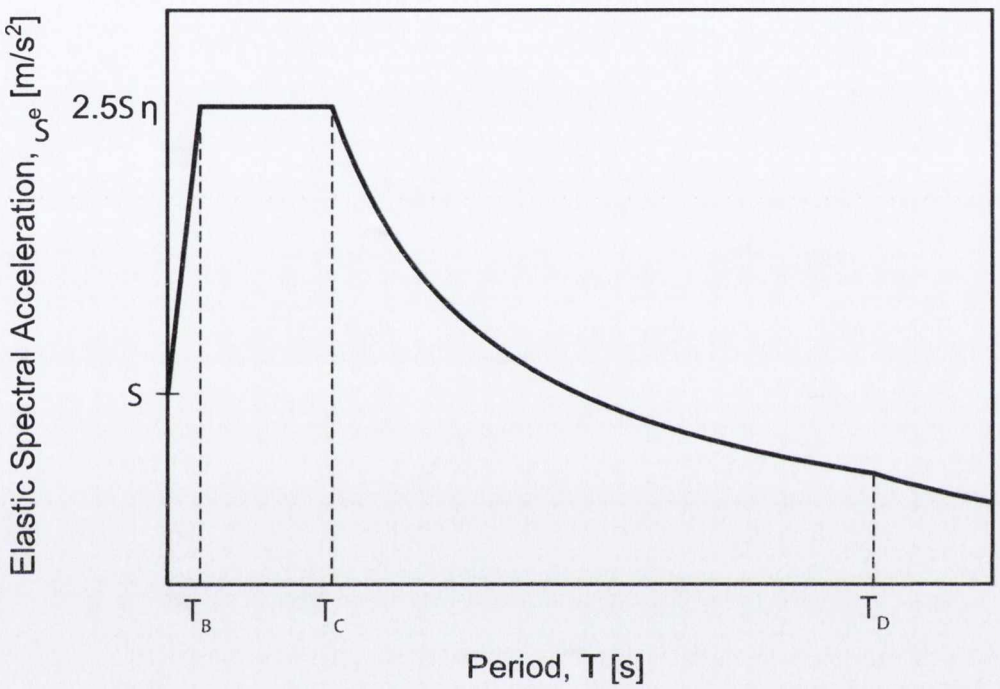

Figure 2.2 – Eurocode 8 elastic response spectrum shape with period values T_B, T_C and T_D and soil factor S describing the shape of spectrum corresponding to a specific ground type.

The lateral force method applies equivalent lateral static loads to the structure, in two orthogonal directions. However, some restrictions are in place concerning its applicability. Eurocode 8 (CEN, 2004a) limits this method only to structures whose response is dictated by its fundamental mode in each direction. Furthermore, a structure must be regular in elevation and its fundamental period of vibration T_1 must remain less than both $4T_C$ and $2.0\ s$ where T_C is a transition period described in the elastic response spectrum (Figure 2.2). If these criteria are not fulfilled then a modal response spectrum analysis shall be carried out. The base shear force F_b for each of the horizontal directions is defined as:

$$F_b = S_d(T_1)m\lambda \qquad 2.2$$

where $S_d(T_1)$ is the value of the design spectrum for the fundamental period, m is the total mass of the building and λ is a correction factor for the modal mass participation of buildings with more

than two stories. The base shear force is typically converted into a set of lateral inertia forces. For the lateral force method this can be conducted using weighted ratios of storey mass and their respective horizontal displacements or vertical heights from ground level. For a modal response spectrum analysis the response of all significant modes of vibration are considered. An eigenmode-eigenvalue analysis is carried out and for each significant mode, the natural period, mode shape vector and modal participation factor are calculated for each direction of interest. These are combined with the spectral displacement to establish a nodal displacement vector for each direction. Nodal displacement vectors are then used to compute deformations of storeys or members for each mode. These exact peak modal responses can be combined to form an approximate overall response.

Two non-linear methods are described in Eurocode 8 as non-linear static (pushover) analysis and non-linear dynamic analysis. In its simplest form, a pushover analysis is carried out under constant gravity loads and monotonically increasing lateral loads to reach a target displacement. As the monotonic loads increase, inelastic deformation development in structural members is considered. A form of non-linear static analysis is carried out in the present study in the form of a displacement-controlled pseudo-static cyclic load on a single member CBF test structure (Chapters 4.4).

Where the pushover method of a structure requires an approximation of global deformation for suitable target displacements or forces, a non-linear dynamic analysis requires the response be obtained through the direct numerical integration of the structure's differential equations of motion. This is done using time-dependant accelerograms as motion input. Non-linear time history analysis is carried out for the BRACED project and is presented in Chapter 8.

In Eurocode 8, capacity design procedures for diagonal frames assume that only the tension diagonals contribute to the design lateral resistance, while dissipative zones in CBFs are also assigned to the tension diagonals. The remaining members are non-dissipative and are required to remain elastic; they are designed to have sufficient overstrength to ensure inelastic development in the brace members only. As a result, the actual maximum yield strength of the dissipative brace members must be carefully controlled and should not exceed $1.1\gamma_{ovr}$ where the overstrength factor, $\gamma_{ovr} = 1.25$. All frames designed in this study are diagonal frames, despite their immediate appearance as V-frames. This layout of the frames in this study permits out-of-plane brace deformation without interaction between the braces.

Specific maximum q values are defined for diagonal frames and V-frames (Table 2.1). Depending on the q values employed, the sizing of brace members is selected taking into account brace slenderness and width-to-thickness ratios (local slenderness):

- To avoid overloading the columns in the pre-buckling stage, the non-dimensional brace slenderness, $\bar{\lambda}$, in diagonal frames is limited to $1.3 < \bar{\lambda} \leq 2.0$ and for V-frames $\bar{\lambda} \leq 2.0$. Eurocode 3 (CEN, 2005a) defines non-dimensional slenderness as:

$$\bar{\lambda} = \sqrt{\frac{Af_y}{N_{cr}}} = \frac{L_{cr}}{i}\frac{1}{\lambda_1} \qquad 2.3$$

for Class 1, 2 and 3 cross-sections in which

$$\lambda_1 = \pi\sqrt{\frac{E}{f_y}} \qquad 2.4$$

where A is the section area, f_y is the yield strength, N_{cr} is the elastic critical force for the relevant buckling mode, L_{cr} is the relevant buckling length, i is the relevant radius of gyration and E is the modulus of elasticity for steel.

- Maximum width-to-thickness limits are imposed for the compression elements of cross-sections for different section classes (Class 1, 2, 3 and 4) by Table 5.2 in Eurocode 3. Within the behaviour factor limits of Table 2.1, further cross-section class requirements are defined by Eurocode 8 for specific ranges of q.

Table 2.1 - Maximum behaviour factors, q, for dissipative diagonal frames and V-frames.

CBF Type	Ductility Class	
	DCM	DCH
Diagonal Frames	4	4
V-Frames	2	2.5

When capacity design is complete, displacements under the seismic action are estimated. These are checked to comply with the damage limitation limits of Eurocode 8. If the limits are exceeded, redesign of structural members is required by increasing member sizes, to increase member stiffness.

In the AISC Seismic Provisions (AISC, 2010) two distinct categories of concentrically braced frame systems are defined: Ordinary Concentric Braced Frames (OCBF) and Special Concentric Braced Frames (SCBF). OCBFs have low ductility demand expectations and are designed for large base shears and limited inelastic deformation capacity. SCBFs are specifically designed for significant inelastic deformation capacity primarily through brace buckling in compression and yielding of the brace in tension. They require lower base shear capacity and are expected to sustain forces matching the yielding capacity of the braces through relatively large drifts. The response

modification coefficient R (ASCE, 2010) provides a rational relationship between response spectrum demand and the inelastic response reduction capabilities of a structural system:

$$V_s = \frac{V_e}{R} \tag{2.5}$$

where V_s is the design base shear force and V_e is the elastic design base shear force. As is apparent from Equation 2.1, R fulfils an equivalent function to the European behaviour factor q. For elastic design, the base shear values that have been reduced by R are multiplied by a system overstrength factor Ω_0 to estimate the internal forces in force-controlled members for capacity design. In order to estimate the maximum inelastic drift values D_u (under elastic design), story drift values D_s are multiplied by a deflection amplification factor C_d:

$$D_u = D_s C_d \tag{2.6}$$

The inelastic drift values D_u are checked to ensure that they do not exceed the allowable storey drift limits as set out in ASCE 7 (ASCE, 2010). The R, Ω_0 and C_d factors pertaining to OCBFs and SCBFs are listed in Table 2.2 below.

Table 2.2 – Design coefficients and factors for OCBFs and SCBFs as set out in ASCE 7 (ASCE, 2010).

CBF Category	Response Modification Coefficient, R	System Overstrength Factor, Ω_0	Deflection Amplification Factor, C_d
OCBFs	6	2	5
SCBFs	3.25	2	3.25

2.2.2 Displacement-Based Seismic Design

The displacement-based design method has been under development for over 20 years (Priestley, 1997; Priestley et al., 2007) with a framework design code developed as recently as 2012 (Sullivan et al., 2012). The formulation characterises the structure to be designed by a SDOF oscillator whose properties represent performance at peak displacement response, rather than by its initial elastic characteristics. The fundamentals of this process are illustrated in Figure 2.3 below. Figure 2.3(a) shows the SDOF representation of a frame building while Figure 2.3(b) shows the bi-linear lateral-force displacement curve with initial stiffness K_i, followed by post yield stiffness rK_i. In contrast to force-based design where a structure is characterised by elastic pre-yield properties (initial stiffness and elastic damping), displacement-based design characterises the structure using the secant stiffness K_e at maximum displacement Δ_d and equivalent viscous damping ξ_{eq}. The equivalent viscous damping represents the elastic damping combined with hysteretic inelastic energy dissipation (Figure 2.3(c)). Using the established design displacement and damping ratio, the

effective period T_e is determined for the effective mass m_e measured at the effective height H_e. The effective secant stiffness K_e of the SDOF system is as follows:

$$K_e = 4\,\pi^2 m_e / T_e^2 \qquad 2.7$$

As a result, the lateral SDOF force F can be determined and used for distribution of base shear forces V_{Base}:

$$F = V_{Base} = K_e \Delta_d \qquad 2.8$$

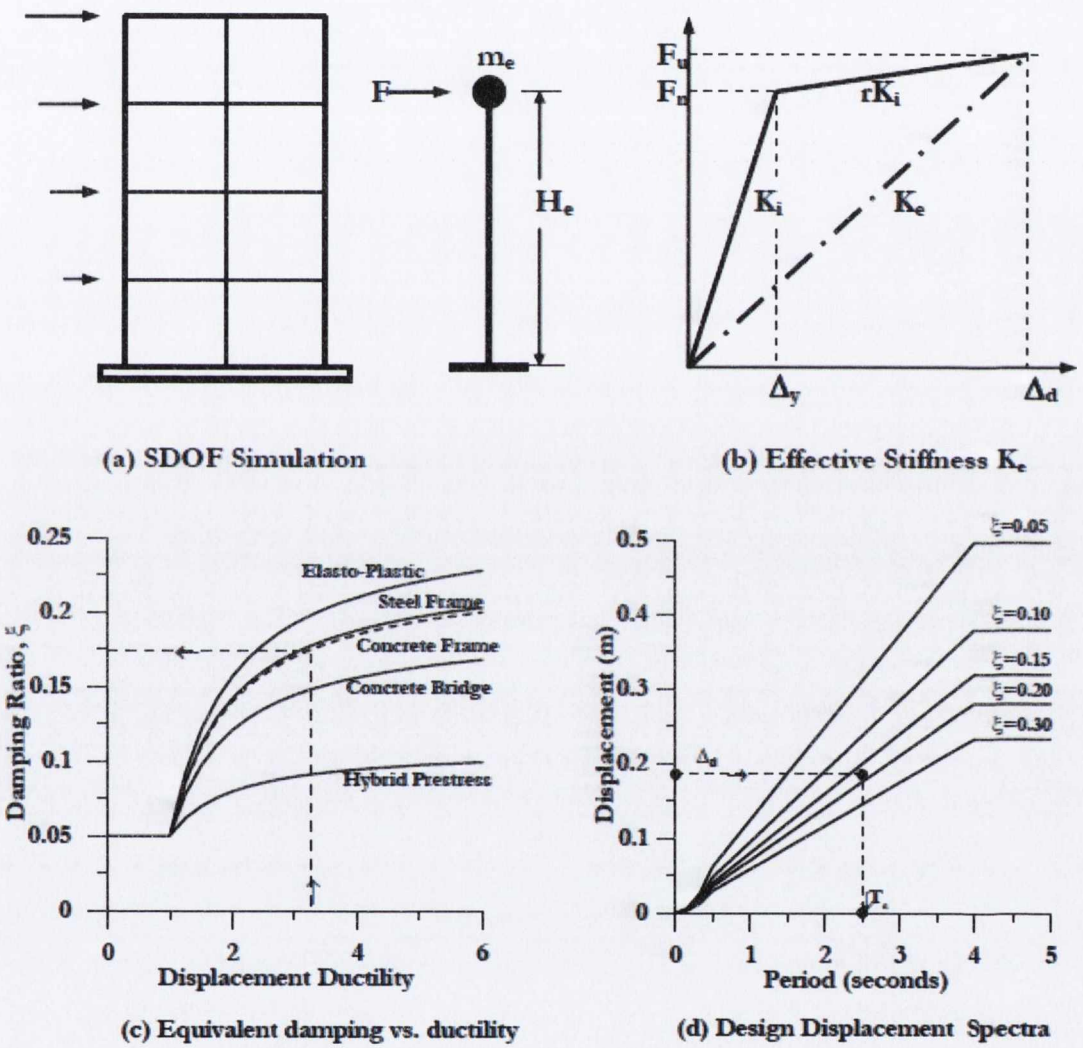

Figure 2.3 – Outline of the displacement-based design process illustrating the SDOF approximation, equivalent viscous damping representation and effective period determination (Priestley et al., 2007).

While this method was developed with the aim of mitigating deficiencies of the force-based method, it was primarily developed in the context of reinforced concrete frame design. It is

acknowledged that several outstanding issues exist for the application of the displacement-based design method for steel CBFs (Priestley et al., 2007). A study by Medhekar and Kennedy (2000) applied the displacement-based design method to a two-storey and an eight-storey building with steel CBFs used for lateral resistance. Having compared the seismic response with static and dynamic time-history analyses, they found that inconsistencies existed with the assumed displaced shape from design examples. This was particularly noticeable with the eight-storey building where ductility demand exceeded the assumed demand due to higher modes of vibration. Furthermore the need for properly calibrated equivalent viscous damping values was also highlighted. Several equations exist for evaluating ξ_{eq} for different structural types (concrete wall buildings, concrete frame buildings, steel frame buildings) but more research is required to establish a specific equivalent viscous damping equation that accounts for the pinched hysteresis of CBFs. The data gathered from this body of work will aid in the understanding of damping of CBFs.

2.3 Concentrically Braced Frames for Seismic Resistance

Concentrically braced frames are widely employed in seismic resistant steel frames due to their inherent strength and stiffness, which allows them to efficiently resist design seismic forces and restrict inter-storey drifts. As well as providing a source of energy dissipation through the alternate cyclic yielding and post-buckling deformation of their braces, the stiffness of CBFs also helps minimise non-structural damage and residual deformations.

2.3.1 Brace Hysteretic Behaviour

Figure 2.4 illustrates the features displayed in the hysteretic behaviour of a brace member. An initially stiff axial force-deformation response is limited by buckling in compression or yielding in tension. Brace buckling generally occurs with seismic forces somewhat lower than those required for brace yielding. During brace buckling, plastic hinges develop within the brace length (usually at mid-length but sometimes at the brace ends, depending on the rotational restraint provided by the brace connections). With increasing axial deformation, the compression resistance of the brace is dramatically reduced as the lateral deflection increases. Upon load reversal, a residual axial deformation is observed at zero load due to the accumulated plastic rotation of the plastic hinge(s). When the brace is loaded in tension, the lateral deflection decreases, and a significant axial force is required to develop the full tensile stiffness and, subsequently, yield resistance of the brace. The load deflection hysteresis plot in Figure 2.4 demonstrates this behaviour for an asymmetrical axial loading pattern. The low stiffness of the brace in the post-buckling and load reversal phases lead to the archetypal 'pinched' hysteretic plots used to assess brace performance. This feature is more severe with slender braces. After several inelastic loading cycles, yield points of the same displacement magnitude will degrade for each subsequent cycle. This is known as the Bauschinger

effect (1886) (cited by Buckley and Entwistle (1956)). The result is that lower axial force is required to reverse the direction of strain than to continue deforming with strain hardening in the same direction.

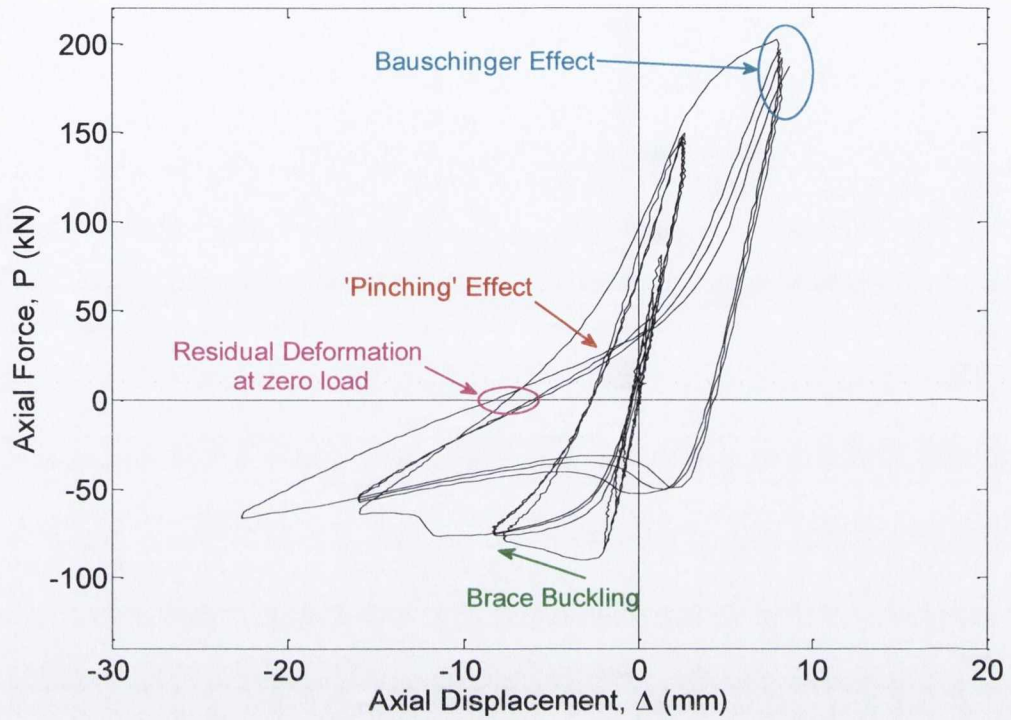

Figure 2.4 – Typical brace hysteresis force-displacement plot demonstrating pinched behaviour due to brace buckling and the Bauschinger effect.

Experimental studies have examined the influence of parameters such as brace slenderness, section slenderness and end conditions on the hysteretic response of axially loaded brace members. More recently the ductility capacity of steel braces has also been studied within several experimental programmes. These are identified in sub-sections below.

2.3.2 Previous Testing of Brace Members for CBFs

The complex hysteresis behaviour of CBFs has prompted a substantial body of research and experimental investigation. In the 1970s many applications of CBFs were used in fixed offshore platforms and power transmission towers. More stringent design requirements for offshore platform design were implemented by the American Petroleum Institute (1977) . Given that designing such structures on an elastic basis was prohibitively expensive and impractical, this encouraged a large body research to be carried out to investigate the inelastic cyclic performance of steel braces. Early experimental work was carried out by Popov, Jain, Roeder, Goel, Tang and Black amongst others, as detailed below. These investigations were initially aimed at establishing suitable analytical models to characterise the overall hysteretic performance of steel braces. Early

theoretical models used experimental results to characterise the general cyclic force-deformation behaviour, but the quantitative behaviour could not be predicted with a high degree of accuracy, especially in the peak loading ranges.

It is generally understood that under cyclic axial loading, steel members exhibit a net elongation after repeatedly reaching their compressive and tensile yield strengths. This was one of the primary findings noted by Kahn and Hanson (1976) in their experimental program to determine the hysteretic characteristics of sixteen 25.4×12.7 mm hot-rolled rectangular hollow section (RHS) steel bars. The bars were of varying length and had a fixed-end condition. Equations developed to form analytical hysteresis curves were found to generally agree with experimental results. Comparing the different hysteresis plots for each specimen, it was shown that at zero load the percentage residual elongation relative to the original specimen length was greater for shorter specimens than for longer ones.

Jain et al. (1977) examined the hysteresis behaviour of axially loaded members with gusset plate end restraints. Twenty-four 25.4mm square hollow sections (SHS) with various sizes gusset plate connections were tested under a series of static and dynamic axial load tests. Shorter members with lower slenderness ratios exhibited greater energy dissipation than longer, more slender members. Further to these experimental conclusions, a comparative study showed that the theoretical predictions of Prathuangsit (1976) did not adequately represent the hysteretic behaviour for members with slenderness, $\lambda < 50$. The progressive reduction in maximum compressive strength and elongation with number of cycles were the most noticeable shortcomings of the hysteresis model. The discrepancies can be attributed to not considering the effects of strain-hardening and the Bauschinger effect. Similar discrepancies in the maximum compressive and tensile ranges can be seen in theoretical solutions developed by Higginbotham and Hanson (1976). In fact, Higginbotham and Hanson (1976) suggest including initial member curvature imperfections to improve accuracy in the maximum compressive force regions and a formulation that permits zones of plastic behaviour.

In later work, Jain et al. (1978) further developed their studies on brace members by conducting an experimental programme that considered the influence of the rotational end restraint provided by connections. The influences of connection stiffness and change in member length on hysteretic behaviour were also analysed. It was found that the effective slenderness ratio had a more significant influence on the shape of the hysteresis curves than connection strength or stiffness.

Popov et al. (1979) carried out cyclic loading tests on six Ø100 mm tubular members with pin-ended and fix-ended constraints. The one-sixth scale members had similar diameter-to-thickness ratios D/t and were annealed to eliminate the large amount of work-hardening produced at such a

scale. A reduction in buckling load capacity with each subsequent cycle was noted. In the tensile loading range, rapid deterioration of the axial member stiffness resulted in larger displacement amplitudes. After the development of plastic hinges at mid-length, local buckling occurred during compressive cycles, however the cross-sectional shape was restored upon reloading in tension. When the members re-entered the compression range, the cross-sections became distorted once more and during subsequent cycles tearing of the steel was observed in the local buckling regions. Thereafter, significant deterioration of both stiffness and strength was seen in the load-displacement plots. Overall, specimens with smaller D/t ratios exhibited less rapid strength deterioration due to local buckling and therefore higher tensile and compressive capacities. An analytical model implemented by Roeder and Popov (1977) achieved good representation of the experimental hysteretic loops. The model included the deterioration of buckling strength for consecutive cycles, however it only accounted for idealised pinned and fixed end conditions. It was concluded that further analytical investigations were needed to clarify models for the intermediate boundary conditions between the classical pin and fixed connections.

To improve the deficiencies of the hysteresis models used by Higginbotham and Hanson and Roeder and Popov, Jain et al. (1980) proposed a model that exhibited good agreement with a series of experimental tests on seventeen tube and eight angle specimens. It is interesting to note that this experimental program featured realistic gusset plate connections which were representative of those utilised in CBFs of the time. To develop the model two important parameters were quantified: maximum compressive loads and residual elongation. The reduction in maximum compressive loads in successive cycles can be expressed as a function of the effective slenderness ratio:

$$F_{max} = \frac{30F_y}{\frac{KL}{i}} \tag{2.9}$$

for the second cycle and:

$$F_{max} = \frac{25F_y}{\frac{KL}{i}} \tag{2.10}$$

for the third and subsequent cycles. These expressions were considered adequate for slenderness ratios in the range $50 < \lambda < 150$. Residual elongation was determined to be directly proportional to maximum compressive displacement and inversely proportional to the effective slenderness ratio KL/r as expressed in the empirical relationship:

$$\varepsilon = \frac{0.55\delta_u}{\frac{KL}{i}} + 0.0002\delta_u^2 \tag{2.11}$$

where, ε is residual strain, K is the effective length factor, L is the member length and i is the radius of gyration. Similar to the maximum compressive load prediction, this equation is not valid for members with an effective slenderness ratio of less than 60. The shape of the cross section had a noticeable influence on the hysteretic behaviour. This was attributed to the differing effects of heat treatment, strain hardening, residual stress in corner regions, the Bauschinger effect and local buckling for different cross section shapes.

To improve upon previous phenomenological models in which plastic hinges were modelled as an elasto-perfectly plastic material, Ikeda and Mahin (1986) undertook research to formulate a refined physical theory brace model based on a simplified geometric representation consisting of simply-supported bracing member with a plastic hinge at mid-span. Physical theory models do not require empirical information on cyclic behaviour as per phenomenological models. Physical theory input parameters are based on measurable material or geometrical properties derived from engineering principles. The model was compared to data from quasi-static testing of a single brace member and dynamic analyses of a three-storey diagonally braced frame. Overall, the model achieved very good representation of the hysteretic loops and featured degradation in energy dissipation and buckling load. However, when compared with a phenomenological model by Ikeda et al. (1984) , the phenomenological model demonstrated superior results provided that sufficient experimental data was available prior to the analyses. This research further developed the concept of limiting user input to information on brace geometry and material properties, as is commonly employed in current computer modelling software (Uriz and Mahin, 2008). More recently, a physical theory model development by Jin and El-Tawil (2003) included a distributed inelasticity element model without limitations on boundary conditions. However, it was acknowledged that the model is calibrated for the specific brace sections used in their experimental study.

As CBFs dissipate seismic energy input through cyclic inelastic buckling of braces, ductility can be considered as an additional design parameter that represents the ability of a structure to undergo large plastic deformations without losing strength (Gioncu, 2000a). Therefore, ductility is mainly concerned with post-yield and pre-failure structural performance regions, and can be used as an indicator of seismic energy dissipation capacity. It is related to the concept of yielding mechanisms within a structure (see Chapter 3). In the seismic response of CBFs, ductility is determined by the fracture life of braces under a tensile load (often initiated by brace tearing due to local buckling under compression). Hence, fracture resistance is a key parameter for ductility design. Several ductility definitions are outlined by Gioncu (2000a), however the pertinent definition for this study is as follows:

$$\mu_\Delta = \frac{\Delta_u}{\Delta_y} \qquad 2.12$$

where Δ_u refers to the ultimate deformation at fracture and Δ_y refers to the deformation at first yield.

Shaking table tests carried out by Uang and Bertero (1986) on a 0.3-scale six-storey steel structure displayed significant local buckling in the diagonal braces which led to brace rupture. The test results also indicated that once brace rupture occurred, a soft storey developed resulting in reduced lateral stiffness and consequently little shear resistance in that storey. Furthermore, studies by Lee and Goel (1987) and Liu and Goel (1987) showed that local buckling initiation was very sensitive to the width-to-thickness ratio (and to a lesser extent brace slenderness and steel material properties). Lower width-to-thickness ratios delayed local buckling and consequently increased the fracture life.

In order to predict the fracture life of bracing members, a method of converting general deformation cycles into an equivalent number of standard cycles was developed by Tang and Goel (1987). This normalisation of cyclic deformation history provided a mechanism to compare experimental data to theoretical predictions of fracture life. A typical cyclic loading history was classified in three distinct groups: small cycle, simple cycle and incremental cycle. The number of standard cycles in each group allowed any cyclic deformation history to be converted into a simple standardised history. Based on these results empirical formulae for fracture life were proposed:

$$N_f = C_s \frac{(b/d)\,(KL/i)}{[(b-2t)/t]^2} \qquad 2.13$$

for $KL/r > 60$ and:

$$N_f = C_s \frac{(b/d)\,(60)}{[(b-2t)/t]^2} \qquad 2.14$$

for $KL/r \leq 60$, where N_f is the number of cycles to fracture, $C_s = 262$, a numerical constant for the test results, d is the gross depth of the section, b is the gross width of the section and t is the wall thickness. Local buckling is considered based on the theory of elasticity in which the local buckling strength of a plate is inversely proportional to the square of the width-to-thickness ratio. Hence, the width-to-thickness ratio of the compression flange is represented in Equations 2.13 and 2.14 by the term $(b-2t)/t$. Higher brace slenderness values KL/r were found to reduce local buckling, however in short members with $KL/r \leq 60$ slenderness did not appear to influence fracture life. Formulations based on Equations 2.13 and 2.14 by Archambault et al. (1995) were further refined by Shaback and Brown (2003) with additional data sets.

A survey of nine experimental studies by Tremblay (2002) examined the inelastic ductile response of diagonal bracing systems with various displacement histories. During seismic loading, a critical condition occurs in CBF when the tension brace yields just after the compression brace has buckled (Figure 2.5), with tension yielding at $T_y = A_g F_y$ (where A_g is the gross cross sectional area, F_y is the yield strength) and compressive resistance C_u.

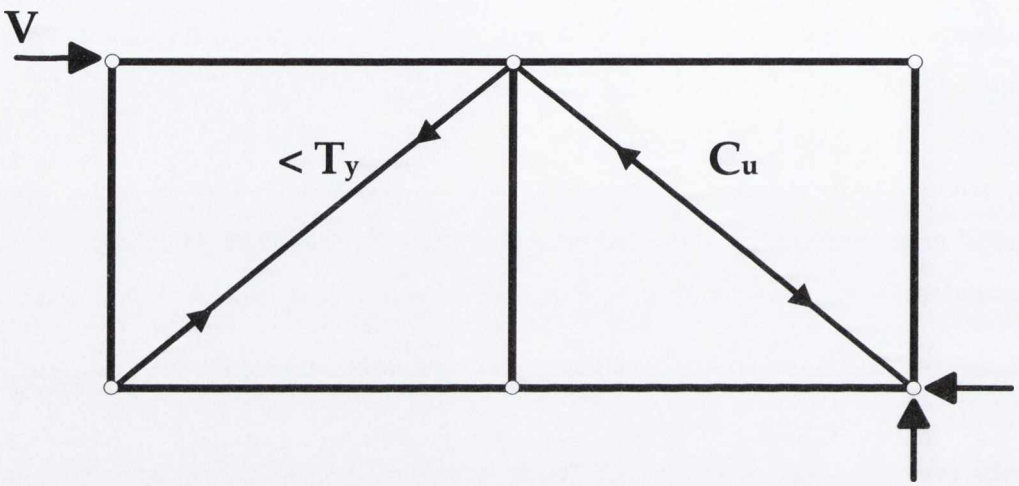

Figure 2.5 – Inelastic response of tension-compression CBF (Tremblay, 2002)

It was found that in symmetrical CBFs with slenderness values $\bar{\lambda} \leq 1.0$, braces could maintain a compressive resistance C_u at a deformation level sufficient to develop tensile yielding, T_y, in the corresponding brace. For slenderness values $\bar{\lambda} > 1.0$ buckling occurs at a smaller deformation level, and the force in the compression brace should be assumed to equal $0.8C_u$ when tension yielding occurs in the other brace. However, it was observed that for specimens loaded in tension prior to buckling, this effect was minimised due to the Bauschinger effect. The maximum tension force $F_{y,max}$ achieved in each test depended upon the loading history, with higher deformation demands in earlier stages of a test leading to larger $F_{y,max}$ values.

Minimum compressive strength formulations were presented for various levels of ductility ($\mu_\Delta = 2$, 3 and 5). From a design perspective compressive strength at a specific ductility level can represent a critical loading condition. Under symmetrical loading conditions, it was observed that the compression resistance of the brace at any plastic hinge rotation depends on prior cyclic loading history due to the cumulative elongation of the brace during tension loading. It was anticipated that brace load data for this formulation would be selected from the range of tests. The load was selected where the compression ductility was reached for the first time having reached the corresponding tension ductility level. However, the variability between all of the tests led to a tension ductility level of 0.5 units the target ductility level being used instead. Thus, the non-linear regression formula is as follows:

$$C'_u = A_g F_y(\mathrm{a} + \mathrm{b}\bar{\lambda}^{-c}) \leq C_u \quad 2.15$$

where C'_u is the post-buckling compressive capacity, C_u is the buckling capacity, and a, b and c are constants defined for ductility values of 2, 3 and 5.

It was found that slender braces possess higher ductility capacities as strain demand in plastic hinges reduces with slenderness, limiting the extent of local buckling. Cross-section width-to-thickness ratio was also found to have a limited influence on ductility capacity, which agrees with the findings of Tang and Goel (1987). A model to predict displacement ductility capacity was proposed using the linear physical theory model for cold-formed members:

$$\mu_\Delta = 8.3\bar{\lambda} + 2.4 \quad 2.16$$

in which μ_f is the ductility reached at fracture. It was acknowledged in a subsequent paper by Tremblay et al. (2003) that while Equation 2.16 is suitable for single bracing members it is unconservative for diagonal frames. It was suggested that further refinement was required to include effects such as width-to-thickness ratio, steel types and different section shapes such as RHS and tubular sections. These parameters were specifically explored by Goggins et al. (2006) in an assessment of the cyclic performance of cold-formed square and rectangular hollow section brace members. Having considered the effects of material yield strength, the influence of non-dimensional slenderness and width-to-thickness ratio was implemented in two distinct equations for displacement ductility capacity:

$$\mu_\Delta = 26.2\bar{\lambda} - 0.7 \quad 2.17$$

$$\mu_\Delta = 29.1 - 1.07(d/t) \quad 2.18$$

These equations were derived from a limited limited set of cyclic tests on members with normalised slenderness in the range 0.4 to 0.9, as longer length specimens were not tested to fracture. Experimental work carried out by Nip et al. (2010) considered a wider range of slenderness values (0.34 to 1.40) for hot-rolled carbon steel, cold-formed stainless and carbon steel. Displacement ductility predictions for the three materials were set out as follows:

Hot-rolled carbon steel:

$$\mu_\Delta = 3.69 + 6.97\bar{\lambda} - 0.05(d/t\varepsilon) - 0.19(\bar{\lambda})(d/t\varepsilon) \quad 2.19$$

Cold-formed carbon steel:

$$\mu_\Delta = 6.45 + 2.28\bar{\lambda} - 0.11(d/t\varepsilon) - 0.06(\bar{\lambda})(d/t\varepsilon) \quad 2.20$$

Cold-formed stainless steel:

$$\mu_\Delta = -3.42 + 19.86\bar{\lambda} + 0.21(d/t\varepsilon) - 0.64(\bar{\lambda})(d/t\varepsilon) \quad 2.21$$

where $\varepsilon = \sqrt{235/f_y}$. When compared with the results of their experimental study, the proposed equations showed an improvement on ductility capacity predictions given by Equations 2.16 to 2.18. This result emphasised the need to consider the full range of slenderness values and constituent material types that may be encountered in a given application. Equations 2.17 and 2.18 were found to overestimate the experimental ductility capacity results observed by Nip et al.

2.3.3 Lateral Deformations of Brace Members

A set of simple equations for lateral deformation were proposed by (Tremblay et al., 2003) to assess brace damage to non-structural elements. They were formulated for pin and fixed end conditions and later developed for single and diagonal frame members at peak compression ductility μ_c following a peak ductility in tension μ_t (Tremblay et al., 2003). For a single brace member:

$$\Delta = 0.7\sqrt{(\mu_c + \mu_t - 1)\delta_y L_H} \qquad 2.22$$

with δ_y representing the tension yield displacement and L_H representing the distance between the rotational hinges that form near the ends of the brace (Figure 2.6). When Equation 2.22 is applied to case of a diagonal frame:

$$\Delta = \frac{1}{\sqrt{1 + L_H/L_{HE}}}\sqrt{\delta_y L_{HE}} \qquad 2.23$$

where L_{HE} is the distance between the brace mid-length and the plastic hinge near the brace end. These equations demonstrated good agreement with the results of tests carried out by Tremblay et al. (2003). Equation 2.22 was also assessed by Goggins et al. (2006) using results from a separate series of cyclic tests, with good agreement generally observed, except for large axial displacements where experimental values were under-predicted.

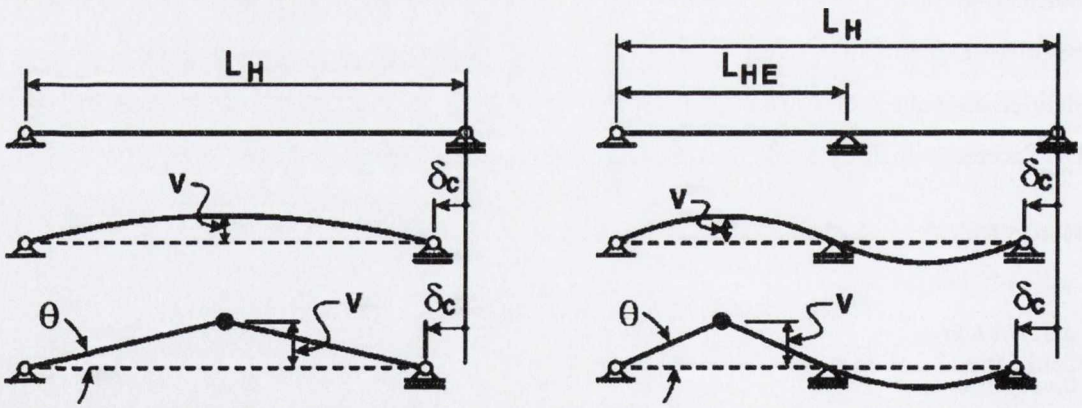

Figure 2.6 – Simplified deformed shapes for a single brace member (Tremblay et al., 2003)

Nine experimental tests on hollow structural steel (HSS) specimens were carried out by Shaback and Brown (2003). A formulation to predict the out-of-plane deformation of a single brace with gusset plate connections was calibrated using this series of tests. It was found that out-of-plane

deformation was heavily influenced by plastic hinge rotation near the gusset plate connections and brace mid-length. A simple geometrical formulation was found to be heavily dependent on ductility level, however the calibrated form showed acceptable correlation with experimental results:

$$\Delta = L(2\mu - \frac{1}{9}\mu^{1.9}) \tag{2.24}$$

2.4 Measuring Damping in CBFs

All oscillatory systems undergo a resistance to motion known as damping. This damping arises from energy dissipation through elastic springs and friction forces caused by structural joints, bearing supports, fluid resistance and so forth. Combinations of such mechanisms lead to energy losses in free vibration systems which result in decay of response amplitude. The simple linear model for mathematical analysis assumes that the damping force remains proportional to velocity as is seen in the formulation of the SDOF equation of motion:

$$m\,\ddot{u}(t) + c\,\dot{u}(t) + k\,u(t) = -m\,\ddot{v}(t) \tag{2.25}$$

where m is the mass, $\ddot{u}(t)$ is the relative acceleration, c is the system damping coefficient, $\dot{u}(t)$ is the relative velocity , k is the system stiffness $u(t)$ is the relative displacement and $\ddot{v}(t)$ is the ground acceleration. The restoring force, $Q(t)$ is composed of:

$$Q(t) = F_c(t) + F_{nc}(t) \tag{2.26}$$

with

$$F_c(t) = k\,u(t) \tag{2.27}$$

and

$$F_{nc}(t) = c\,\dot{u}(t) \tag{2.28}$$

where $F_c(t)$ is a conservative force and $F_{nc}(t)$ is a non-conservative force. The stiffness is based on structural geometry and material properties; but the damping coefficient cannot be calculated from such measurable parameters. Free vibration decay can be used to evaluate the damping coefficient. However this only applies under low amplitude input acceleration within elastic limits. Under these conditions, Equations 2.27 and 2.28 remain as valid linear relationships. For elastic shake table testing this can be accomplished using the half-power bandwidth method outlined in sub-section 2.4.1 below.

Conversely, under larger amplitude seismic input with inelastic deformation, these equations no longer hold true as the damping coefficient is amplitude dependent implying that early high-amplitude cycles yield higher damping ratios than subsequent low-amplitude cycles. This amplitude dependency is caused by changes in stiffness and damping mechanisms of the system.

Frequency-independent damping (or 'hysteretic' damping) is associated with static hysteresis due to plastic strain, localised plastic deformation, crystal plasticity and plastic flow. The analytical solution for the free vibration of nonlinear hysteretic damping has been derived by Chen et al. (1994) and was further refined by Chen and You (1997). The governing equation of an SDOF system for the hysteretic damping model is formulated as:

$$m\ddot{u} + \frac{h}{|\bar{\omega}|}\dot{u} + ku = \bar{p}(\bar{\omega})e^{i\bar{\omega}t} \tag{2.29}$$

Although Equation 2.29 remains valid for harmonic vibration, it is invalid for free vibration as the presence of $|\bar{\omega}|$ is ambiguous when the forcing term $\bar{p}(\bar{\omega})e^{i\bar{\omega}t}$ is set to zero. Therefore only the stead state solution can be obtained:

$$-m\bar{\omega}^2\bar{x} + k(1 + sgn(\bar{\omega})i\eta)\bar{x} = \bar{p} \tag{2.30}$$

where η is the loss factor, $k\eta$ is equal to h, and $sgn(\bar{\omega})$ is $+1$ when $\bar{\omega} > 0$ and is -1 when $\bar{\omega} < 0$ and sgn is sign function. To solve for the time domain using the Fast Fourier Transform for $\bar{p} = 1$

$$x(t) = \frac{1}{2\pi}\int_{-\infty}^{\infty} \frac{e^{i\bar{\omega}t}}{(k - m\bar{\omega}^2 + sgn(\bar{\omega})ik\eta)} d\bar{\omega} \tag{2.31}$$

By taking the inverse Fourier transform of Equation 2.30 the governing equation in the time domain is as follows:

$$m\ddot{x}(t) - \frac{k\eta}{\pi}\int_{-\infty}^{\infty} \frac{x(u)}{(t-u)} du + kx(t) = p(t) \tag{2.32}$$

with conditions at $t = -\infty$ being

$$x(t)|t = -\infty = 0, \dot{x}(t)|t = -\infty = 0, \tag{2.33}$$

To construct the hysteresis loop in the time domain, the forcing function $p(t)$, in Equation 2.32 must be harmonic excitation. In order to solve the integral-differential equation for Equation 2.32 by using the iteration technique, Equation 2.32 can be reduced to the following form:

$$\ddot{x}_{n+1}(t) + 2\xi\omega\dot{x}_{n+1}(t) + \omega^2 x_{n+1}(t) = 2\xi\omega\dot{x}_n(t) + \frac{\omega^2\eta}{\pi}\int_{-\infty}^{\infty} \frac{x_n(u)}{(t-u)} du + \frac{p(t)}{m} \tag{2.34}$$

where $x_n(t)$ denotes the n^{th} iteration state for $x(t)$ and $\omega = \sqrt{k/m}$. Using the Duhamel integral and considering the terms in the right hand side of Equation 2.34 as external forces, Equation 2.34 can be reduced to the following iteration form:

$$x_{n+1}(t) = \frac{1}{\omega\sqrt{1-\xi^2}} \int_{-\infty}^{\infty} e^{-\xi\omega(t-\tau)} \sin(\omega\sqrt{1-\xi^2}(t - \tau)) \left\{ \frac{\omega^2\eta}{\pi} \int_{-\infty}^{\infty} \frac{x_n(u)}{(\tau-u)} du + 2\xi\omega x_n(\tau) + \frac{p(\tau)}{m} \right\} d\tau \quad 2.35$$

By iterating $x_n(t)$ in Equation 2.35, a hysteresis loop can be constructed after setting harmonic loading for $p(t)$ and a convergent solution can be obtained as follows:

$$\int_{-\infty}^{\infty} |x_n(t) - x_{n+1}(t)|^2 \, dt < \epsilon, if \; n > N \quad 2.36$$

where ϵ is the error tolerance and N is the number of iterations. In summary, Equation 2.29 is the governing equation of hysteretic damping in the time domain for an SDOF system. A solution has been formed in Equation 2.36 where a hysteresis loop can be constructed. This is relevant for the series of shake table tests described in Chapter 8 where the plastic behaviour of bracing members is investigated within an SDOF system.

2.4.1 Damping for Elastic Tests (Half-Power Bandwidth Method)

To obtain the natural (fundamental) frequency, ω_n of a CBF system, the system can be subjected to white noise or sweep excitation within its elastic limits. The resulting response is typically recorded in the time-domain. Using the Fast Fourier Transform the frame response can be converted to the frequency-domain and ω_n and frequencies from other modes can be extracted from the response peaks. Goggins (2004) carried out elastic shake table tests and found the natural frequency ω_n to be proportional to the brace size A_s and inversely proportional to the brace slenderness $\bar{\lambda}$. However, these results were largely influenced by initial brace loading in tension or compression after brace installation. Initial brace camber was usually indicative of the presence of these axial brace forces.

To determine system damping, the half-power bandwidth (HPB) method is commonly used for its simplicity, and accurate results can be expected for SDOF systems with small values of damping (Chopra, 2006). The method is based on measuring the maximum amplitude observed on a frequency response curve (displacements, velocities or accelerations) due to applied harmonic loads of different frequencies. The two frequencies at which the response equals $1/\sqrt{2}$ the maximum amplitude are then obtained, as shown in Figure 2.7. The damping ratio is then defined as

$$\xi = \frac{\omega_b - \omega_a}{2\omega_n} \quad 2.37$$

where ω_a and ω_b are the frequencies either side of the natural frequency ω_n.

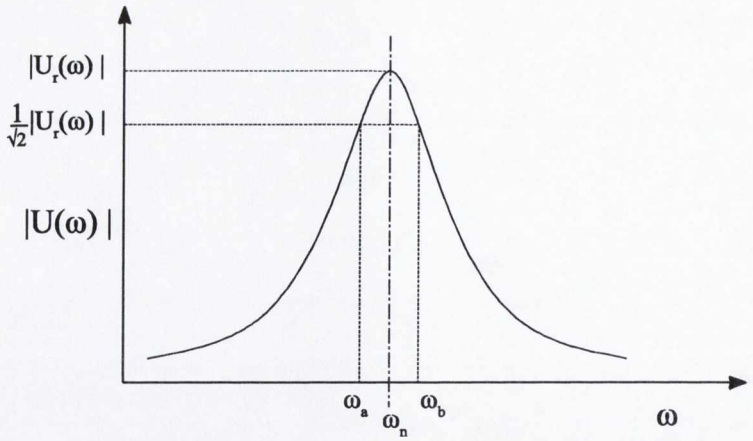

Figure 2.7 – Definition of half-power bandwidth method.

In fact, in an investigation by Olmos and Roesset (2009) of the accuracy of this method when used with MDOF systems, continuous systems and systems with nonlinear viscous damping showed accurate predictions of damping estimates. For systems with mass proportional damping the results were accurate in several modes with constant modal damping. Systems with stiffness proportional damping showed valid results in the first few modes.

A similar study by Papagiannopoulos and Hatzigeorgiou (2011) focussed on examining the accuracy of the half-power method with single- and multi-degree-of-freedom systems with linear viscous damping. They assumed several values of ξ for three different systems: a linear SDOF structure with a fundamental frequency 1.674 Hz, a seven-storey, two-bay moment resisting steel frame structure with the first four natural frequencies ranging from 0.946 to 8.084 Hz and a three-storey, two-bay frame with a non-uniform distribution of damping over the structure height. The assumed values for ξ were then compared with the damping values obtained after constructing the acceleration frequency response transfer functions and examining their moduli at the peak amplitude for each structural configuration. The standard expression for the half-power bandwidth method shown in Equation 2.37 was used to estimate ξ for displacement frequency transfer functions. However accuracy issues arise when acceleration frequency transfer functions are used with this definition. To account for this, a third order correction applied by Wang (2011) produces acceptable results:

$$2\xi + 8\xi^3 = \frac{\omega_b - \omega_a}{\omega_n} \qquad 2.38$$

For the first SDOF structure it was observed that Equation 2.37 produced good upper bound results for $\xi \leq 0.15$ and Equation 2.38 produced good lower bound results for $\xi \leq 0.20$. The first four frequencies of the MDOF moment-resisting frame were well separated and damping was uniformly distributed throughout the frame. Both Equations 2.37 and 2.38 produced very accurate predictions for the first two modes with $\xi \leq 0.10$, and the third mode with $\xi \leq 0.05$. At higher modes both equations become inaccurate.

Therefore, for concentrically braced frames subjected to low amplitude loading, as in the case of elastic shake table tests, the half-power bandwidth method is suitable for estimating the damping properties. In the case of stronger amplitude time histories, plastic regions are expected to develop in the structure, thus changing the damping properties making the assumption of linear viscous damping invalid.

2.4.2 Rayleigh Damping

Rayleigh damping is a technique often used in evaluating damping properties of nonlinear systems. It assumes that the damping matrix is proportional to the mass and stiffness matrices:

$$[C] = \alpha[M] + \beta[K] \tag{2.39}$$

where $[C]$ is the system damping matrix, $[M]$ is the mass matrix, $[K]$ is the stiffness matrix of the system and α and β are the constants of proportionality. The damping ratio for the Rayleigh damping equation is:

$$\xi = \frac{\alpha}{2\omega} + \frac{\beta\omega}{2} \tag{2.40}$$

When β is discounted ($\beta = 0$), the α value is calculated from a known value of damping ξ (i.e. $\alpha = 2\omega\xi$). This is known as alpha damping and damps out the lower modes of vibration. Conversely, beta damping ($\alpha = 0$) damps out the higher modes of vibration. In cases of even distribution of natural system frequencies, Rayleigh damping formulation is suited for accurate damping representation (Papagiannopoulos and Hatzigeorgiou, 2011). This damping technique is typically used in nonlinear computer simulations where an explicit damping matrix definition is needed. In this body of work it is employed in the OpenSees (McKenna, 1997) finite element models as described in Chapter 4.

3 Background: Design of CBFs with Gusset Plate Connections

3.1 Introduction

As mentioned in Chapter 2, the performance of CBFs under strong ground motions is primarily determined by its bracing members and connections. To provide sufficient lateral frame resistance, the diagonal bracing members are designed to resist large axial forces which are transferred to the other frame members via gusset plate connections. In the seismic design of diagonal CBFs to Eurocode 8 (CEN, 2004a) normally only the resistance of the tension braces is included in the analysis of seismic action effects. For V-frames both compression and tension diagonals are considered. Because brace compression resistance need not be taken into account for diagonal frames, European design practice tends to employ bracing members that are more slender than those encountered in other regions where brace compression strength contributes to the design lateral resistance of the CBF.

In accordance with capacity design procedures, the diagonal brace members are identified as the dissipative elements of the CBF, and the structural design must ensure that yielding occurs in these elements before failure occurs in the connections, and before yielding or buckling occurs in the beams and columns. To obtain the required design resistance of these non-dissipative structural components, the design resistance of the brace member is increased by an 'overstrength' factor, and the force equilibrium used to determine a consistent set of forces in beams, columns and connections. Thus, these elements are provided with sufficient resistance to avoid failure. In addition, the detailed design of the CBF must ensure that the expected yielding mechanism occurs, and remains stable within the anticipated range of seismic drift. Conventional seismic design achieves this objective by specifying allowable ranges for global and local brace slenderness (as described in Chapter 2), and detailing rules for gusset plate brace connections that incorporate the Standard Linear Clearance model (described in Section 3.2).

In Section 3.3., the inelastic behaviour of brace-gusset plate assemblies undergoing cyclic response due to earthquake loading is examined and alternative gusset designs are proposed for use in the experimental programmes in Chapter 5 and Chapter 8.

3.2 Gusset Plate Design – Standard Linear Clearance

When subjected to strong ground motions, diagonal bracing members in CBFs are expected to undergo large inelastic deformations in the post-buckling range leading to the formation of plastic

hinge regions. As bracing members are susceptible to local buckling, the large flexural stains at the mid-length plastic hinge locations can lead to brittle failure due to fracture (see Chapter 2). This behaviour, which may occur at low storey drifts, results in reduced system ductility and can induce excessive ductility demands on beams and columns. . If brittle fracture of the brace member can be delayed, energy may still be dissipated after local buckling has occurred.

The gusset plate connections commonly used at either end of the brace members can be designed as rotationally restrained or unrestrained. Generally, for out-of-plane rotation the gusset plate is unrestrained (unless crossed gusset plates are used) to accommodate brace end rotation. This is the premise of the design rules specified for gusset plate connections in 'Special Concentrically Braced Frames' (SCBF), as set out by the AISC Seismic Design Provisions (AISC, 2005a) and the AISC Uniform Force Method (UFM) (AISC, 2005c).

Gusset plates are the predominant method used to connect brace members to the rest of the structural frame. Typically, the gusset plate is aligned in-plane with the frame in a vertical direction. The direction in which compression braces buckle is dependent on the orientation of the section shape and the brace end restraints provided by the gusset plate. For out-of-plane brace buckling, member end rotations induce weak axis bending in the gusset plate.

At larger storey drifts, the end rotation in the post-buckled brace is accommodated by the formation of plastic hinges in the gusset plates (Cochran, 2003). To permit this, a free length is incorporated in the gusset plate perpendicular to the end of the brace and the assumed line of restraint (Figure 3.1). This gusset design method is known as the Standard Linear Clearance (SLC) model. The recommended size of the free length is between $2t_p$ - $4t_p$ where t_p represents gusset plate thickness. For all SLC specimens used in this study, a free length of $3t_p$ was used as recommended by Astaneh-Asl et al. (1981) and Cochran (2003).

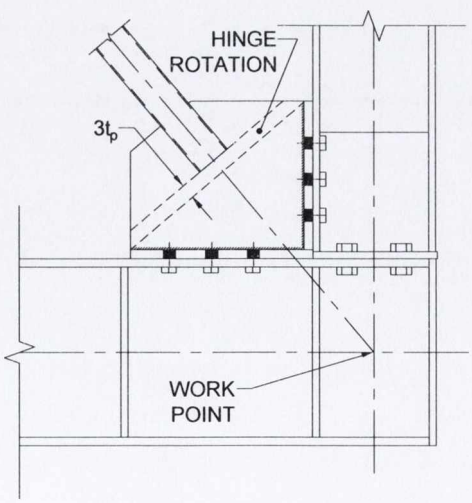

Figure 3.1 – Standard Linear Clearance design method with clearance length of 3tp.

Gusset connections are typically designed with initial overall dimensions l_h and l_v (Figure 3.2a) governed by the alignment of the brace centreline with the intersection of the beam and column centrelines known as the work point, in Figure 3.1. Typically, gusset plates are welded to beam and column flanges. However for ease of brace installation and removal during experimentation in this work, bolted connections were used. This is reflected in Figure 3.1 and Figure 3.2. Once the maximum forces to be transferred from the brace have been established, the welds or bolts used to connect the brace to the gusset plate can be specified. If welds are used, their lengths will be determined by the initial sizing of the gusset plate dimensions l_h and l_v and the specified clearance length.

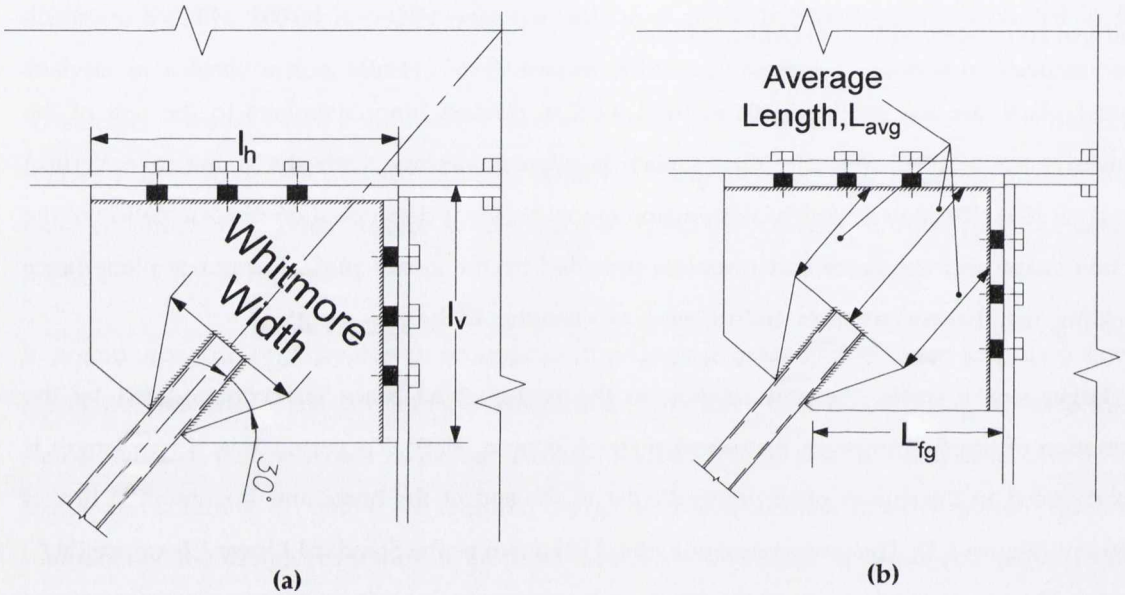

Figure 3.2 – Schematic of (a) Whitmore width b_{ww} and (b) Thornton method for establishing average length L_{avg} of gusset plate section under compression. Unsupported edge length L_{fg} also shown.

The gusset plate yield and buckling strengths may then be calculated. This part of the design procedure is developed on the concept of the Whitmore section (Whitmore, 1950) which proposes that the axial force of the brace member is transferred through a section with a predefined width, b_{ww}. This axial force can be distributed as a uniform stress over the section, which is sized to remain elastic. The Whitmore width is defined with projection lines extending at 30° from the intersections of the brace with edge of the gusset plate to a line through the end of the brace (Figure 3.2a). The design tension resistance is then given by the product of the gusset plate yield stress and the area of the Whitmore section.

The Thornton model (Thornton, 1984; Thornton, 1991) allows the design plate buckling resistance to be determined by treating the gusset plate as a slender strut element with an assumed effective length and uniform cross-section equal to the area of the Whitmore section. The effective strut length is taken as the average of three lengths (L_{avg}) projected from the Whitmore width to the beam and column flanges (Figure 3.2b). Given the restrained boundary conditions on two sides of the plate, an effective length coefficient of $K = 0.65$ can be justified, consistent with the assumption that the gusset plate is nearly fully restrained against rotation at each end and sidesway buckling is prevented (Roeder et al., 2004). Other methods suggested by Yam and Cheng (1994) include the Modified Thornton Method which recommends a 45° projection angle, introduced to take into account the effects of thin plate behaviour, and employs the single length along the centroid of the brace (known as the 'centroidal length') as the effective gusset length. However, when the column buckling formula is used, the load redistribution due to yielding is neglected as the formula considers a rectangular column directly beneath the Whitmore section.

Brown (1988) addressed the edge buckling strength of the gusset plate by recommending a maximum value for the unsupported edge length (L_{fg}) between the beam or column flange and the point at which the brace intercepts the plate edge (Figure 3.2(b)). This study used an Euler-type equation for the average longitudinal buckling stress in a flat strip plate simply supported at both ends. The recommendation can be expressed as:

$$\frac{L_{fg}}{t_p} \leq 0.83\sqrt{\frac{E}{F_y}} \qquad 3.1$$

where L_{fg} is the length of the gusset free length, t_p is the plate thickness and F_y is the steel yield stress. As before, this model of buckling is based on test results that suggest that the gusset plate edges buckle in a manner analogous to column buckling. This criterion is suitable for elastic buckling of free edge lengths of thin gusset plates but does not hold true under large cyclic loads (Astaneh-Asl, 1998). A series of cyclic load tests on gusset plate specimens representing V-braced connections were carried out by Astaneh-Asl et al. (1989) who proposed an alternative criterion to account for cyclic buckling of the free edge before the gusset plate reaches its compression capacity.

$$\frac{L_{fg}}{t_p} \leq 0.75\sqrt{\frac{E}{F_y}} \qquad 3.2$$

Roeder et al. (2005) compared several sets of experimental data from previous gusset plate tests with the above edge buckling models by examining the ratio of the ultimate load reached during testing to the design load predicted by each model. The Brown and Astaneh-Asl models displayed conservative predictions of gusset strength with significant variation. Although the Thornton

model also exhibited some variation and conservatism, these were less than with the other two models. In order to adjust for the conservative predictions Roeder suggests solutions including; increasing the projection angle of the Whitmore width (thereby increasing the effective section area); and reducing the effective length of the gusset plate.

As previously discussed, the Modified Thornton Method utilises a larger projection angle offering a possible solution to the over-conservative predictions. Roeder's results showed that this leads to a marked reduction in the conservation of the prediction, with some unconservative results arising. Roeder proposed using a variation on the Modified Modified Thornton Method which employs the 45° projection, but an average effective gusset length (as in the standard Thornton method) instead of the centroidal length. The analysis showed slight improvements in the mean ratio and standard deviation but results in greater underestimates of buckling resistance in more slender plates.

In an parametric study by Sheng et al. (2002) using splice members to connect the brace member to gusset plate, it was recommended to use stiffeners on the splices and the gusset free edges to increase the ultimate load of the gusset plate. However, compared to an analytical study, loads calculated were overpredicted using the Whitmore width. Using the Thornton and the Modified Thornton method produced conservative results. An alternative method was proposed based on an inelastic plate buckling formulation where bounded edge conditions are considered. The proposed method was based on rectangular shape gusset plates only with 45° splice-brace connections.

Implications for current study

This study incorporates two series of tests on earthquake resistant bracing members in CBFs: cyclic quasi-static tests on single brace planar test models and shaking table tests on single-storey models with a pair or brace members. In the design of test specimens for both the cyclic tests (Chapter 4.4) and shaking table tests (Chapter 8) the Whitmore section and standard Thornton methods were used to ensure equivalence with previous experimental studies (Roeder et al., 2011a) and common engineering practice (AISC, 2005a). In particular, the use of these methods was important to facilitate comparison with the extensive studies carried out by Roeder and Lehman (2008). At this stage it is important to note that the sets of experimental results examined by Roeder were largely obtained from tests with idealised or simplified experimental conditions in which the brace members did not buckle or undergo any large inelastic deformation. In real structural connections, large tensile and compressive force and deformation demands arise in the brace and additional rotational restraints exist in the connections. The test set-ups described in Chapters 5 and 8 are designed to capture these important factors that can influence gusset plate performance. Roeder noted that three preliminary results from tests on a full-scale, three-storey braced frame were significantly underestimated using the Modified Modified Thornton Method, with ultimate load to

design load ratios of approximately 0.5. In the current study, plate thicknesses as small as 4 mm are used in the experimental programmes. This indicates that neither form of the Modified Thornton Method should be employed as these have been observed to perform poorly with thin gusset plates. The edge buckling Equations 3.1 and 3.2 are relevant to the tests performed in the current study, and they are employed as initial checks when selecting the overall gusset plate geometry of the individual test specimens.

3.3 Gusset Plate Design – Elliptical Clearance

The methods described in the previous section are typically used in engineering practice for the seismic design of gusset plate brace connections. However, these methods are premised on the concept that satisfactory CBF response depends largely on the dissipative behaviour of the brace member alone. Consequently, capacity design requires the tension and compression resistances of the connection to be much larger than those of the brace member, and the connection itself is not considered as a potential dissipative zone. However, the need to facilitate global brace buckling in compression means that it is not possible to ensure that the gusset plate remains elastic at all times. Hence, the formation of adequate plastic hinges in the gusset plates is ensured by the SLC design method, meaning that gusset plate yielding due to plate bending is accommodated during brace compression, while gusset plate yielding over the effective Whitmore width must be prevented during brace tension. Moreover, gusset plate buckling must be prevented during brace compression, even in the presence of the gusset plate plastic hinges. The twin requirements that the gusset plate should remain elastic in tension and stable but ductile in compression can lead to large gusset plates that are often sub-optimal. At large inelastic deformation demands, local damage can occur in beam, column and brace members adjacent to stiff gusset plates. In testing of beam-column connections with attached gusset plates, Uriz and Mahin (2004a) demonstrated the fracture susceptibility of stiff gusset plates through brittle fracture during plastic hinge formation. The efficient application of conventional gusset plate design methods is also affected by the inaccuracies discussed in the previous section.

The potential therefore exists to achieve improved and more reliable overall CBF behaviour by allowing some limited tensile yielding in carefully sized and detailed gusset plates. This has led to the development of the balanced design approach by Roeder (2002). In seismic design provisions following the capacity design approach, a yielding hierarchy is established in which the strengths of energy-dissipating elements are evaluated and other structural elements are provided with adequate reserve strength capacities through the use of appropriate overstrength factors. In the case of CBFs, the overstrength tensile resistance of the brace member is used to identify the required connection resistances to ensure that the brace members yield before connection yielding

occurs. This modular view of CBF design does not adequately consider the potentially brittle behaviour of proportionally stronger and stiffer connections under low cycle fatigue conditions. Furthermore, the conventional approach does not differentiate between different connection failure modes which are all required to have the same overstrength resistance.

Roeder's balanced design approach develops the capacity design approach through the balancing of yield mechanisms in both the brace and the connection. The methodology distinguishes between yielding of an element which implies significant changes in stiffness and inelastic deformation while maintaining reasonably stable resistance, and failure modes leading to fracture initiation which imply reduced resistance and inelastic deformation capacity. In Figure 3.3 below, the yielding mechanisms and failure modes in CBFs are identified. Roeder summarises the desirable yield mechanism balance equation as follows:

$$\underline{\textit{Brace Buckling} < \textit{Brace Yielding} < \textit{Connection Yielding} < \textit{Brace Tearing}} \qquad 3.3$$

Equation 3.3 ensures that undesirable failure modes are restricted and yield mechanisms are balanced to allow optimal frame ductility. From a design perspective this can be expressed as follows:

$$R_y F_y A_g < \beta R_n \qquad 3.4$$

where β is a balance factor, R_n is the resistance of a yield mechanism or failure mode in the connection, R_y is a ratio of the expected yield strength to the minimum specified yield strength of steel F_y (as in the AISC Seismic Provisions for Structural Steel Buildings (AISC, 2010)) and A_g is the gross section area of the brace. Expanding this out in a series for many yield mechanisms where the brace resistance is the primary controlling yield mechanism:

$$R_y F_y A_g = R_y R_{yield} \leq \beta_{y1} R_y R_{yield,1} \leq \beta_{y2} R_y R_{yield,2} \leq \cdots \leq \beta_{yi} R_y R_{yield,i} \qquad 3.5$$

If this is combined with failure mode resistances to ensure that failure modes occur after the primary and first secondary yield resistance, the expression is as follows:

$$R_y F_y A_g = R_y R_{yield} \leq \beta_{y1} R_y R_{yield,1} \leq \beta_{fail,1} R_{fail,1} \leq \beta_{fail,2} R_{fail,2} \leq \cdots \leq \beta_{fail,i} R_{fail,i} \qquad 3.6$$

The introduction of the β ratio establishes the idea of controlling yielding modes in the frame system. The magnitude of β is adjusted so that there is a greater range difference between undesirable or difficult to predict failure modes (i.e. low β ratios). For more favourable yield mechanisms to occur, β ratios can approach a value of 1.0. This is manifested in the gusset connection through permitting tensile yielding of the gusset plate.

When the balanced design method is applied to gusset plates in CBF design, gusset plate yielding is permitted, requiring smaller, thinner gusset plates. In an extensive experimental study featuring thirty-four full-scale 1-, 2- and 3-storey SCBFs Roeder et al. (2011b) and Roeder et al. (2011a) found that the balanced design method greatly increases the deformation capacity of SCBF systems. When the balanced design method was implemented with rectangular gusset plates, a 46% increase in drift capacity was demonstrated. A smaller increase in drift capacity was also observed for tapered gusset plates because tapered plates sustain greater damage due to their reduced reserve capacity.

While smaller, thinner gusset plates offer potentially a more ductile global CBF response, they are more susceptible to plate buckling - an unacceptable failure mode. This is addressed by an alternative detailing proposal by Roeder et al. (2006) which theorises an elliptical yield line shape occurring in the gusset plate, rather than the conventional SLC detail. This leads to smaller overall gusset plate dimensions, shorter effective lengths and increased plate buckling resistance. This elliptical clearance offset from the beam and column edges is shown in Figure 3.4 as N times the plate thickness t_p. Lehman et al. (2008) and Roeder et al. (2011b), observed that specimens with a free length of $8t_p$ performed well achieving large drift capacities without weld fracture and consequently this free length is used in all experimentation design in this study.

The balanced design method incorporating the elliptical clearance model is implemented in both the Complementary Cyclic Test (Chapter 5) and BRACED Shake Table Test (Chapter 8) series where direct comparison is made with the conventional design approach incorporating the SLC method. To quantify the balance of the primary yield mechanism (brace tensile yielding) with the secondary yield mechanism (gusset plate yielding) the balance factor for each specimen was calculated as follows:

$$\beta_{ww} = \frac{R_{y,brace} F_{y,brace} A_{net,brace}}{R_{y,gusset} F_{y,gusset} b_w t_p} \qquad 3.7$$

The R_y values are obtained from Table A3.1 in the AISC Seismic Provisions (AISC, 2010). The R_y value is the ratio of the expected yield stress to the specified minimum yield stress of the steel material. In specimens used by Lehman et al. (2008), the materials used were ASTM A500 for HSS sections and ASTM A572 for gusset plates with $R_{y,brace} = 1.4$ and $R_{y,gusset} = 1.1$ respectively. To maintain fidelity with these experimental results the R_y values from Table A3.1 are used in calculating β_{ww} ratios for the test specimens in the Complementary Cyclic Tests (Chapter 5) and BRACED Shake Table Tests (Chapter 8).

An alternative solution for establishing an accurate effective area for gusset plate yield capacity is suggested by English and Goggins (2012). In their study a series of experimental tests were carried

out on gusset plate specimens to examine different gusset failure modes. The specimens were then modelled using ABAQUS (2009) to validate numerical models. From the force-strain plots post-processed from the analyses, the corresponding yield force was calculated for each specimen. Thus, the effective area of each gusset plate was calculated using the yield force divided by the expected yield stress of the material. The effective area was then defined as follows:

$$A_e = t_p \times b_e \tag{3.8}$$

where

$$b_e = \beta_i \times b \tag{3.9}$$

where b is the total width of the elliptical curve and b_e is the effective width based on the β_t modification factor established from equations below. The modification factor takes into account that not all of the plate is utilised in resisting the demand from the brace. The β_t value is the ratio of the width obtained from the numerical analysis to the actual measured experimental width. Several β_t values exist for different gusset plate shape factors:

$$\beta_1 = 0.67; \quad \beta_2 = \beta_1 + 2\tan\alpha(1-\beta_1) \leq 1.0; \quad \beta_3 = 1.0 \tag{3.10}$$

where β_1 is for rectangular plates, β_2 is for tapered plates connected to beam and column and β_3 is for plates connected to beams only. The α value represents the angle of inclination of the taper.

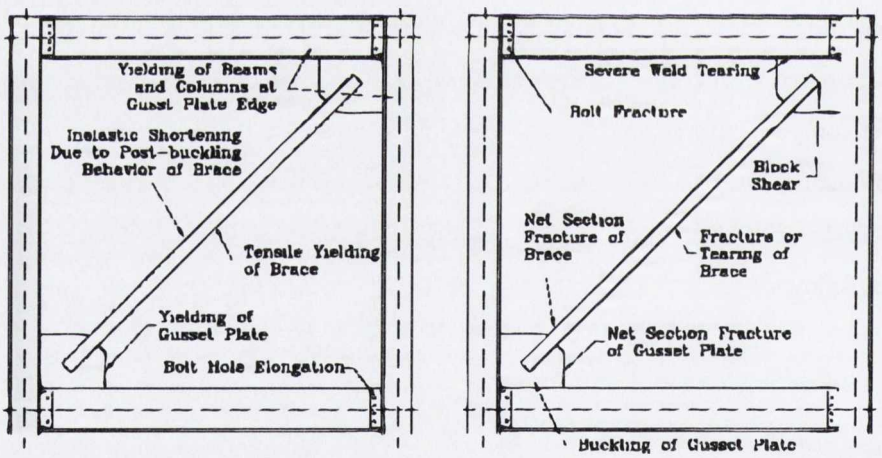

Figure 3.3 – (a) Yielding mechanisms and (b) failure modes for CBFs (Roeder et al., 2004).

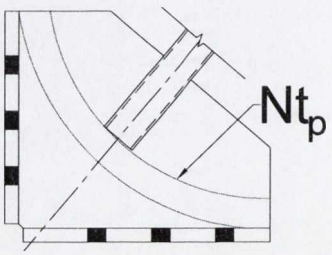

Figure 3.4 – Elliptical clearance geometrical layout where the plastic hinge length is N times the plate thickness t_p.

3.4 Connection Type

In the previous sections, design options were explored for detailed gusset plate design that allows plastic hinge development under frame rotation induced by earthquake ground motions. The behaviour of the brace-gusset element is not only dependent on its out-of-plane and axial stiffness, but also on the manner in which this element is connected to other parts of the CBF. In Figure 3.5 two common connection configurations are illustrated. In cases where the gusset is connected to both beam and column flanges (the 'CA' type), for a tensile brace load, the plate experiences tensile strains in the direction of the brace and compressive strains induced by the lateral deformation of the frame (which causes the beam-column connection angle to reduce). For a compression brace load, the connection angle opens and these strains are reversed, while the connection to both beam and column restrains out-of-plane plate rotation. In the case where the gusset is connected to the beam flange only (the 'CB' type), secondary strains are not induced due to changes in the beam-column connection angle and free plate rotation is permitted in the out-of-plane direction.

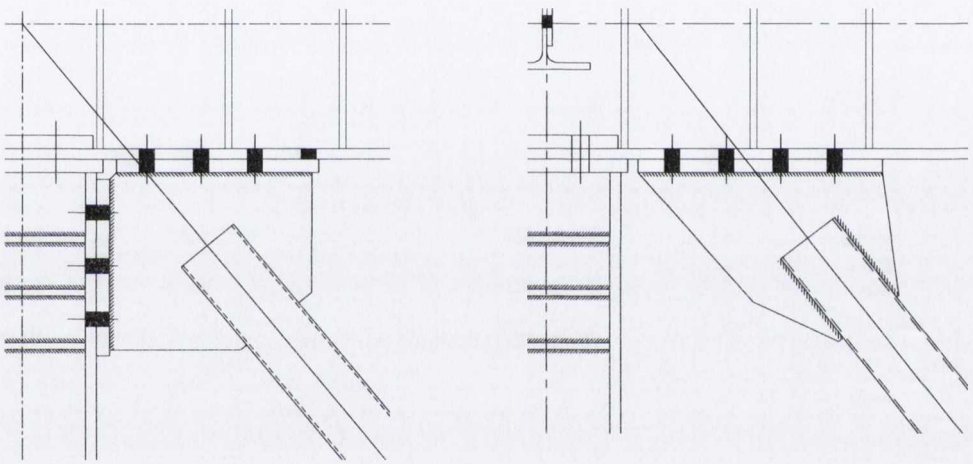

Figure 3.5 – Common connection types showing (a) gusset joint with beam and column (CA) and (b) gusset joint with beam only (CB).

The frame beam-to-column connection stiffness is also affected by the characteristics of the gusset plate connection. While in general design practice, the connections in CBFs are considered to be pinned connections, CA type connections can effectively increase the depth of the beam-column connection, leading to substantial rotation stiffness and resistance. Thus, both gusset configurations were investigated within the experimental programmes in this study. The additional restraint provided by the CA connection (high stiffness) increases the overall stiffness of the frame with the CB type connection (low stiffness) only transferring axial and bending forces to the beam. In Chapter 5 and Chapter 8, the test setup for these connections is outlined for the cyclic loading and shake-table testing programmes respectively.

3.5 Chapter Overview

In this chapter, the principles behind the design of gusset plate connections for earthquake resistant bracing members were described and codified design procedures were explained. Some design codes (e.g. AISC Seismic Provisions) permit plastic hinge development in the gusset plate along a linear free length that is a function of plate thickness, while preventing plate yielding in tension. These codified procedures can lead to early fracture development in the brace tube. This behaviour is a product of capacity design methods in which the connection is required to be much stronger than the brace and the connection itself is not considered as a potential dissipative zone. This can have the effect of increasing the occurrence of brittle fracture, thereby reducing system ductility.

To improve system ductility, alternative gusset design principles were explored. One of the primary proposals by Lehman et al. (2008) permits controlled tensile yielding in the gusset plate by balancing brace tensile yielding with gusset yielding. A yielding hierarchy is established with β_{ww} values introduced to indicate the ratio of yielding strengths of brace tube and gusset plates. Thinner gusset plates can be utilised to permit tensile axial yielding in this plate. However, to prevent plate buckling, an elliptical-shaped plastic hinge model (as an alternative to the standard linear model) can be used to produce smaller overall plate dimensions and therefore reduced buckling lengths and increased plate buckling capacities for thin plates.

The fundamental behaviour and seismic design concepts for brace members and their connections as outlined in this chapter merit further investigation, especially under realistic earthquake loading. The experimental programmes outlined in Chapters 5 and 8 compare the seismic performance of brace members and CBFs with a different connection designs in both cyclic and shaking table tests.

4 Numerical Modelling of Concentrically Braced Frames with OpenSees

4.1 Introduction

The relatively larger stiffness of CBFs compared to that of moment-resisting frames helps reduce interstorey drifts. However, the seismic performance of these frames is sensitive to the pinched hysteretic behaviour of the braces (Khatib et al., 1988). This behaviour combined with several other CBF design methods are explored through two sets of experimental tests that are discussed in Chapters 4.4 to 10.

As part of this research, numerical models of CBFs were developed alongside the experimental studies. Using OpenSees (McKenna, 1997), an object-orientated framework for finite element analysis, numerical models of braced frames were developed to examine their reliability in relation to specific performance parameters. Prior to developing complete numerical simulation models of full CBFs, a tiered hierarchical approach was used in employing OpenSees for this research with fundamental modelling aspects investigated first, progressing to model optimisation using advanced models with greater detail. Firstly, different aspects of the available OpenSees modelling techniques were examined in a parametric study where simplified tube members were used. The optimum parameter properties were established and used in developing full-scale brace member models. Using the brace member models, a correlation study was carried out to demonstrate the capabilities and limitations of the OpenSees physical theory model for hollow section shapes as investigated by Goggins (2004). The cyclic response of the brace members was examined for acceptable agreement with the results obtained by Goggins. This formed the finer level of model development where full finite element models of both the Complementary Cyclic Test specimens and BRACED project specimens were used to predict their respective responses (using the previously established optimum parameters).

Two types of distributed plasticity models are available in OpenSees: force-based elements (FBE) and displacement-based elements (DBE) utilising the flexibility and stiffness methods accordingly. In contrast to concentrated plasticity models, they permit yielding to occur at any location along the element. However, when using such element types, different modelling techniques are required to achieve comparable accuracy. In order to demonstrate the modelling options and select a method most suited to this study, a brief derivation by Neuenhofer and Filippou (1997) for both displacement and stiffness methods is applied to a simplified 2D beam-column element below.

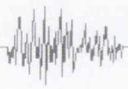

Displacement-Based Element (Stiffness Method)

The DBE interpolates section deformations from an approximate displacement field. Using the principle of virtual displacements, an equilibrium relationship is established between section forces and element forces. Considering a 2D beam-column element based on the Euler-Bernoulli beam theory (Figure 4.1), it is necessary to assume constant axial deformation and a linear curvature distribution along the element length. Thus, the displacement fields of the element are discretised and interpolated in terms of n_{DoF} element end displacement degrees of freedom $\mathbf{q}$ such that:

$$\boldsymbol{u}(x) = \boldsymbol{N}(x)\boldsymbol{q} \tag{4.1}$$

where $\mathbf{N}(x)$ is the interpolation matrix containing the shape functions based on the theory of Hermition polynomials. Implementing for the 3DOF, 2D beam-column element:

$$\begin{bmatrix} u_a(x) \\ u_t(x) \end{bmatrix} = \begin{bmatrix} N_1(x) & 0 & 0 \\ 0 & N_2(x) & N_3(x) \end{bmatrix} \begin{bmatrix} q_1 \\ q_2 \\ q_3 \end{bmatrix} \tag{4.2}$$

where $u_a(x)$ and $u_t(x)$ represent axial displacement and transfer displacement respectfully. Based on kinematic strain-displacement relationships an expression for the deformation fields can be developed:

$$\boldsymbol{d}(x) = \begin{bmatrix} \varepsilon_a(x) \\ \kappa(x) \end{bmatrix} = \begin{bmatrix} u_a'(x) \\ u_t''(x) \end{bmatrix} = \boldsymbol{B}(x)\boldsymbol{q} \tag{4.3}$$

where axial strain deformation $\varepsilon_a(x)$ and curvature $\kappa(x)$ along element length are contained by the matrix $\mathbf{B}(x)$. Internal or sectional force fields

$$\boldsymbol{D}(x_i) = \begin{bmatrix} N(x_i) \\ M(x_i) \end{bmatrix} \tag{4.4}$$

are axial force $N(x)$ and bending moment $M(x)$ leading to a summation for every discrete section fibre i. For an incremental section relation:

$$\boldsymbol{\Delta D} = \boldsymbol{k_{sec}}\boldsymbol{\Delta d} \tag{4.5}$$

where $\mathbf{k_{sec}}$ is the section stiffness matrix established from the user-defined stress-strain material relationship:

$$\boldsymbol{k_{sec}} = \frac{\partial \boldsymbol{D}}{\partial \boldsymbol{d}} \tag{4.6}$$

Developing Equation 4.5 into a constitutive relationship according to Equation 4.3 yielding the force field increment:

$$\boldsymbol{\Delta D}(x) = \boldsymbol{k_{sec}}(x)\boldsymbol{\Delta d}(x) = \boldsymbol{k_{sec}}(x)\boldsymbol{B}(x)\boldsymbol{\Delta q} \tag{4.7}$$

Given that the principle of virtual displacements requires that internal virtual displacements are in equilibrium with external virtual displacements an approximate equilibrium solution between sectional forces and basic forces, **Q**, can be formulated:

$$\boldsymbol{Q} = \int_0^L \boldsymbol{B}^T(x)\boldsymbol{D}(x)\,dx \approx \sum_{i=1}^{Np} \boldsymbol{B}^T(x_i)\boldsymbol{D}(x_i) \tag{4.8}$$

where L represents element length. However, this equilibrium approximation causes error in force boundary conditions leading to discrepancy between sectional and basic forces.

A system tangent stiffness matrix, $\mathbf{k_{sys}}$, can be assembled to represent the complete element:

$$\boldsymbol{k_{sys}} = \frac{\partial \boldsymbol{Q}}{\partial \boldsymbol{q}} \int_0^L \boldsymbol{B}^T(x)\boldsymbol{k_{sec}}(x)\boldsymbol{B}(x)\,dx \tag{4.9}$$

The equilibrium approximation deviates from the exact solution requiring a finer mesh discretisation (increase in number of elements) and consequently a significant computational effort.

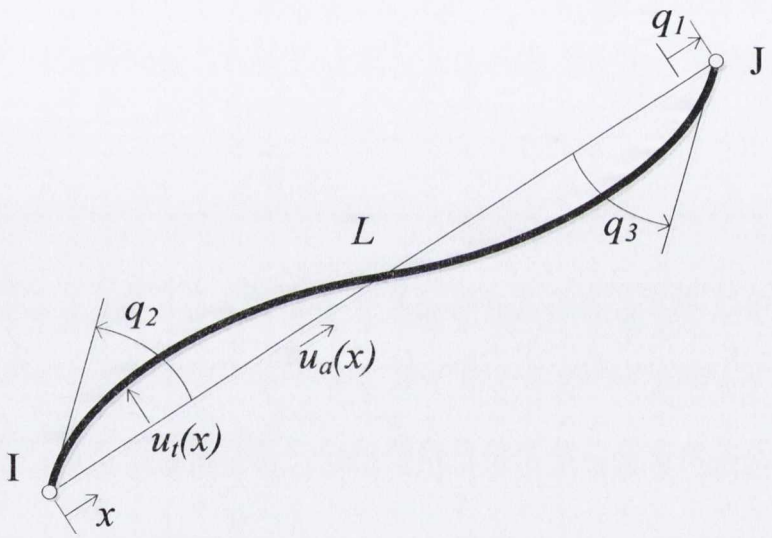

Figure 4.1 – 2D displacement-based element of length L between nodes I and J.

Force-Based Element (Flexibility Method)

Using the FBE requires the availability of an exact equilibrium solution between element and section forces. In contrast to the stiffness method, section forces are determined from the basic forces by interpolation within the basic system. Following this, the principle of virtual forces is used to formulate compatibility between section and element displacements.

In the flexibility method, force fields are described as:

$$\boldsymbol{D}(x) = \boldsymbol{b}(x)\boldsymbol{Q} \tag{4.10}$$

with the shape function matrix represented by $\mathbf{b}(x)$, relating the generalised nodal forces $\mathbf{Q}$ to the sectional forces $\mathbf{D}(x)$. Implementing this for the 2D element:

$$\boldsymbol{D}(x) = \begin{bmatrix} N(x) \\ M(x) \end{bmatrix} = \begin{bmatrix} b_1(x) & 0 & 0 \\ 0 & b_2(x) & b_3(x) \end{bmatrix} \begin{bmatrix} Q_1 \\ Q_2 \\ Q_3 \end{bmatrix} \tag{4.11}$$

Pre-multiplying Equation 4.5 by the inverse section stiffness matrix yields the form:

$$\boldsymbol{\Delta d} = \boldsymbol{f_{sec}} \boldsymbol{\Delta D} \tag{4.12}$$

in which the section flexibility matrix $\boldsymbol{f_{sec}} = \boldsymbol{k_{sec}^{-1}}$. Applying the relation from Equation 4.10:

$$\boldsymbol{\Delta d}(x) = \boldsymbol{f_{sec}}(x)\boldsymbol{b}(x)\boldsymbol{Q} \tag{4.13}$$

Similar to the stiffness method, the principle of virtual forces established compatibility between element end displacements and sectional displacements:

$$\boldsymbol{q} = \int_0^L \boldsymbol{b}^T(x)\boldsymbol{d}(x)\, dx = \sum_{i=1}^{Np} \boldsymbol{b}^T(x_i)\boldsymbol{d}(x_i) \tag{4.14}$$

Finally, a system flexibility matrix can be established for the complete element:

$$\boldsymbol{f_{sys}} = \frac{\partial \boldsymbol{q}}{\partial \boldsymbol{Q}} \int_0^L \boldsymbol{b}^T(x)\boldsymbol{f_{sec}}(x)\boldsymbol{b}(x)\, dx \tag{4.15}$$

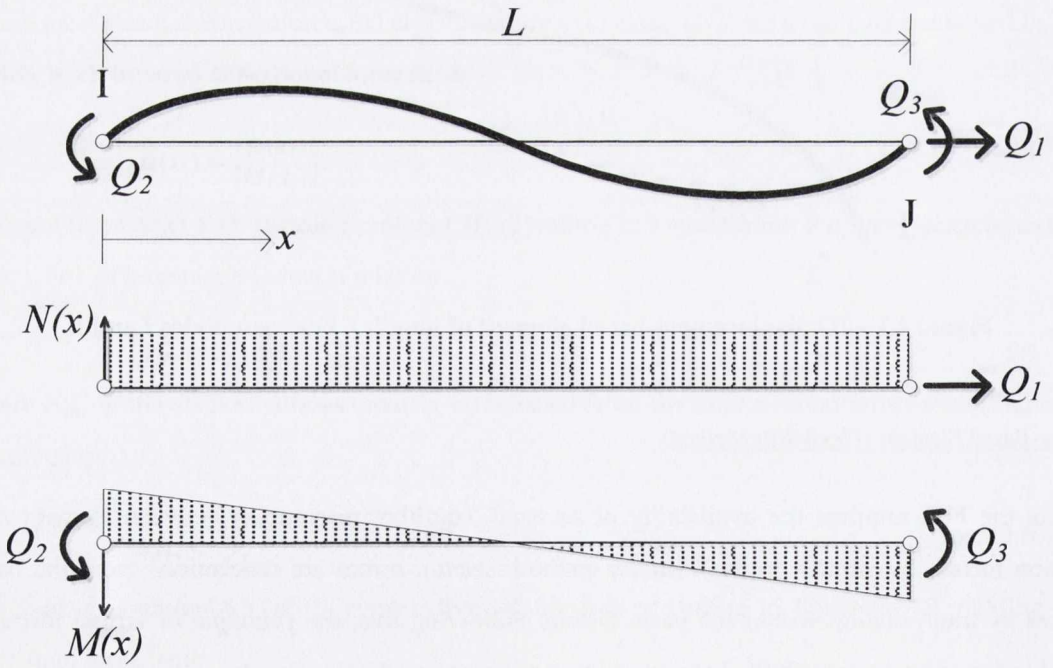

Figure 4.2 – 2D force-based element of length *L* between nodes *I* and *J*.

The favourable behaviour of the flexibility approach is based on the fact that the force interpolation functions satisfy force equilibrium exactly in contrast to the stiffness method where displacement

interpolation functions produce large deviations from exact results. The accuracy of the FBE can be improved by increasing the number of integration points or the number of elements. Error can only be improved for the DBE by increasing the number of elements with larger computational effort required to achieve comparable accuracy to the FBE.

Furthermore, the capabilities of the FBE have been found to accurately represent the response of hollow and filled steel section braces under cyclic loading in a validation study conducted by Hunt and Broderick (2010). Such errors accumulate during the iteration of each time step during non-linear analysis in OpenSees and can lead to inaccurate response prediction. Based on the advantages of FBEs compared to DBEs, FBEs have been utilised in all OpenSees modelling for this study.

To capture steel material behaviour for the axial and bending moment sectional forces, the Giuffré-Menegotto-Pinto uniaxial material model ('Steel02' in OpenSees) (Menegotto and Pinto, 1973) was specified (Figure 4.3). This material offers more input parameters than other available steel materials (including defining the transition curve between elastic and plastic branches, not available in 'Steel01') and has been used extensively in previous work modelling CBFs (AISC, 2005c; Hsiao et al., 2012; McCrum and Broderick, 2010; Salawdeh, 2012; Santagati et al., 2012; Uriz et al., 2008). However some limitations exist for plasticity based models, in particular their basis in small deformation theory (Uriz et al., 2008). Small deformation theory is based on the assumption that plane sections remain plane and shear distortion has no contribution after deformation so that section shape is retained. In physical terms, this implies that local buckling of braces is not modelled which imposes limitations on the ability of the beam-column element to model fracture initiation. However, a proposed solution to address this is discussed in greater detail in Section 4.3.

4.2 Parametric Study

The response of the physical theory fibre model is sensitive to the influence of several modelling parameters. This section investigates the degree of influence of each of these parameters on the ability of the fibre model to replicate a realistic response of brace members under monotonic and cyclic loading regimes. As the results of this parametric study are used in the correlation study with experimental data in section 4.3.2, identical brace lengths and sections are employed here for consistency in modelling. Two section types are modelled in OpenSees for each parameter being investigated; 40×40×2.5 SHS and 50×25×2.5 RHS. To consider the influence of different end conditions, these members are modelled under both pin-pin (PP), fix-pin (FP) and fix-fix (FF) boundary conditions. The specimens have a complete length of 1100 mm and are modelled with stiffener plates at both ends to simulate the connection setup used in real experimentation.

When a brace undergoes compression there is an interaction between axial force and bending moment. The combination of a force-based, nonlinear beam-column element with a uniaxial material element accounts for this interaction by integrating the material model over the cross section of the brace. Several effects are considered including kinematic and isotropic hardening and the Bauschinger effect. However as discussed above, some effects are not considered including local effects.

4.2.1 In- and Out-of-Plane Camber

For realistic buckling to occur in OpenSees, an initial camber must be specified along at the brace mid-length. A similar suggestion by Higginbotham and Hanson (1976), recommended augmenting their analytical brace hysteresis solution with the inclusion of initial curvature imperfection to remove the discrepancy in predicting maximum compressive force regions. In OpenSees, this imperfection is usually set as a proportion of the length of the brace. However, using nodal geometry, it can be set as an in-plane imperfection, out-of-plane imperfection or a combination of both. This is illustrated in Figure 4.3(e). The effects of this are examined for a 40×40×2.5 SHS of length 1100 mm, with four nonlinear beam-column elements and five integration points per element. The stiffener plates at both ends of the specimen determine the weak axis of bending for the square section. When an initial camber is prescribed as in-plane, brace buckling will occur about the weak axis. For an out-of-plane initial camber, bending is induced about the stronger axis, hence increasing the buckling capacity of the brace. The stiffener plates have a thickness of 8 mm and a length of 125 mm.

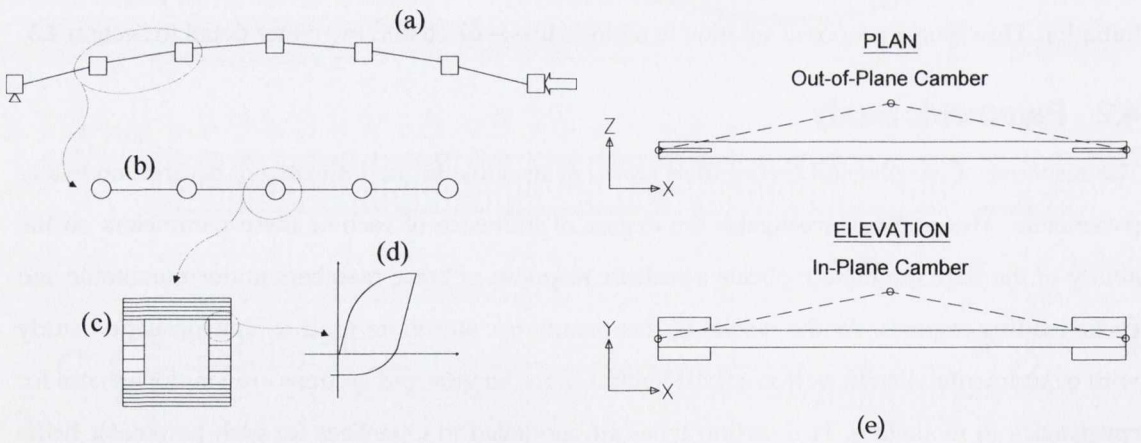

Figure 4.3 – Operation of nonlinear beam column element in OpenSees showing (a) brace finite element mesh with elements and nodes, (b) force-based beam column element with integration point sections, (c) predefined section discretized into smaller fibres, (d) material stress-strain response specified to give resultant behaviour and (e) overall brace diagram with geometrical camber overlay.

Figure 4.4(a – b) shows the monotonic compression response of the brace specimen for both in-plane and out-of-plane camber. In the FF end condition, the in-plane camber restricts the tube to rotation about the strong axis only. Therefore, the increased end stiffness associated with the stiffener plates reduces the effective length and demonstrates a larger in-plane buckling capacity compared to the out-of-plane model. In the FP boundary condition models, the limited rotational restraint at one end produces a minimal increase in buckling capacity.

Figure 4.5(a) demonstrates a similar outcome with larger compressive resistance in the post-buckling region demonstrated by the in-plane specimen. This pattern is repeated until final excursions into the compression range where both in- and out-of-plane resistances match. In the fix-pin case (Figure 4.5(b)), the difference between the two specimens is minimised because the bending stiffness of only one gusset plate is effective.

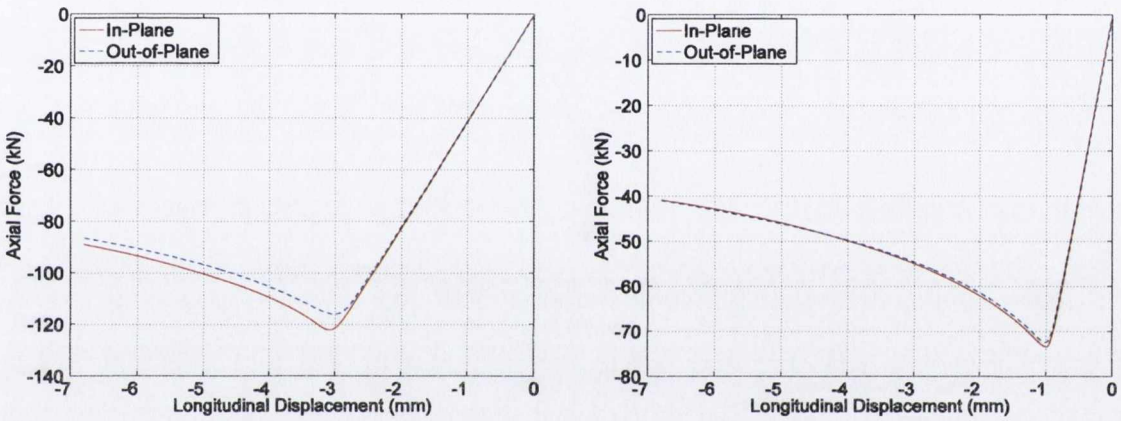

(a) fix-fix end conditions (b) fix-pin end conditions

Figure 4.4 – Monotonic compression response of (a) fix-pin and (b) pin-pin end conditions for in-plane and out-of-plane initial prescribed camber.

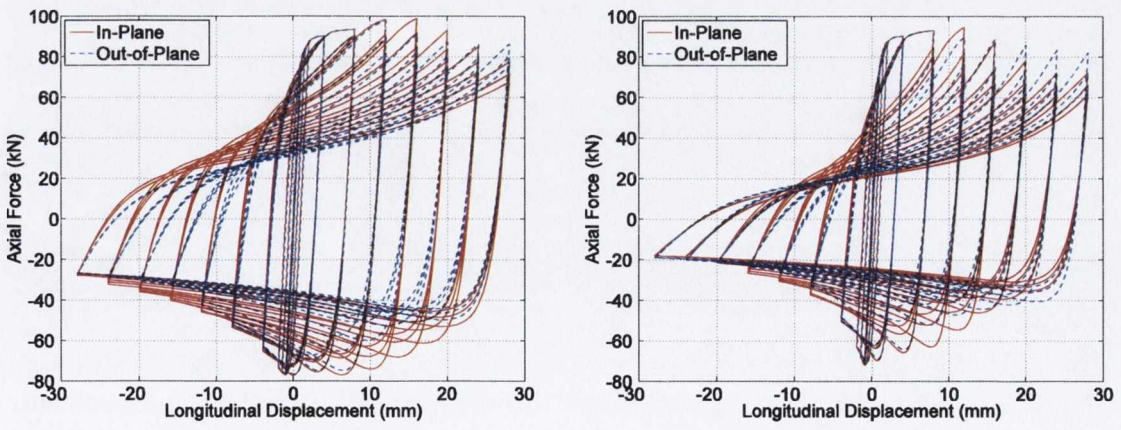

(a) fix-fix end conditions (b) fix-pin end conditions

Figure 4.5 – Hysteretic response of (a) fix-pin and (b) pin-pin end conditions for in-plane and out-of-plane initial camber.

The curvature distribution along the length of each brace model with fix-fix conditions is shown in Figure 4.6(a) below. The differences in response are much more apparent compared to the hysteresis responses discussed above. In-plane, the section up to 125 mm shows minimal section curvature. However, in the out-of-plane direction the lower section stiffness exhibits larger curvature compared to other sections in the model. The discrete changes in curvature that occur at 125 mm are caused by the immediate change in section definition from SHS tube with plate section to just SHS tube. Overall, the curvature in-plane has a larger order of magnitude compared to the curvature out-of-plane. This is explained by the rigid in-plane sections at the fixed ends where buckling is induced over a shorter brace length focussing large curvature at mid-span.

Similar outcomes are derived from the fix-pin conditions (Figure 4.6(b)). The discrete curvature changes are observable at 125 mm and to a lesser extent 975 mm. As mentioned earlier, the curvature order of magnitude is increased for in-plane measurements due to the larger bending moment introduced at the brace ends.

Under ideal conditions (perfectly pinned connections), the orientation of the buckling shape of a square hollow steel strut is influenced by imperfections in the steel material and residual stresses due to the uneven cooling of steel sections after hot rolling (Ding, 2000). Therefore, buckling deformation can occur in any orientation. However, as described above, the stiffener plates have a strong influence on the orientation of brace deformation. As such, it is prudent to prescribe an initial camber in both planes for a realistic response where the direction of buckling can be controlled. This is particularly useful for inducing out-of-plane buckling CBF systems with plastic hinge zones in gusset plate connections.

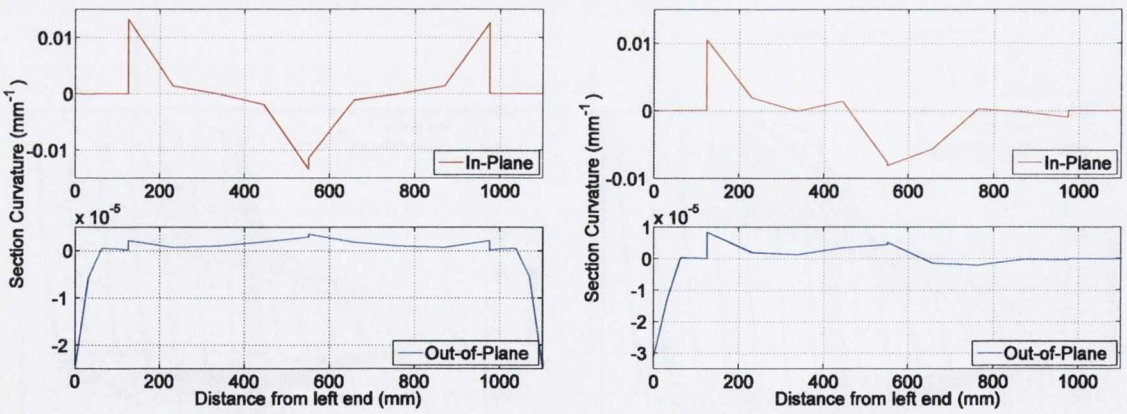

(a) fix-fix end conditions

(b) fix-pin end conditions

Figure 4.6 – Curvature recorded at each integration point for the four nonlinear beam column elements along the length of the brace model.

4.2.2 Initial Camber Magnitude

The degree of initial camber assigned influences the maximum buckling load achieved by the brace model. As in the previous section, this is carried out using a geometric imperfection in OpenSees. Several degrees of initial camber were tested: 0.01%; 0.1%; 1.0% and 3.0% of brace length. Although an initial camber of 3% is unlikely to occur in real-life, it is used in this study solely to examine the extremities of each case. In section 6.2, measured initial camber values from complementary tests are presented and discussed. The plots shown in Figure 4.7 (a – b) illustrate that, as expected, a prescribed initial camber helps initiate buckling of a strut in a realistic manner. As the magnitude of the initial camber is increased the compressive capacity is decreased. In a Pacific Earthquake Engineering Research Centre (PEER) report compiled by Uriz and Mahin (2008) similar cambers were considered for a parametric study and a range of 0.05%-0.1% was deemed acceptable for accurate buckling representation. The design buckling resistances for both end conditions of the member being examined were calculated according to Eurocode 3 (CEN, 2005a), $N_{b,Rd}$, and for LRFD design provisions according to AISC Specification for Structural Steel Buildings (AISC, 2005b), $\phi_c P_n$, are shown in Table 4.1.

Table 4.1 - Design Buckling Resistances (AISC, 2005b; CEN, 2005a) and OpenSees Buckling Resistances

	$N_{b,Rd}$ (kN)	$\phi_c P_n$ (kN)	$N_{b,0.1\%}$ (kN)
Fix-Pin	74.55	72.37	82.86
Pin-Pin	70.10	67.09	76 42

In both cases using an initial camber of 0.1% provides a buckling resistance ($N_{b,0.1\%}$) that matches closely with the design predictions from Eurocode 3 with some over estimation. The buckling strength in Eurocode 3 is established from buckling curves which are related to the shape of sections, axis of buckling and thickness of material. These curves are based on experimental studies on real columns by the European Convention for Constructional Steelwork (ECCS, 1976). As these nondimensional curves account for the geometrical imperfections and material inhomogeneities that are inherent with industrially manufactured columns they provide a realistic prediction of the associated buckling strength.

An examination of the hysteresis plots in Figure 4.8 (a – b) shows results typical of a fix-pin and pin-pin connection. In Figure 4.8(a) a larger residual compressive resistance is observable for all initial cambers compared to Figure 4.8(b). However, large initial cambers reduce the initial buckling load and buckling loads at subsequent cycles. A similar characteristic occurs with the

larger non-zero tangent stiffness for each cycle in the fix-pin setup compared to the pin-pin setup. A large initial camber of 3.0% affects the strain hardening significantly for both cases.

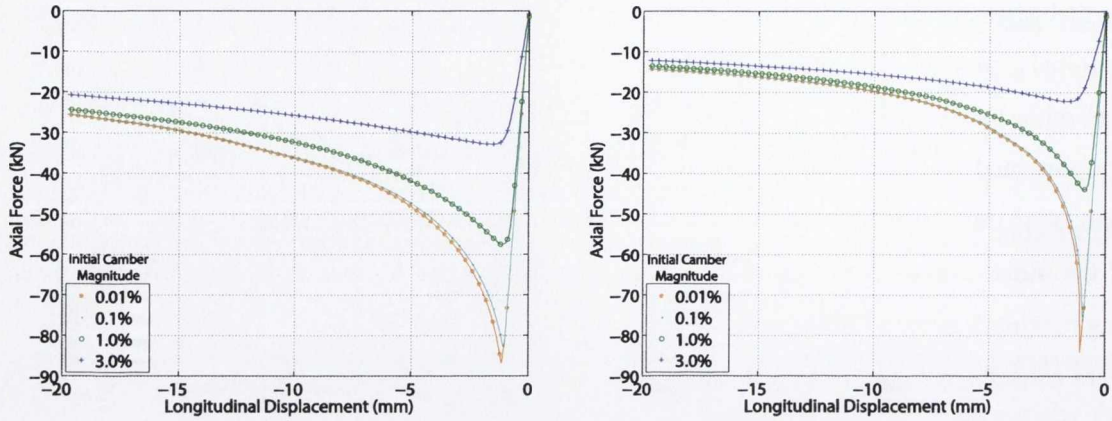

(a) fix-pin end conditions (b) pin-pin end conditions

Figure 4.7 – Monotonic compression response of (a) fix-pin and (b) pin-pin end conditions for four magnitudes of initial camber.

Global displacements of the central midspan node of each model for the ideal pinned case are shown in the hysteresis plots in Figure 4.9 (a – b). It is interesting to note the significant influence higher degrees of initial camber have on the lateral deformations. When the brace enters the compressive loading half-cycle with a large initial camber most of the buckling occurs in the in-plane direction. If the initial camber is reduced to the lower range of camber values, the brace buckles more evenly between the two planes. Hence, at the peak lateral displacements at the end of the compressive half-cycles in Figure 4.9, an initial camber of 0.01% exhibits reduced lateral displacements to those of an initial camber of 3% due to the more balanced distribution of displacements.

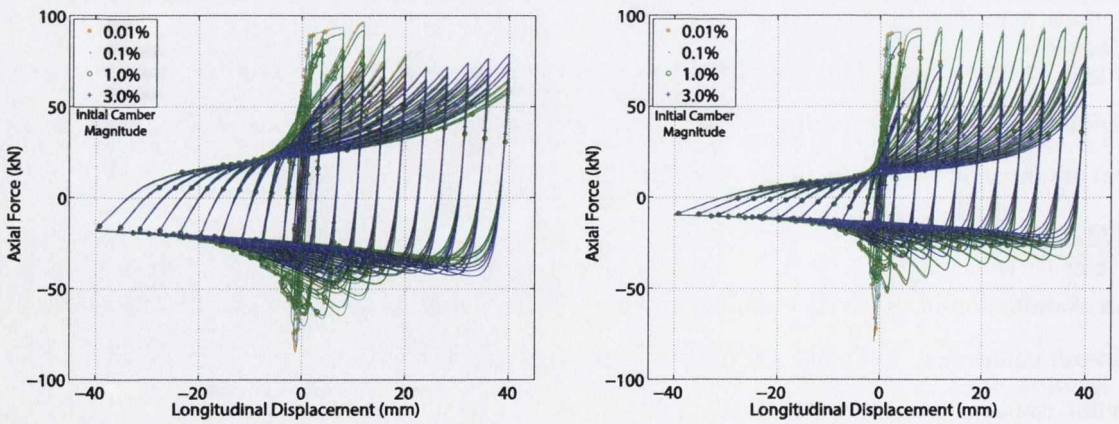

(a) fix-pin end conditions (b) pin-pin end conditions

Figure 4.8 – Hysteretic response of (a) fix-pin and (b) pin-pin end conditions for four magnitudes of initial camber.

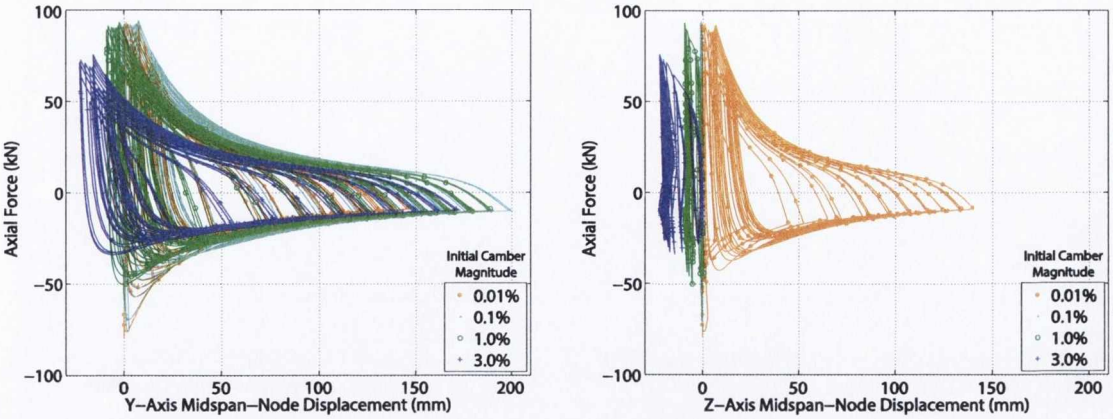

(a) In-plane displacements (y-axis) (b) Out-of-plane displacements (z-axis)

Figure 4.9 – Hysteretic response of brace midspan the ideal pin boundary conditions.

4.2.3 Number of Elements per Brace

Similar to the influence a prescribed geometrical camber can have on brace characteristics, the effects of the number of nonlinear beam-column elements defined along the brace length were investigated. All other variables were kept constant: five integration points are specified for each element; the initial camber is maintained at 0.1% as recommended above and the same material properties are used.

Examining the monotonic compression plots in Figure 4.10 it is clear that the effect of increasing the number of elements is negligible. The buckling capacity is practically identical for the fix-pin case (Figure 4.10(a)), and there exists a 4.5% difference in capacity between maximum and minimal mesh definition for the pin-pin case (Figure 4.10(b)). The difference in the rate of strength loss in the post-buckling range is more noticeable in the fix-pin case with a larger number of elements showing a greater degradation of strength. It was anticipated that this would have stronger implications for the hysteretic performance of the brace.

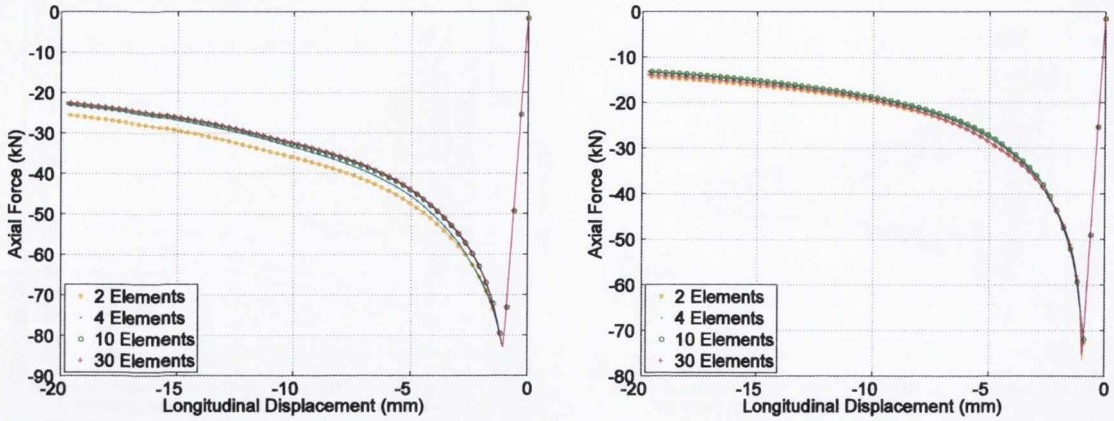

(a) fix-pin end conditions (b) pin-pin end conditions

Figure 4.10 – Monotonic compression response of (a) fix-pin and (b) pin-pin end conditions for different degrees of finite element mesh resolution.

Upon carrying out the cyclic analyses, as expected, a more significant influence was observed in the hysteretic characteristics of the brace model as displayed in Figure 4.11. The influence on the rate of strength loss derived from the monotonic analyses was observed in the brace cyclic performance. For the fix-pin instance (Figure 4.11(a)), the initial tensile and compressive peaks were identical but for all target displacements thereafter reduced capacities were present for mesh definitions greater than four elements. In the latter tensile half-cycles, a marginal decrease in tangent stiffness is exhibited for these mesh definitions also. This is manifested through slightly less concave curves for the two-element case. Overall, the performance of the pin-pin case remains unaffected for all mesh scenarios (Figure 4.11(b)).

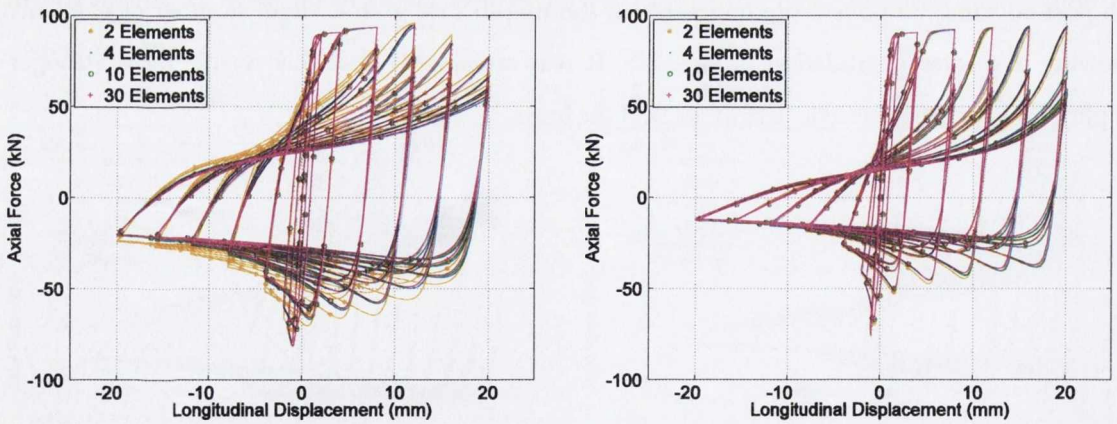

(a) fix-pin end conditions (b) pin-pin end conditions

Figure 4.11 – Hysteretic response of (a) fix-pin and (b) pin-pin end conditions for different degrees of finite element mesh resolution.

As encountered in Section 4.2.1, the effects on the recorded curvature are more evident as illustrated by the plots of in-plane curvature in Figure 4.12. For the fix-pin case (Figure 4.12(a)), a plastic hinge forms just after the fixed end stiffener approximately between 125 mm and 220 mm. A second plastic hinge formed at the right end just before the adjacent stiffener. This hinge forms at approximately 750 mm when more refined meshes were used. However, as less information is supplied with the two-element analysis, this can lead to an incorrect interpretation of the plastic hinge developing at approximately 600 mm. For this case it is recommended that at least four elements are used for the brace span. In the case of pin-pin conditions (Figure 4.12(b)) the information loss has a minimal influence on hinge location interpretation. This can be attributed to the near-symmetrical boundary conditions.

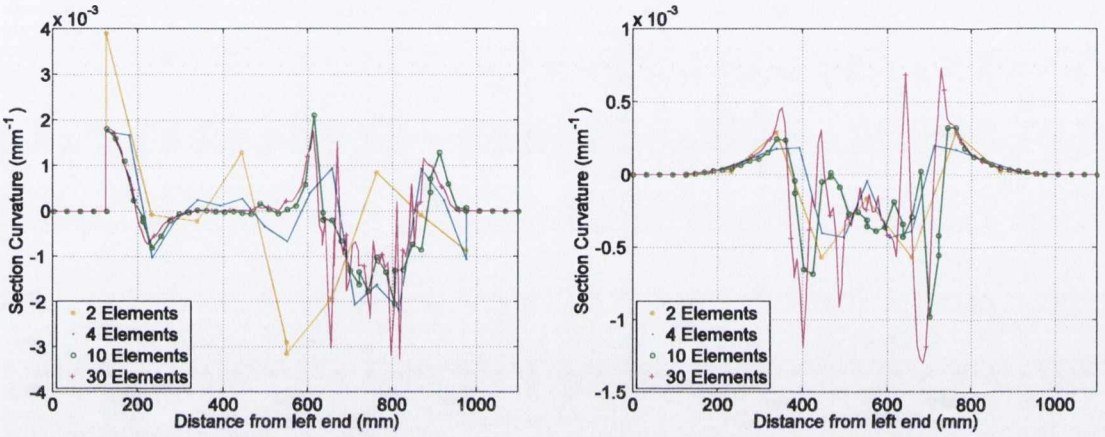

(a) fix-pin end conditions (b) pin-pin end conditions

Figure 4.12 – In-plane curvature recorded at each integration point for each case of mesh refinement.

4.2.4 Number of Integration Points per Element

As discussed previously in the chapter, the nonlinear beam-column element is based on the force (flexibility) method that considers the spread of plasticity throughout the element. Numerical integration is carried out along the element length however an approximation of the integral is reached using a weighted sum of the force function values at specified points. A larger number of integration points will yield an integral approximation that approaches the definite integral. The nonlinear beam-column element requires the specification of the number of integration points along the element length. This type of element employs the Lobatto quadrature rule where integration points are included at both element ends by default (Abramowitz and Stegun, 1965). Increasing the number of integration points leads to a more numerically accurate analysis at the expense of computation time. This section determines an optimum balance of these considerations that leads to a reasonably accurate and practical analysis.

The first set of analyses comprises the monotonic compression responses depicted in Figure 4.13 below. The difference in response is negligible for the fix-pin case in Figure 4.13(a), but the pin-pin case Figure 4.13(b) demonstrates a marginally slower decrease in compressive resistance for an increased number of integration points. The same effects are noticed in the hysteretic responses shown in Figure 4.14. The responses of five integration points or greater are nearly identical. Therefore, to capture a realistic post-buckling response with practical computational expense, a minimum of five integration points per element is recommended.

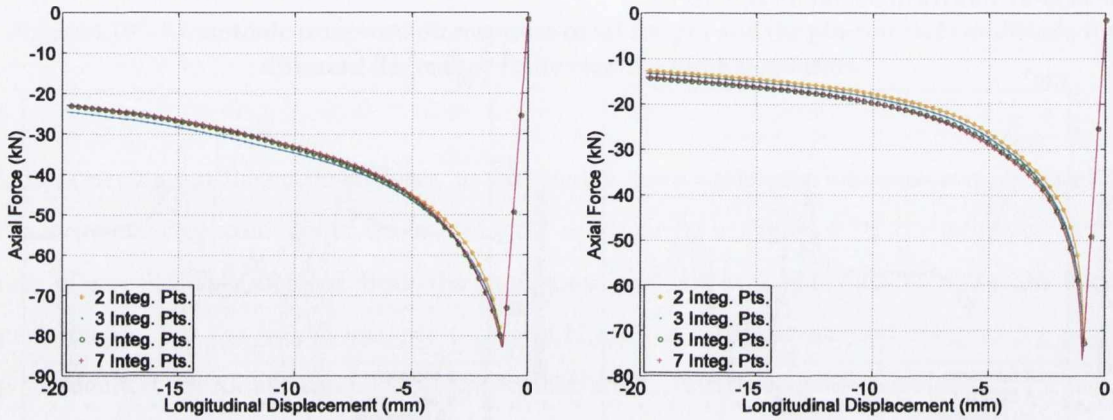

(a) fix-pin end conditions (b) pin-pin end conditions

Figure 4.13 – Monotonic compression response of (a) fix-pin and (b) pin-pin end conditions for different quantities of integration points along each element.

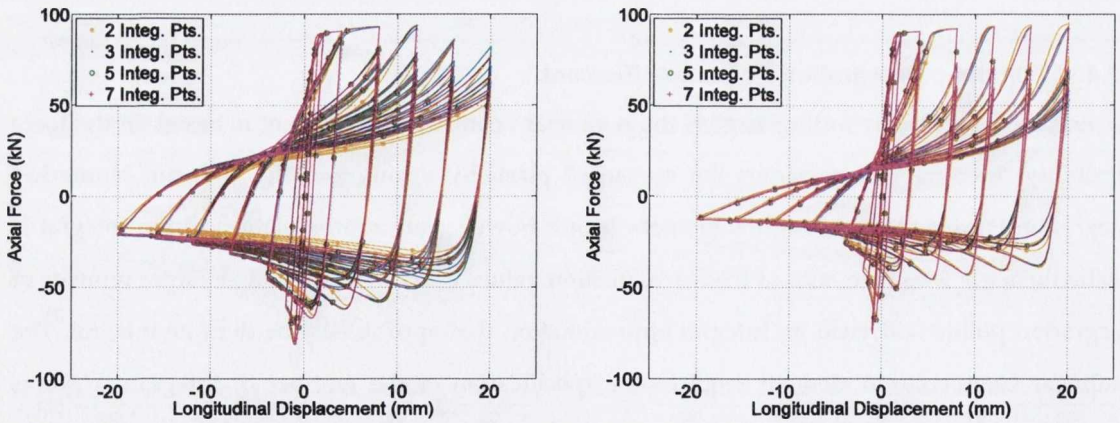

(a) fix-pin end conditions (b) pin-pin end conditions

Figure 4.14 – Hysteretic response of (a) fix-pin and (b) pin-pin end conditions for different quantities of integration points along each element.

4.2.5 Summary of Observations

The parametric study examined the influence of important parameters that are involved in the fundamental decision-making process when initially developing an OpenSees model. Idealised conditions were employed to eliminate case-specific factors from influencing the recorded responses. The parameter cases considered to produce the most desirable results are utilised in the more advanced finite element models developed throughout this thesis. An overview of the recommendations is as follows:

- Due to the uncertainty associated with SHS buckling direction, prescribing an initial camber curvature in both buckling planes produces the most realistic result.
- The order of magnitude of initial camber strongly influences the initial buckling capacity producing larger buckling loads with decreased camber magnitude. Conversely, reduced loads are observed with cambers approaching unrealistically large values. A value of 0.1% camber at brace mid-length is recommended to achieve buckling loads approaching those predicted by design standards.
- The effect of varying the number of elements was minimal when examining the monotonic compression and hysteretic performance of the test models. However, the optimum curvature response was observed when using at least four elements for the brace span.
- To reduce computation time whilst maintaining an accurate analysis, a minimum of five integration points per element was recommended.

4.3 Brace Member Model

In this section, the capability of the inelastic beam-column element for modelling the monotonic and hysteretic response is demonstrated for use in CBF models. As mentioned in the introduction of this chapter, the beam-column element is not capable of modelling local buckling modes which can lead to fracture. This would suggest that the numerical response of sections susceptible to local buckling would be affected. It was therefore necessary to investigate the significance of this numerical modelling drawback. It was anticipated however, that for sections with larger global slenderness values that the OpenSees models would demonstrate more reasonable fidelity.

Firstly, it was necessary to describe how fracture is considered in the OpenSees simulations. Following this, in light of the parametric study previously described, the OpenSees modelling method is validated through a correlation study with hollow steel braces of square and rectangular cross-sections tested by Goggins (2004) using a series of monotonic and cyclic tests. These experiments form a benchmark for the correlation studies which assess the optimum parameters that have been derived from the parametric study.

4.3.1 Fracture due to Low Cycle Fatigue (LCF)

As described in Chapter 2, braces that undergo uniaxial loading buckle out of plane, and at large deformations develop plastic hinges at one or more locations along their length. Typically, large strains will accumulate at these regions especially at the onset of local buckling, eventually leading to fracture initiation (Jain et al., 1977; Lee and Goel, 1987; Tremblay et al., 2003). It has been observed by Gugerli and Goel (1980) and Ikeda and Mahin (1986) that once fracture has initiated, significant deterioration in brace hysteretic performance is exhibited, with associated loss in member strength and stiffness. Therefore it is essential to consider fracture initiation when modelling CBFs under seismic excitation.

Different methodologies exist to predict ductile crack initiation using numerical simulations. Generally, a micromechanics-based approach is employed where, under cyclic loading, member ductility capacity will decay according to a damage rule (Fell et al., 2006). This can be expressed through a damage index (DI):

$$DI = \frac{Demand}{Capacity} \qquad 4.16$$

Such a rule allows a limit state to be calculated at a specific point based on material parameters (Kanvinde and Deierlein, 2004). A high damage index indicates imminent ductile fracture for a material. The study carried out by Fell et al. (2006) utilised the finite element program ABAQUS to predict fracture for 7 HSS brace specimens. It was found that fracture in steel HSS braces was governed by local buckling in corner regions rather than cold working strains at opposite corners. Unlike OpenSees, ABAQUS is capable of modelling local buckling through the use of continuum shell finite elements. However, this is a computationally expensive procedure and as discussed below, local buckling simulation is not necessary to predict fracture.

A method proposed by Uriz and Mahin (2004b) describes a material model that accounts for the effects of low cycle fatigue. Experimentally, it is typical for fracture life to be determined by constant amplitude tests for a specific material. Due to the variability in amplitude associated with earthquake excitations, a load cycle-counting method can be employed and the average strain amplitude from the hysteretic response of a fibre section obtained. Member failure is initiated when this average strain reaches the pre-defined limit state in Equation 4.16.

In OpenSees, strain histories can be recorded for each fibre across a member section. As a result, a rainflow counting algorithm is used to reduce the varying strains to a histogram of simple strain reversals. The rainflow counting concept was first proposed by Matsuishi and Endo (1968) but has been defined using explicit analytical formulae by Rychlik (1987). More recently, ASTM (2011)

recommends a rainflow counting algorithm for simplifying complex strain history data for material testing.

The rainflow cycle algorithm is used in combination with a linear strain accumulation model (Miner's Rule) based on the log-log relationship for low cycle fatigue proposed by Coffin (1954) and Manson (1965) as shown in Figure 4.15:

$$\frac{\Delta\varepsilon_p}{2} = \varepsilon'_f(2N_f^C) \qquad 4.17$$

where:

$\frac{\Delta\varepsilon_p}{2}$	is the plastic strain amplitude;
ε'_f	is the empirical fatigue ductility coefficient (failure strain for single reversal);
$2N_f$	is the number of reversals to failure (N_f cycles to failure);
C	Is an empirical fatigue ductility coefficient.

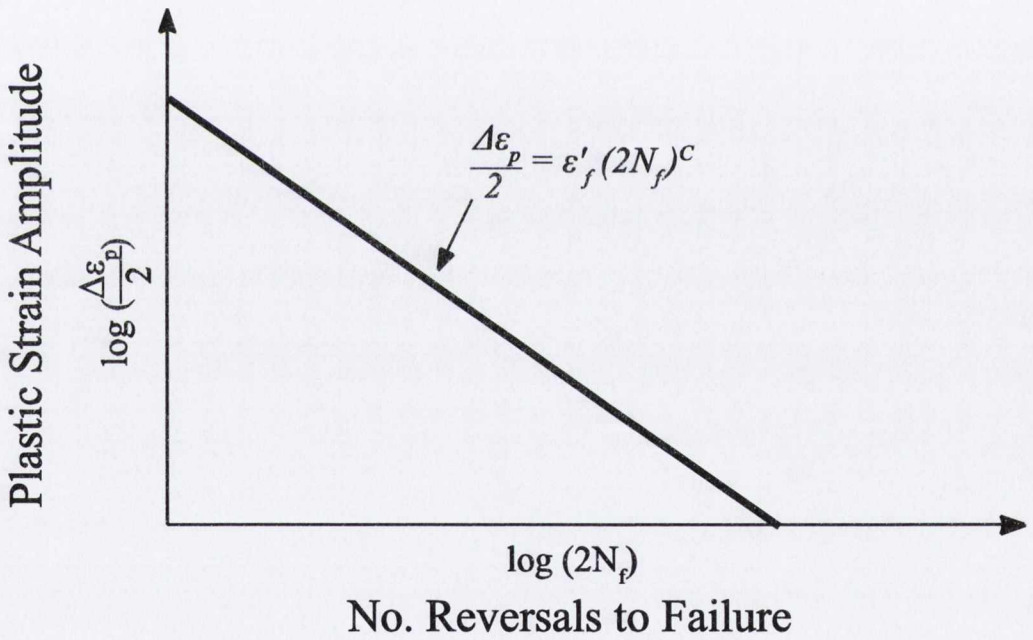

Figure 4.15 – Linear Coffin-Manson relationship.

Equation 4.17 represents a linear relationship that the log of the number of constant amplitude cycles to failure N_f and the log of the strain amplitude $\Delta\varepsilon_p$ expressed in each cycle. When the strain of a monitored fibre fails, the fibre is removed from the element model. This allows fibres to be progressively removed, thus replicating the deterioration of the brace hysteretic properties. This procedure is implemented in OpenSees through a uniaxial fatigue material wrapped around the

parent material (e.g. Giuffré-Menegotto-Pinto material) and has no influence on the stress-strain behaviour of the parent material. A thorough discussion of this process is provided by Uriz and Mahin (2008). The accumulation of damage in the fatigue material is represented by a damage index that varies between 0 and 1. When the damage index reaches 1.0, the force of the parent material becomes zero and failure is triggered. The two primary input parameters for this material model are strain that causes failure after one cycle ε_0 (fatigue ductility coefficient), and the slope of the log-log Coffin-Manson relationship m. The default values are 0.191 and -0.458 respectively. These parameters were calibrated by Uriz and Mahin (2008) using data from a series of tests on HSS (Hollow Structural Section) struts carried out by Yang and Mahin (2005) for sections with and without net section area reinforcement. For each of the 6 full-scale uniaxial brace specimens, an OpenSees analytical model was developed and the strain history was examined at the location of fracture. An average strain amplitude was established for the outer compression fibre at the brace mid-length section. The plastic strain range values were then plotted against the number of cycles to failure for each specimen on a log-log scale to form specific Coffin-Manson plots as described above. The slope of the Coffin-Manson plot was evaluated for each specimen. The process was repeated to evaluate suitable parameters for other common sections. Low-cycle fatigue tests conducted by Ballio and Castiglioni (1995) were used for obtaining calibrated parameters for wide flange beam sections. The recommended values for the different section configurations are listed in Table 4.2 below. These values were determined on the ability of the OpenSees models to predict low-cycle fatigue failure within one cycle of the observed experimental result.

Table 4.2 – Recommended values for the fatigue model input parameters (Uriz and Mahin, 2008).

	m	ε_0
HSS braces with reinforced net area	-0.5	0.095
HSS braces without reinforced net reduced area	-0.458	0.091
Wide flange beam sections	-0.458	0.191

Santagati et al. (2012) considered the experimental investigations of several single brace and one-storey frame testing programmes (Archambault et al., 1995; Roeder et al., 2004; Shaback and Brown, 2003). Data was collated for 32 SHS and RHS brace types where failure was achieved at the brace mid-length to further calibrate the fatigue model input parameters for HSS braces. Each test was simulated numerically in OpenSees and the ductility coefficient correlated with the corresponding experimental behaviour assuming a constant slope of $m = -0.458$. The study showed a large scatter in the range of ε_0 values required for each specimen with maximum, minimum and mean values reported as 0.17, 0.07 and 0.12 respectively. These values are employed

for use as starting values for similar iterative procedure use in the correlation study in sub-section 4.3.2.

A similar study conducted by Lignos et al. (2012) calibrated the fatigue model based on a database of 20 major steel brace experimental programmes that gathered various properties of steel braces with a range of section shapes. Most significantly, the database includes digital load-deformation hysteretic data, brace geometry and relevant material properties. An optimisation procedure was used to calibrate the ε_0 and m parameters for the OpenSees model of each brace within the database:

$$H(\varepsilon_0, m) = \sqrt{\sum_{i=1}^{N} \left[F_{exp.}(\delta_i) - F_{sim.}(\delta_i)\right]^2} \qquad 4.18$$

where H is the objective function of the constrained optimisation problem and $F_{exp.}$ and $F_{sim.}$ are the axial force of the brace for each axial displacement δ_i given N number of points. It was found that the m parameter is constant and independent of the shape of steel section calibrated (i.e. effective slenderness ratio KL/r and section slenderness b/t). However, the KL/r and b/t ratios were shown to affect the ε_0 strain parameter (Figure 4.16). At the time of writing, this investigation was still underway and Figure 4.16 only represents preliminary results. Therefore the conclusions drawn by Lignos et al. (2012) are not considered for use in these models until further results are published.

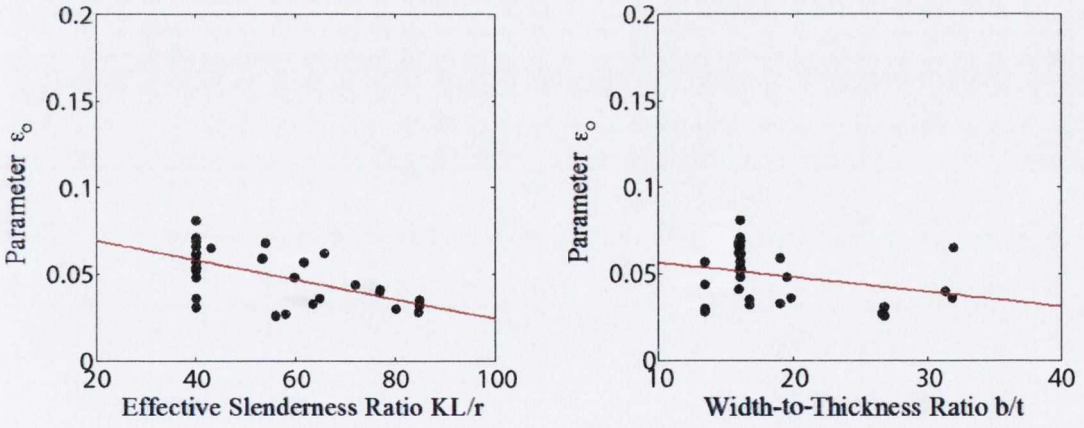

(a) (b)

Figure 4.16 – Influence of effective slenderness ratio and width-to-thickness ratio on ε_0 and m parameters (Lignos et al., 2012).

4.3.2 Correlation Study

Although hollow cold-formed members are effective at resisting compressive axial loads, the onset of local buckling can prevent the steel from developing its full yield strength in compression,

reduce ductility and may lead to brittle failure (Uy, 1998). Thin-walled sections are most susceptible to local buckling as the occurrence of local buckling in struts is influenced by section properties such as width-to-thickness ratio. Studies have been performed on the hysteretic response of steel braces that examined the effect of brace slenderness, cross-sectional shape and end conditions on buckling capacity (Black et al., 1980; Tremblay et al., 2003). Their main findings showed that the slenderness of a brace appears to be the most important factor in determining the hysteretic behaviour and their ductility is reduced significantly due to local buckling in the sections. Therefore, to assess the capabilities of OpenSees, numerical models were compared with experimental results conducted by Goggins (2004) which considered specimens with a range of global and local slendenesses.

The three section shapes tested by Goggins (2004) were 40×40×2.5 SHS, 20×20×2.0 SHS and 50×25×2.5 RHS and are all classified as or Class 1 cross-sections according to Eurocode 3 (CEN, 2005a). The specimen details used in the correlation study are scheduled in Table 4.3. Boundary conditions for the specimens were fully fixed in all directions for all of the cyclic displacement tests. The non-dimensional slenderness ratio $\bar{\lambda}$ was calculated about the weak axis providing a normalised ratio of the slenderness of each specimen. Eurocode 3 [12] defines $\bar{\lambda}$ as $(N_{pl,Rd}/N_{cr})^{0.5}$ where $N_{pl,Rd}$ is the plastic section resistance and N_{cr} is the theoretical (Euler) elastic critical buckling force based on the gross section properties and effective length. Stiffener plates with 8 mm thickness and 125 mm height run through the centre of the faces of the hollow steel sections along the y-axis in order to influence the direction of buckling. The length of the specimens (L_T) was 1100 mm but the stiffener plates provided an unstiffened length (L_O) of 850 mm for all specimens (see Figure 4.17).

Table 4.3 - Correlation study specimen details (Goggins, 2004).

	L_O (mm)	L_T (mm)	$\bar{\lambda}$	b/t
40×40×2.5 SHS	850	1100	0.4	16
20×20×2.0 SHS	850	1100	0.9	10
50×25×2.5 RHS	850	1100	0.6	20

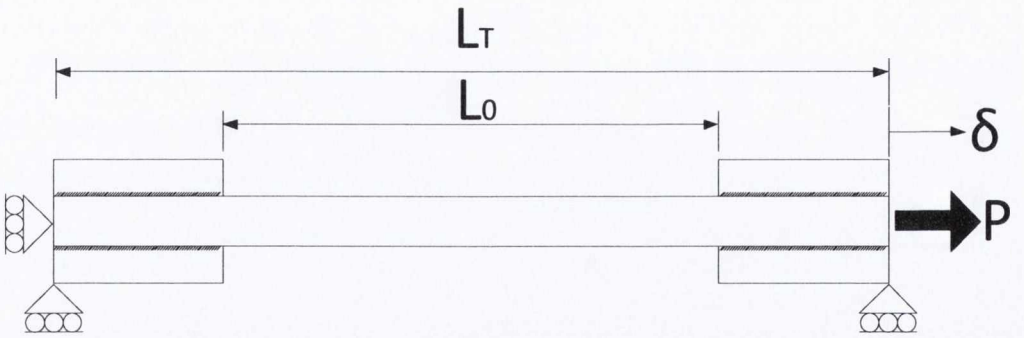

Figure 4.17 – Test specimen dimensions from Goggins (2004).

The OpenSees model implements the recommendations concluded from the parametric study in Section 4.2: a geometrical brace camber of 0.1% is prescribed; four elements are defined for the brace span L_0; five integrations points are used for each nonlinear element. Furthermore eight fibre sections are used across the section thickness with two fibres around the section perimeter. As before, the Giuffré-Menegotto-Pinto material model is used to represent the uniaxial stress-strain relationship of the steel. The steel model uses fibre sections with a combined linear kinematic and isotropic hardening material model. Values for yield strength and the Young's modulus were determined from the material strength coupon tests carried out by Goggins.

Two specimen pairs of each specimen type were tested by Goggins (2004) to assess their buckling capacity, hysteretic performance and overall ductility. The results of three tests are compared in Figure 4.18 to Figure 4.20 which show the force-axial displacement hysteresis for the 40×40×2.5 SHS, 20×20×2.0 SHS and the 50×25×2.5 RHS specimens respectively.

The 40×40×2.5SHS specimens experienced uniaxial buckling and failed by a combination of both overall lateral buckling and local buckling at plastic hinge mechanisms located at mid-length and close to the end stiffeners. Comparison of the hysteretic response of the 40×40×2.5SHS specimens in Figure 4.18 shows very reasonable fidelity to the experimental results. In the tensile half-cycle range the numerical analysis agrees very well with peak tensile loads nearly identical to those of the experiment. The only loss of information occurs in the later cycles of increased displacement demand, with minimally lower peak tensile load predictions. In the compressive loading range, the initial buckling load matches closely to the test result. This continues for peak compression loads up to a target displacement of approximately -9.4 mm. Thereafter, there is an over-estimation in the prediction of compressive capacity. This can be accounted for by the model's inability to represent local buckling. In these cycles, the strength of the cross section at the plastic hinge has been significantly affected by the presence of local buckling. It was anticipated that this phenomenon

would be mitigated using the 20×20×2.0 SHS section due to its lower b/t ratio. Using the default value for ε_0, the fatigue material predicted fracture one displacement target cycle ahead of experimental fracture initiation. The mean value (0.12) established by Santagati et al. (2012) led to fracture prediction 5 cycles earlier than the actual fatigue life of the brace. Through an iterative procedure, an ε_0 strain parameter value of 0.167 was found to match the numerical prediction of fracture with the experimentally-observed fracture cycle. Rapid strength loss is triggered at the same displacement amplitude cycle at approximately +15 mm.

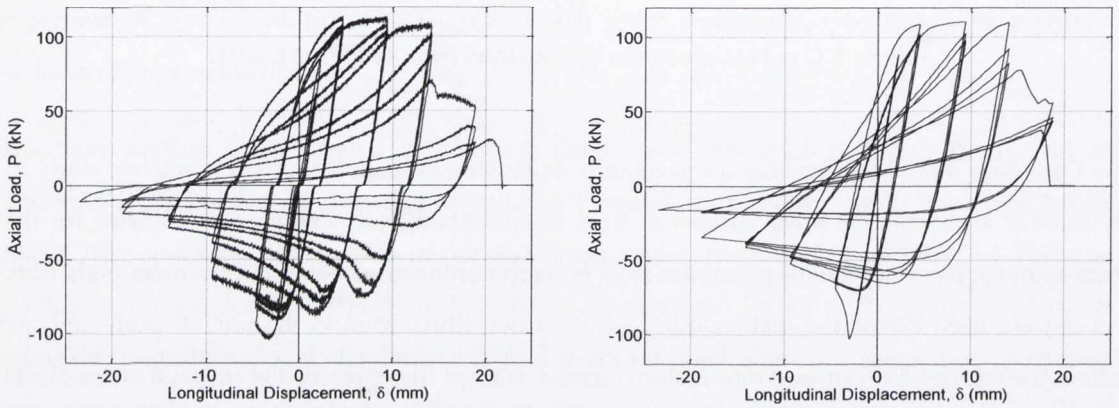

(a) experimental (Goggins, 2004) (b) numerical analysis

Figure 4.18 – Hysteretic response correlation of 40x40x2.5 SHS specimens.

The non-dimensional slenderness value of the 20×20×2.0SHS specimens is the highest, and the sectional slenderness ratio, b/t, the lowest of the three sections tested, leading to the specimen failing without experiencing local buckling. This is reflected in the numerical model results in Figure 4.19 where both the tensile and compressive resistances agree closely with the experimental results. Strength degradation is also represented very accurately during successive loading cycles with the inclusion of the Bauschinger effect in the steel material, where the yield strength of the material decreases following a prestrain in the reverse direction. This effect is particularly refined in the tensile loading cycles. The only exception to this can be seen in the compressive loading range where the compressive resistance over-estimation was still present but had been significantly minimised as discussed above. The specimen maintains a concave stiffness curve which is also reasonably represented in the numerical model. Although necking resulted in a reduction in cross section in these specimens, this had negligible effects on the numerical model results. Experimental failure occurred on the first tensile displacement cycle approaching +23 mm. Similar to the 40×40×2.5 specimen, the default values for the fatigue model predicts fracture ahead of the experimental value, in this case 4 cycles after experimental fracture. The mean value for the fatigue ductility coefficient ($\varepsilon_0 = 0.12$) simulated failure 4 cycles before experimental failure, however the value $\varepsilon_0 = 0.165$ showed greatest fidelity to the brace hysteretic performance.

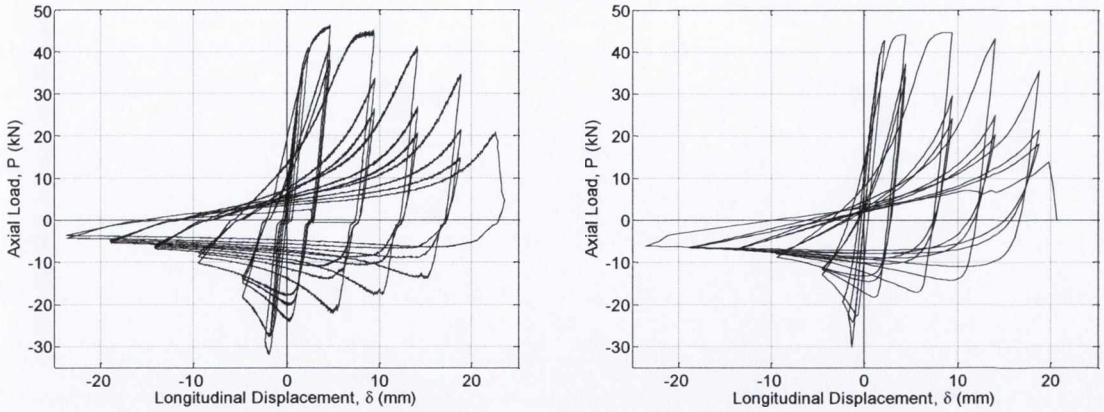

(a) experimental (Goggins, 2004) (b) numerical analysis

Figure 4.19 – Hysteretic response correlation of 20×20×2.0 SHS specimens.

The experimental response of the 50×25×2.5RHS was similar to that of the 40×40×2.5SHS specimen. Due to a larger slenderness value, the combination of both overall lateral buckling and local buckling at plastic hinges did not prove difficult to replicate in the numerical model. In this analysis, the over-prediction of the residual compressive strength was not as great (Figure 4.20). As before, the reduction in compressive resistance in the specimen is explained by the accumulated longitudinal strains at plastic hinge locations. Similar to the 40×40×2.5SHS specimen, peak tensile loads corresponded very well with the tensile strength evolution of the experimental specimen. The use of the default value of the fatigue material model predicts fracture one cycle ahead of experimental fracture and overestimates residual tensile section strength. A recommended value of $\varepsilon_0 = 0.163$ produced a very accurate fatigue life prediction, only one half cycle ahead of actual brace failure.

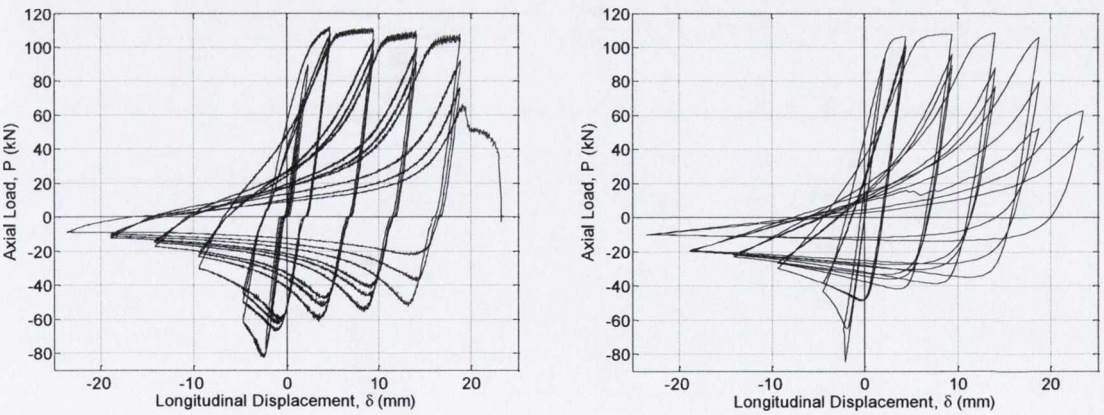

(a) experimental (Goggins, 2004) (b) numerical analysis

Figure 4.20 – Hysteretic response correlation of 50×25×2.5 RHS specimens.

Overall, the results in Figure 4.18 to Figure 4.20 display excellent agreement between the experimental and numerical responses, validating the prediction capabilities of OpenSees for single hollow section steel brace members under cyclic loading.

4.4 Chapter Overview

This chapter introduced the OpenSees finite element software that is used for modelling brace-gusset plate test specimens and CBF test frames in this research project. First, the stiffness and flexibility methods were reviewed followed by a parameter study on brace member modelling. Important modelling parameters highlighted in previous research were examined for application to this study. Using the recommended parameters, a general brace model is presented which includes the modelling of fracture due to fatigue. This general brace model is correlated with quasi-static cyclic loading tests. In Chapter 7, the methods employed to implement the single brace member model within a full CBF system are described with a correlation study of the Complementary Cyclic Tests. In Chapter10 the OpenSees models are used in dynamic analyses that are carried out for comparison with experimental shake table tests.

5 Complementary Cyclic Tests – Experimental Program and Setup

5.1 Introduction

This chapter presents the experimental setup and programme for a series of quasi-static cyclic loading tests on a model CBF with different combinations of connection types and brace sizes. The behaviour of selected hollow section brace sizes with two different connection types designed using two gusset plate design methods investigated. These experiments were undertaken in the Structures Laboratory at Trinity College Dublin (TCD), to act as complementary tests for the shake table tests carried out at CEA Saclay as part of the BRACED project (Chapter 8), and to support the development of OpenSees finite element models for this form of structure (Chapter 4).

5.2 Preliminary Experimental Considerations

The experimental programme was designed to match as closely as possible the test conditions planned for the BRACED project at CEA Saclay. Thus, different types of full-scale gusset plate connections were tested, in each case using a single diagonal brace member. The test parameters examined the following variables: brace size, gusset plate and geometry (G1 and G2); and gusset plate connection conditions (CA and CB).

Brace slenderness values were similar to those subsequently examined in the BRACED specimens. This was achieved by using similar and slightly smaller brace cross-section sizes, limiting brace length and inclination angle. In line with actuator capacity, section sizes were limited to a maximum of 60×60×2.5 SHS. Although 60×60×3.0 section size was used in the BRACED project, it was not readily available from suppliers at the time of carrying out the complementary tests.

The gusset plates connections were fixed to the beam and column members of the test frame using a bolted connection to allow for straightforward installation and removal of specimens and an efficient turnaround between tests (Figure 5.1). The same arrangement was envisaged for the BRACED shake table experiments, and the Complementary Tests provided an essential prior validation of this approach. In contrast to the shaking table tests, however, the brace members were welded to the gusset plates in situ, i.e. after the gusset plates flanges had been bolted to the test frame. This was done to accommodate larger fabrication and erection tolerances. The brace member tubes were slotted to ensure that this was performed without preloading the brace specimens prior to testing.

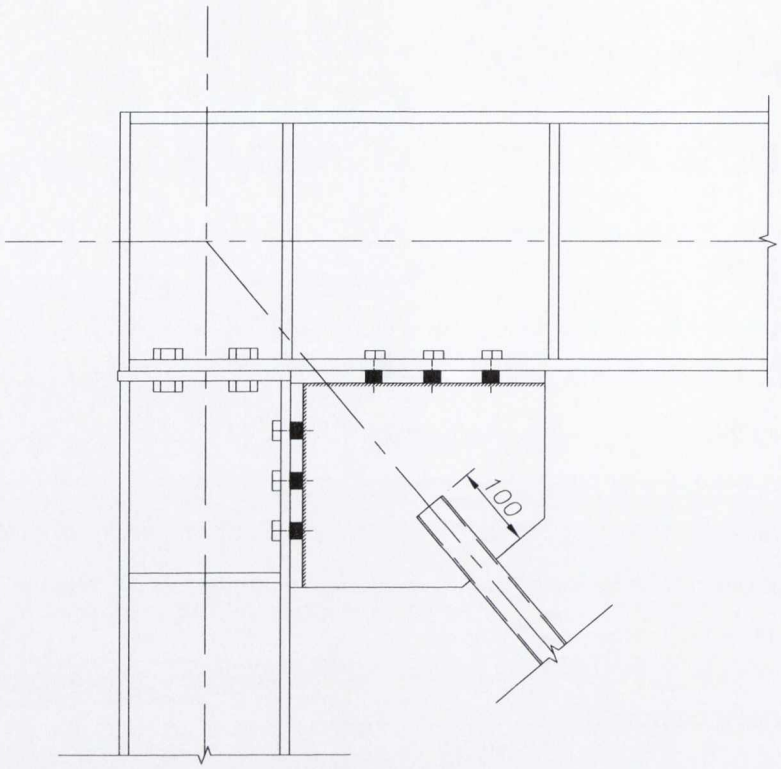

Figure 5.1 – Modified beam-column connection for cyclic tests.

The test frame that was used to test the specimens had previously been used to test an X-braced CBF system. Therefore modifications were carried out to accommodate suitable connections for the cyclic tests. The original frame setup is shown in Figure 5.2 before augmentations took place. The original frame featured short lengths of UC 'column stubs' at the column-ground connections and at the beam-column connections creating pinned connections at these locations. The connections of the BRACED frame required more realistic beam-column connections with the column end plates bolted directly to the beam flange. As a result the short column lengths at the top of the support columns were removed and the beam was bolted directly to the column (Figure 5.1).

To compensate for the loss in frame height due to the removal of the top column lengths, the frame was raised using similar short column lengths that were reinforced with 12 mm thick stiffener plates, ensuring a rigid base connection to the reaction frames. This arrangement was selected to maintain a similar inclination of the brace member and overall frame height to that of the BRACED frame. Also, by eliminating the need to move the actuator, time required to calibrate instrumentation was minimised.

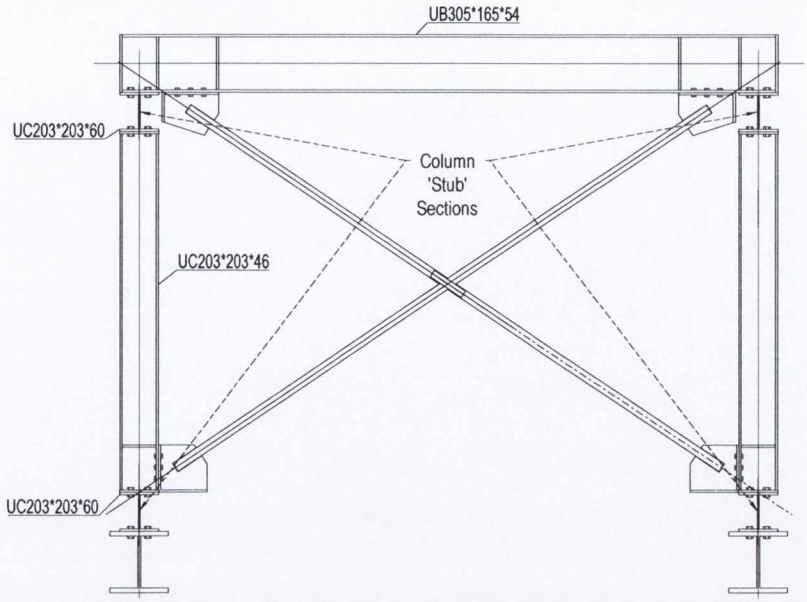

Figure 5.2 – Original X-braced frame configuration prior to complementary tests.

5.3 Experimental Specimens and Parameters

Six tests were carried out each featuring a different combination of gusset plate sizes (G1 and G2 influencing drift and β_{ww}), gusset plate constraints (CA and CB influencing frame stiffness K_{fr}) and brace sizes (S40 and S60 influencing non-dimensional slenderness $\bar{\lambda}$). The gusset plate and brace specimens were fitted to a single storey plane frame forming a CBF structure (Figure 5.3).

The testing facility at TCD consists of a MTS actuator system (MTS Systems Corporation) and parallel reaction frames. The MTS hardware comprises of a Series 111 MTS Accumulator and a high speed linear hydraulic actuator with a 150 kN capacity, 250 mm (± 125 mm) stroke and pinned bearings at both ends. The actuator was fixed to in-plane dual reaction frames and then fitted to the top left corner of the test frame to apply a horizontal cyclic force. The specimens were tested in the single-storey plane frame through a cyclic inelastic deformation history based on the ECCS (1986) testing protocol. The response during the initial cycles in the elastic range were used to determine the elastic stiffness and yield displacement of the structure, while repeated inelastic deformation cycles at increasing ductility levels determined compressive and tensile strengths and strength degradation.

The tests were designed to explore the key design considerations for CBF braces and connections, specifically with both high and low ranges of β_{ww}occurring from the gusset design methods. The specific influential parameters are outlined in Table 5.1 and a drawing of Specimen S40-CA-G1 showing typical dimensions is shown in Figure 5.6. Time and cost limitations permitted six tests to be carried out. As a result the S60-CB combination was not included, as large frame rotations were expected (and hence frame deformation) and it was to be tested in the BRACED project.

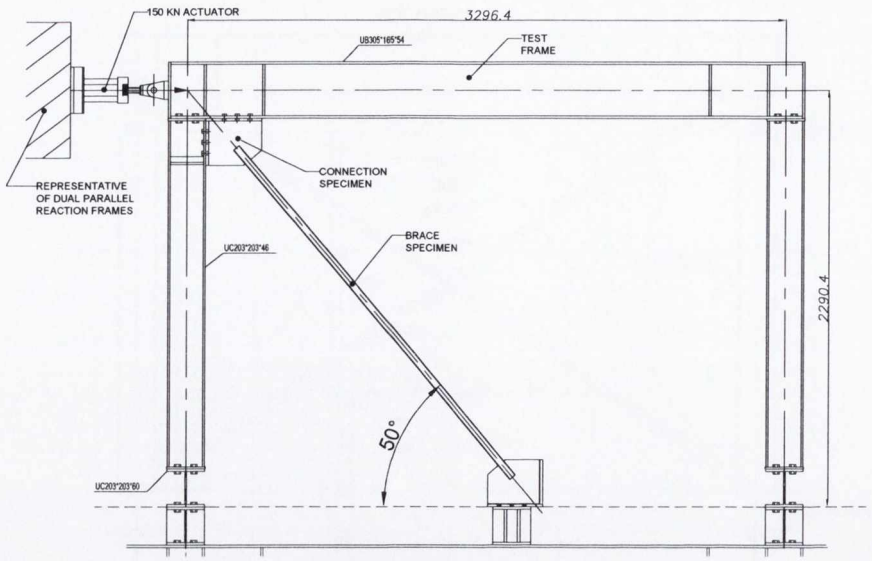

(a)

(b)

Figure 5.3 – Cyclic Test Configuration Setup with (a) schematic and (b) photograph.

Table 5.1 – Programme for cyclic testing of brace members with gusset plates connections.

Specimen	Brace Section Size	Conn-ection Type	Clearance Model	t_p (mm)	b_{ww} (mm)	l_h (mm)	l_v (mm)	Brace Length, L_b (mm)	β_{ww}
S40-CA-G1	40×40×2.5	CA	Standard ($3t_p$)	8	155	285	240	2368	0.38
S40-CA-G2	40×40×2.5	CA	Elliptical ($8t_p$)	4	155	270	230	2503	0.75
S40-CB-G1	40×40×2.5	CB	Standard ($3t_p$)	8	155	265	240	2368	0.38
S40-CB-G2	40×40×2.5	CB	Elliptical ($8t_p$)	4	155	250	230	2503	0.75
S60-CA-G1	60×60×2.5	CA	Standard ($3t_p$)	8	175	285	240	2368	0.52
S60-CA-G2	60×60×2.5	CA	Elliptical ($8t_p$)	4	175	270	230	2467	1.03

One of the key requirements for the cyclic test programme was to replicate, as closely as possible, the design of the BRACED shake table test frame. In this respect, the two main connection types to be examined in the shaking table tests were also investigated in the complementary cyclic test programme, as shown in Figure 5.4. In connection type A (CA), the gusset plate flanges are bolted

to both the column flange and beam flange, effectively restraining the gusset plate on two sides (see Section 3.4). In connection type B (CB) the gusset is connected to the beam flange only which allows free plate rotation in the out-of- plane direction, and less restraint against beam-to-column joint rotation.

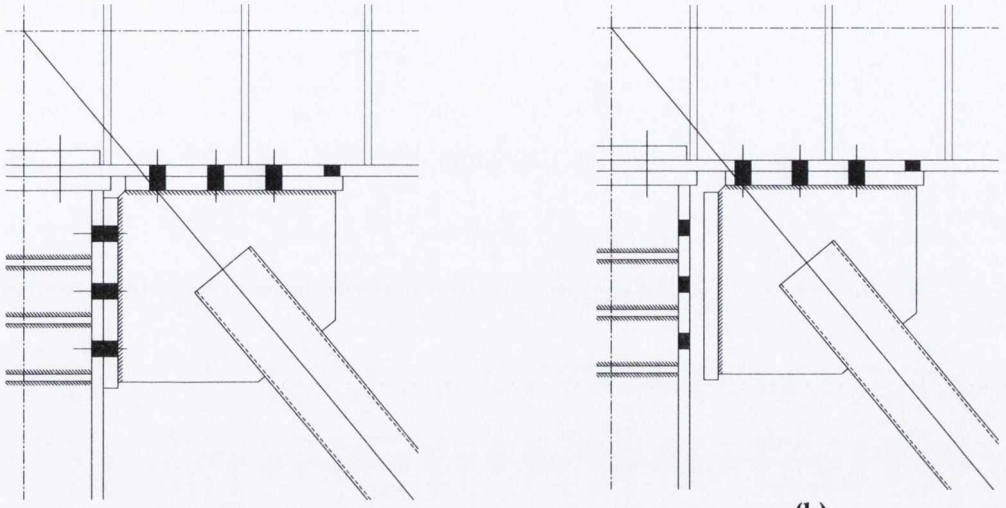

Figure 5.4 – Schematic of (a) connection type CA (b) and connection type CB.

The 150 kN capacity of the MTS actuator (Figure 5.5) constrained the maximum axial load that could be imposed on the brace member and its gusset plates. Therefore, to allow investigation of ultimate response, the maximum brace section sizes for the complementary tests were limited to the smallest section size planned to be used the shake table tests (60×60×2.5 SHS). The square hollow sections and gusset plates were manufactured from cold formed S235JRH steel, with a nominal yield strength of 235 MPa and an ultimate strength between 360 and 510 MPa (CEN, 2006a).

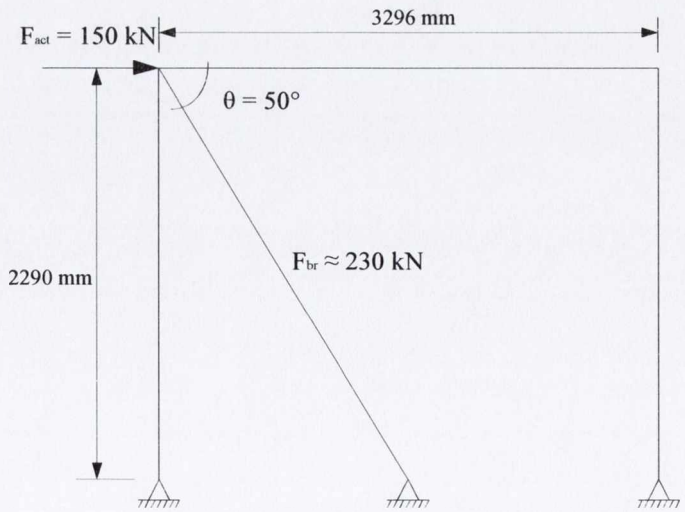

Figure 5.5 – Complementary cyclic test frame; primary forces.

Given an actuator capacity $F_{act} = 150kN$, and an inclination angle of $\theta = 50°$ the resultant maximum theoretical applied force is as follows:

$$F_{br} = \frac{F_{act}}{\cos(\theta)} = \frac{150}{\cos(50)} \approx 230\ kN \qquad 5.1$$

Therefore, based on the Eurocode 3 (CEN, 2005a) section resistances calculated in Table 5.2 (design plastic capacity $N_{pl,Rd}$ and design buckling capacity $N_{b,Rd}$), 40×40×2.5 and 60×60×2.5 SHS brace sizes were selected for testing. These capacities are based on the nominal yield strengths stated above. $\bar{\lambda}$ values are based on assumed theoretical effective length factors $K = 0.7$ for CA and $K = 1.0$ for CB connections.

Table 5.2 – Complementary cyclic test section resistances based on nominal yield strengths.

Specimen	b/tε	$\bar{\lambda}$	$N_{pl,Rd}$ (kN)	$N_{b,Rd}$ (kN)
S40-CA-G1	16	1.16	86.5	48.0
S40-CA-G2	16	1.23	86.5	44.4
S40-CB-G1	16	1.66	86.5	27.0
S40-CB-G2	16	1.75	86.5	24.5
S60-CA-G1	24	0.75	133.5	101.3
S60-CA-G2	24	0.80	133.5	97.9

5.3.1 Gusset Plate Designs

Standard gusset plate design principles are dealt with primarily in a conceptual manner in Eurocode 8 (CEN, 2004a) leaving designers to adopt details available from current literature (Elghazouli, 2009). For both of the connection types (CA and CB), considered in the experimental programme, two gusset plate design methods were investigated: the conventional design method and the balanced design method. Specimens designed using the conventional method are designated as 'G1', and the Standard Linear Clearance (SLC) model (AISC, 2005a) is used detail the gusset plate to ensure that a stable plastic hinge forms in the gusset plate during brace buckling, as illustrated in Figure 5.6. Specimens designed using the balanced method are designated as 'G2', and the Elliptical Clearance (EC) model (Lehman et al., 2008) is used to detail the gusset plate. The EC model leads to more compact gusset plates than the SLC method, providing the shorter plate buckling lengths required to avoid buckling in the thinner gusset plates that a feature of balanced design.

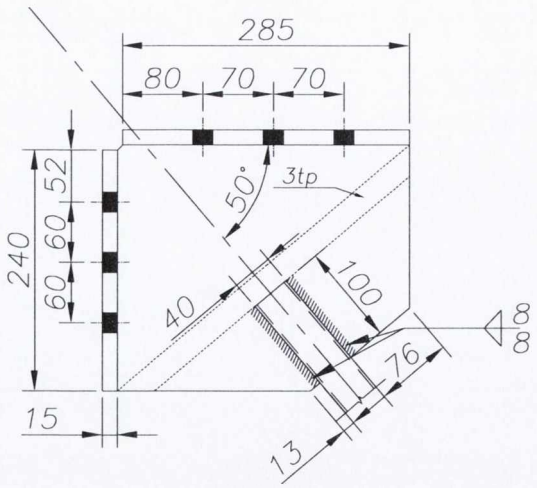

Figure 5.6 – Specimen S40-CA-G1 details.

During the design and detailing of all gusset plates, the length of the weld joining the brace tube to gusset plate was kept constant at 100 mm to reduce variability (Figure 5.6). The calculated Whitmore width, b_{ww}, is a function of this weld length and width of the brace section. For G1 designs, gusset plate thickness, t_p, is selected to ensure that the factored design resistances, for each connection failure mode, are greater than the axial force capacity of the brace member ($N_{pl,Rd,Brace}$) with the overstrength factor (γ_{ovr}) applied. At gusset plate tensile yielding:

$$N_{pl,Rd,Gusset} \geq \gamma_{ovr}(N_{pl,Rd,Brace}) = \gamma_{ovr}(Af_y) \qquad 5.2$$

where A is the section area (determined by b_{ww} and t_p) and f_y is the specified yield stress (i.e. the yield resistance of the connection is designed to be stronger than that of the brace member). Consideration of the tensile resistances of the brace members in Table 5.3 leads to a selected t_p value of 8 mm. This value for t_p leads to low β_{ww} values that are associated with the large, stiff connections associated with the conventional design approach. The β_{ww} ratios presented in Table 5.3 were calculated in accordance with Equation 3.7. As discussed in Section 3.3, the pertinent R_y values are obtained from the AISC Seismic Provisions for the equivalent materials used in this programme. In this case the R_y values were 1.4 and 1.1 for the brace tubes and gusset plates respectively.

The design procedure for G2 plates used the geometrical design recommendation as set out by (Lehman et al., 2008) to establish plate dimensions l_h and l_v. An $8t_p$ offset was used for the shape of the elliptical yield line. The Whitmore width was calculated as before for use in the section resistance calculations. To achieve β_{ww} ratios that approach 1.0, a plate thickness of 4 mm was specified. As the strength balancing method concerns tensile yielding only, all the gusset plate buckling resistances were checked to ensure they were greater than the buckling capacity of the brace tubes.

Table 5.3 – SLC and EC Design Parameters (with design capacities).

Clearance Design Method	Section Size (SHS)	Brace $N_{pl,Rd}$ (kN)	b_{ww} (mm)	t_p (mm)	Gusset $N_{pl,Rd}$ (kN)	β_{ww}
G1 (SLC)	**40×40×2.5**	86.5	155	8	292.3	0.38
	60×60×2.5	133.5	175	8	329.9	0.52
G2 (EC)	**40×40×2.5**	86.5	155	4	146.1	0.75
	60×60×2.5	133.5	175	4	164.9	1.03

5.4 Experimental Preparation Procedures

5.4.1 Material Coupon Tests

The design strength, f_y, of the brace-gusset plate specimens was 235 N/mm² except for the flange plates welded to the gusset plates for which a yield strength of 275 N/mm² was specified to prevent yielding. Thus, the steel ordered for the brace tube was cold formed S235 JRH; the gusset plates comprised hot rolled sheet S235JR plates; and the gusset connection plate cleats were hot rolled sheet S275JR plates.

Mill test reports (CEN, 2004c) quoted upper yield strengths, R_{eH}, tensile strengths, R_m, and elongation ratios, A, for each of the steel types used. These values are reported in Table 5.4. Material coupon tests were carried out to determine the actual tensile yield and ultimate strengths of the steel brace tubes and gusset plates. Coupon shapes were machined from the 40×40×2.5 and 60×60×2.5 SHS tube lengths and from the 4 mm and 8 mm gusset plates. The longitudinal tensile coupons were tested as specified by the European Standard BS EN ISO 6892-1 (CEN, 2009) for tensile testing of metallic materials. The cross section of all the test pieces was maintained as a rectangular cross sectional area, S_o (Figure 5.7). In the ISO 6892-1 standard, preferred test pieces have an original gauge length, L_o, that is proportional to S_o. In this series of tests, non-proportional test pieces were used due to limited length of available material.

Table 5.4 – Material Properties from mill certificates.

Component	Grade	R_{eH} (MPa)	R_m (MPa)	R_m/R_{eH}	A (%)
40×40×2.5 SHS Tube	S235JRH	323	400	1.23	43
60×60×2.5 SHS Tube	S235JRH	353	422	1.19	26
Gusset Plates	S235JR	260	422	1.61	33
Flange Plates	S275JR	284	419	1.47	35

The coupon shape prescribes a transition radius between the gripped ends and the parallel length L_C, to restrict the material strain to the original gauge length. The original gauge length, L_o, was marked using finely scribed lines to an accuracy of ± 1 %. The original cross sectional area S_o is calculated as the average of three cross section measurements for each test piece. Three test pieces were machined from the faces of the brace tube sections with the exception of the face containing the seam weld and tested to establish the steel characteristic properties (Faces A, B and C in Table 5.7 and Table 5.8). This was carried out for both section sizes resulting in six test samples for the brace tubes. Two test pieces were cut from the pair of gusset plates that were used at the top and bottom connections of each specimen (Plates A and B respectively, as in Table 5.9 to Table 5.14). Using these properties, plastic and buckling capacities were calculated for the brace sections and are presented in Table 5.6 for reference. As the gusset plate dimensions varied between specimens, the test pieces were cut along the longest side. This resulted in twelve test pieces in total for the gusset plates. The dimensions for each test piece type are summarised in Table 5.5 below as per the relevant appendix of BS EN ISO 6892-1:2009.

Table 5.5 – Coupon test piece dimensions.

Component	Specimen Type	L_t (mm)	L_c (mm)	L_o (mm)	b_o (mm)	B (mm)	r (mm)	a_o (mm)	S_o (mm²)
Brace Tube	40×40×2.5	298.3	75	55	12.5	20	20	2.5	31.25
	60×60×2.5	298.3	75	55	12.5	20	20	2.5	31.25
Gusset Plate	G1	Varies	90	80	20	30	12	8	160
	G2	Varies	90	80	20	30	12	4	80

The test samples were tested to failure in a 250 kN Denison Universal Testing Machine (Model No. T42B4). The test pieces were held in place using jaw grips to ensure that the tensile force is applied along the longitudinal axis so that bending is minimised. An extensometer of 50 mm gauge length was clamped to the specimen and used to control the longitudinal strain rate, $\dot{e}_{L_e}$. In the ranges where yielding has finished a second estimated strain rate, $\dot{e}_{L_c}$, measured over the parallel length, L_c, is used. The parallel length strain rate $\dot{e}_{L_c}$ is achieved by controlling the crosshead separation rate, v_c, at a velocity that is equal to the desired strain rate multiplied by L_c.

In the range up to the determination of the upper yield strength, R_{eH}, the 0.2 % plastic proof strength (plastic extension only), $R_{p,0.2}$, and the 0.5 % total proof strength (elastic and plastic extension) $R_{t,0.5}$ the strain rate $\dot{e}_{L_e}$ was set to 0.00025 s^{-1}. For the ranges following this (lower yield strength, R_{eL}, and tensile strength, R_m), the strain rate $\dot{e}_{L_c}$ was set to 0.002 s^{-1}. In reference to BS EN ISO 6892-1, the test control modes can be abbreviated as ISO 6892-1:2009 A233. The values for R_{eH},

R_{eL}, $R_{p,0.2}$, $R_{t,0.5}$ and R_m were all determined from the force extension curves of each test with the proof strengths based on the specified percentages of the initial extensometer gauge length L_e (where $0.5L_o \leq L_e \leq 0.9L_c$). The percentage elongation after fracture, A, expressed as a percentage of L_o was determined as follows:

$$A = \frac{L_u - L_o}{L_o} \times 100 \qquad 5.3$$

where L_u is the final gauge length between the scribe marks measured after rupture. This is measured ensuring the pieces fit back together in order that their axes lie in a straight line. In addition, the percentage reduction in cross section area was defined as:

$$Z = \frac{S_o - S_u}{S_o} \times 100 \qquad 5.4$$

where S_u is the minimum cross sectional area after fracture.

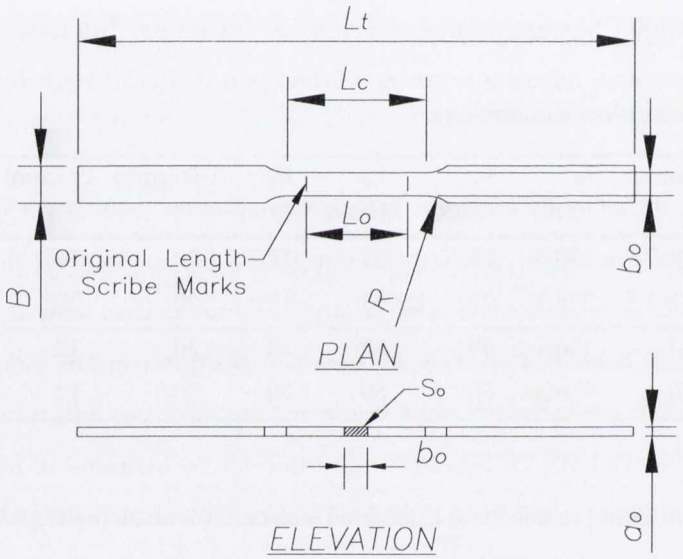

Figure 5.7 – Machined test piece dimensions for rectangular cross sections.

Table 5.6 – Complementary test section capacities based on yield strengths from coupon tests.

Specimen	$N_{pl,coup}$ (kN)	$N_{b,coup}$ (kN)
S40-CA-G1	129.4	52.8
S40-CA-G2	129.4	48.1
S40-CB-G1	129.4	28.1
S40-CB-G2	129.4	25.3
S60-CA-G1	191.3	140.0
S60-CA-G2	191.3	133.4

Table 5.7 – Measured results of 40×40×2.5 SHS tube coupon tests.

Face	L_c (mm)	L_o (mm)	L_u (mm)	L_t (mm)	$\bar{a}_o$ (mm)	$\bar{b}_o$ (mm)	$\bar{S}_o$ (mm²)	$\bar{a}_u$ (mm)	$\bar{b}_u$ (mm)	$\bar{S}_u$ (mm²)	R_{eH} (MPa)	R_m (MPa)	R_m/R_{eH}	A (%)	Z (%)
A	75	55	63.67	332.5	2.33	12.11	28.21	1.39	8.36	11.62	329.69	375.77	1.14	15.76	58.81
B	75	55	63.78	314.2	2.31	12.39	28.66	1.28	8.51	10.89	355.87	436.11	1.23	15.96	62.00
C	75	55	61.73	323	2.33	12.19	28.40	1.39	9.73	13.52	369.68	440.10	1.19	12.24	52.38
Mean	*75*	*55*	*63.06*	*323.23*	*2.32*	*12.23*	*28.42*	*1.35*	*8.87*	*12.01*	*351.75*	*417.33*	*1.19*	*14.65*	*57.73*
StDev	*0*	*0*	*1.15*	*9.15*	*0.01*	*0.15*	*0.23*	*0.06*	*0.75*	*1.36*	*20.31*	*36.04*	*0.04*	*2.10*	*4.90*
C_v	*0.000*	*0.000*	*0.018*	*0.028*	*0.004*	*0.012*	*0.008*	*0.047*	*0.085*	*0.113*	*0.058*	*0.086*	*0.036*	*0.143*	*0.085*
P-Value											*0.134*	*0.493*	*0.238*	*0.002*	

Table 5.8 – Measured results of 60×60×2.5 SHS tube coupon tests.

Face	L_c (mm)	L_o (mm)	L_u (mm)	L_t (mm)	$\bar{a}_o$ (mm)	$\bar{b}_o$ (mm)	$\bar{S}_o$ (mm²)	$\bar{a}_u$ (mm)	$\bar{b}_u$ (mm)	$\bar{S}_u$ (mm²)	R_{eH} (MPa)	R_m (MPa)	R_m/R_{eH}	A (%)	Z (%)
A	75	55	69.57	318.1	1.83	12.41	22.75	1.06	8.35	8.85	329.65	342.83	1.04	26.49	61.10
B	75	55	69.01	318.5	1.88	12.25	23.08	1.05	8.89	9.33	390.00	400.83	1.03	25.47	59.55
C	75	55	68.97	312.9	1.79	12.47	22.36	1.11	8.65	9.60	290.66	353.26	1.22	25.4	57.06
Mean	*75*	*55*	*69.18*	*316.5*	*1.84*	*12.38*	*22.73*	*1.07*	*8.63*	*9.26*	*336.77*	*365.64*	*1.09*	*25.79*	*59.24*
StDev	*0*	*0*	*0.34*	*3.12*	*0.05*	*0.11*	*0.36*	*0.03*	*0.27*	*0.38*	*50.05*	*30.92*	*0.10*	*0.61*	*2.03*
C_v	*0.000*	*0.000*	*0.005*	*0.010*	*0.025*	*0.009*	*0.016*	*0.030*	*0.031*	*0.041*	*0.149*	*0.085*	*0.096*	*0.024*	*0.034*
P-Value											*0.631*	*0.087*	*0.270*	*0.606*	

Table 5.9 – Measured results of S40-CA-G1 (Test 1) gusset coupon tests.

Plate	L_c (mm)	L_o (mm)	L_u (mm)	L_t (mm)	$\bar{a}_o$ (mm)	$\bar{b}_o$ (mm)	$\bar{S}_o$ (mm²)	$\bar{a}_u$ (mm)	$\bar{b}_u$ (mm)	$\bar{S}_u$ (mm²)	R_{eH} (MPa)	R_m (MPa)	R_m/R_{eH}	A (%)	Z (%)
Upper	90	80	110.37	274	7.91	19.68	155.73	3.35	12.41	41.57	295.37	404.53	1.37	37.96	73.30
Lower	90	80	109.13	274	7.93	19.42	154.04	3.44	12.24	42.11	246.69	383.02	1.55	36.41	72.67
Mean	*90*	*80*	*109.75*	*274.00*	*7.92*	*19.55*	*154.89*	*3.40*	*12.33*	*41.84*	*271.03*	*393.78*	*1.46*	*37.19*	*72.99*
StDev	*0.00*	*0.00*	*0.88*	*0.00*	*0.01*	*0.19*	*1.20*	*0.06*	*0.12*	*0.38*	*34.42*	*15.21*	*0.13*	*1.10*	*0.45*
C_v	*0.00*	*0.00*	*0.01*	*0.00*	*0.00*	*0.01*	*0.01*	*0.02*	*0.01*	*0.01*	*0.13*	*0.04*	*0.09*	*0.03*	*0.01*
P-Value											*0.729*	*0.232*	*0.351*	*0.117*	

Table 5.10 – Measured results of S40-CA-G2 (Test 2) gusset coupon tests.

Plate	L_c (mm)	L_o (mm)	L_u (mm)	L_t (mm)	$\bar{a}_o$ (mm)	$\bar{b}_o$ (mm)	$\bar{S}_o$ (mm²)	$\bar{a}_u$ (mm)	$\bar{b}_u$ (mm)	$\bar{S}_u$ (mm²)	R_{eH} (MPa)	R_m (MPa)	R_m/R_{eH}	A (%)	Z (%)
Upper	90	80	96.82	264.18	4.01	20.07	80.53	2.60	15.24	39.62	285.59	347.68	1.22	21.03	50.80
Lower	90	80	99.55	265.45	4.01	19.95	79.95	2.44	14.48	35.33	337.73	445.30	1.32	24.44	55.81
Mean	*90*	*80*	*98.19*	*264.82*	*4.01*	*20.01*	*80.24*	*2.52*	*14.86*	*37.48*	*311.66*	*396.49*	*1.27*	*22.73*	*53.30*
StDev	*0.00*	*0.00*	*1.93*	*0.90*	*0.00*	*0.08*	*0.42*	*0.11*	*0.54*	*3.04*	*36.86*	*69.03*	*0.07*	*2.41*	*3.54*
C_v	*0.00*	*0.00*	*0.02*	*0.00*	*0.00*	*0.00*	*0.01*	*0.04*	*0.04*	*0.08*	*0.12*	*0.17*	*0.06*	*0.11*	*0.07*
P-Value											*0.298*	*0.693*	*0.093*	*0.105*	

Table 5.11 – Measured results of S40-CB-G1 (Test 3) gusset coupon tests.

Plate	L_c (mm)	L_o (mm)	L_u (mm)	L_t (mm)	$\bar{a}_o$ (mm)	$\bar{b}_o$ (mm)	$\bar{S}_o$ (mm²)	$\bar{a}_u$ (mm)	$\bar{b}_u$ (mm)	$\bar{S}_u$ (mm²)	R_{eH} (MPa)	R_m (MPa)	R_m / R_{eH}	A (%)	Z (%)
Upper	90	80	108.78	256	7.96	19.74	157.04	3.62	12.42	44.96	280.19	395.45	1.41	35.98	71.37
Lower	90	80	109.51	254.49	8.02	19.50	156.30	3.49	11.98	41.81	287.91	385.16	1.34	36.89	73.25
Mean	*90*	*80*	*109.15*	*255.25*	*7.99*	*19.62*	*156.67*	*3.56*	*12.20*	*43.39*	*284.05*	*390.30*	*1.37*	*36.43*	*72.31*
StDev	*0.00*	*0.00*	*0.52*	*1.07*	*0.04*	*0.17*	*0.52*	*0.09*	*0.31*	*2.23*	*5.46*	*7.27*	*0.05*	*0.65*	*1.33*
C_v	*0.00*	*0.00*	*0.00*	*0.00*	*0.01*	*0.01*	*0.00*	*0.03*	*0.03*	*0.05*	*0.02*	*0.02*	*0.04*	*0.02*	*0.02*
P-Value											*0.101*	*0.102*	*0.094*	*0.084*	

Table 5.12 – Measured results of S40-CB-G2 (Test 4) gusset coupon tests.

Plate	L_c (mm)	L_o (mm)	L_u (mm)	L_t (mm)	$\bar{a}_o$ (mm)	$\bar{b}_o$ (mm)	$\bar{S}_o$ (mm²)	$\bar{a}_u$ (mm)	$\bar{b}_u$ (mm)	$\bar{S}_u$ (mm²)	R_{eH} (MPa)	R_m (MPa)	R_m / R_{eH}	A (%)	Z (%)
Upper	90	80	103.66	247.34	4.01	20.08	80.57	2.06	14.08	29.00	310.27	428.18	1.38	29.58	64.00
Lower	90	80	101.22	245.48	4.01	19.93	79.93	2.09	14.04	29.34	294.00	429.11	1.46	26.53	63.29
Mean	*90*	*80*	*102.44*	*246.41*	*4.01*	*20.01*	*80.25*	*2.08*	*14.06*	*29.17*	*302.13*	*428.64*	*1.42*	*28.05*	*63.65*
StDev	*0.00*	*0.00*	*1.73*	*1.32*	*0.00*	*0.10*	*0.45*	*0.02*	*0.03*	*0.24*	*11.51*	*0.66*	*0.06*	*2.16*	*0.50*
C_v	*0.00*	*0.00*	*0.02*	*0.01*	*0.00*	*0.01*	*0.01*	*0.01*	*0.00*	*0.01*	*0.04*	*0.00*	*0.04*	*0.08*	*0.01*
P-Value											*0.121*	*0.044*	*0.132*	*0.190*	

Table 5.13 – Measured results of S60-CA-G1 (Test 5) gusset coupon tests.

Plate	L_c (mm)	L_o (mm)	L_u (mm)	L_t (mm)	$\bar{a}_o$ (mm)	$\bar{b}_o$ (mm)	$\bar{S}_o$ (mm²)	$\bar{a}_u$ (mm)	$\bar{b}_u$ (mm)	$\bar{S}_u$ (mm²)	R_{eH} (MPa)	R_m (MPa)	R_m / R_{eH}	A (%)	Z (%)
Upper	90	80	111.2	277	7.95	19.71	156.69	3.33	12.05	40.13	274.42	384.19	1.40	39.00	74.39
Lower	90	80	108.82	277.5	7.93	19.57	155.16	3.22	12.55	40.41	283.57	395.71	1.40	36.03	73.77
Mean	*90*	*80*	*110.01*	*277.25*	*7.94*	*19.64*	*155.93*	*3.28*	*12.30*	*40.27*	*279.00*	*389.95*	*1.40*	*37.51*	*74.08*
StDev	*0.00*	*0.00*	*1.68*	*0.35*	*0.01*	*0.10*	*1.08*	*0.08*	*0.35*	*0.20*	*6.47*	*8.15*	*0.00*	*2.10*	*0.44*
C_v	*0.00*	*0.00*	*0.02*	*0.00*	*0.00*	*0.01*	*0.01*	*0.02*	*0.03*	*0.00*	*0.02*	*0.02*	*0.00*	*0.06*	*0.01*
P-Value											*0.150*	*0.113*		*0.202*	

Table 5.14 – Measured results of S60-CA-G2 (Test 6) gusset coupon tests.

Plate	L_c (mm)	L_o (mm)	L_u (mm)	L_t (mm)	$\bar{a}_o$ (mm)	$\bar{b}_o$ (mm)	$\bar{S}_o$ (mm²)	$\bar{a}_u$ (mm)	$\bar{b}_u$ (mm)	$\bar{S}_u$ (mm²)	R_{eH} (MPa)	R_m (MPa)	R_m / R_{eH}	A (%)	Z (%)
Upper	90	80	103.24	268.76	4.01	19.99	80.15	2.06	14.15	29.15	318.17	427.97	1.35	29.05	63.63
Lower	90	80	102.1	266.9	3.98	20.05	79.80	2.08	14.54	30.24	313.29	428.58	1.37	27.63	62.10
Mean	*90*	*80*	*102.67*	*267.83*	*4.00*	*20.02*	*79.97*	*2.07*	*14.35*	*29.70*	*315.73*	*428.27*	*1.36*	*28.34*	*62.87*
StDev	*0.00*	*0.00*	*0.81*	*1.32*	*0.02*	*0.04*	*0.25*	*0.01*	*0.28*	*0.77*	*3.45*	*0.43*	*0.02*	*1.01*	*1.08*
C_v	*0.00*	*0.00*	*0.01*	*0.00*	*0.01*	*0.00*	*0.00*	*0.01*	*0.02*	*0.03*	*0.01*	*0.00*	*0.01*	*0.04*	*0.02*
P-Value											*0.028*	*0.031*	*0.025*	*0.096*	

5.4.2 Cold-Formed Section Strengths

The use of cold-formed sections for the brace tube material introduces several considerations that are not generally encountered with hot rolled steel. The most significant aspect is the non-uniform distribution of material properties that originates from cold-working. Increased yield strength is prominent in the cold-worked corner regions, and as the coupons are cut from the flat faces for material testing, it is important to consider the overall section yield strength. Part 1-3 of Eurocode 3 (CEN, 2006b) allows for the increased yield strength and reduced ductility of cold-formed sections by defining an average cross section yield strength, f_{ya}, that is used in subsequent design calculations for the basic yield strength, f_{yb}. The average yield strength f_{ya} may be determined from the results of full size tests or alternatively from the formulation:

$$f_{ya} = f_{yb} + (f_u - f_{yb})\frac{knt^2}{A_g} \text{ but } f_{ya} \leq \frac{(f_u + f_{yb})}{2} \qquad 5.5$$

where:

A_g is the gross cross-sectional area;

k is a numerical coefficient that depends on the type of forming as follows:

- $k = 7$ for roll forming;
- $k = 5$ for other methods of forming;

n is the number of 90° bends in the cross section with an internal radius $r \leq 5t$ (fractions of 90° bends are counted as fractions of n);

t is the design core thickness of steel material before cold-forming, exclusive of metal and organic coatings

f_{yb} is the basic yield strength of the hot rolled sheet for S235 from BS EN 10025-2:2004 (CEN, 2004b) according to Table 3.1a of BS EN 1993-1-3 (235 N/mm²);

f_u Is the tensile (ultimate) strength of the hot rolled sheet according to Table 3.1a of BS EN 1993-1-3 (360 N/mm²).

A similar consideration is provided in North American Specification for the Design of Cold-Formed Steel Structural Members (AISI, 2007) where an average yield stress for a section F_{ya} is substituted for the typical yield stress used for design F_y. For axially loaded tension and compression members, this can be determined from full section tensile tests, column stub tests or from the following definition:

$$F_{ya} = CF_{yc} + (1 - C)F_{yf} \leq F_{uv} \qquad 5.6$$

in which:

$$F_{yc} = \frac{B_c F_{yv}}{(R/t)^m} \quad \text{when } F_{uv}/F_{yv} \geq 1.2,\ R/t \leq 7 \qquad 5.7$$

$$B_c = 3.69(F_{uv}/F_{yv}) - 0.819(F_{uv}/F_{yv})^2 - 1.79 \quad 5.8$$

$$m = 0.192(F_{uv}/F_{yv}) - 0.068 \quad 5.9$$

where:

F_{ya} is the average yield stress of full unreduced section of compression members or full flange sections of flexural members;

C is; for compression members, a ratio of the total corner cross-sectional area to total cross-sectional area of full section; and for flexural members, a ratio of total corner cross-sectional area of controlling flange to full cross-sectional area of controlling flange:

F_{yv} is the tensile yield stress of virgin steel;

R is the inside bend radius;

t is the thickness of section;

F_{uv} is the tensile strength of virgin steel;

F_{yf} is the weighted average tensile yield stress of flat portions or virgin steel yield stress.

To compare the two methods from both standards (Equations 5.5 - 5.6) the yield strength of both sections was calculated using; the nominal specified strengths; the quoted mill certificate strengths and the strengths established from the coupon tests, in Table 5.15 below. The nominal strengths were obtained from Table 3.1a in Eurocode 3 Part 1-3 as described above.

Table 5.15 - Calculated cold formed yield strengths

Section Size	r_i (mm)	r_o (mm)	A_g (mm²)	f_{ya}[a] (N/mm²)	F_{ya}[a] (N/mm²)	f_{ya}[b] (N/mm²)	F_{ya}[b] (N/mm²)	f_{ya}[c] (N/mm²)	F_{ya}[c] (N/mm²)
40×40×2.5	2.5	5	359	295.9	271.3	360.5	329.9	383.7	358.1
60×60×2.5	2.5	5	559	274.1	258.3	374.6	357.1	345.8	339.0

a) Calculated using nominal specified yield strengths.
b) Calculated using yield strengths reported in mill certificates.
c) Calculated using yield strengths obtained from coupon tests.

5.4.3 Specimen Manufacture and Installation

Specimen materials were delivered from the steel provider to the TCD Structures Laboratory in the form of 7 m tube lengths and gusset plates welded to cleats as specified. The specification also required the steel fabricator to construct the gusset plates in a jig assembly to avoid distortion of thin plates due to heat effects during welding. The weld widths were 4 mm fillet welds.

For each test, the bolts connecting the beam and column members of the test frame were first tightened and then each gusset pair was fitted to the test frame and the associated bolts were tightened to a torque of 400 Nm. This procedure avoided preloading of the specimens prior to testing. After subsequent testing, when the test frame was brought back to its zero position, the angle between the beam and columns varied outside of 90° due to plastic deformation in the stub connections. In such cases, this created alignment problems when connecting the gusset plates for the subsequent test. To counteract this problem the edges of the cleat plates were ground helping in the alignment of the bolt holes.

The brace tube lengths were cut according to the measured diagonal length between the in-situ gusset plates. This measured length was always within a tolerance of ± 5 mm compared to the design drawings. Slots of length 100 mm (equal to the gusset-to-tube weld length) were then cut at each end of the tube length to accommodate the gusset plate thicknesses. The tube ends were then welded to the gusset plates using 4 No. 8 mm fillet welds at each end. Once the welds had cooled the instrumentation was installed on the test frame and specimen as described in Section 5.6 below.

5.5 Testing Methods

The specimens were tested using cyclic inelastic deformation histories based on the ECCS (1986) testing protocol. The protocol is designed as a reference to provide a unified method of testing for characterising the behaviour of structural steel components under cyclic loading. This form of testing accounts for the cumulative damage experienced by a structural element during successive seismic actions (Krawinkler, 2009).

There are two testing procedures defined in the ECCS protocol: the complete testing procedure and the short testing procedure. The complete testing procedure is comprised of preliminary monotonic displacement increase tests for tension and compression ranges and a cyclic test with displacement increases. The short testing procedure consists of the cyclic test only. For this set of experimental tests, an augmented form of the short testing procedure was employed which is described below

5.5.1 Simulating Monotonic Tests

Horizontal cyclic displacements of increasing amplitude are applied to the test frame via the MTS actuator system. The displacement histories were applied at increasing ductility levels based on initial yielding of the brace cross sections. Such initial yield displacements are obtained from the monotonic tests for the complete testing procedure or from initial small displacement steps for the short testing procedure.

As outlined in Chapter 4, numerical models were developed in OpenSees and these were used to simulate the static tensile and compressive monotonic displacement controlled tests. This was carried out instead of applying initial small displacements as part of the short testing procedure. In this way, estimates for the yield displacements of each specimen were obtained from the pushover analyses.

The influence of strain rate during monotonic and cyclic tests is important to consider, however the procedure of the ECCS protocol limits these effects. Early research performed by Manjoine (1944) through a series of tensile tests at different temperatures indicated a significant increase in yield strength associated with an increase in the rate of strain. While there is an effect on the ultimate tensile strength, it is less important in relation to the yield strength. Additionally, the influence of strain rate on the elastic and strain-hardening moduli is negligible (Tremblay and Filiatrault, 1996). The effects are particularly noticeable at strain rates equal to and greater than 10^{-1} sec^{-1}. The effect of ground motion velocities can induce high strain rate demand during the dynamic loading of structures (Gioncu, 2000b). For recent earthquakes such as the 1994 Northridge and 1995 Hanshin/Awaji (Kobe) earthquakes, the peak velocities recorded lie within the range of 10^{-1} to 10^{1} sec^{-1}. Overall, from a structural perspective, this has the effect of narrowing the range between yield and ultimate strengths, thereby transforming a ductile plastic deformation to a more brittle fracture. This is an important consideration prior to carrying out experimental monotonic tests, but the material model used in the analyses is not rate-dependent by default. This is because the current time during an analysis is not passed to an element, which in turn cannot communicate the strain rate to the embedded material. Therefore the influence of strain rates is not experienced by the finite element models. During the shake table tests, data presented in Chapter 9 shows that significant peak strain rates of 50^{-1} sec^{-1} were reached.

The simulated monotonic tests aim to deduce the load limit of the elastic range F_y and the corresponding yield displacement e_y for use in defining the waveform displacement history in the cyclic tests. Figure 5.8 illustrates these parameters for an excursion into the tension range (F_y^+, e_y^+) but this can also be applied to the compression range (F_y^-, e_y^-) These parameters are evaluated from the output F-e curves using the following process:

- Establish the tangent at the origin of the F-e curve to produce a tangent modulus $E_t = tg\alpha_y$;
- Locate the tangent that has a slope of $E_t/10$;
- At the intersection of the two tangents the corresponding ordinate on the vertical axis defines the F_y value;

- At the same intersection the ordinate on the horizontal axis defines the yield displacement value e_y.

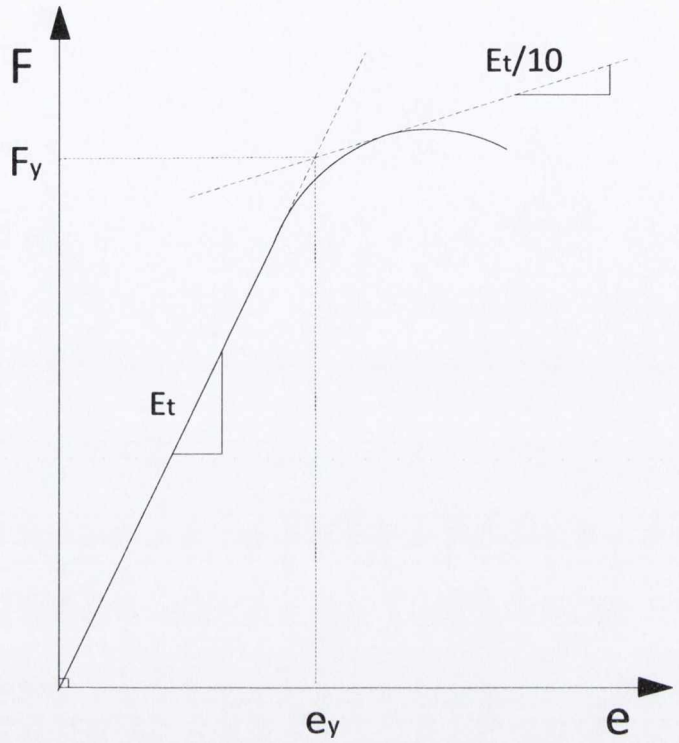

Figure 5.8 – Force-displacement curve.

5.5.2 Cyclic Test Displacement History

The cyclic tests were displacement-controlled using a displacement history waveform generated from the estimated yield displacements with increasing amplitude. The waveform has the following characteristics:

- One cycle in the $^{e_y^+}/_{4}$, $^{e_y^-}/_{4}$ range;
- One cycle in the $^{2e_y^+}/_{4}$, $^{2e_y^-}/_{4}$ range;
- One cycle in the $^{3e_y^+}/_{4}$, $^{3e_y^-}/_{4}$ range;
- One cycle in the e_y^+, e_y^- range;
- Three cycles in the $2e_y^+$, $2e_y^-$ range;
- Three cycles in the $(2 + 2n)e_y^+$, $(2 + 2n)e_y^-$ range for $n = 1, 2, \ldots$;

More cycle ranges may be added if necessary, and the test is continued until specimen failure. The generalised waveform shape generated is shown in Figure 5.9. As was expected the compression yield values, e_y^- were of a smaller magnitude compared to the tension yield values, e_y^+. Therefore, to maintain a symmetric response, the compression yield values were used instead of the tension yield values to generate the waveform and were used as the starting target yield values during the cyclic testing. The period between cycles was maintained at 50 seconds to reduce risk of overheating associated with the hydraulic pumps providing pressure to the actuator system.

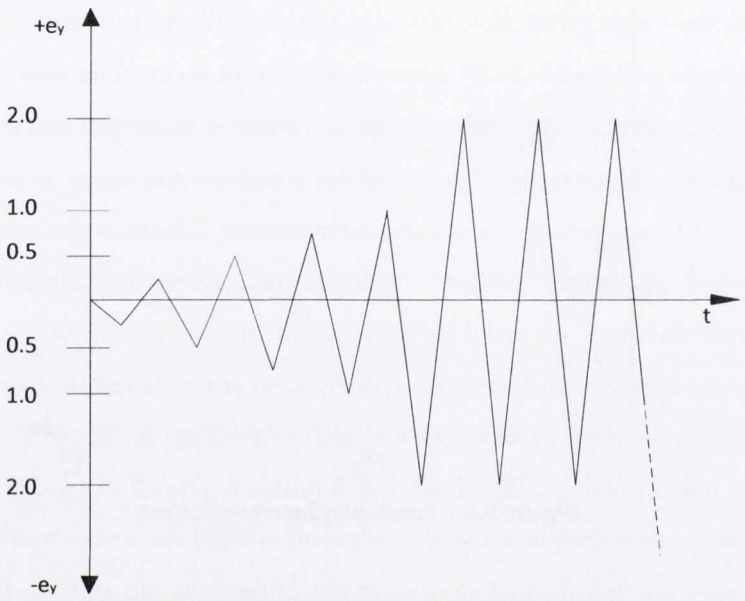

Figure 5.9 – Displacement time-history waveform.

5.6 Test Control System and Instrumentation

5.6.1 Test Control System

The testing hardware used during this series of tests featured a MTS real-time hybrid test system, however the cyclic tests only required specific actuator control functionality. A detailed description of the real-time hybrid test system can be found in the work of McCrum and Broderick (2010). The MTS actuator system consists of a Series 111 MTS Accumulator and a high speed linear hydraulic actuator with a 150 kN capacity and 250 mm (± 125 mm) stroke. The computer hardware consists of a HP Compaq Pentium IV Test PC (Test PC), a two-channel MTS 493 Real-Time Controller (Servo-Controller) and a Dell Optiplex with a Vishay Measurements Group System 5000 data acquisition system (twin Model 5100 Scanners) as shown in Figure 5.10.

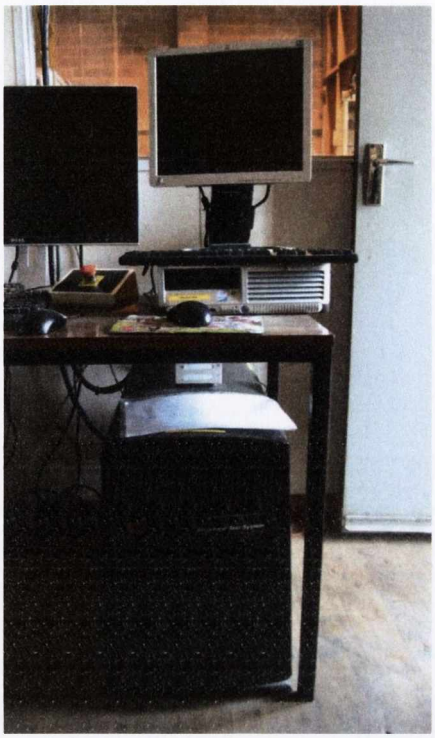

(a) Test PC and Servo-Controller

(b) System5000 Scanners and StrainSmart PC

Figure 5.10 – Control system computer hardware.

An overview of the control system layout is shown in Figure 5.11. The servo-hydraulic actuator is controlled using a method known as Proportional Integral Derivative (PID) control. PID control operates through a feedback loop that measures the error in a process and minimises it by adjusting the process control inputs. The Structural Test System (STS) provides a graphical user interface (GUI) for the Servo-Controller and calibration of the actuator. The Servo-Controller allows control of the actuator through closed loop PID control (McCrum, 2012). The displacement history waveform is input for each specimen and transformed for use as the target displacements in the STS Software. The target command displacements are sent from the Servo-Controller to the MTS actuator. An internal load cell and Linear Variable Differential Transformer (LVDT) Displacement Transducer record the measured force and displacement at the actuator. The force and displacement data are sent back to the Servo-Controller and recorded on the Test PC.

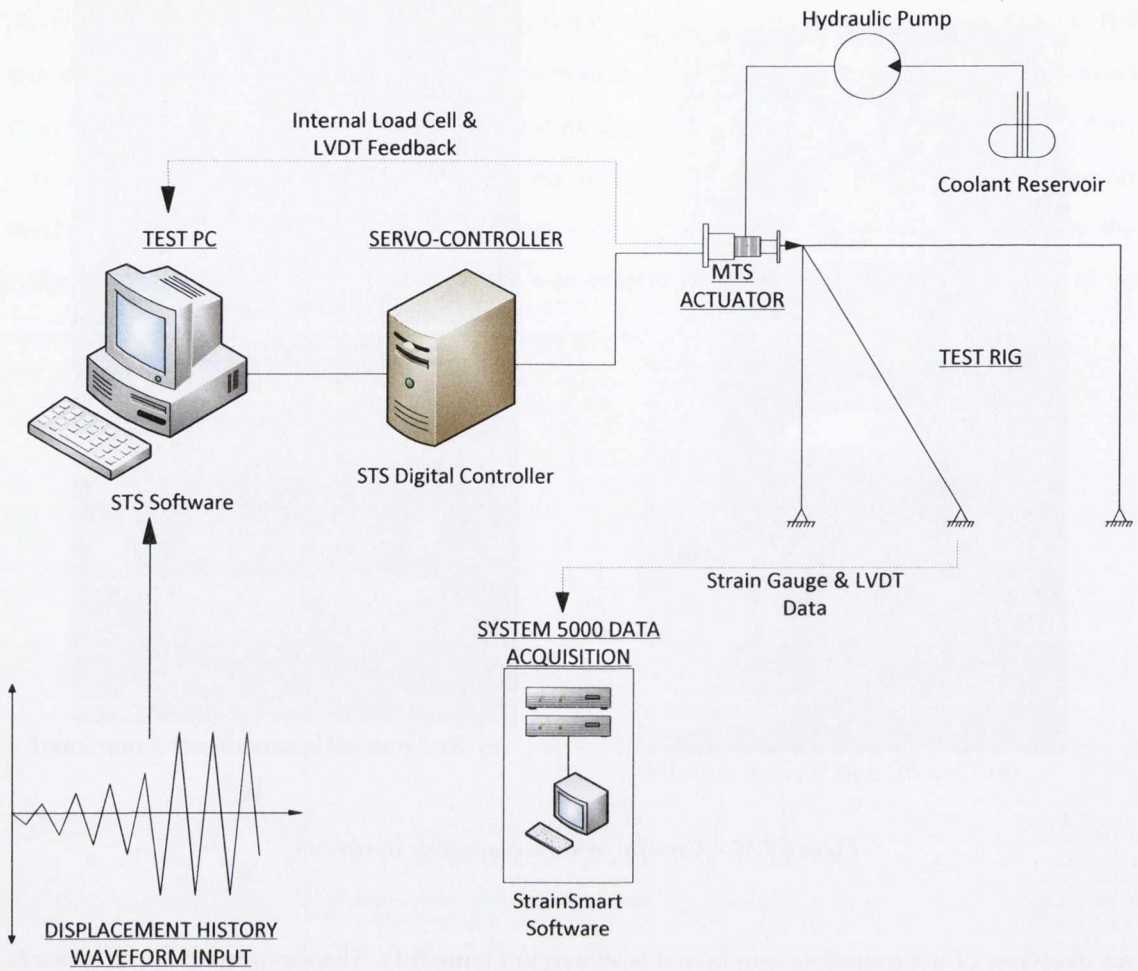

Figure 5.11 – Schematic of test hardware and rig setup.

5.6.2 Instrumentation

Measurements of the hysteretic behaviour in both the overall frame response and the local brace response were required in each test. Internal instrumentation of the actuator featured a 150 kN load cell and LVDT depicted as D1(INT) and LC1(INT) in Figure 5.12. External instrumentation to measure displacement consisted of a LVDT fixed to the top left corner of the test frame measuring horizontal frame movement; a LVDT measuring vertical deformation of the channel section connection; and a string potentiometer attached to the lower brace connection measuring longitudinal deformation of the brace member. As above, these are shown as D2, D3 and SP1 respectively in Figure 5.12. The external LVDT, D2 was used as a reference to calibrate the internal LVDT, D1. D2 and D3 were calibrated using a vernier caliper. The external displacement measurements were made using an RDP Electronics Ltd. ACT2000 LVDTs with a ± 50 mm range.

Strain gauges were assigned to specific locations on the test rig and the brace specimen as shown in Figure 5.13 (designated S1 to S21). The strain gauges were used for; carrying out an experimental stress analysis; to measure the degree of local deformation in the brace specimen and monitor the

test rig for undesired plastic behaviour. To ensure optimum performance of the strain gauges, the application surface was cleaned, abraded and neutralised using an aerosol cleaning solvent prior to bonding. An epoxy adhesive was used to form a bond and allowed to cure as specified by the manufacturer. For unidirectional normal strain measurement (S4 to S21), Radionics 632-168 mild steel foil gauges (Part No. N11MA512011) were used. The 632-168 strain gauges had a gauge length of 5 mm, an operational temperature range of -30° C to +180° C and a nominal resistance of 120 Ω. Strain gauges at the column mid-heights (S17 to S20) were used to calculate the axial load of the columns and S21 fixed at the beam mid-span ensured that negligible bending occurred in the beam. The design of the test frame lower connections ensured that hinge rotation was limited to the column 'stub' sections. Strain gauges S13 to S16 were positioned to monitor the strain levels in the stub sections and ensure that plastic behaviour was never approached during testing.

On the gusset plates Strain Gauge Rosettes were used for the directions S1 to S3 and unidirectional gauges for S4 to S6. The rosette gauges were FRA-5-11 three-element gauges with manufactured by TML Tokyo Sokki Kenkyujo Co.,Ltd with a gauge length of 5 mm and a nominal resistance of 120 Ω. The strain gauge rosettes have an arrangement of three closely positioned gauge grids orientated to measure three independent normal strains along different directions. This enables the principal stresses and strains to be determined. In this series of tests, the strain rosette gauges have a delta gird arrangement with the second and third grids orientated at 60° and 120°, respectively, from the first grid. Strain gauges S7 to S11 were attached to the faces of the tube element for each specimen to monitor plastic deformation due to bending and buckling at key locations. Figure 5.12 and Figure 5.13 provide a general overview of strain gauge locations. Complete detail drawings with dimensioned instrumentation locations are provided in Appendix A.

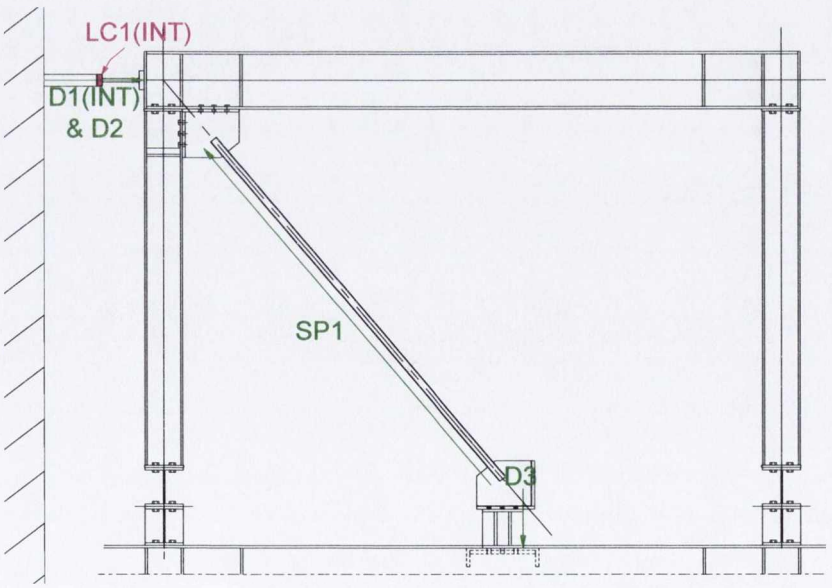

Figure 5.12 – LVDT and Load Cell instrumentation used for cyclic tests (INT. signifying internal instrumentation). Channel section is shown with dashed line type.

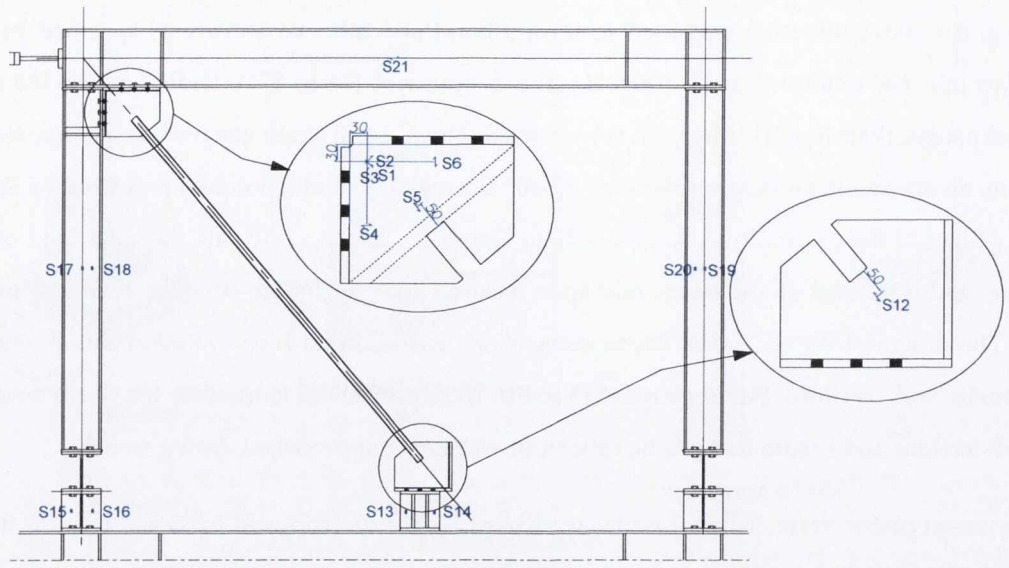

(a)

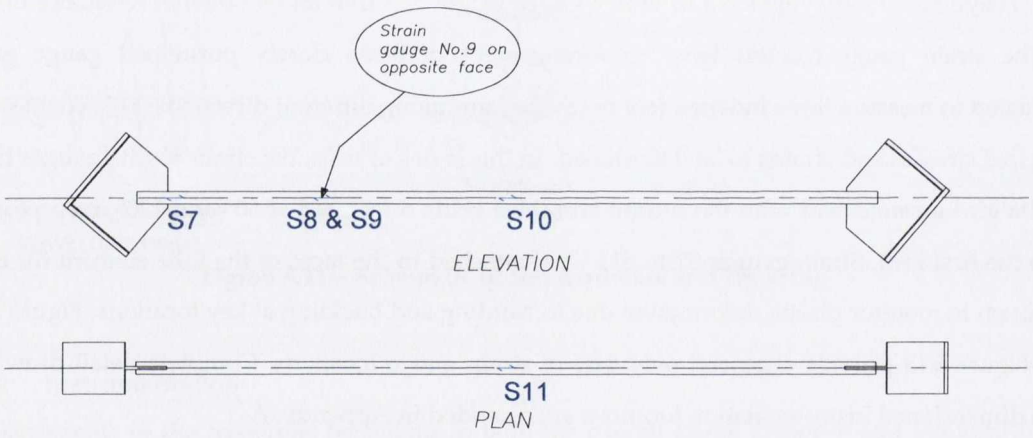

(b)

Figure 5.13 – Strain gauge locations for (a) test rig and gusset plates and (b) tube specimens.

5.7 Chapter Overview

This chapter outlined the experimental preparation and set-up for a series complementary cyclic tests carried out at TCD. The process used in the G1 and G2 gusset designs was outlined and used as a platform to describe the test specimen design and parameters selected for investigation in this series of tests, taking into account the capacity of the available laboratory equipment. Material strength tests using coupon test pieces were also described. Finally, the relevant parts of the employed cyclic testing method were summarised and the setup for the test control hardware and measurement instrumentation was also provided. The following chapter (Chapter 6) presents and analyses the results obtained in these complementary cyclic tests.

6 Complementary Cyclic Tests – Experimental Results and Analysis

6.1 Introduction

The previous chapter presented the test setup, material properties and specimen details for a series of complementary cyclic tests carried out at Trinity College Dublin in support of the BRACED project shake table tests. In this chapter the results and analysis of these complementary cyclic tests are presented and discussed in detail. This is followed by an examination of the test results analysing different performance parameters.

6.2 Specimen Profile Shapes

Prior to each test, the initial deformation of each brace member was measured in both the in-plane and out-of-plane directions (Table 6.1). These measurements were made by attaching a datum line to both ends of the brace and measuring the offset distance using a vernier caliper and a set square. Although efforts were made to reduce any preloading of the brace (Section 5.4.3), the heat effects of welding the tube to the gusset plate introduced a small camber in the brace tube. The initial deformation measurements were important for determining the initial direction of buckling. This facilitated the correct placement of the string potentiometer so that it was not influenced by the out-of-plane movement of the specimen. As discussed in section 4.2.2, the degree of initial camber has a significant influence on the initial buckling load and buckling loads in subsequent cycles. . The maximum pre-test camber for a given direction is shown in brackets in Table 6.1. These values agree with the initial camber recommended for modelling in section 4.2.2.

Measurements of initial deformation were taken using the local axes of the brace member as the frame of reference (Figure 6.1). To minimise error in carrying out these small measurements, error correction methods were employed. Firstly, the datum line could not always be placed exactly parallel to the brace ends. The associated error was calculated and removed from every measurement along the length of the brace tube (X-axis). Error originating from measurements recorded using the vernier calliper was minimised by establishing the average of several measurements.

Three different profile shapes were observed, and these can be approximated with shapes of the letters 'm', 'Ω' and 'S' (Figure 6.2(a)). The 'Ω' and 'S' shapes are similar to the first and second buckling mode profiles of a fixed-ended strut.

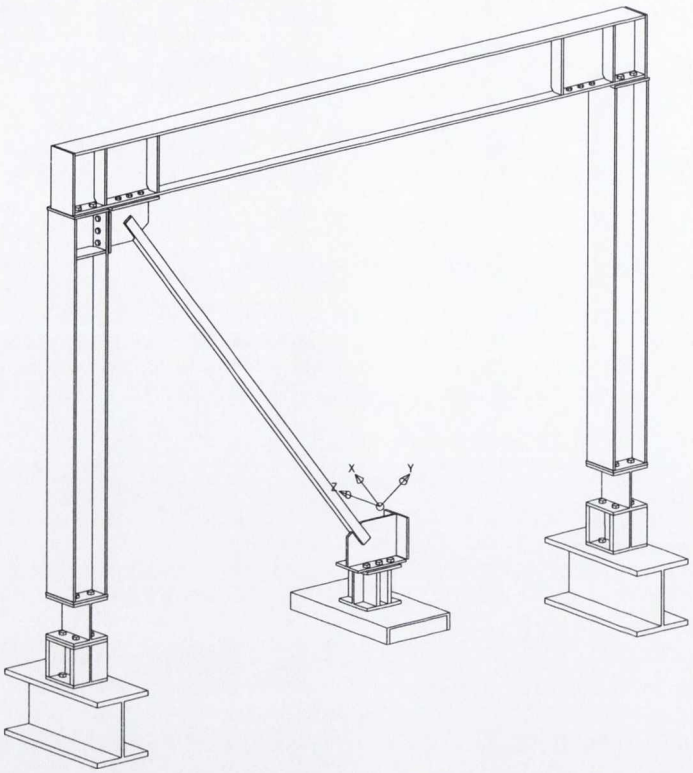

Figure 6.1 – Test frame and specimen drawing showing local brace member axes designation.

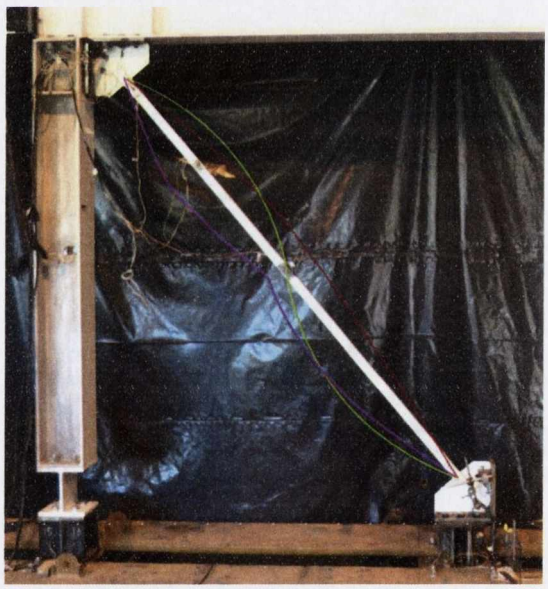

(a) 'Ω', 'S' and 'm' profiles depicted in red, green and magenta arcs respectively

(b) Original alignment shown in red

Figure 6.2 – Photographs of test rig and specimen with (a) front elevation showing observed profile shapes and (b) end elevation showing out-of-plane buckling.

Table 6.1 – Measured deformation of brace specimens. Values in brackets indicate maximum camber expressed as a percentage of brace length.

Specimen ID	Pre-Test			Post-Test		
	x (mm)	y (mm)	z (mm)	x (mm)	y (mm)	z (mm)
S40-CA-G1	0	0	0	0	0	0
	592	-1.06 (0.04%)	2.42	592	0.92	54.73
	1184	-0.70	2.71 (0.11%)	1184	4.09	123.60
	1776	0.71	1.89	1776	1.44	58.47
	2368	0	0	2368	0	0
	Profile	S	Ω	Profile	Ω	Ω
S40-CA-G2	0	0	0	0	0	0
	625	1 (0.04%)	-0.41	575	-0.25	84.67
	1252	0.50	-0.92 (0.04%)	1150	-2.50	158.23
	1877	1	-0.45	1725	0.25	69.10
	2503	0	0	2300	0	0
	Profile	m	Ω	Profile	S	Ω
S40-CB-G1	0	0	0	-	-	-
	592	-1.04	0.72	-	-	-
	1184	-0.43	1.04 (0.04%)	-	-	-
	1776	-1.41 (0.06%)	0.76	-	-	-
	2368	0	0	-	-	-
	Profile	m	Ω	-	-	-
S40-CB-G2	0	0	0	-	-	-
	625	0.17	1.55	-	-	-
	1252	0.04	1.70 (0.07%)	-	-	-
	1877	1.11 (0.04%)	0.82	-	-	-
	2503	0	0	-	-	-
	Profile	m	Ω	-	-	-
S60-CA-G1	0	0	0	-	-	-
	592	-0.09	0.27	-	-	-
	1184	-0.27	0.73 (0.03%)	-	-	-
	1776	-0.41 (0.02%)	0.68	-	-	-
	2368	0	0	-	-	-
	Profile	Ω	Ω	-	-	-
S60-CA-G2	0	0	0	-	-	-
	625	-0.93	-0.03	-	-	-
	1252	-0.76	-0.18 (0.01%)	-	-	-
	1877	-1.12 (0.04%)	-0.14	-	-	-
	2503	0	0	-	-	-
	Profile	m	Ω	-	-	-

6.3 Cyclic Tests

This series of tests examined six brace-gusset plate specimens installed in a test frame that was tested under a displacement-controlled horizontal cyclic load (Section 5.5). Detailed geometrical and instrumentation drawings for each specimen are presented in Appendix A and material properties for the steel used are given in Sections 5.4.1 and 5.4.2.

Key test results are presented in Table 6.2 below. For each design type, the global and section slenderness is shown together with the experimental brace ultimate tension and buckling compression loads, brace yield displacement (δ_y) and maximum brace elongation (δ_{max}). The displacement δ_y, was established through: identifying the initial yield point on the elastic range of the brace hysteresis plot (using the intersection of E_t and $E_t/10$ method as described in sub-section 5.5.1); and finding the corresponding ordinate on the displacement axis.

Observations made on the measured performance parameters of each specimen are provided below with the aid of hysteretic data recorded during the test.

Table 6.2 – Summary of experimental cyclic results.

Specimen	b/tε	$\bar{\lambda}$	β_{ww}	Brace Buckling Load (kN)	Brace Ult. Tensile Load (kN)	δ_y (mm)	δ_{max} (mm)
S40-CA-G1	16	1.16	0.38	-66.81	178.64	0.72	-
S40-CA-G2	16	1.23	0.75	-48.60	211.32	2.76	21.67[a]
S40-CB-G1	16	1.66	0.38	-53.46	197.10	4.80	23.76
S40-CB-G2	16	1.75	0.75	-34.75	205.29	5.12	30.46
S60-CA-G1	24	0.75	0.52	-117.95	208.53	2.95	13.00
S60-CA-G2	24	0.80	1.03	-89.94	202.28	2.80	8.67

[a] Maximum displacement ductility demand survived by specimen.

Observations and results from each of the cyclic tests are presented in the sub-sections below. The data is presented in a consistent format for all tests:

Global Response Data

- Base shear and horizontal roof displacement hysteresis plot;
- Input actuator command displacement and frame response displacement time history plot;

Local Response Data

- Brace axial force and longitudinal deformation hysteresis plot with brace capacities shown in dashed lines (from coupon yield strengths);

- Brace axial force time history plot;
- Strain hysteresis of upper gusset plate (SG5) and brace mid-length (SG10) as shown in the sketch in Figure 6.3.

In comparing the strain results for SG5 it is important to note that the strain readings are reversed in sign for specimens S40-CA-G2 and S60-CA-G2 due to the alternate directions of out-of-plane buckling of the brace member in these tests.

Figure 6.3 – Strain gauge locations for SG5 and SG10

Brace axial force is determined from the resolved component of the force measured by the actuator load cell. In this regard, the brace and frame members are assumed to behave as a simple truss. This leads to an error in the brace axial load results as the partially-restrained nature of the test frame provides a small resistance in addition to that due to the axial deformation of the brace.

6.3.1 Cyclic Test 1: S40-CA-G1

In the first cyclic test, a 40×40×2.5 SHS tube was connected to the test frame using the CA connection with a gusset plate designed using the SLC layout. The gusset plates were 8 mm thick forming the stiffest connection types of the test series. During the test, unanticipated plastic deformation was observed in the lower channel section that connected the lower portion of the brace to the reaction frames. Visual inspection indicated that yielding had occurred in the channel section web. This lower channel section was mounted between the two reaction frames to support (in compression) and anchor (in tension) the lower brace connection (Figure 5.12). The web deformation was noticed during the latter cycles of the test. The test was suspended and the channel section was removed and replaced with a strengthened channel section. The modified channel section included the addition of 20 mm stiffener plates along its length including a 20 mm plate welded to the web (Figure 6.4). The test was resumed at the same displacement cycle prior to suspending the test and the brace tube failed at a tensile axial load of 98.91 kN without further deformation of the channel section.

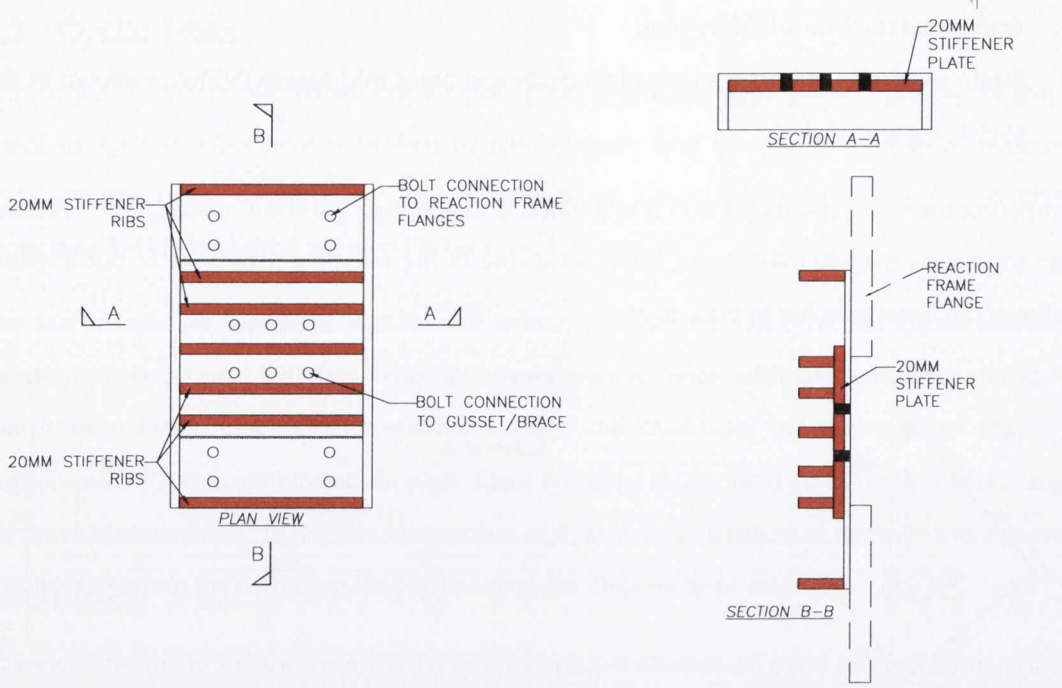

Figure 6.4 – Modified channel section including stiffener plates highlighted with solid red hatching.

As anticipated for a single brace CBF structure, the frame response was asymmetrical. The plot of frame lateral displacements and actuator reaction load in Figure 6.5(a) demonstrates this behaviour. The smooth transitions between the tensile and compressive loading half-cycles lack the characteristic pronounced pinched cyclic behaviour often exhibited by braced frames. This was incurred due to the aforementioned yielding in the web of the channel section, and this behaviour was not observed in successive tests. Figure 6.5(b) compares the actuator target displacements and the measured frame lateral roof displacements (Frame Fbk) and these show good agreement.

As indicated by Figure 6.5(c) initial buckling was observed at an axial load of approximately -66.81 kN and involved brace bending in the +z direction (Figure 6.1). This was followed by substantial out-of-plane deformation with local buckling observed at the mid-span (photographs in Figure 6.6(a) and (b)). The recorded brace hysteresis was affected by the yielding of the channel section web and the out-of-plane brace deformation pushing against the string-pot line used to measure longitudinal displacement. This is particularly noticeable in the compression ranges where the brace buckled and introduced a large error into the measured brace displacement. The axial load time-history shown in Figure 6.5(d) is also influenced by this behaviour. The target displacement triplets are not clearly distinguishable in the time-history due to the intensifying plastic deformation of the support/anchor channel.

Figure 6.5(e) shows the normalised strain hysteresis response in the upper gusset plate (SG5) and at brace mid-length (SG10). The strains are normalised using the yield strains established from the coupon tests for the plates and tubes. Even with the plasticity of the channel section, inelastic response and local buckling occurred in the brace leading to large accumulated strains at mid-length. At the SG5 location the strains remain largely elastic but minor permanent deformation is observable in the photograph in Figure 6.6(c). Limited plastic strains have developed in the gusset plate because of the increased bending resistance offered by the 8 mm plate and it is also important to note that the gauge SG5 located just outside the linear plastic hinge zone.

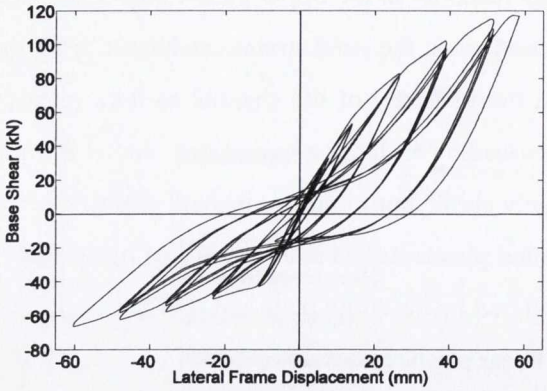

(a) Frame hysteretic response

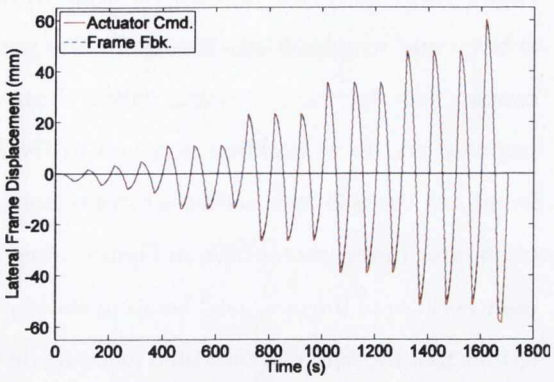

(b) Lateral frame fisplacement time-history

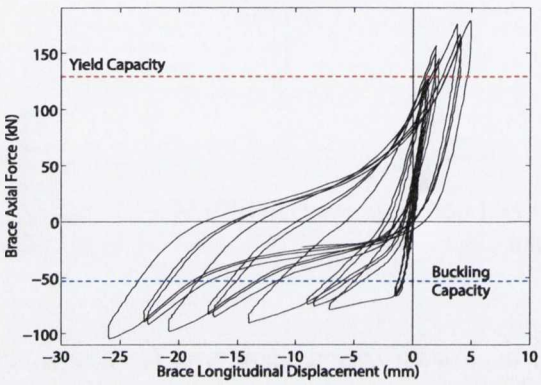

(c) Local brace hysteretic response, with brace capacities from coupon tests

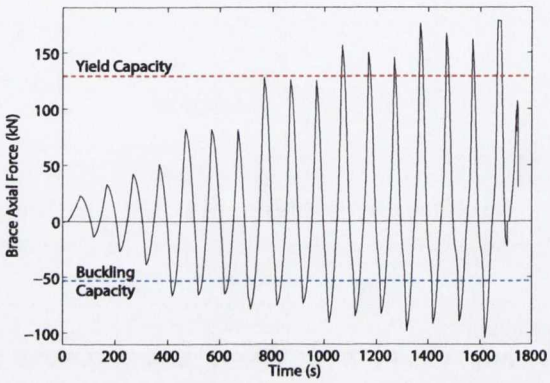

(d) Brace axial force time-history, with brace capacities from coupon tests

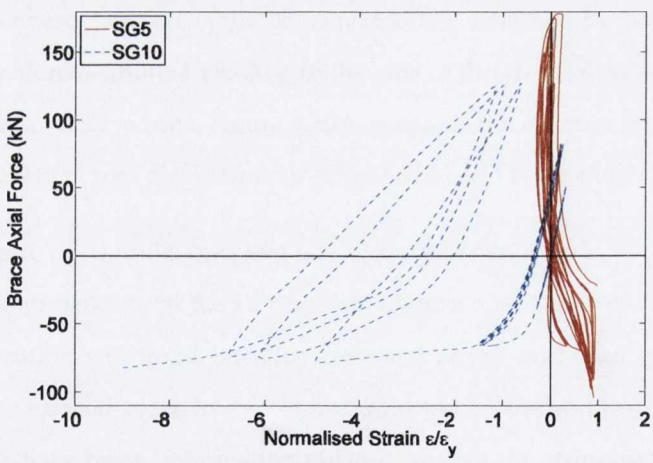

(e) Strain hysteresis at brace mid-length (SG10) and in upper gusset plate plastic hinge zone (SG5)

Figure 6.5 – Recorded responses in Cyclic Test 1; Specimen S40-CA-G1.

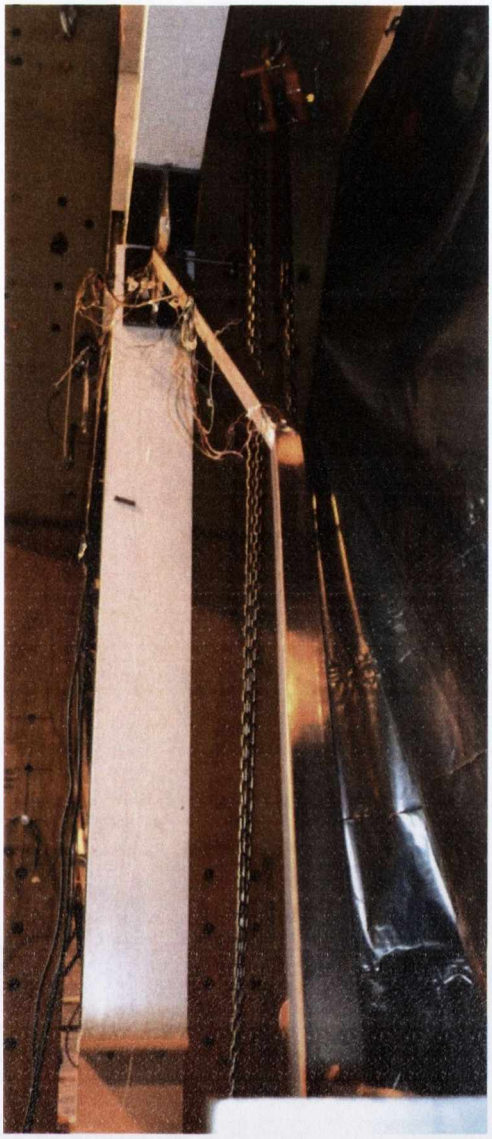

(a)

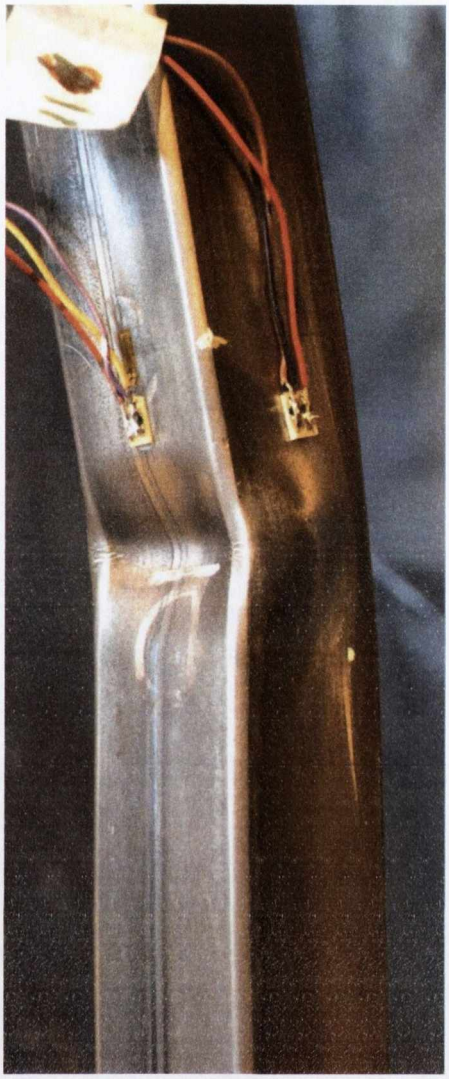

(b)

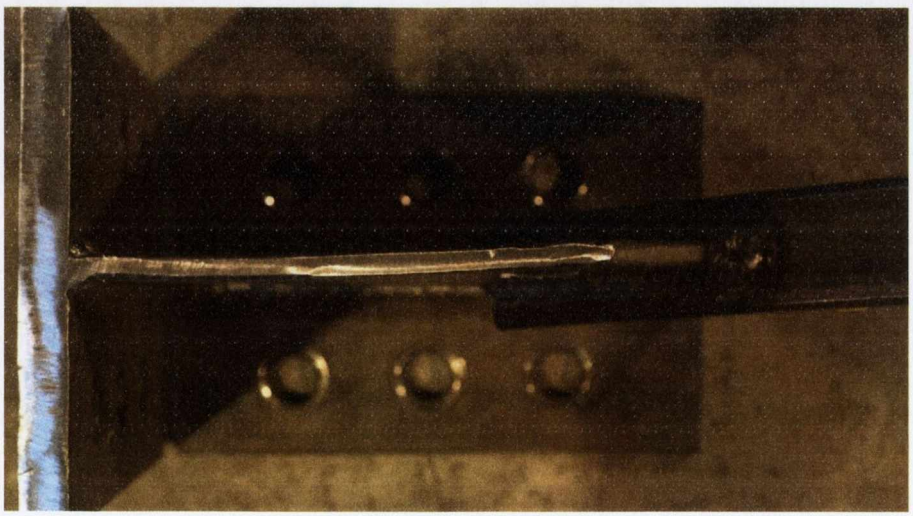

(c)

Figure 6.6 – Cyclic Test 1; Specimen S40-CA-G1 after testing showing (a) overall brace deformation (b) local buckling mode at brace mid-length and (c) gusset plate deformation.

6.3.2 Cyclic Test 2: S40-CA-G2

In this specimen, the gusset layout design was changed from the linear (SLC) layout used in previous specimen to the elliptical (G2) layout. The second specimen had a thinner gusset plate and a higher strength balancing factor, β_{ww}, than the first specimen The primary results for specimen S40-CA-G2 are shown in Figure 6.7. These are comparable to the results of specimens S40-CA-G1 and S40-CB-G2 in sections 6.3.2 and 6.3.4 respectively. With the strengthened channel section, the frame response displays the characteristic base shear-lateral displacement plot of a CBF (Figure 6.7(a)). Good agreement is achieved between the command and feedback displacements as exhibited in Figure 6.7(b). However, as is shown in this plot, an extra displacement cycle was added due to the pausing and resuming of test operations. This was caused by unexpected temperature increases on the actuator pump and associated cooling system. This restricted the test duration which was terminated before complete brace member failure. Limited local buckling occurred at the brace tube mid-length when the buckling capacity was reached but this was much less than in all other tests. Bending and yielding of the gusset plates during brace compression allowed flexural member buckling to occur without local buckling in the brace tube, as seen by the deformed shape in Figure 6.8. This absence of buckling-induced damage may contribute the larger tensile capacity observed with this specimen compared to other tests.

In Figure 6.7(c) and (d) the brace response is shown with the predicted tensile yield and buckling capacity ranges based on the characteristic strength tests (coupon tests). Initial buckling capacity reached -48.6 kN with out-of-plane brace buckling in the –z direction. As discussed previously, the calculated quantity 'Brace Axial Force' includes the contributions to resistance provided by both the brace member and the test frame. This is evident in the brace plots as an increase in compressive resistance owing to the frame action.

The strain hysteresis in Figure 6.7(e) illustrates the significant yielding observed at brace mid-length and within the elliptical gusset clearance zone. At brace mid-length (SG10), large plastic deformations occurred during the later cycles. Plastic deformation of the gusset plate (SG5) occurred over a larger range of displacement cycles. This response is in line with the expected performance of a brace-gusset plate combination with a strength balancing factor β_{ww} close to 1.0. In contrast to the S40-CA-G1 specimen, this test developed a full plastic hinge zone in the gusset plate owing to the reduced thickness of the G2 plate design.

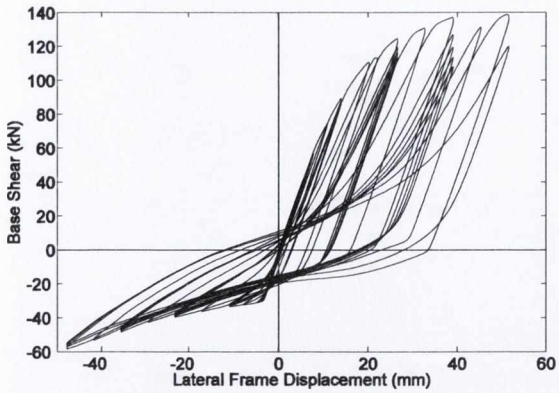

(a) Frame hysteretic response

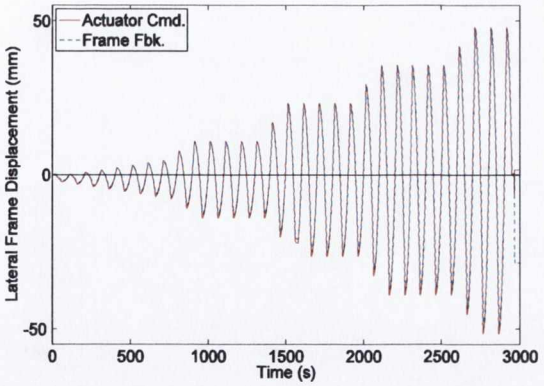

(b) Lateral displacement time-history

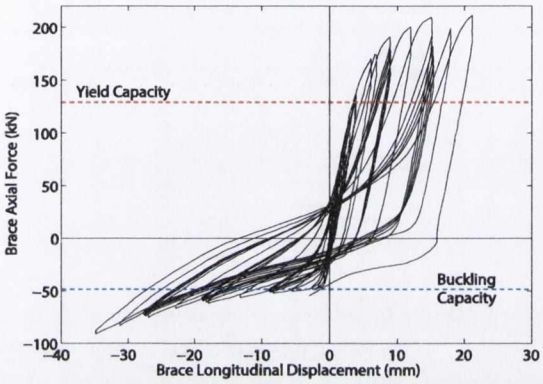

(c) Local brace hysteretic response, with brace capacities from coupon tests

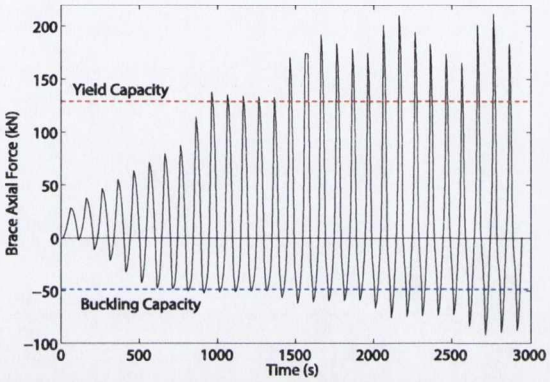

(d) Brace axial load time-history, with brace capacities from coupon tests

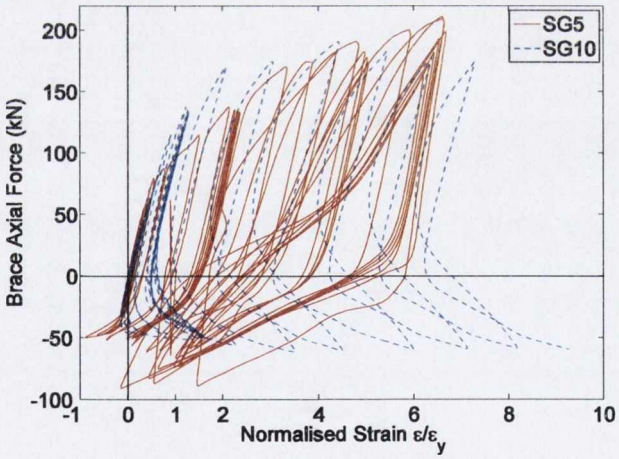

(e) Strain hysteresis at brace mid-length (SG10) and in the upper gusset plate plastic hinge zone (SG5)

Figure 6.7 – Recorded responses in Cyclic Test 2; Specimen S40-CA-G2.

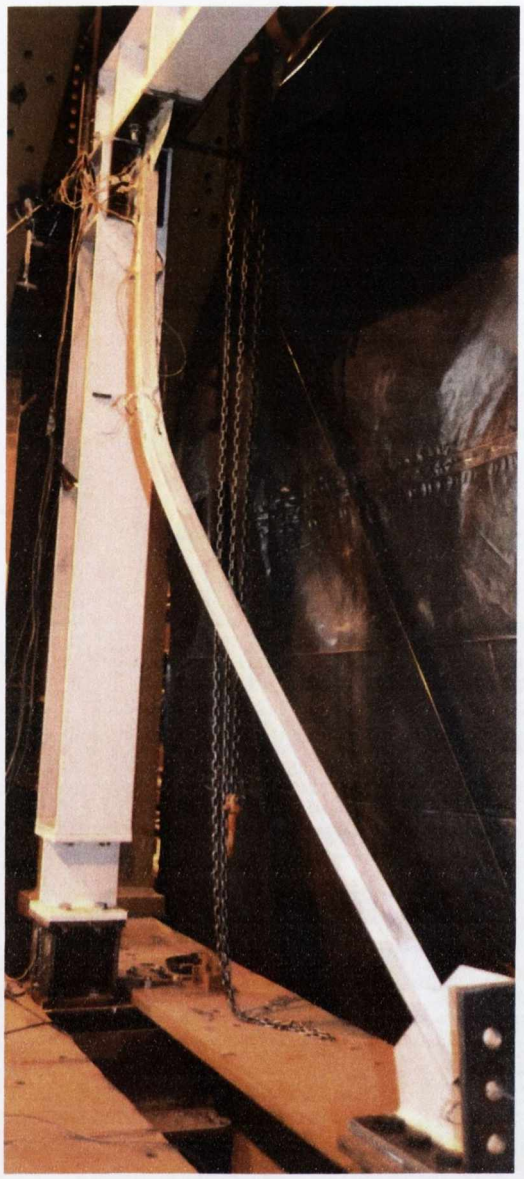

(a)

(b)

(c)

Figure 6.8 – Cyclic Test 2; Specimen S40-CA-G2 after testing showing (a) overall brace deformation (b) brace mid-length and (c) gusset plate deformation.

6.3.3 Cyclic Test 3: S40-CB-G1

This specimen employed the conventional G1 gusset plate design with a CB type connection. The frame hysteretic response in Figure 6.9(a) shows that the maximum compression load is attained at initial buckling of the brace. In contrast to the CA specimens (where the brace connection increased the rotational stiffness of the beam-to-column joint), no increase in compressive strength is observed thereafter. Good agreement between the applied actuator displacement history and the lateral frame response is exhibited in Figure 6.9(b). Due to minor cooling issues a momentary pause was applied during the last cycle of the $6\delta_y$ amplitude displacement cycles.

The brace axial response in Figure 6.9(c) and (d) indicates that design calculations (based on characteristic strength tests) provide a conservative estimate of buckling capacity. A plastic hinge developed at the brace mid-length (Figure 6.10(a)) leading to a gradual reduction in compressive capacity due to accumulated residual deflection in the brace member combined with the Bauschinger effect. On reloading in the reverse direction plastic elongation accumulates in the brace following tensile yielding, and for displacement triplets of the same amplitude, a reduction in the tensile load required to reach each target displacement is observed in the brace axial load time-history in Figure 6.9(d).

Comparing the strain response at brace mid-length (SG10) and in the upper gusset plate (SG5) in Figure 6.9(e) shows that significant yielding was confined to the brace only. The large brace strains caused plastic hinge rotation and local buckling. High strains in the local buckles lead to eventual fracture at the brace mid-length, as shown in the photograph Figure 6.10(c). The gusset plate remained elastic throughout most of the test until the latter cycles (Figure 6.10(b)). This reflects the lower strength balancing factor β_{ww} for this specimen.

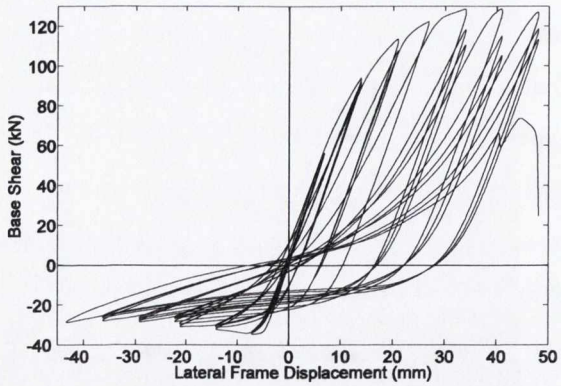

(a) Frame hysteretic response

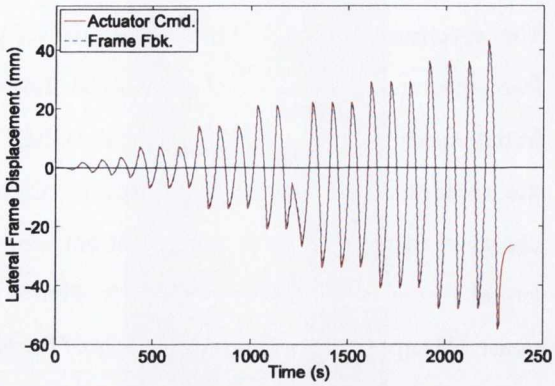

(b) Lateral displacement time-history

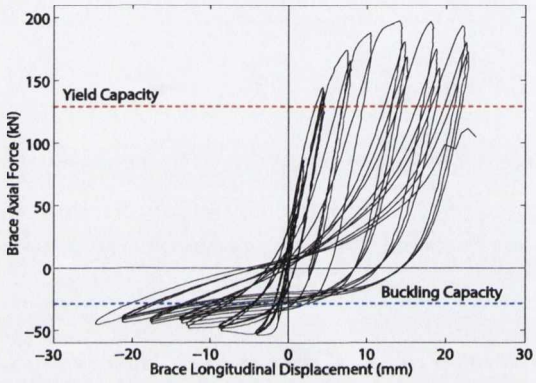

(c) Local brace hysteretic response, with brace capacities from coupon tests

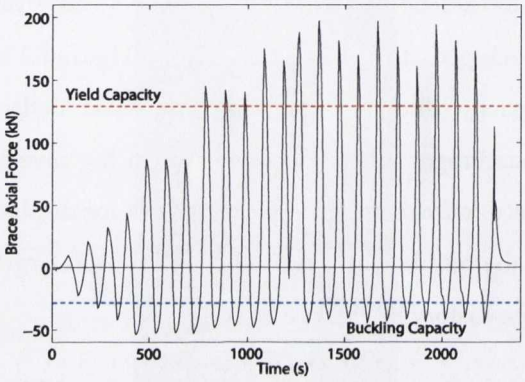

(d) Brace axial load time-history, with brace capacities from coupon tests

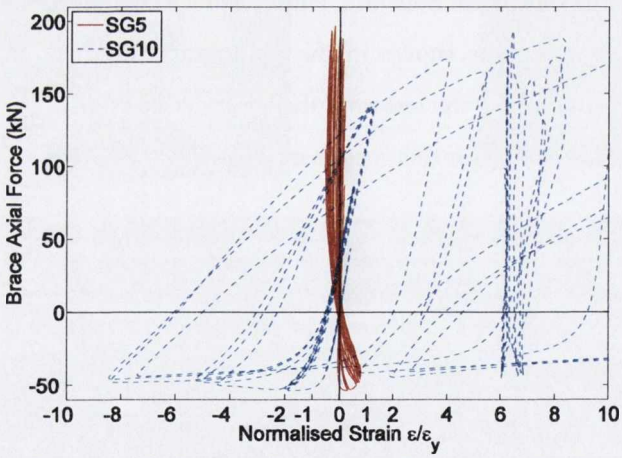

(e) Strain hysteresis at brace mid-length (SG10) and in the upper gusset plate plastic hinge zone (SG5)

Figure 6.9 – Recorded responses in Cyclic Test 3; Specimen S40-CB-G1.

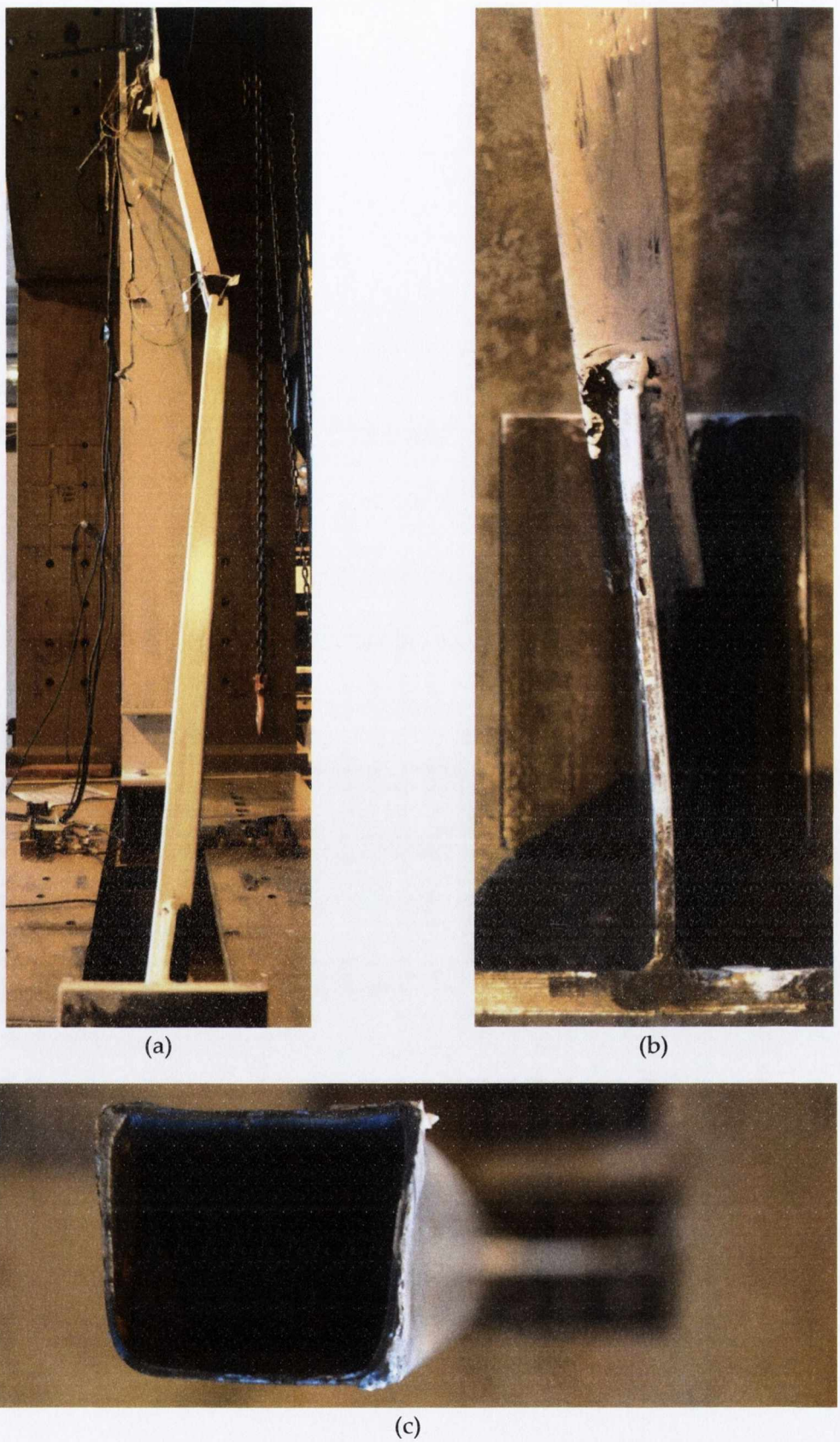

Figure 6.10 – Cyclic Test 3; Specimen S40-CB-G1 after testing showing (a) overall brace deformation with plastic hinge at mid-length (b) gusset plate bending and (c) complete brace failure.

6.3.4 Cyclic Test 4: S40-CB-G2

This specimen was similar to Cyclic Test 3, except the elliptical layout (EC) was employed in the gusset design. In a similar manner to Test 2, this resulted in a thinner gusset plate and an increase in the β_{ww} factor. The primary results are shown in Figure 6.11 and are comparable to the previous Cyclic Test 3.

Unlike the previous Test 3, the maximum compression load is not achieved at initial buckling of the brace. The peak compressive load is achieved at the final compression loading cycle. Prior to this force being reached, there is an increase in the compressive resistance that is seen in both frame and actuator hysteresis plots (Figure 6.11(a) and (c)). This can be attributed to the stiffness contribution of the bolted beam-column connection. It was observed towards the end of the test due to the frame undergoing large displacement demands that had not been reached during previous tests. The buckling capacity prediction is shown to be very accurate until the large displacement demands are reached.

Further cooling issues required a momentary pause and resulted in the third $+6\delta_y$ target not being fully reached Figure 6.11(b). However, there is good agreement between the actuator and frame feedback displacements.

A local buckle formed at brace midspan (Figure 6.12(a)) and causes a reduction in the compressive capacity until the connection stiffness dominates the response. As observed in the previous test, in the tensile range, there is a reduction in the load required to reach subsequent target displacement of the same amplitude.

The strain measurements in Figure 6.11(e) show that significant yielding was more prominent in the brace at the local buckle (SG10) compared to the plastic hinge zone of the upper gusset plate (SG5). The strains at SG5 just reached the elastic limit, however visual inspection of the plate indicates that there was greater deformation in the plate compared to Test 3 (Figure 6.12(c)).

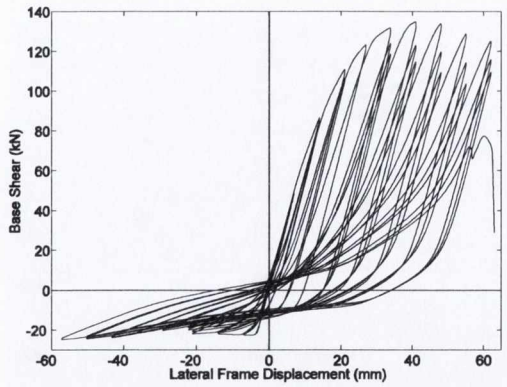

(a) Frame hysteretic response

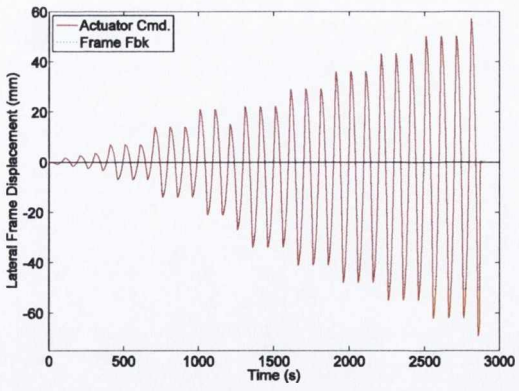

(b) Lateral displacement time-history

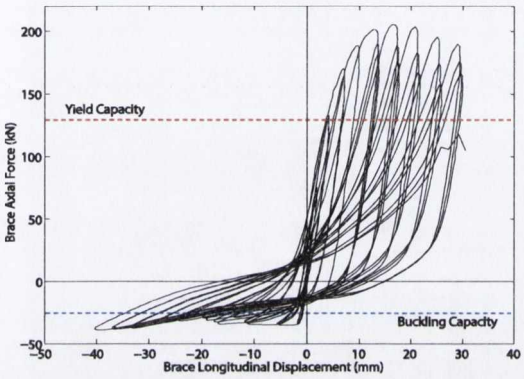

(c) Local brace hysteretic response, with brace capacities from coupon tests

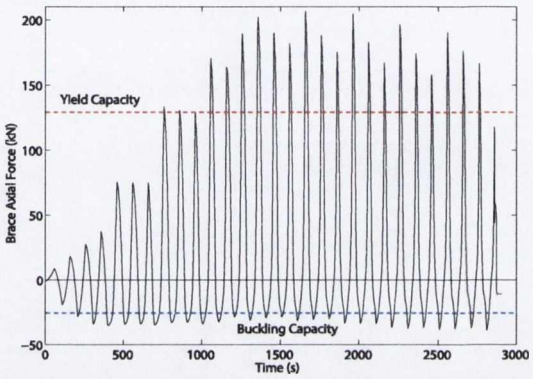

(d) Brace axial load time-history, with brace capacities from coupon tests

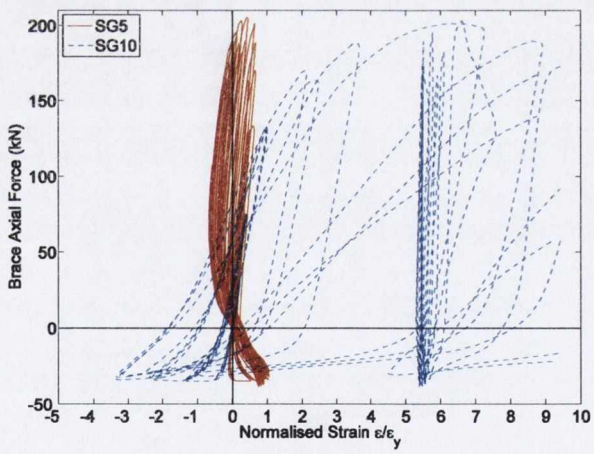

(e) Strain hysteresis at brace mid-length (SG10) and in the upper gusset plate plastic hinge zone (SG5)

Figure 6.11 – Recorded responses of Cyclic Test 4; Specimen S40-CB-G2.

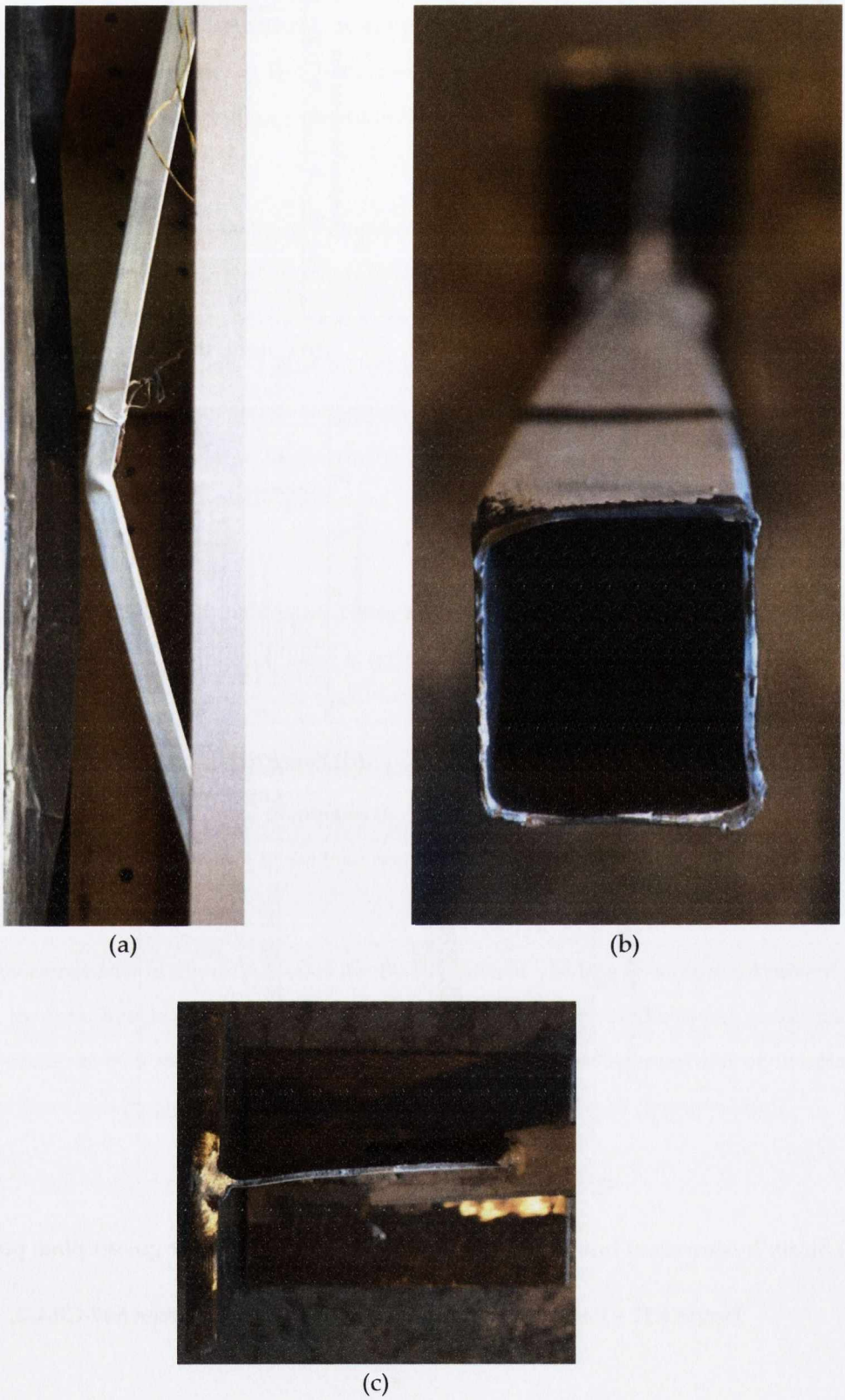

Figure 6.12 – Cyclic Test 4; Specimen S40-CB-G2 after testing showing (a) overall brace deformation with plastic hinge at mid-length (b) brace section failure and (c) gusset plate bending.

6.3.5 Cyclic Test 5: S60-CA-G1

This was the first test to employ the S60 section size and is comparable to Cyclic Test 6. This test had a low β_{ww} factor due to the conventional G1 gusset plate design.

The plots in Figure 6.13(a) and (b) show a lower number of displacement demand cycles sustained by this specimen. In Figure 6.13(c) the initial buckling capacity of the brace is the peak compressive force achieved in the test. Thereafter, small increases in compressive resistance offered by the brace-gusset specimen are observed. A local buckle formed at the compressive δ_y peak at brace midspan (Figure 6.14(a)) followed by cracks in the corners, tearing of the face during the tensile $4\delta_y$ cycles and eventual failure during the first $6\delta_y$ cycle (Figure 6.14(b)).

The strain measurements for SG5 and SG10 in Figure 6.13(e) show large plastic strain achieved at the brace midspan as in previous tests. The SG5 data showed erroneous 'spikes' recorded during plate bending under large brace forces at the tension fibre. After testing was complete, investigation showed that this was caused by strain gauge debonding from the steel plate surface. Disregarding the error spikes, it is found that yield strain limits are only just reached at SG5 in the gusset plate, as in Cyclic Test 4 and 3. Minimal bending was visibly observed in the gusset plate.

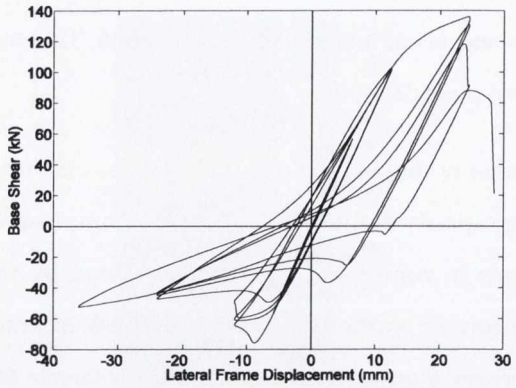

(a) Frame hysteretic response

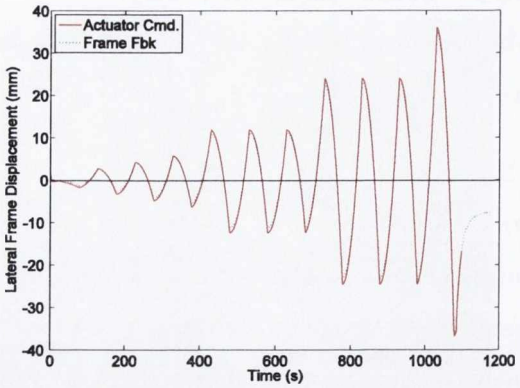

(b) Lateral displacement time-history

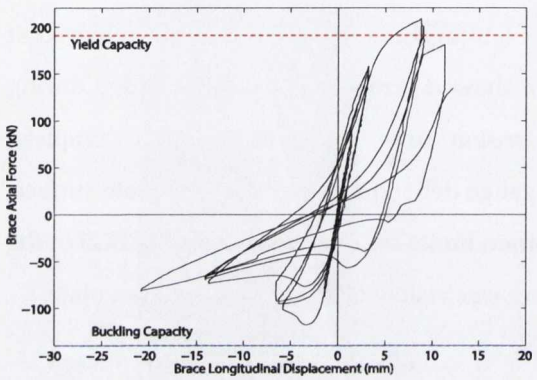

(c) Local brace hysteretic response, with brace capacities from coupon tests

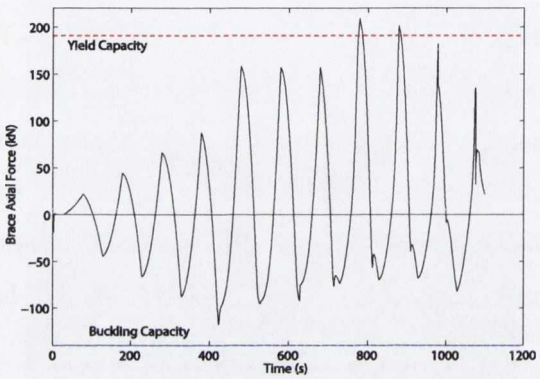

(d) Brace axial load time-history, with brace capacities from coupon tests

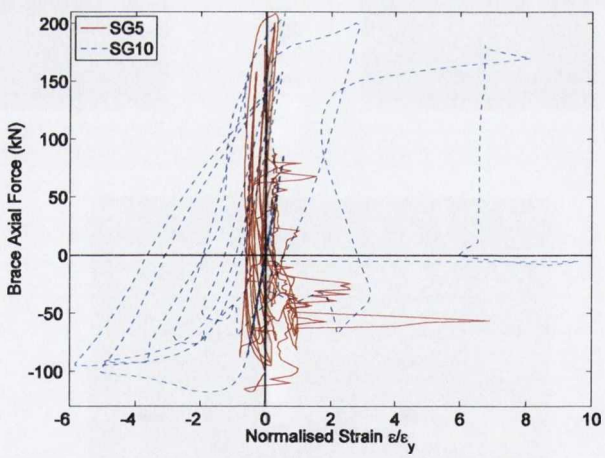

(e) Strain hysteresis at brace mid-length (SG10) and in the upper gusset plate plastic hinge zone (SG5)

Figure 6.13 – Recorded responses of Cyclic Test 5; Specimen S60-CA-G1.

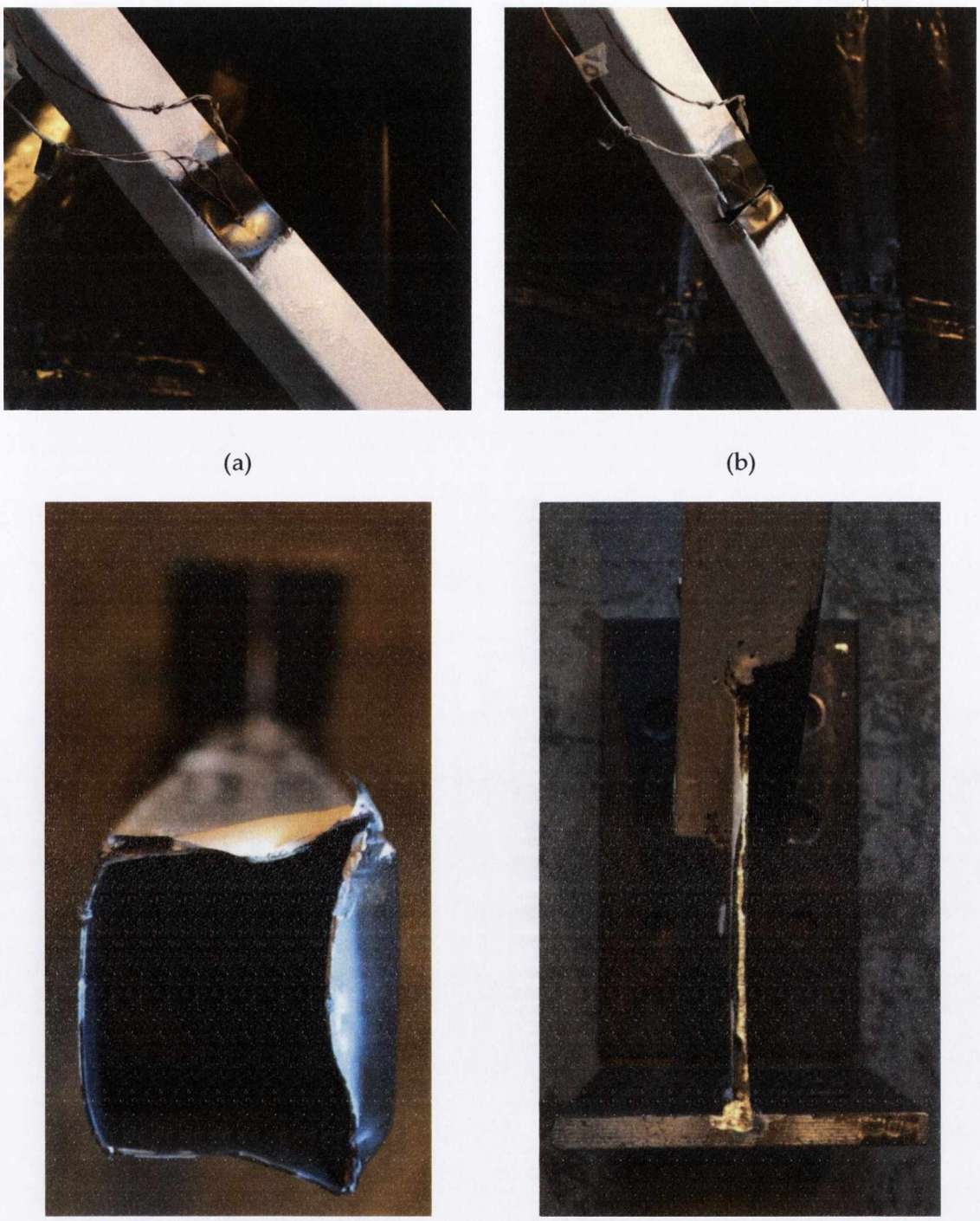

Figure 6.14 – Cyclic Test 5; Specimen S60-CA-G1 after testing showing (a) brace local buckle at midspan (b) brace tearing (c) failed brace section shape and (d) gusset plate bending shape.

6.3.6 Cyclic Test 6: S60-CA-G2

This test is similar to Cyclic Test 5 but uses the alternative SLC gusset design and therefore has a higher β_{ww} factor. The lateral displacement time-history in Figure 6.15(b) shows that excellent agreement was attained between command and feedback displacements. Also, complete brace section failure occurs at the same target displacement $6\delta_y$.

Buckling capacity is reached at the δ_y cycle and the brace undergoes more noticeable compressive resistance degradation in subsequent cycles, observed as uneven saw tooth shapes in the brace axial load time-history in Figure 6.15(d). Calculated buckling capacity is not achieved during this test. In the tensile loading range the Bauschinger effect is observable with a decrease in applied force for a given displacement demand at $4\delta_y$. As in Cyclic Test 2, the brace buckled out-of-plane in the –z direction.

The strain measurements at SG5 in Figure 6.15(d) show very large strains reached during the $4\delta_y$ and $6\delta_y$ displacement cycles. This indicates that a plastic hinge formed in the gusset plate.

Similar plastic strain is also recorded at the plastic hinge at SG10, indicating that a plastic hinge developed at brace mid span during the δ_y cycle. As the gauge was located on the tension flange, the development of the local buckle was not represented. This is in agreement with the design intentions of a larger β_{ww} value that approaches 1.0. However, no clear increase in brace elongation capacity, and consequently, frame drift is discernable.

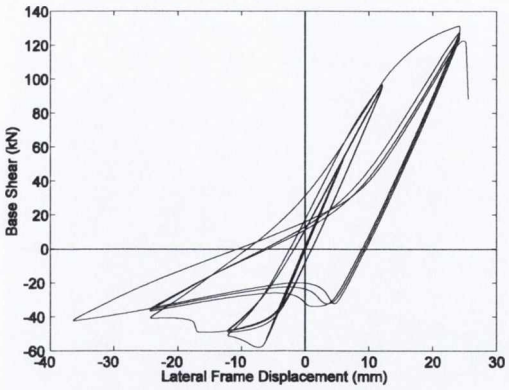

(a) Frame hysteretic response

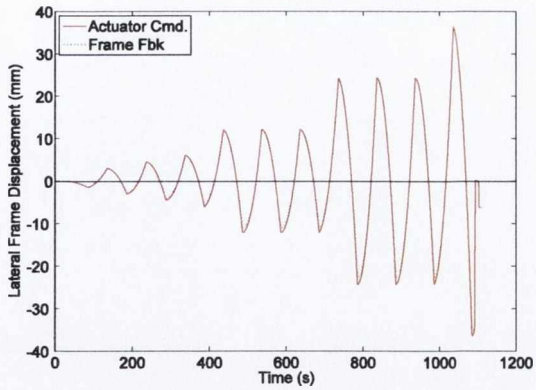

(b) Lateral displacement time-history

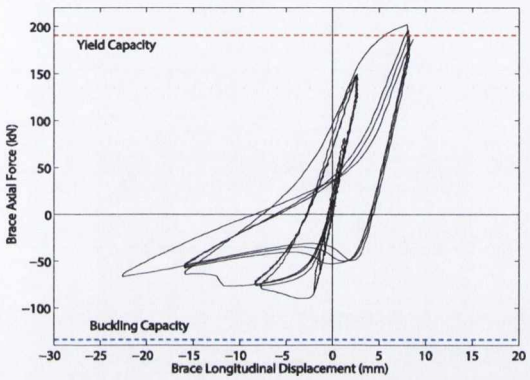

(c) Local brace hysteretic response, with brace capacities from coupon tests

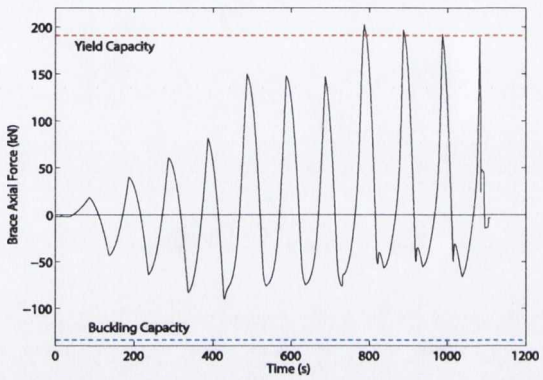

(d) Brace axial load time-history, with brace capacities from coupon tests

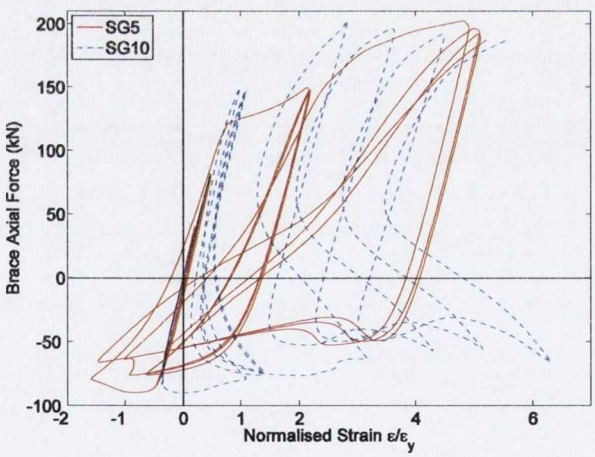

(e) Strain hysteresis at brace mid-length (SG10) and in the upper gusset plate plastic hinge zone (SG5)

Figure 6.15 – Recorded responses of Cyclic Test 6; Specimen S60-CA-G2.

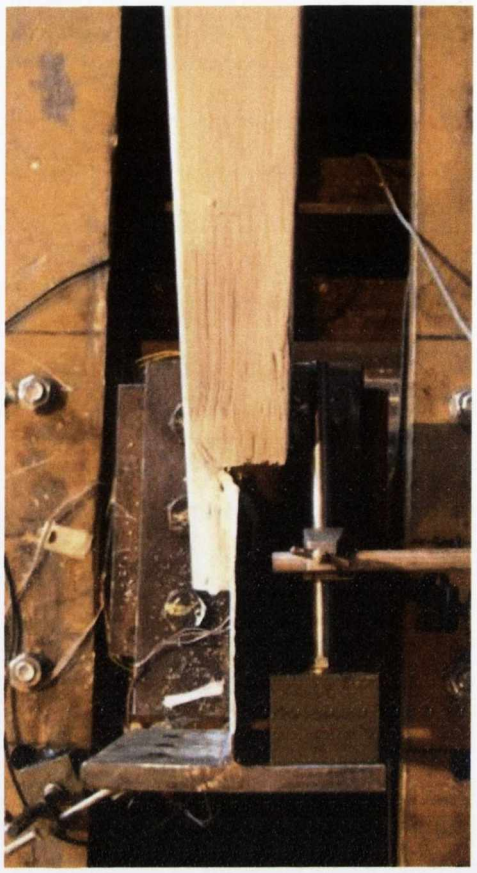

(a)

(b)

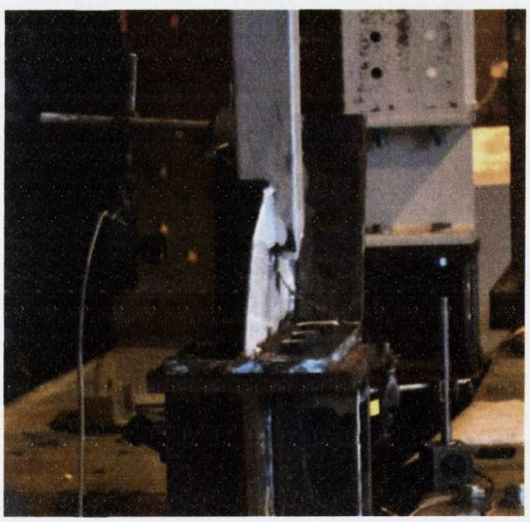

(c)

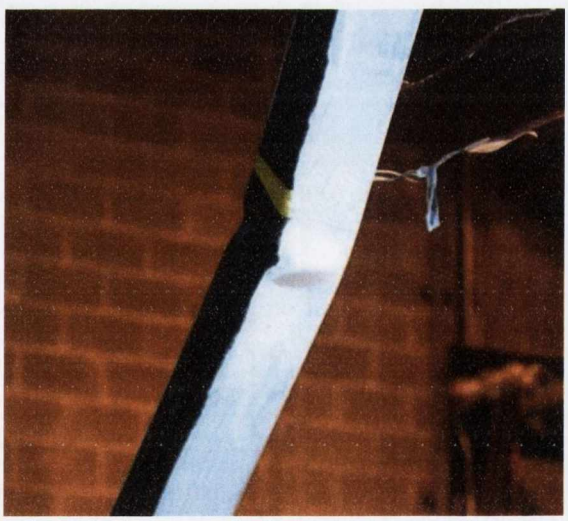

(d)

Figure 6.16 – Cyclic Test 6; Specimen S60-CA-G2 after testing showing (a) lower gusset plate connections (b) column and upper gusset plate connection (c) bending of lower gusset plate and (d) local buckle at brace midspan.

6.4 Analysis of Cyclic Test Results

In the previous section, measured data were reported for each test and observations were made on the execution of the experiments. This section presents an analysis of the data collected in all six tests to evaluate how frame performance was influenced by the different brace member and gusset plate configurations. The influence of the CA and CB connection types on initial frame stiffnesses and overall frame behaviour is examined. The effects on brace buckling and tensile capacities and gusset plate deformation zones are also investigated. The influence of gusset designs G1 (SLC) and G2 (EC) is assessed through the number of cycles completed to failure and drift range. Finally, displacement ductility capacity is evaluated for each specimen and compared with prediction models, and the influence of the balance design factor on energy dissipation is assessed.

6.4.1 Connection Type (CA and CB)

The influence of connection type on frame response can be evaluated in different ways. Table 6.3 presents the measured initial stiffness, K_{fr}, of the test frame in each test. This value was obtained by establishing the tangent stiffness between the yield point and the origin on the base shear-lateral deformation plot. These values are compared with an estimate of the tensile stiffness of a single brace, $K_{br} = cos(\theta)^2 EA/L$, where $\theta = 50°$. The K_{br}/K_{fr} ratios are larger than unity for all tests, ranging between 1.6 and 2.69. This indicates that there are other significant sources of flexibility in the frame. With the exception of S40-CA-G1, larger K_{fr} values were observed for the CA connections compared to the CB connections. This is explored in the following paragraphs through detailed comparisons the responses of specimen pairs.

Table 6.3 – Frame stiffness properties

Specimen	b/tε	$\bar{\lambda}$	Brace Stiffness K_{br} (N/mm)	Measured Frame Stiffness K_{fr} (N/mm)	K_{br}/K_{fr}	Brace Buckling Load (kN)	Brace Ult. Tensile Load (kN)
S40-CA-G1	16	1.16	13486	5013[a]	2.69	-66.81	178.64
S40-CA-G2	16	1.23	12774	7992	1.60	-48.60	211.32
S40-CB-G1	16	1.66	13486	7883	1.71	-53.46	197.10
S40-CB-G2	16	1.75	12774	6814	1.87	-34.75	205.29
S60-CA-G1	24	0.75	20485	9405	2.18	-117.95	208.53
S60-CA-G2	24	0.80	19403	8752	2.22	-89.94	202.28

[a] Initial stiffness recorded with unanticipated inelastic behaviour.

The recorded global frame hysteretic responses provide evidence of the influence of connection type on overall frame stiffness. In comparing specimens S40-CA-G2 and S40-CB-G2 (in Figure

6.17(a) and (b) respectively), the end conditions of the CB connection type exhibits a more 'pinched' hysteretic plot characteristic that is archetypal of CBF behaviour. The extra rotational restraint provided by the CA connection reduces the brace effective length thereby increasing the brace buckling load by 35.7%. During initial loading, the brace member provides the main source of lateral resistance, and when buckling is initiated in the brace, frame lateral resistance is dramatically reduced in this loading direction. However during the post-buckling response of specimens with CA connections, the post-buckling resistance of the brace is supplemented by the frame joint rotation resistance provided by the connection of the gusset plate to both beam and column flanges. This is observable in the post-buckling response of specimen S40-CA-G2, where the compressive loading half-cycles are distinguished by a gradual increase in tangent stiffness. The compressive resistance increases by 93.4% above the initial buckling capacity reaching a base shear of -58.4 kN. Initial elastic tensile cycles display CA frame stiffness 12.7% larger than that demonstrated by the CB frame.

A similar pattern is observable when comparing the initial elastic cycles of specimens S40-CB-G1 and S60-CA-G1 (Figure 6.17(c) and (d) respectively), with the CA specimen displaying a larger initial tangent stiffness. For example, in the elastic tensile cycles, the CA frame stiffness is 4.25% larger than the CB frame. The relative stiffness of CA and CB specimens with G2 (EC) gusset plate designs can be compared in Table 6.3. The CA specimen (S60-CA-G2) displayed a 30.3% higher stiffness than the CB specimen (S40-CB-G2). Reducing the gusset plate thickness has the effect of minimising its contribution to frame stiffness when bending is induced in the gusset.

Strain gauges were located on the test frame and all test specimens to record the development of localised strains. The positions of strain gauges on the specimen gusset plates are shown in Figure 6.18. The brace force-strain relationships recorded with these gauges are shown in Figure 6.19. Comparison of Figure 6.19 (a) and (c) demonstrates that in the CB connection much greater inelastic strains occur at the top plate boundary (SG6) than at the bottom boundary (SG4). The CA connection shows a more balanced distribution of strain across the plate without reaching the yield strain limit ε_y. However in Figure 6.19(b), the effects of using a thinner gusset plate is emphasised with SG6 reaching strain values almost five times the nominal material yield strain. The asymmetrical layout of the thin plate in the S60-CA-G2 specimen considered in Figure 6.19(d) resulted in gauge SG4 lying within the elliptical plastic hinge zone and experiencing larger strains than SG6. SG6 was positioned on the outer end of the plastic hinge zone and only yielded during the final loading cycle.

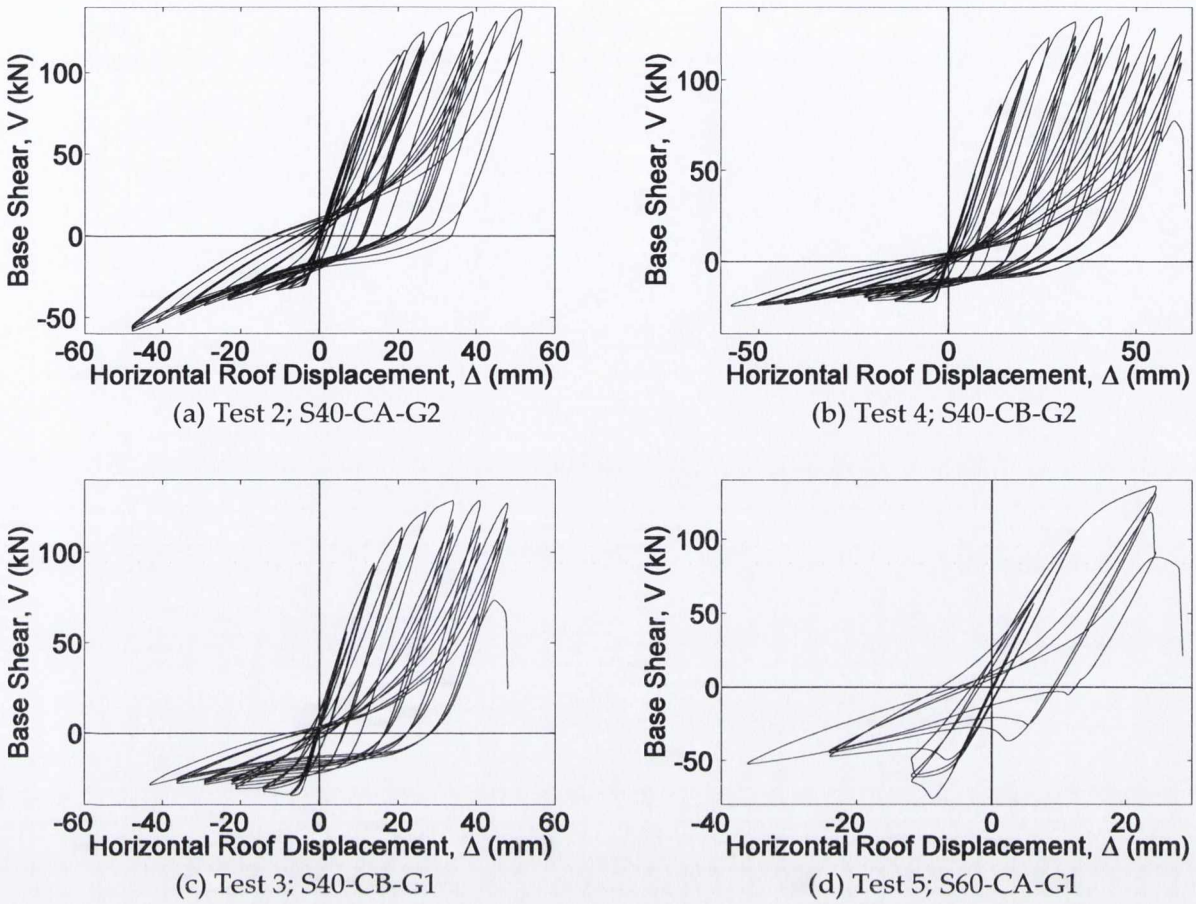

Figure 6.17 – Frame hysteretic behaviour (global) plots showing variation of base shear with horizontal roof displacement.

Figure 6.20 demonstrates the reduction in frame stiffness trend with increasing brace slenderness observed with both CA and CB connection types. These observations agree with the anticipated contribution of stiffness for each connection type, with CA connections demonstrating K_{fr} stiffness values at least 17.3% larger than CB connections of the same brace section size.

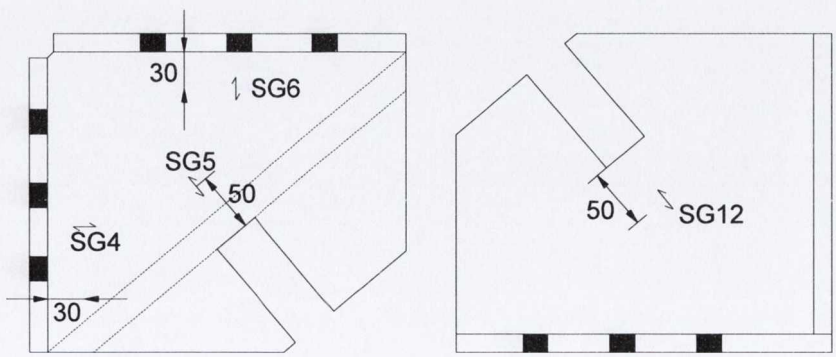

Figure 6.18 – Strain gauge locations on gusset plates.

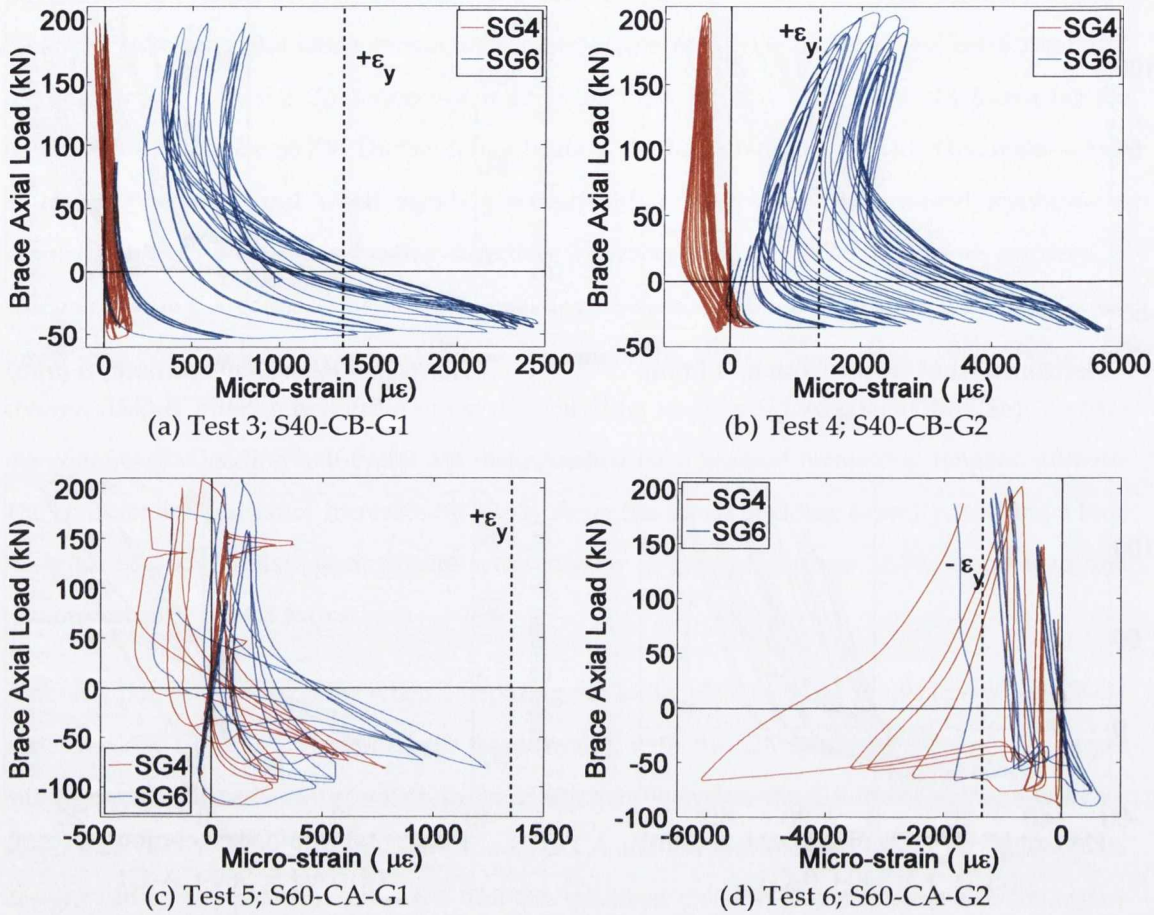

Figure 6.19 – Recorded brace axial load-strain plots for strain gauges located on gusset plates.

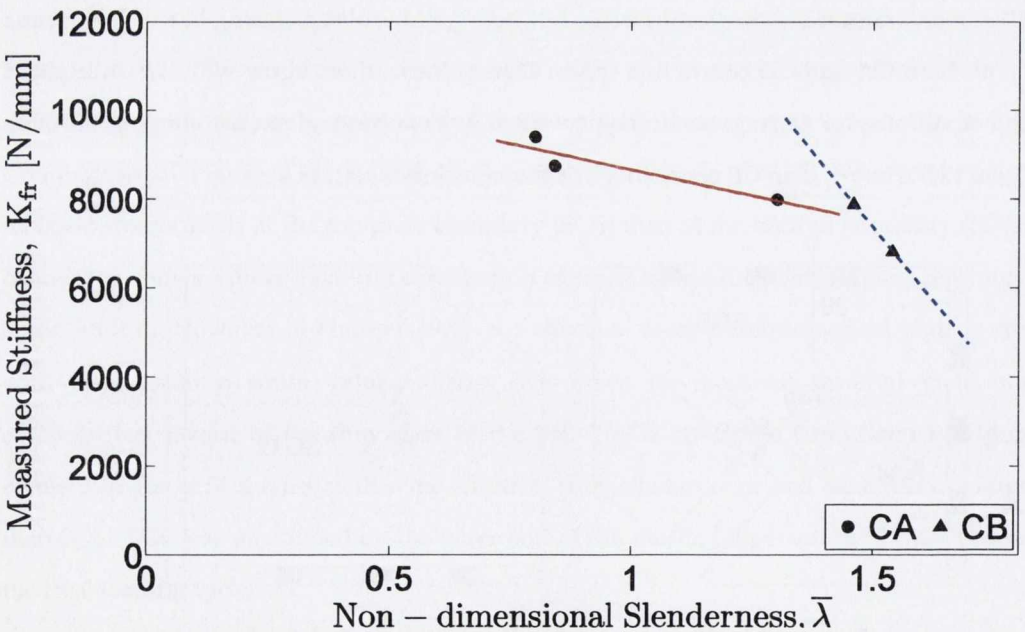

Figure 6.20 – Measured frame stiffness, K_{fr} plotted against non-dimensional brace slenderness, $\bar{\lambda}$ for both connection types CA and CB.

6.4.2 Gusset Design (G1 and G2)

One aim of this experimental series was to examine the hypothesis that greater brace ductility capacity could be achieved using β_{ww} ratios near 1.0 (G2 plates) than with lower β_{ww} ratios (G1 plates). The performance of specimens with G1 and G2 gusset designs can be assessed by examining the number of cycles to brace failure N_f in each test (Table 6.4). As an indication of overall global ductility capacity, the minimum and maximum storey drift values (Δ_{min} and Δ_{max} respectively) are combined to obtain the drift range Δ_{range} for each specimen. From Table 6.4, comparison of tests S40-CB-G1 and S40-CB-G2 identifies a larger drift capacity and therefore larger ductility capacity for the G2 design. For S60-CA-G1 and S60-CA-G2, the high cross-section slenderness dominated brace fracture behaviour leading to the same N_f and Δ_{range} values identical for this specimen pair.

The performance of G1 and G2 gusset designs can be further evaluated from brace hysteresis response plots shown in Figure 6.21. On comparing tests S40-CB-G1 and S40-CB-G2 (Figure 6.21(a) and (b) respectively), the G2 design out-performs the standard G1 design, extending seven target displacement cycles beyond the G2 failure limit. This effect is not manifested in the 60×60×2.5 SHS specimens (Figure 6.21(c) and (d)). The high cross-section slenderness ratio in these specimens resulted in significant localised strains at brace mid-length during early compression cycles. Large local buckling strains developed in the cross-section corners after several cycles of inelastic buckling leading to fracture initiation. Upon reloading in tension, cracks formed in the corner regions of both specimens beginning in the +10 mm displacement cycles. Local buckling was the dominant failure mode for these specimens, thus limiting the ability of the gusset plates to contribute to energy dissipation through plastic yielding.

Table 6.4 – Brace fracture and frame drift

Specimen	$b/t\varepsilon$	$\bar{\lambda}$	β_{ww}	No. Cycles to Fracture, N_f	Frame Drift		
					Δ_{min} (%)	Δ_{max} (%)	Δ_{range} (%)
S40-CA-G1	16	1.16	0.38	16	-2.76	2.67	5.43
S40-CA-G2[a]	16	1.23	0.75	28	-2.19	2.36	4.55
S40-CB-G1	16	1.66	0.38	21	-1.98	2.52	4.50
S40-CB-G2	16	1.75	0.75	28	-2.62	3.16	5.78
S60-CA-G1	24	0.75	0.52	10	-1.65	1.68	3.33
S60-CA-G2	24	0.80	1.03	10	-1.67	1.67	3.33

[a] Maximum demand values sustained by specimen.

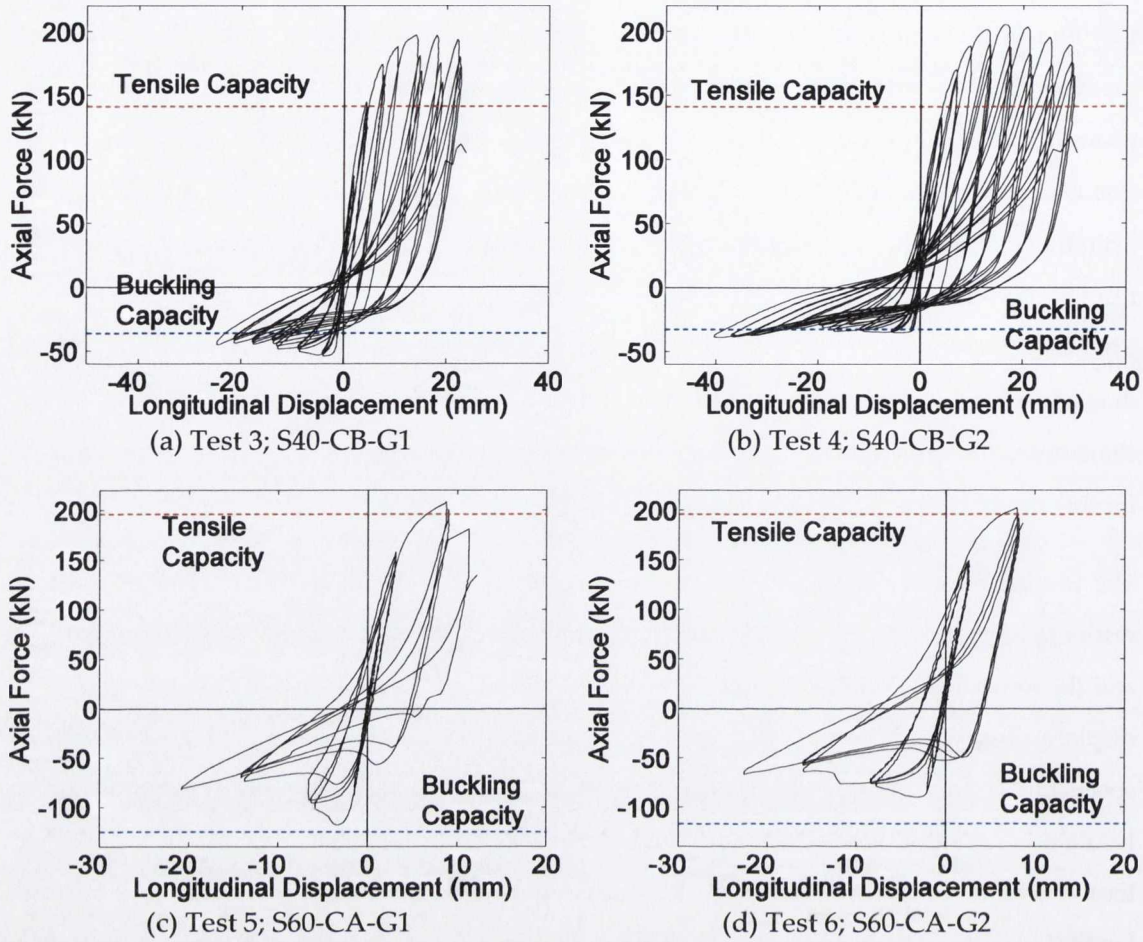

Figure 6.21 – Brace hysteretic behaviour (local) plots showing the variation of brace axial force with brace elongation.

Strain gauges SG5 and SG12 were located just outside the boundary of the free rotation zone in which plastic hinge rotation occurs during brace buckling (Figure 6.18). High strains at these locations can arise due to both plastic hinging in compression and gusset plate yielding in tension. Considering the strains measured at these locations shows that much higher strains were observed with G2 gusset plates in CA type connections, but not with CB type connections (Figure 6.22). For the S40-CA-G1 test (Figure 6.22(a)) minor yielding occurred in the gusset compared to specimen S40-CA-G2 (Figure 6.22(b)) where strains at SG5 reached 700% of yield strain. In S40-CB-G1 (Figure 6.22(c)) plastic hinge development was limited implying the concentration of plastic deformation at brace mid-length, and the complementary test S40-CB-G2 cycles through only a slightly larger strain range.

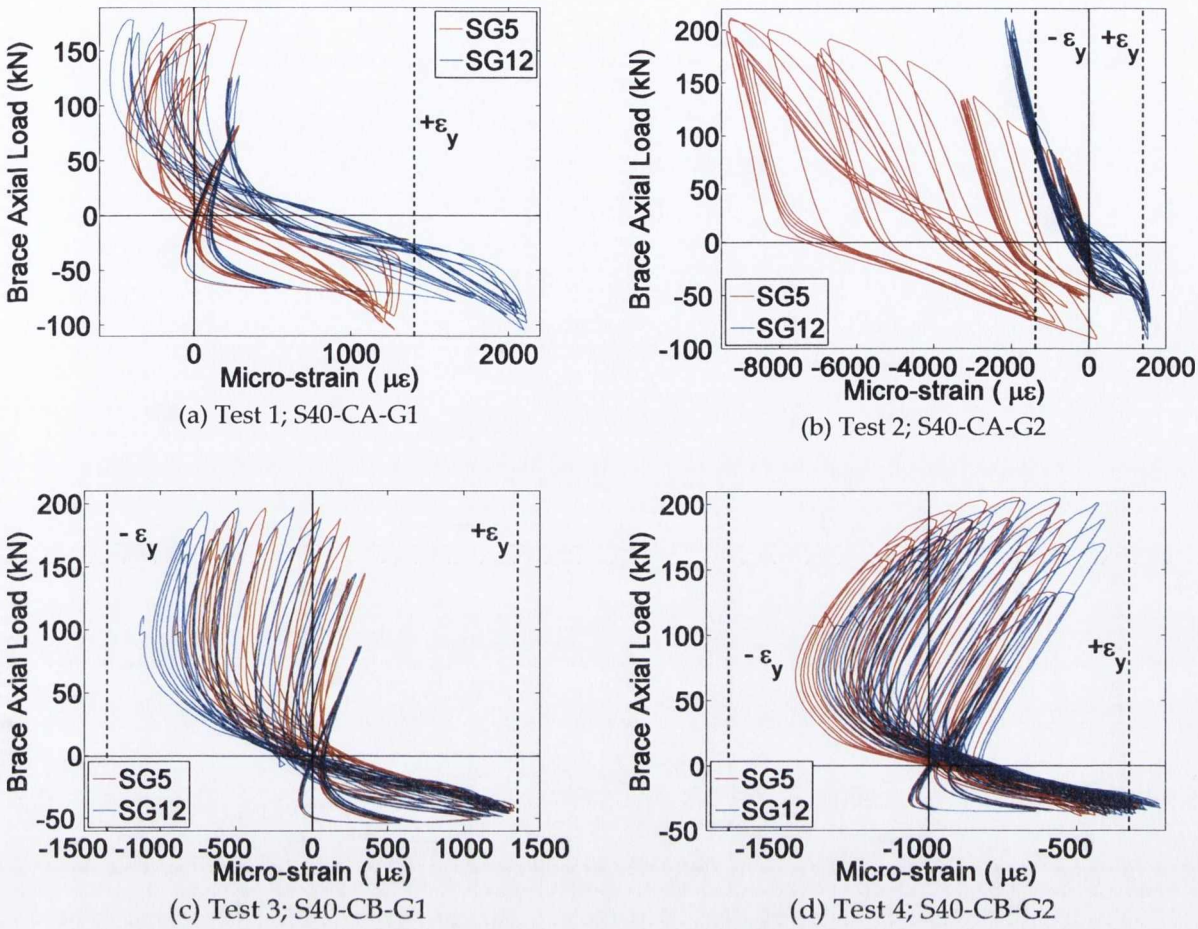

Figure 6.22 – Local hysteretic behaviour showing plots of brace axial force and longitudinal displacement

6.4.3 Displacement Ductility and Energy Dissipation

Brace displacement ductility – defined as the ratio of maximum to yield displacement (see Chapter 2) – is a key performance parameter that provides an indication of the energy dissipation capabilities of each specimen. The measured ductility capacities μ_Δ of the test presented in Table 6.5 ranged from 2.54 to 8.12.

Table 6.5 – Displacement ductility and energy dissipation for cyclic tests.

Specimen	$b/t\varepsilon$	$\bar{\lambda}$	β_{ww}	Displacement Ductility		Energy Dissipation	
				δ_y (mm)	μ_Δ	E_{tot} (m.kN)	E_{10} (m.kN)
S40-CA-G1	16	1.16	0.38	0.72	-	6.20	0.65
S40-CA-G2	16	1.23	0.75	2.76	5.67[a]	22.42	1.13
S40-CB-G1	16	1.66	0.38	4.80	7.69	16.32	1.23
S40-CB-G2	16	1.75	0.75	5.12	8.12	33.45	1.28
S60-CA-G1	24	0.75	0.52	2.95	3.07	6.55	5.44
S60-CA-G2	24	0.80	1.03	2.80	2.54	7.86	6.12

[a] Maximum displacement ductility demand survived by specimen.

In Figure 6.23, predictions of the displacement ductility capacity of each specimen made using the model proposed by Nip et al. (2010) and set out in Equation 2.20 are compared with the measured experimental values. The trend shows that for higher non-dimensional slenderness ($\bar{\lambda}$) members, there is an increase in displacement ductility capacity (μ_Δ). Assuming uniform curvature, this is attributable to plastic strains being reached at a lower member rotation in low $\bar{\lambda}$ members compared to high $\bar{\lambda}$ members for a given drift demand. For specimens with lower cross-section slenderness (S40), the prediction slope underestimates the measured ductility capacities. This may be attributable to the influence of the gusset plate connections, (including the G2 specimens designed for greater gusset plate yielding) in the test specimens, which contrast with the fixed-end stiffened connections employed in the specimens tested by Nip et al. (2010). For specimens with high cross-section slenderness ratios, the predicted values overestimate the measured ductility capacity. The prediction methods of Tremblay (2002) and Goggins et al. (2006) overestimated the measured ductility capacities. The relationships provided by Goggins et al. (2006) were calibrated against tests using hot rolled steel sections only and for specimens with different member and local slendernesses.

As discussed in Chapter 2, the energy dissipated in a single response cycle can be evaluated as the closed integral of the force-displacement curve for that cycle:

$$E_i = \oint ku(t)\frac{du}{dt}dt = \oint Fu(t)dt = = \frac{1}{2}Fu(t) \qquad 6.1$$

The total energy dissipated E_{tot} was calculated for each test and these results shown are in Table 6.5. Similar to the work of Goggins (2004) energy dissipation values at the end of the tenth cycle E_{10} were used to compare the energy dissipated in different tests. The plots in Figure 6.24 display an increase in energy dissipation (for both section types) for larger β_{ww} values. While this is more

obvious in the plot of total dissipated energy in Figure 6.24(a), a more direct comparison is made in Figure 6.24(b) where the brace size is shown to significantly influence the energy dissipated in a single displacement cycle. After ten displacement cycles the S60 specimens had nearly attained their final energy dissipation values shown in Figure 6.24(a). In contrast, at this stage the S40 specimens have only dissipated a fraction of their eventual test totals.

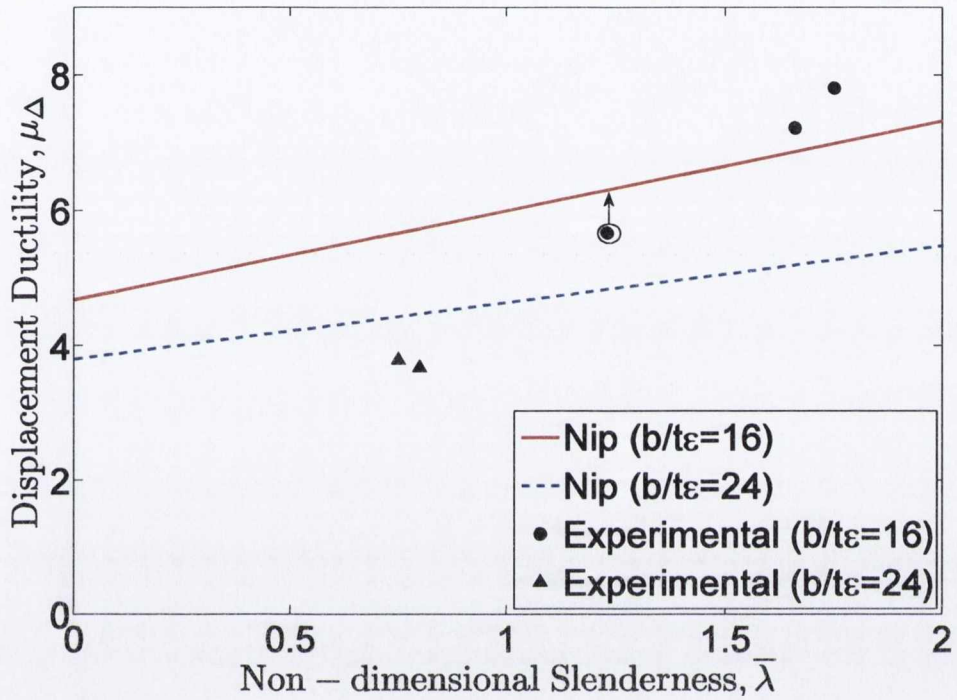

Figure 6.23 – Displacement ductility plotted against non-dimensional brace slenderness. Predicted values by Nip et al. (2010) are compared with experimental results.

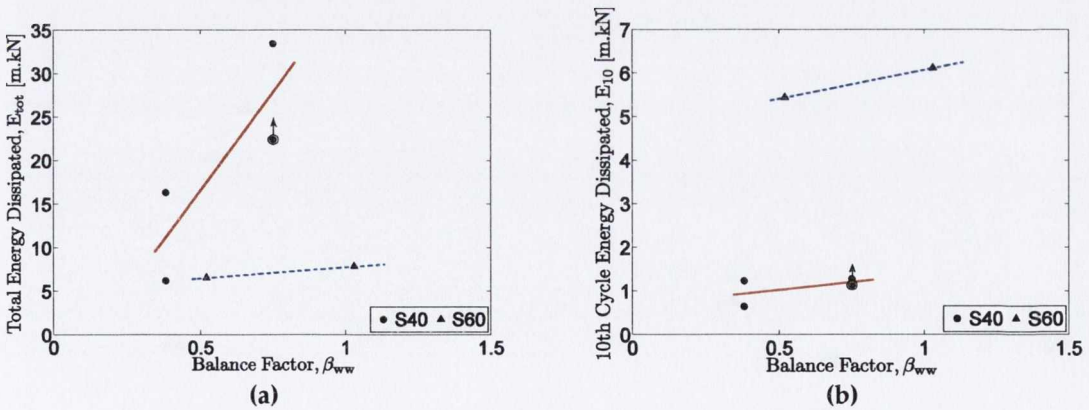

Figure 6.24 – Energy dissipation values compared with balance factor β_{ww}.

6.5 Chapter Overview

This chapter presented the results and analysis of the cyclic testing phase of the overall experimental programme. The measured specimen profile shapes were first presented and shown to influence the direction of out-of-plane brace deformation during buckling. The specimen response measurements were then presented for each test. These results were then analysed to identify the influence of the experimental parameters on the overall performance, and to make comparison between different brace-gusset plate designs. The experimental observations of the behaviour of the different brace-gusset plate specimens and of the test frame as a whole are of particular value in preparing for the series of shaking table tests on similar specimens described in Chapters 8 and 9. The observations and results presented in this chapter are also employed in the following Chapter 7 for the further development and validation of OpenSees models of CBFs.

7 Complementary Cyclic Tests – Correlation with Numerical Models

7.1 Introduction

In Chapter 4, different methods of modelling brace members in OpenSees were identified. Recommended values were presented for the input model variables, and these recommendations were validated against experimental tests that examined, in particular, the hysteresis performance and fracture life of each specimen. This chapter describes how these procedures are implemented in a full-scale single-storey test CBF structure. The CBF frame considered is the plane frame structure tested in the Complementary Cyclic Tests at Trinity College Dublin (Chapter 5). The aim of developing this model is to investigate the capabilities of OpenSees for CBFs. This test frame incorporates all of the essential features of the BRACED project CBF test structure investigated in the shake table tests at CEA Saclay (Chapter 8).

7.2 CBF Structure and Connectivity

The model comprises a single-storey plane-frame CBF with lateral resistance provided by a single brace member. The beam and column members were designed to remain elastic throughout each test while the brace specimen and connected gusset plates responded inelastically. Further details of the test frame design are presented in Chapter 5.

An overview of the test frame with constituent nodes and elements is shown in Figure 7.1 below. The numbering scheme is arranged so that the elements are numbered with the suffix 'e' and the nodes with the suffix 'n'. The specific UB and UC cross-section geometries were defined for application to the beam-column elements in the frame. As the frame was expected to perform elastically, only one main element was defined for each member, with more detailed modelling of the member connections. These connection details are summarised below.

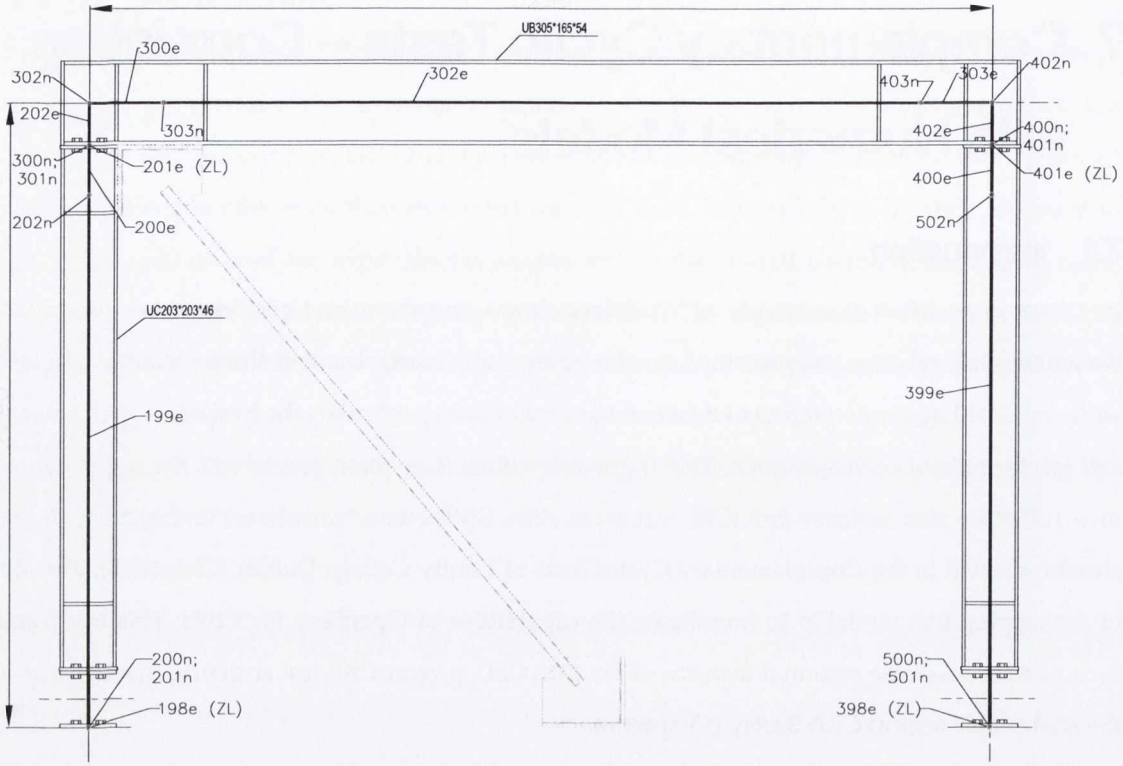

Figure 7.1 – OpenSees model for Complementary Cyclic Test frame. Numbers denoted with 'n' signify node numbers and 'e' signify element numbers.

7.2.1 Beam-Column-Gusset Connection Configuration

In the beam-column connections in the test frame, the bottom beam flange is bolted to the top of the columns using flush end plates. The semi-rigid nature of this connection implies that it cannot be accurately modelled as either a simple pinned or continuous connection. The partially-restrained bolted connection model employs elastic springs to constrain three translational degrees of freedom and two rotational degrees of freedom about the in-plane axes. A specific elastic rotational spring is used to model rotation about the out-of-plane axis. This follows the methodology used by Hsiao et al. (2012) to model shear tab connections. Hsiao et al. used the moment-rotation model developed by Liu and Astaneh-Asl (2004) to obtain estimates for initial rotational stiffness and maximum positive and negative moment capacities. Liu and Astaneh-Asl provided guidelines for estimating the behaviour of composite and non-composite shear tab connections based on experimental results from tests on different shear tab connections. The results of this study showed that both shear tab connection types exhibit non-negligible rotational strength and stiffness leading to partially restrained connection behaviour.

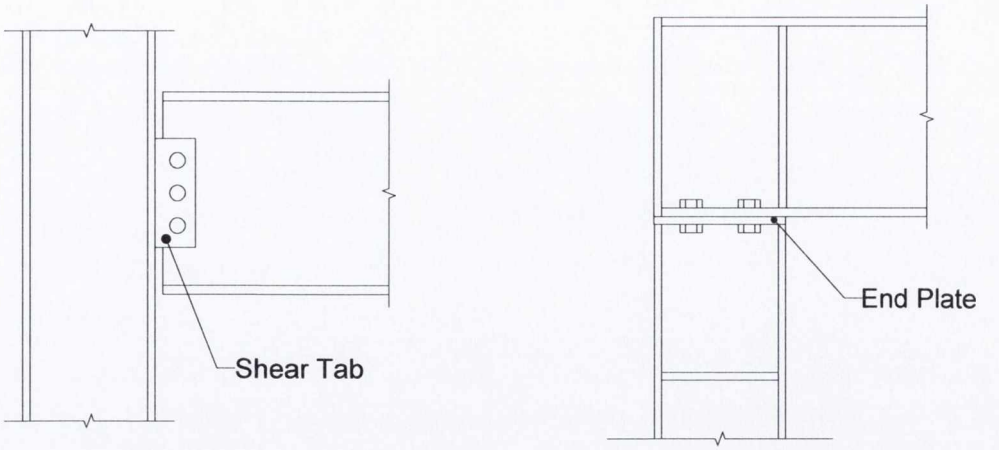

Figure 7.2 – (a) Shear tab connection (normally treated as a 'pin' connection), and (b) end plate connection (treated as partially restrained).

Numerical models are developed for both of the gusset connection configurations considered in the test series in this project. In connection type A (CA), gusset plate flanges are bolted to both the column flange and beam flange, while in connection type B (CB), the gusset is connected to the beam flange only, allowing free plate rotation in the out-of-plane direction (see Figure 7.3 and Section 3.4 for further details). In order to apply a modelling methodology similar to that used by Hsiao et al., the rotational spring method needs to be adapted for the CB connections and for the right-hand frame connection (where there is no brace connection). In this configuration the gusset plate boundary conditions make a negligible contribution to the beam-column connection moment capacity. In the CA connections, the gusset plate boundary conditions have the effect of effectively restraining joint rotation, and were treated as fully restrained connections using a simplified fixed connection model. However, once brace buckling occurs, large frame rotations induce tension forces within the gusset plate with the effect of stretching and flattening the plate. This is in opposition of the action of the brace bending the plate out of plane. In essence, the complex behaviour is difficult to capture with the analysis techniques used in this work.

Therefore, for the CB connections, an initial rotational stiffness for the flush end plate connection system is required for the elastic spring material model. A study conducted by Thomson (2001) developed a prediction model for the moment-rotation response of end plate connections. The prediction model formulates a moment-curvature relationship based on material and geometric properties of a generic beam-column flush end plate connection. The force-displacement relationship is then predicted based on different failure mode classifications of equivalent T-stubs and bolts. The elastic behaviour of T-stub systems has been studied by Yee and Melchers (1986). A deformation model is provided for stiffened and unstiffened connections. The extensive set of

equations has been simplified for the stiffened case in (Figure 7.4) below with the loads represented as P for the T-stub web force; B for the bolt force and Q for the prying force. The T-stub is modelled as a beam under simple bending with the T-stub deflection shown as Δ. These notional T-stubs are also used in Eurocode 3 Part 1-8 (CEN, 2005b) to model certain joint typologies for bending of column flanges, end-plates and flange cleats. Using Thomson's model, the rotational stiffness of the beam-column connection in the test CBF structure was calculated. As this model was adapted for a connection featuring a beam connected to a column end plate rather than the opposite, it was expected that the calculated provisional stiffness would require further refinement during the model validation phase in Chapter 7 and Chapter 10.

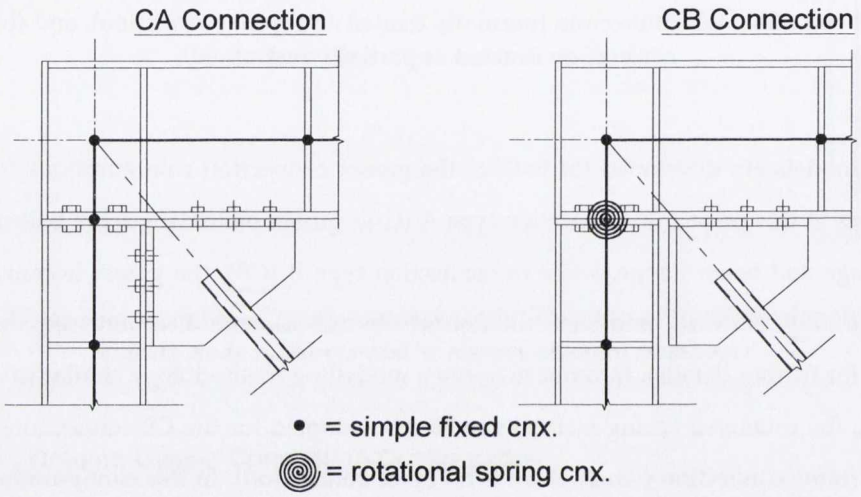

Figure 7.3 – Modelling methods for CA connection (treated as fully restrained) and CB connection (treated as partially restrained).

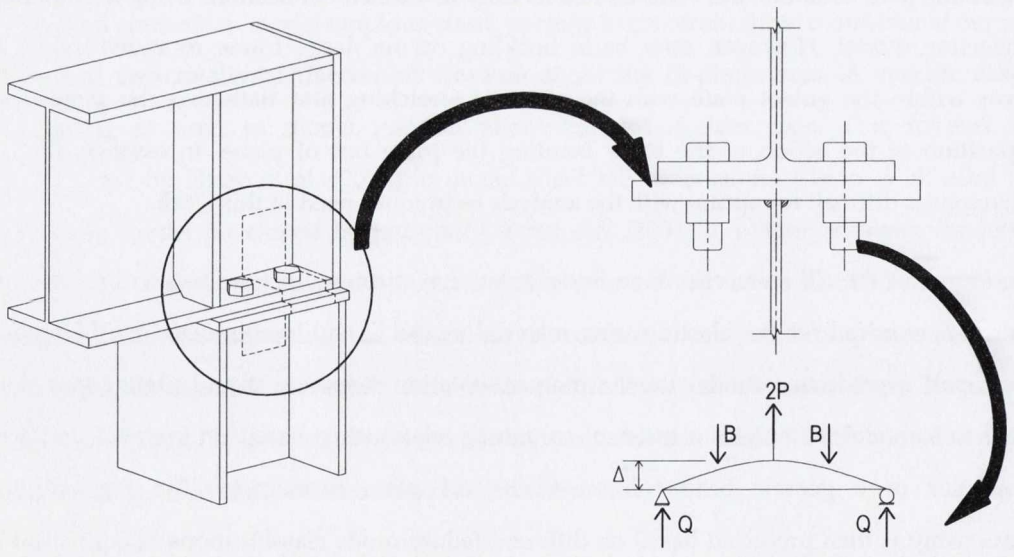

Figure 7.4 – T-stub notional component for the beam-column connection in use in the test CBF structure similar to that described by Thomson (2001).

7.2.2 Beam-Column-Gusset Rigid Zone Elements

At the beam-column-gusset connection significant rigidity is provided by the gusset plate and by the additional stiffener plates used to prevent beam and column flange buckling. Furthermore, as previously described in Chapter 3, the plastic hinge that forms in the gusset plate to permit out-of-plane brace buckling reduces the rotational demand on the bolts or welds used to connect the gusset to the beam and column flanges. Two options were explored to account for the associated increase in stiffness of portions of the beam and column lengths: equal degree of freedom nodal constraints (EqualDOF) and rigid links. Both options were implemented by creating rigid zones designated as elements 200e, 202e, 300e and 304e; 303e, 402e and 400e (Figure 7.5) dependent on the connection type. The details of each option are as follows:

- EqualDOFs impose the exact rotations and translations of a master node to a slave node. The example in Figure 7.6(a) shows unit translations and rotation θ of the master node (MN) and the corresponding displacements of the slave node (SN). The overall effect is that the constrained nodes always stay parallel.
- Rigid links connect node pairs and influence their behaviour as if they were connected by an 'infinitely stiff element'. In physical terms, this means that the element assumes small rotations and includes the arc an element would travel. This can be explained using the same example as above, shown in Figure 7.6(b). The slave node rotates along the rotation arc that is centred on the master node with a radius equal to the distance between the nodes. This results in the changes dX and dY applied to the linear translations.

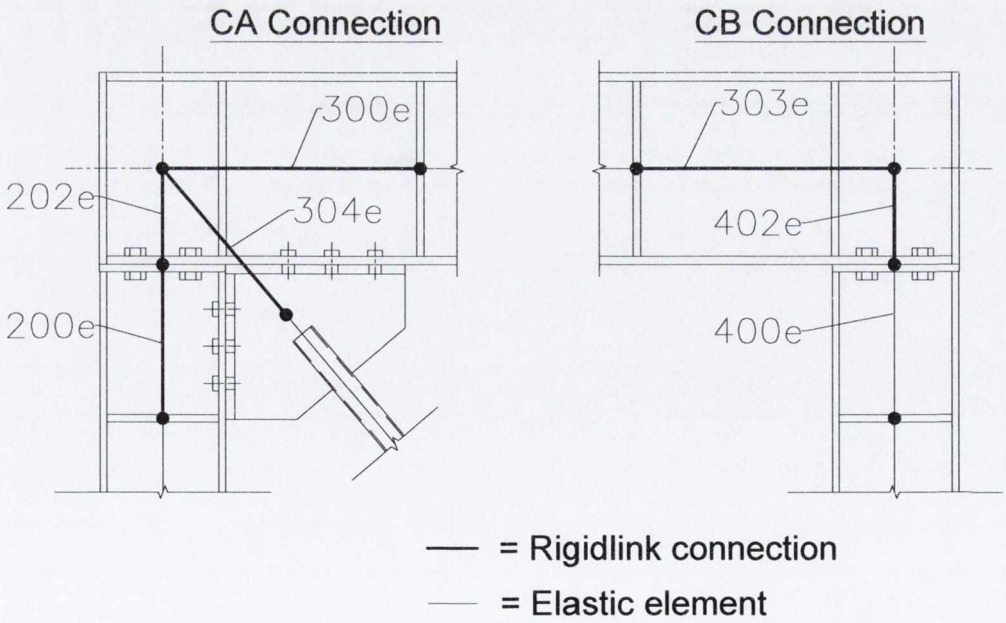

Figure 7.5 – High stiffness zone elements for CA and CB connections.

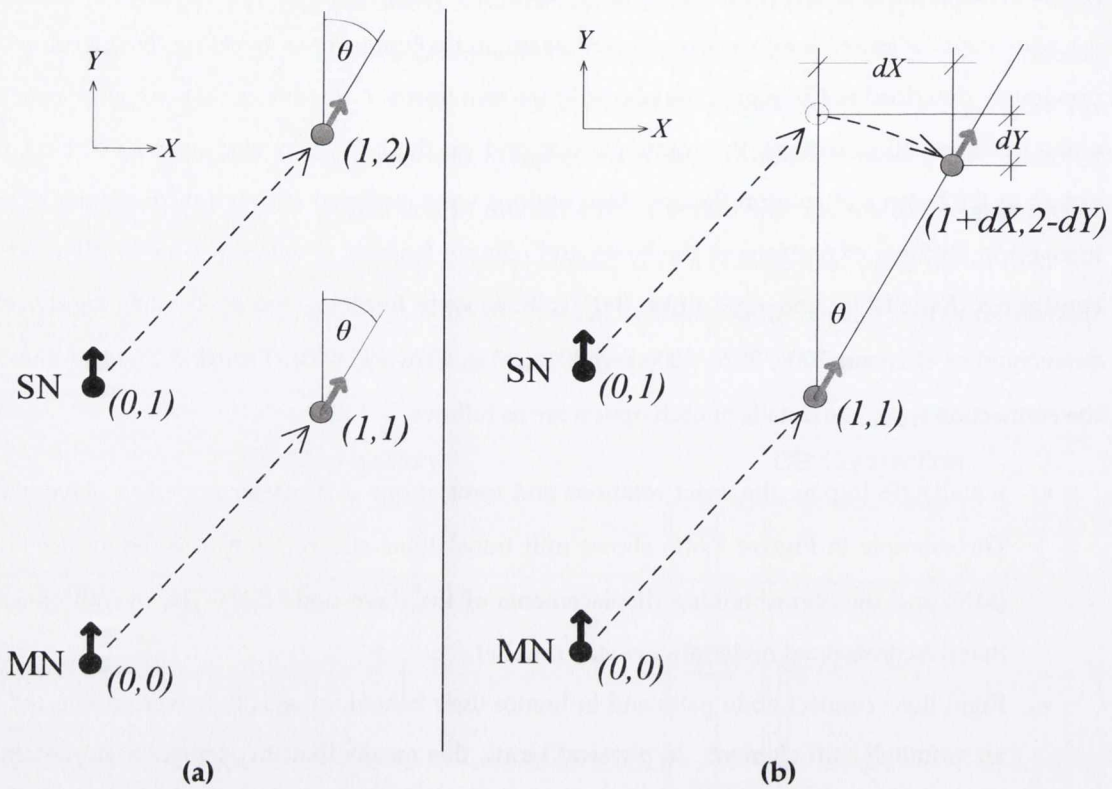

Figure 7.6 – (a) EqualDOF nodes with master node (MN) imposing unit translations and unit rotation θ to slave node (SN). (b) nodes connected using rigid links demonstrating the 'infinitely stiff element' concept.

7.2.3 Column Base Plate-Reaction Frame Connection

To isolate the experimental response of the brace specimens and their connections, the test frame employed pinned connections free to rotate in plane. This was implemented using short lengths of I-shaped UC sections, orientated with the lateral displacement of the frame (Figure 7.7). The web of these UC sections was designed to undergo plastic deformation forming nominally pinned connections. The web length could be considered as a cantilever structure with stiffness K equivalent to $3EI/L^3$. Similar to the beam column connections discussed above, these connections were modelled using a ZeroLength elastic rotational spring element. The initial stiffness calculated using the cantilever formulation was used as the Young's modulus of the spring. If required, the structural model can be simplified; actual pinned connections can be used with no in-plane rotational restraint, eliminating the requirement of ZeroLength springs. It was anticipated that these connection types would be implemented for later tests where plastic hinges fully developed in the web component.

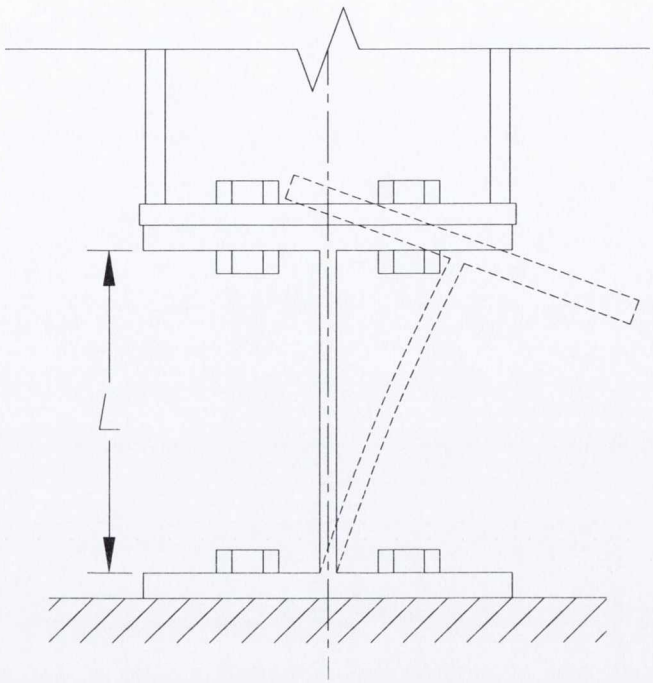

Figure 7.7 – Nominally pinned anchor points with UC 203×203×60 stub sections. By analysing the web length L the stiffness of the nominal pin can be calculated.

7.3 Brace Tube and Gussets

The parametric and correlation studies conducted in sections 4.2 and 4.3 identified optimum modelling parameters for brace tube specimens. These were employed for the brace and gusset specimens used in the test CBF structure including a prescribed initial camber of 0.1% of brace length. Both the standard and elliptical gusset designs (Chapter 3) were modelled and are represented as G1 and G2 respectively in Figure 7.8. As detailed in Chapter 3, both gusset types have specific yielding patterns dependent on the plate profile geometry and thickness. The specific plastic hinge sizes are modelled using a method proposed by Hsiao et al. (2012) where the out-of-plane stiffness is computed using rotational spring models similar to those used in the beam-column connections and the UC column stubs. In Figure 7.8 these are identified as elements 304e and 600e connecting the coincident node pairs 304n, 305n and 604n and 605n respectively. The spring model uses the same nonlinear steel material model as the rest of the brace. The initial stiffness of the gusset plate is a function of the plate profile geometry and thickness, therefore the stiffness for the spring model was calculated using the average gusset length L (Thornton, 1991) using:

$$K_{gus} = \frac{E}{L}\left(\frac{b_{ww}t_p^3}{12}\right) \qquad 7.1$$

Equation 7.1 is based on the Whitmore width concept where the axial force of the brace is transmitted through a beam-column element of width b_w and thickness t_p. Its suitability for finite element analysis was verified by Hsiao et al. based on the results of Yoo (2006). Minimal in-plane rotation occurs in the gusset plate. This rigidity is modelled using very high stiffness values to simulate rigidity.

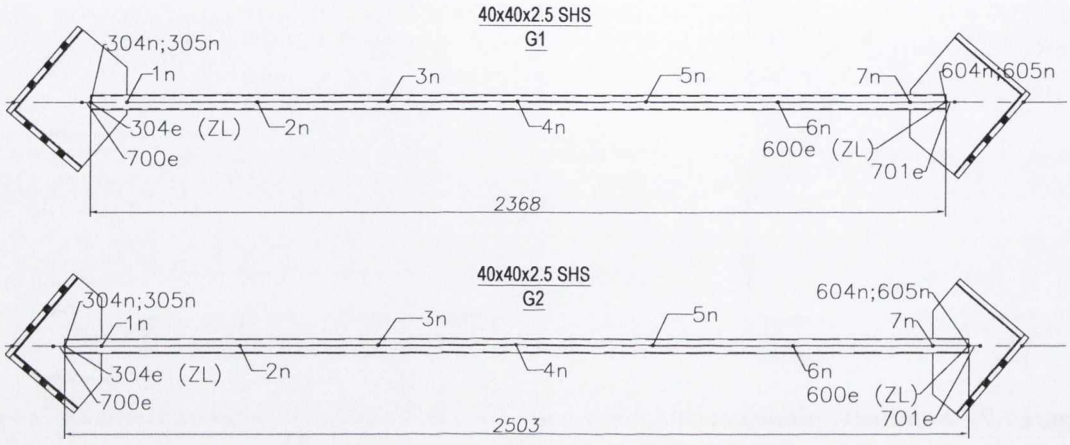

Figure 7.8 – Node pair locations for 304n, 305n and 604n, 605n. These locations are similar for both SLC (G1) and EC (G2) gusset designs.

7.4 Correlation with Numerical Models

In this section, the output from OpenSees models are compared with the cyclic experimental test results from Chapter 6. The models are constructed using the techniques discussed in Section 7.2 and 7.3. The results of Cyclic Tests 2 to 6 are correlated with their experimental frame hysteresis results. In this way, both the brace resistance and frame action are included in the correlations.

The comparison results are shown in Figure 7.9. The models employed rigid link elements in the corner beam-column connections with continuous connectivity for the CA connection configuration (Figure 7.5(a)). The rotational stiffness from Thomson (2001) was calculated for the beam-column connection. The rotational stiffness was prescribed for the right-hand beam-column connection in all tests and both connections in Tests 3 and 4 (CB connection configuration) as shown in Figure 7.1. To represent the bending stiffness of the gusset plate connection, a rotational spring with a stiffness value from Equation 7.1 was implemented connecting the brace and gusset elements and similarly for the UC stubs as in Figure 7.7. The fatigue model was employed for the brace elements using $\varepsilon_0 = 0.165$ based on the values used in sub-section 4.3.2.

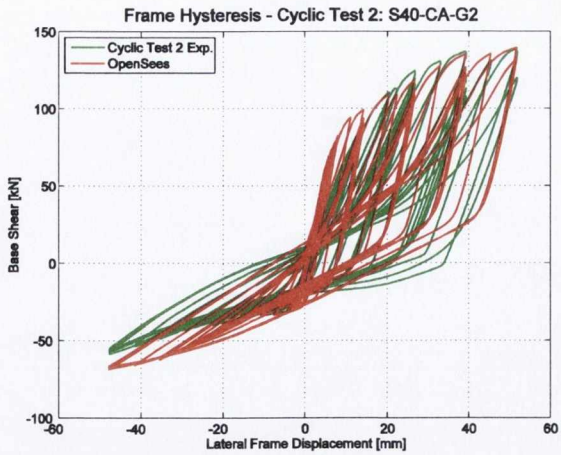

(a) Cyclic Test 2; S40-CA-G2

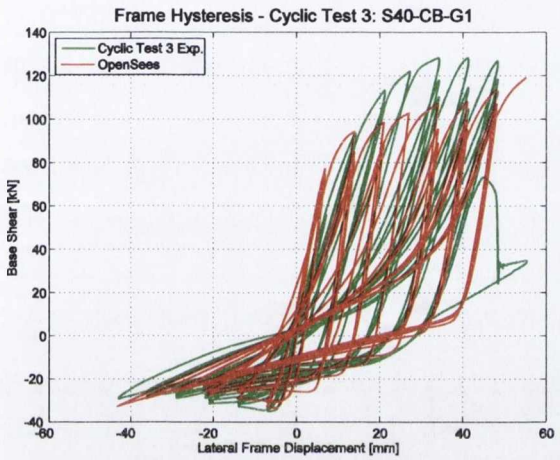

(b) Cyclic Test 3; S40-CB-G1

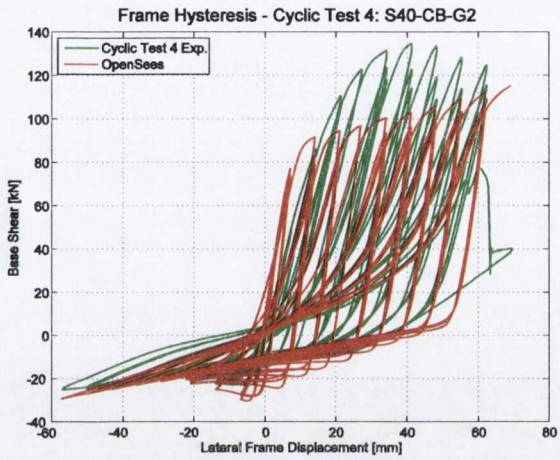

(c) Cyclic Test 4; S40-CB-G2

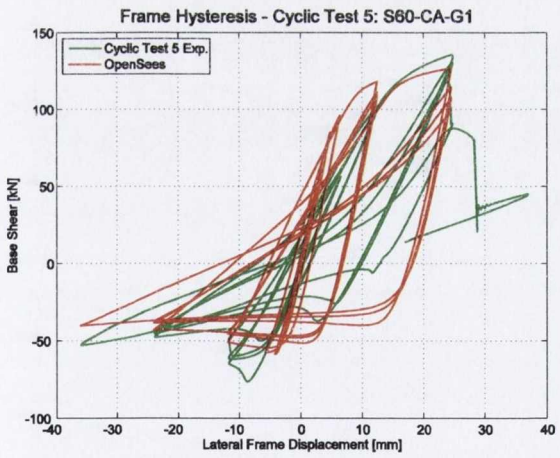

(d) Cyclic Test 5; S60-CA-G1

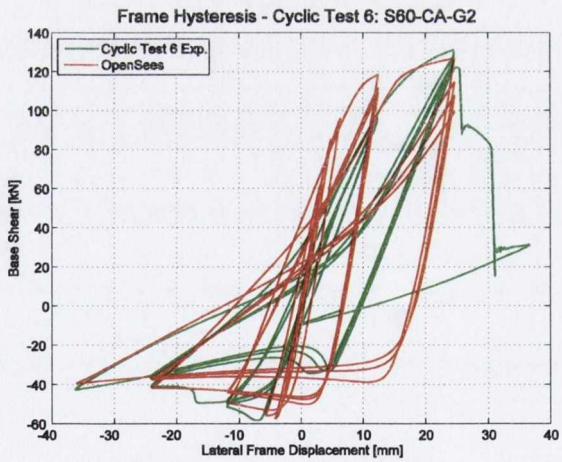

(e) Cyclic Test 6; S60-CA-G2

Figure 7.9 – Frame hysteresis correlation plots for Cyclic Tests 2 to 6. Experimental responses are denoted with 'Exp.' and simulated responses with 'OpenSees'.

Figure 7.9(a) shows the response comparison for Cyclic Test 2 with S40-CA-G2 specimen. In the compression range, the predicted initial buckling capacity of the frame is accurate with approximately 2.7% overestimation. Thereafter, the increase in compressive resistance of the frame

(controlled by the post-buckling strength of the brace and the rotational stiffness of the beam-column connections) is captured reasonably well at each target displacement with slight overestimations of up to 16.7%. This difference is more pronounced at larger displacement demands where the experimental connection has sustained large plastic rotations. In the unloading half-cycles returning to the tensile range, the OpenSees model displays a close prediction of the experimental unloading curve. This is continued at large tensile displacement demands. The initial tangent stiffness of the frame is overestimated for the loading cycles up to δ_y displacement. This is a noticeable trend across all of the subsequent model correlations. In the unloading half-cycles returning to the compression range, a larger frame stiffness is predicted by the model.

Cyclic Test 3 was the first test with the CB configuration at the left–hand (brace-gusset) connection. The calculated moment-rotation stiffness was prescribed for this connection. The large drift demands of the previous tests caused significant yielding in the right-hand beam-column connection. Consequently, to replicate the reduced stiffness of the right-hand connection, the elements 400e and 402e were joined using a pinned connection. The correlation of the model and test is shown in Figure 7.9(b). As before, the initial frame stiffness is overestimated. After the yield displacement is reached, the tensile capacity of the frame is underestimated but an accurate representation of the Bauschinger effect is still maintained. The initial brace buckling capacity is marginally underestimated by 5.8%. The tangent stiffness in the unloading half-cycles is accurately represented in both the compression and tension ranges.

The correlation of experimental and model results for Cyclic Test 4 is presented in Figure 7.9(c). As in Test 3, the left-hand connection was modelled with a nominally pinned connection with the calculated rotational stiffness used in the right-hand connection. A similar simulated response is observed in Figure 7.9(c) with good representation of compressive resistance and underprediction of tensile resistance at large target displacements. The initial buckling capacity is overestimated by 23.3%. This indicates that the gusset plate stiffness calculated using Equation 7.1 has reduced accuracy for thin gusset plates with a single edge restraint.

In the final two tests (Tests 5 and 6) the pinned connection conditions of the right-hand beam-column connection were maintained as in Tests 3 and 4. As Tests 5 and 6 featured CA connection specimens, continuous connection conditions were modelled at the left-hand connection (as in Test 2). In Figure 7.9(d), it is seen that the initial buckling capacity observed in Test 5 is underestimated by 21%. This underestimation decreases at greater displacement amplitudes in the compression range. In the tensile range, the yield capacity is overestimated by 15.3%. The responses of Test 6 are presented in Figure 7.9(e) with very accurate simulated initial buckling capacity and subsequent

compressive resistance degradation. Similar to Test 5, the simulated response demonstrates overprediction in the vicinity of δ_y displacement amplitudes.

Overall most test models demonstrated reasonable accuracy when the plastic damage of the beam-column connections was considered. Assumptions were required to model specific aspects of the frame (i.e. UC stubs, lower gusset plate boundary conditions). The cyclic test models explored the capabilities of the modelling techniques for use in a reference model (in Chapter 10) for dynamic testing of a test frame with more idealised connections and boundary conditions. For all the cyclic test models, a fatigue parameter of $\varepsilon_0 = 0.165$ was employed, and fracture was not predicted by the fatigue material in any test. This is investigated in greater detail in Chapter 10.

7.5 Chapter Overview

This chapter implemented the OpenSees brace model (presented in Chapter 4) in a model CBF. Several modelling considerations were discussed including the interaction between the columns and beam; the column anchor points and the gusset-brace connection bending stiffness. These methods were then utilised in the CBF model. A correlation study was performed, where the experimental responses from the Complementary Cyclic Tests are compared with the output from the OpenSees CBF model. Important considerations for accurate response, such as a rotational stiffness value at beam-column connections and correct initial tangent stiffness of the frame, are noted for use in the development of the dynamic CBF model described in Chapter 10.

8 BRACED Project – Experimental Programme & Setup

8.1 Introduction

This chapter describes the experimental programme and set-up for the BRACED (Brace Response Assessment – Computation, Experiments and Design) project. This experimental programme investigated the influence of different brace and gusset connection configurations on the performance of a CBF under dynamic seismic loading. Section 8.2 provides an overview of the experimental programme, while detailed descriptions of the test frame and brace member specimen designs are given in sections 8.3 and 8.4 respectively. The arrangement of experimental instrumentation on the test frame and specimens is reported in section 8.5. Finally, in section 8.6 the test schedule used in the experimental campaign is described, and the shake table control and changeover procedures for setting up each test configuration are outlined.

8.2 BRACED Project Overview

The series of shake table tests performed within the BRACED project aimed to investigate the ultimate behaviour of CBFs through dynamic earthquake testing of a CBF incorporating pairs of brace specimens with different brace member and gusset plate characteristics. The seismic performance of such structures is affected by the ductility capacity of brace members under low cycle fatigue conditions. It has been shown in Chapter 3 that proposed design and detailing guidance for gusset-plate connections can extend the fatigue life of hollow brace section members. Thus, current design methods (SLC) are compared with the proposed methods (EC) in the specimen design. Furthermore it was necessary to investigate recently-developed models for the ductility capacity of hollow section bracing members.

The BRACED project was initiated as part of the Transnational Access programme offered by the European Commission's Seventh Framework Programme (FP7) project SERIES (Seismic Engineering Research Infrastructures for European Synergies). In total, the BRACED project involved collaboration between researchers in Trinity College Dublin, National University of Ireland Galway, University of Ljubljana, Imperial College London, University of Liege and the Commissariat à l'Énergie Atomique (CEA). The experimental phase of the BRACED project was carried out at the TAMARIS Laboratory in the Laboratoire d'Etudes de Mécanique Sismique (EMSI) at CEA Saclay, France, where the tests were carried out on the AZALEE shake table, illustrated in Figure 8.1.

The AZALEE table is fixed in a pit within the middle of a 2700 tonne concrete reaction mass, and uses eight hydraulic actuators (four for horizontal excitations and four for vertical excitations). Its maximum payload is 100 tonnes and it has a platform area of 6 m^2. Each horizontal actuator has a maximum force of 1000 kN similar to the vertical actuators with a capacity of 1000 kN. Four static pneumatic supports are placed under the table to support and balance the weight of the table and the specimen. The maximum displacement amplitude range is ±125 mm for the two horizontal axes and ±100 mm for the vertical axis.

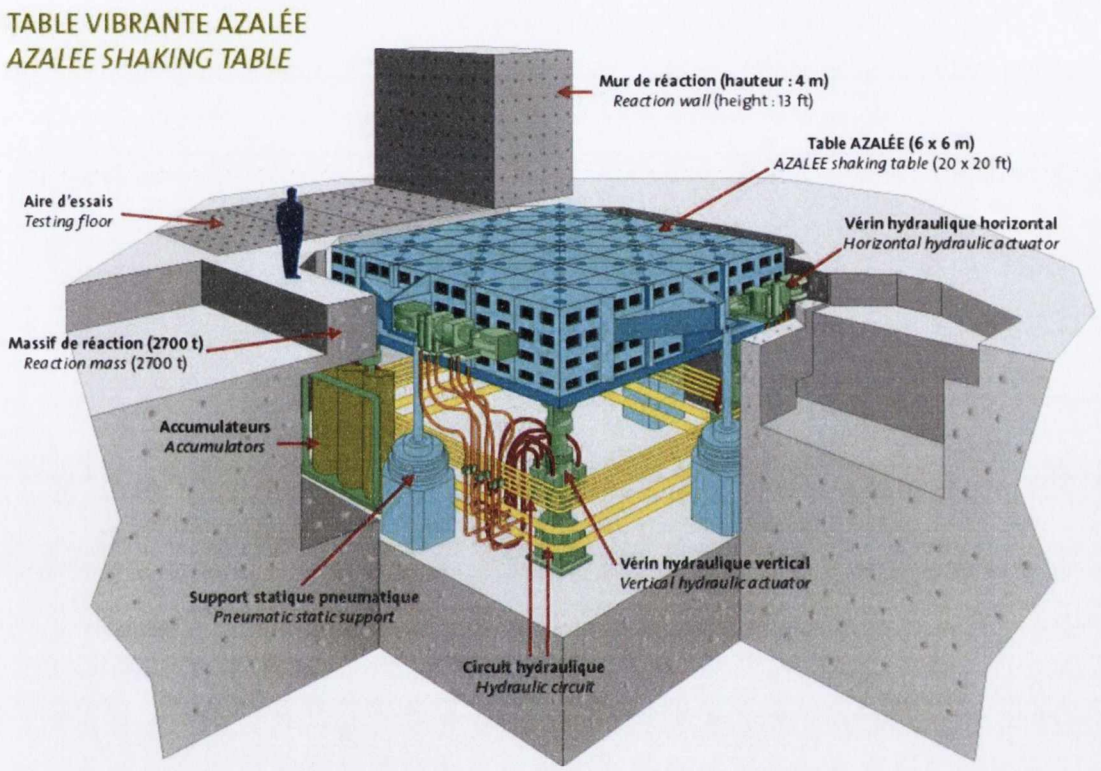

Figure 8.1 – Overview of AZALEE shake table (CEA, 2011)

The test frame was designed to accommodate experimental brace member specimens that were changed between tests. The brace member and connection details were varied between experiments to investigate the range of global and local member slenderness found in European design practice. In each experiment, it was intended that three separate tests would be performed with table excitations scaled to produce elastic response, brace buckling and/or yielding and brace fracture. The principal outcomes included measurements of the displacement ductility capacity of the brace specimens; an evaluation of the influence of gusset plate detailing on connection ductility; observations on the contributions of brace and connection yielding to overall inelastic

deformation of CBFs; measurements of equivalent viscous damping in CBFs; assessment and improvement of Eurocode 8 design guidance for CBFs; and validation of numerical models.

The defined objectives of the project were to:

- Obtain essential experimental evidence of the ultimate dynamic response of CBFs to realistic earthquake loading;
- Validate recent models of ductility capacity during low cycle fatigue failure of hollow section brace members;
- Investigate the behaviour of practical gusset-plate bracing connections, including the validation of recently proposed design models and detailing rules (EC);
- Support the development of Eurocode 8 through improved design guidance for CBFs;
- Validate numerical models of the earthquake response of CBFs and the inelastic response of SHS and RHS brace members and gusset plate connections; and
- Obtain experimental data required for the development of a displacement-based design methodology for CBFs.

The model CBF test frame was designed to Eurocode 8 and included two nominally identical brace members. The test frame (or 'mock-up') used for the BRACED experiments on the AZALEE shake table was designed to facilitate the testing of multiple pairs of brace-gusset plate specimens, by allowing the specimens to be exchanged between experiments. Twelve distinct experiments were performed using different pairs of brace members. The tests were conducted in EMSI Laboratory according to the schedule detailed in Table 8.1.

Table 8.1 – Execution of BRACED tests runs.

Test number	Test sequence description	Run Number	Dates (2013)
Preliminary	Preliminary testing of two configurations	1 to 21	March 25th to April 4th
1 to 8	Different geometries of referenced braces	22 to 119	April 8th to April 26th
9 to 12	Different geometries of referenced braces	120 to 160	May 13th to May 23th

To meet the objectives listed above, three different test parameters were examined (similar to the test parameters in the cyclic tests in Chapter 5): brace section size; connection configuration and

gusset plate design. The range of test parameters and the notation used to identify the twelve specimen pairs are described below:

- Brace Section Size
  - **S1** 80×80×3.0 SHS
  - **S2** 100×50×3.0 RHS
  - **S3** 80×40×3.0 RHS
  - **S4** 60×60×3.0 SHS
- Connection Configuration
  - **CA** Gusset connection to beam and column flange
  - **CB** Gusset connection to beam flange only
- Gusset Plate Design
  - **G1** Conventional design with Standard Linear Clearance (SLC)
  - **G2** Balanced design with Elliptical Clearance (EC)

While it was desirable to use similar section sizes to those of the complementary tests, identical section sizes could not be used because of limitations in sourcing brace lengths of required yield strength. In total 48 brace specimens were fabricated for 24 tests. However, the number of tests was limited to 12 due to the time frame for project completion. It was intended that the extra specimens could be tested in future experimentation. The subsequent tests will expand the parameter ranges and allow for repeat tests where necessary. The schedule of tests in Table 8.2 below is designed to address all of the above test parameters within these 12 tests. The sequence of testing was determined by the availability of the specified materials. Due to undesirable characteristic strength values of the S2 section, newer S2 brace lengths were ordered and this brace section was first tested in Test 4. The non-dimensional slenderness, $\bar{\lambda}$, is predicted based on the assumption of nominal area, pinned-pinned boundary conditions with bending about the minor axis ($K = 1.0$) and nominal material yield strength ($f_y = 235$) for pre-test comparison purposes. The predicted scaled earthquake Peak Ground Acceleration (PGA) to achieve failure ('Target PGA 2%/50') is also shown in units of g. The PGA values were selected based on brace size and PGA required for fracture from preliminary tests (further discussion in section 8.7.2). Two strain gauge configurations are described using 'D' and 'S' to indicate detailed and standard strain gauge layouts respectively (section 8.5.1). Once testing was completed the post-processed data was used for comparing the key test parameters (Section 9.4). In Chapter 10 this data is also utilised in a correlation study using time-history analyses.

Table 8.2 – Overview of BRACED test schedule and specimen properties.

Test	Specimen	Brace Cross Section	Area (mm²)	$\bar{\lambda}_{Rd}$	b/tε	β_{ww}	Target PGA (2%/50) (g)	Strain Config.*
1	S1-CA-G1	80×80×3.0	915	0.83	26.67	0.33	0.60	D
2	S3-CA-G1	80×40×3.0	674	1.59	26.67	0.36	0.44	S
3	S4-CA-G1	60×60×3.0	674	1.11	20.00	0.39	0.41	S
4	S2-CA-G1	100×50×3.0	854	1.24	33.33	0.28	0.57	S
5	S1-CA-G2	80×80×3.0	915	0.86	26.67	0.79	0.60	D
6	S2-CA-G2	100×50×3.0	854	1.28	33.33	0.85	0.57	S
7	S3-CA-G2	80×40×3.0	674	1.64	26.67	0.72	0.44	S
8	S1-CB-G1	80×80×3.0	915	0.82	26.67	0.33	0.60	S
9	S2-CB-G1	100×50×3.0	854	1.23	33.33	0.28	0.45	S
10	S4-CB-G2	60×60×3.0	674	1.12	20.00	0.79	0.41	D
11	S2-CB-G2	100×50×3.0	854	1.25	33.33	0.85	0.57	S
12	S3-CB-G2	80×40×3.0	674	1.58	26.67	0.72	0.44	D

* Maximum Strain gauge configuration: 'D' indicating detailed layout and 'S' indicating standard layout.

8.3 Test Frame Design

The test frame was designed as a dedicated single-storey model CBF structure capable of accommodating the full range of brace and gusset-plate connection specimens set out in Table 8.2. These specimens were designed so that they could be tested to failure within the capacity of the shaking table. The following requirements drove the primary test frame and specimen design:

- The test frame should have a realistic storey height and natural period;
- The mass supported by the test frame should not exceed 50 tonnes.
- The PGA required to fracture the brace specimens should not exceed 1.0g.
- The displacement ductility demand required for brace fracture ($\mu_\Delta > 4$) should be accommodated by the test frame (including allowable frame drift limits of ≈ 2° frame rotation);
- Brace lengths should be realistic; non-dimensional slenderness should be within or close to Eurocode 8 limits;
- Braces members should possess class 1 cross-sections, but small b/t and d/t ratios should be avoided to ensure that local buckling and fracture is observed;
- The brace-gusset plate specimens should be easily exchanged between tests;
- Brace connections to beam and column (CA) and beam only (CB) should be accommodated;

- Two gusset plate designs should be included: conventional design (G1) with SLC plastic hinging and balanced design (G2) with EC plastic hinging;
- Load cells shall be accommodated to measure the brace axial forces directly;

Figure 8.2 shows the resulting design of the test frame with the direction of excitation shown and Figure 8.3 provides photographs of the frame assembly. More detailed drawings that illustrate all aspects of the frame design are included in the attached DVD media. The lateral resistance of the frame was provided by the pair of brace specimens in Frame B which were positioned in the same plane to prevent any significant torsional response. Two additional unbraced frames (Frame A and C) were located on either side of the CBF model to provide lateral stability and to facilitate the lateral beams which support the added mass. All column members in Frames A and C were pinned at top and bottom ends. Columns in Frame B were pinned at their bottom end and connected to the primary beam by a flush end plate bolted connection at their top end.

The principal elements of the test frame are:

- a main beam in Frame B (IPE 400), length 7500 mm,
- two columns in Frame B: (HE 220 B) supporting the IPE 400,
- two columns each on Frames A and C (HE 120 A),
- six beams (IPE 270), forming a square horizontal roof grid, supported by the outer columns and fixed to the main IPE 400 beam in Frame B,
- four transverse braces (100 x 20 mm solid cross-section) to provide lateral frame stability in the direction perpendicular to Frames A-C,
- two MTS swivel bearings (described below) with load cells assemblies,
- the two brace members, which are the elements tested, mounted in the main plane between the swivels and the IPE 400 / HE 220 angle,
- two mechanical devices designed to return the frame to the vertical after each test.

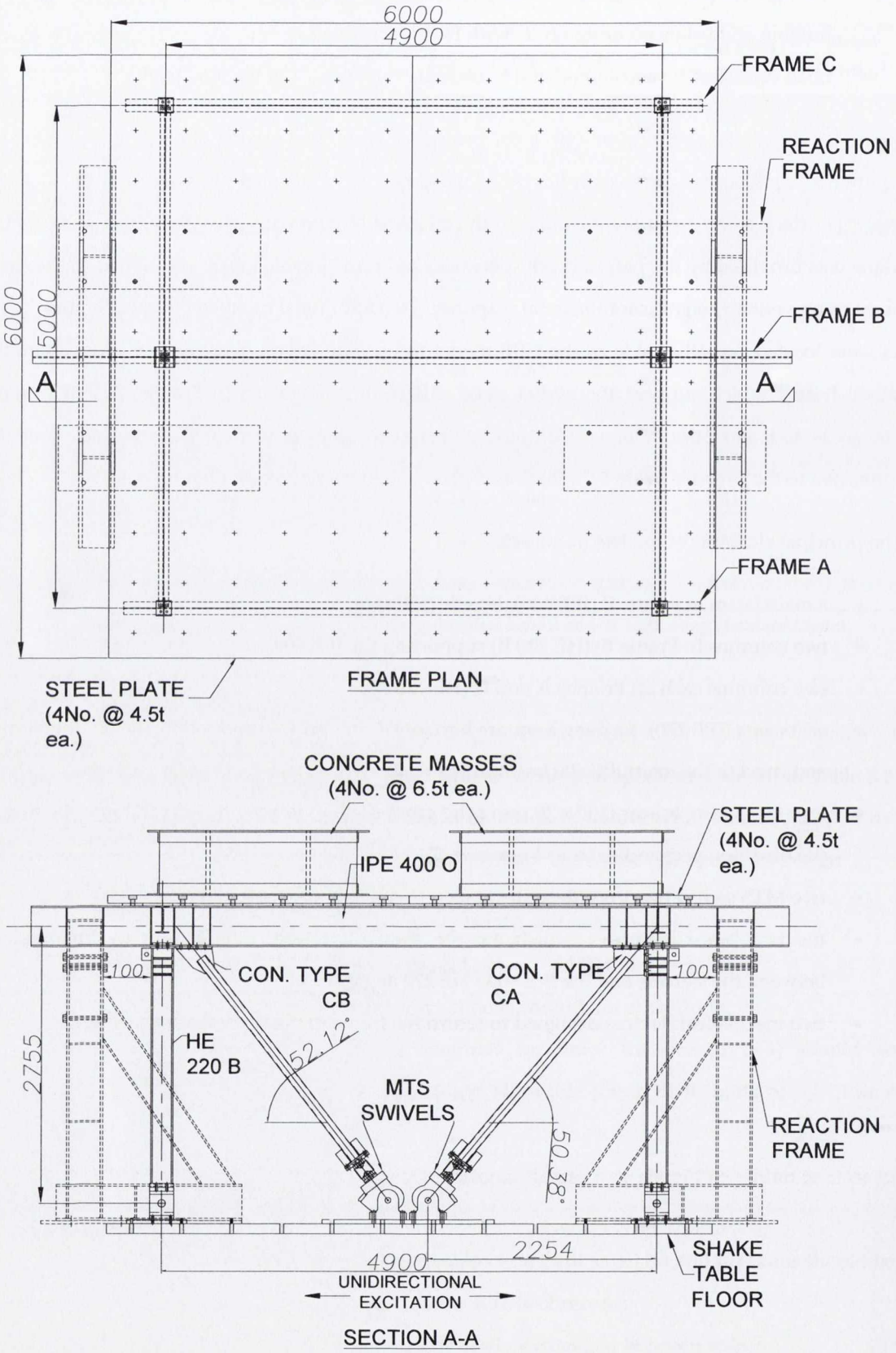

Figure 8.2 – Schematics of BRACED test frame. CA and CB connections shown for illustration, identical brace specimen pairs were used in all tests. Dimensions in mm.

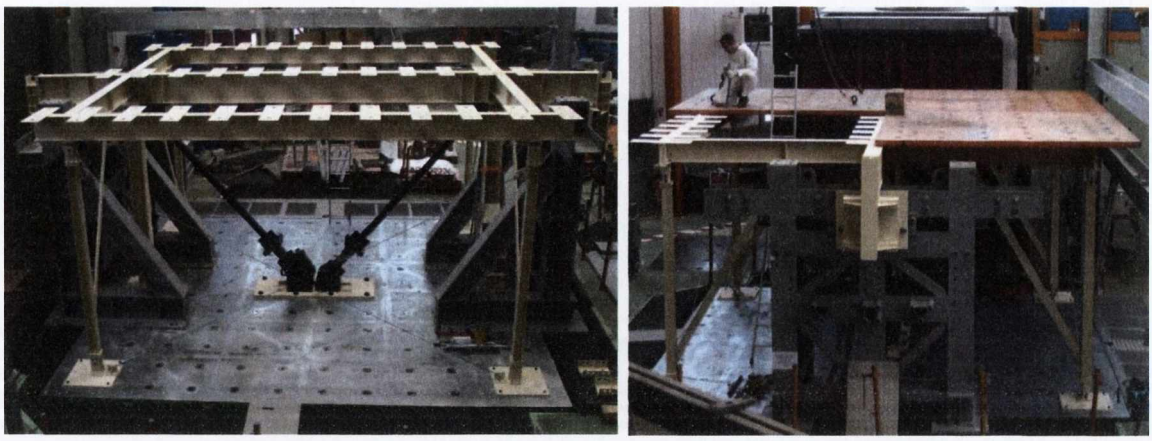

(a) (b)

Figure 8.3 – BRACED test frame (a) side elevation with no plate or concrete masses in place and (b) end elevation with three plate masses secured to frame.

The different steel frame elements were assembled together by bolts (M24 in Frame B and M12 in Frames A and C). The six columns were supported by hinge bearings bolted to AZALEE shaking table by M18 bolts (Figure 8.4 (b)). Four similar hinge bearings connected the top of the columns in Frames A and C to the top IPE 270 beam assembly. These hinge bearings ensure that lateral resistance was provided by Frame B alone. The transverse beams were linked to the main IPE400 by M12 bolts.

The two beam-column joints in Frame B, where the IPE400 beam was connected to the HE220 columns, were designed to remain elastic during all tests, taking into account the maximum force transferred from the brace members connected to these joints.

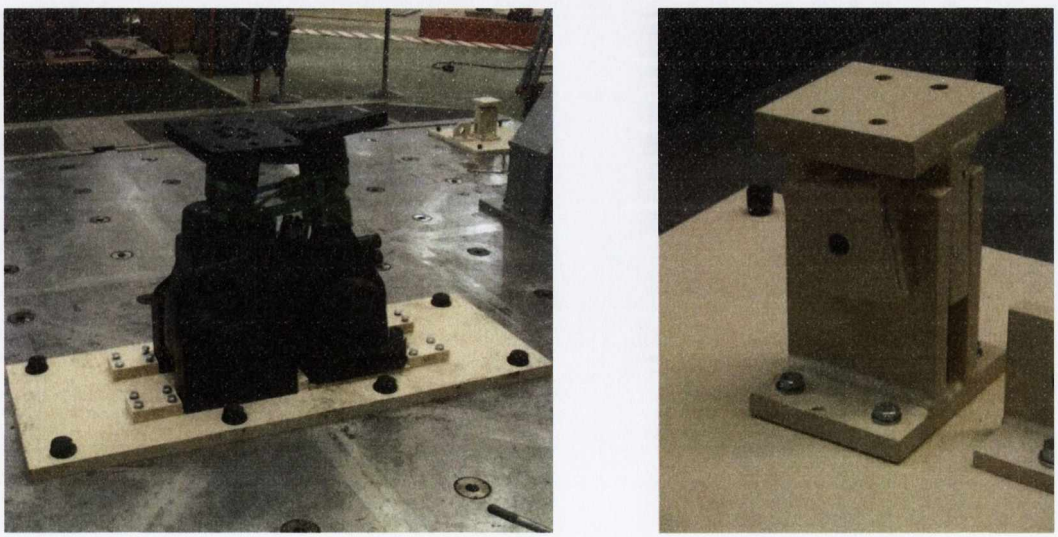

(a) (b)

Figure 8.4 – (a) MTS swivel bearings fixed to shaking table and (b) an outer column bearing.

The total height of the frame was 3167 mm. The overall width (4900 mm) and depth (5000 mm) of the test frame were limited by the dimensions of the AZALEE platform (6m x 6m). This led to the composition of the added test mass as four steel plates supporting four concrete masses. These provided a total added mass of 44 tonnes, which combined with the mass of the beam members gave a total mass at or above roof level of approximately 46 tonnes. The added masses comprised of

- four steel plates (3 X 3 m, 4.5 tons) placed on top of the steel frame to form a square roof 6 x 6 m. They were fixed to the IPE beams in Frames A, B and C by 72 M38 bolts,
- four concrete blocks (1.97 x 1.97 x 0.66 m, 6.5 tons each) bolted to each steel plate by 32 M22 bolts.

The mechanics team of EMSI laboratory handled and tightened these masses at the maximum torque value for these bolts.

The total mass of the frame was approximately five tonnes. The mass of the reaction frames was four tonnes each. So, the total mass on the AZALEE table was approximately 52 tonnes.

As it was intended that the maximum experimental response would extend beyond fracture of the brace member specimens in Frame B, two reaction frames (Figure 8.5) were positioned on either side of the test frame (under the main middle beam IPE 400) to support the structure following brace fracture. A dedicated steel bumper was installed on both of these reaction frames that was designed to take the impact from the main column if the frame continued to move horizontally following brace fracture.

To provide for the significant drift demand required to attain the axial displacement ductility capacity of some of the brace specimens, a maximum test frame displacement of ± 100 mm (equal to a storey rotation of approximately ±2°) was provided between the reaction frames.

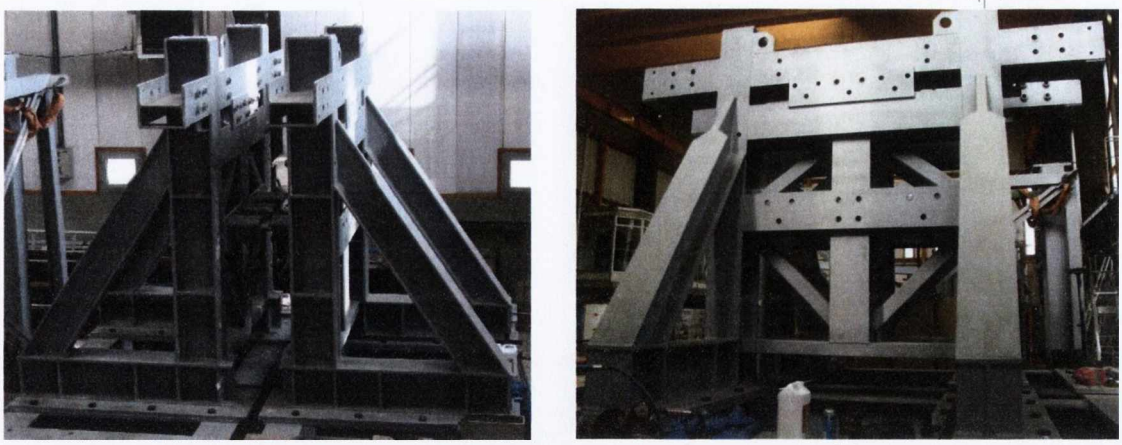

(a) (b)

Figure 8.5 – Reaction frames (a) side elevation and (b) end elevation.

8.3.1 Brace Dimensions and Resistance

The columns, beams and connections of the test frame were designed with excess resistance to ensure that they remained elastic and stable throughout all tests. The dimensions and design strengths of these components were selected considering the maximum brace size that could be tested to failure on the AZALEE shake table. Two considerations limited this maximum brace size: the maximum seismic force that could be imposed on the test frame, and the instrumentation available to measure brace axial force.

Considering the available seismic force, to ensure that sufficient ductility demand could be imposed on the brace specimens, the lateral yield resistance of the test frame (design base shear) was limited to less than 35% of shake table capacity (maximum base shear), estimated as:

- Test mass = 46 tonnes
- Maximum table acceleration = 1.0g
- Assumed response acceleration amplification = 2.5
- Maximum base shear = 46 × 1.0 × 9.81 × 2.5 = 1128 kN
- Maximum design base shear = 0.35 x 1128 = 395 kN

The maximum design base shear led to the largest brace section size being identified as 80 × 80 × 3.0 ('S1'), with a predicted maximum tensile capacity of 329 kN. This selection took into account the likely contribution to lateral resistance provided by both tension and compression braces, and brace angle of inclination. The ultimate tensile capacity of this brace size is also below the capacity of the two 500 kN load cells which were available for brace axial force measurement (described below).

To maintain realistic brace lengths whilst remaining within the geometrical constraints of the shake table floor, a frame width of 4.9 m was selected. This length and the frame height determine the brace length, and their combined values needed to ensure that the non-dimensional brace slenderness values remained within the desired range. This led to the selected storey height of 2.755 m, which also provided a realistic natural period (≈ 0.3 s) for the CBF.

8.3.2 Brace Boundary Conditions

To accommodate the load cells required to measure brace axial force, MTS swivel bearings (normally used as actuator bearings) were used to connect the lower end of the brace specimens to the shake table platform. Each swivel was connected through four M30 bolts to a 40 mm thick plate, which was itself bolted to the AZALEE shaking table by M36 bolts. These bearings provide a boundary condition at the lower end of the brace with swivel angle ranges of -30°, +90° (in-plane) from vertical and tilt angle (out-of-plane) of ±7° from vertical.

An existing swivel (Model No: 204.81, .82 – 02) was employed for the right-hand brace and a new swivel (Model No: 249B.M730) was acquired for the left-hand brace (Figure 8.6). As these models had slightly different overall dimensions, the details of their connection to the brace specimens were varied to ensure equal brace lengths. During initial tests the new left-hand swivel offered unanticipated rotational resistance that was not observed in the older right-hand swivel.

This restraint influenced the effective lengths of the braces in the preliminary and initial tests. However following these initial tests, and individual adjustment of the clamping force of the swivel jaws, both braces displayed similar low rotational stiffness from the beginning of Test 2 (see section 9.3). The MTS swivel bearings have a force rating of 730 kN, which exceeds the predicted maximum tensile capacity of the largest S1 brace size.

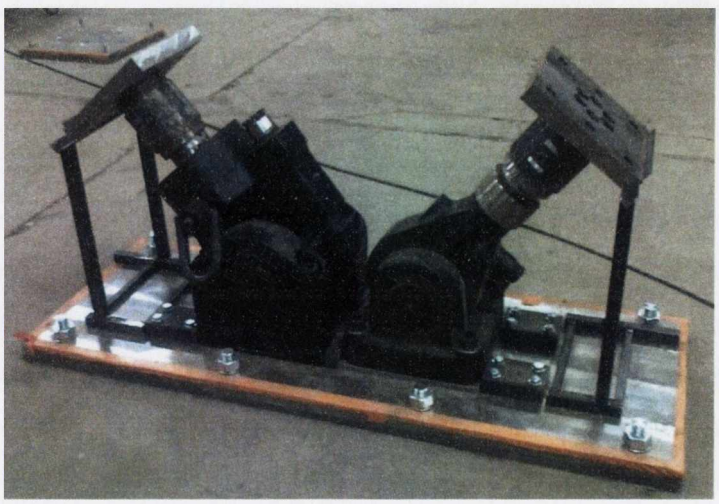

Figure 8.6 – MTS swivels with new model 249B.M730 on left and old model 204.81, .82 – 02 on right.

The upper boundary condition of the brace was formed by its gusset-plate connection to the test frame. The diagram in Figure 8.2 shows two different experimental specimens with CA and CB connection configurations to illustrate the difference in brace inclination angle and length that arise with the two configurations. However, in all tests, identical brace specimen pairs were utilised. The brace-gusset plate specimens were bolted to the beam and column (CA) or beam (CB) members of Frame B to permit easy changeover between tests. For this purpose, the gusset plates were welded to flange plates, which were bolted to the flanges of the primary beam (IPE 400 O) and columns (HE 220 B), which were strengthened using stiffener plates. The positions of bolt holes and stiffener plates accommodated both CA and CB connection types and G1 and G2 gusset plates.

8.4 Brace Member Specimen Design

The detailed design of the brace-gusset plate specimens comprised two main components: brace tube design and gusset plate design. Nominal material strengths were used for all calculations. Material characteristic strength tests were later performed on coupon samples from the brace tube lengths and gusset plates. The coupon tests were carried out according to the European Standard BS EN ISO 6892-1 (CEN, 2009). This testing method has previously been described in relation to the cyclic tests in section 5.4. Consequently, two sets of specimen properties are presented in each design phase below. These are designated with the subscripts 'Rd' and 'meas' for calculations using nominal and characteristic strengths, respectively.

8.4.1 Brace Tube Design

Twenty-four identical brace tube pairs were designed using four different cross-section sizes for two connection types (CA and CB) and two gusset plate types (G1 and G2). S235 JRH steel with a nominal design yield strength, f_y, of 235 N/mm^2 was specified for all tube lengths. This grade was selected to limit the ultimate tensile resistance of the brace specimens (see Section 8.3.1), while also keeping the member slenderness within the acceptable range. The two sets of yield and buckling capacities (based on nominal and measured characteristic steel strengths) are presented in Table 8.3 below. The corresponding non-dimensional slenderness values are also presented.

8.4.2 Gusset Connection Design

The SLC and EC gusset design methods are outlined in Chapter 3. Both of these designs were employed for the four section sizes and two connection types. The connection types CA and CB are shown in Figure 3.5.

Table 8.3 – Overview of brace tube design parameters.

Test	Specimen	Section Type	Brace Length (mm)	Mean Measured Strength		Yield Capacity		Non-dimensional Slenderness		Buckling Capacity	
				R_{eH} (MPa)	R_m (MPa)	$N_{pl,Rd}$ (kN)	$N_{pl,meas}$ (kN)	$\bar{\lambda}_{Rd}$	$\bar{\lambda}_{meas}$	$N_{b,Rd}$ (kN)	$N_{b,meas}$ (kN)
1	S1-CA-G1	80×80×3.0	2413	372.5	437.0	214.8	340.8	0.83	1.04	167.6	217.3
2	S3-CA-G1	80×40×3.0	2427	384.3	430.5	158.4	259.0	1.59	2.03	53.6	56.3
3	S4-CA-G1	60×60×3.0	2425	347.5	404.0	158.4	234.2	1.11	1.35	93.0	103.4
4	S2-CA-G1	100×50×3.0	2413	341.5	377.7	200.7	291.6	1.24	1.49	102.0	110.0
5	S1-CA-G2	80×80×3.0	2502	337.8	389.0	214.8	308.7	0.86	1.03	163.6	199.7
6	S2-CA-G2	100×50×3.0	2509	341.7	380.2	200.7	291.8	1.28	1.55	96.2	102.9
7	S3-CA-G2	80×40×3.0	2504	370.5	429.7	158.4	249.7	1.64	2.05	50.8	53.0
8	S1-CB-G1	80×80×3.0	2395	336.5	388.8	214.8	307.6	0.82	0.98	168.4	208.7
9	S2-CB-G1	100×50×3.0	2395	340.0	377.8	200.7	290.4	1.23	1.48	103.1	111.3
10	S4-CB-G2	60×60×3.0	2437	347.5	404.0	158.4	234.2	1.12	1.36	92.4	102.6
11	S2-CB-G2	100×50×3.0	2433	341.5	377.7	200.7	291.6	1.25	1.50	100.7	108.4
12	S3-CB-G2	80×40×3.0	2420	370.5	429.7	158.4	249.7	1.58	1.99	53.9	56.4

First the initial overall dimensions l_h and l_v (Figure 3.2a) were determined based on the alignment of the brace centreline with the intersection of the beam and column centrelines and the weld lengths connecting the end plates to the gusset plate. The maximum force to be transferred through the brace was established from the ultimate tensile strength of the brace section S1. Following this, the weld sizes connecting the brace to the gusset plate were specified as 150 mm for all specimens. Throughout the design process, all welds and bolts were considered critical connection components. Therefore, the shear, bearing and tensile loads transferred from the S1 brace size were multiplied by a safety overstrength factor of 2.0. Four sample connection layouts are shown in Figure 8.7, and complete detail drawings are included in the attached DVD media.

Subsequently, the gusset plate yield and buckling strengths were calculated. Similar to the tube lengths, material characteristic tests were carried out for the large steel plates from which the gusset plates were cut. Therefore in

Table 8.4, both nominal and characteristic strengths are listed for each specimen. The area used for the calculation of these strengths is derived from the Whitmore width and the gusset plate thickness t_p.

The G1 (SLC) and G2 (EC) gusset design layouts were the primary design considerations particularly in relation to gusset tensile yield strength. The concept of balancing the brace tensile yielding and gusset yielding mechanisms has been encapsulated using the balance factor β_{ww} (Equation 3.7). Design of the G1 gusset, resulted in low (~0.2-0.3) β_{ww} values (i.e. very high overstrength of gussets in tension design). This occurred for two reasons: the overstrength requirement of the gusset to be proportionally stronger than the brace under tension; and as the linear clearance zone produces large sized gusset plates (l_h and l_v) and longer effective lengths, thicker plates are required to prevent plate buckling. Thicker plates increase the size of the Whitmore section thereby increasing the plate tensile capacity and reducing the β_{ww} ratio. A higher range of β_{ww} values (~0.6-0.75) was expressed for the G2 designs because the elliptical design results in smaller dimensioned plates with shorter buckling lengths. For all G1 specimens a plastic hinge length of $3t_p$ was used, while an elliptical clearance zone of $8t_p$ (based on recommendations of Lehman et al. (2008), see section 3.3) was used for G2 plastic hinge designs. Values for expected yield stress ratio R_y (as recommended in Chapter 3) were used for $\beta_{ww,Rd}$ calculations. In calculating values of $\beta_{ww,meas}$, characteristic strengths were used and therefore R_y ratios were not required.

Having established the balancing factor, β_{ww}, for each specimen, the Thornton model was employed to check for gusset plate buckling. The gusset plate was modelled as a slender strut with

a length established from the average of three lengths projected from the Whitmore width to the gusset boundaries, L_{avg}. Roeder et al. (2004) applied an effective length factor of $K = 0.65$ to this length, considering both ends of the gusset plate strut to be the effectively restrained against rotation and translation. In this project, however, to ensure that plate buckling is avoided in all tests, a more conservative value for the effective length factor of $K = 1.2$ was used to calculate the gusset plate buckling capacity. This value assumes fixed rotation and free translation at the brace end of the gusset plate (Figure 8.8) to account for large out-of-plane brace deformation that occurs at high drift demands. A sample of the gusset design worksheets is shown in Figure 8.9 and the complete design sheets for brace and gusset specimens are stored on the included DVD media.

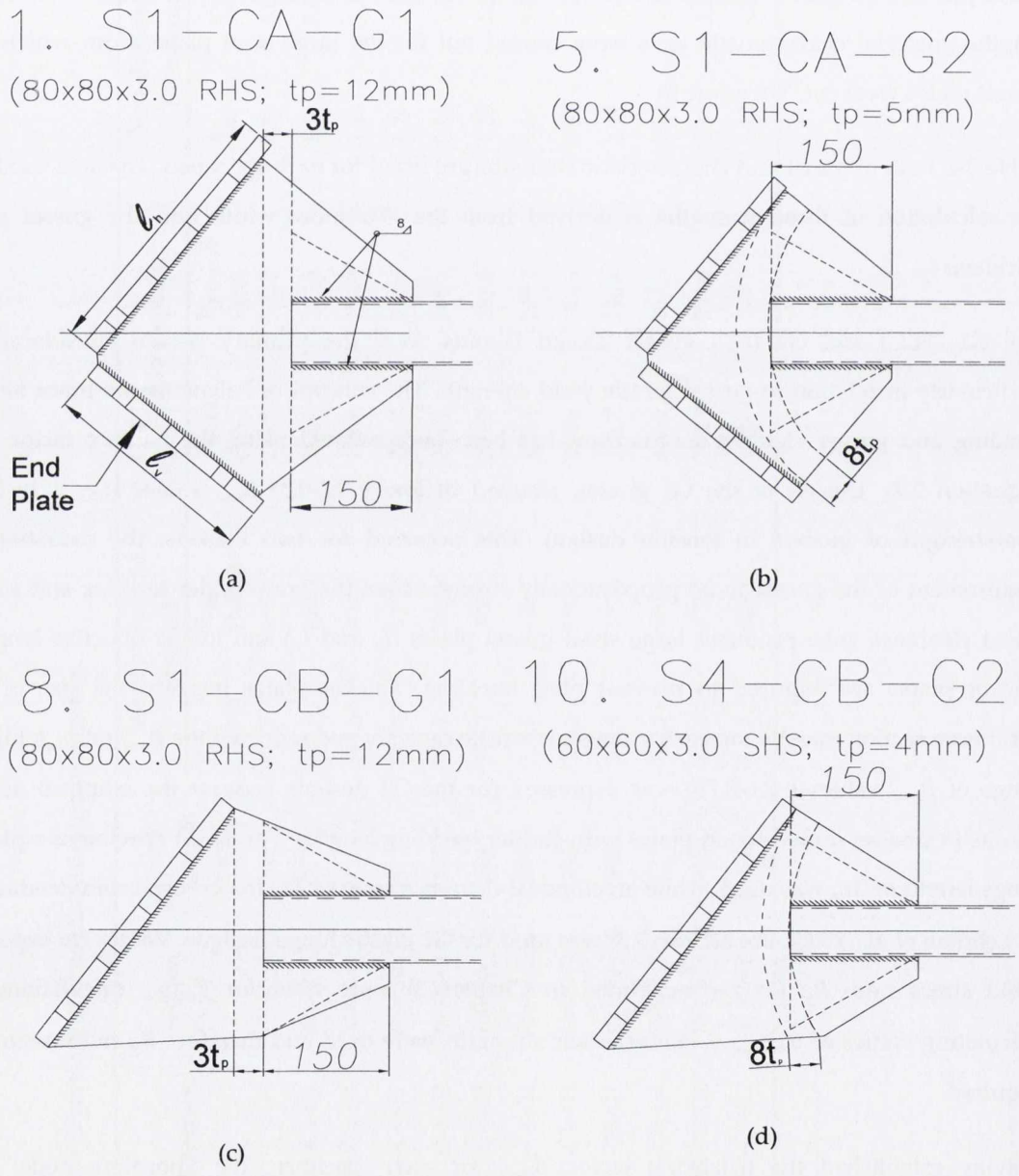

Figure 8.7 – Drawings illustrating examples of the four primary gusset/connection designs from (a) CA-G1 (b) CA-G2 (c) CB-G1 and (d) CB-G2.

Table 8.4 – Overview of gusset plate connection design parameters.

Test	Specimen	Gusset Type	Drawing No. (Appendix B)	t_p (mm)	Mean Measured Strength		Yield Capacity		Balance Factor		Buckling Capacity	
					R_{eH} (MPa)	R_m (MPa)	$N_{pl,Rd}$ (kN)	$N_{pl,meas}$ (kN)	$\beta_{ww,Rd}$	$\beta_{ww,meas}$	$N_{b,Rd}$ (kN)	$N_{b,meas}$ (kN)
1	S1-CA-G1	SLC	SK005-TCD	12	369.0	506.7	835.6	1121.2	0.33	0.28	737.5	941.4
2	S3-CA-G1	SLC	SK006-TCD	8	337.0	490.0	557.1	682.6	0.36	0.35	412.6	461.6
3	S4-CA-G1	SLC	SK006-TCD	8	337.0	490.0	513.1	628.7	0.39	0.36	370.5	411.4
4	S2-CA-G1	SLC	SK005-TCD	12	369.0	506.7	901.6	1209.8	0.28	0.23	804.8	1032.8
5	S1-CA-G2	EC	SK008-TCD	5	336.0	444.7	348.2	425.4	0.79	0.73	302.6	356.3
6	S2-CA-G2	EC	SK008-TCD	4	388.0	488.0	300.5	424.0	0.85	0.68	260.3	341.5
7	S3-CA-G2	EC	SK012-TCD	4	388.0	488.0	278.5	393.0	0.72	0.62	233.5	299.9
8	S1-CB-G1	SLC	SK007-TCD	12	369.0	506.7	835.6	1121.2	0.33	0.27	747.6	960.6
9	S2-CB-G1	SLC	SK007-TCD	12	369.0	506.7	901.6	1209.8	0.28	0.24	798.1	1020.2
10	S4-CB-G2	EC	SK009-TCD	4	388.0	488.0	256.5	361.9	0.79	0.64	126.0	134.6
11	S2-CB-G2	EC	SK010-TCD	4	388.0	488.0	300.5	424.0	0.85	0.69	140.7	149.5
12	S3-CB-G2	EC	SK012-TCD	4	388.0	488.0	278.5	393.0	0.72	0.62	109.1	114.1

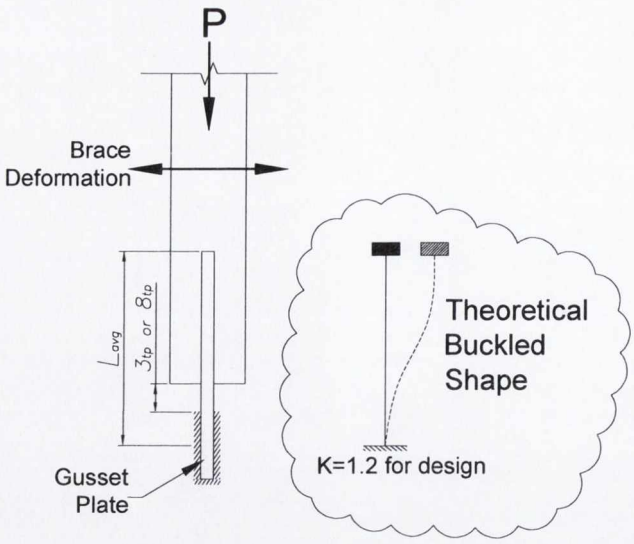

Figure 8.8 – Schematic showing section of gusset plate and treatment of boundary conditions for buckling capacity.

(1) Input			(2) Calcs			(3) Output		
Test5 S1-CA-G2-E1 (80x80x3.0								
b_{brace} =	80	mm	a' =	230	mm	b_w =	253	mm
l_{weld} =	150	mm	b' =	210	mm	l' =	190	mm
			ρ =	1.095238				
a =	270	mm	y' =	182.5764	mm			
b =	250	mm	x' =	113.6405	mm			
t_p =	5	mm	β =	-74.8599				
α =	50	deg	Corr =	-24.8191				
c =	40	mm						

(a) Initial geometrical sizing for elliptical (EC) design

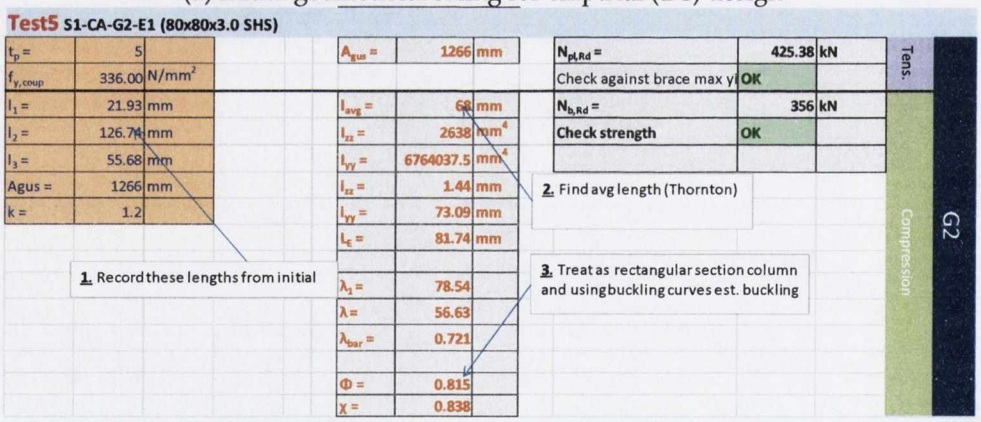

(b) Calculations for gusset yielding and buckling

Figure 8.9 – Samples of gusset design work sheets.

8.5 Instrumentation

Several sets of instrumentation were used throughout the testing programme. They are described below categorised according to the type of measurement recorded. Using the data acquisition system, all data was recorded at a frequency of 512 Hz. It is worth noting that photogrammetry

measuring technology was employed using tracking targets and stereo correlation. However, at the time of writing no data had been analysed and as such a description of the photogrammetry systems is provided in the BRACED project report Broderick et al. (2013).

8.5.1 Strain Gauges

For the purposes of this project the strain gauges were categorised into two sets:

1. Permanent strain gauges fixed to the frame. Throughout the project they are designated a number prefixed with 'SGF'.
2. Short-term use gauges fixed to each specimen. They are designated a number prefixed with 'SG'.

The primary function of the SGF gauges was to provide strain information to check for undesirable behaviour in the test frame. Such behaviour could include yielding of the primary beam due to bending, bending of beam or column flanges, or significant development of inelastic strain at critical locations. The avoidance of these behaviours ensures that the response is dominated by the behaviour of the brace-gusset plate specimens, and that the test frame properties do not change during the experimental programme.

Three SGF gauges were located in each column of Frame B (see Section 8.3) permit column axial loads to be estimated. The gauges were placed on the outer edges of the column flanges. Two gauge pairs were positioned on the primary beam in Frame B to check the bending moment in this member. Eight gauges were placed on the beam and column flanges where the gusset plates are connected. These facilitated checks for inelasticity in the beam and column flanges. Detailed structural drawings showing the SGF gauge locations and all data recorded for these gauges can be found in the attached DVD media.

All SGF strain gauges utilised were Tokyo Sokki Kenkyujo WFLA-6-11-5LT single axis encapsulated strain gauges. The attachment cables were pre-welded on the gauge pads and the strain range was ±3% with leadwire resistance of 0.44 Ω per meter.

The SG gauges were positioned in standard layouts on the brace and gusset specimens to complement the analysis provided by the photogrammetry systems described in Section 8.5. To allow the photogrammetry system to function effectively, no strain gauges were placed on the left-hand brace. On some specimens, extra gauges were employed to supplement the standard strain gauge layout. The corresponding strain gauge layouts are indicated as 'D' and 'S' in Table 8.2. An example of the two layouts is shown in Figure 8.10. Detailed drawings of SG layouts for all specimens are included in the attached DVD media. Gauges are located at and near the brace mid

length (SG1, 2, 8, 9 & 16) to estimate bending in the brace and the degree of plastic hinge development in the brace. SG4 and SG5 are located within and outside of the plastic hinge zones of the gusset plate, respectively. SG6 and SG7 are positioned to monitor the compression and tension induced in the gusset plate during frame rotation.

For all SG gauges, linear pattern Vishay CEA-06-125UW-120 were used. Their strain range was ±5% with a gauge length of 3.18 mm and with a resistance of 120±0.3% Ω.

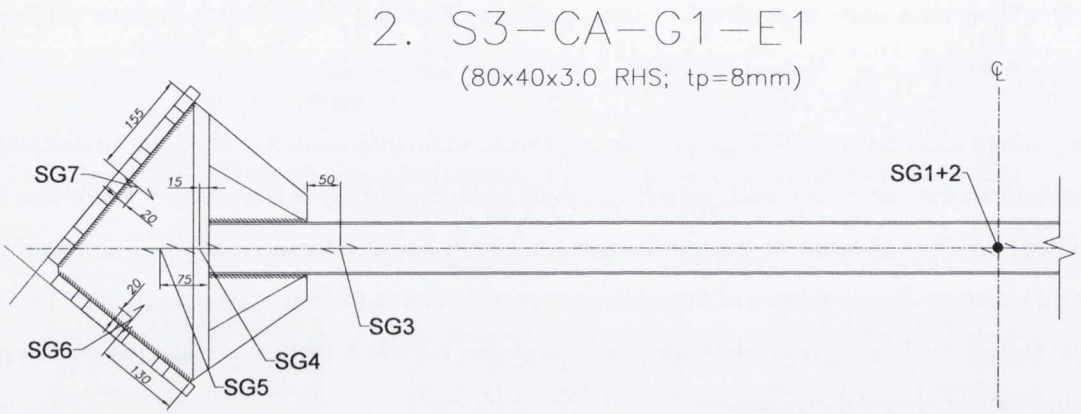

(a) 'STANDARD' specimen strain gauge layout

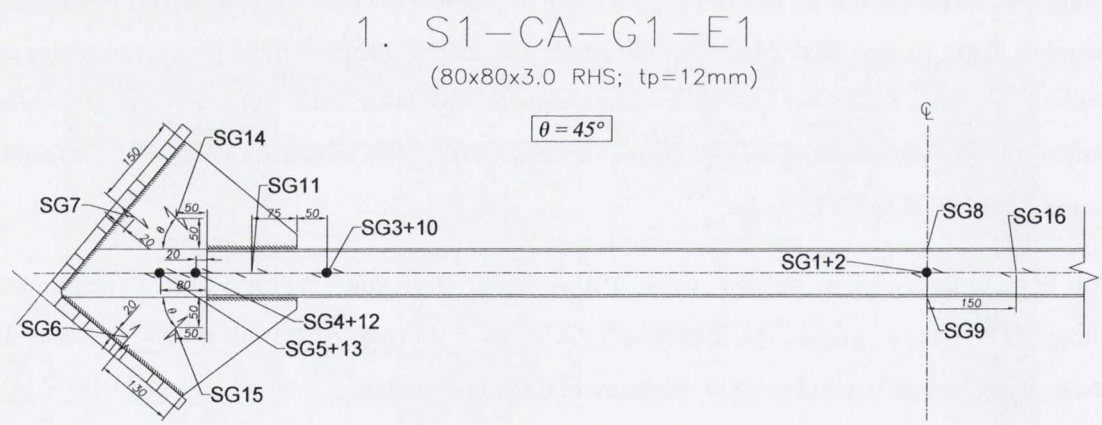

(b) 'DETAILED' specimen strain gauge layout

Figure 8.10 – Example drawings of two SG-type strain gauge layout configurations.

8.5.2 Accelerometers

Two primary triaxial accelerometers (PCB Piezotronics, type pcb3711b1110g, range: +/- 10 g – frequency range: 0 – 1500 Hz) were utilised for recording acceleration in all three directions. Their

locations are indicated as 'AxTop' and 'AxTab' in Figure 8.11. AxTop and AxTab are the channel designations for acceleration in the longitudinal x-direction (i.e. the direction of excitation) at the roof level and ground level (shake table), respectively. Secondary accelerations were also recorded to monitor and check y and z direction accelerations at these locations, but are not included in the main analysis of test results in Chapter 9.

In addition, another set of accelerometer instrumentation consisted of a proprietary MTS system located within the AZALEE shake table. These recorded acceleration in all three directions and rotations (i.e. rotational acceleration for roll, pitch and yaw). As before these were recorded for checking for any undesirable table-structure interaction and were not used in the main set of analyses.

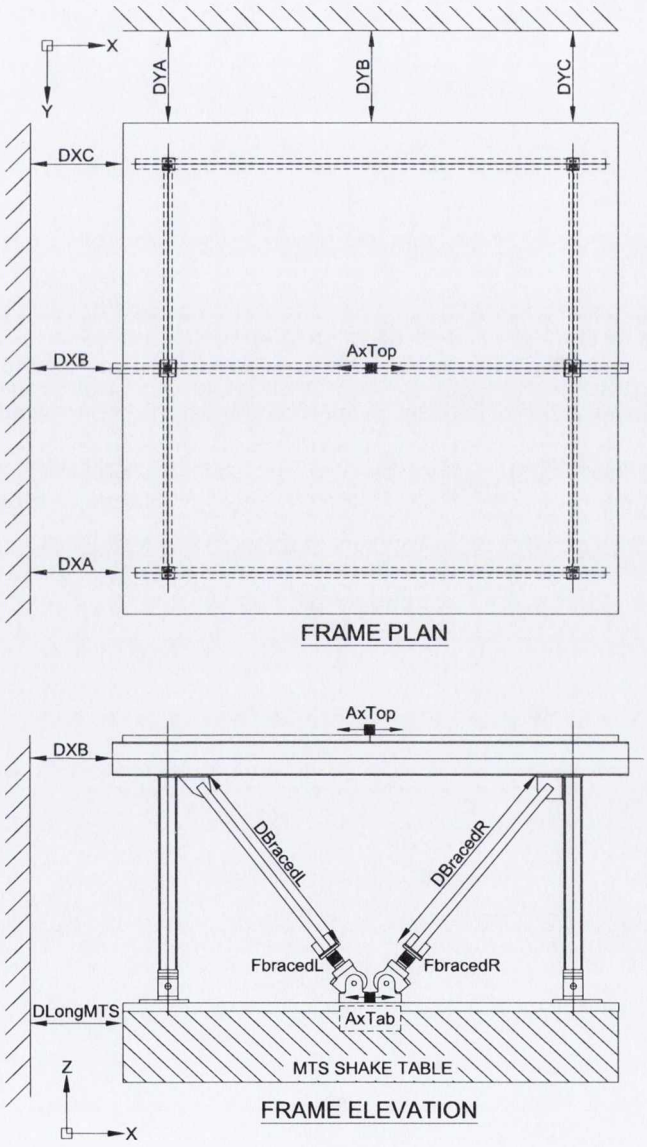

Figure 8.11 – Schematic diagram showing primary measurement instrumentation positioning

8.5.3 Displacement Transducers

Six displacement cable sensors (FGP, type 1850-040 range: +/- 500 mm) were located at the roof level as indicated in Figure 8.11. Those labelled 'DXA', 'DXB' and 'DXC' measured displacement response in the x-direction and those labelled 'DYA', 'DYB' and 'DYC' measured displacement in the lateral y-direction. 'DLongMTS' measured the shake table displacements in the x-direction. The displacement cable sensors for these measurements were attached to a fixed reference frame as shown in Figure 8.12.

Figure 8.12 – Photograph of displacement cable sensor (blue) attached to fixed reference position. Cable is linked to test frame (orange).

Furthermore, two displacement cable sensors were positioned between the brace end attached to the bottom flange of the primary beam and the brace end plate connected to the MTS swivel. These cable sensors were designated 'DBracedL' and 'DBracedR' and measurement brace elongation across the total brace length for left and right braces, respectively.

8.5.4 Load Cells

Two MTS load cells with 500 kN capacity (Model No: 661.23B-02) were used to measure the axial load transferred to the MTS swivels. They were located between the lower brace end and the MTS swivel mounts and are designated 'FbracedL' and 'FbracedR' in Figure 8.11 for the left-hand and right-hand braces, respectively. The load cells and their mounting on the MTS swivel bearings are illustrated in Figure 8.13.

(a) MTS Load Cell

(b) Load cell attached to swivel

Figure 8.13 – Photographs of MTS load cell.

8.5.5 Video Recording

Two cameras were used to record the response throughout all tests. One camera was dedicated to a general side view of the frame (Figure 8.14(a)) and the other was fixed to the right-hand reaction frame to view the out of plane deformations of the braces (Figure 8.14 (b)).

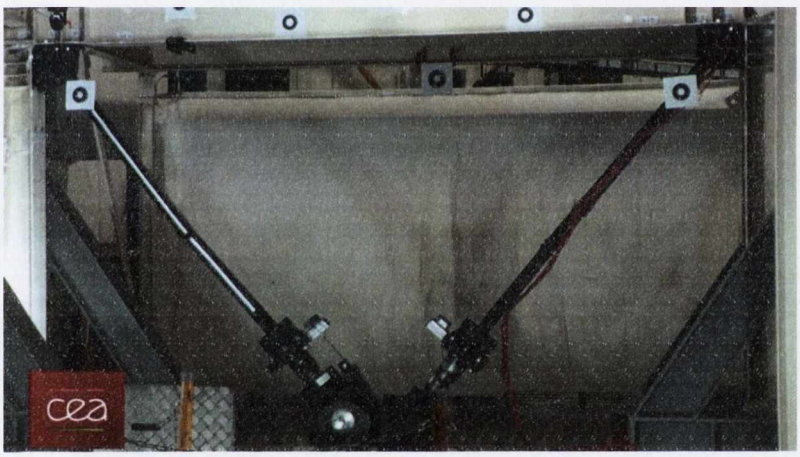

(a)

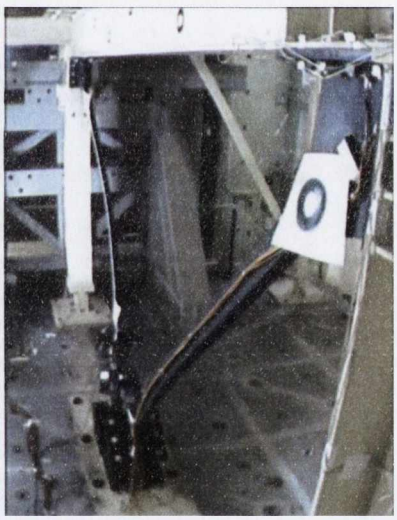

(b)

Figure 8.14 – Video camera views; (a) general view of test frame, (b) zoom view of out-of-plane brace deformation

8.5.6 Data Acquisition

Two data acquisition systems were employed in the BRACED project. The data channels acquired with the Pacific Instruments system and the MTS data recorder are listed in Appendix B1. The acquisition files have the same data structure for all the configurations even if the number of sensors is not exactly the same. The acquisition duration was 50 seconds in each test.

The following parameters were used for data acquisition with the Pacific Instruments system:

- Acquisition duration: 50 seconds.
- Acquisition sample rate: 512 Hz.
- Value of the anti-aliasing filter: 150 Hz.
- No computed channels.
- No recording of the pre-test sequences.
- Zeroing offsets: Only measurements by the accelerometer sensors and displacement sensors were zeroed for each new configuration. In particular, initial measurements of load cells and gauges were retained to determine if the braces were prestressed in the frame before the tests sequence. Balance of the load cells and braces gauges (SG) was performed when the brace bolts were still loose, just before they were tightened. The frame gauges (SGF) were zeroed only once, before the first test on the first configuration.

The MTS data recorder was used to acquire the displacement, acceleration and forces measurements from the eight actuators of the table.

8.6 Testing Procedure

All tests were carried out following the same methodology. Once a test sequence on a pair of braces was completed, the frame had to be returned to its original vertical position and a new pair of braces installed. Before initiating test runs, the test frame was aligned so that the primary columns were vertical. All data readings for instrumentation on the frame (displacement transducers and SGF strain gauges) were zeroed in a way that ensured that any initial loading of the brace member was recorded.

8.6.1 Test Runs

As a whole, 160 test runs were performed on the frame from March 2013 to May 2013. Summary details of these runs are presented in Appendix B2. For each brace configuration, test runs were executed in the following sequence:

- 0.05 g - MTS white noise test from which initial natural frequency (eigen-frequencies) and damping were identified;
- 0.1 g - ISTAR pretest for initializing shaking table control; this was done in two steps: identification of the minimum level of solicitation, and then, first ISTAR drive identification using a white noise at this level ;
- low level (≈ 0.05 g) - seismic test (for improvement of transfer function),
- low level (≈ 0.05 g) - seismic test (for improvement of transfer function),

- **low level (≈ 0.1 g) - seismic test (elastic behavior of the braces expected),**
- 0.05 g - MTS white noise test (eigenfrequency identification),
- **medium level (≈ 0.2 g) - seismic test (brace buckling and yielding expected),**
- 0.05 g - MTS white noise test: (eigenfrequency identification),
- **high level (≈ 0.5 and 1 g) - seismic test (fracture of braces expected).**

In some tests, a second high level seismic test was executed to achieve brace fracture. All the MTS white noises had the following parameters:

- random, flat,
- frequency between 0.7 and 50 Hz,
- acceleration 0.1 g RMS,
- span between 20 and 30%,
- acquisition 60 s on Pacific Instruments system, 120 sec on MTS data recorder.

8.6.2 Preliminary Testing

Before beginning the testing programme, two preliminary tests were performed. These had several goals:

- to check the table monitoring in experimental conditions, i.e. with the full mass on the table;
- to check the frame behaviour;
- to check the operational procedure for exchanging pairs of brace-gusset-plate specimens;
- to confirm estimates of the level of seismic excitation required to achieve brace fracture.

The first preliminary test was carried out with a pair of S1-CA-G1 specimens, and the second one with a pair of S1-CB-G1 specimens.

8.6.3 Operations Between Two Test Sequences

After each test sequence on a pair of brace-gusset plate specimens, the specimens were exchanged according to a technical procedure written by the frame fabricator.

A new set of gauges cables were welded on the next instrumented brace for the next test sequence. The cables of the two sensors measuring the overall length of the braces were disconnected and the damaged braces were removed. If necessary damaged bolts from connections of the IPE400 beam to the HEB220 columns were also removed. The frame was straightened back using a dedicated system and the new pair of braces was positioned in the frame.

To align the frame correctly between tests, 'Matjack' high pressure air bags were placed at the impact panels between the reaction frames and the test frame (Figure 8.15(a)). The air bags were then inflated until the desired alignment was reached. At this point, the brace members were 'offered-up' to the frame and bolted in place. All bolts in the frame and specimen connections were tightened to the torque reference values in BS EN 1090 (CEN, 2008) for k-class K2 bolts.

(a)

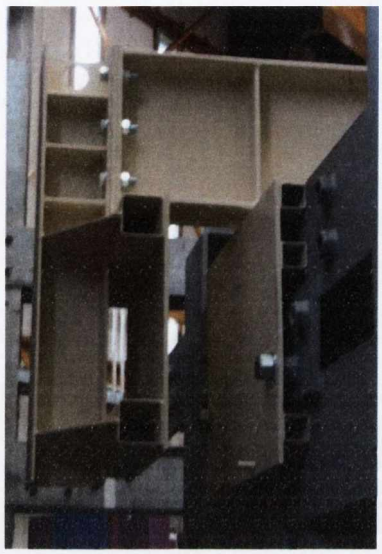

(b)

Figure 8.15 – Photographs of (a) high pressure air bag and (b) impact panel.

The balance of the load cells and brace gauges was performed before the tightening of the bolts. The tightening of the bolts between the swivels and the lower ends of the braces was recorded and numbered as a dedicated test run.

8.6.4 Shaking Table Control

Shaking table control was performed by a two-stage system:

- SIGNALSTAR software Version 4.4.0.3, developed by Data Physics and loaded on industrial computer (IS140755), sends the electric drive for each degree of freedom needed by the MTS controller to achieve a seismic acceleration signal that fits with the required spectrum. The initial drive is computed through an initial operation called 'pretest' which is divided into two steps:
  i. The identification of the minimum drive voltage necessary to obtain a significant response of the system (table with installed test frame). The criterion is that the ratio of acceleration feedback signal to measurement noise, is higher than a value fixed by the user (typically 3 dB).

ii. The monitoring of the system (table with test frame) with a white noise scaled at the minimum drive voltage in order to compute the first drive and first transfer function. The criteria are the acceptable quality of the transfer function and coherence of the acceleration signal.

The electric drive is then adjusted after each seismic run by comparing the spectrum obtained in the previous run with the theoretical spectrum. This iterative process permits to improve the monitoring of the table to fit the spectrum in several steps.

- The drive is sent to the MTS controller monitored by the software 469D, loaded on computer DELL PRECISION 490 (IS145516), which transforms this drive dedicated to one degree of freedom, into electric signals sent to each of the eight table actuators. The 469D software uses the monitoring parameters or 'settings' tuned for the system to be monitored (table with installed test frame).

The feedback acceleration is measured by reference accelerometers fixed within the AZALEE shake table, in the center of its top surface. Only one accelerometer was used for feedback. For the MTS controller, the settings file was '124_BRACED.set'.

8.6.5 Post-Test Measurements

After the final test on each configuration, the deformations of the test frame and the brace-gusset plate specimens were measured manually. These measurements included the distances between test frame and reaction frames, buckling or fracture location along brace length, and the out-of-plane deformation profile of any unfractured brace specimens remaining as one length after failure.

Detailed measurements were made of the cross-section dimensions (width, depth and thickness) of the brace tubes to evaluate variations due to manufacturing and testing. Furthermore, the geometry of the fracture and local buckle location were measured for an assessment of the local brace deformation profile. For Tests 1 – 4, both tube lengths were cut into sections at 200 mm intervals. The remaining tests were cut at both ends near the connection plates, and on both sides of the fracture or buckle. Dimensional measurement obtained at these cross sections were used to calculate mean cross-section areas for each specimen. The application of these measurements is discussed in section 9.2.1.

8.7 Seismic Excitation

As indicated above, twelve specimens were tested under uniaxial seismic excitation using a single earthquake record scaled to three different levels. The signal is a natural ground record from the PEER database, recorded in Imperial Valley (California, USA) during the 1940 earthquake. The

chosen ground motion was determined using hazard spectra for a specific benchmark site, as described in sub-section 8.7.2. It was originally intended to test twenty-four specimen pairs with duplicate specimens to be tested under different seismic excitations. However, due to time constraints, twelve core specimens were tested using a single ground motion record allowing comparison between main specimen parameters.

8.7.1 Application of Seismic Signal

The spectrum of the input seismic signal was normalised to the lowest seismic level expected in the test sequence, that is a PGA level at 0.1 g. This level is considered as the 0 dB level, and the signal is then amplified for different excitation levels.

The original signal was filtered at low frequency to limit the maximum displacement to less than the ± 100 mm limit value for the AZALEE table. A high pass filter eliminates the frequencies under 0.7 Hz. This filtering is also needed to obtain a null value of table displacement at the end of the test. The signal duration is 40 seconds with five seconds at null value added at the beginning in order to provide the operators with time to check the correct triggering of the data acquisition system. The normalised ground motion employed in the shake table tests is shown in Figure 8.16, including the original signal and filtered signal.

As indicated in sub-section 8.6.1, before the scaled earthquake level tests were applied, a number of low level earthquake tests were performed to optimise the shake table transfer function so that the table motion matched the spectrum of the earthquake record.

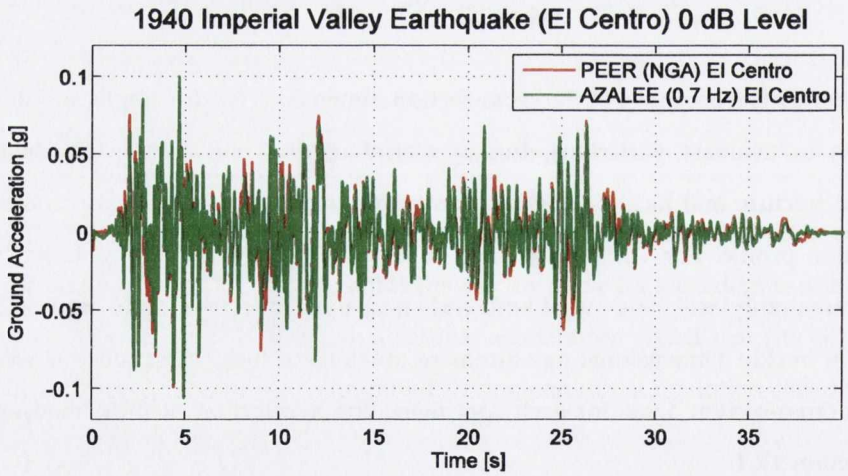

Figure 8.16 – PEER NGA and filtered AZALEE ground motion records normalised to 0 dB.

8.7.2 Selection of Earthquake Ground Motions

The three scaled earthquake ground motion levels correspond to the three levels of design earthquake typically specified in design codes; serviceability limit state (level 1); damage control

limit state (level 2) and life-safety limit state (level 3). Two of these design earthquake levels have been discussed in Chapter 2 in relation to the no-collapse (level 3) and damage limitation (level 2) requirements in Eurocode 8. The Level 2 requirement has probability of exceedence of 10% in 50 years and is treated as the reference hazard level. For many existing design codes, three probabilities of exceedance are defined as 50% in 50 years, 10% in 50 years and 2% in 50 years. Hereafter, these are denoted by 50%/50, 10%/50 and 2%/50 respectively. In design codes, Level 1 and Level 3 hazard levels can be specified as scaled versions of the Level 2 hazard. For example, in Eurocode 8 (CEN, 2008) the ratio between Level 2 and Level 1 hazard levels is 0.4.

There are some existing drawbacks of using this approach, two of which are briefly discussed. Firstly, as noted by Priestley et al. (2007), this method of scaling the Level 2 hazard to obtaining Level 1 and 3 hazard levels is reasonable for areas of high seismicity but becomes less relevant for areas of infrequent, high intensity shaking. This is especially important in generating displacement spectra. Secondly, Bommer and Pinho (2006) have highlighted the issue of anchoring spectral acceleration to the PGA and soil despite the fact that PGA has no geophysical significance and also that the actual spectral shape is strongly influenced by the earthquake magnitude. An approach offered by Priestley et al. (2007) establishes a corner period (T_D in Eurocode 8) and the displacement of the displacement spectra given the expected magnitude and distance to the casual earthquake, which is based on the formulations developed by Faccioli et al. (2004). This forms the basis of a Probabilistic Seismic Hazard Analysis (PSHA) where site-specific hazard assessment is used to establish distinct spectra for each hazard level rather than simply applying factors to a related level (e.g. Level 2). However, similar to Eurocode 8, the resulting spectra are still anchored to the PGA. Without consideration of the magnitude in the spectral shape, the spectra will not have uniform hazards at all periods.

In order to achieve a Uniform Hazard Spectrum (UHS), a PSHA of a design site can be carried out and the spectral acceleration values can be plotted for each period. Consequently, each period value on the design spectra has the same probability of exceedence (Algermissen and Leyendecker, 1992). A hazard analysis for a particular facility considers nearby faults, source-site distance, source-site conditions and facility location. This can be performed efficiently using the hazard maps and an online interactive deaggregation tool developed by the United States Geological Survery (USGS). The deaggregation process separates the contributions to the seismic hazard from different magnitudes and site-source distances. In addition, individual seismic sources controlling the seismic hazard at a given period can be identified.

In this respect, a PEER benchmark site used by Haselton et al. (2008) was selected for choosing ground motion input in this experimental campaign. The benchmark site allows for future comparisons between different studies. It is situated at the LA Bulk Mail Facility located in Bell, Los Angeles, California and demonstrates good representation of the general characteristics of the Los Angeles area. A disaggregation plot for the benchmark site with a period of 1.0 s and a 10% in 50 years probability of exceedence is depicted in Figure 8.17. It is shown that a large contribution to the hazard is caused by magnitude M_w 6.6-7.0 earthquakes from a source with a distance 8-15 km from the site. At this period, a spectral acceleration of 0.5599g is returned. This procedure was repeated for a period range with the three hazard levels and a UHS was generated as illustrated in Figure 8.18.

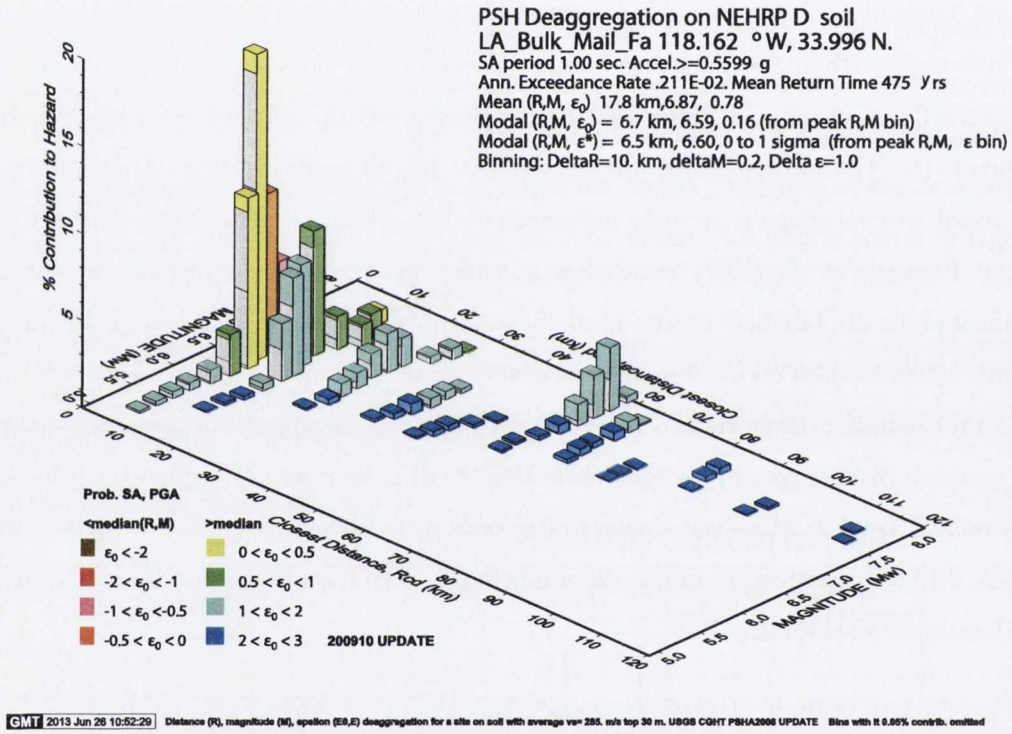

Figure 8.17 – Hazard deaggregation plot produced from USGS (2013) for LA Bulk Mail Facility site with 10% in 50 years probability of exceedence and at a period of 1.0 s.

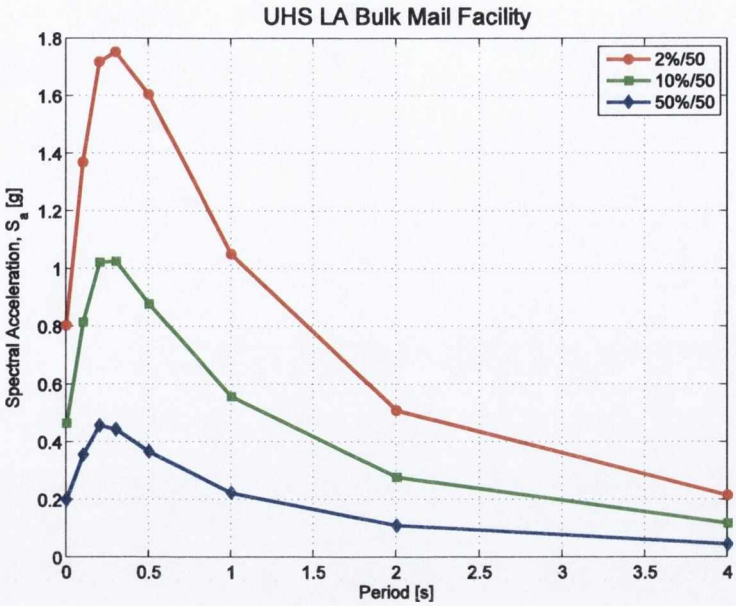

Figure 8.18 – Uniform Hazard Spectra for LA Bulk Mail Facility site with three hazard levels.

Based on the deagreggation analysis a short list of ground motion records were selected for similar magnitude, site-source distance and epsilon value. The significance of the epsilon value pertaining to ground motion record selection is discussed in detail by Baker et al. (2011). Site conditions at each recording station were also important and records with soil sites considered as NEHRP C or D (NEHRP, 2009) were selected to be consistent with the LA Bulk Mail Facility soil condition.

Although it was desirable to capture the variation in causal sources for the UHS using more than one ground motion record, the existing set of experimental parameters resulted in one record being used for testing purposes. The selected record was from the 1940 Imperial Valley earthquake recorded at the USGS El Centro Array with NGA #0006 in the PEER NGA Database (PEER, 2010). The spectra for the El Centro ground motion are shown in Figure 8.19 with the UHS as above. The reason for selecting this record was twofold: sufficient response acceleration is shown in the response spectrum near the natural period of the test frame (≈ 0.2s); and strong motions are observed in groups towards the beginning and end of the record (Figure 8.16), encouraging yield development throughout the duration of the time history. It is noted that one cannot represent a UHS with a single ground motion. However, the record selected for the shake table tests matched the UHS over the period range that was of interest in the tests (0.15 – 0.3 s), as shown in Figure 8.19.

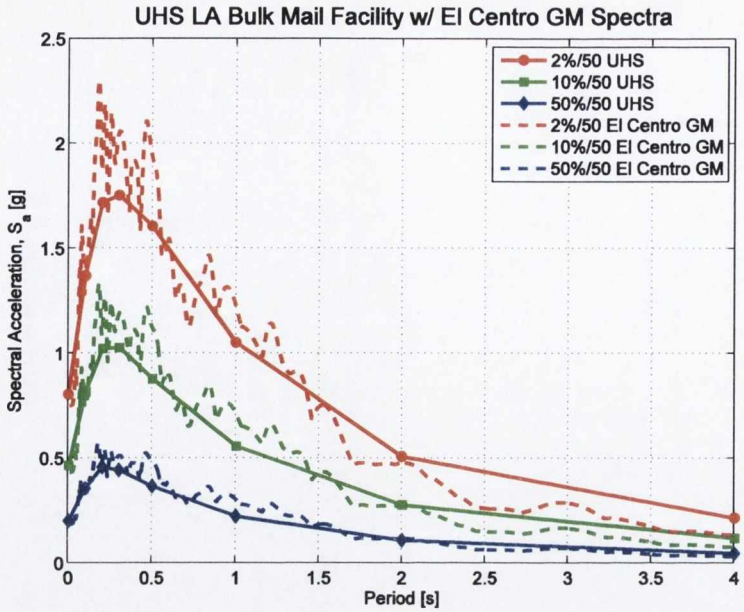

Figure 8.19 – El Centro ground motion spectra matched to UHS at 2% in 50 years. The spectra were scaled to match at lower levels.

The selected signal was filtered as described in sub-section 8.7.1. With the retained signal frequency range of 0.7 to 50 Hz, the AZALEE table could operate from 0.1g to 1.0g within its displacement limits. The result of the filtering is shown in Figure 8.20 (a) and (b) with negligible effects in the period range of interest (0.1 – 1.0 s) for the acceleration and displacement response spectra.

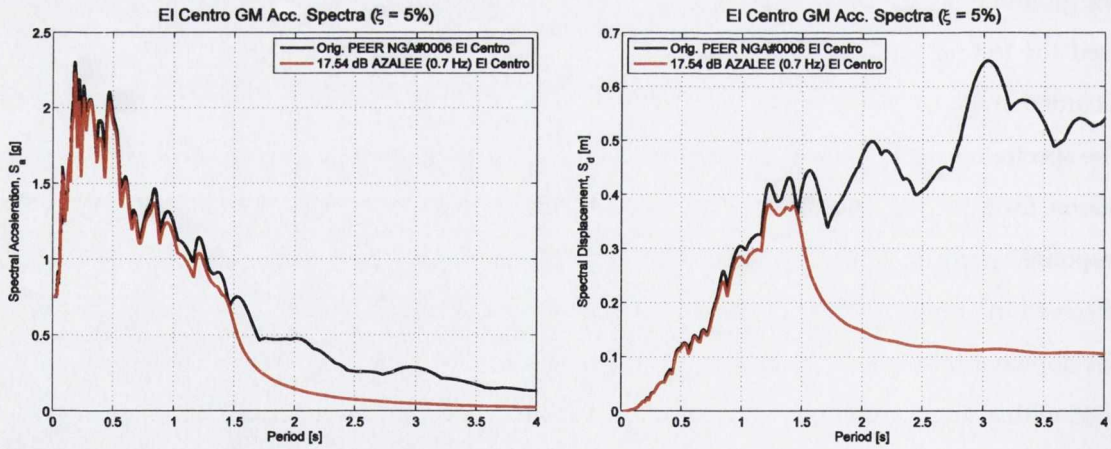

(a) (b)

Figure 8.20 – Earthquake excitation (a) acceleration and (b) displacement spectra for the original PEER NGA record and the filtered reference record (scaled up to 17.54 dB) for application to the AZALEE shake table.

Two preliminary shake table tests were carried out using brace section S1 to establish a realistic PGA for fracture for the largest section size (0.60g). This was representative of the 2%/50 hazard

level. The ground motions for the 10%/50 and 50%/50 levels were scaled using the ratios between the PGAs of the UHS in Figure 8.18. Therefore, the three ground motions scale factors and PGAs for testing were established for all experiments with S1 sections. The same methodology was applied to sections S2 – S4 except that the PGA for fracture (2%/50) for each section size was reduced based on its proportion to the S1 section size. This process is shown in Table 8.5.

Table 8.5 – Overview of ground motion PGA levels based on UHS for three hazard levels and brace section yield strengths.

Brace Section	Ratio of Brace Yield Strengths	Hazard Level	Ratio from UHS	PGA for testing (g)
S1	1.000	2%/50	1.000	0.60†
		10%/50	0.580	0.35
		50%/50	0.250	0.15
S2	0.856	2%/50	1.000	0.57
		10%/50	0.580	0.33
		50%/50	0.250	0.14
S3	0.735	2%/50	1.000	0.44
		10%/50	0.580	0.25
		50%/50	0.250	0.11
S4	0.686	2%/50	1.000	0.41
		10%/50	0.580	0.23
		50%/50	0.250	0.10

†PGA for fracture based on preliminary experiments.

8.8 Chapter Overview

This chapter presented the BRACED project shake table testing programme, with an overview of the testing facility, a list of the project objectives and the collaborative effort of the organisations involved, followed by a description of the test frame design and a detailed description of the design of the brace-gusset plate specimens. The location of both permanent (for AZALEE shake table) and temporary (for BRACED structure) instrumentation was illustrated for each category of data measurement. Testing procedures relating to the test frame, specimens and shaking table control were described. To support the use of UHS for ground motion selection, a brief background highlighted the design code approach and the PSHA approach. The UHS for the selected benchmark site were presented and the procedures before and after specimens were tested have been described.

9 BRACED Project – Experimental Results and Analysis

9.1 Introduction

In this chapter the experimental observations and results from the shake table test programme of the BRACED project are presented. Results from the application of earthquake and white noise excitations to the test frame are first reported. These are then analysed to explore the effects of the key experimental parameters on the observed response.

9.2 Measured Test Conditions

Each pair of brace-gusset plate specimens was tested using scaled site-specific ground motions for three different probabilities of exceedence of 2%, 10% and 50% in 50 years representing high, intermediate and low level earthquake events respectively. The actual dimensions of the brace specimens and the characteristics of the applied seismic excitation were monitored throughout the experimental programme.

9.2.1 Measured Brace Tube Section Area

The actual yield strengths of the steel in the brace and gusset plates of the individual brace-gusset plate specimens were measured in tensile coupon tests and presented in Table 8.3 and

Table 8.4. Due to manufacturing tolerances the actual cross-section dimensions of the steel tubes used in the fabrication of the brace specimens also vary from their nominal values. To obtain an accurate value of the cross-section area for the calculation of brace yield and buckling resistances, and for the validation of OpenSees models, the cross-section area of each specimen was measured after testing. Measurements were obtained at regular intervals along the brace tube length where the brace was cut using an electric hacksaw. At one end of each of the cut lengths three thickness measurements were made on each of the four faces of the tube, along with three depth and height measurements. For the first four tests (Test 1 – 4), the brace was cut into eleven short lengths and measurements obtained from each, while for the remaining tests (Test 5 – 12) the brace was cut into four lengths. Dimensional measurements were made using a digital calliper (with a resolution of 0.01mm). Measured cross-section areas were calculated from weighted mean t, B and D values for each tube length. Table 9.1 presents the nominal and measured cross-section areas of the left-hand and right-had braces in each test. The presented reduction factors show that nearly all actual cross-section areas were smaller than their nominal values; the differences are usually less than 5%. Figure 9.1 demonstrates the method used to measure square and rectangular cross-sections. The

numbers 1, 2, 3 indicate the location and orientation of each of the thickness measurements; the three cross-section depth and width measurements were also obtained at these locations.

Table 9.1 – Summary of nominal and measured brace tube areas for left and right braces.

Test	Specimen	Section Type	Nominal Area (mm^2)	Measured Area Reduction Factor		Measured Area (mm^2)	
				Left	Right	Left	Right
1	S1-CA-G1	80×80×3.0 SHS	915	0.962	0.928	880.230	849.120
2	S3-CA-G1	80×40×3.0 RHS	674	0.927	0.935	624.798	630.190
3	S4-CA-G1	60×60×3.0 SHS	674	0.967	0.965	651.758	650.410
4	S2-CA-G1	100×50×3.0 RHS	854	0.972	0.966	830.088	824.964
5	S1-CA-G2	80×80×3.0 SHS	915	0.990	1.003	905.850	917.745
6	S2-CA-G2	100×50×3.0 RHS	854	0.993	0.992	848.022	847.168
7	S3-CA-G2	80×40×3.0 RHS	674	0.948	0.980	638.952	660.520
8	S1-CB-G1	80×80×3.0 SHS	915	0.967	0.977	884.805	893.955
9	S2-CB-G1	100×50×3.0 RHS	854	0.983	0.985	839.482	841.190
10	S4-CB-G2	60×60×3.0 SHS	674	0.950	0.982	640.300	661.868
11	S2-CB-G2	100×50×3.0 RHS	854	0.994	0.999	848.876	853.146
12	S3-CB-G2	80×40×3.0 RHS	674	0.949	0.979	639.626	659.846

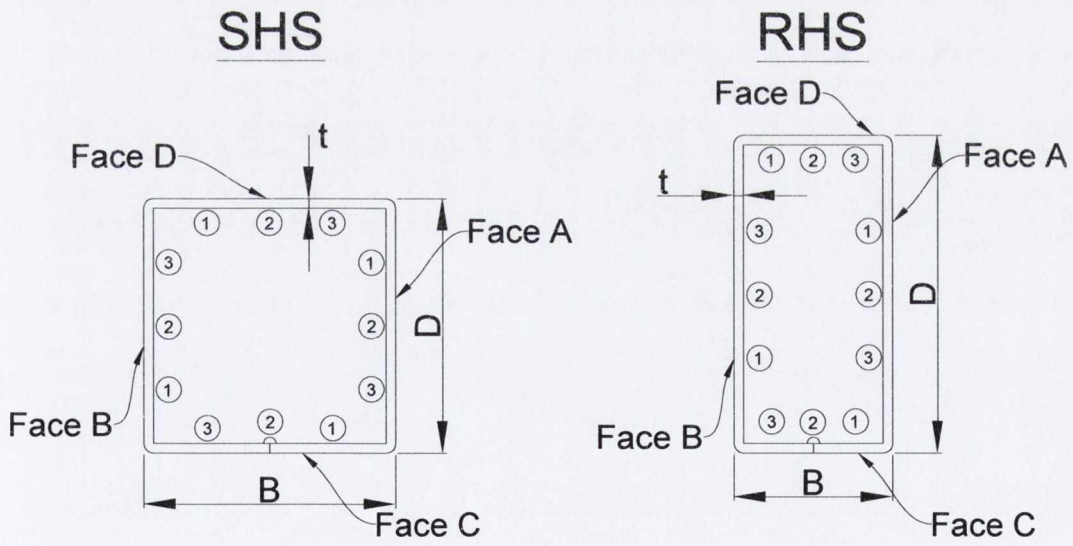

Figure 9.1 – Measurement locations for both section types showing twelve thickness measurement locations and three depth and width measurement locations.

9.2.2 Ground Motion Response Spectra

The El Centro ground motion (used for all earthquake excitation runs) was selected from the PEER NGA database and filtered for use with the AZALEE shake table as outlined in Chapter 8. Prior to testing each specimen, a number of low level earthquake tests were performed to optimise the shake table transfer function (Figure 9.2). This was carried out so that table motions were controlled to ensure that the original (target) accelerations were reproduced. The method employed compared the spectrum of the filtered record (input) with the spectrum of the actual table acceleration measured during the test. This process was also carried out for the hazard level tests to check the reproduction of the target accelerations at higher PGA levels.

Figure 9.3 presents the normalised response spectra obtained from the recorded table motions in the different runs in Test 5. Reasonable fidelity to the reference 'AZALEE 0.7 Hz' spectrum is shown in the 0.18 – 0.22 s period range of the natural frequency of the test frame. At larger acceleration amplitudes the actual run spectrum can deviate from the reference spectrum in a manner that varies from run to run. Plots for all of the hazard level tests for each specimen are compared with the reference spectra in Appendix B4.

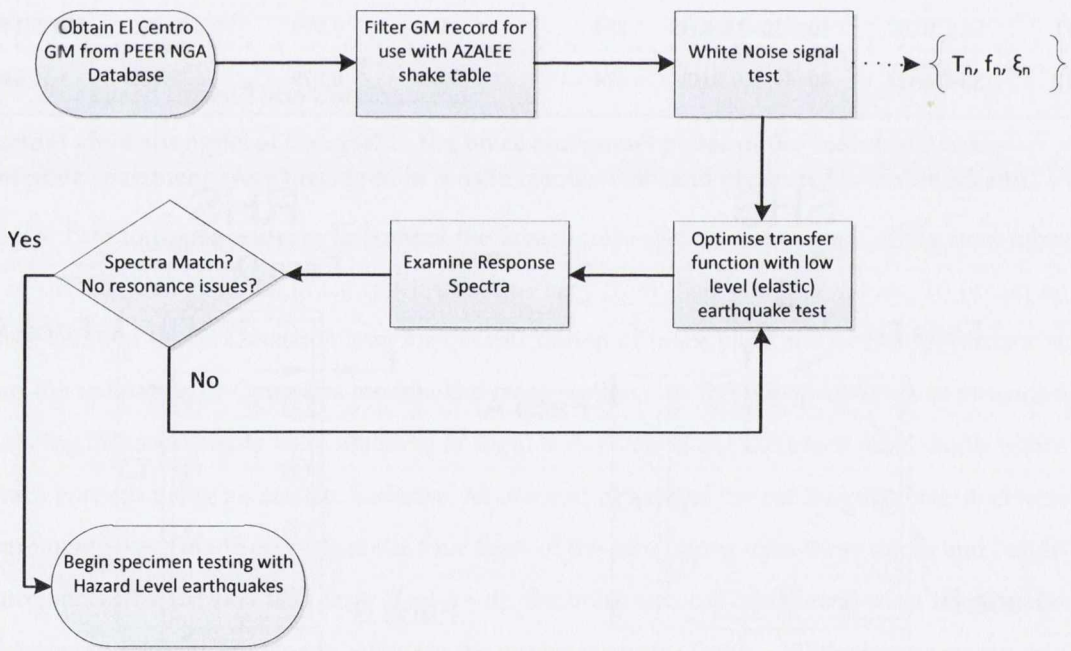

Figure 9.2 – Flow chart of shake table testing process.

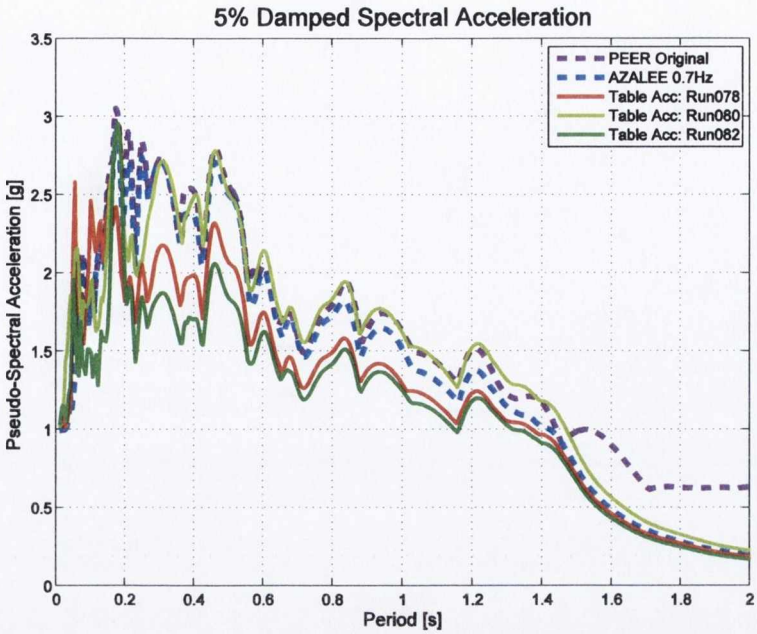

Figure 9.3 – Normalised response spectra from runs in Test 5 compared to reference spectra.

9.3 Earthquake Excitation Tests: Results and Observations

A schedule of the twelve scaled earthquake ground motion shake table tests performed is shown in Table 9.2, along with peak global acceleration and drift results from the earthquake excitation runs. In this section, the primary results recorded during these tests are presented along with observations made during the tests. In most tests, three scaled earthquake ground motion runs (50%/50, 10%/50 and 2%/50) were employed, however for some tests in which full fracture did not occur in either braces during the 2%/50 run, extra earthquake tests were carried out to achieve complete brace failure. For Test 8, the presence of resonance and shake table-structure interaction, necessitated an intermediate earthquake test to be performed after the 50% level for diagnostics related to the shake table transfer function.

In the each of the test descriptions below, measured response plots from the final two levels are presented. In most tests these feature the 10%/50 and 2%/50 runs, while in others the 2%/50 and Failure Level runs are shown. Results from any preceding low level earthquake tests are presented in Appendix B3. For brace axial load plots yield and buckling capacities (based on characteristic strengths and measured brace section area) are indicated with dashed lines. Similarly for strain measurement plots, yield strain thresholds (based on characteristic strengths) are indicated with dashed lines.

Table 9.2 – Overview of earthquake excitation test runs with peak global response results.

Shake Table Test	Specimen	Exp. Run No.	Earthquake Ground Motion	Target PGA (g)	Actual PGA (g)	DAF	Max. Drift (%)
P1	S1-CA-G1 (Pre-test)	Run010	Elastic	0.1	0.157	1.631	0.224
		Run011	Elastic	0.2	0.242	2.255	0.360
		Run012	Inelastic	0.4	0.466	1.699	0.672
		Run013	Inelastic	0.5	0.497	1.734	0.879
		Run014	Inelastic	0.5	0.620	1.561	0.948
P2	S1-CB-G1 (Pre-test)	Run017	Elastic	0.1	0.186	1.982	0.358
		Run019	Inelastic	0.3	0.319	2.592	0.816
		Run021	Inelastic	0.5	0.564	1.542	1.068
1	S1-CA-G1	Run028	50%/50	0.15	0.185	1.915	0.202
		Run030	10%/50	0.35	0.327	2.091	0.414
		Run032	2%/50	0.6	0.624	1.579	1.000
2	S3-CA-G1	Run037	50%/50	0.11	0.158	1.547	0.180
		Run039	10%/50	0.25	0.383	1.285	0.449
		Run041	2%/50	0.44	0.517	1.631	1.525
		Run043	Failure Level	0.6	0.670	3.454	2.135
3	S4-CA-G1	Run048	50%/50	0.1	0.131	1.742	0.154
		Run050	10%/50	0.23	0.250	1.924	0.353
		Run052	2%/50	0.41	0.431	1.519	0.829
		Run054	Failure Level	0.55	0.718	1.128	2.546
		Run056	Failure Level	0.55	0.577	1.434	2.911
4	S2-CA-G1	Run065	50%/50	0.14	0.207	1.611	0.221
		Run067	10%/50	0.33	0.401	1.604	0.634
		Run069	2%/50	0.57	0.640	1.448	1.536
5	S1-CA-G2	Run078	50%/50	0.15	0.182	1.958	0.255
		Run080	10%/50	0.35	0.345	1.988	0.667
		Run082	2%/50	0.6	0.768	1.792	1.726
6	S2-CA-G2	Run088	50%/50	0.14	0.186	1.715	0.177
		Run090	10%/50	0.33	0.363	1.902	0.651
		Run092	2%/50	0.57	0.813	1.375	2.083
		Run094	2%/50	0.57	0.720	1.976	2.436
7	S3-CA-G2	Run099	50%/50	0.11	0.180	1.333	0.199

		Run101	10%/50	0.25	0.386	1.202	0.545
		Run103	2%/50	0.44	0.578	1.438	1.933
		Run105	Failure Level	0.6	0.592	5.734	3.238
8	**S1-CB-G1**	Run113	50%/50	0.15	0.165	3.228	0.345
		Run115	Diagnostics Level	0.2	0.230	2.006	0.413
		Run117	10%/50	0.35	0.425	3.886	0.699
		Run119	2%/50	0.6	0.825	4.900	1.693
9	**S2-CB-G1**	Run125	50%/50	0.14	0.187	2.294	0.249
		Run127	10%/50	0.33	0.367	2.337	0.891
		Run129	2%/50	0.45	0.416	1.382	1.151
10	**S4-CB-G2**	Run134	50%/50	0.1	0.175	2.332	0.360
		Run136	10%/50	0.23	0.313	2.147	0.446
		Run138	2%/50	0.41	0.497	1.450	1.799
		Run140	Failure Level	0.55	0.746	7.434	3.763
11	**S2-CB-G2**	Run146	50%/50	0.14	0.170	2.993	0.219
		Run148	10%/50	0.33	0.413	1.595	0.746
		Run150	2%/50	0.57	0.681	1.567	1.857
12	**S3-CB-G2**	Run156	50%/50	0.11	0.148	2.080	0.276
		Run158	10%/50	0.25	0.348	1.945	0.947
		Run160	2%/50	0.44	0.466	1.577	2.093

After the final earthquake test run with each pair of specimens, the fracture and buckling locations on each brace member were measured. In most cases, these locations correspond to the positions when plastic hinges formed during brace compression. This position varied between braced specimens due to differences in the rotation stiffnesses of the gusset plates and swivel bearings at the upper and lower ends of the brace member. These data are relevant for assessing the effects of the boundary conditions imposed by different gusset plate designs and the two MTS swivels. Knowledge of the plastic hinge position can also help to identify the effective buckling length of each brace and the locations of local buckling and fracture.

These locations were recorded as a measured distance from the top end of the brace tube attached to the gusset. The measured locations are listed in Table 9.3. The difference between the fracture/buckling locations of the left- and right-hand braces is also noted.

Table 9.3 – Summary of buckling and fracture locations in left and right braces.

Test	Specimen	Buckling/Fracture Location L_{bu}[mm]		$\lvert\delta L_{bu}\rvert$[mm]
		Left	Right	
1	S1-CA-G1	-	493	-
2	S3-CA-G1	1328	1283	45
3	S4-CA-G1	1205	1215	10
4	S2-CA-G1	1835	1655	180
5	S1-CA-G2	1560	1670	110
6	S2-CA-G2	1364	1212	152
7	S3-CA-G2	1158	1215	57
8	S1-CB-G1	1592	1605	13
9	S2-CB-G1	1692	1695	3
10	S4-CB-G2	1208	1201	7
11	S2-CB-G2	1233	1169	64
12	S3-CB-G2	1264	1354	90

9.3.1 Shake Table Pre-test 1: S1-CA-G1

This was the first pilot test used to assess the behaviour of the test frame and specimens. It examined the response of two braces with a CA type connection configuration. Unlike the reference tests (Test 1-12), no coupon tests were carried out to characterise the steel used in the pre-tests, hence an accurate prediction of the PGA required to cause brace fracture could not be made in advance. Consequently, low PGA values in initial runs were simply incremented until failure occurred in one of the brace members. Results from two of these runs are plotted in Figure 9.4. Initial low level elastic earthquake runs were performed to ensure appropriate matching of the input and shake table response spectra. For Run010 and Run011, the frame performed elastically with no signs of global buckling in the brace tubes or bending in the gusset plates.

During Run012 at a realised PGA of 0.466 some resonance due to the uncontrolled interaction of the test frame and shaking table was experienced towards the latter half of the test. Run014 with a PGA of 0.620g proved to be the failure event with brace fracture occurring. The maximum drift at failure of just below 1% of storey height was within the limits of the bumper catching system and the frame remained stable and upright after failure.

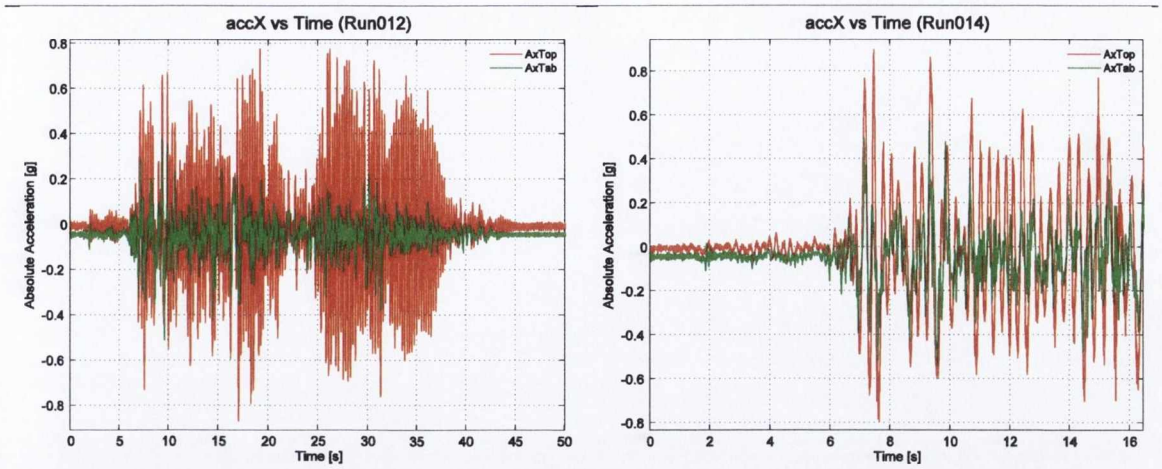

(a) Input (AxTab) and response (AxTop) absolute acceleration time history in x-direction

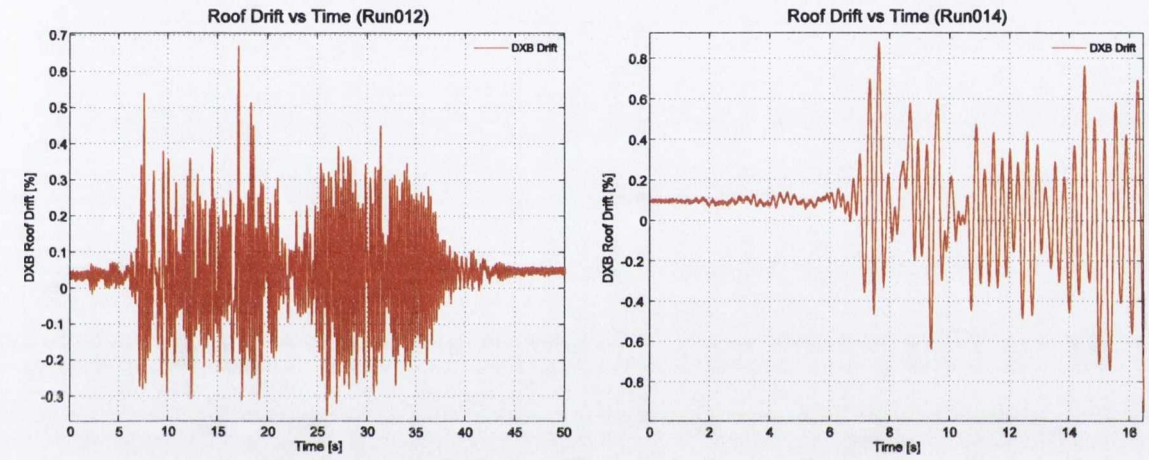

(b) Roof level drift (DXB Drift) time history in x-direction

Figure 9.4 – Recorded responses Shake Table Pretest 1; S1-CA-G1.

9.3.2 Shake Table Pre-test 2: S1-CB-G1

The second pilot test assessed the dynamic characteristics and behaviour of the test frame associated with a CB connection. Results from two of test runs are plotted in Figure 9.5. The test frame-table resonance experienced in Pretest 1 also occurred in this test, but at a lower realised PGA of 0.319 (Run012). Brace fracture occurred after 27 seconds of Run021 which had a PGA of 0.564g. As expected, maximum storey drift demand of just over 1% remained within the displacement limit allowed in the test frame design, and as in Pretest 1, the test frame remained upright after failure.

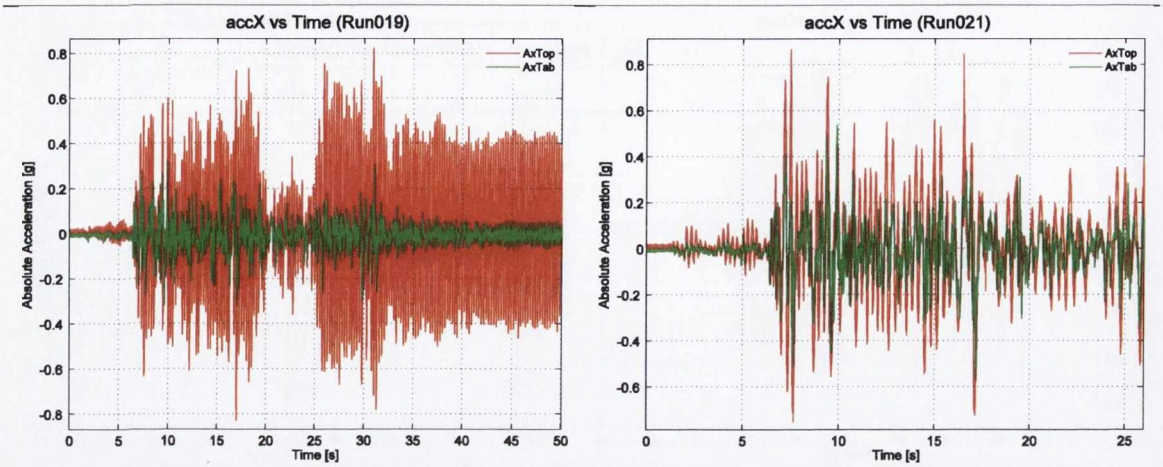

(a) Input (AxTab) and response (AxTop) absolute acceleration time history in x-direction

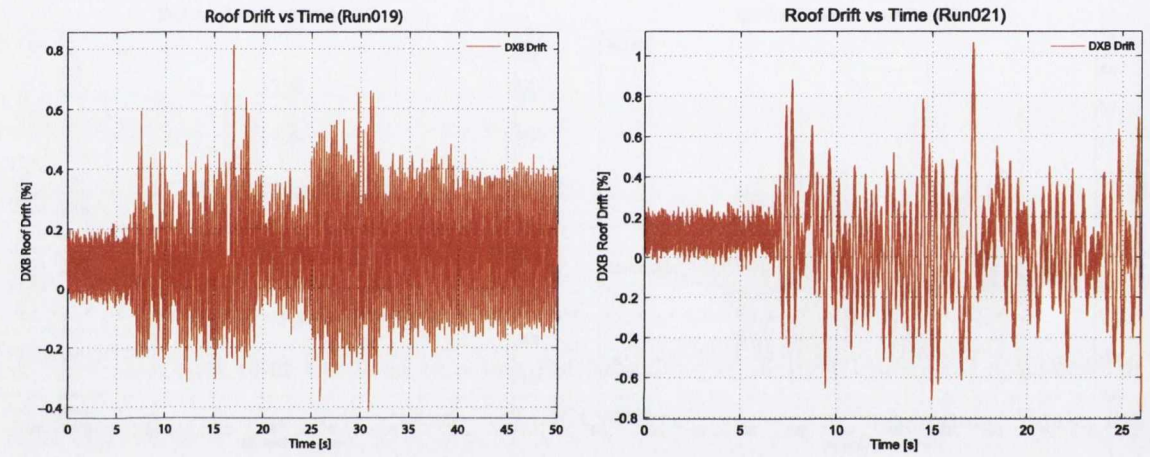

(b) Roof level drift (DXB Drift) time history in x-direction

Figure 9.5 – Recorded responses Shake Table Pretest 2; S1-CB-G1.

9.3.3 Shake Table Test 1: S1-CA-G1

The first four referenced shake table tests (Tests 1-4) all investigated the response of braces connected to the frame by conventionally designed gusset plates with SLC detailing, and as such are directly comparable. In Test 1, the largest section size (S1: 80×80×3.0 SHS) was examined. During the 50%/50 and 10%/50 levels the specimens were observed to perform elastically with no buckling or yield strains observed. The test frame strain data showed that the beam and column members in the test frame remained elastic for all the earthquake runs of this test. Also in all runs of this test, the newer MTS swivel used with the left-hand brace did not rotate freely, providing a stiff boundary condition and a reduced effective length for this brace. This was visually observable during all earthquake runs, while the right brace exhibiting free out-of-plane movement.

In the 2%/50 level (Run032), a PGA of 0.624g was realised and brace fracture occurred after 33 seconds with a maximum frame drift of 1.0% (Figure 9.6). Global buckling developed first in the

right-hand brace after around 7 seconds of the 2%/50 level test. Once global buckling had initiated, large out-of-plane deformation was present in both braces, leading to local buckling and fracture in the right brace where a tear originated in the corner regions of the cross-section. Upon post-test inspection, it was observed that this tear had propagated across half the section area of the right brace (Figure 9.7). The left brace exhibited residual out-of-plane deformation with no local buckling or cracking present.

The resolution of the load cell data obtained in this test was reduced due to application of a 50 Hz AC data acquisition filter, however, comparison of base shear values derived from roof level acceleration data and from brace axial force data display reasonable agreement (Figure 9.6(c)).

In Figure 9.6(f) yield strains are displayed by gauges SG1 and SG2 (located near brace mid-length) in the 2%/50 run. This indicated that tensile yield occurred across the whole section. In the gusset plate, SG4 lies within the $3t_p$ plastic hinge zone and displays large yield strains. SG5 is positioned close to the plastic hinge zone and does not achieve sustained yield strains, indicating plastic strains were limited to the plastic hinge clearance zone. This is reflected in the residual deformation of the gusset plate in Figure 9.7(c). This is in contrast to Test 8 (section 9.3.10) where the CB connection was used and large strains exceeding yield are observable in SG5.

10%/50 (Run030) **2%/50 (Run032)**

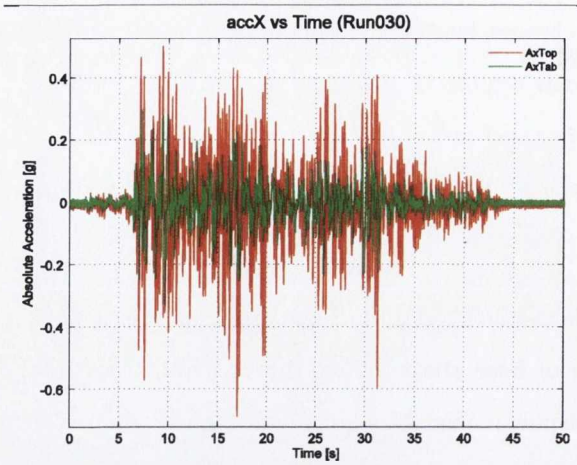

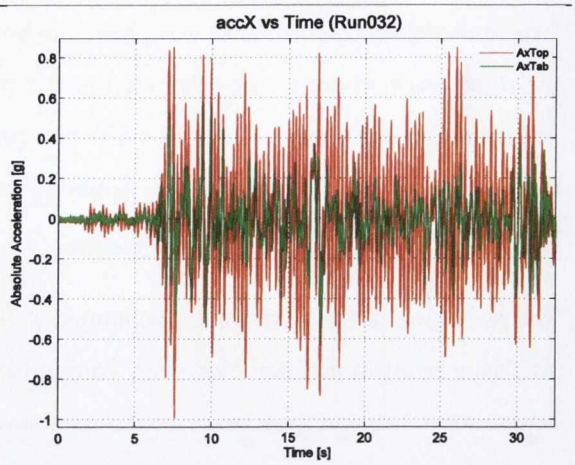

(a) Input (AxTab) and response (AxTop) absolute acceleration time history in x-direction

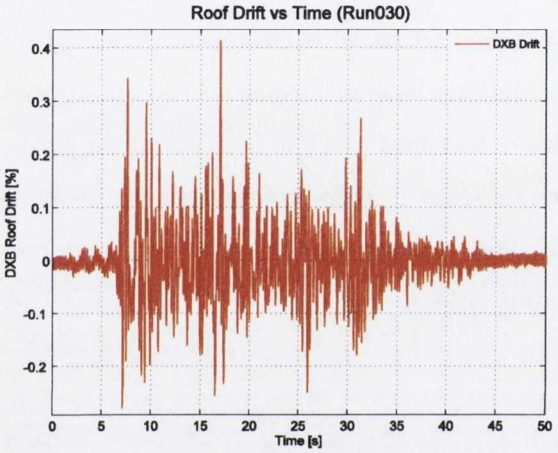

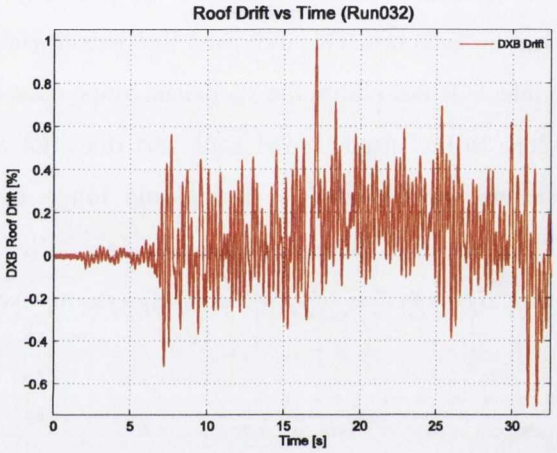

(b) Roof level drift (DXB Drift) time history in x-direction

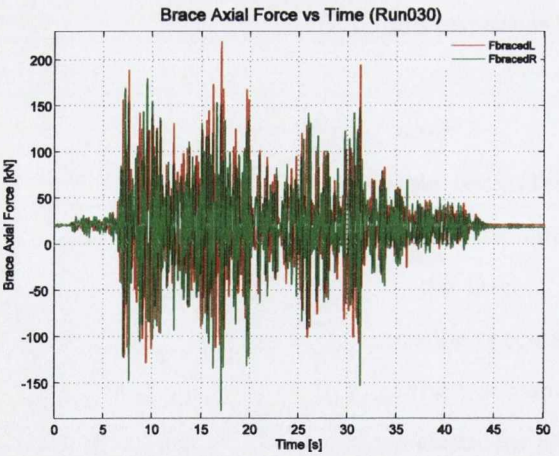

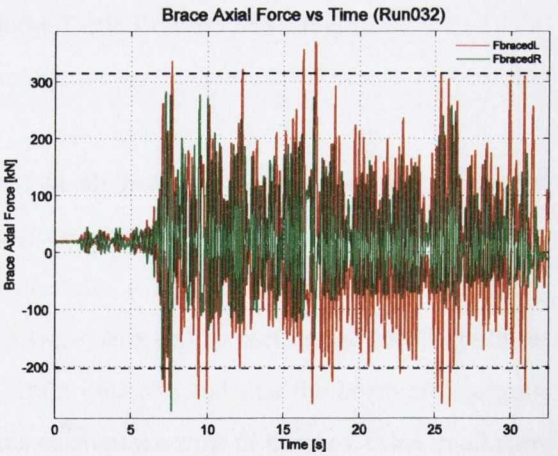

(c) Brace axial load time history for left (FbracedL) and right (FbracedR) braces. Dashed lines indicate yield and buckling capacities (based on characteristic strengths and measured brace section area).

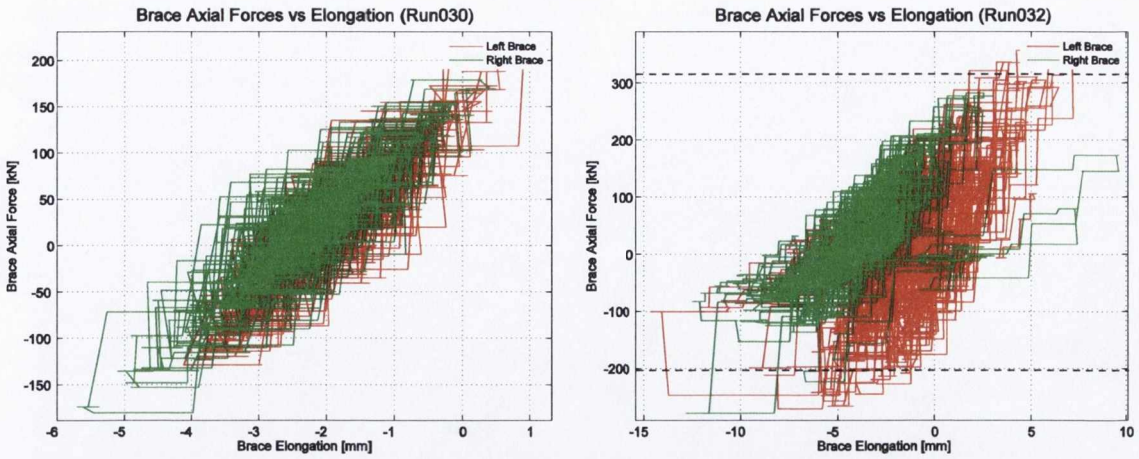

(d) Brace axial load hysteresis for left and right braces. Dashed lines indicate yield and buckling capacities (based on characteristic strengths and measured brace section area).

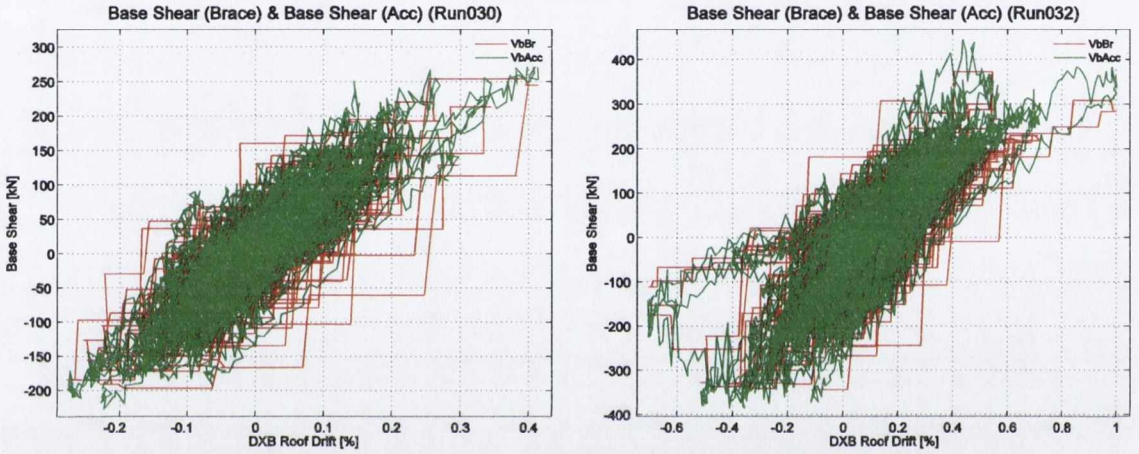

(e) Base shear from brace axial forces plotted against roof drift

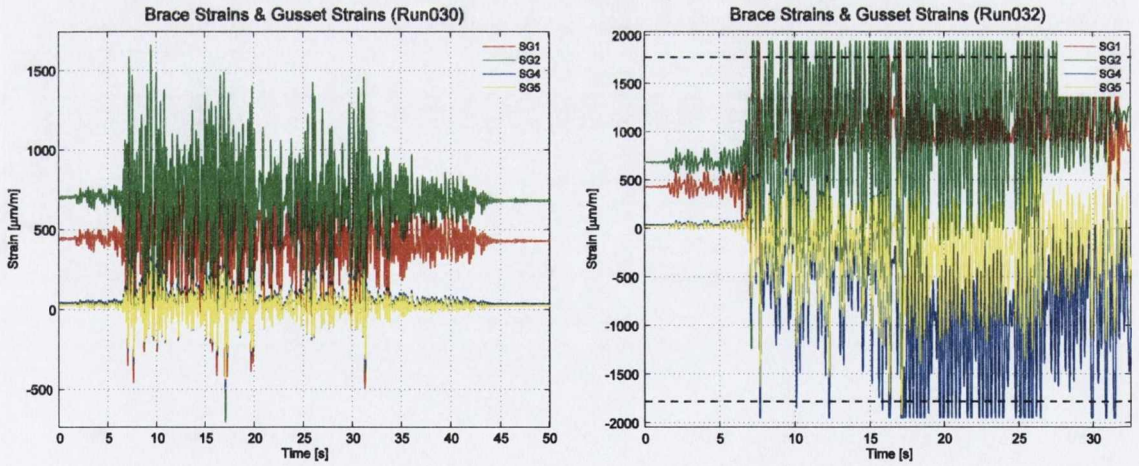

(f) Strain gauge measurements located on the right brace and gusset plate specimen. Dashed lines indicate yield strain thresholds (based on characteristic strengths).

Figure 9.6 – Recorded responses Shake Table Test 1; S1-CA-G1.

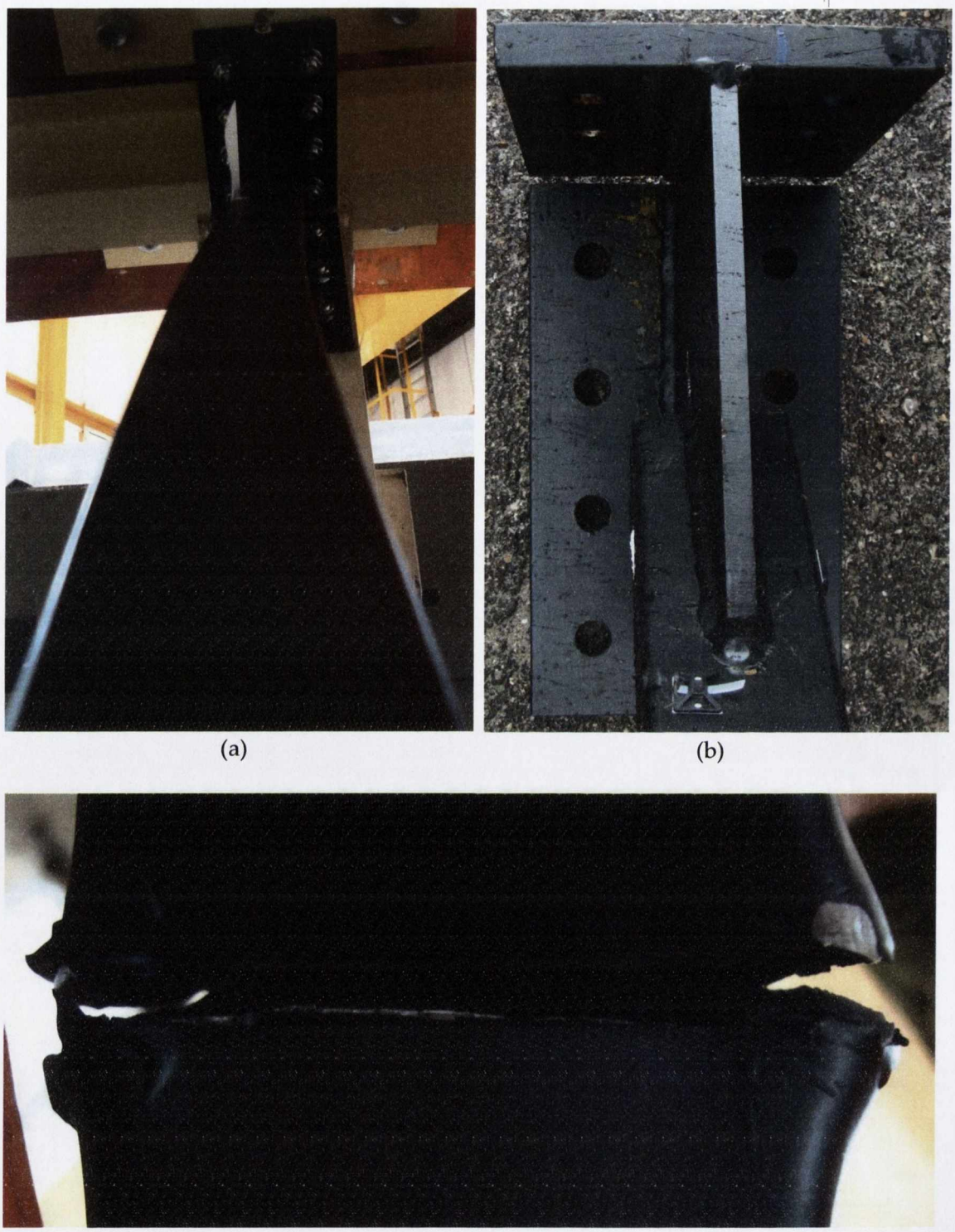

(a) (b)

(c)

Figure 9.7 – Test 1; S1-CA-G1 after testing: (a) overall brace bending shape with global buckling in left brace (b) minimal bending deformation of right gusset plate and (c) fracture across the near face of the right brace.

9.3.4 Shake Table Test 2: S3-CA-G1

Prior to the initial run in this test, adjustments were made to the new MTS swivel used with the left-hand brace. These adjustments were performed to ensure that both braces possessed a true unrestrained pinned connection and therefore matching effective lengths. During the 50%/50 run all components responded elastically. In the 10%/50 run yield thresholds were just reached with minor yield strains developed in the gusset plate and the theoretical buckling loads attained in both braces. In the 2%/50 level (Run041) with target PGA of 0.44g, global buckling occurred in both braces and residual out-of-plane deformations were present in both braces after the test. The deformed brace profile shapes appeared visually similar indicating that both braces experienced similar boundary conditions. However, no local buckling was observable in either brace. Consequently, a higher scale earthquake run was performed (Run043) with target PGA of 0.60g with the aim of causing fracture in the brace-gusset plate specimens.

As this final run began with residual drift present (Figure 9.8(b)) and both braces had experienced elongation in the previous run, non-zero initial compression loads existed in both braces, as shown in Figure 9.8(c). During large amplitude response at approximately 10 seconds, a local buckle was observed in the right-hand brace. Following this, fracture initiated in the right-hand brace and, subsequently during large tension force and displacement demands at 16.5 seconds, complete section failure occurred. Simultaneously, a local buckle developed in the left-hand brace.

Post-test inspection showed that only limited local buckling had developed in the braces. In the right-hand brace necking typical of tensile rupture was observable, with minimal evidence of buckling in the compression flange, as shown in Figure 9.9(a). In the left-hand brace a very slight local buckle was observed with slight bulging of the corner regions and no cracking or fracture visible. The plastic hinge locations measured along either brace length differed by only 45mm, suggesting that similar end restraint conditions existed in the two braces.

The SLC layout of the gusset plates was reflected in the form of plastic hinging developed in these elements, as illustrated by the paint flaking along the hinge length visible in Figure 9.9(c). The strain gauge measurements from SG4 and SG5 in Figure 9.8(f) indicate that (approaching brace failure, Run043) yielding was mainly limited to the plastic hinge zone (SG4) with minor exceedences of the yield strain limit observed in SG5. Permanent deformation of the gusset plate is observable in the drift of the SG4 readings into the compression range. In Test 7 (section 9.3.9), the strain measurements of SG4 demonstrated a larger absolute range between maximum and minimum strain peaks. In that instance, plastic deformation was not limited to the elliptical clearance zone, as SG5 shows several large excursions beyond elastic strain limits.

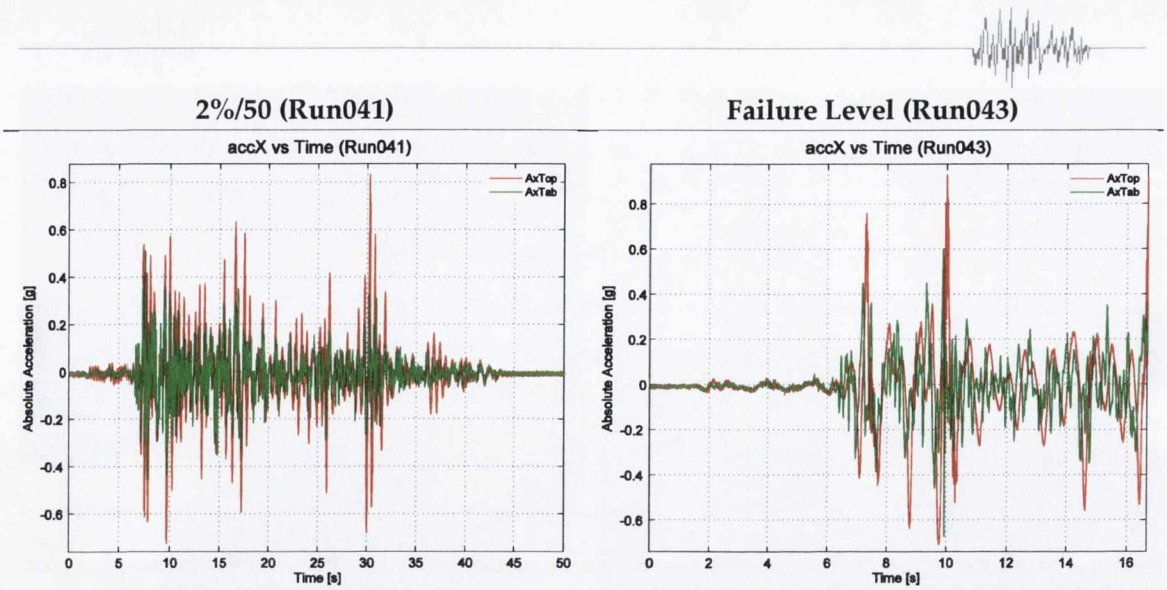

(a) Input (AxTab) and response (AxTop) absolute acceleration time history in x-direction

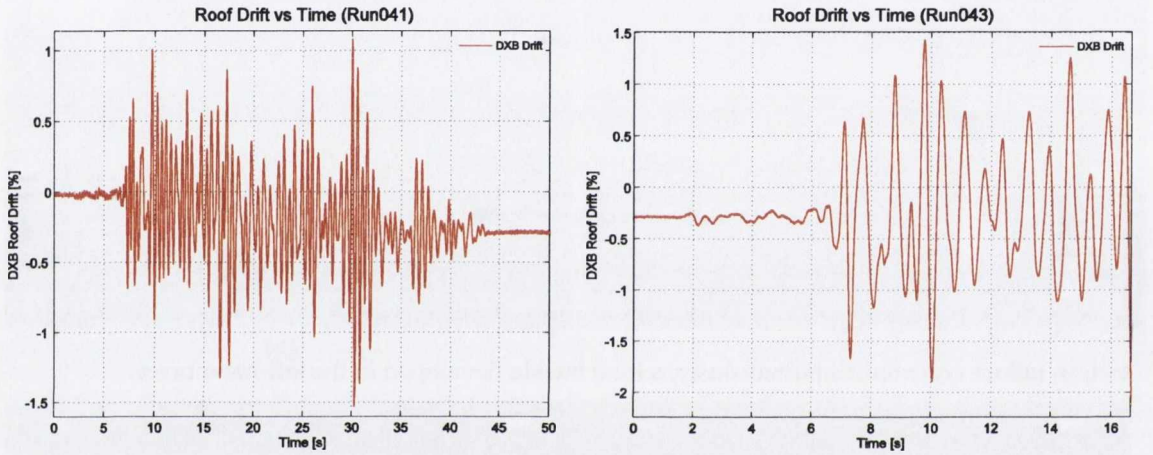

(b) Roof level drift (DXB Drift) time history in x-direction

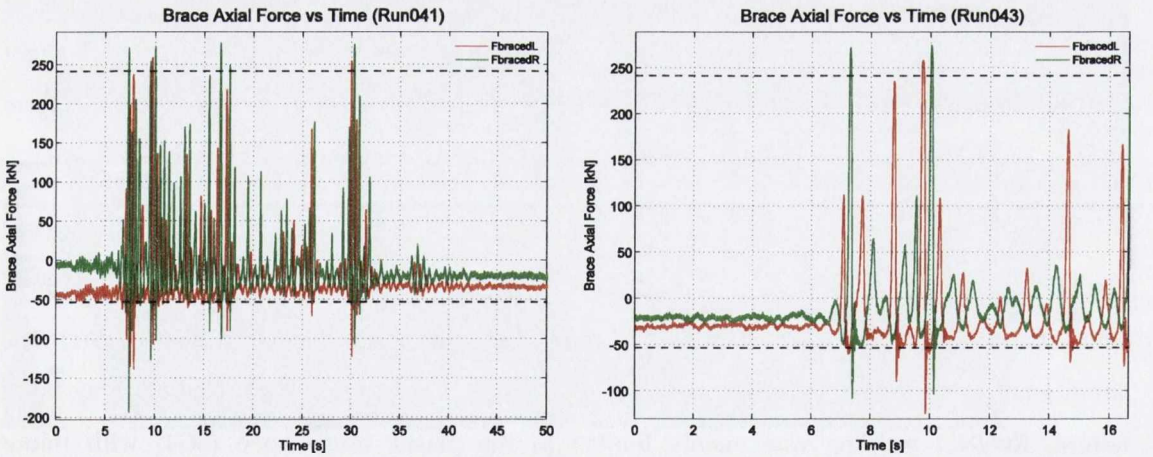

(c) Brace axial load time history for left (FbracedL) and right (FbracedR) braces. Dashed lines indicate yield and buckling capacities (based on characteristic strengths and measured brace section area).

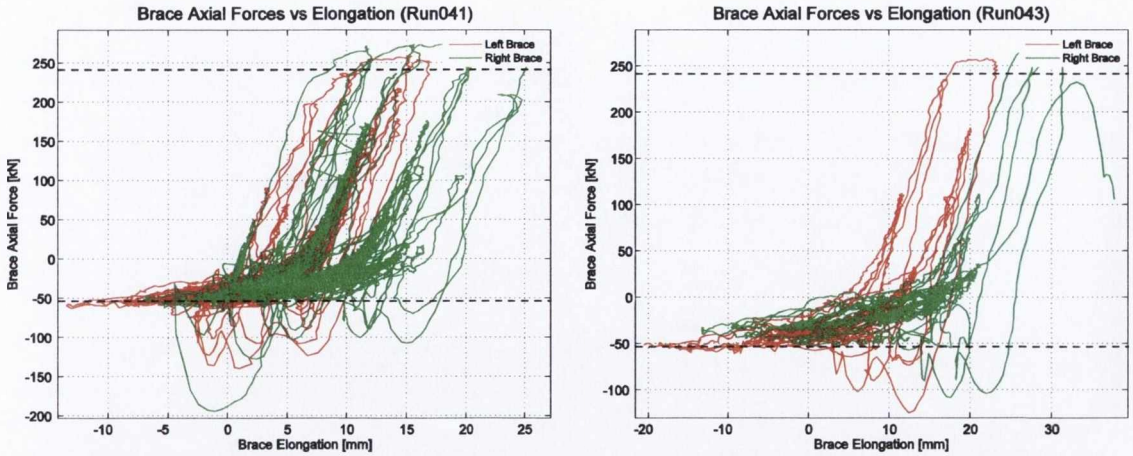

(d) Brace axial load hysteresis for left and right braces. Dashed lines indicate yield and buckling capacities (based on characteristic strengths and measured brace section area).

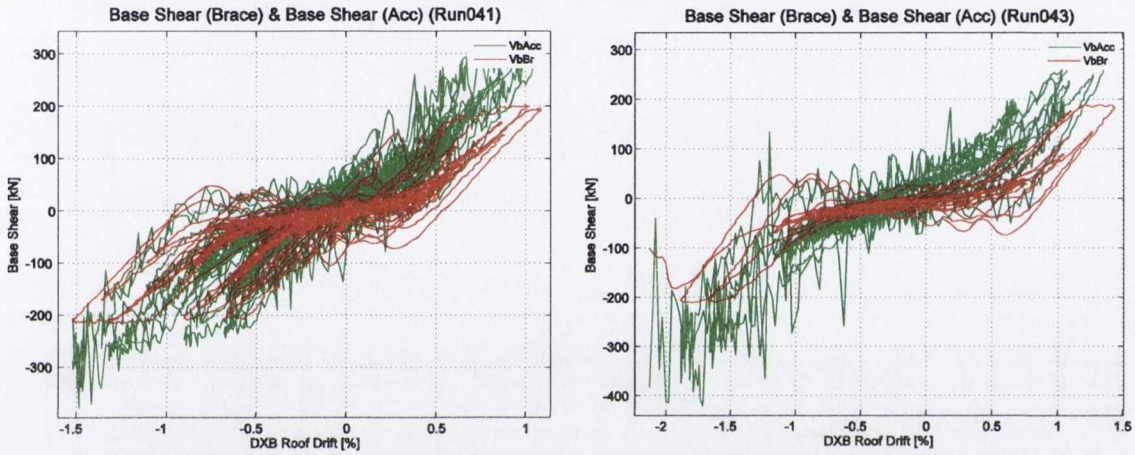

(e) Base shear from brace axial forces plotted against roof drift

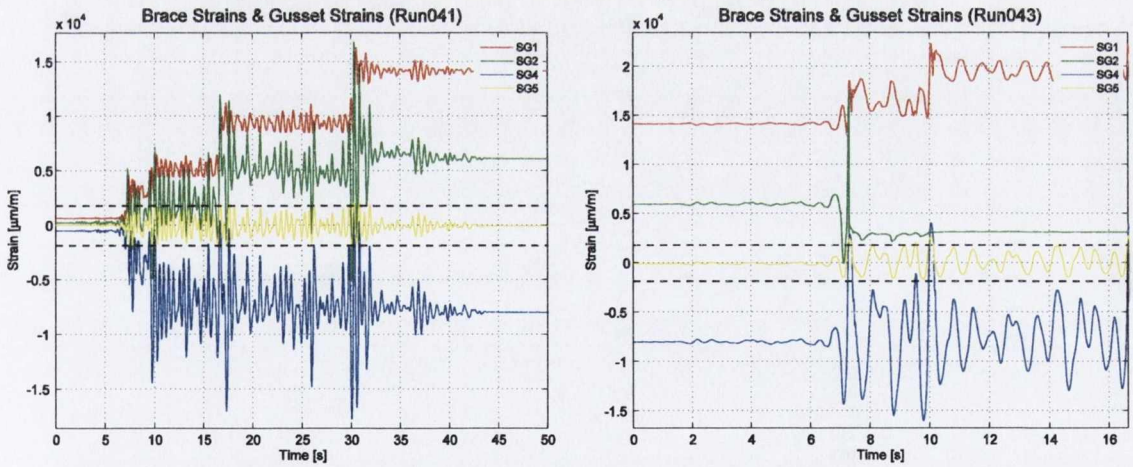

(f) Strain gauge measurements located on the right brace and gusset plate specimen. Dashed lines indicate yield strain thresholds (based on characteristic strengths).

Figure 9.8 – Recorded responses Shake Table Test 2; S3-CA-G1.

(a)

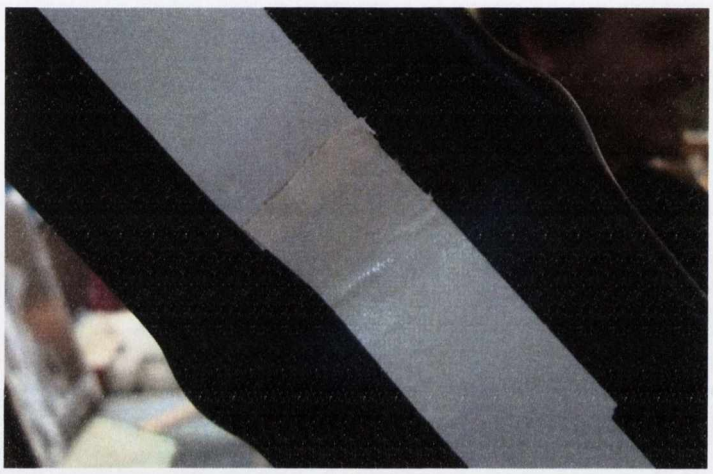

(b)

(c)

Figure 9.9 – Test 2; S3-CA-G1 after testing: (a) section failure of right brace (b) local buckling in left brace and (c) plastic hinge patterns in right-hand gusset.

9.3.5 Shake Table Test 3: S4-CA-G1

During this test, elastic performance was observed in the 50%/50 and 10%/50 levels. In the 2%/50 level (Run052) significant buckling and yielding occurred in the plastic hinge zone only but no local buckling or fracture occurred. Consequently, as with Test 2, a higher scale earthquake run was performed twice with a target PGA of 0.55g to achieve failure of the specimens, i.e. two failure level runs were performed. Test 10 (section 9.3.12) had equally scaled excitations for both 2%/50 and Failure Levels.

In the 2%/50 level test global buckling occurred in both braces. There were no indications of local buckling in the braces but very large inelastic strains were accumulated in the gusset plate hinge at SG4 (Figure 9.10(f)).

Initial local buckling was observed in the right-hand brace after 17.4s of the first failure level run (Run054), as evident in the brace axial load plot in Figure 9.10(c). This was followed by large out-of-plane deformation of the right-hand brace and further increasing inelastic strain in the gusset plate hinge at SG4 (Figure 9.10(f)). Only an out-of-plane global buckling response was observed in the left-hand brace. The brace hysteresis plot in Figure 9.10(d) shows more excursions in the post-buckling range during the failure level run than in the 2%/50 level run, and the maximum brace elongation during the failure level run was ~76 mm compared to 21 mm during the 2%/50 level run. At the end of this run fracture was limited to the corner regions of the right-hand brace local buckle with two small tears visible at the corners and all four faces intact.

In the second failure level run (Run056), the right-hand brace experienced complete fracture and local buckling was initiated in the left-hand brace. The left-hand brace sustained two large compression and tension cycles before experiencing complete failure under tension. The form of failure featured necking and minimal local buckling of the cross-section shape (Figure 9.11(a)), similar to Test 2. This contrasts with the distortion of the right brace section shape in Figure 9.11(b). With both braces completely fractured, the stability offered by the CA connection configuration preserves the test frame in an upright position with minimal residual drift.

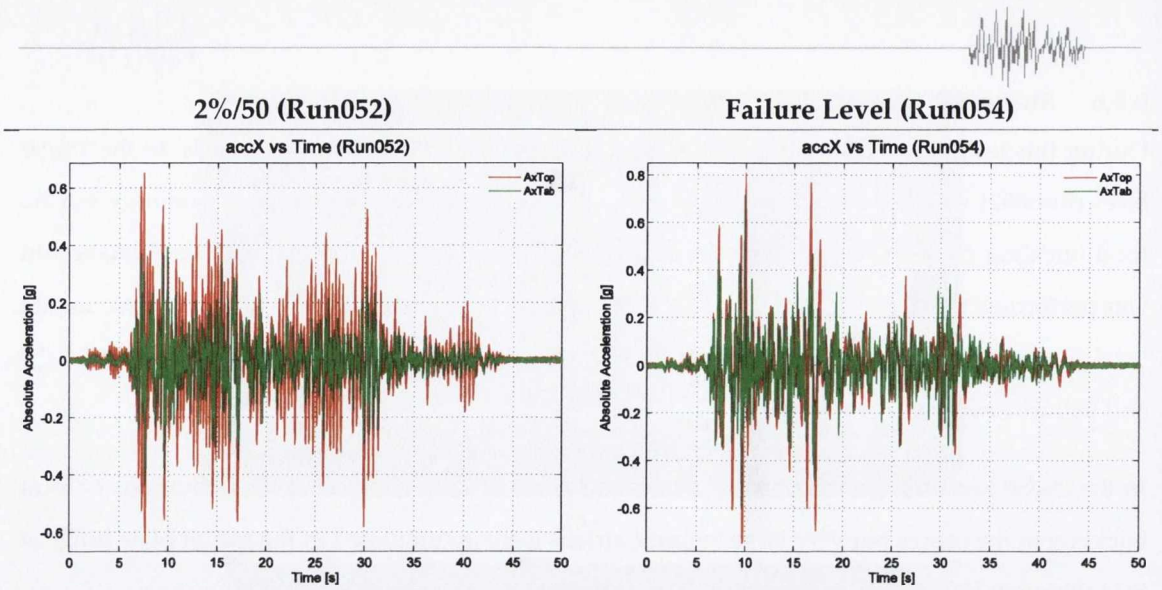

(a) Input (AxTab) and response (AxTop) absolute acceleration time history in x-direction

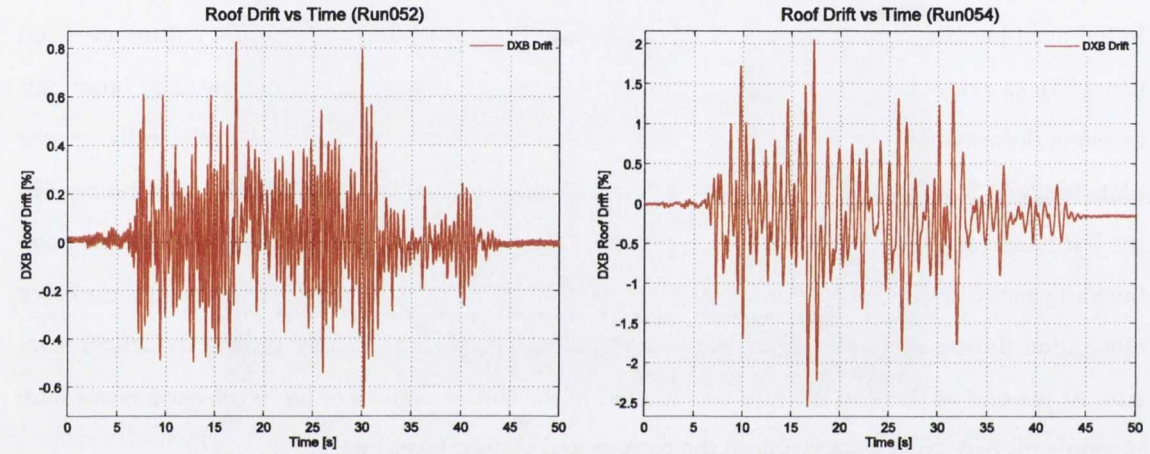

(b) Roof level drift (DXB Drift) time history in x-direction

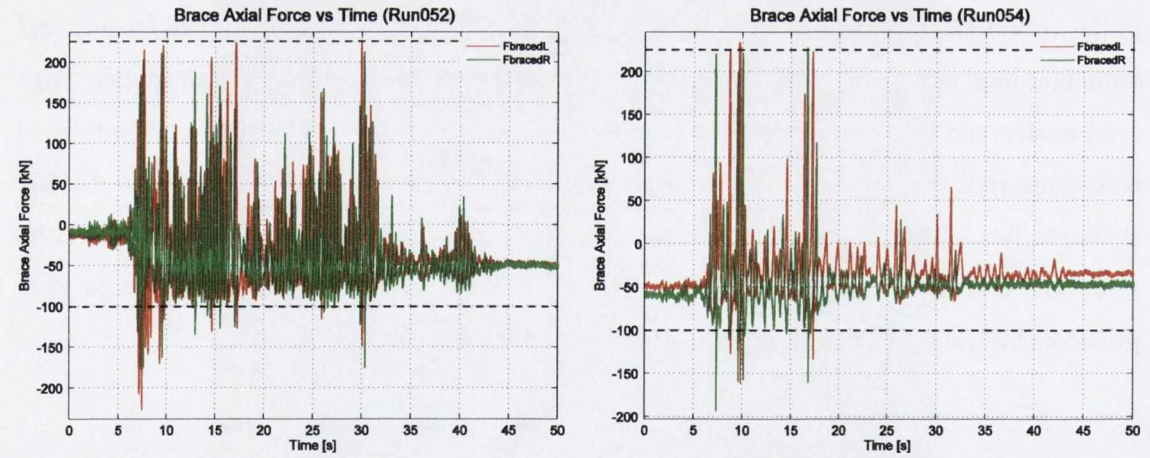

(c) Brace axial load time history for left (FbracedL) and right (FbracedR) braces. Dashed lines indicate yield and buckling capacities (based on characteristic strengths and measured brace section area).

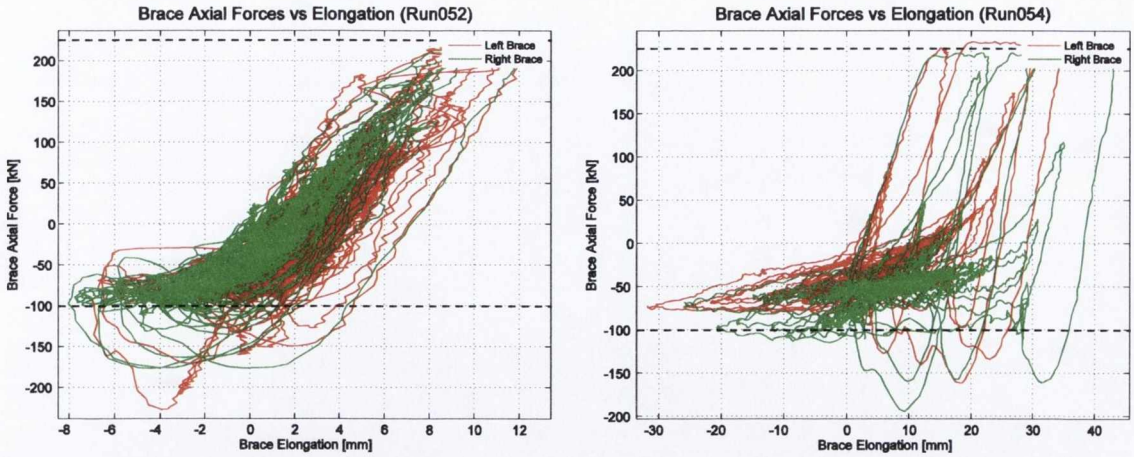

(d) Brace axial load hysteresis for left and right braces. Dashed lines indicate yield and buckling capacities (based on characteristic strengths and measured brace section area).

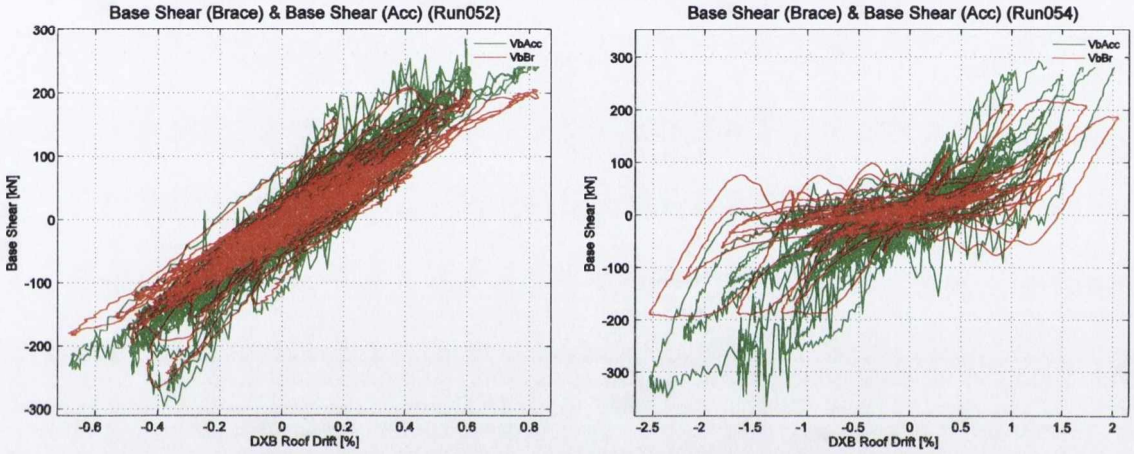

(e) Base shear from brace axial forces plotted against roof drift

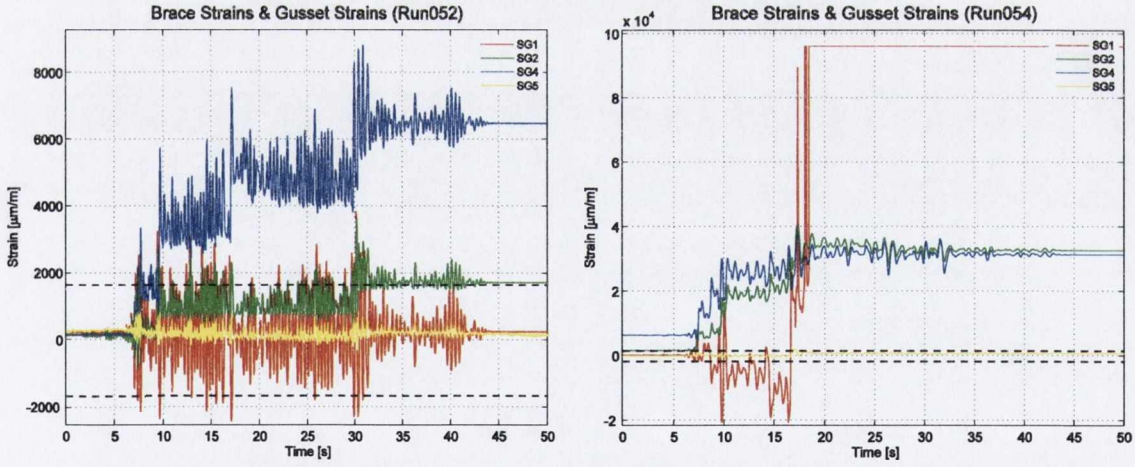

(f) Strain gauge measurements located on the right brace and gusset plate specimen. Dashed lines indicate yield strain thresholds (based on characteristic strengths).

Figure 9.10 – Recorded responses Shake Table Test 3; S4-CA-G1.

(a)

(b)

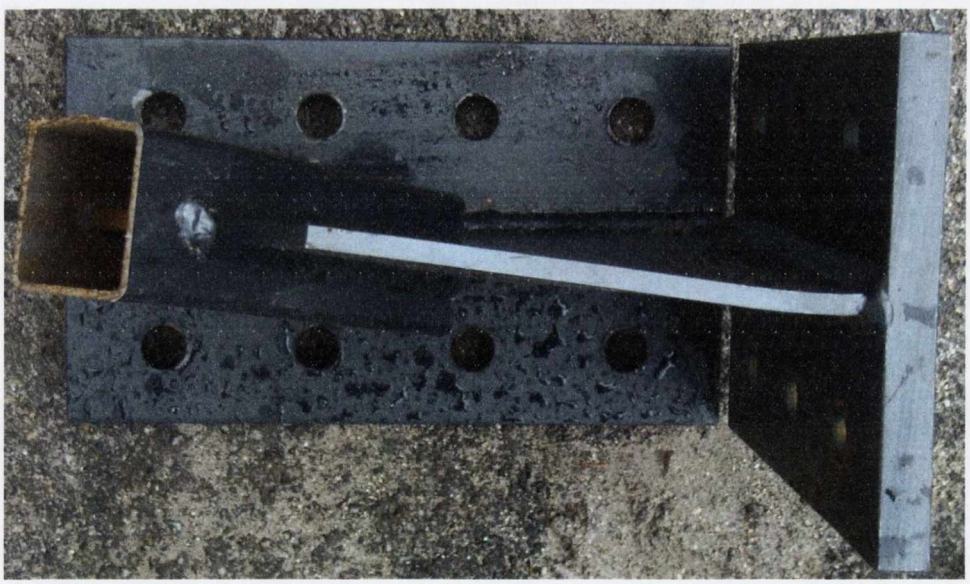

(c)

Figure 9.11 – Test 3; S4-CA-G1 after testing: (a) fractured cross-section of left-hand brace (b) local buckling of cross-section in right-hand brace and (c) plastic hinge bending in right-hand gusset.

9.3.6 Shake Table Test 4: S2-CA-G1

The 50%/50 and 10%/50 runs in this test performed as anticipated with a completely elastic response during the 50%/50 run and brace buckling loads and yield strains exceeded in the 10%/50 run (Figure 9.12(c) and (f)). Consequently, negligible residual drift existed at the end of Run067. During Run067 the pretension force in the displacement cable sensor on the right-hand brace was lost, which resulted in erroneous elongation measurements for that brace.

By the end of the 2%/50 run, complete section failure had occurred in both braces. Local buckling was first induced in the right-hand brace, followed nearly immediately by a local buckle in the left-hand brace. This process happened within a short duration (~1.5 s). At 15.44 s the axial load in the right-hand brace reached +250 kN (very near its yield capacity), followed by a large demand in the opposite direction with the axial load reaching -105 kN at 15.53 s and the development of the first local buckle. Following this, further compressive demands were induced in the right-hand brace but were sustained through tensile loading of the left-hand brace (~+250 kN) and a sudden compression demand nearing -100 kN. This process left both braces with significant local buckles near the lower third of their span with tearing initiating in their cross-section corners. Further lateral loading demands from strong motion cycles resulted in the left-hand brace section failing completely at 30 s, with the same occurring in the right-hand brace 1 s after. The brace cross section shapes after failure are shown in Figure 9.13(a) and (b).

Large increments in plastic strain were observed in strain gauges SG1 and SG2 located at mid-length of right-hand brace. A similar pattern of inelastic strain development is also evident in the response of SG4 which monitored the expected gusset yield mechanism. The drift of the SG4 readings indicate the permanent residual bending shape of the gusset plate in the direction of the SG4 gauge. The G2 plate in Test 6 (section 9.3.8) showed large drifts in both compression and tension ranges for SG4. The strain response at SG5 mostly remained within the elastic limits for the duration of the test. The gusset plates in this test were the same thickness as those used in Test 1 and similar minimal bending deformation was visible at the end of the test (Figure 9.13(c)).

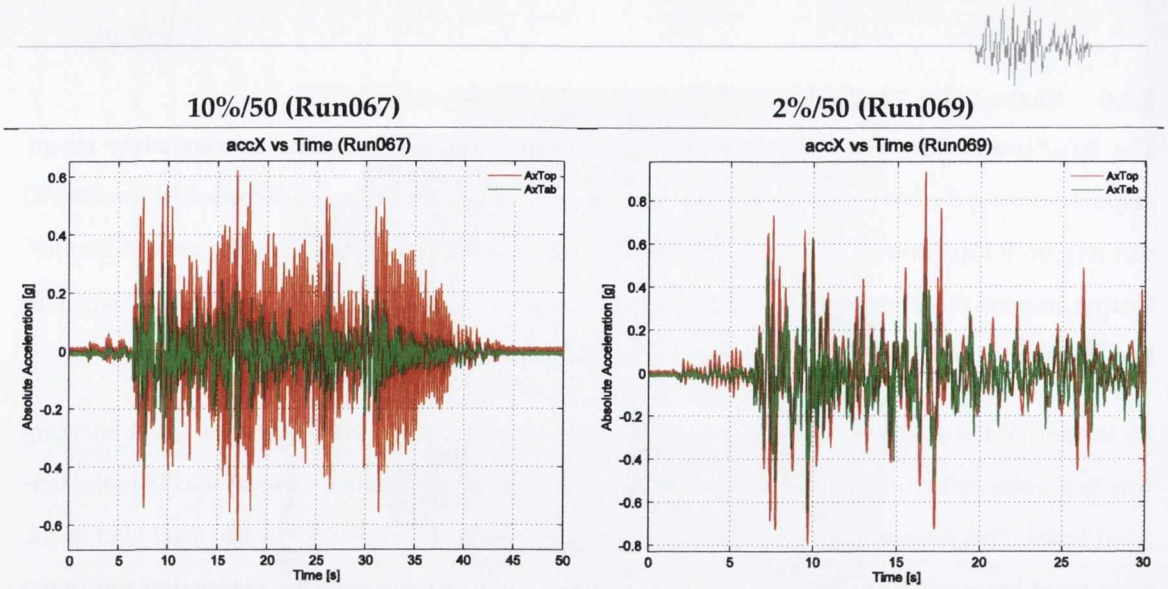

(a) Input (AxTab) and response (AxTop) absolute acceleration time history in x-direction

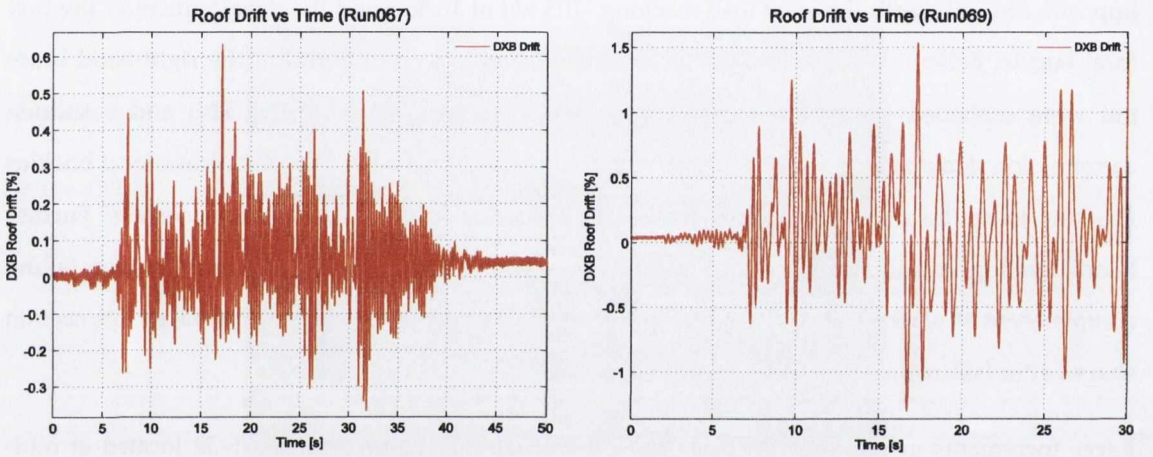

(b) Roof level drift (DXB Drift) time history in x-direction

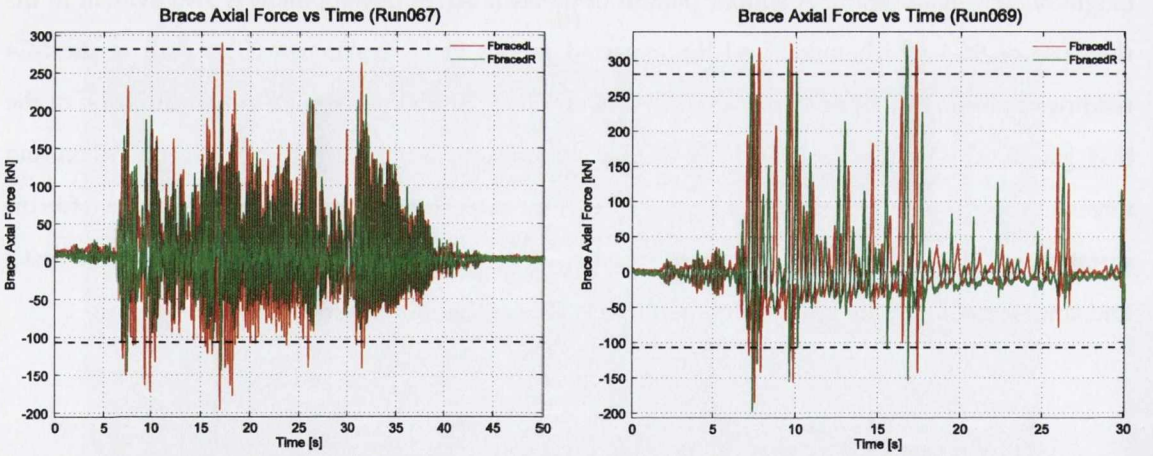

(c) Brace axial load time history for left (FbracedL) and right (FbracedR) braces. Dashed lines indicate yield and buckling capacities (based on characteristic strengths and measured brace section area).

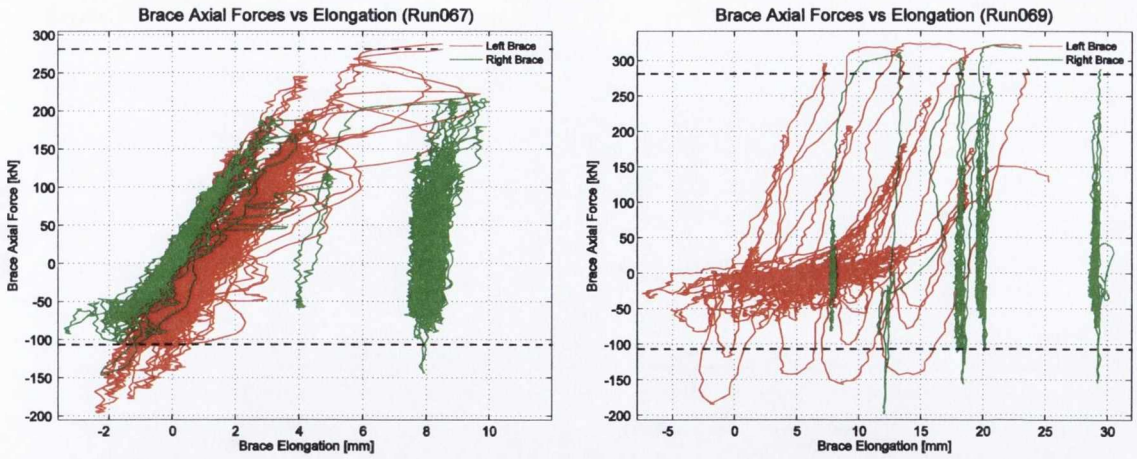

(d) Brace axial load hysteresis for left and right braces. Dashed lines indicate yield and buckling capacities (based on characteristic strengths and measured brace section area).

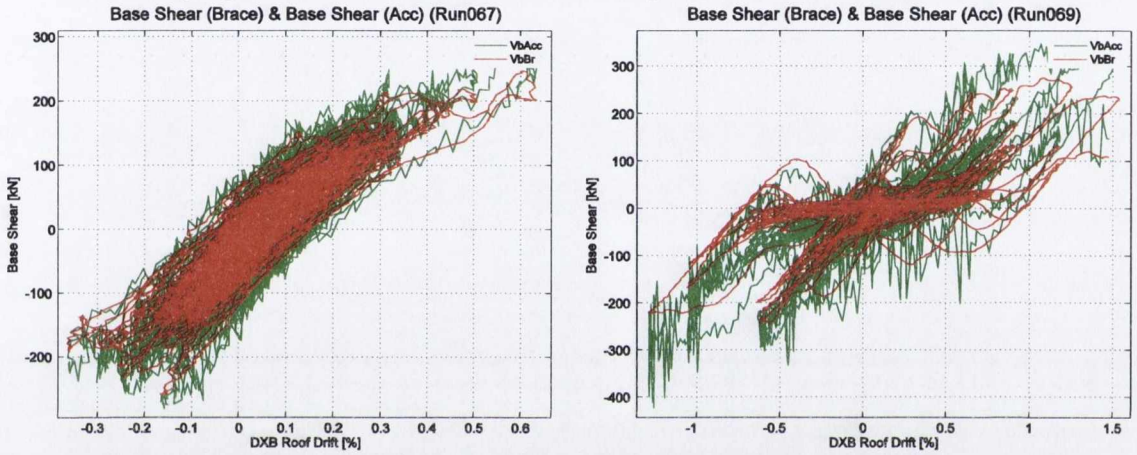

(e) Base shear from brace axial forces plotted against roof drift

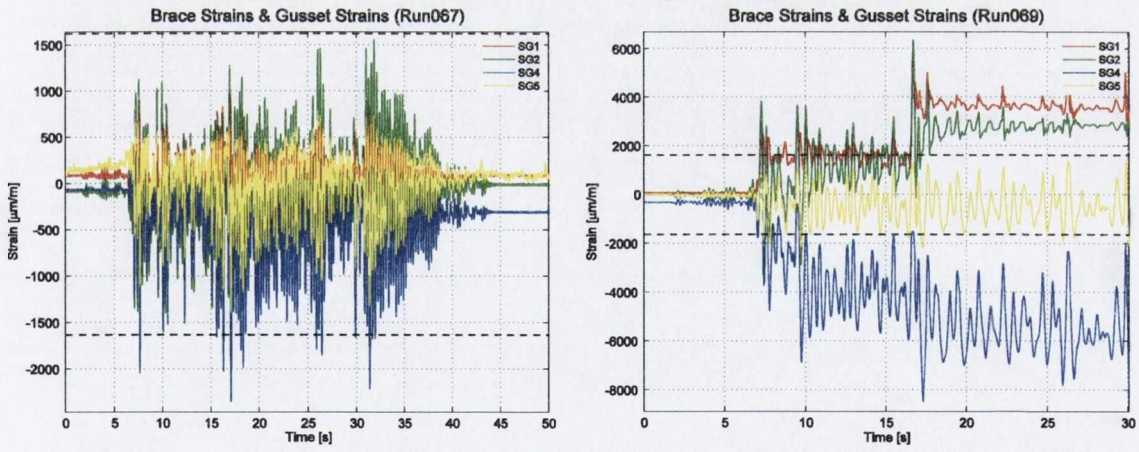

(f) Strain gauge measurements located on the right brace and gusset plate specimen. Dashed lines indicate yield strain thresholds (based on characteristic strengths).

Figure 9.12 – Recorded responses Shake Table Test 4; S2-CA-G1.

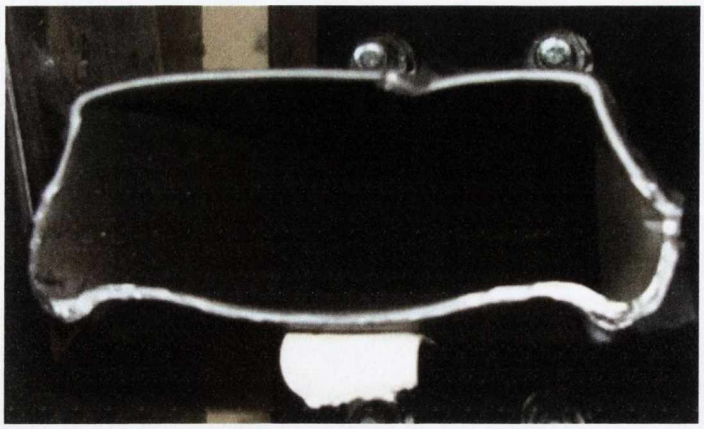

(a)

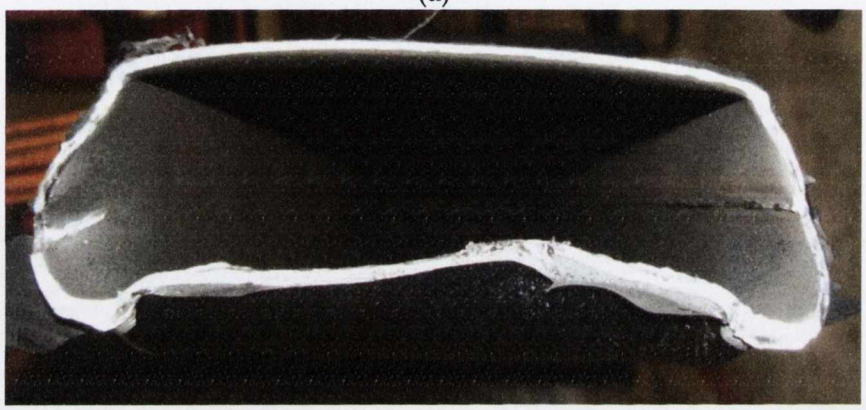

(b)

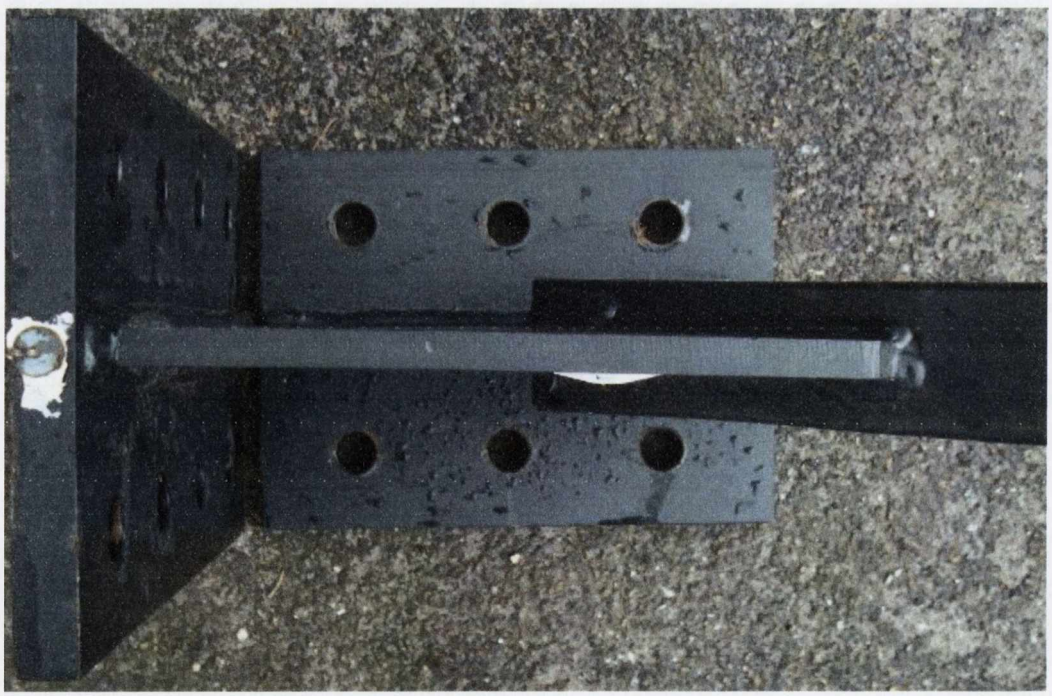

(c)

Figure 9.13 – Test 4; S2-CA-G1 after testing showing (a) fractured section shape of left-hand brace (b) fractured section shape of right-hand brace and (c) minimal deformation of left-hand gusset.

9.3.7 Shake Table Test 5: S1-CA-G2

This test saw the first investigation of the G2 gusset plate design and is directly comparable to Test 1 (section 9.3.3). The first 50%/50 level (Run078) was an elastic test, while in the 10%/50 level run (Run080) some yielding was observed and brace compression forces reached their theoretical buckling values. However no local buckling was observed in either test. In the 10%/50 level run (Run080) more severe global buckling was observed in the right-hand brace compared than in the left-hand brace. The brace hysteresis plots shown in Figure 9.14(d) display several loading excursions into the compression range, with forces reaching ~220 kN in the left brace. However, the axial load of the right brace only approached this compression load once, with lower compression resistances displayed in subsequent cycles. This suggests that the braces possessed different buckling capacities, indicating different effective lengths. The severe global buckling in the right brace is reflected in the strain reading from SG1 in Figure 9.14(f). The plastic strain limit is reached and residual strain remains at the end of the test.

At the 2%/50 level (Run082) the prescribed PGA was 0.6g but the realised PGA was higher at 0.768g. A maximum drift of 1.73% was experienced but this remained within the displacement limits of the experimental set-up. This was larger than the absolute maximum drifts reached in Test 1 (1.00% storey height) where frame rotation was limited due to the CA connection and a lower realised PGA of 0.624g. During the strong motion cycles at ~17s local buckling occurred in both braces within 0.5s of each other. This was followed by fracture in the left-hand brace and, after table motion reversal, fracture in the right-hand brace. The fracture propagated in both braces as a tear spreading across all three faces leaving one face intact, as shown in the photographs in Figure 9.15(a) and (b).

Inspection of strain gauge plots shows that SG4 which was located within the elliptical plastic hinge zone of the gusset plate experienced larger plastic strains than SG5 which was located just outside this zone. After testing, the gusset plates were shown to exhibit a 'C' shaped deformation profile due to the elliptical shape of the plastic hinge. Due to the thin gusset plate design, frame connection rotation may have also contributed to formation of this deformed shape (Figure 9.15 (c) and (d)), which is more exaggerated in this test than with the thicker plates used in Tests 1 – 4.

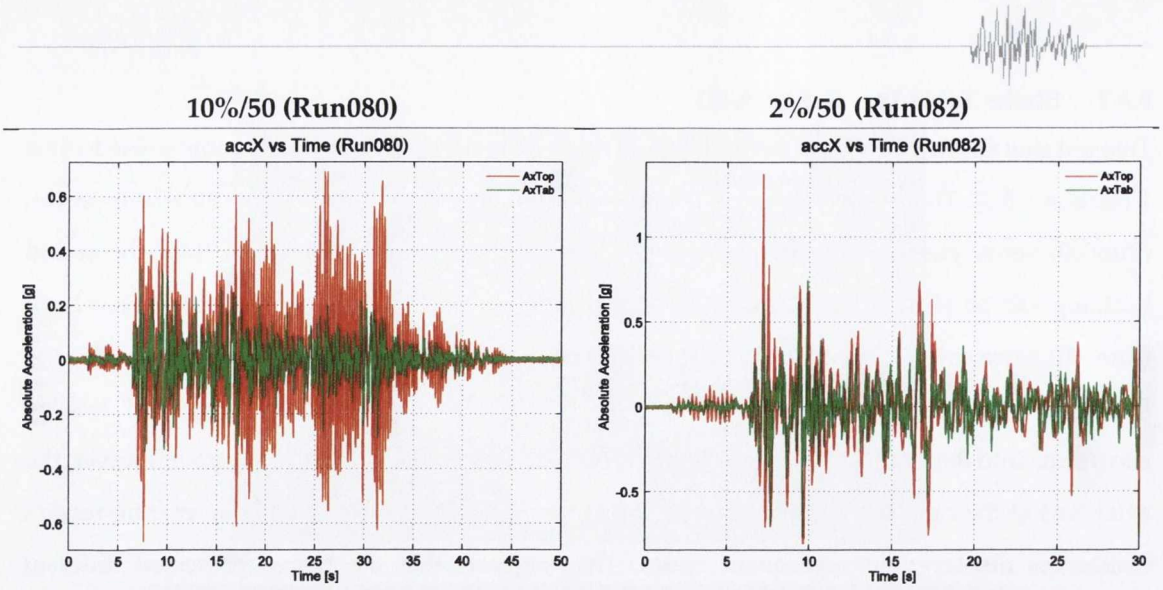

(a) Input (AxTab) and response (AxTop) absolute acceleration time history in x-direction

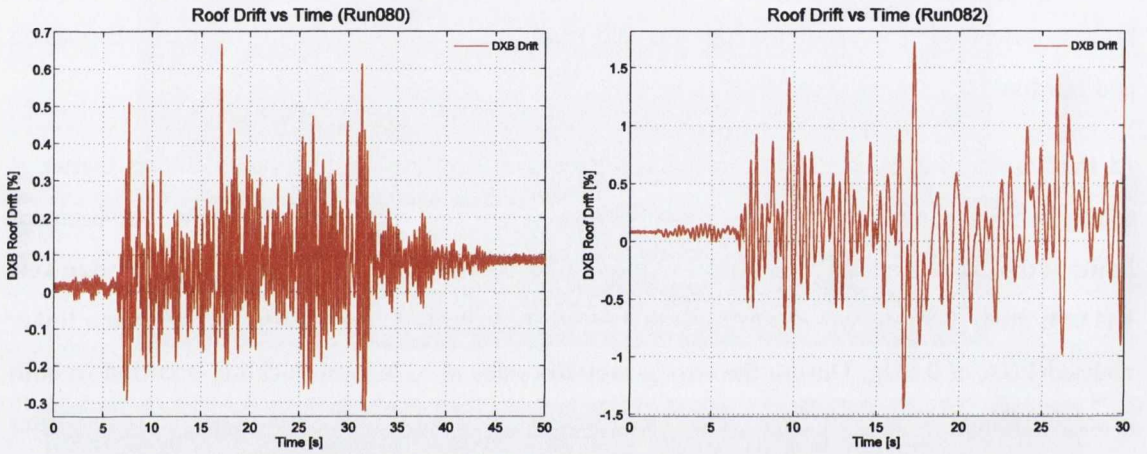

(b) Roof level drift (DXB Drift) time history in x-direction

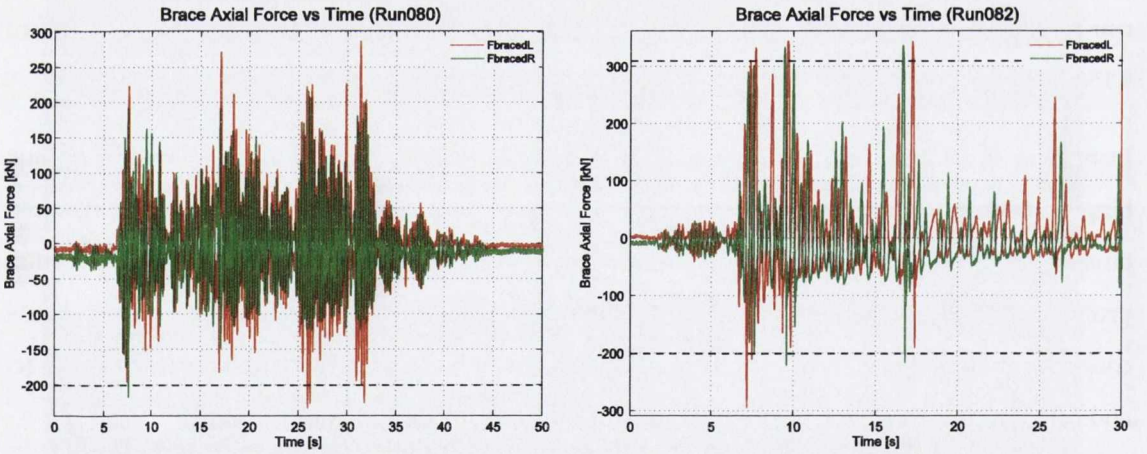

(c) Brace axial load time history for left (FbracedL) and right (FbracedR) braces. Dashed lines indicate yield and buckling capacities (based on characteristic strengths and measured brace section area).

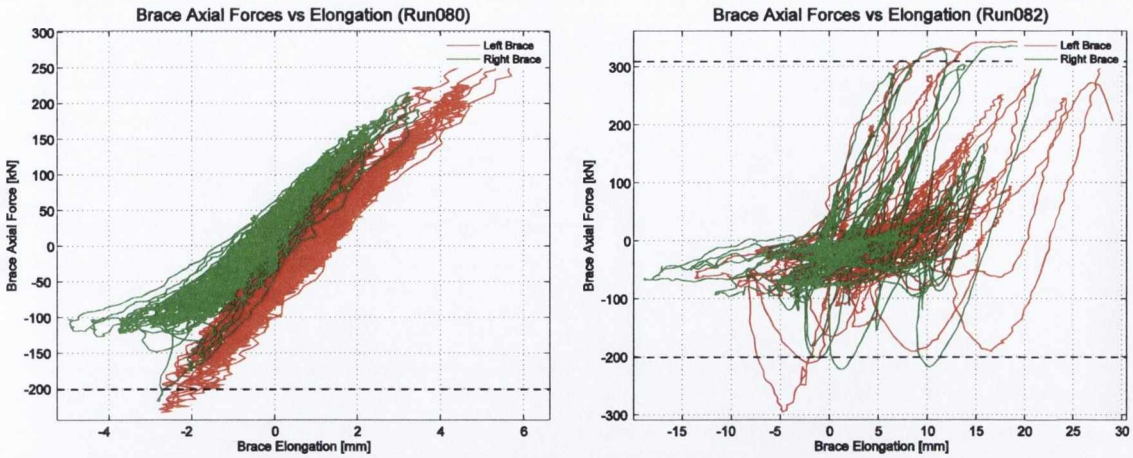

(d) Brace axial load hysteresis for left and right braces. Dashed lines indicate yield and buckling capacities (based on characteristic strengths and measured brace section area).

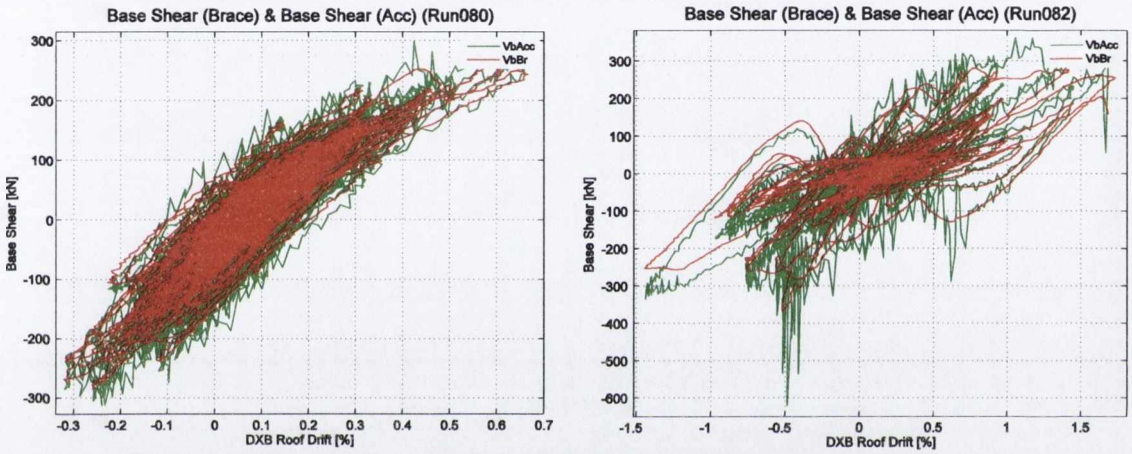

(e) Base shear from brace axial forces plotted against roof drift

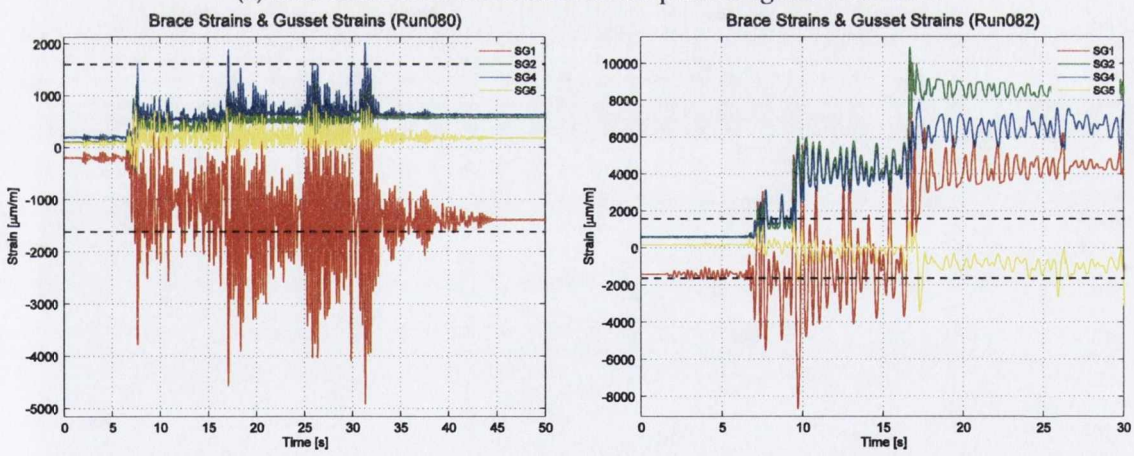

(f) Strain gauge measurements located on the right brace and gusset plate specimen. Dashed lines indicate yield strain thresholds (based on characteristic strengths).

Figure 9.14 – Recorded responses Shake Table Test 5; S1-CA-G2.

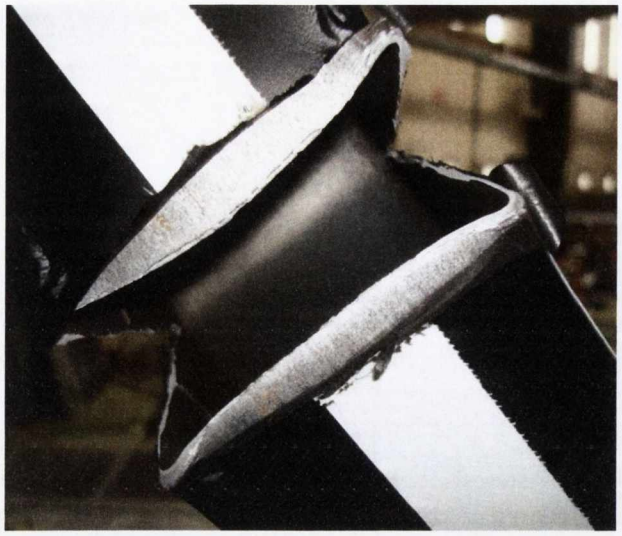

(a)

(b)

(c)

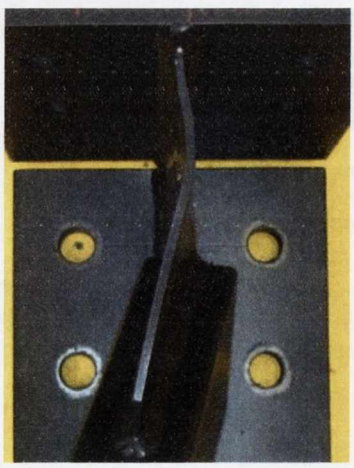

(d)

Figure 9.15 – Test 5; S1-CA-G2 after testing showing (a) tear in left-hand brace (b) tear in right-hand brace, and deformation shape of (c) left-hand gusset plate and (d) right-hand gusset plate.

9.3.8 Shake Table Test 6: S2-CA-G2

For this test the 50%/50 (Run088) and the 10%/50 (Run090) levels performed as expected. However the 2%/50 level run (Run092) was interrupted, so this level was repeated (Run094), and brace failure occurred during this run.

Figure 9.16(c) and (d) show that the right-hand brace axial load reached its initial buckling capacity after approximately 17 s during Run090, with a residual compressive resistance of approximately 60 kN remaining thereafter. Buckling in the left-hand brace did not occur until 25.4 s. The strain recordings from SG1 and SG2 presented in Figure 9.16(f) show that the strains in the brace compression flange exceeded the elastic limit, similar to the SG1 and SG2 readings in Test 4 (section 9.3.6). Overall the hysteresis cycles from the base shear plot in Figure 9.16(e) show larger frame drift limits reached and larger sized hysteresis loops compared to Test 4.

During Run092 local buckling occurred first in the right-hand brace and in the left-hand brace shortly after. The test was halted at 19 s due to sudden, unexpected snapping noise. Upon inspection it was found that both braces suffered from out-of-plane deformation and that local buckling was most severe in the left brace. As in Test 5, large gusset plate distortion was observed in both plates, but no tearing had occurred in the brace plastic hinge. The test was repeated and complete section failure occurred in the left-hand brace after only three seconds of excitation (Figure 9.17(a)). One face of the right-hand brace section sustained a partial tear spreading from the fracture that had developed in all corners, as illustrated in Figure 9.17(b) and (c).

10%/50 (Run090) **2%/50 (Run092)**

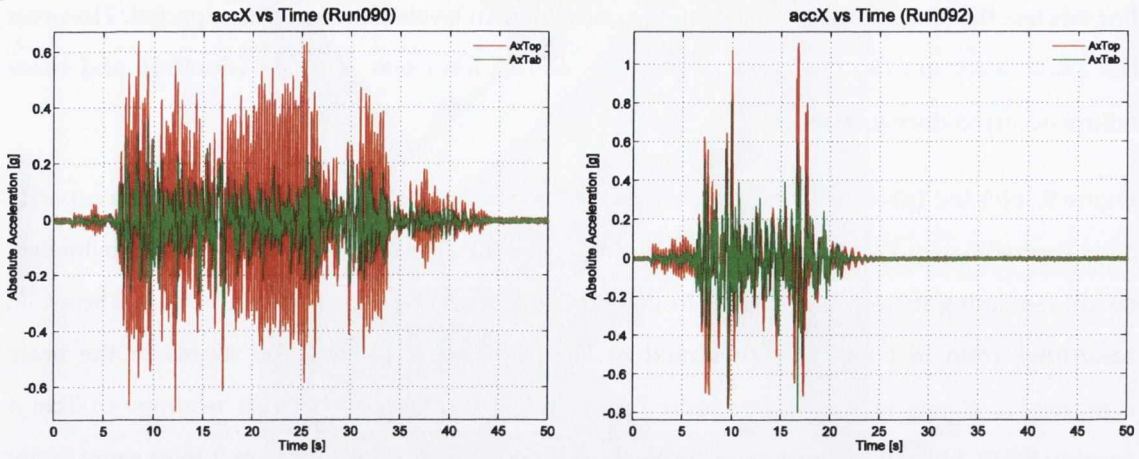

(a) Input (AxTab) and response (AxTop) absolute acceleration time history in x-direction

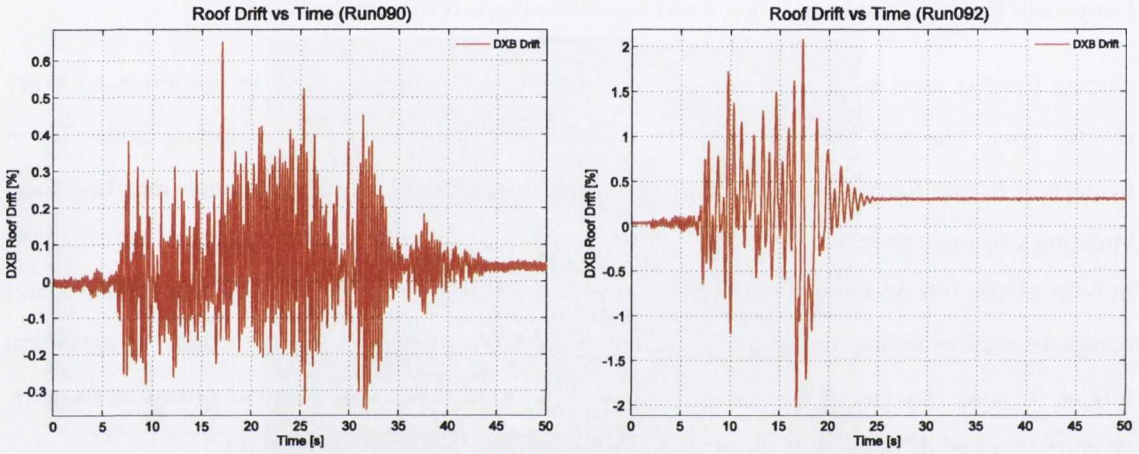

(b) Roof level drift (DXB Drift) time history in x-direction

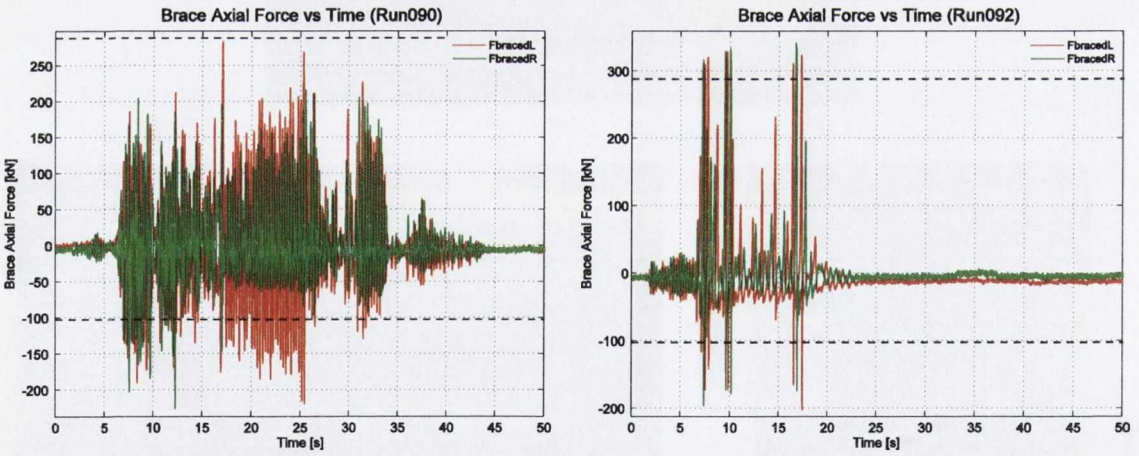

(c) Brace axial load time history for left (FbracedL) and right (FbracedR) braces. Dashed lines indicate yield and buckling capacities (based on characteristic strengths and measured brace section area).

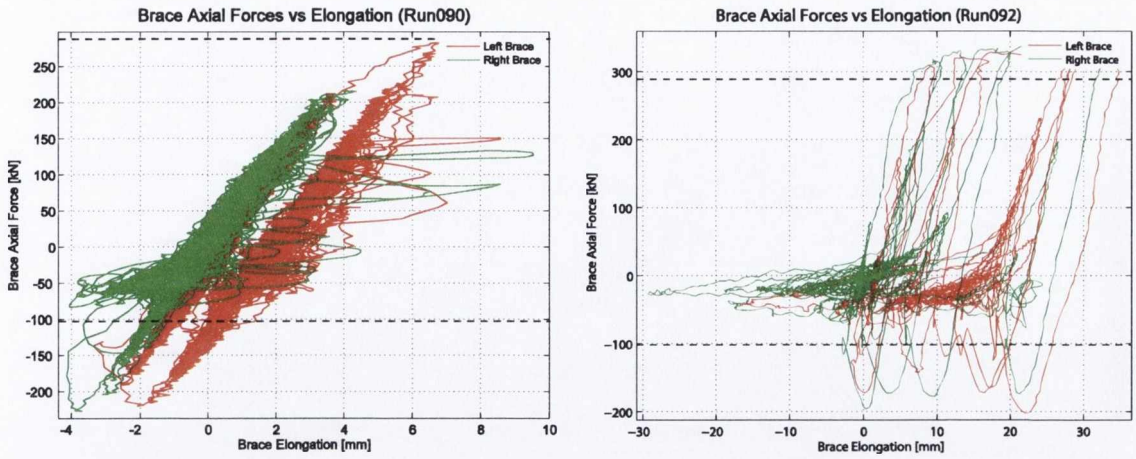

(d) Brace axial load hysteresis for left and right braces. Dashed lines indicate yield and buckling capacities (based on characteristic strengths and measured brace section area).

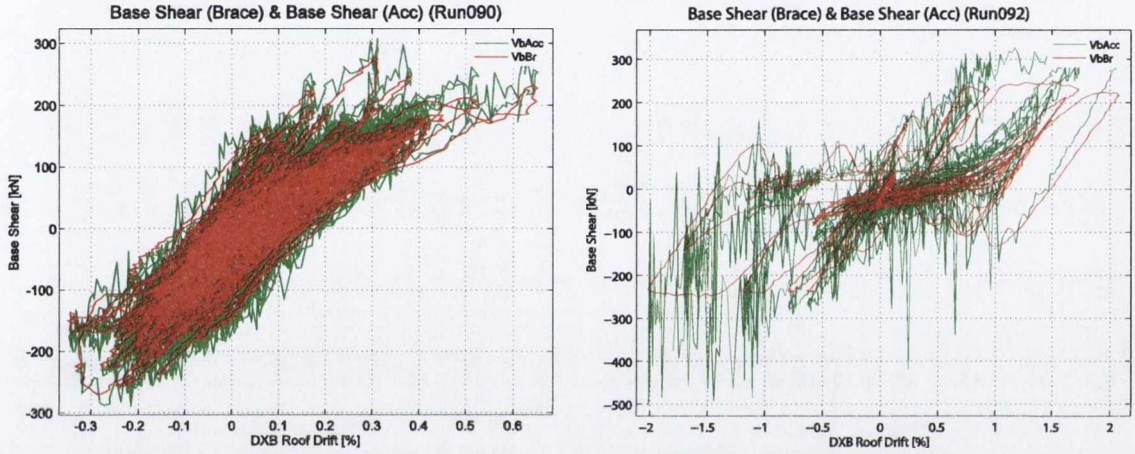

(e) Base shear from brace axial forces plotted against roof drift

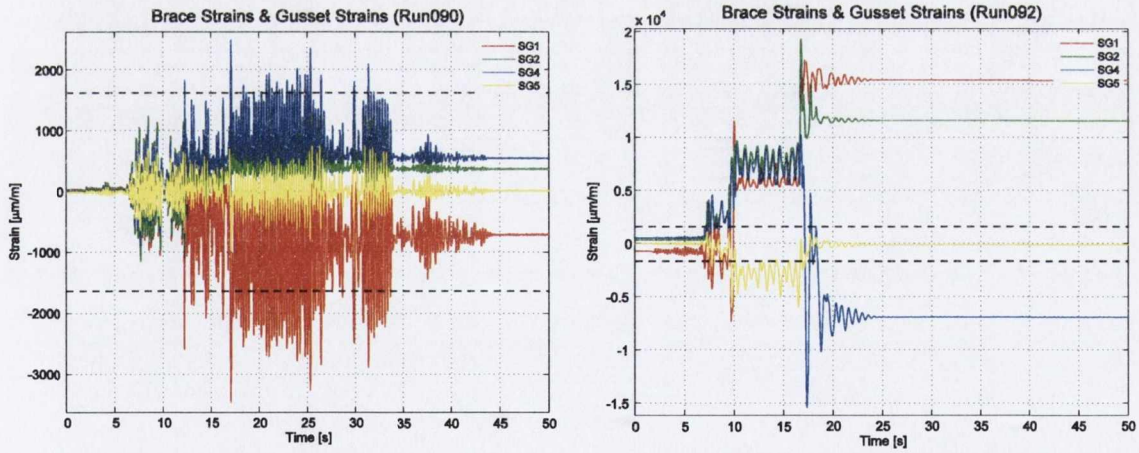

(f) Strain gauge measurements located on the right brace and gusset plate specimen. Dashed lines indicate yield strain thresholds (based on characteristic strengths).

Figure 9.16 – Recorded responses Shake Table Test 6; S2-CA-G2.

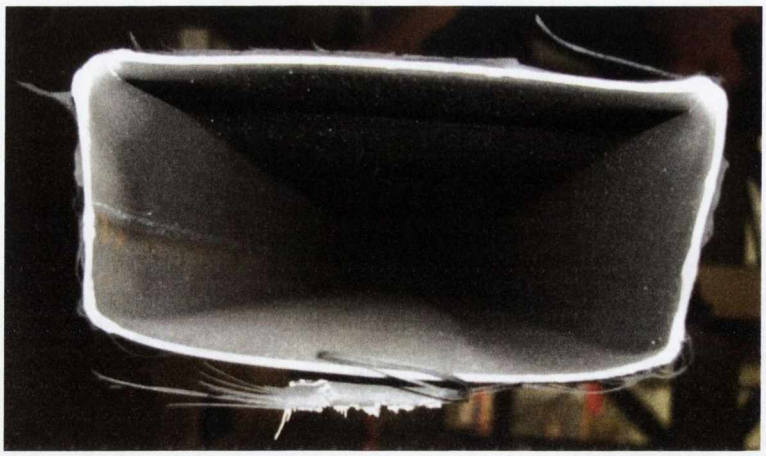

(a)

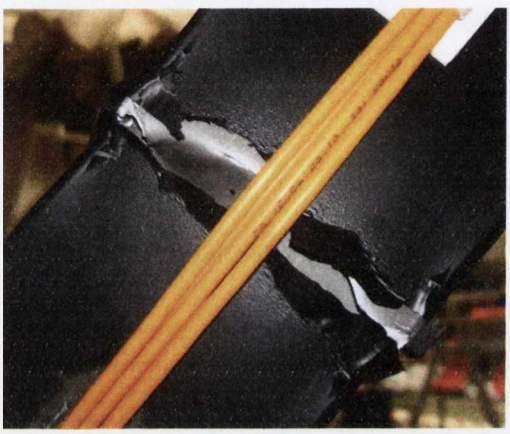

(b)

(c)

(d)

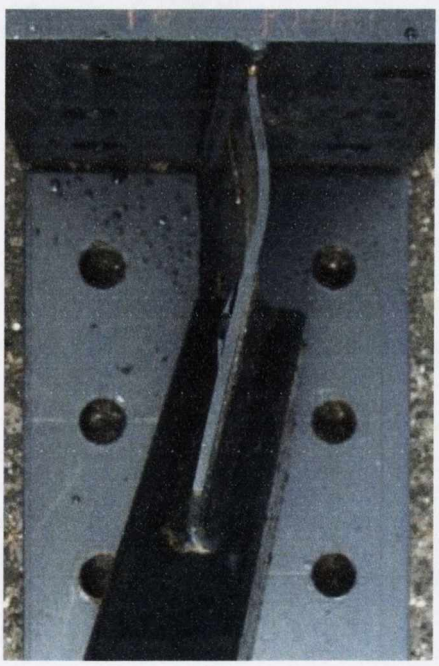

(e)

Figure 9.17 – Test 6; S2-CA-G2 after testing showing (a) section of left-hand brace (b) right-hand brace face with fracture in corner regions and tear running from bottom right to top left (c) corner regions fractured in right-hand brace and deformation shape of (d) left gusset and (e) right gusset.

9.3.9 Shake Table Test 7: S3-CA-G2

During the 50%/50 run (Run099) all recorded data indicated a fully elastic response in the brace-gusset plate specimens. The 10%/50 run (Run101) displayed global brace buckling and plastic hinging in the right-hand gusset plate. Large out-of-plane buckling displacements were observed in both braces, attributable to the low flexural stiffnesses of the rectangular brace cross-section and the thin G2 gusset plate. In Test 2 (section 9.3.4) where G1 gusset designs were employed, out-of-plane brace deformations were lower and a larger frame stiffness was observable in the frame drift results.

The 2%/50 run (Run103) displayed more exaggerated buckling in both braces. The brace tubes buckled in opposite directions with the left brace deforming away from the front of the frame (-Y direction) and the right towards the front of the frame (+Y direction). A local buckle developed in the right brace at approximately 17 s and the left brace remained globally buckled. Drift measurements approached 2% during this run (Figure 9.18(b)) (frame rotation limit ≈ 3.2%), however, no signs of brace fracture were observed at the end of the test. Consequently, a final failure level run (Run105) was performed. Substantial tearing of the compression flange of the right brace occurred at 9.7 s, and this is reflected in a pulse in the acceleration response time history in Figure 9.18(a). At 16.7 s complete section failure occurred in the right-hand brace and simultaneously a local buckle formed in the left brace. Very clear distortions were observable in the gusset plates (Figure 9.19(c) and (d)) associated with the high frame displacement demands (drift larger than 3%). After testing, strain gauge readings and visual inspection of the gussets showed that inelastic strains were significant but not limited to the elliptical plastic hinge zone. It is likely that the rotation of the test frame and the associated change in the angle of the beam-column connections caused additional compression and tension forces perpendicular to the gusset plate edges, exaggerating the distorted shape of both gusset plates (Figure 9.19(d)). In Test 2 such distortions were not observed in the gusset plates and a smaller range of strains for SG4 and SG5 were recorded for Run043. SG4 and SG5 in Figure 9.18(f) for Run105 show larger maxima strains reached in the gusset plate for Test 7.

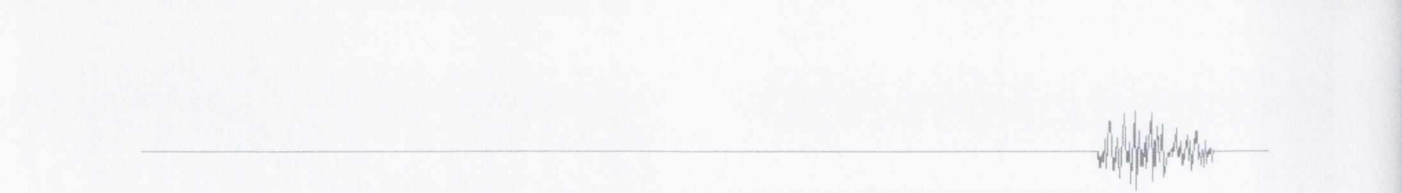

2%/50 (Run103)	Failure Level (Run105)

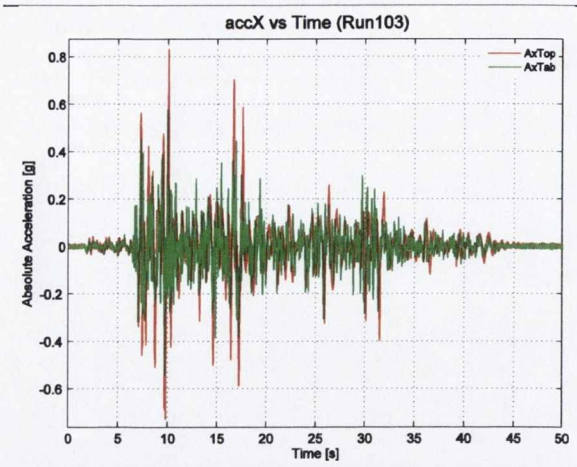

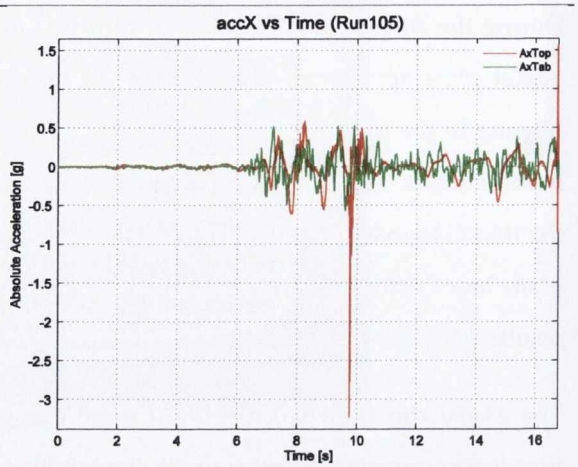

(a) Input (AxTab) and response (AxTop) absolute acceleration time history in x-direction

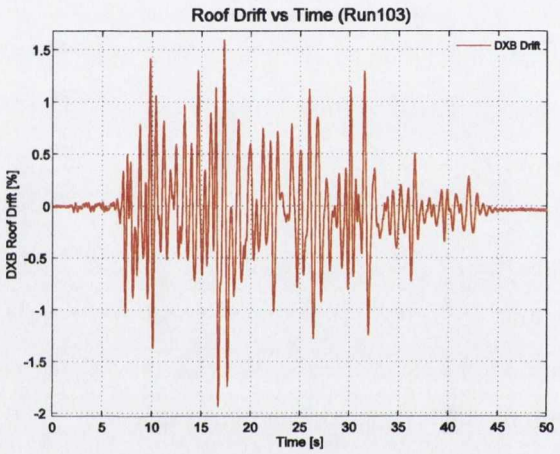

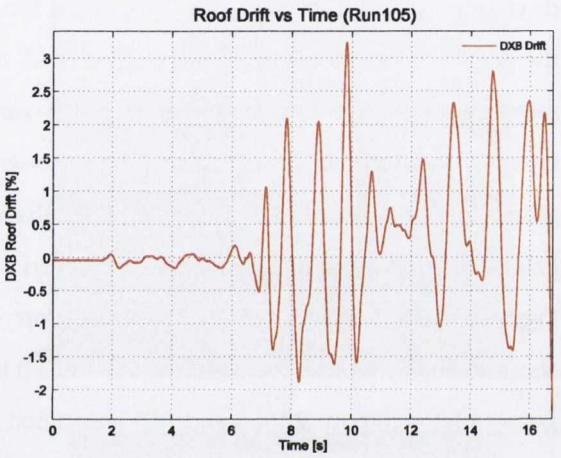

(b) Roof level drift (DXB Drift) time history in x-direction

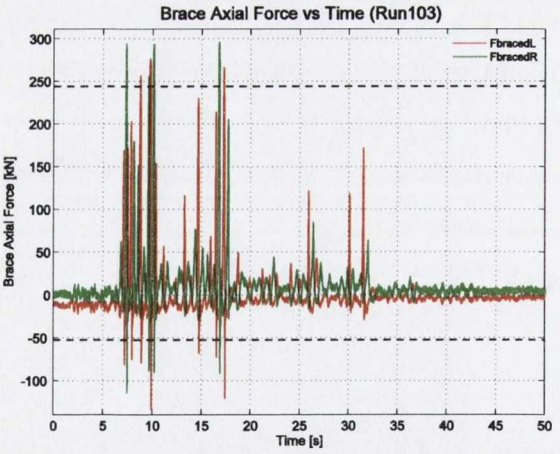

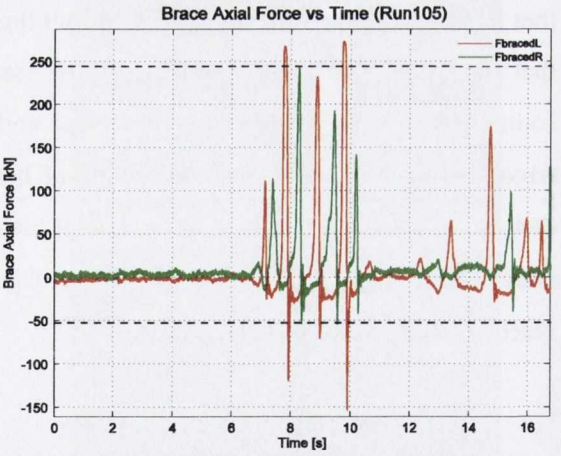

(c) Brace axial load time history for left (FbracedL) and right (FbracedR) braces. Dashed lines indicate yield and buckling capacities (based on characteristic strengths and measured brace section area).

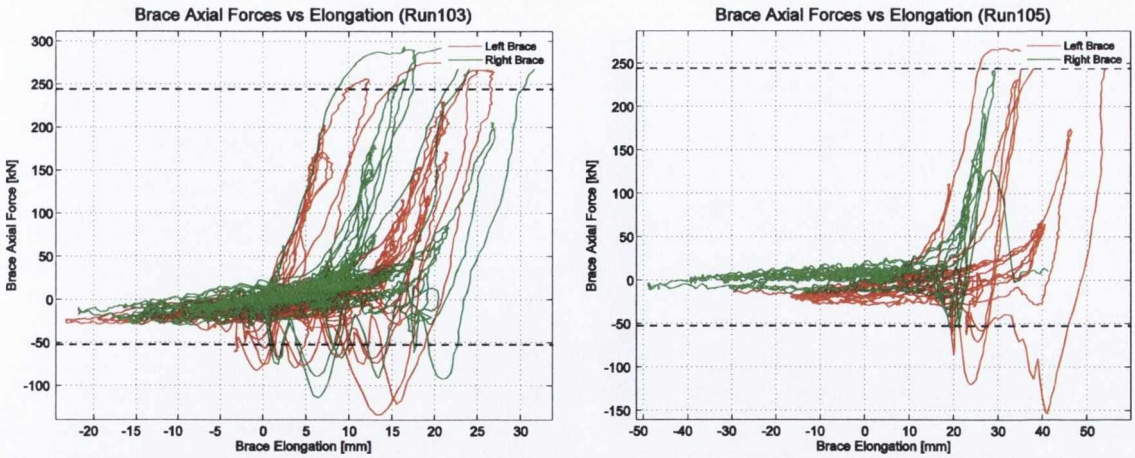

(d) Brace axial load hysteresis for left and right braces. Dashed lines indicate yield and buckling capacities (based on characteristic strengths and measured brace section area).

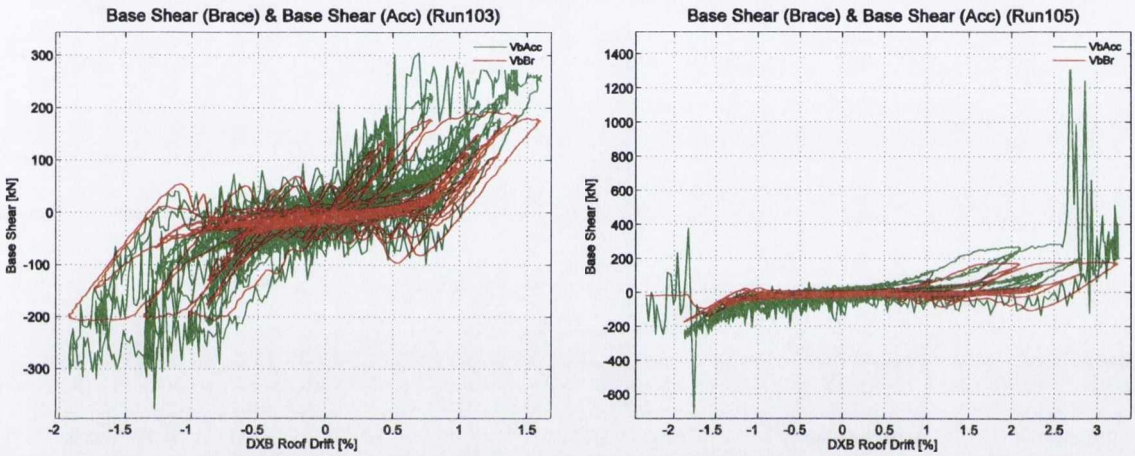

(e) Base shear from brace axial forces plotted against roof drift

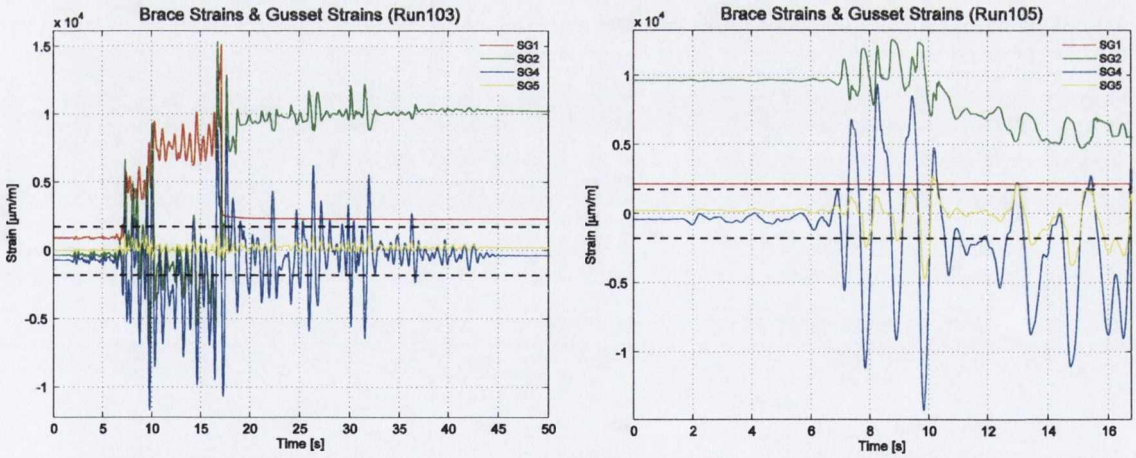

(f) Strain gauge measurements located on the right brace and gusset plate specimen. Dashed lines indicate yield strain thresholds (based on characteristic strengths).

Figure 9.18 – Recorded responses Shake Table Test 7; S3-CA-G2.

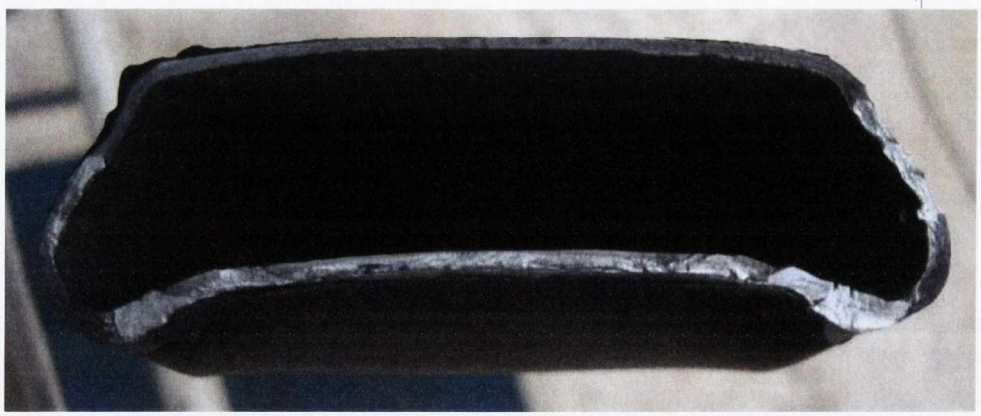

(a)

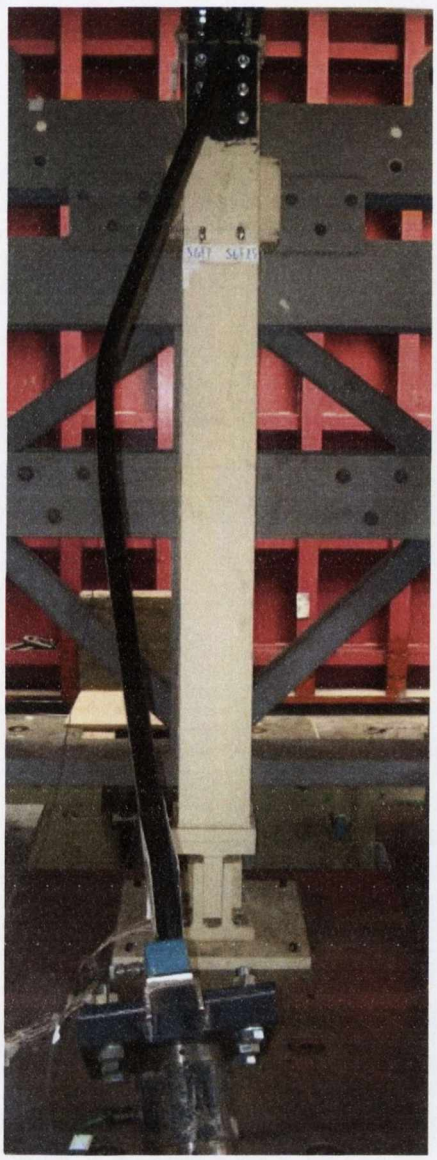

(b)

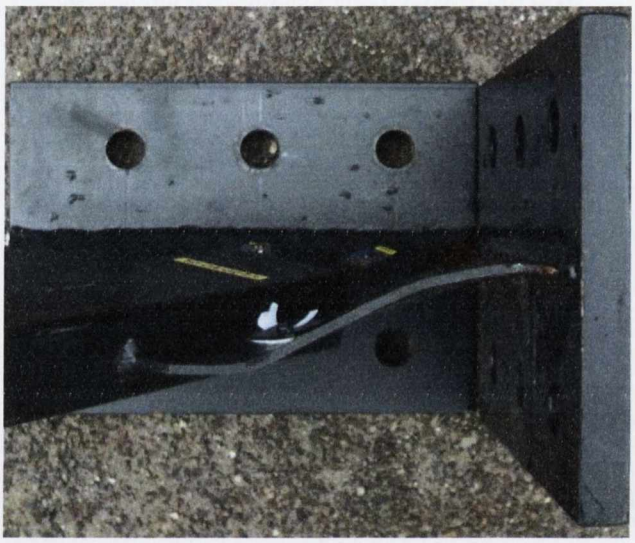

(c)

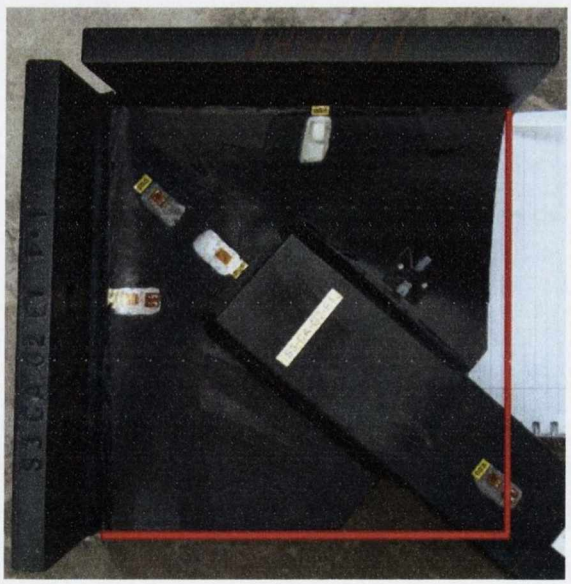

(d)

Figure 9.19 – Test 7; S3-CA-G2 after testing showing (a) right brace section failure (b) deformation of left brace and (c) and (d) distortion of right gusset with red line indicating original shape.

9.3.10 Shake Table Test 8: S1-CB-G1

Test 8 featured the first investigation of brace-gusset plate specimens with CB type connections. During the initial 50%/50 run (Run113) uncontrolled resonance due to table-test frame interaction was experienced in the frame response. Therefore, for further calibration purposes, an extra elastic run was inserted in the testing schedule before the 10%/50 level record (Run117).

During Run117 several loud snapping noises were heard throughout the test. After the test, all welded and bolted connections were inspected for damage. It was established that the noises were a result of bolt slippage; where the shear force transferred to the connection from the tension brace overcame the bolt friction due to torque in the tightened bolts. The effects of the bolt slippage are displayed in the acceleration response as large impulse peaks in Figure 9.20(a). The plots shown here have been carefully filtered to reduce the effect of these peaks. A detailed description of the filtering process is discussed in sub-section 9.3.15. As with other 10%/50 tests, brace buckling was limited to global buckling only, with no local buckling observed.

Brace fracture occurred after 16.6 s of the 2%/50 run (Run119). Further loud snapping noises resulting from bolt slippage were heard just before 8 s and 10 s. At 8 s, local buckling formed in the right brace and was exacerbated by the sudden displacement demand at 10 s. The left brace developed a local buckle at 13.2 s. Complete failure of the right brace at 16.6 s resulted in the frame impacting on the impact bumper located on the right-hand reaction frame. Upon load reversal, the left brace failed completely under tension with the frame impacting on the left-hand impact bumper. Both impact bumpers were damaged by these impacts (Figure 9.21(a)). The large frame displacement demand caused large rotations in the beam-to-column joint, elongating the bolts connecting the main beam to the columns. Both sets of bolts failed under tension with the nuts tearing the threads from the bolts as in Figure 9.21(e). Although this behaviour was foreseen at frame design stage, it had not occurred in any of the previous tests because the CA type connections provided more rigid beam-to-column joints. In Figure 9.20(f), the gusset plate strain recordings show that the plastic strain was concentrated in the plastic hinge zone at SG4, but significant yielding occurred outside of the zone at SG5. In Test 1 (section 9.3.3) the strains in SG5 remained mostly within elastic strain limits.

10%/50 (Run117) **2%/50 (Run119)**

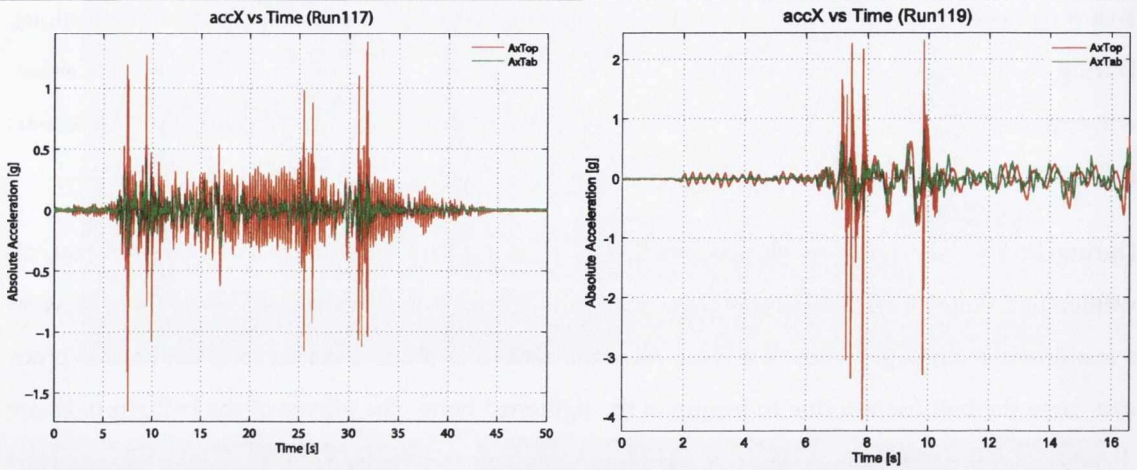

(a) Input (AxTab) and response (AxTop) absolute acceleration time history in x-direction

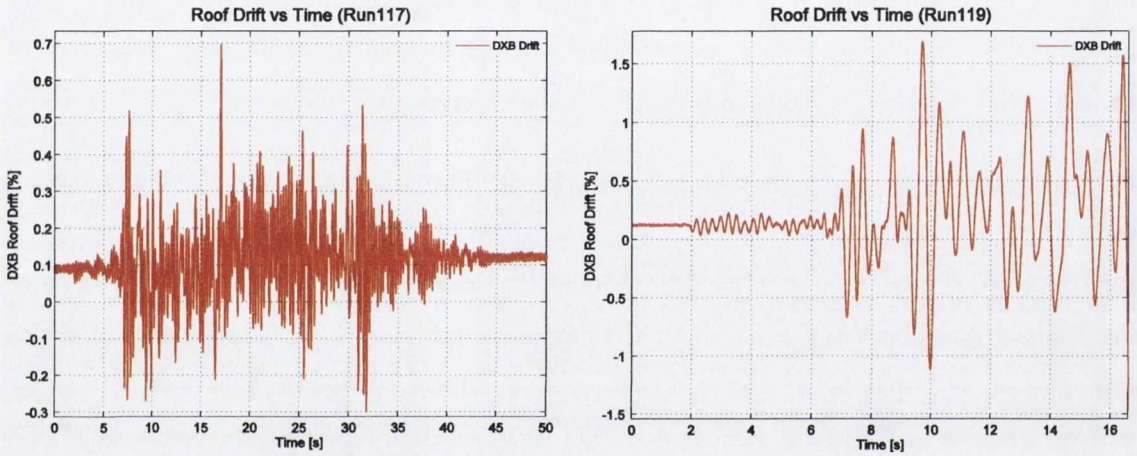

(b) Roof level drift (DXB Drift) time history in x-direction

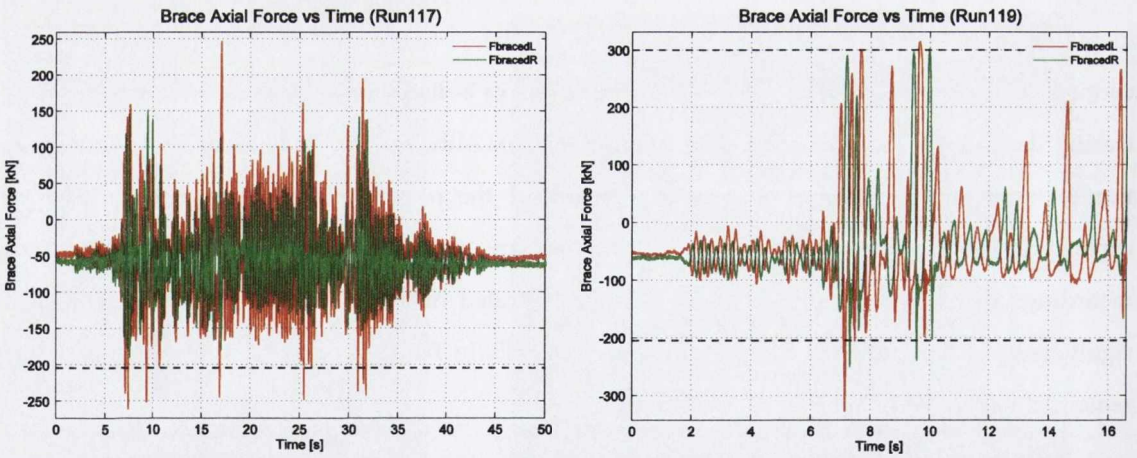

(c) Brace axial load time history for left (FbracedL) and right (FbracedR) braces. Dashed lines indicate yield and buckling capacities (based on characteristic strengths and measured brace section area).

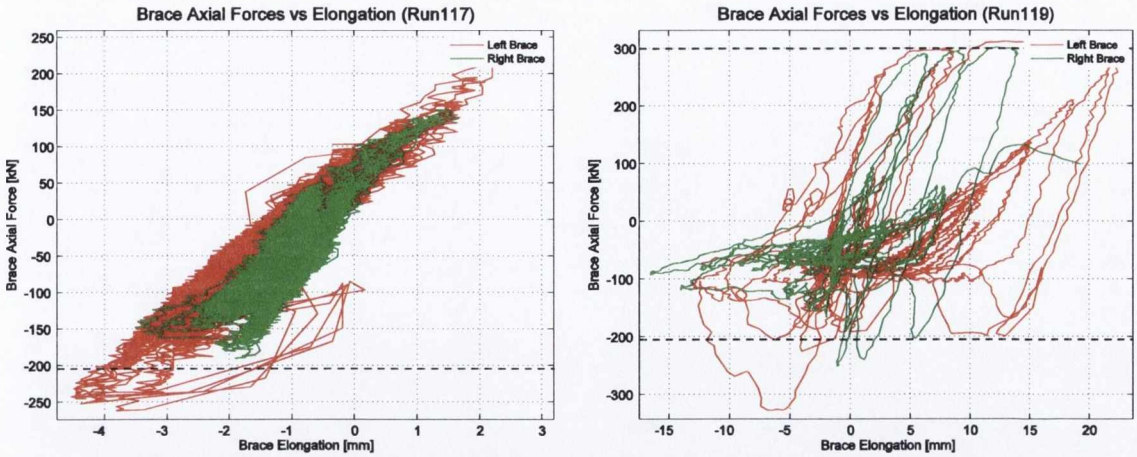

(d) Brace axial load hysteresis for left and right braces. Dashed lines indicate yield and buckling capacities (based on characteristic strengths and measured brace section area).

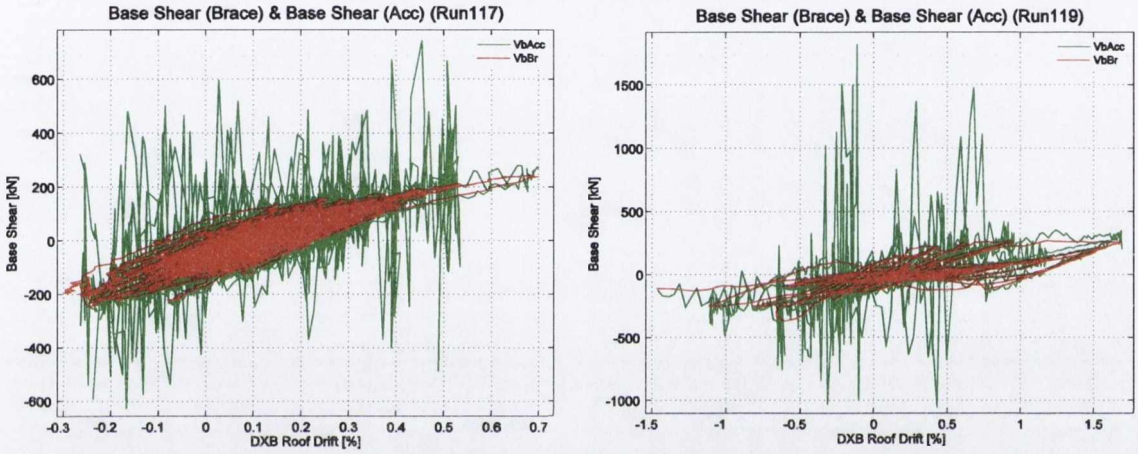

(e) Base shear from brace axial forces plotted against roof drift

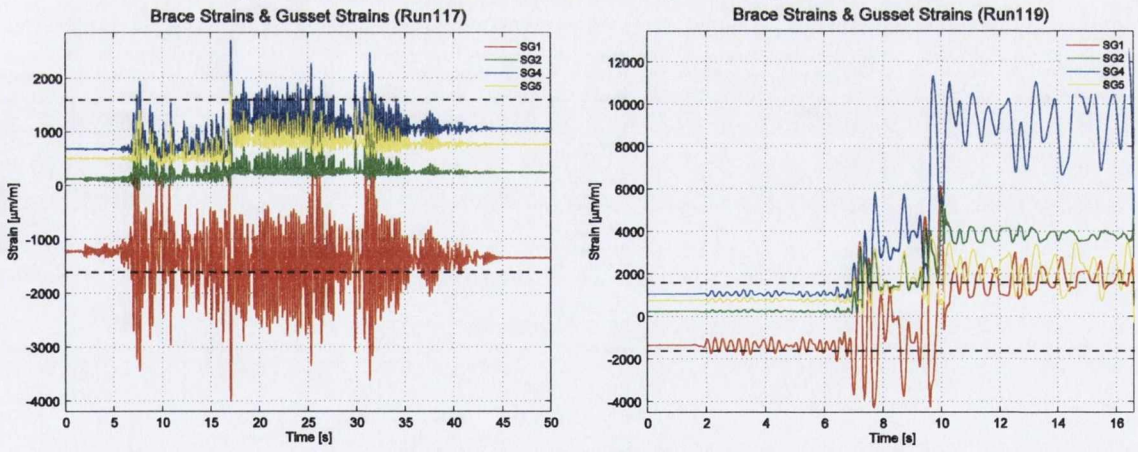

(f) Strain gauge measurements located on the right brace and gusset plate specimen. Dashed lines indicate yield strain thresholds (based on characteristic strengths).

Figure 9.20 – Recorded responses Shake Table Test 8; S1-CB-G1.

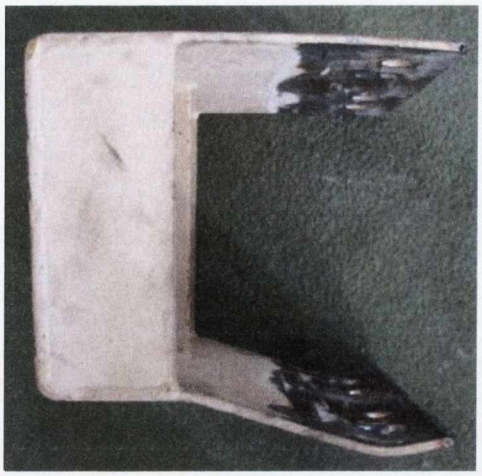

(a)

(b)

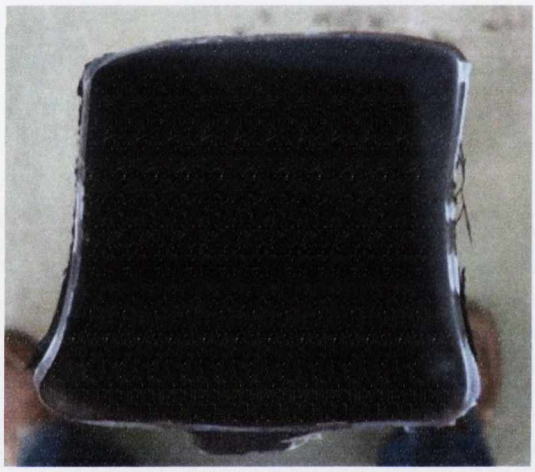

(c)

(d)

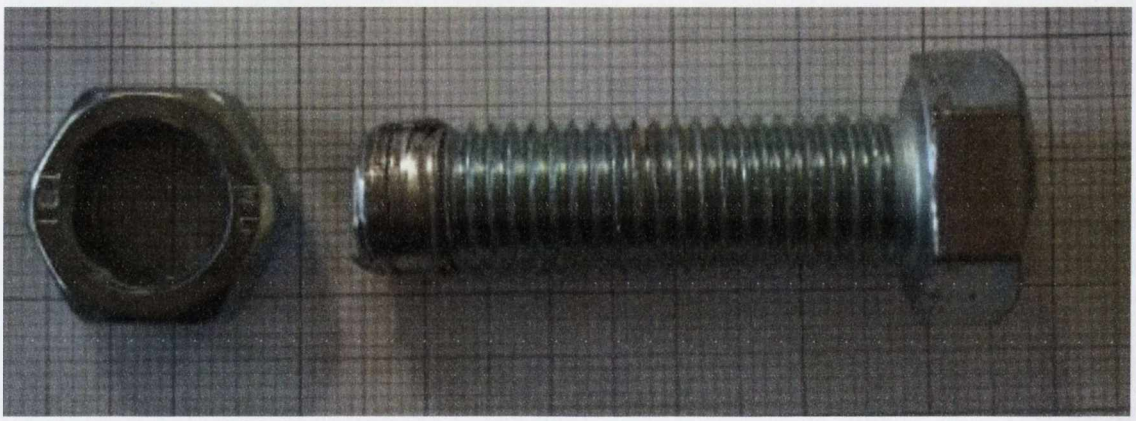

(e)

Figure 9.21 – Test 8; S1-CB-G1 after testing showing (a) damaged impact bumper (b) elongation of bolt hole on impact bumper (c) deformed cross-section of right-hand brace (d) plastic hinging in left-hand gusset plate (e) failed nut and bolt from main beam-column connection.

9.3.11 Shake Table Test 9: S2-CB-G1

Three hazard level earthquake runs were employed in this test, with brace fracture occurring during the 2%/50 run (Run129). A data logging problem was experienced with the right-hand load cell in this experiment as a loose cable connection caused erroneous axial load results to be recorded for the right-hand brace.

During the 10%/50 run (Run127), the specimen behaved as anticipated. Two impulse peaks associated with bolt slippage have been filtered from the recorded acceleration response Figure 9.22(a). The maximum drift reached 0.89% storey height with elastic strain limits being just reached at the mid-length brace strain gauges SG1 and SG2 in Figure 9.22(f). Local buckling formed at locations in the lower third of both braces (Figure 9.23(a)).

Failure occurred in the left-hand brace at the beginning of the strong motion cycles at 9.5 s during the 2%/50 run (Run129). Maximum drift just before failure was recorded as 1.15% storey height. The right-hand brace remained intact with small fracture cracks beginning in the corner regions as shown in the photograph in Figure 9.23(a). Large out-of-plane deformation was experienced by both braces. In this test, the out-of-plane rotation limits of the MTS swivel bearings were reached, resulting in additional brace bending close to the brace-swivel connection. After testing, slight local buckling of the brace cross-section was observed at this location, as shown in Figure 9.23(b). As in Test 8, relatively small residual out-of-plane deformations were observable in the gusset plates (Figure 9.23(d)). The deformed section shape of the cross-section of the left-hand brace (Figure 9.23(c)) was similar to that previously observed in Test 6 (section 9.3.8).

This Shake Table Test 6: S2-CA-G2test is comparable with Test 11 (where a G2 plate design was used). For the same 2%/50 hazard level, strain measurements for SG4 reached similar maximum peaks for both tests. However, in Test 11 , much larger strains at mid-length of the brace SG1, were observed.

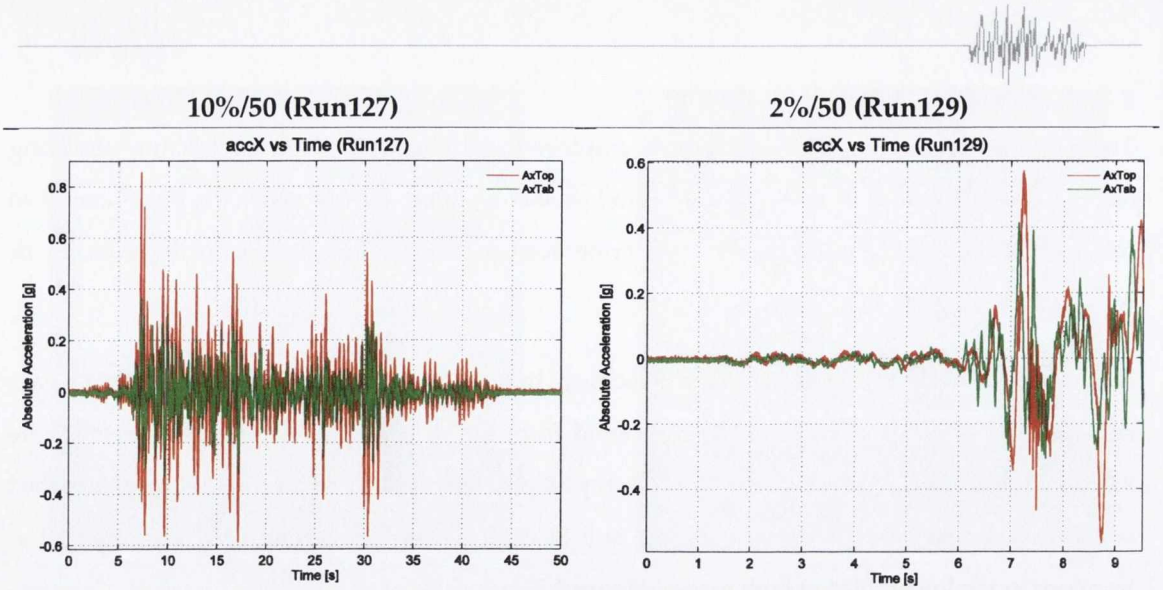

(a) Input (AxTab) and response (AxTop) absolute acceleration time history in x-direction

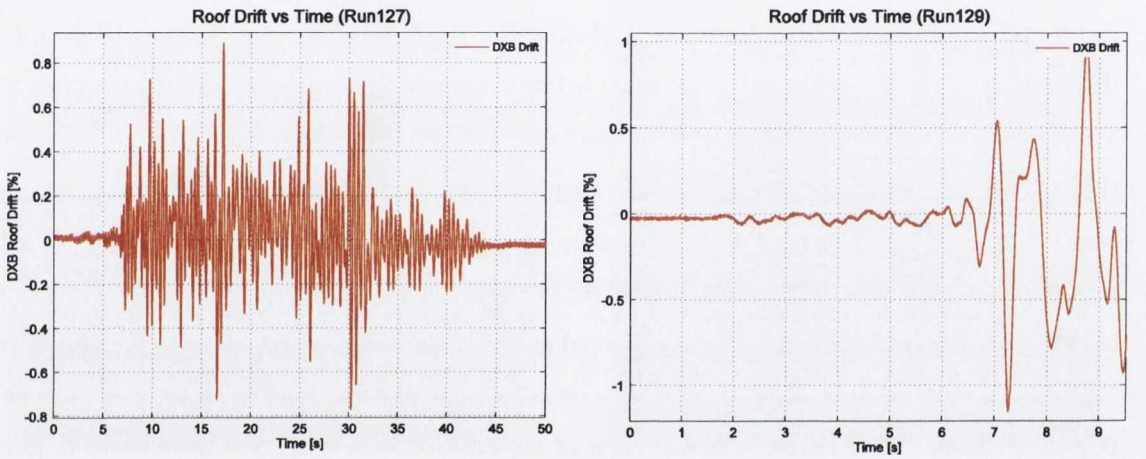

(b) Roof level drift (DXB Drift) time history in x-direction

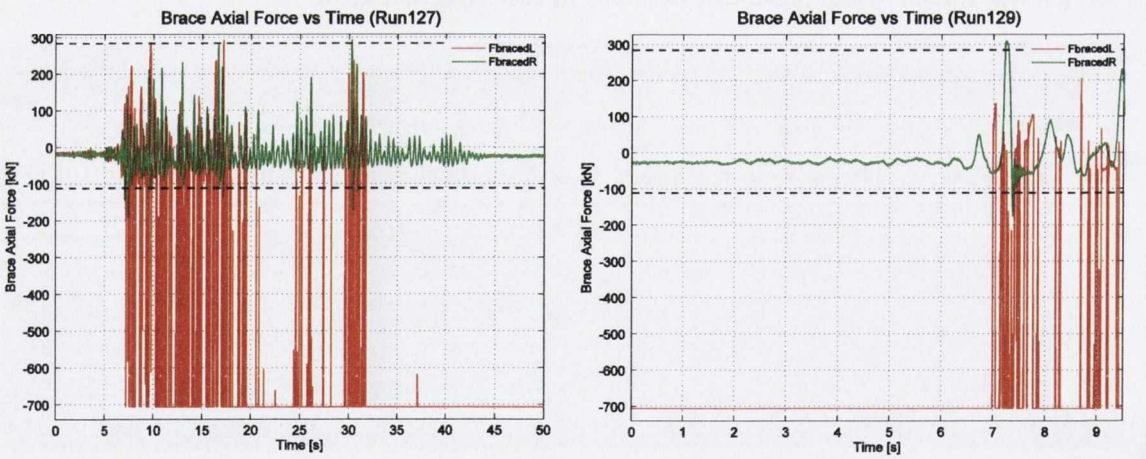

(c) Brace axial load time history for left (FbracedL) and right (FbracedR) braces. Dashed lines indicate yield and buckling capacities (based on characteristic strengths and measured brace section area).

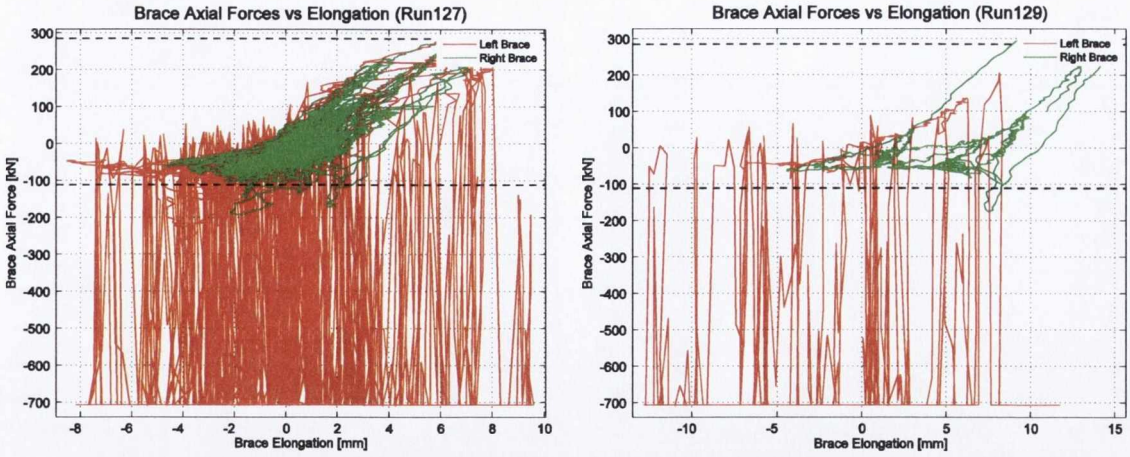

(d) Brace axial load hysteresis for left and right braces. Dashed lines indicate yield and buckling capacities (based on characteristic strengths and measured brace section area).

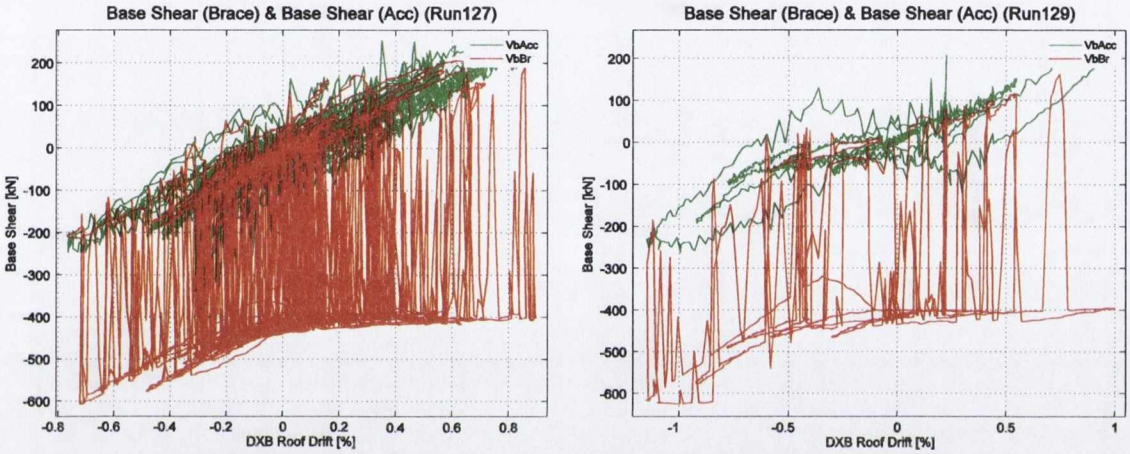

(e) Base shear from brace axial forces plotted against roof drift

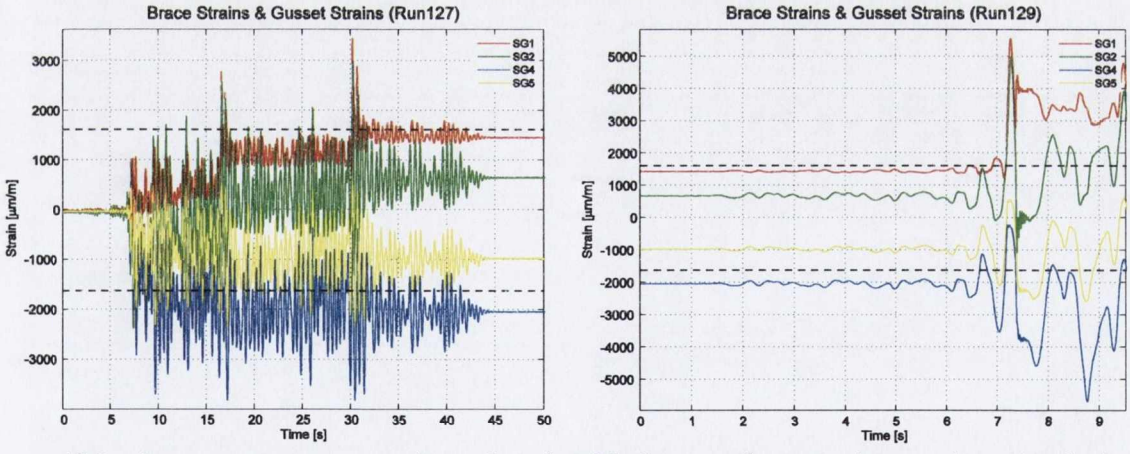

(f) Strain gauge measurements located on the right brace and gusset plate specimen. Dashed lines indicate yield strain thresholds (based on characteristic strengths).

Figure 9.22 – Recorded responses Shake Table Test 9; S2-CB-G1.

(a)

(b)

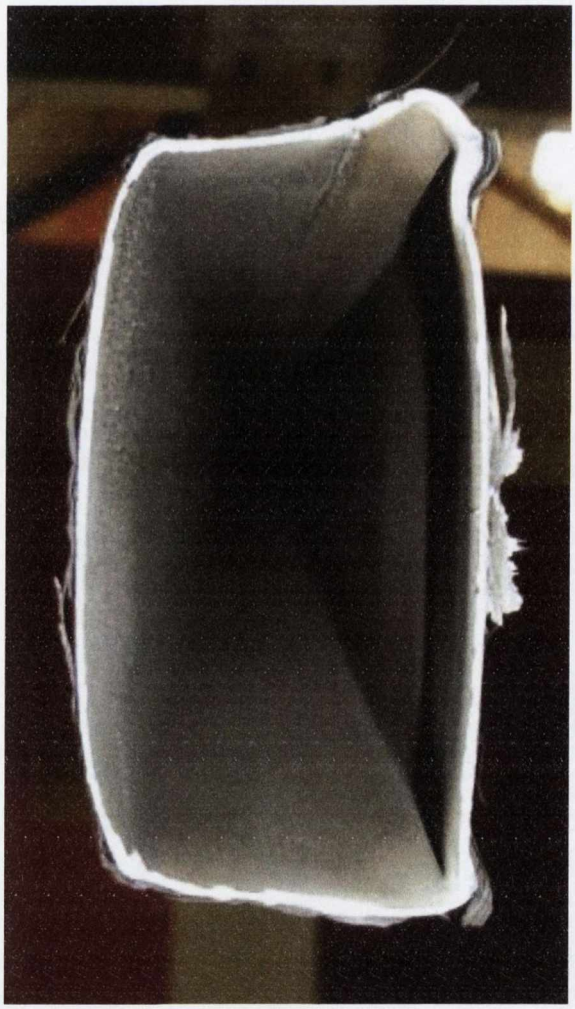

(c)

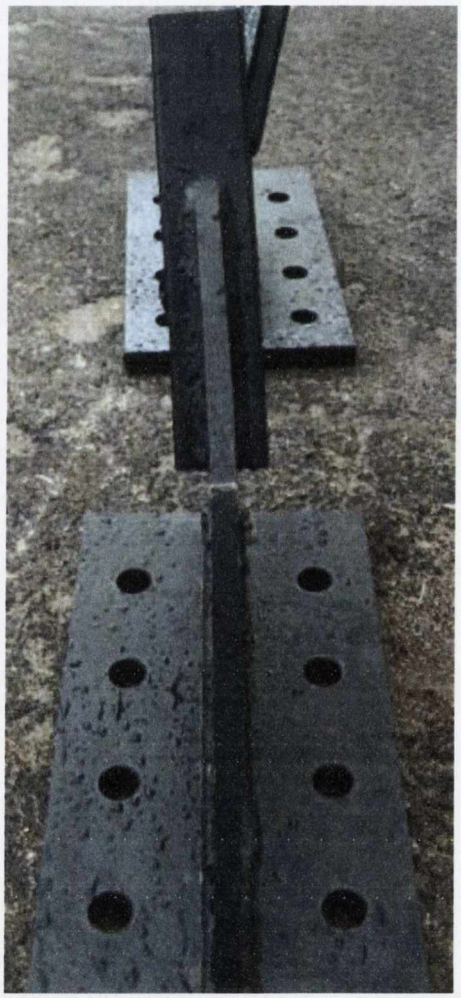

(d)

Figure 9.23 – Test 9; S2-CB-G1 after testing showing (a) fracture cracks beginning in local buckle in right-hand brace (b) local buckling of brace at brace-swivel connection (c) deformed cross-section of left-hand brace (d) deformed shape of right-hand gusset plate.

9.3.12 Shake Table Test 10: S4-CB-G2

In these tests, brace fracture occurred during an additional failure level run (Run140) in which the excitation was scaled to equal the excitation in the failure level run of Test 3 (section 9.3.5) as the same brace size (60×60×3.0) was used in both tests. No plastic deformations in the braces were observed in the 50%/50 level (Run134). Some global buckling was observed in both braces during the 10%/50 level (Run136), and this was more pronounced in the right-hand brace.

During the 2%/50 level (Run138) no signs of local buckling or necking were observed in either brace, despite a large drift demand of 1.8%. The brace axial load plots and base shear plots demonstrate larger, less 'pinched' hysteresis loops similar to those displayed in Test 3. Strains in the brace mid-length gauges (SG1 and SG2) exceeded the yield strain threshold by almost 1400% and 700% in tension and compression, respectively.

In the failure level run, drifts of over 3.7% were reached with one large bolt slippage impulse peak displayed in the measured acceleration response. A local buckle formed at mid-length in the right-hand brace at 9.8 s, which progressed to cross-section rupture at 16.8 s. Simultaneously, a local buckle formed in the left brace (Figure 9.25(b)) and all bolts at the primary beam-to-column joint underwent tensile failure due to the large, post-failure drift demands. The relatively thin and flexible gusset plates arising from the application of the balanced design approach combined with the less restrained CB type connection configuration resulted in large out-of-plane bending (Figure 9.25(e)) to accommodate brace buckling, but plate buckling did not occur.

The elevated strain measurements in SG2 are attributable to the formation of the brace local buckle at exactly this gauge location Figure 9.24(f). SG2 was positioned on the compression flange of the buckled brace, as indicated in Figure 9.25(c).

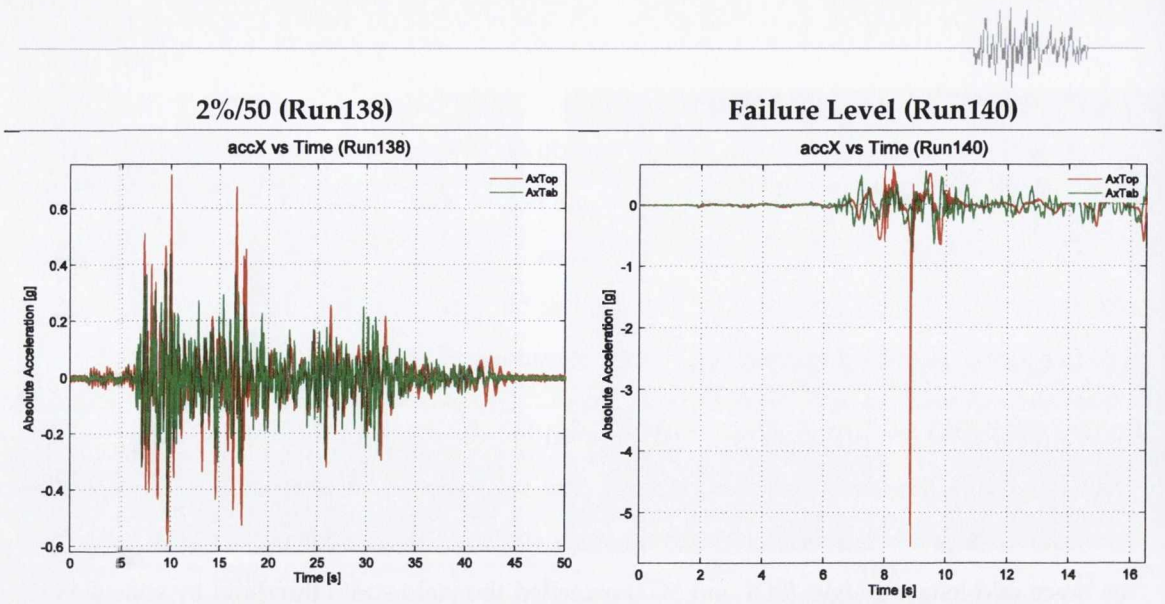

(a) Input (AxTab) and response (AxTop) absolute acceleration time history in x-direction

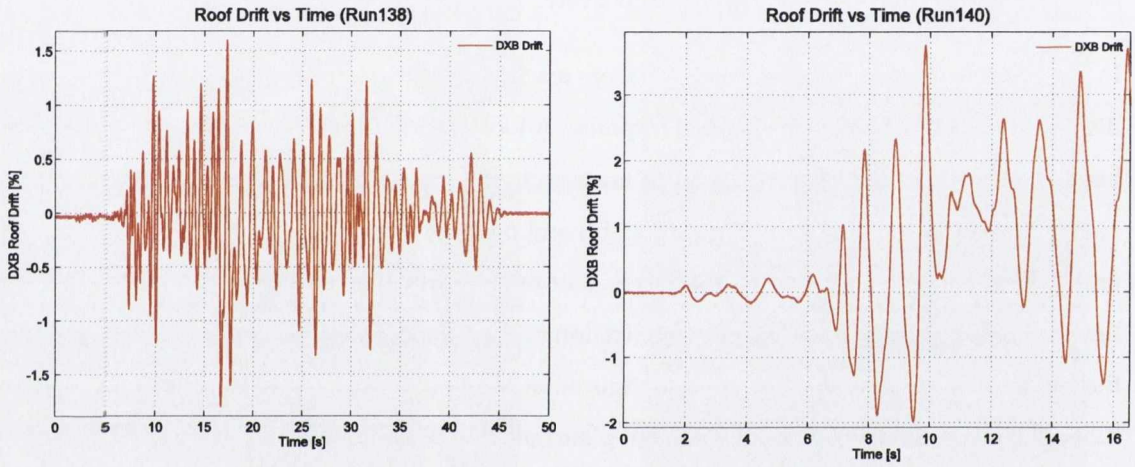

(b) Roof level drift (DXB Drift) time history in x-direction

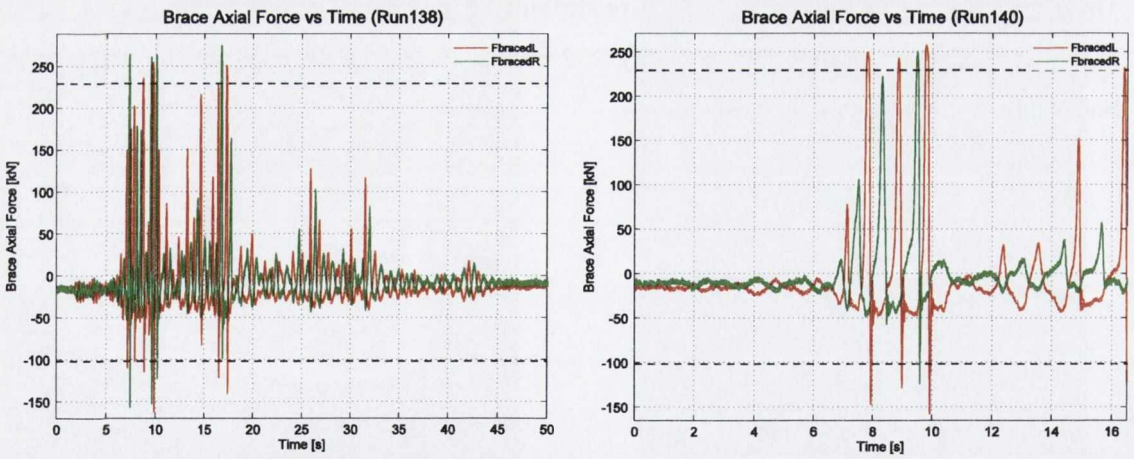

(c) Brace axial load time history for left (FbracedL) and right (FbracedR) braces. Dashed lines indicate yield and buckling capacities (based on characteristic strengths and measured brace section area).

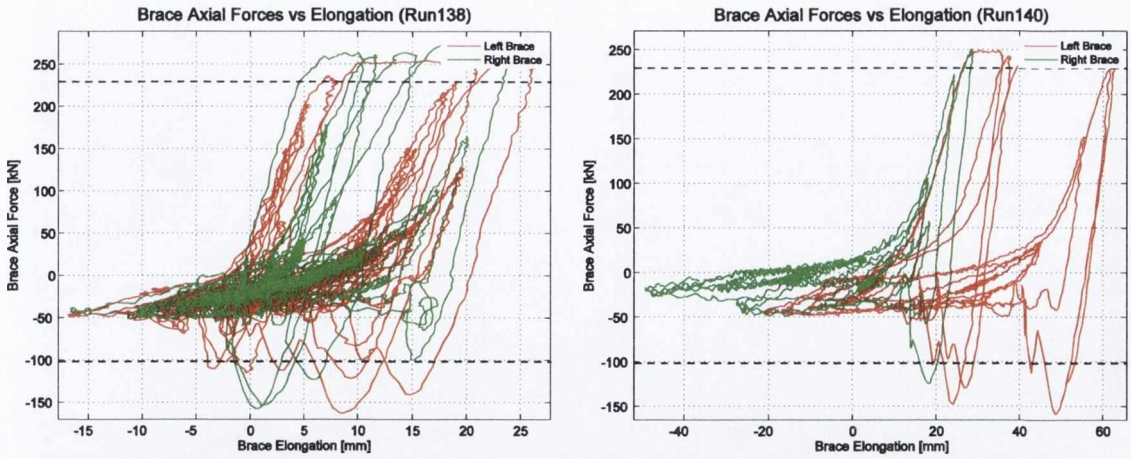

(d) Brace axial load hysteresis for left and right braces. Dashed lines indicate yield and buckling capacities (based on characteristic strengths and measured brace section area).

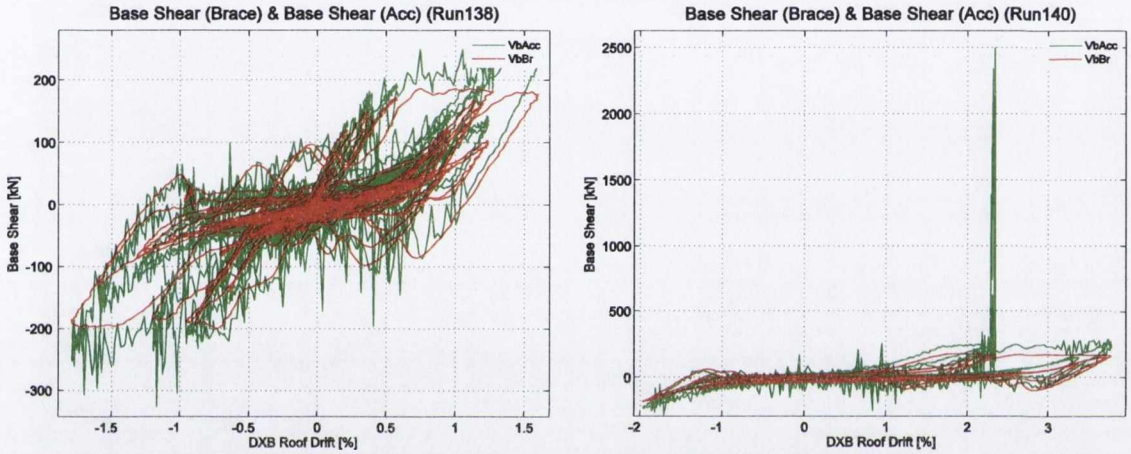

(e) Base shear from brace axial forces plotted against roof drift

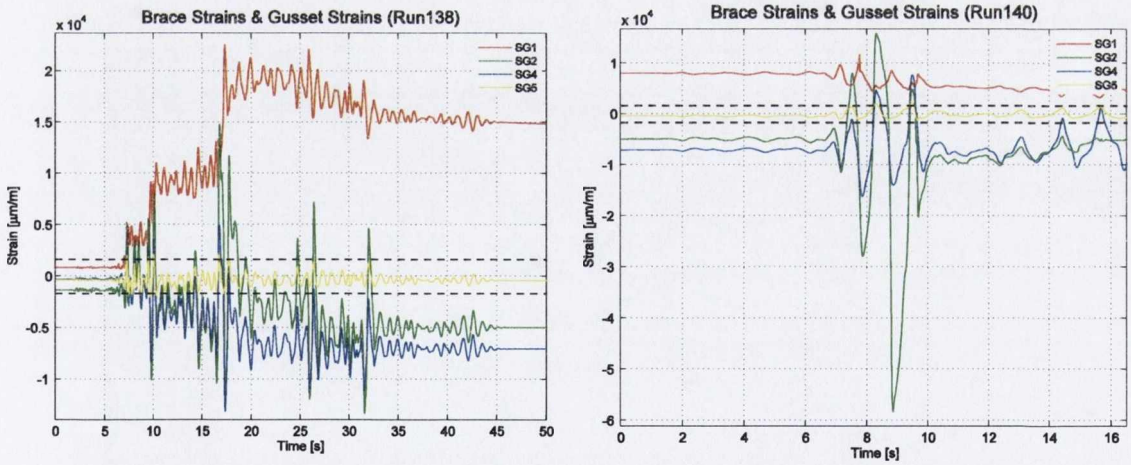

(f) Strain gauge measurements located on the right brace and gusset plate specimen. Dashed lines indicate yield strain thresholds (based on characteristic strengths).

Figure 9.24 – Recorded responses Shake Table Test 10; S4-CB-G2.

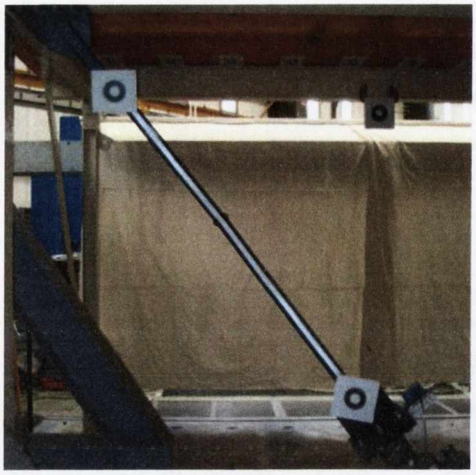

(a)

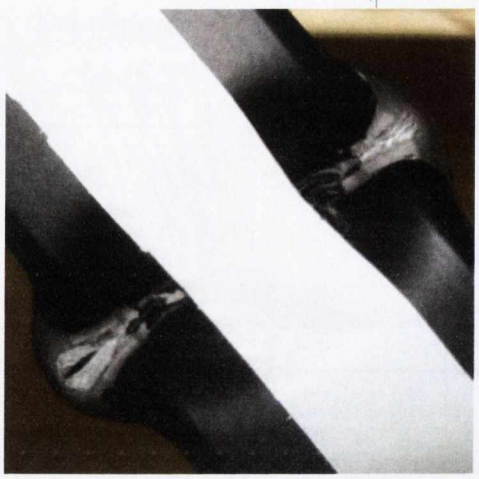

(b)

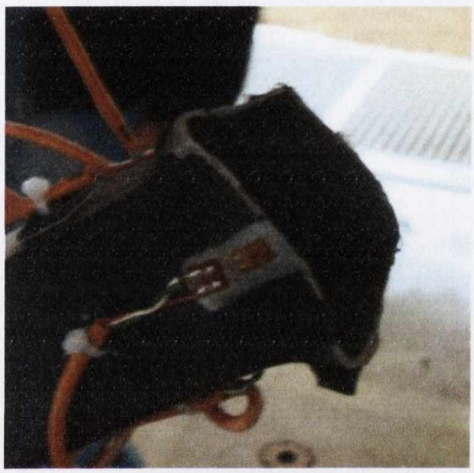

(c)

(d)

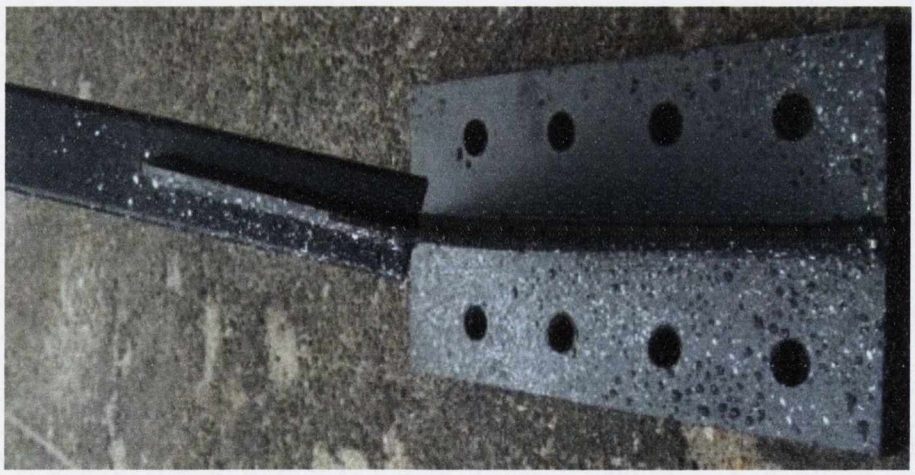

(e)

Figure 9.25 – Test 10; S4-CB-G2 after testing showing (a) residual local buckle in left-hand brace (b) close-up of local buckle with tears at corners of cross-section (c) deformed cross-section of right-hand brace with strain gauges (d) damaged right-hand impact bumper with honeycomb shock absorber and (e) residual bending in left-hand gusset plate.

9.3.13 Shake Table Test 11: S2-CB-G2

Three earthquake runs were carried out in this test at the three hazard levels. During the 50%/50 level run (Run146), some resonance was observed towards the end of the run, though all measurements showed that the response remained within the elastic range.

For the 10%/50 run (Run148) global buckling was observed in both braces. Response drifts reached 0.75% with yielding and buckling limits just being reached in the brace axial load plot (Figure 9.26(c)). Strain gauge SG2 had debonded from the brace surface causing erroneous measurements to be recorded.

Partial brace fracture occurred in the 2%/50 run with drift demand approaching 2% and both braces forming large local buckles at mid-length. At the end of the test, both braces remained intact but partial fracture had occurred at the corners of both locally-buckled cross-sections, as shown in Figure 9.27(a) and (b). Figure 9.26(f) shows that the strains in the gusset plate exceeded the elastic limits, but as shown in Figure 9.27(d) the gusset plates remained substantially undeformed without excessive bending and without buckling. This is largely in agreement with the visual inspection of the gusset plates used in Test 9 (section 9.3.11) where a G1 design was used.

10%/50 (Run148) **2%/50 (Run150)**

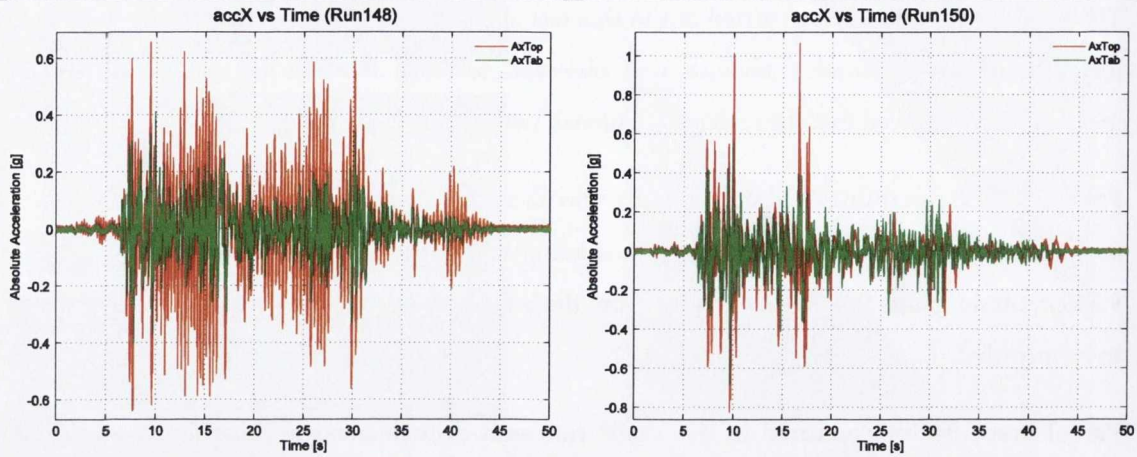

(a) Input (AxTab) and response (AxTop) absolute acceleration time history in x-direction

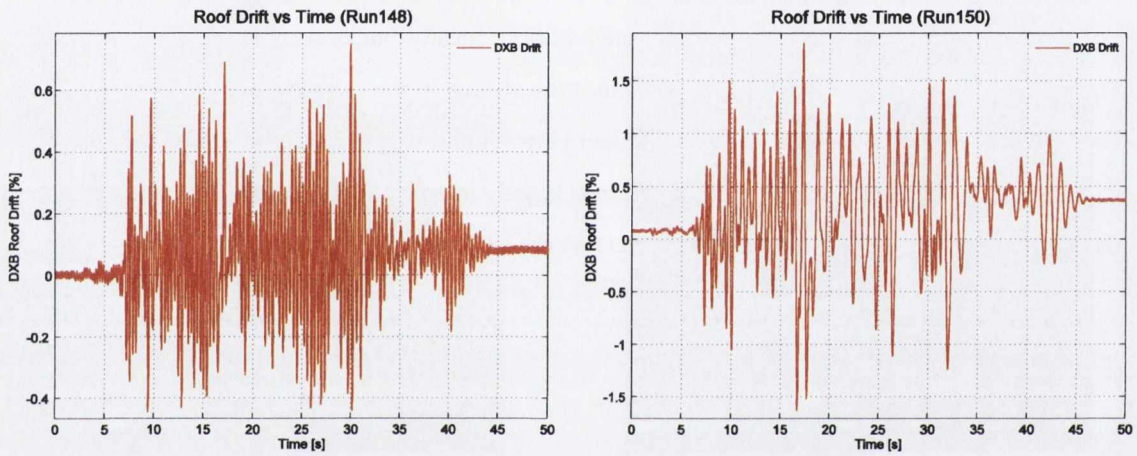

(b) Roof level drift (DXB Drift) time history in x-direction

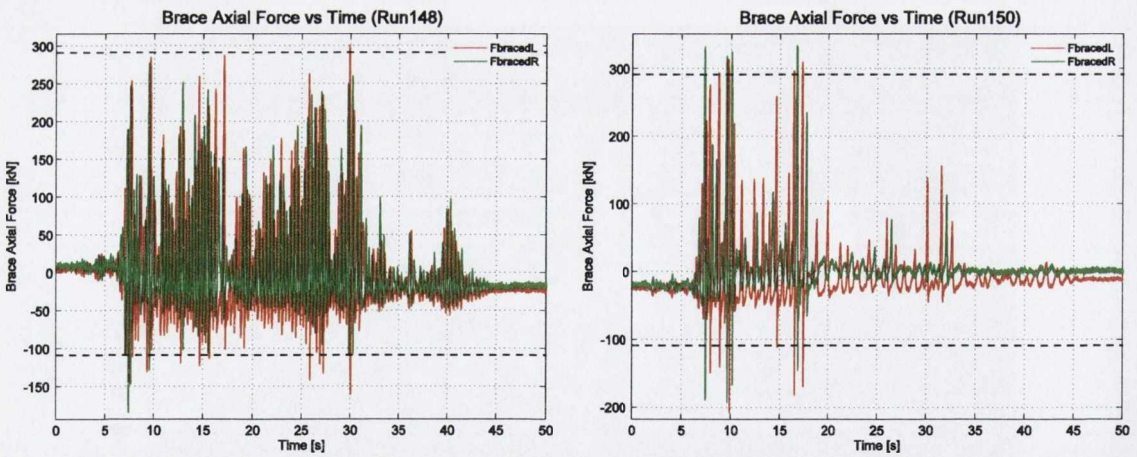

(c) Brace axial load time history for left (FbracedL) and right (FbracedR) braces. Dashed lines indicate yield and buckling capacities (based on characteristic strengths and measured brace section area).

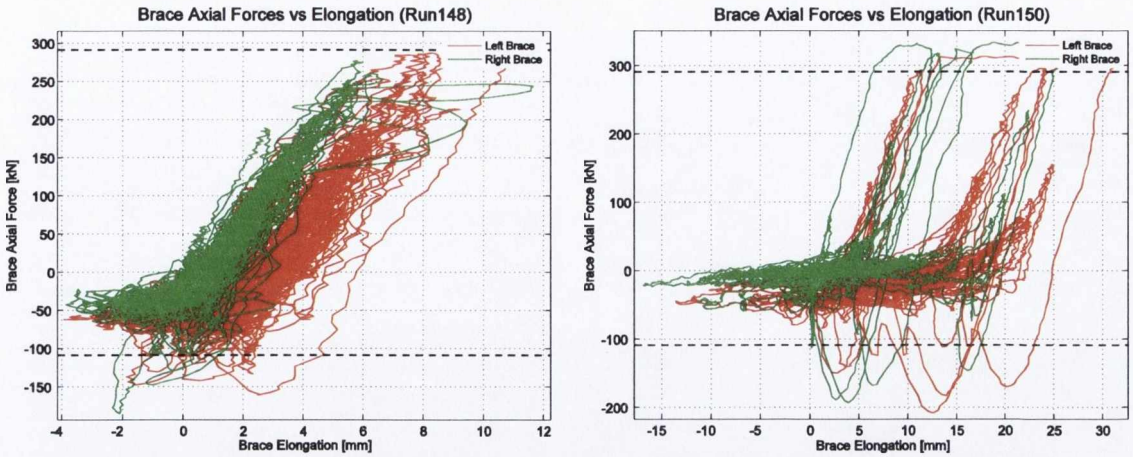

(d) Brace axial load hysteresis for left and right braces. Dashed lines indicate yield and buckling capacities (based on characteristic strengths and measured brace section area).

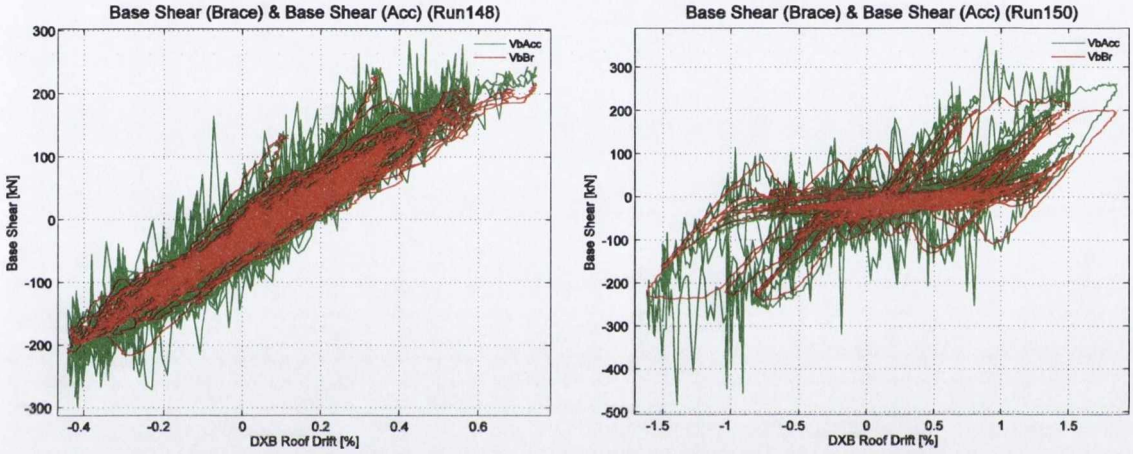

(e) Base shear from brace axial forces plotted against roof drift

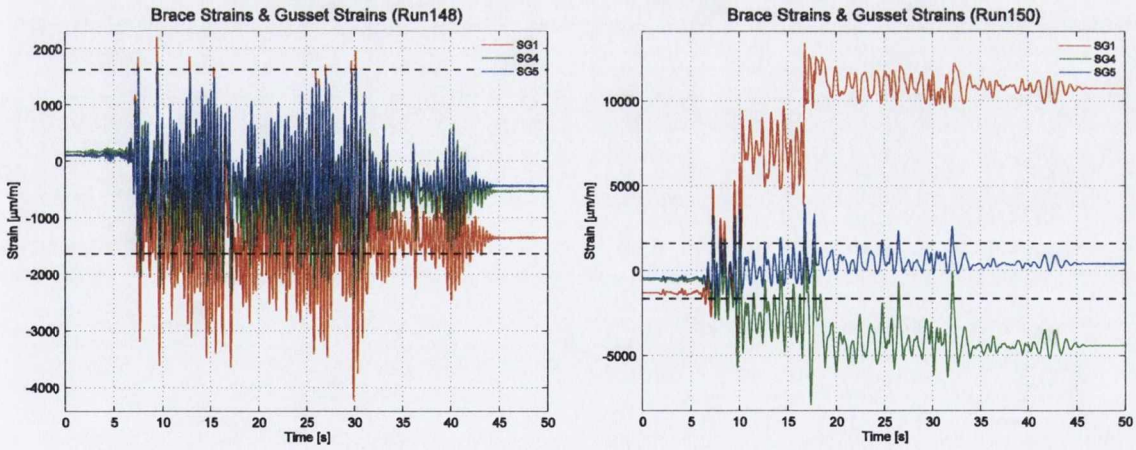

(f) Strain gauge measurements located on the right brace and gusset plate specimen. Dashed lines indicate yield strain thresholds (based on characteristic strengths).

Figure 9.26 – Recorded responses Shake Table Test 11; S2-CB-G2.

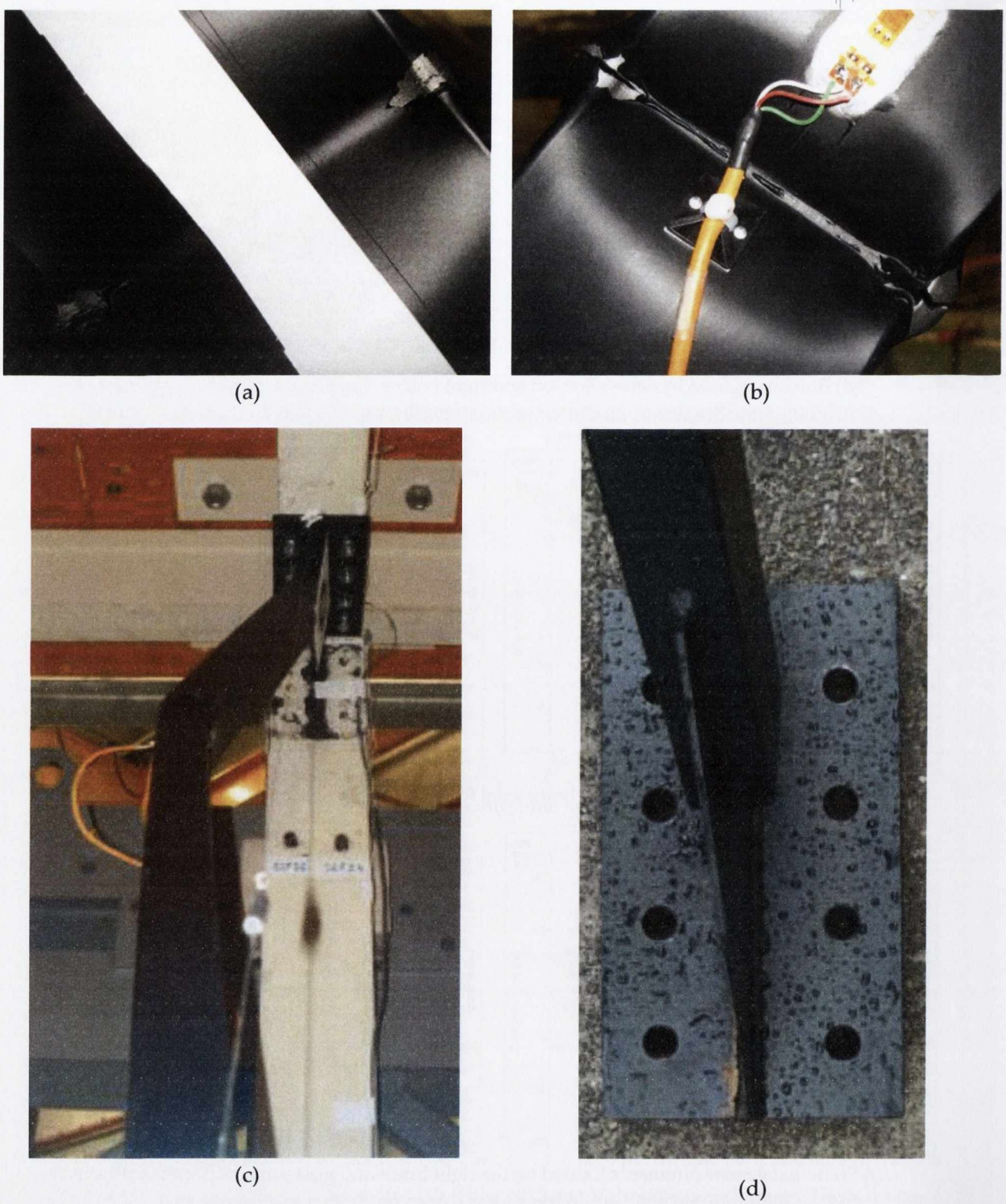

Figure 9.27 – Test 11; S2-CB-G2 after testing showing local buckle and fracture forming in (a) left-hand brace and (b) right-hand brace; (c) residual out-of-plane deformation of left-hand brace; (d) minimal deformation in right-hand gusset.

9.3.14 Shake Table Test 12: S3-CB-G2

Three hazard level earthquake runs were performed in this test. As anticipated, the overall response of the frame and specimens remained elastic during the 50%/50 run (Run156). The drift demand reached 0.9% in the 10%/50 level (Run158) with brace yielding and buckling limits being just reached. The brace strain gauges showed that the flange monitored by SG2 remained in the tensile range once the plastic limit had been exceeded Figure 9.28(f). The SG1 flange mostly remained within the elastic range, with both tension and compression yield limits reached intermittently.

Failure occurred in the 2%/50 level (Run160) with both braces forming local buckles and the right brace failing completely. Large plastic strains were observed in the gusset plate plastic hinge (SG4), with a mostly elastic response occurring outside the elliptical clearance zone (SG5), as shown in the strain measurements of Figure 9.28(f). The view of the right-hand brace cross-section after failure (Figure 9.29(b)) shows that local buckling was not severe and some necking is observable. No rupture was observed in the left-hand brace local buckle, as indicated in the photograph in Figure 9.29(a). There was very little residual deformation in either gusset plate Figure 9.29(d) compared to the distortion observed in the gusset plates in Test 7 (section 9.3.9) where a CA connection was used.

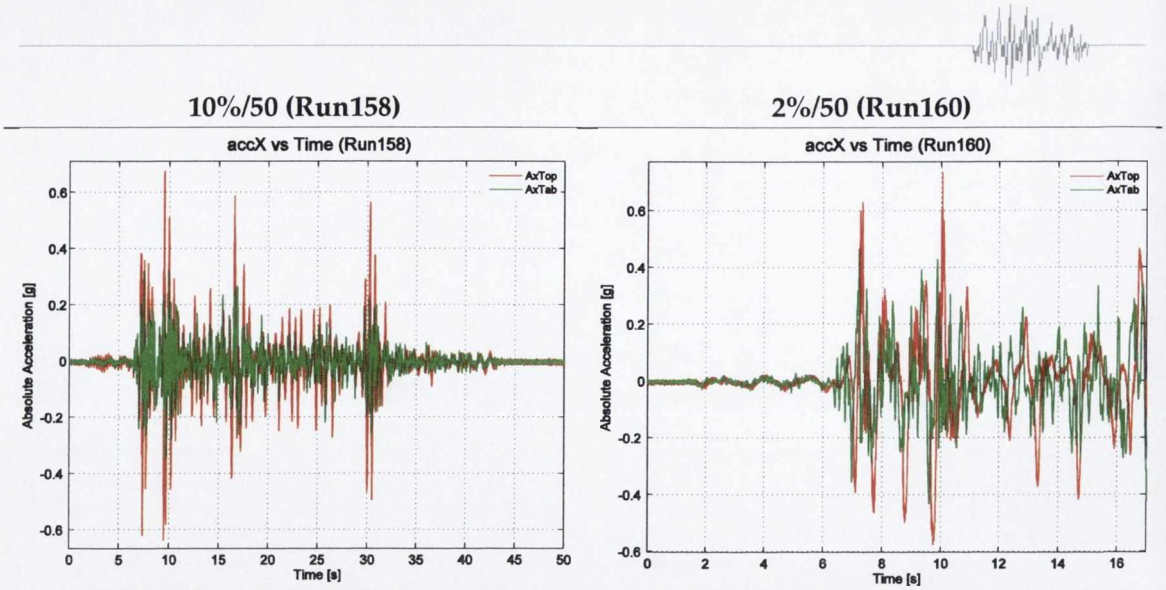

(a) Input (AxTab) and response (AxTop) absolute acceleration time history in x-direction

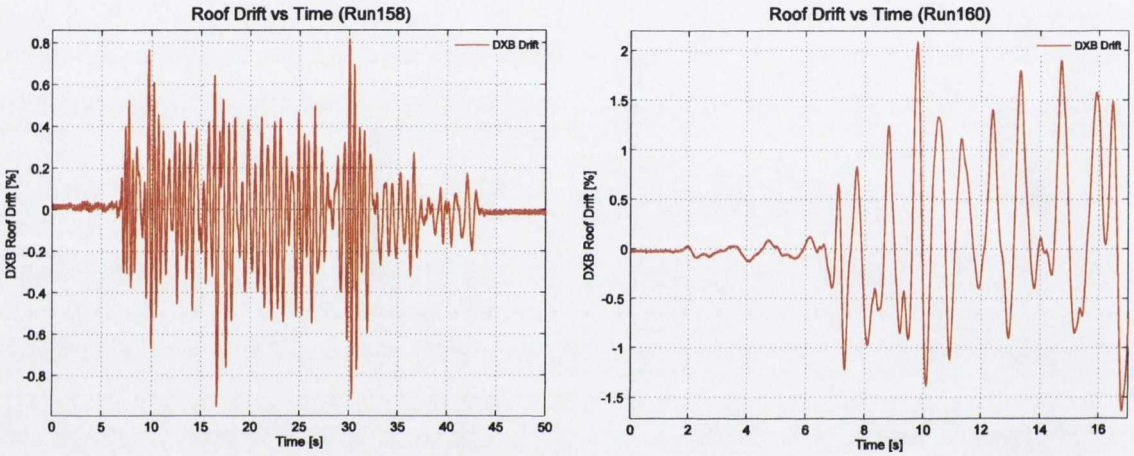

(b) Roof level drift (DXB Drift) time history in x-direction

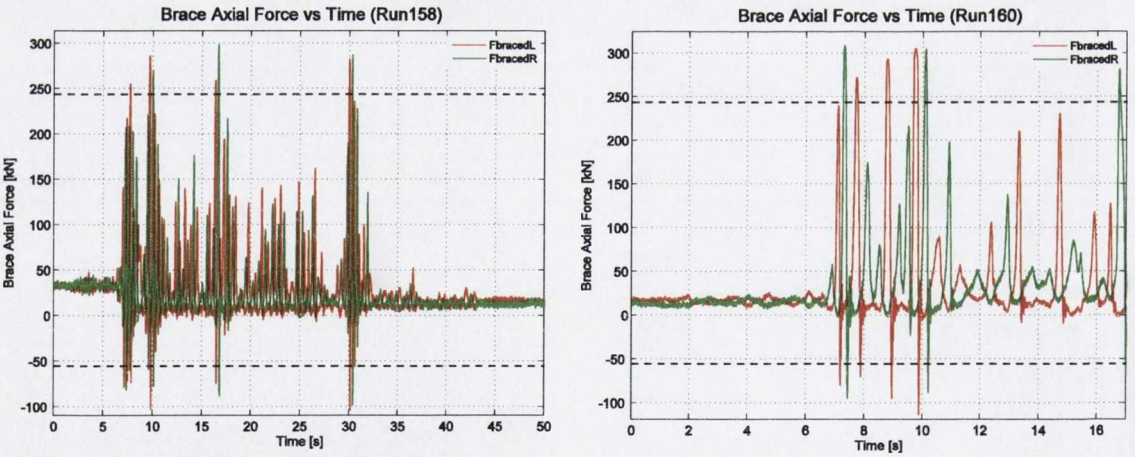

(c) Brace axial load time history for left (FbracedL) and right (FbracedR) braces. Dashed lines indicate yield and buckling capacities (based on characteristic strengths and measured brace section area).

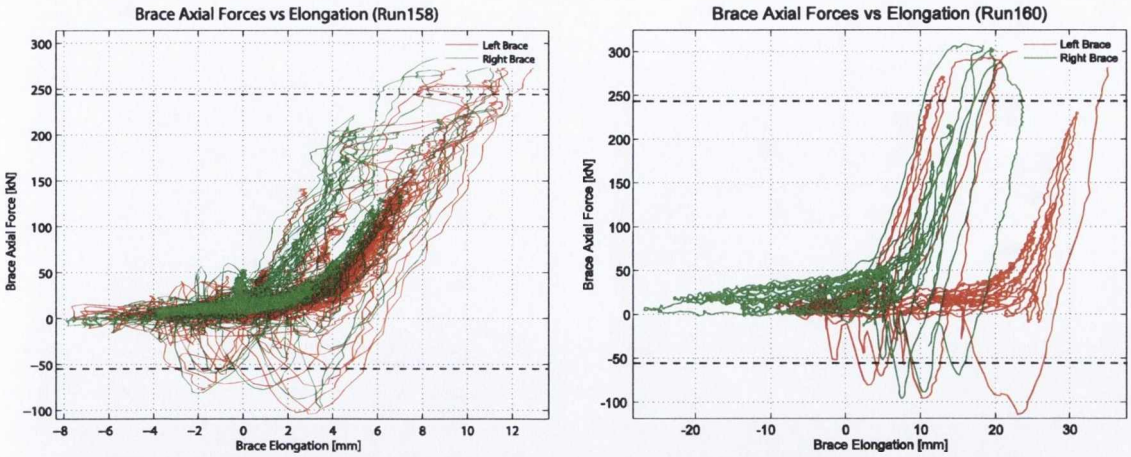

(d) Brace axial load hysteresis for left and right braces. Dashed lines indicate yield and buckling capacities (based on characteristic strengths and measured brace section area).

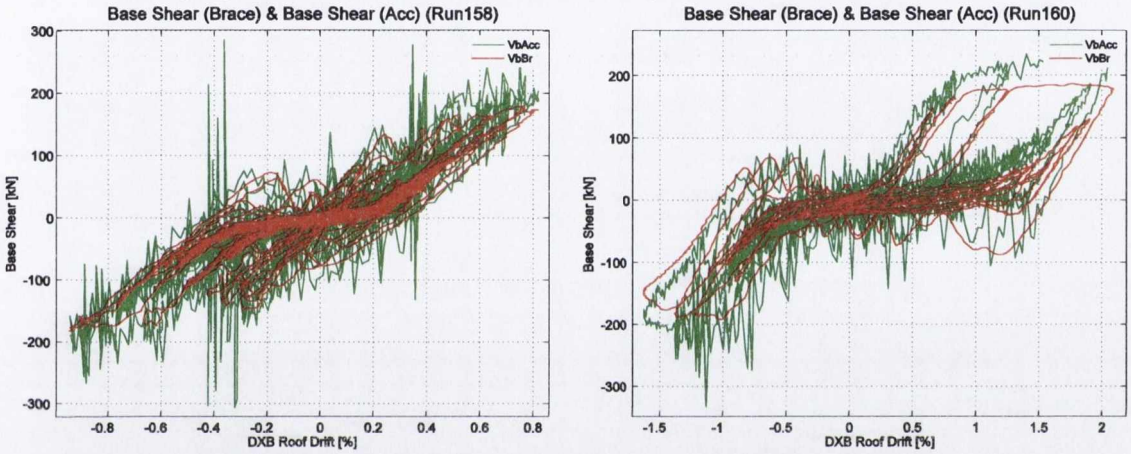

(e) Base shear from brace axial forces plotted against roof drift

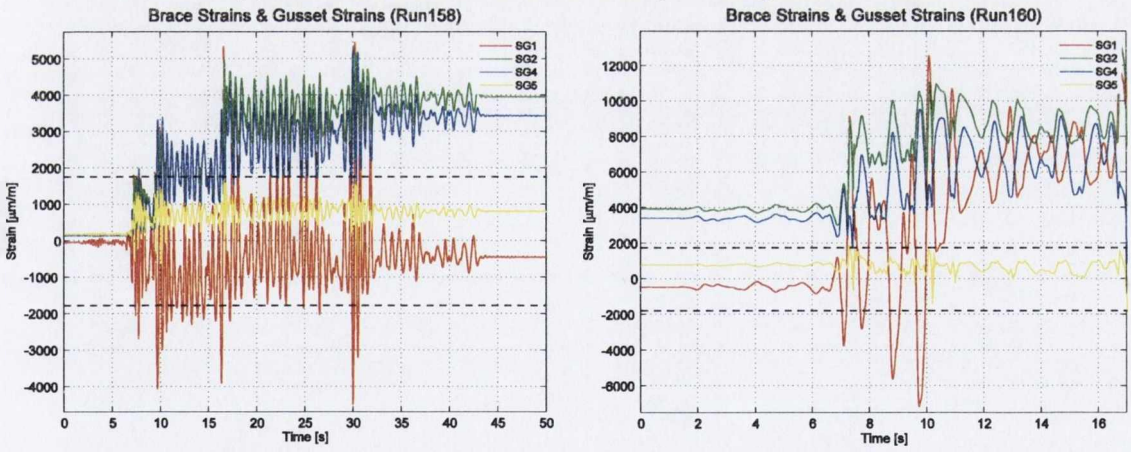

(f) Strain gauge measurements located on the right brace and gusset plate specimen. Dashed lines indicate yield strain thresholds (based on characteristic strengths).

Figure 9.28 – Recorded responses Shake Table Test 12; S3-CB-G2.

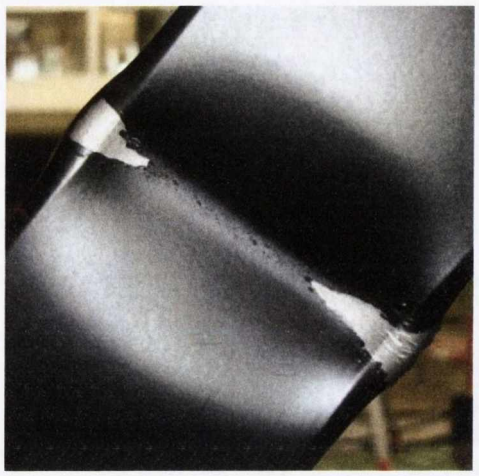

(a)

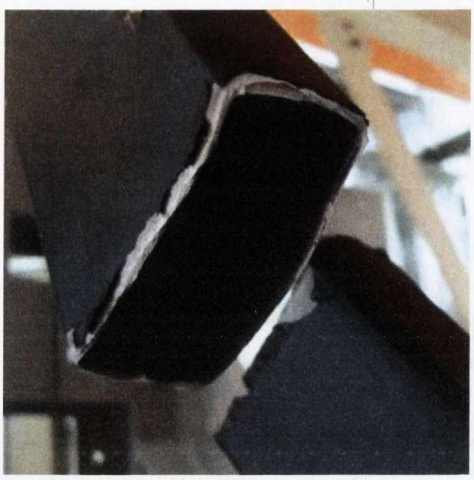

(b)

(c)

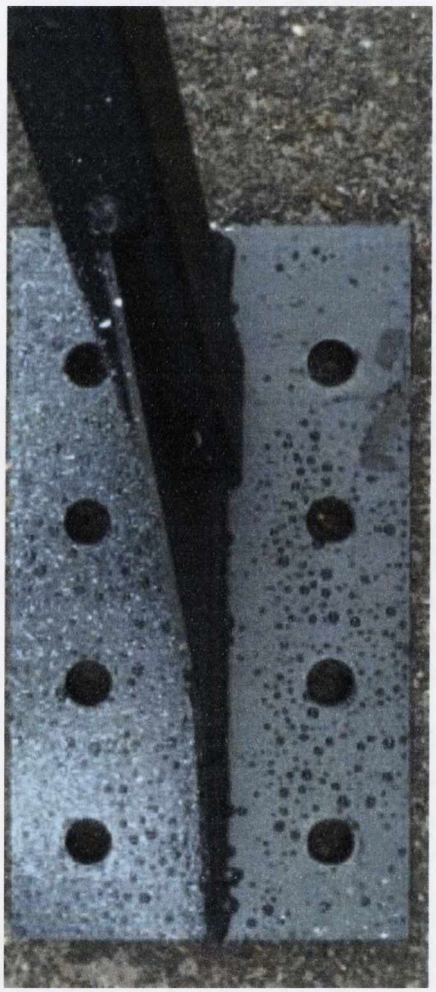

(d)

Figure 9.29 – Test 12; S3-CB-G2 after testing showing local buckle and fracture forming in (a) left-hand brace and (b) right-hand brace; (c) residual out-of-plane deformation of left-hand brace; (d) minimal deformation in right-hand gusset.

9.3.15 Treatment of Acceleration Impulses

In some of the earthquake runs of the tests on brace-gusset plate specimens with CB type connections (Tests 8 – 12), loud sharp emissions of noise were heard. After the first earthquake run in which this occurred, all welds and bolts in the test frame and specimens were closely inspected but no signs of failure were observed. After further investigation it was found that these noises were caused by bolt slippage caused by the large shear forces in the bolts connecting the brace-gusset plate specimens to the beams of the test frame that arise when the beam-only CB type connection configuration is employed. Except for the recording of sudden large peaks in the measured acceleration response recorded, this slip did not appear to affect overall frame or specimen response. However, the large recorded acceleration peaks did pose a problem in establishing realistic values for the maximum and minimum table and response accelerations for the run, and for the dynamic amplification factors and base shear plots calculated from these acceleration data. Two typical impulses from Run127 are highlighted in green ellipses in Figure 9.30(a).

To resolve this issue, the use of smoothing filters to reduce these peaks throughout data post-processing was investigated. However, this approach resulted in undesirable corruption of the data. Instead, the adopted approach involved identifying the relevant acceleration peaks, setting the extreme values as 'NaN' values and applying a filter to the affected data in the vicinity. The runs where this approach was applied were Runs 117 and 119 in Test 8, Run 127 in Test 9, Run 134 in Test 10 and Run 158 in Test 12.

Firstly, the problematic impulses were identified and isolated by inspection of the acceleration response, and the use of video and sound recordings of the test runs. The typical impulse duration was very short lasting between 0.0103 – 0.0274 seconds, and with its characteristic waveform shape, was immediately distinct from peaks due to other sources of shock or impulse, such as brace fracture. The second step involved removing the impulses by setting them as NaN values. Figure 9.30(b) shows the resulting plot when applied to Run127. Finally, the Savitzky-Golay filter (Savitzky and Golay, 1964) was applied to adjacent data that was considered to influence the lower frequency response as in Figure 9.30(c). This filter performs a linear least-squares fit of a selected polynomial, and was carefully selected to perform lightweight smoothing with a quadratic polynomial.

For the affected runs (with the exception of Run117), smoothing was considered necessary for either one or two impulses. Overall, this process produced more realistic response plots and calculated response variables that are uncorrupted by the effects of bolt slip with minimal data removal.

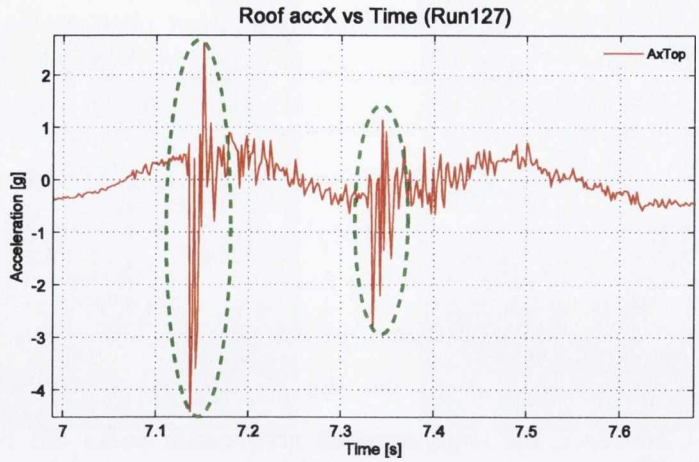

(a) Original record with acceleration impulses at approximately 7.143 and 7.342 seconds.

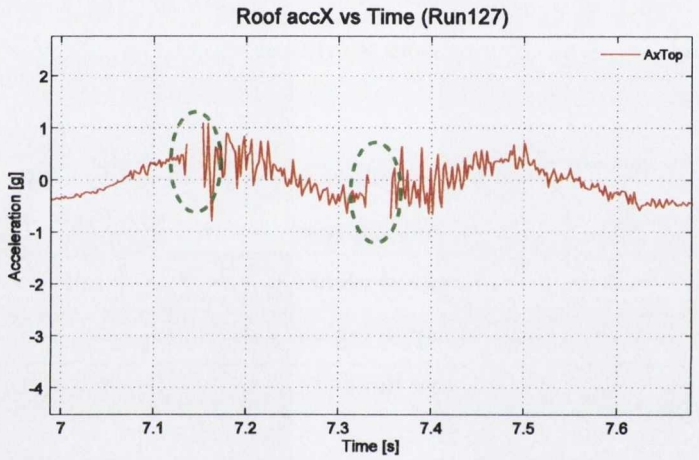

(b) Data with extreme values set as NaN

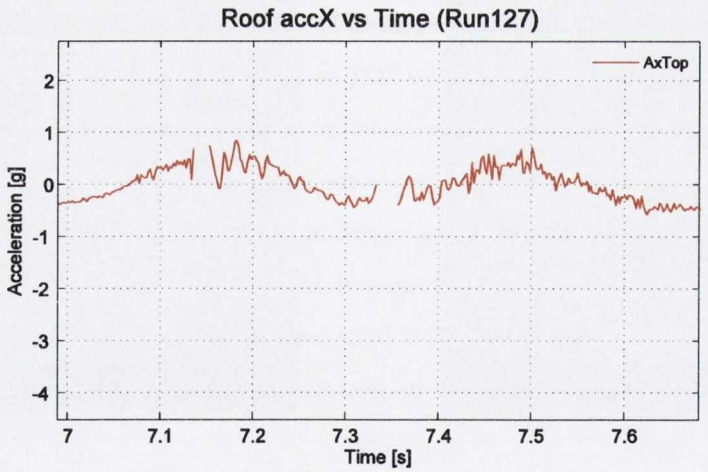

(c) Data with extreme values set as NaN and Savitzky-Golay filter applied between 7.15 and 7.43 seconds.

Figure 9.30 – Filtering of recorded roof acceleration response for Test 9, Run127.

9.3.16 Lateral and Supplementary Displacement Measurements

In all tests, three lateral displacement measurements were recorded as detailed in Chapter 8. The test frame was designed and constructed to have no plan irregularity, with an even distribution of mass throughout the structure and with lateral stiffness in single plane at the centre of the structure. Therefore only a translational response was expected with a uni-directional excitation. The measurements DXY, DYB and DYC were recorded to check for any indication of a torsional response and overall lateral stability of the test frame. Small lateral frame displacements were observed in all tests, with no indication of plan torsion response. A typical sample of the data obtained is shown in Figure 9.31(a) and demonstrates that at one of the largest PGAs in the experimental programme (0.813g), the lateral frame drift reaches 0.45% of storey height during the strong motion cycles at approximately 17s. These displacements may be attributable to the lateral component of the brace axial compression force following out-of-plane buckling. Note that the frame has a low stiffness in this direction, and these displacements did not have any influence on the response of the frame in the longitudinal direction.

Longitudinal displacement measurements DXA DXB and DXC were also recorded and their locations were detailed in Chapter 8. These were in place to check that the roof level beams and connections exhibited rigid diaphragm action. An example of this is shown in Figure 9.31(b) where all three measurements are nearly identical.

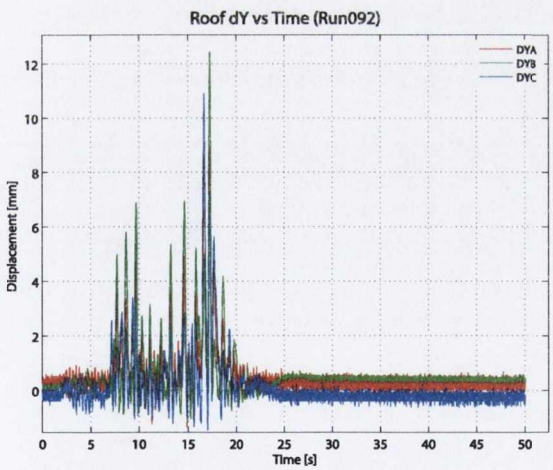

(a) Lateral displacements of DYA, DYB and DYC showing peak displacement at 17s.

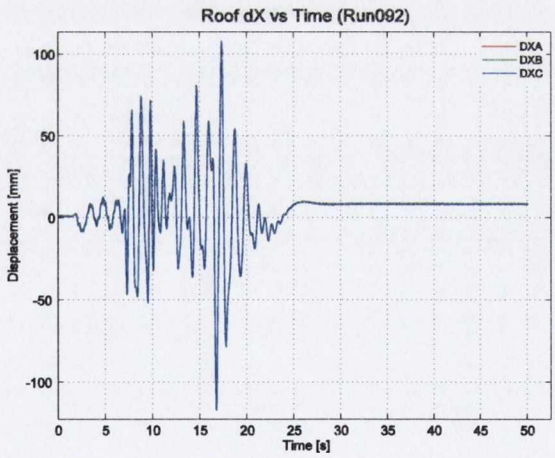

(b) Longitdudinal displacements DXA, DXB and DXC showing roof rigidty

Figure 9.31 – Sample of recorded displacement checks for Run092 with a realised PGA of 0.813.

9.4 Results of White Noise Tests

Table 9.4 presents the results of the white noise tests which were conducted in different runs at the start of each set of tests on a pair of brace-gusset plate specimens, and again after each earthquake excitation test in which brace failure did not occur. Details of the white noise excitation applied are

given in Chapter 8. The objectives of these tests were to evaluate the elastic properties of the structure prior to testing, and the evolution of these properties as the level of excitation applied to the structure increased. In particular, the variation of beam-to-column joint rotation stiffness between brace connection types and designs can influence initial frame stiffness, and the presence of residual global brace deformations following buckling was expected to lead to deterioration of frame stiffness during each earthquake test.

Converting a white noise response signal from the time domain to the frequency domain enables its frequency components to be identified. The structural period can then be identified from the dominant frequency and the structural damping ratio can be established from the HPB method (see Chapter 2). To convert to the frequency domain the Fast Fourier Transform (FFT) algorithm (Cooley and Tukey, 1965) was performed on the original response signal for each white noise test. As an example, the results from Run071 in Test 5 are presented in Figure 9.32. Figure 9.32(a) and (b) show the original white noise response in the time domain and the resulting discrete Fourier transform (DFT) respectively. Accurate experimental measurements using the DFT caused difficulties due to the effect of measurement noise. Therefore, for each DFT, a spectral plot was produced using Welch's method (Welch, 1967). Welch's method is a smoothing algorithm that reduces noise caused by imperfect data in an estimated power spectrum. The resulting spectral density estimation is shown in Figure 9.32(c), where the fundamental frequency is identified at 4.56 Hz and the HPB damping value is estimated at 3.14%.

Table 9.4 presents the target PGA and the actual PGA achieved in each white noise run. The target PGA in nearly all cases was 0.05g, and while the actual values vary about the target value, they are nearly all less than 0.1g. The results presented in the previous section confirm that at this level of excitation, frame response can be expected to remain elastic, without initial brace buckling. Table 9.4 also presents the measured natural frequency (and natural period) and damping of the test frame in each white noise excitation run. These data are examined in more detail in Figure 9.33 - 9.36.

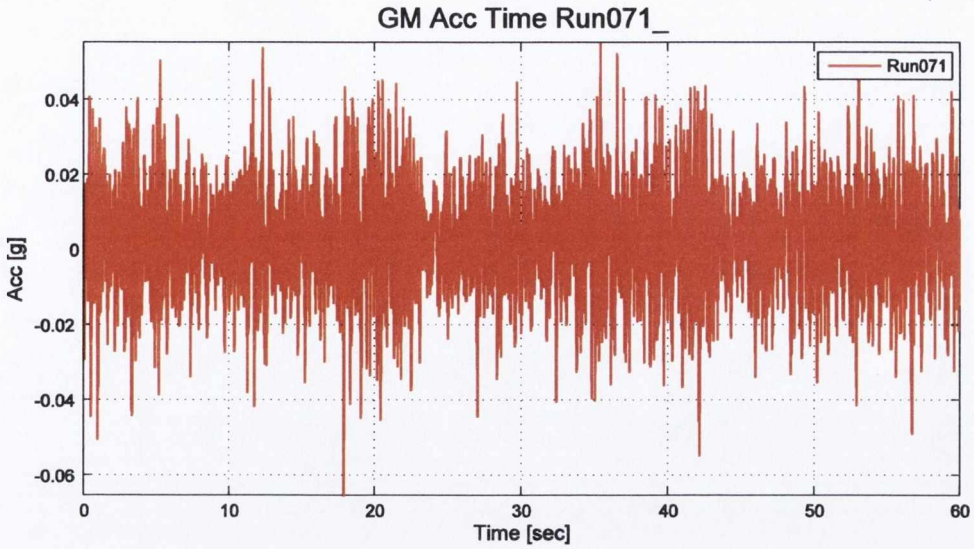

(a) Time history response signal

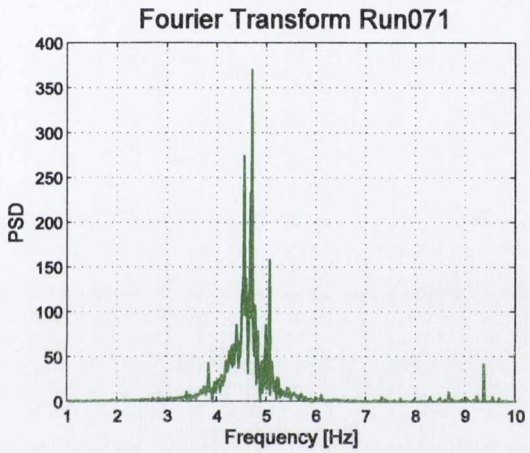

(b) Discrete Fourier transform using FFT algorithm

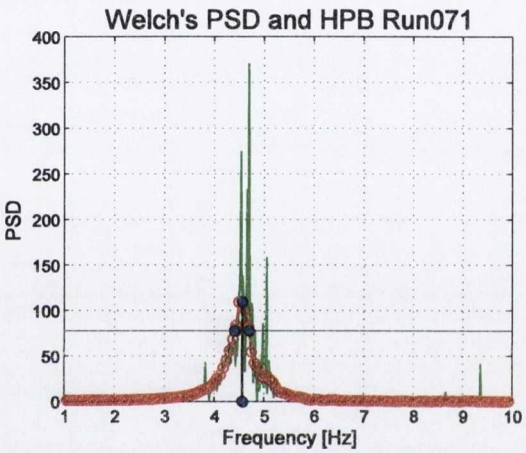

(c) PSD using pwelch (red) and FFT (green) algorithms. HPB points shown in blue.

Figure 9.32 –White noise results and analysis for acceleration response of Run071 (Test 5).

Figure 9.34 compares the initial damping displayed by each test frame before any earthquake tests were performed. The variation is greater than that observed in the natural frequency data, ranging from just below 2% to just over 4.5%. No definite trends are observable in the measured damping data, but frames with CB connections tend to have lower damping than frames with CA connections, and frames with G2 connections tend to have lower damping than frames with G1 connections.

Table 9.4 – White noise test results.

Shake Table Test	Specimen	Run No.	Target PGA (g)	Actual PGA (g)	f_n (Hz)	T_n (s)	ξ_n (%)
P1	S1-CA-G1 (Pre-test)	Run002	0.1	0.087	4.688	0.213	3.53
		Run009	0.1	0.082	4.375	0.229	4.08
P2	S1-CB-G1 (Pre-test)	Run015	0.1	0.064	4.438	0.225	2.67
		Run018	0.1	0.078	4.438	0.225	3.98
		Run020	0.1	0.067	4.313	0.232	3.99
1	S1-CA-G1	Run023	0.05	0.636	4.625	0.216	3.56
		Run029	0.05	0.081	4.625	0.216	3.12
		Run031	0.05	0.086	4.594	0.218	3.13
2	S3-CA-G1	Run034	0.05	0.067	4.25	0.235	2.5
		Run038	0.05	0.064	4.25	0.235	3.55
		Run040	0.05	0.066	3.313	0.302	4.61
		Run042	0.05	0.071	1.813	0.552	6.5
3	S4-CA-G1	Run045	0.05	0.090	4.438	0.225	4.58
		Run049	0.05	0.074	4.438	0.225	4.17
		Run051	0.05	0.101	4.25	0.235	3.04
		Run053	0.05	0.062	2.688	0.372	5.19
		Run055	0.05	0.075	1.5	0.667	6.16
4	S2-CA-G1	Run057	0.01	0.011	-	-	-
		Run058	0.05	0.071	4.5	0.222	4.05
		Run066	0.05	0.091	4.5	0.222	3.62
		Run068	0.05	0.081	4.063	0.246	3.31
5	S1-CA-G2	Run071	0.05	0.068	4.563	0.219	3.14
		Run079	0.05	0.078	4.438	0.225	3.45
		Run081	0.05	0.075	4.063	0.246	3.48
6	S2-CA-G2	Run083	0.01	0.010	-	-	-
		Run084	0.05	0.058	4.438	0.225	2.6
		Run089	0.05	0.076	4.5	0.222	3.61
		Run091	0.05	0.071	3.813	0.262	4.37
		Run093	0.05	0.051	1.563	0.64	5.98
7	S3-CA-G2	Run095	0.01	0.028	-	-	-
		Run096	0.05	0.064	4.063	0.246	3.6

		Run100	0.05	0.061	3.813	0.262	3.94
		Run102	0.05	0.091	2.375	0.421	13.61
		Run104	0.05	0.070	1.5	0.667	6.23
		Run106	0.01	0.032	-	-	-
		Run107	0.05	0.052	4.438	0.225	1.98
8	**S1-CB-G1**	Run114	0.05	0.037	4.688	0.213	3.35
		Run116	0.05	0.049	4.375	0.229	1.49
		Run118	0.05	0.048	4.438	0.225	2.41
		Run121	0.05	0.052	3.875	0.258	4.27
9	**S2-CB-G1**	Run126	0.05	0.054	4.063	0.246	3.28
		Run128	0.05	0.045	2.313	0.432	4.84
		Run130	0.01	0.052	-	-	-
		Run131	0.03	0.035	4.125	0.242	1.93
10	**S4-CB-G2**	Run135	0.05	0.043	3.813	0.262	1.25
		Run137	0.05	0.041	3.375	0.296	4.91
		Run139	0.05	0.043	1.25	0.8	11.33
		Run142	0.01	0.040	4.563	0.219	2.93
		Run147	0.05	0.036	4.313	0.232	2.84
11	**S2-CB-G2**	Run149	0.05	0.069	2.75	0.364	4.67
		Run151	0.05	0.042	1.125	0.889	14.6
		Run153	0.01	0.039	4.063	0.246	2.12
12	**S3-CB-G2**	Run157	0.05	0.039	3.688	0.271	3.54
		Run159	0.05	0.050	1.188	0.842	24.94

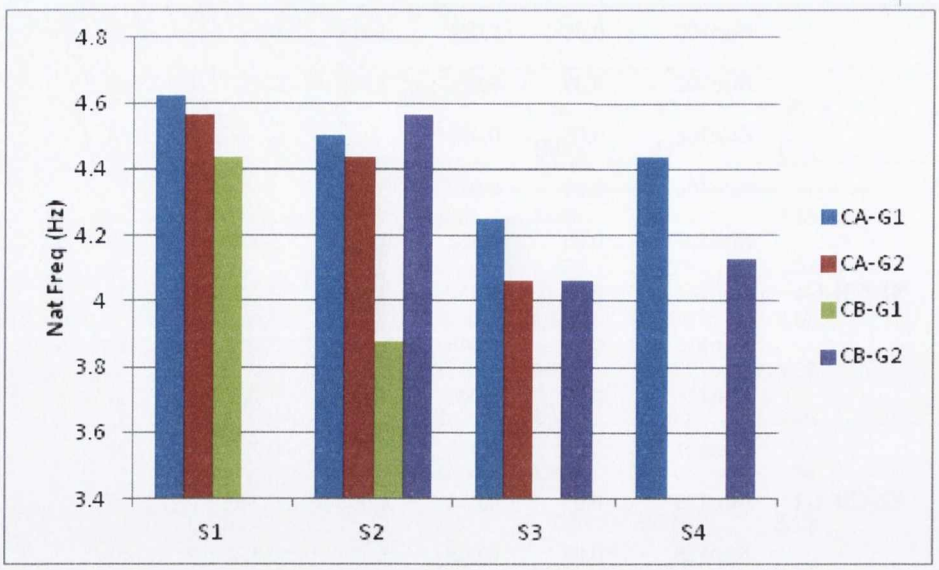

Figure 9.33 – Initial natural frequency of test frame by gusset specimen.

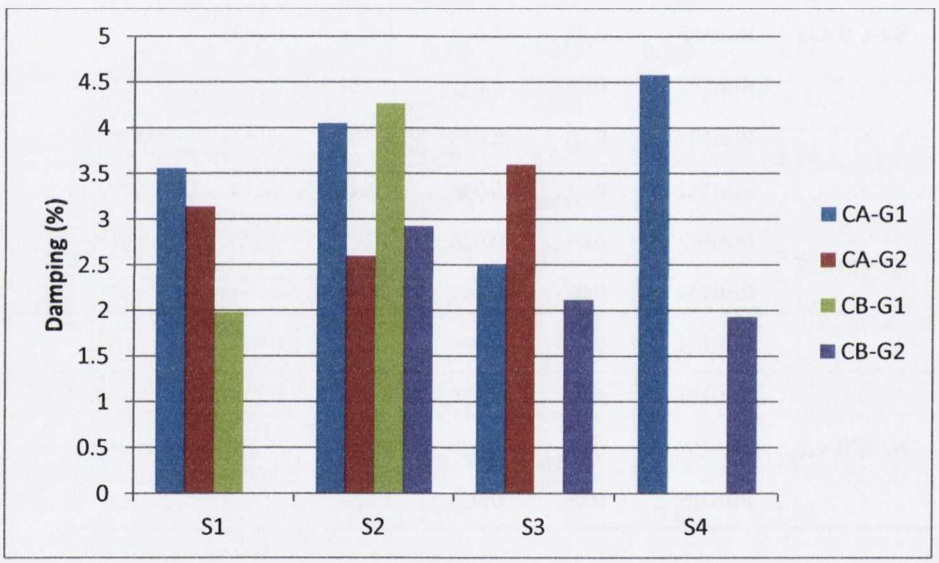

Figure 9.34 – Initial damping of test frame by brace-gusset specimen.

As both stiffness/natural frequency and damping are amplitude dependent, Figure 9.35 presents the variation in these properties with the actual PGA realized in each white noise test. Separate plots are presented for frames with CA and CB brace connections. The data suggest that the differences in excitation level between the white noise tests were not sufficiently large to affect either property in a consistent manner. Comparison of the different plots indicates that when all white noise tests are considered (i.e. not just the initial tests examined in Figure 9.33 and Figure 9.34), frames with CA and CB brace connections do not display substantially different stiffness or damping characteristics.

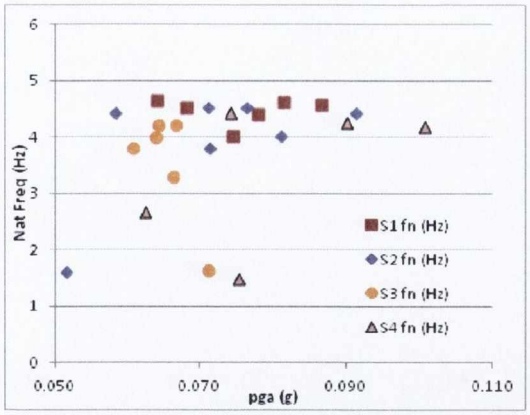

(a) natural frequency, CA connections

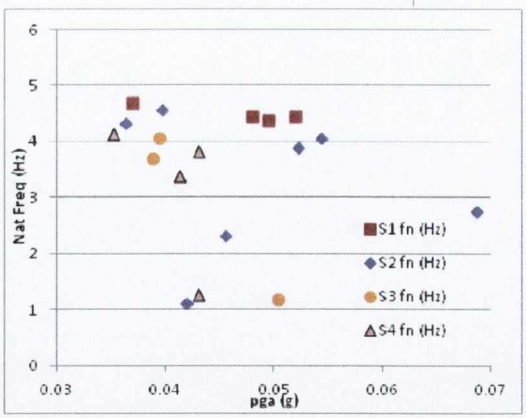

(b) natural frequency, CB connections

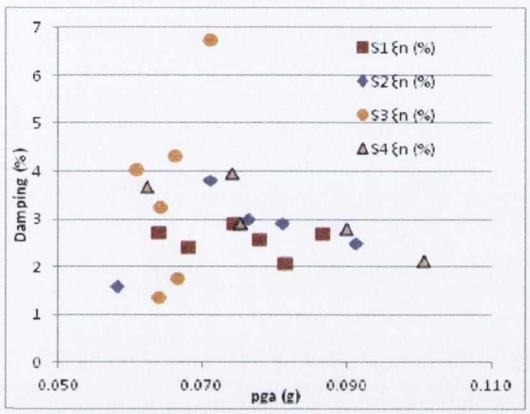

(c) damping, CA connections

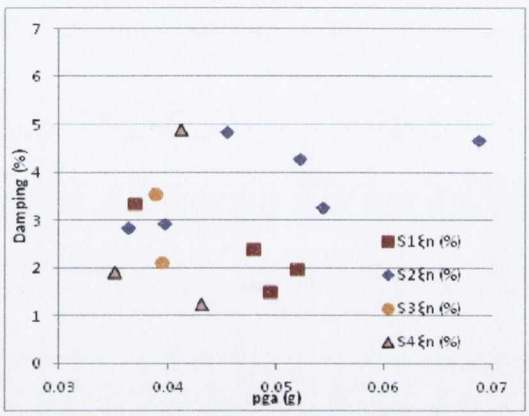

(d) damping, CB connections

Figure 9.35 – Variation of natural frequency and damping with PGA in white noise tests.

Response history, especially in the plastic range, is expected to influence the stiffness and damping characteristics of CBFs. This is investigated in Figure 9.36 which presents the variation in frame natural frequency and damping with the maximum frame drift experienced in the earthquake test run immediately preceding each white noise run. Both frame properties are seen to be strongly influenced by this response variable, which reflects in particular the residual out-of-plane brace deformation at the end of the earthquake test run. Frame stiffness is observed to reduce, and damping is observed to increase, with the previous maximum drift experienced by the frame. These results have implications for the acceleration and displacement response amplification experienced by the test frame in the later earthquake excitation runs in each test.

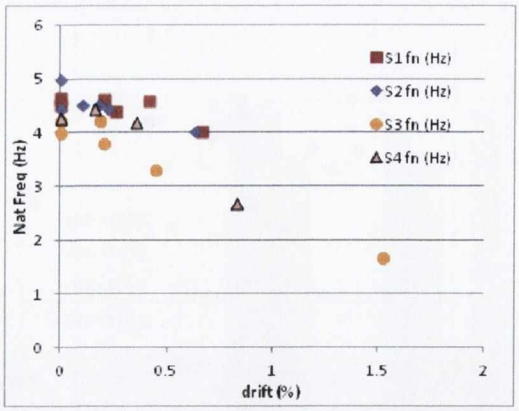

(a) natural frequency, CA connections

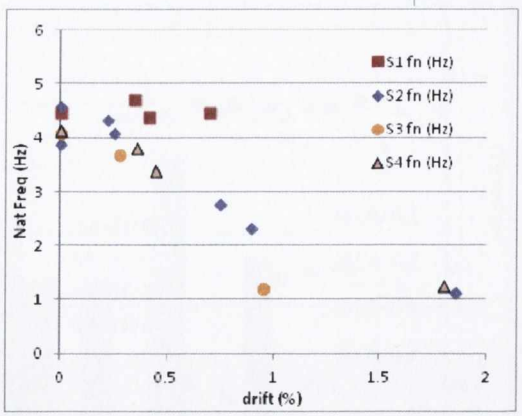

(b) natural frequency, CB connections

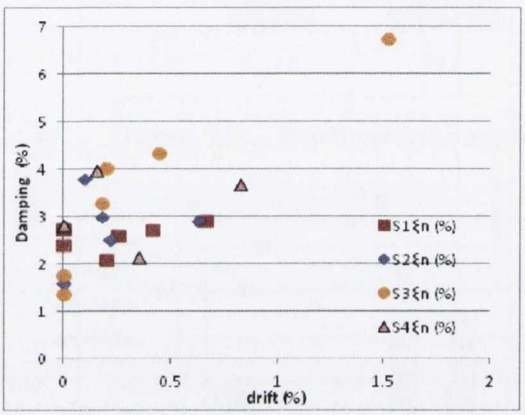

(c) damping, CA connections

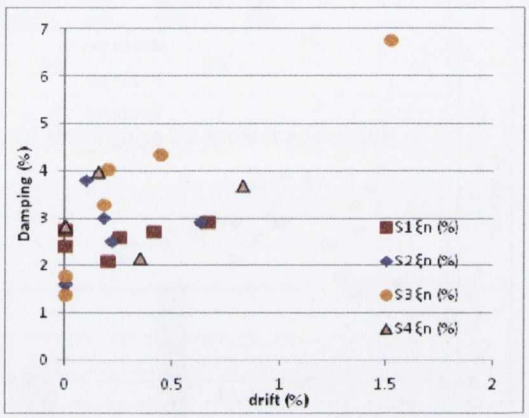

(d) damping, CB connections

Figure 9.36 – Variation of natural frequency and damping in white noise tests with maximum drift demand in previous run.

Figure 9.37 examines the evolution of frame natural frequency in each individual test, grouped by brace-gusset specimen cross-section size. In Figure 9.37(a), the natural frequency of the frame with S1 (80×80×3.0) cross-sections does not reduce much between the initial and final runs because the maximum drift demand (in the 10%/50 earthquake test run) remained less than 1%, and the brace had not experienced large out-of-plane buckling deformations. In contrast, Figure 9.37(b)-(d) display large reductions in natural frequency after the later runs (10%50 and 2%/50 where additional failure level earthquake runs were executed). The S2, S3 and S4 cross-section sizes in these specimens lead to larger out-of-plane brace buckling slendernesses, and larger brace buckling deformations.

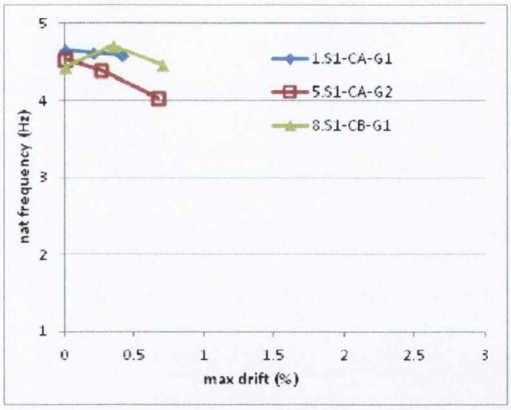

(a) S1

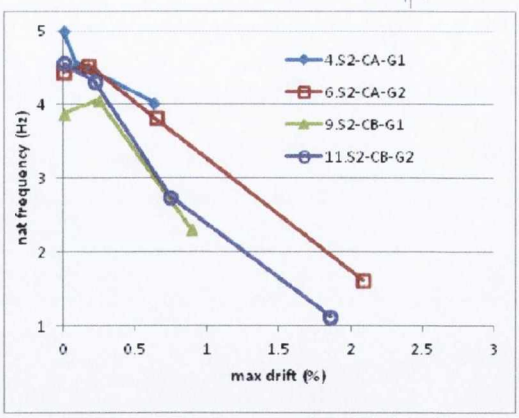

(b) S2

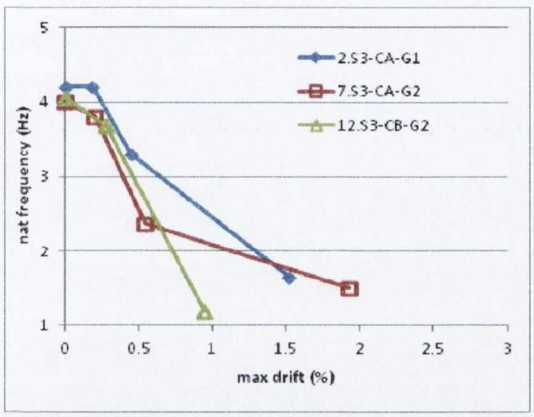

(c) S3

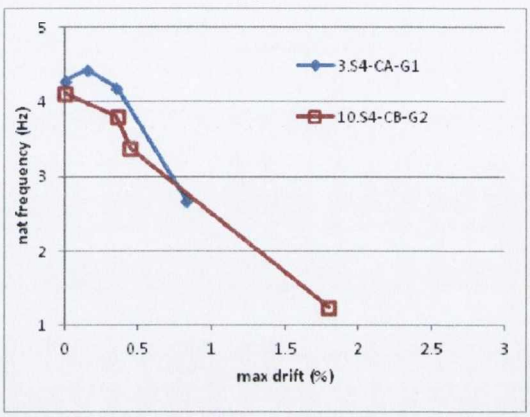

(d) S4

Figure 9.37 – Evolution of natural frequency with previous maximum drift demand in individual tests by brace-gusset plate specimen cross section

9.5 Earthquake Excitation Tests: Analysis of Results

In this section the frame response in the different earthquake excitation tests is compared. The focus is on the variation in maximum response quantities (drift, forces, etc.) between earthquake excitation runs in an individual test, and between different tests. Table 9.5 presents the maximum values of response (roof) acceleration and relative displacement experienced in any of the earthquake runs in a test. The maximum measured brace forces and elongation values are also presented.

Table 9.5 – Overview of BRACED project test specimens with maximum key parameters listed.

Test	Specimen	Max. Actual PGA (g)	Max. Roof Accel. (g)	Max. Relative Disp. (mm)	Max. Brace Tension Force (kN)	Max. Brace Compression Force (kN)	Max. Brace Elongation (mm)
1	S1-CA-G1	0.564	0.869	29.4	349	277	15.3
2	S3-CA-G1	0.670	0.929	58.8	275	193	37.6
3	S4-CA-G1	0.718	0.810	70.1	234	193	43.5
4	S2-CA-G1	0.646	0.936	42.3	325	197	30.45
5	S1-CA-G2	0.766	1.373	47.6	345	294	29.1
6	S2-CA-G2	0.809	1.113	67.1	342	226	40.5
7	S3-CA-G2	0.579	3.224	89.2	296	153	57.0
8	S1-CB-G1	0.825	4.041	46.6	316	326	22.6
9	S2-CB-G1	0.416	0.857	31.7	312	190	14.9
10	S4-CB-G2	0.746	5.543	103.7	275	204	62.6
11	S2-CB-G2	0.681	1.068	51.2	334	207	31.0
12	S3-CB-G2	0.466	0.735	57.7	309	113	35.8

9.5.1 Maximum Drift Demand

Figure 9.38 compares the variation in maximum drift demand with PGA displayed in each test. The results are grouped by brace-gusset plate specimen cross-section size. The larger cross sections (S1 and S2) display a mostly linear relationship between drift and PGA, while the smaller cross sections (S3 and S4) exhibit increasing drift values for higher PGA. This behaviour may be expected in short period structures that are subjected to ground excitations substantially greater than those required for initial yield.

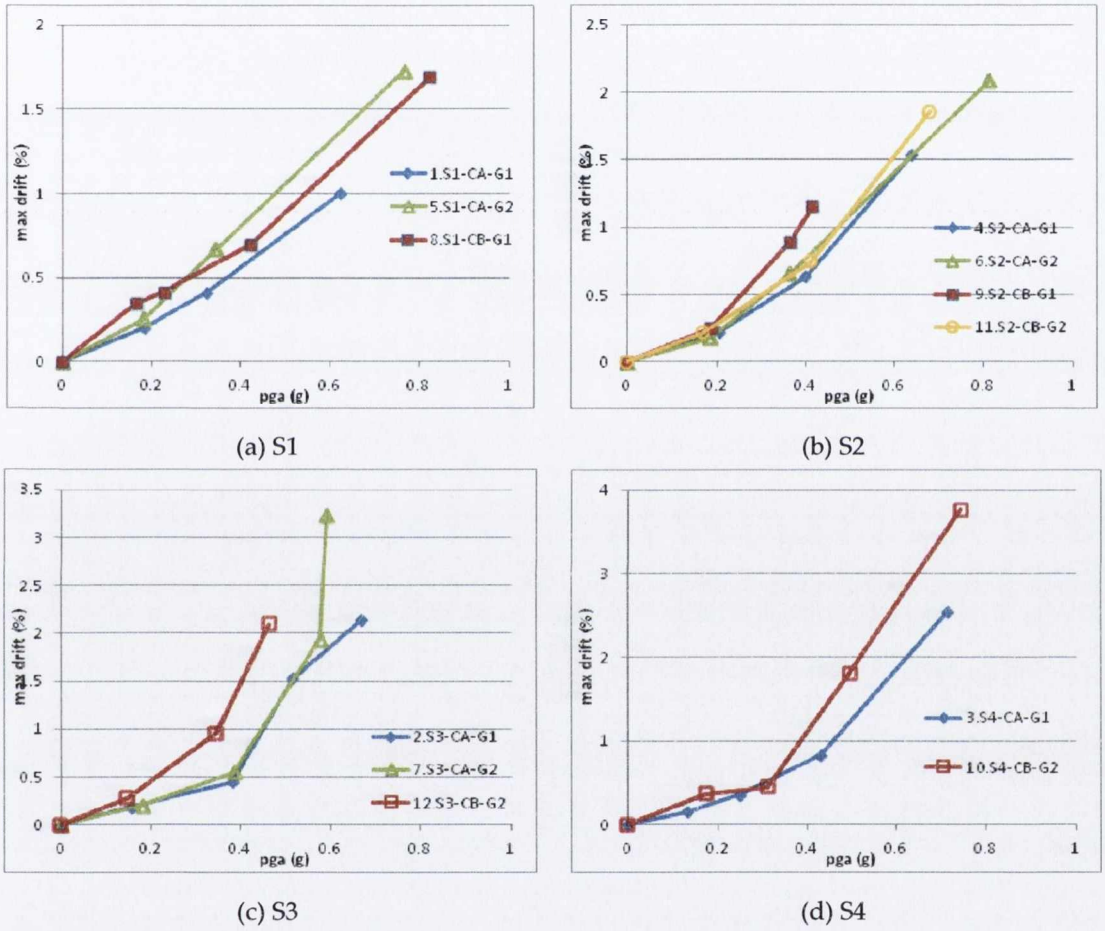

(a) S1 (b) S2

(c) S3 (d) S4

Figure 9.38 – Variation of maximum storey drift demand with PGA by specimen cross section.

Figure 9.39 presents the same variation in maximum drift demand with PGA for test, but with the plots grouped by brace-gusset plate specimen connection type. The individual connection types do not display consistent trends with both practically linear and nonlinear trends displayed in each graph. For example, for the CA-G2 connection type tests examined in Figure 9.39(b), a linear PGA - maximum drift relationship is exhibited in Tests 5 and 6, while a nonlinear relationship is exhibited Test 7. The results indicate that while drift demand is sensitive to brace strength, it is not strongly influenced by connection configuration and design.

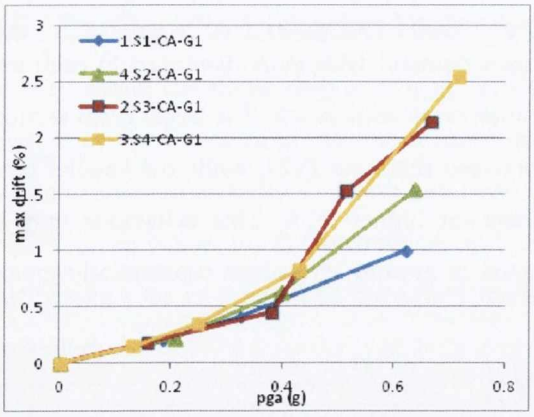

(a) CA-G1

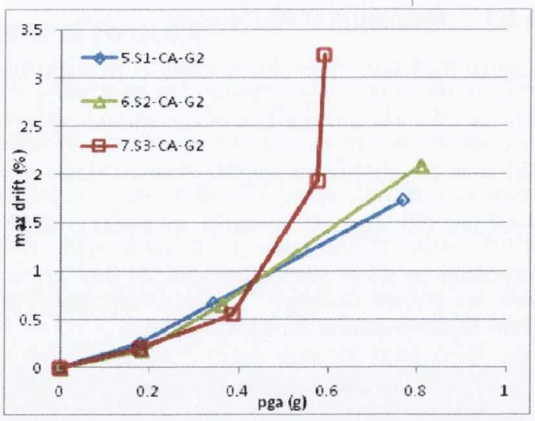

(b) CA-G2

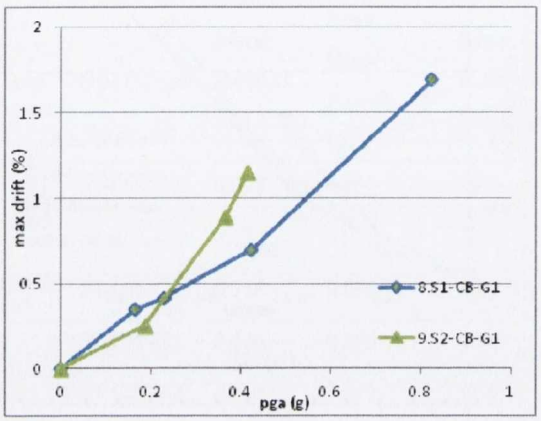

(c) CB-G1

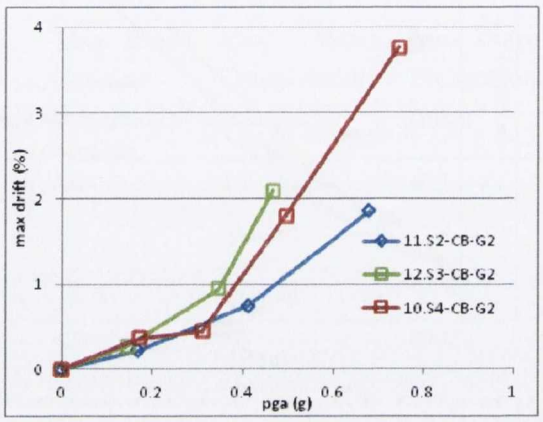

(d) CB-G2

Figure 9.39 – Variation of maximum storey drift demand with PGA by specimen connection type.

9.5.2 Maximum Brace Elongation and Shortening

Brace elongation (in tension) and shortening (in compression) are strongly dependent on frame drift. Figure 9.40 examines the relationship between brace elongation/shortening and both PGA and drift for the case of Test 5. All other tests exhibited similar trends, which in the elongation/shortening versus drift cases is an expression of the kinematic behaviour of the model CBF.

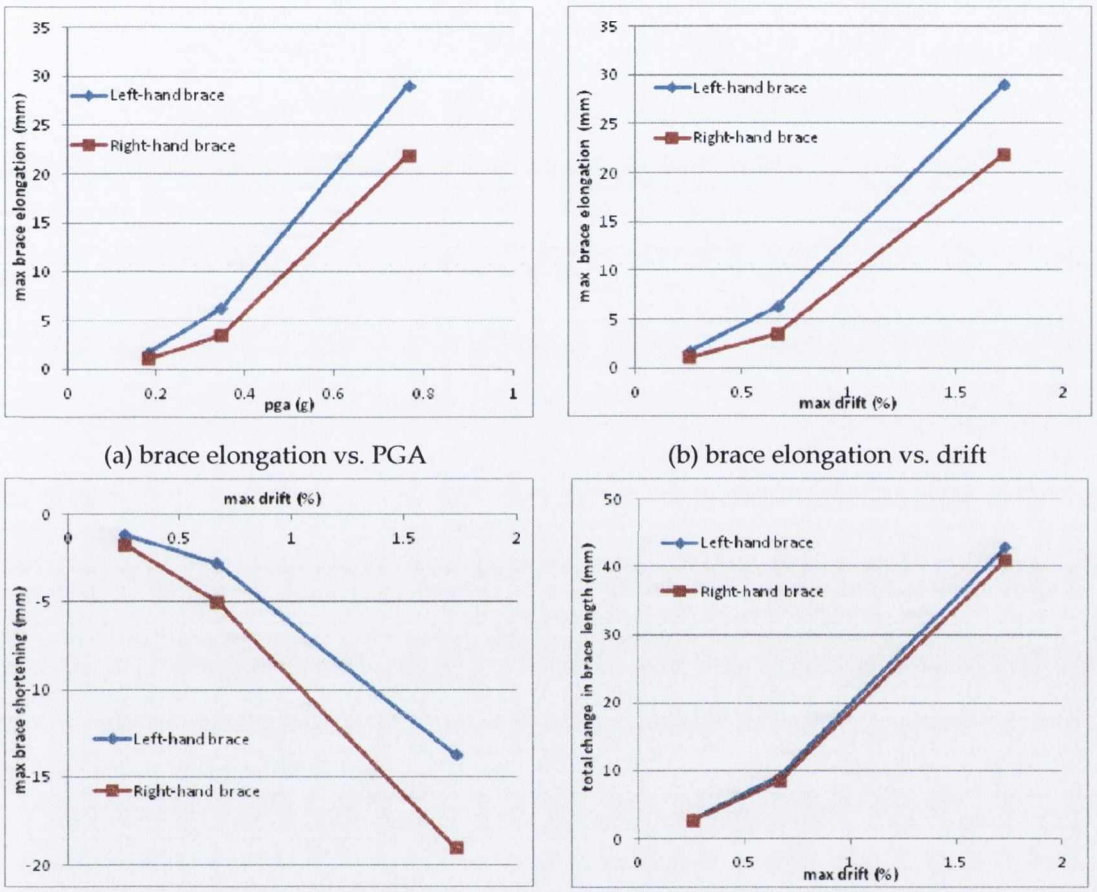

(a) brace elongation vs. PGA

(b) brace elongation vs. drift

(c) brace shortening vs. drift

(d) total length change vs. drift

Figure 9.40 – Maximum brace elongation and shortening in Test 5 runs.

9.5.3 Maximum Brace Forces

The maximum brace forces measured in any earthquake excitation test run are compared in Figure 9.41 – Figure 9.43, which present the variation in normalized brace tension or compression force with PGA. The normalized force values shown are the highest tension or compression forces measured in either test, normalized by the characteristic plastic resistance, $N_{pl,meas}$, of the brace cross-section or the characteristic buckling strength, $N_{b,meas}$, of the brace member. The $N_{pl,meas}$ and $N_{b,meas}$ values employed are presented in Table 8.3 and were calculated using characteristic material strengths measured in coupon tests and an effective length factor of 1.0.

The normalized brace tension forces presented in Figure 9.41 allow the test run in which brace tensile yielding occurred to be identified. In all tests, the maximum tension forces experienced in the 50%/50 level runs remained well below yield, typically in the range 0.3-0.6 $N_{pl,meas}$. Tensile yielding occurred in approximately half of the 10%/50 runs and all but one of the 2%/50 runs. The maximum tension forces experienced in the different tests are in the range 1.0-1.25 $N_{pl,meas}$. The differences between the PGA values at brace yield and brace failure reflect brace ductility capacity in each test. This is discussed in later sections, but in Figure 9.41 appears to be least for the specimens with S1 cross-sections.

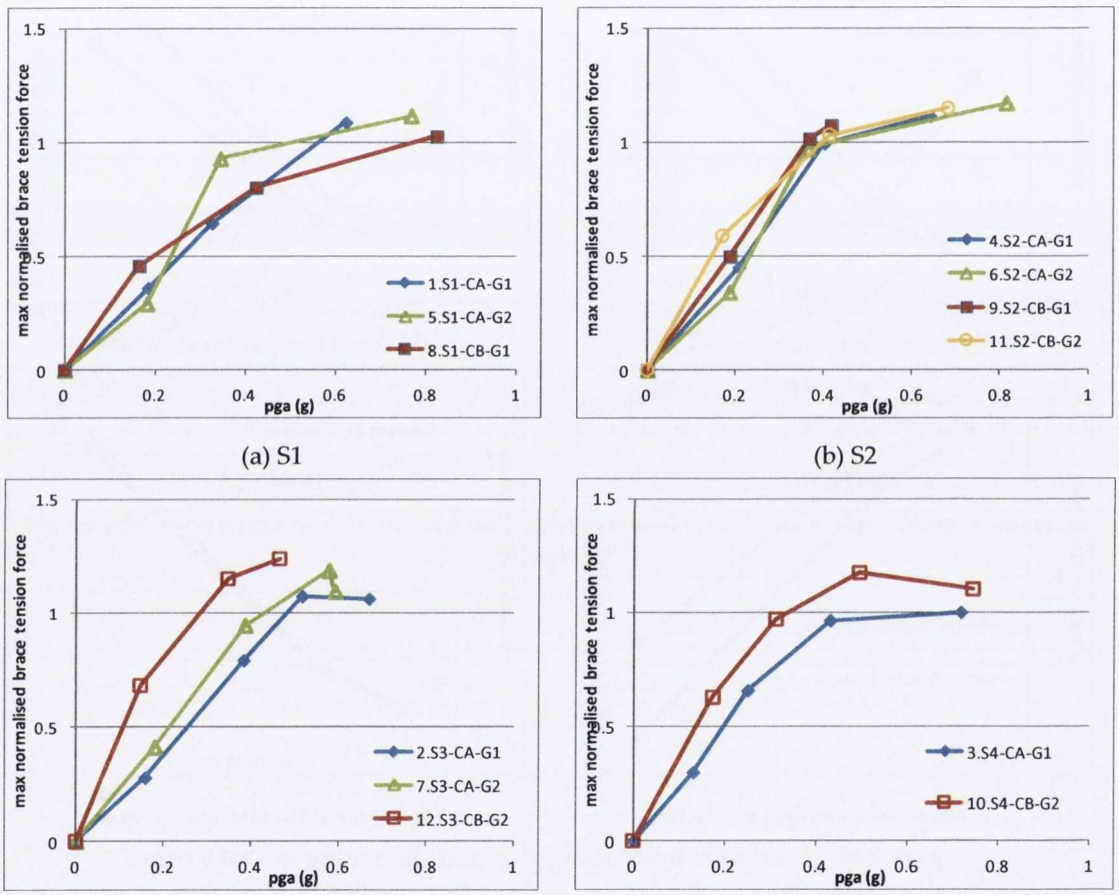

(a) S1 (b) S2

(c) S3 (d) S4

Figure 9.41 – Variation of maximum normalised brace tension force with PGA, by specimen cross-section (maximum brace tension force recorded during experiments normalised with plastic section capacity from characteristic strength tests).

Figure 9.42 compares the observed variations in normalized brace tension force with PGA for each specimen connection type. In Figure 9.42(c), the two CB-G1 specimens tested fractured with PGA values that were only slightly greater than the PGA values for brace yield. The CB-G2 plots shown in Figure 9.42(d) exhibit a more ductile behaviour. The same pattern is observable when comparing the CA-G1 and CA-G2 plots in Figure 9.42(a) and (b), respectively, but the in a less obvious sense.

Overall the results suggest that the use of a G2 (balanced) gusset plate design instead of a G1 (conventional) design leads to brace fracture at higher PGA values and higher maximum brace tension forces. When comparing CA and CB connections (Figure 9.42(a) and (b) with (c) and (d)), no clear patterns emerge from the results as the data set is too small.

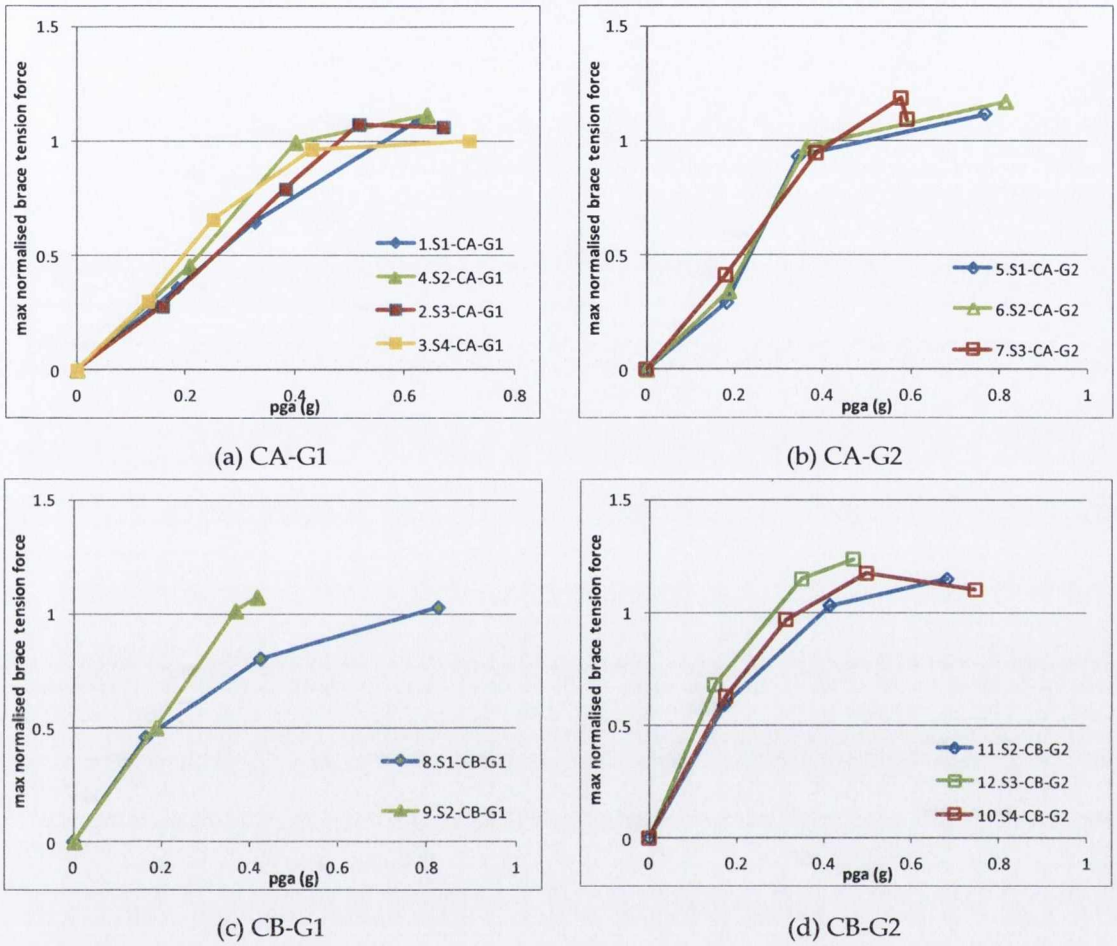

(a) CA-G1

(b) CA-G2

(c) CB-G1

(d) CB-G2

Figure 9.42 – Variation of maximum normalised brace tension force with PGA, by specimen connection type (maximum brace tension force recorded during experiments normalised with plastic section capacity from characteristic strength tests).

Figure 9.43 compares the maximum normalized brace compression forces measured in each test run by brace specimen cross-section size. The maximum values for each test are all significantly higher than 1.0, confirming that the actual effective lengths of the braces are less than the value of 1.0 used to calculated the $N_{b,meas}$ values presented in Table 8.3. These maximum values generally lie in the range 1.5 to 2.0, which is consistent with an effective length factor of approximately 0.75. Clearly there is substantial variation in these values between tests, which are influenced by the rotational restraint imposed by the different gusset plate connection types and, to a lesser extent, the MTS swivel bearing.

The maximum normalized values observed in each test occurred at different excitation levels, but never in the first 50%/50 level run. There is significant between-test variation in the values observed in these 50%/50 runs, and values above 1.0 should not be taken to imply brace buckling due to the effective length factor employed, as described above. The plots do confirm, however, that brace buckling occurred in all 10%/50 level runs.

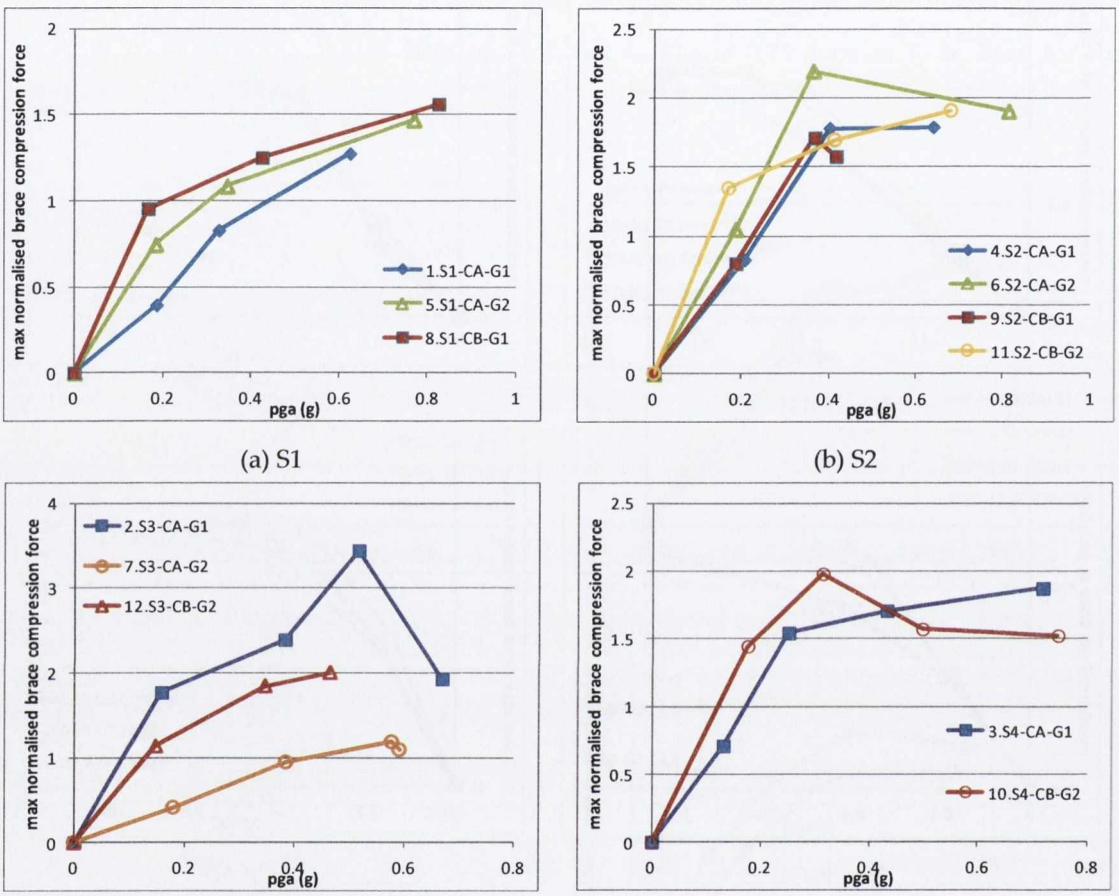

(a) S1 (b) S2

(c) S3 (d) S4

Figure 9.43 – Variation of maximum normalised brace compression force with PGA, by specimen cross-section (maximum brace compression force recorded during experiments normalised with plastic section capacity from characteristic strength tests).

Figure 9.44 examines the maximum normalized brace compression forces by connection type. There is significant variation between the curves presented in each Figure 9.44(a)-(d), and no clear trends are discernable.

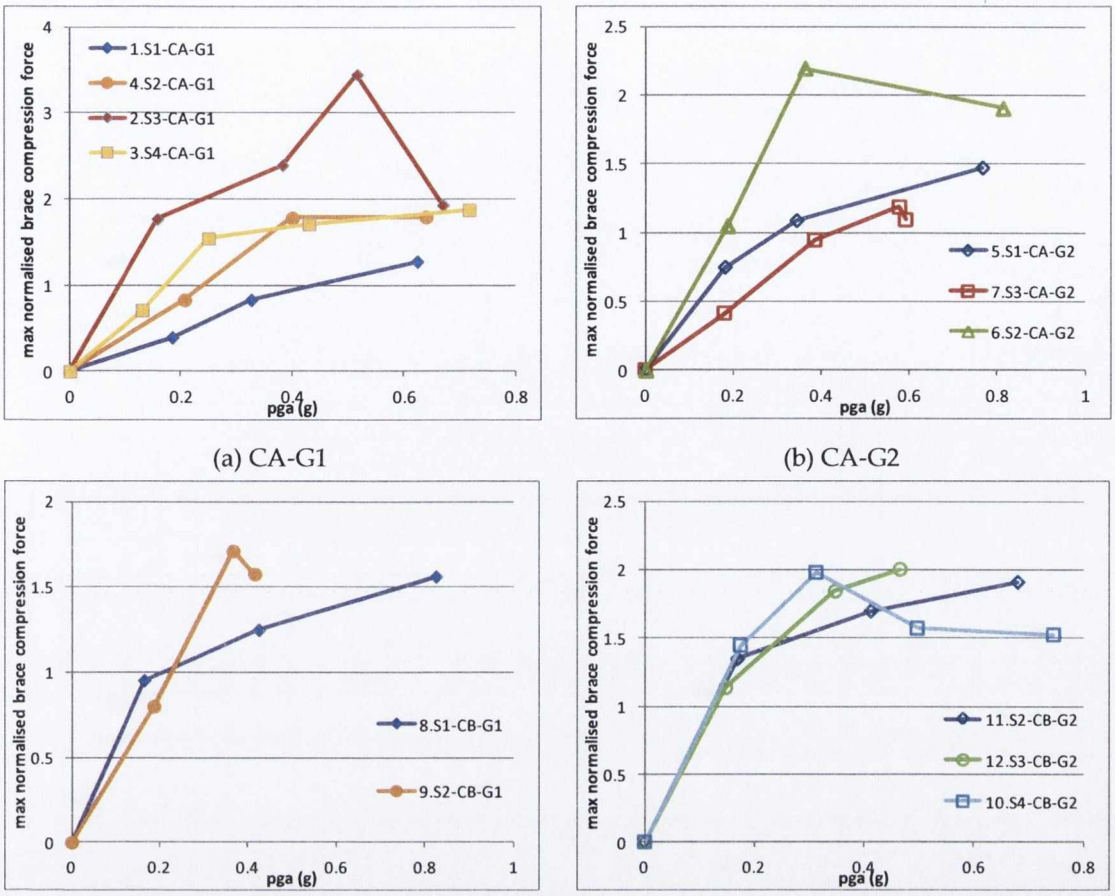

(a) CA-G1

(b) CA-G2

(c) CB-G1

(d) CB-G2

Figure 9.44 – Variation of maximum normalised brace compression force with PGA, by specimen connection type.

9.5.4 Maximum Brace Force-Drift Response

The maximum frame drift and brace force data considered above can be combined to give a high-level indication of the influence of brace-gusset plate specimen connection type on the global ductility capacity of the test frame. The design of the experimental programme provided pairs of tests in which the specimens differ in only one of the main test variables (brace cross-section, connection type and gusset plate design). Figure 9.45 compares the response of pairs of tests which both employed the same brace cross-section, but different connection details. The plots shown compare the variation in the maximum normalized brace force observed in each run (as in Figure 9.41- Figure 9.43) with the maximum drift experienced by the test frame in that run (as in Figure 9.38 and Figure 9.39). The labels indicate the brace cross-section size considered and whether the conventional or balanced gusset-plate design approach was employed. CB-type connections are indicated by the description 'beam only' in brackets.

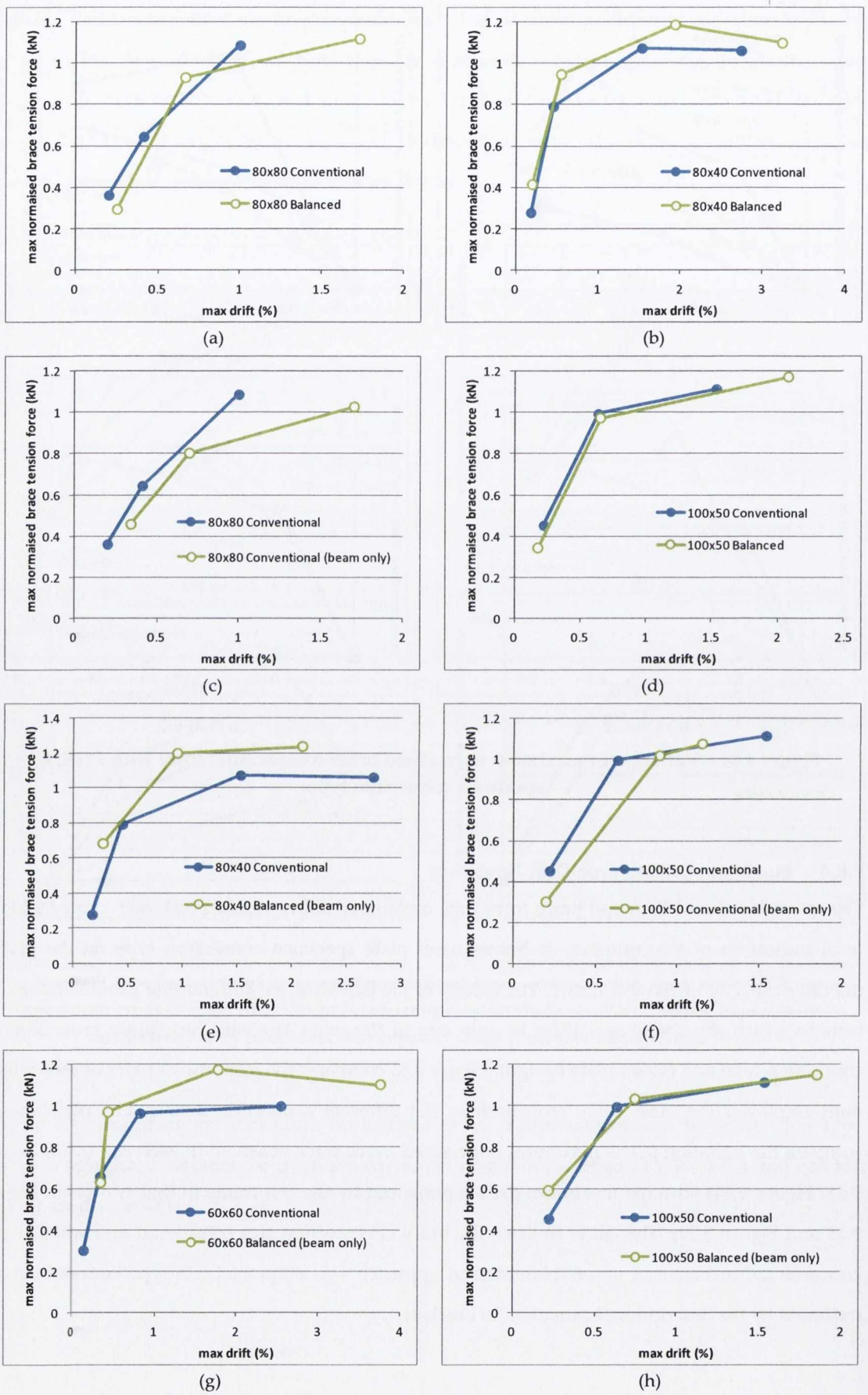

Figure 9.45 – Variation of maximum normalised brace force with maximum drift demand.

Three plots compare the application of the G1 (conventional) and G2 (balanced) design methods to CA-type connections (Figure 9.45(a), (b) and (d)). In each case, the G2 (balanced) design reaches a larger drift before brace fracture. This is especially noticeable with the 80x80 specimens in which the conventional design experienced brace fracture at a drift of only 1%. The maximum brace forces are also greater in the G2 (balanced) design cases.

Two plots compare the behaviour of the test frame with G1 (conventional) gusset plate design, but applied to CA (beam and column) and CB (beam only) connection types (Figure 9.45(c) and (f)). The results are not consistent – for the 80x 80 braces the CB (beam only) connection case experienced fracture at a larger drift than the CA (beam and column) connection case, but the opposite is true for the 100x50 braces.

Three plots compare the behaviour of frame with CA-G1 (conventional, beam and column) connections and with CB-G2 (balanced, beam only) connections (Figure 9.45(e), (g) and (h)). In the 80x40 case, the CA-G1 (conventional) design reached a larger drift in its failure run than the CB-G2 (balanced, beam only) design, but with lower normalized brace resistance. In contrast, with 100x50 and 60x60 braces, larger drifts were reached by the CB-G2 (balanced, beam only) cases without any reduction in maximum brace forces.

Overall, the comparisons presented in Figure 9.45 support the hypothesis that the use of the balanced gusset plate design method leads to a more ductile and dissipative response in CBFs without loss of brace resistance.

9.5.5 Brace Ductility

Table 9.6 presents the observed displacement ductility capacity of the brace-gusset plate specimens. The brace ductility capacity values shown are obtained by normalizing the brace fracture elongation by the brace yield displacement. The brace fracture elongation is the maximum measured change in overall brace length in a fractured brace during the earthquake test run in which that brace fractured. This change in length may be an increase in length (elongation under tension) or a reduction in length (shortening under compression) and includes the effects of axial deformations in the tube length and gusset plate strains. Details of the measurement of this response variable were provided in Chapter 8. The brace yield displacement is obtained by multiplying the length of the unstiffened brace tube by its characteristic yield strain, identified from the results of the characteristic steel strengths measured in the coupon tests presented in Chapter 8.

The measured brace displacement ductility capacities vary between 2.9 and 12.0, with a mean value of $\mu_\Delta = 7.5$. The variation between the values identified in each test is attributable to the main

test specimen parameters: member slenderness, cross-section slenderness, connection type and gusset plate design method. The influence of these parameters is investigated in Figure 9.46 and Figure 9.47.

Figure 9.46Figure 9.47 compares the displacement ductility capacity of the different brace-gusset plate specimens, by cross-section size and connection properties. Figure 9.46(a) indicates that larger ductility capacities were displayed by specimens with smaller cross sections (S3 and S4). Figure 9.46(b) confirms that the use of the balanced gusset design approach (G2) leads to larger brace ductility capacity than the conventional approach (G1). In the four cases where direct comparison can be made, the improvement ranges from 30% to 140%, with a mean improvement of 80%. Figure 9.46(c) suggests that CA type brace connections to the beam and column lead to larger ductility capacity than CB type connections to the beam alone, although the data is not entirely consistent in this regard.

Table 9.6 – Brace displacement ductility capacity.

Test	Specimen	Brace Fracture Elongation (mm)	Brace Yield Displacement (mm)	Brace Ductility Capacity
1	S1-CA-G1	12.8	4.4	2.9
2	S3-CA-G1	37.6	4.5	8.3
3	S4-CA-G1	43.5	4.1	10.6
4	S2-CA-G1	25.3	4.0	6.3
5	S1-CA-G2	29.1	4.1	7.0
6	S2-CA-G2	40.5	4.2	9.7
7	S3-CA-G2	49.1	4.5	10.9
8	S1-CB-G1	24.9	3.9	6.3
9	S2-CB-G1	12.8	4.0	3.2
10	S4-CB-G2	49.5	4.1	12.0
11	S2-CB-G2	25.3	4.1	6.2
12	S3-CB-G2	27.0	4.4	6.2

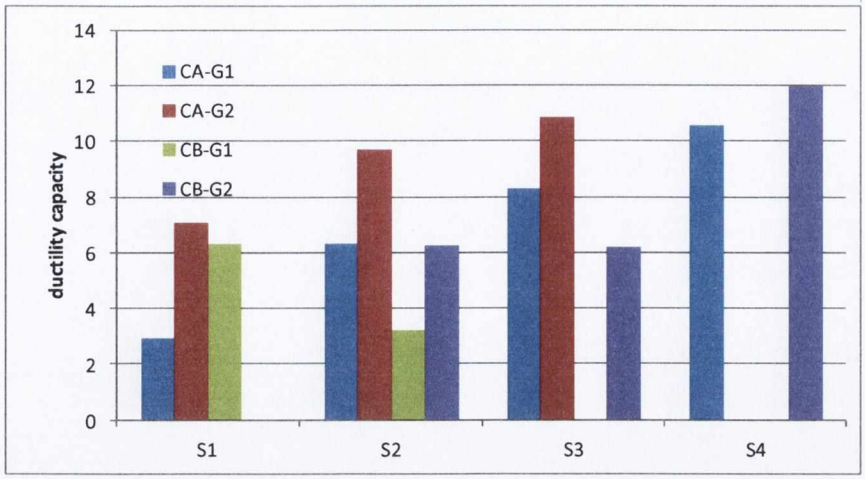

(a) brace displacement ductility capacity by brace-gusset plate specimen characteristics

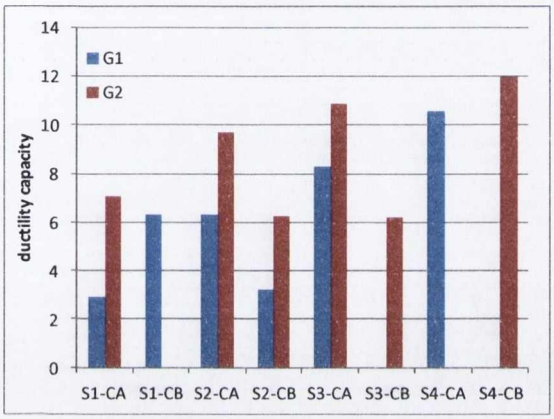

(b) comparison of conventional (G1) and balanced (G2) gusset plate designs

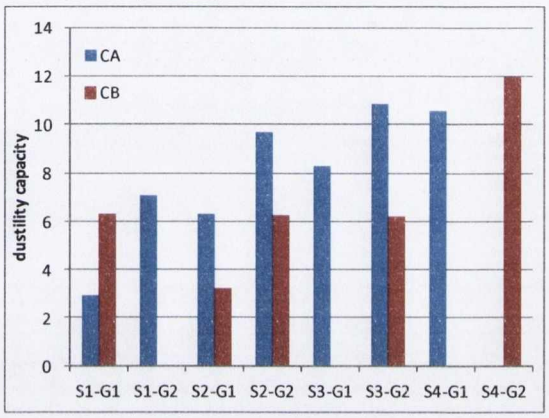

(c) comparison of beam and column (CA) and beam only (CB) brace connections

Figure 9.46 – Brace displacement ductility capacity.

The influence of brace member slenderness, $\bar{\lambda}_{Rd}$, cross-section slenderness, b/t, and gusset plate design factor, β_{ww}, on measured ductility capacity is presented in Figure 9.47(a)-(c) respectively. The expected trends are observable: ductility capacity increases with increasing $\bar{\lambda}_{Rd}$ and β_{ww}, and reduce with increasing b/t ratio. The results display large scatter but the trends are evident.

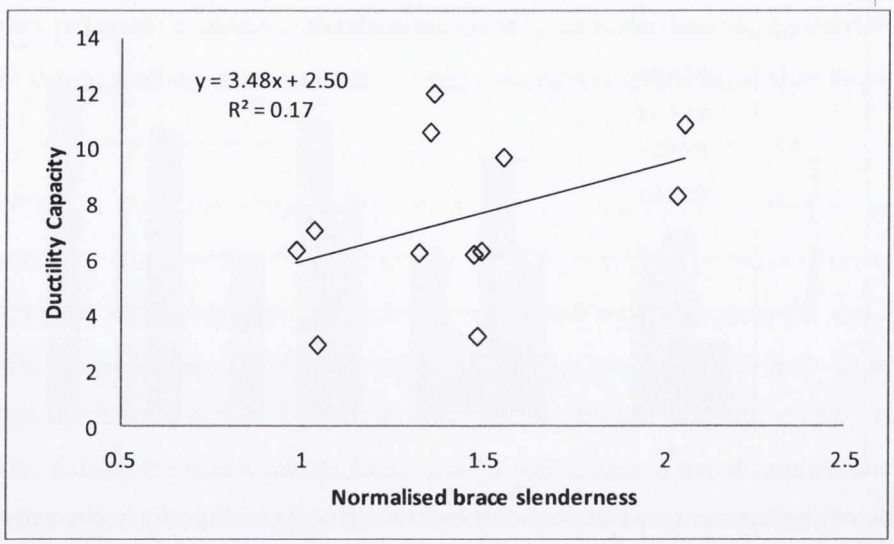

(a)

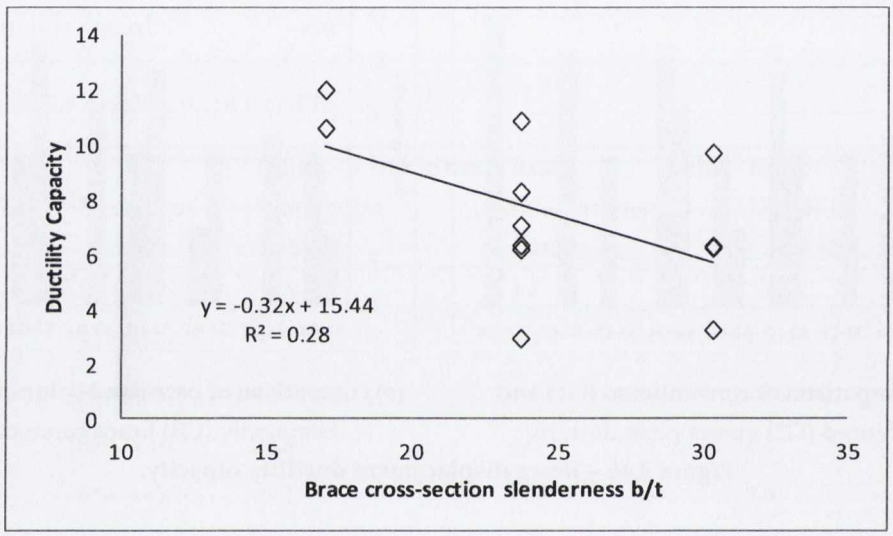

(b)

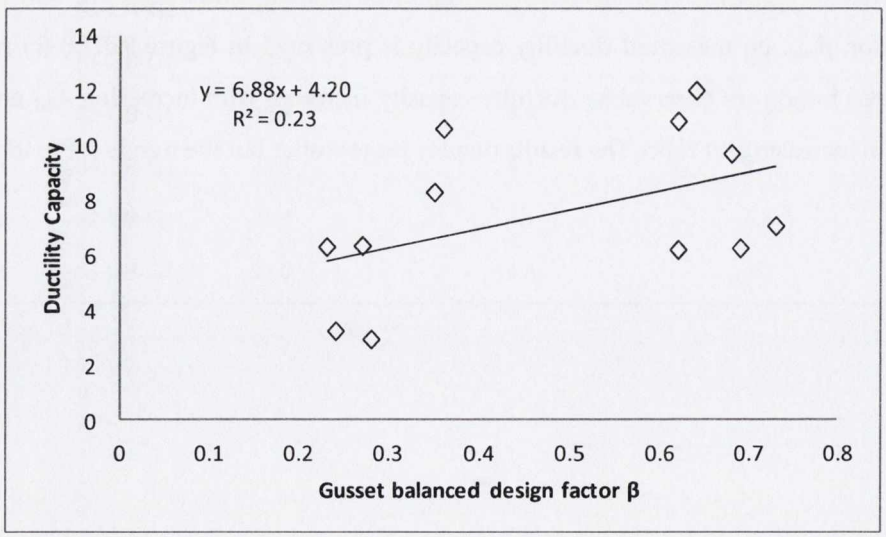

(c)

Figure 9.47 – Variation of measured braced ductility capacity with (a) brace member slenderness,

$\bar{\lambda}_{Rd}$; (b) brace cross-section slenderness, b/t; and (c) gusset plate balanced design factor, β_{ww}.

The variation of ductility capacity with member and section slenderness has been observed in a number of previous experimental studies that examined the response of hollow section steel members under cyclic axial loading. These studies gave rise to the empirical parametric prediction equations for brace displacement ductility capacity presented in Equations 2.16 - 2.21. Figure 9.48 compares the displacement ductility capacity values measured in the dynamic shaking table tests performed in this study with predicted values given by Equations 2.16 - 2.19.

None of the predicted data sets agree well with the measured values. In Figure 9.48(a), Equation 2.16 (Tremblay, 2002) overpredicts the measured values, although a direct comparison in this case should account for the specific manner in which ductility capacity was defined in Tremblay (2002). In contrast, in Figure 9.48(b), Equation 2.19 (Nip et al., 2010) is seen to overpredict the measured values for all but one test. However, the trend of the data evident in this figure suggests that the parameterisation of this model is appropriate for the conditions considered in the experiments performed in this study. Figure 9.48(c) and (d) show that the two prediction equations proposed in Goggins et al. (2006) (Equations (2.17 and 2.18), which consider the member and cross-section variables separately, either significantly underestimate or overestimate the measured values. It is noted that the range of specimen slenderness values considered in Goggins et al. (2006) is different to that of the experiments performed in this study.

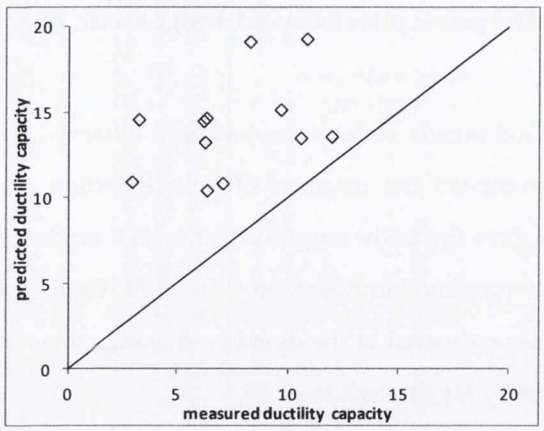

(a) Eqn. 2.16, Tremblay (2002)

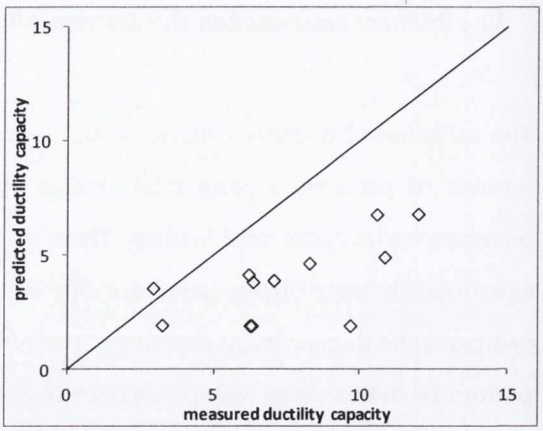

(b) Eqn. 2.19, Nip et al. (2010)

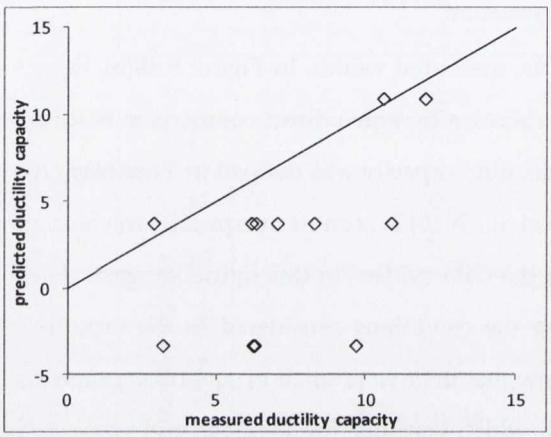

(c) Eqn. 2.17, Goggins et al. (2006)

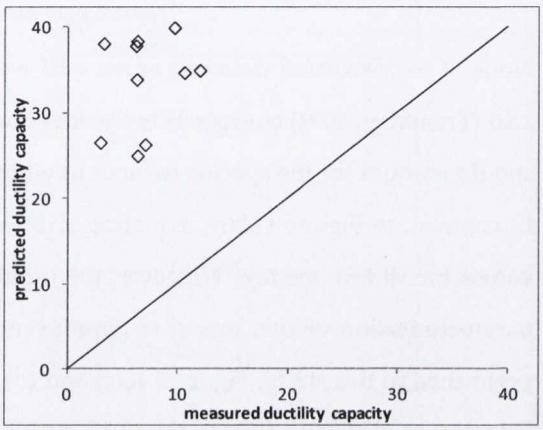

(d) Eqn. 2.18, Goggins et al. (2006)

Figure 9.48 – Variation of maximum normalised brace compression force with PGA, by specimen connection type.

9.6 Chapter Overview

This chapter presented the experimental measurements that were recorded during the BRACED project. The preparation of the earthquake ground motion input using response spectra was outlined. The results of both pre-tests and all reference tests using earthquake ground motions were presented followed by a description of the impulse filtering employed and displacement measurements to check for torsional response or lateral instability. Results from white noise tests carried out before and after each earthquake excitation test in which brace failure did not occur, evaluated the elastic properties and their evolution throughout the experiment. The influence of specimen parameters on these properties was investigated. Finally, an analysis of the earthquake excitation tests was presented focusing on specific maximum response quantities. Results were compared using models from previous studies.

10 BRACED – Correlation with Numerical Models

10.1 Introduction

Numerical modelling techniques were introduced in Chapter 4. Building upon these techniques a numerical model CBF was developed in Chapter 7, with model output correlated with cyclic testing results. In this chapter numerical modelling of CBFs is discussed in the context of the model CBF from the BRACED project. Further modelling techniques are discussed in relation to application for shake table tests. The concept of a 'Reference Model' is presented. Its robustness is examined through comparisons with test results of varying brace member specimens used in the BRACED project. Based on this, several alternative modelling options are explored and recommendations are presented.

10.2 Development of CBF Reference Model

In Chapter 4 recommended modelling procedures were implemented for a planar CBF model. The model was based on the test CBF used in the Complementary Cyclic Tests discussed in Chapter 5. In this section, a similar planar model is presented for the test CBF used in the BRACED project. Due to a number of characteristic differences between the frames, some further modelling recommendations are made here. This forms a simplified Reference Model that was used to predict the test results for all specimens and configurations. After the presentation of the initial correlation of the Reference Model with the experimental results, the sensitivity analysis explores further modelling options.

An overview of the test frame is shown in Figure 10.1. The numbering scheme is consistent with previous models presented so that the elements are numbered with the suffix 'e' and the nodes with the suffix 'n'. Boundary conditions are outlined for the main nodes in the CBF model in Table 10.1. '1' indicates fully restrained and '0' no restraint for a given DOF and as a result all six boundary conditions for a given node can be described as (D_x, D_y, D_z, R_x, R_y, R_z) for descriptive purposes.

All nodes near ground level (n1, 3, 18, 20) are free to rotate about the Y-axis. n18 and n20 are also free to rotate about the X-axis due to the swivel action at these locations. Free rotation about the remaining Z-axis for these nodes was considered but this resulted in excessive drift values. This is discussed in greater depth in the sensitivity analysis in the following section. Roof nodes (n2, 4) are

restricted for translation out-of-plane (Y-axis) representing the support of the outrigger Frames A and C in Figure 8.2. RigidLink elements were utilised between nodes in the top corner connections (Detail A and B in Figure 10.1). This represented the increased bending stiffness in these regions owing to the added stiffener plates. Detail A illustrates the CA connection model. Using a fundamental approach, the connection was modelled as a continuous connection due to the added rotational stiffness of the gusset plate. The CB connection in Detail B was treated as a pinned connection with a ZeroLength element between n602, 6020. The elements connecting the bottom of the brace tubes (n19, 21) to the swivel pivots (n18, 20) were defined using a large elastic column section.

To represent the out-of-plane stiffness of the gusset plates and the formation of the plastic hinge zone, the uniaxial material model ('Steel02' in OpenSees, see section 4.1) was specified for the R_y DOF in the ZeroLength elements connection node pairs n80,505 and n120,555. The plate bending stiffness was defined using the specific plate Whitmore width and thickness for each specimen. The nonlinear Steel02 material was specified for the brace elements; however the fatigue material was used in the subsequent sensitivity analysis.

Mass participation for time-history analysis ('Transient' in OpenSees) was calculated for the steel plate and concrete masses and the self-weight of the beams and columns. This was distributed between nodes n2 and n4 evenly for participation in the X-direction.

Before testing nominal values were used for material strengths, section areas and damping values. Once testing was complete, measured values for these parameters were implemented in the model for improved prediction. In addition, the recorded table motion was used for the acceleration time-history input. For each tested specimen there were at least three experiments performed using hazard level earthquake table motions. For each subsequent run there was an accumulation of damage. To account for this progressive increase in plastic strains in the OpenSees model, the recorded table accelerations for each earthquake run were concatenated forming a single input time history for OpenSees. During the post-processing phase for each specimen, the analysis output was separated corresponding to each run. Appendix C contains a sample OpenSees script for the Reference Model.

Table 10.1 – BRACED project model CBF boundary conditions.

Node No	D_x	D_y	D_z	R_x	R_y	R_z
1	1	1	1	1	0	1
2	0	1	0	1	0	1
3	1	1	1	1	0	1
4	0	1	0	1	0	1
18	1	1	1	0	0	1
20	1	1	1	0	0	1

10.3 Reference Model and Correlation

The Reference Model has been described in the previous section. In this section the OpenSees analysis results for the Reference Model are presented for each test specimen. For brevity one run is compared for each specimen from Test 1 to Test 12 in Figure 10.2 to Figure 10.13 respectively. In each figure, roof level response acceleration, roof level drift and left and right brace axial forces are compared directly with the output recorded from the OpenSees analyses.

Table 10.2 summarises the key indicators for comparing the Reference Model prediction capabilities. The parameters listed correspond to the shake table runs presented in this section. The model structural period was calculated using an eigenvalue analysis in OpenSees and compared with the experimental value from the first white noise test for each specimen. Peak values are shown for the relative response acceleration and drift achieved at the frame roof level.

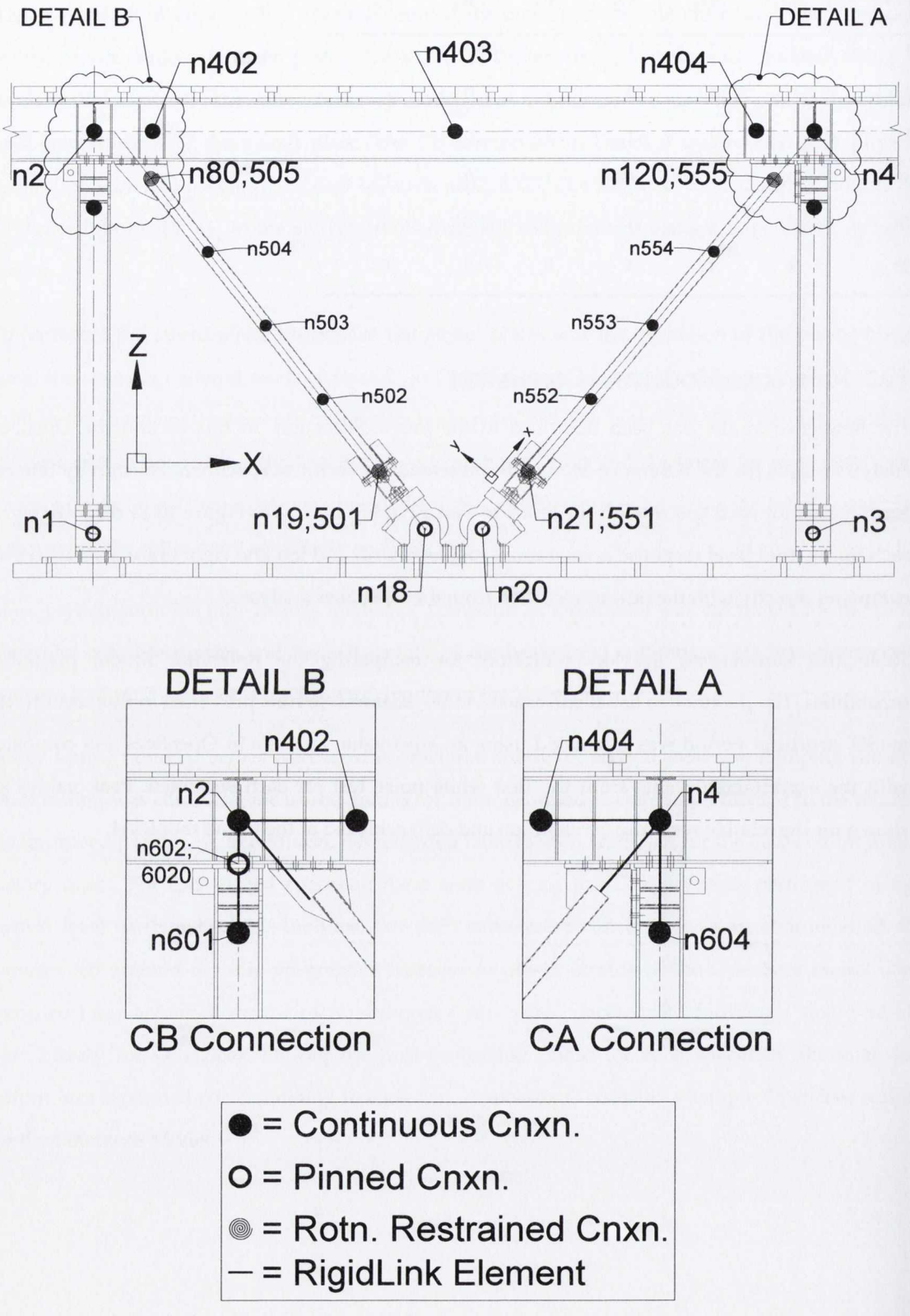

Figure 10.1 – OpenSees Reference Model for BRACED project test CBF.

Table 10.2 – Comparison indicators for Reference Model and experimental results.

Test	Specimen	Structural Period, T (s)		Peak Response Rel. Acc. (g)		Peak Drift (%)		Left Brace Axial Force (kN)				Right Brace Axial Force (kN)			
								Min. Compr.		Max. Tensile		Min. Compr.		Max. Tensile	
		Exp.	Model	Exp.	Model	Exp.	Model	Exp.	Model	Exp.	Model	Exp.	Model	Exp.	Model
1	S1-CA-G1	0.216	0.191	-0.838	0.901	1.00	0.71	-276.6	-136.7	283.1	331.3	-268.9	-151.4	371.1	340.6
2	S3-CA-G1	0.235	0.238	-1.072	-0.950	-1.53	1.40	-193.3	-80.5	278.1	243.7	-138.7	-115.0	259.4	205.9
3	S4-CA-G1	0.225	0.223	0.670	0.634	0.83	0.54	-175.9	-102.1	212.6	211.9	-128.6	-128.6	225.7	213.5
4	S2-CA-G1	0.222	0.201	1.000	-0.736	1.54	0.86	-196.8	-104.3	322.7	289.7	-184.0	-126.8	325.2	290.7
5	S1-CA-G2	0.219	0.185	1.149	0.829	1.73	-0.66	-220.3	-150.3	336.8	305.7	-294.1	-150.9	344.8	311.3
6	S2-CA-G2	0.225	0.202	1.131	1.376	2.08	2.00	-195.9	-112.0	342.4	295.5	-202.3	-109.6	329.3	299.1
7	S3-CA-G2	0.246	0.235	0.849	-0.811	-1.93	1.97	-113.5	-68.1	296.4	259.1	-132.9	-78.3	276.9	250.1
8	S1-CB-G1	0.226	0.188	-1.730	1.639	0.69	-0.33	-189.4	-210.6	152.1	218.8	-260.9	-198.0	247.1	180.7
9	S2-CB-G1	0.258	0.200	0.793	-0.611	0.89	0.30	-190.3	-136.2	294.7	234.6	-	-129.9	294.7	238.1
10	S4-CB-G2	0.242	0.225	-0.761	0.698	-1.80	1.25	-156.4	-111.0	275.3	222.1	-139.9	-109.1	255.1	228.2
11	S2-CB-G2	0.22	0.203	0.997	-0.745	1.86	0.68	-191.9	-124.8	334.6	270.7	-206.9	-151.1	314.3	272.3
12	S3-CB-G2	0.246	0.239	0.899	0.617	2.09	-1.88	-94.95	-54.3	309.2	272.2	-113.2	-50.6	306.1	274.9

10.3.1 Test 1: S1-CA-G1

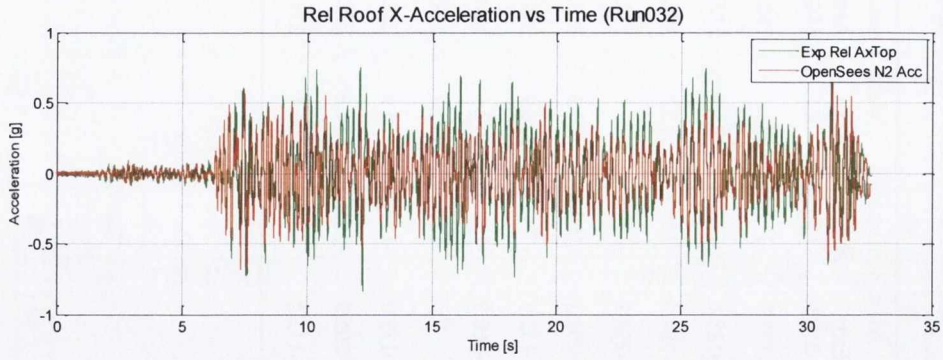

(a) Relative acceleration time history

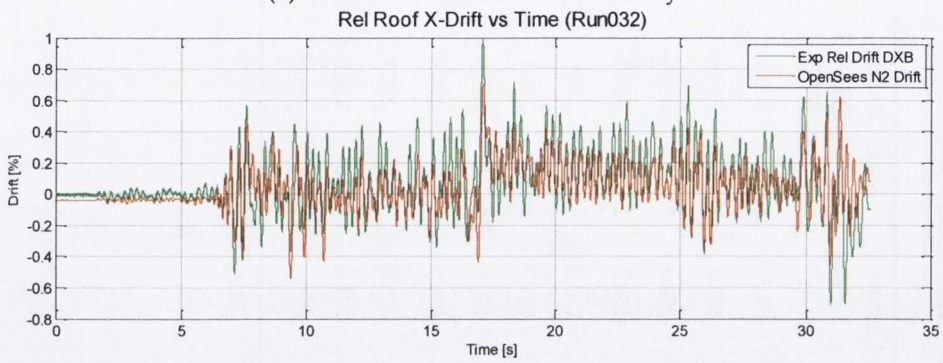

(b) Drift time history

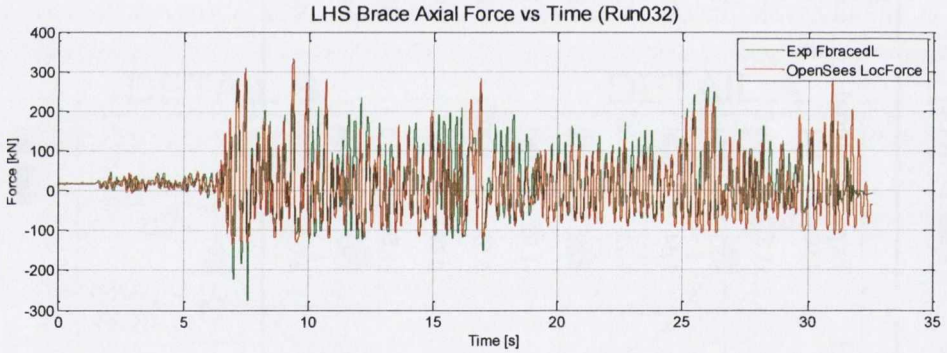

(c) Left brace axial force time history

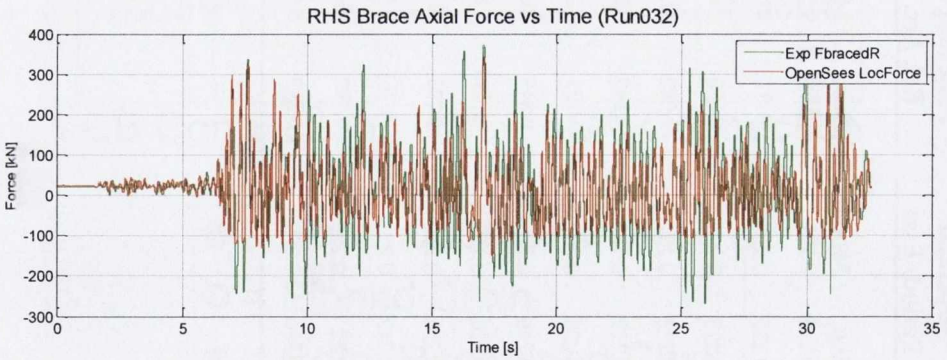

(d) Right brace axial force time history

Figure 10.2 – OpenSees response compared with recorded responses for 2%/50 level (Run032) Shake Table Test 1; S1-CA-G1.

10.3.2 Test 2: S3-CA-G1

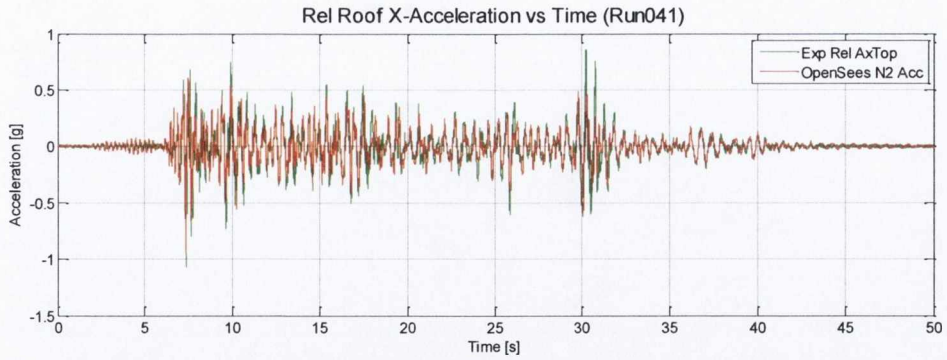

(a) Relative acceleration time history

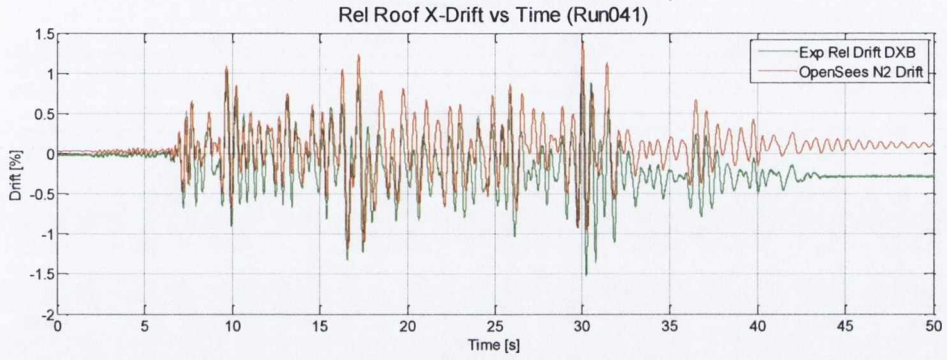

(b) Drift time history

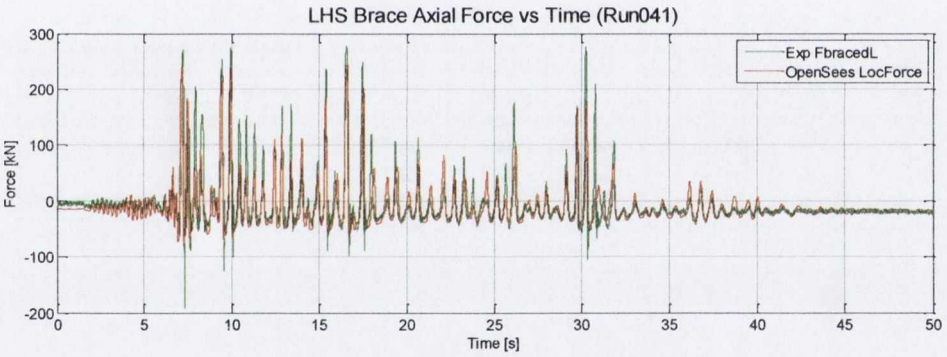

(c) Left brace axial force time history

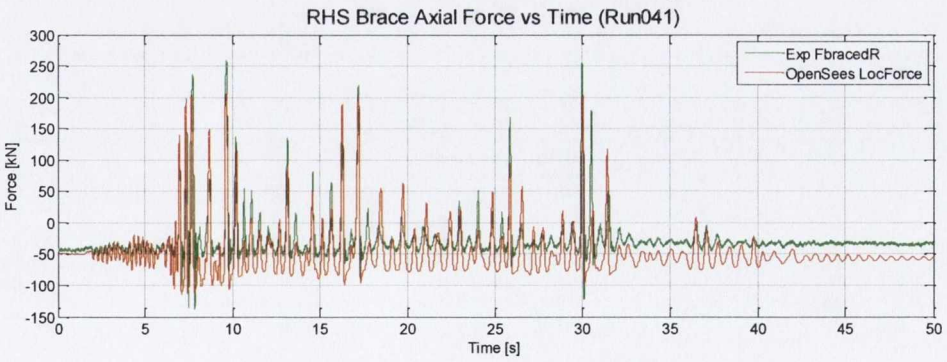

(d) Right brace axial force time history

Figure 10.3 – OpenSees response compared with recorded responses for 2%/50 level (Run041) Shake Table Test 2; S3-CA-G1.

10.3.3 Test 3: S4-CA-G1

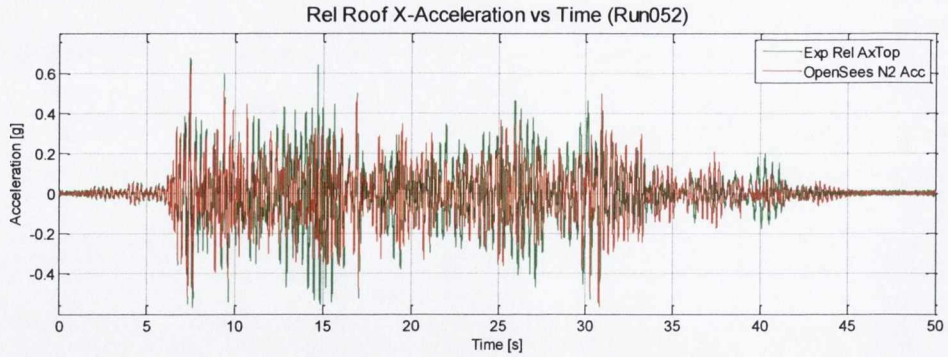

(a) Relative acceleration time history

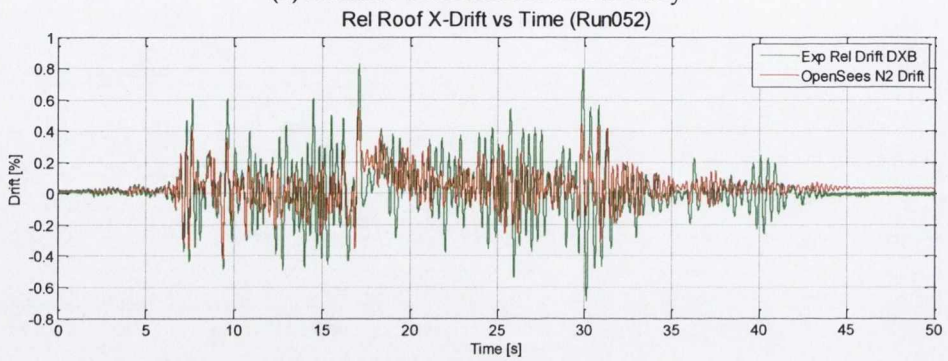

(b) Drift time history

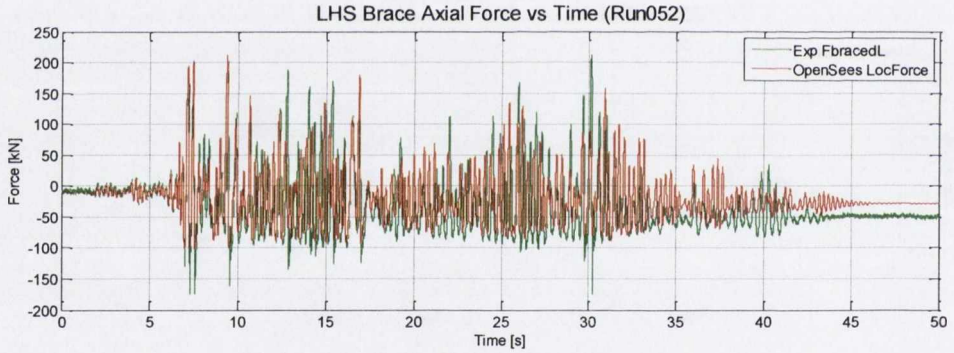

(c) Left brace axial force time history

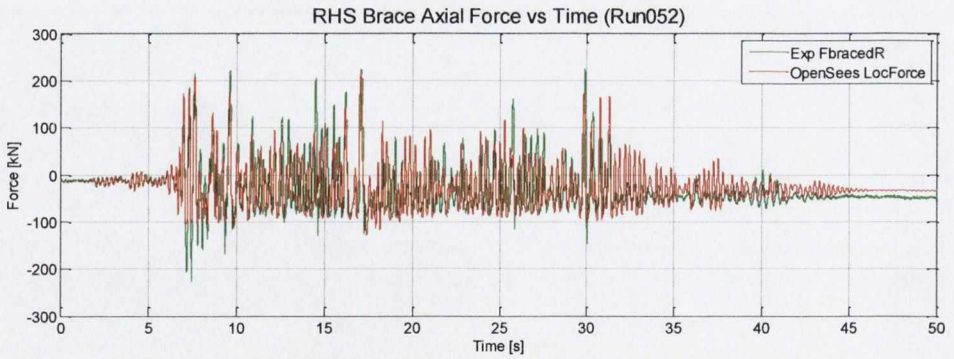

(d) Right brace axial force time history

Figure 10.4 – OpenSees response compared with recorded responses for 2%/50 level (Run052) Shake Table Test 3; S4-CA-G1.

10.3.4 Test 4: S2-CA-G1

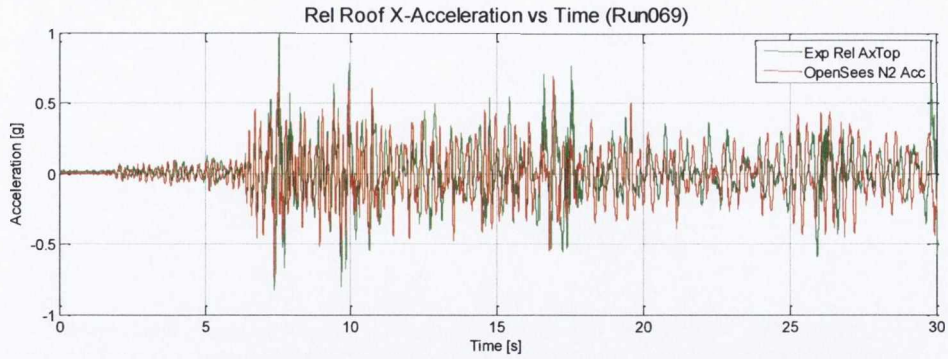

(a) Relative acceleration time history

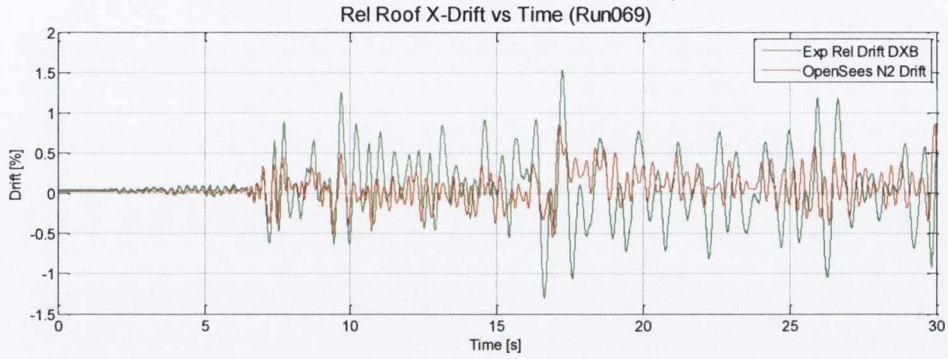

(b) Drift time history

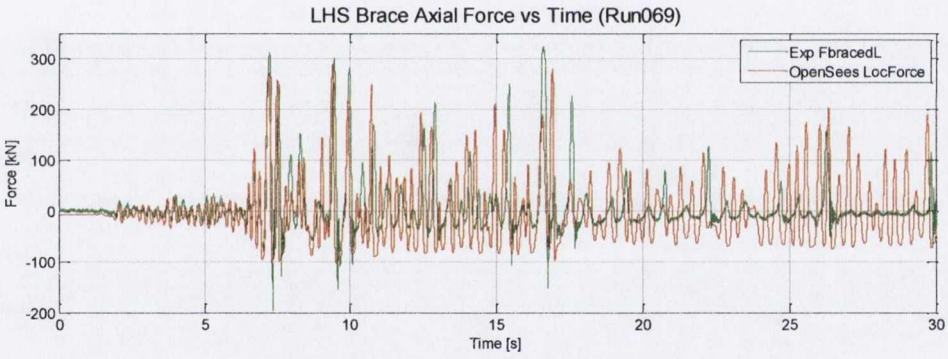

(c) Left brace axial force time history

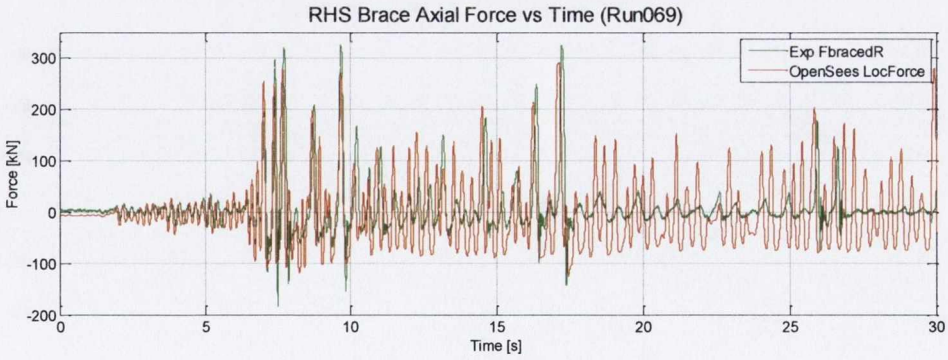

(d) Right brace axial force time history

Figure 10.5 – OpenSees response compared with recorded responses for 2%/50 level (Run069) Shake Table Test 4; S2-CA-G1.

10.3.5 Test 5: S1-CA-G2

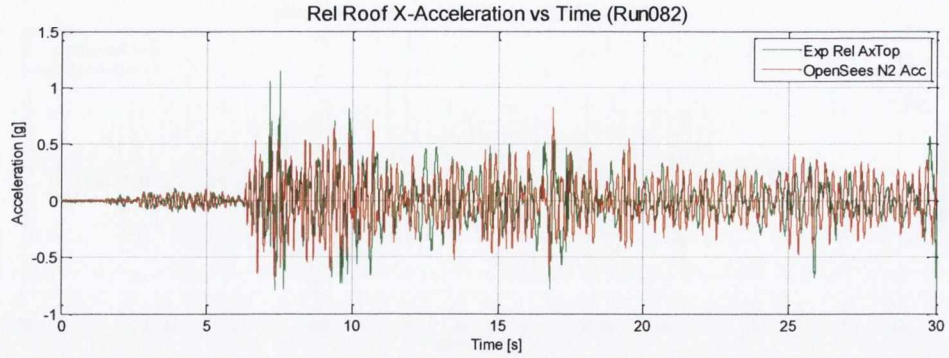

(a) Relative acceleration time history

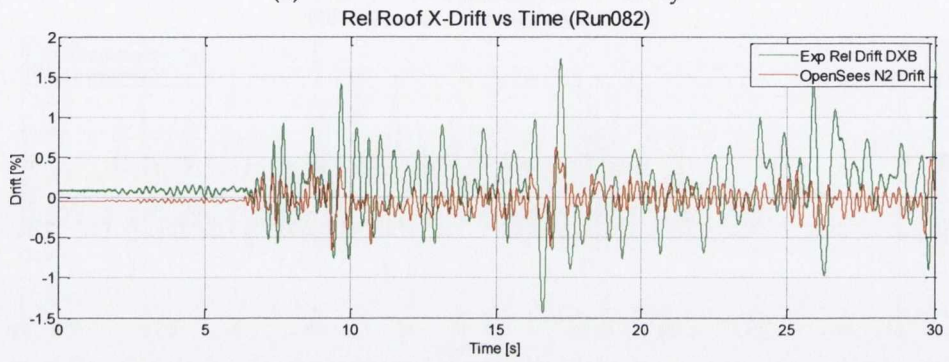

(b) Drift time history

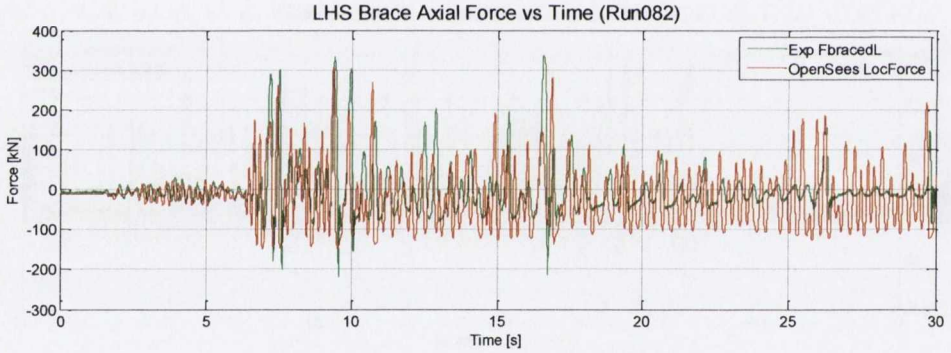

(c) Left brace axial force time history

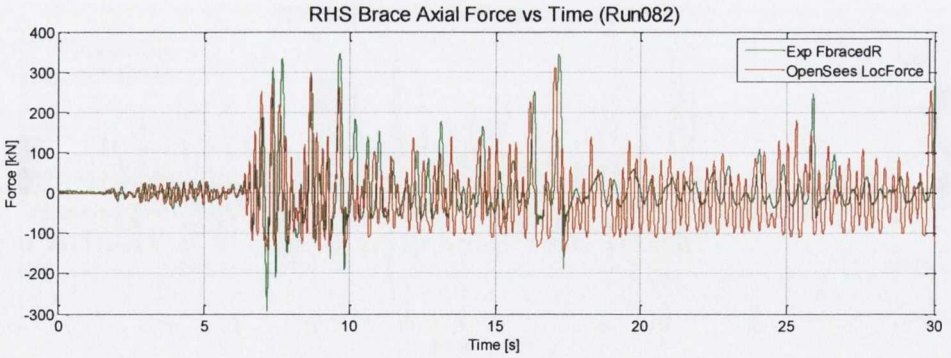

(d) Right brace axial force time history

Figure 10.6 – OpenSees response compared with recorded responses for 2%/50 level (Run082) Shake Table Test 5; S1-CA-G2.

10.3.6 Test 6: S2-CA-G2

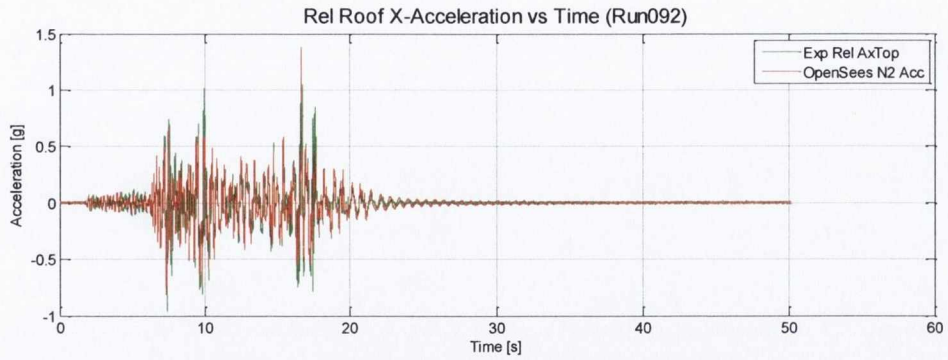

(a) Relative acceleration time history

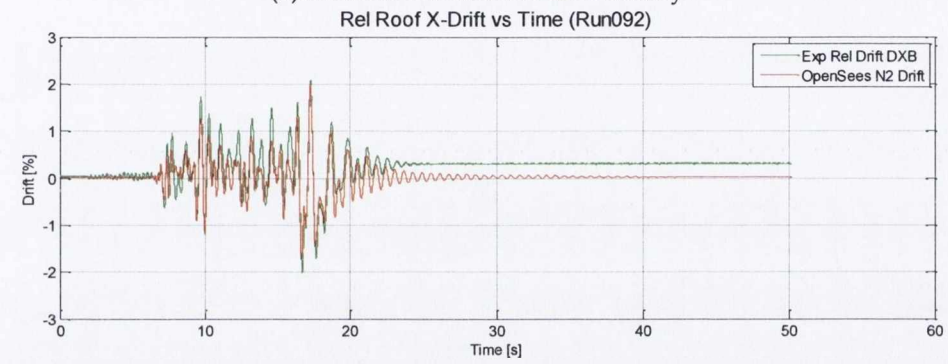

(b) Drift time history

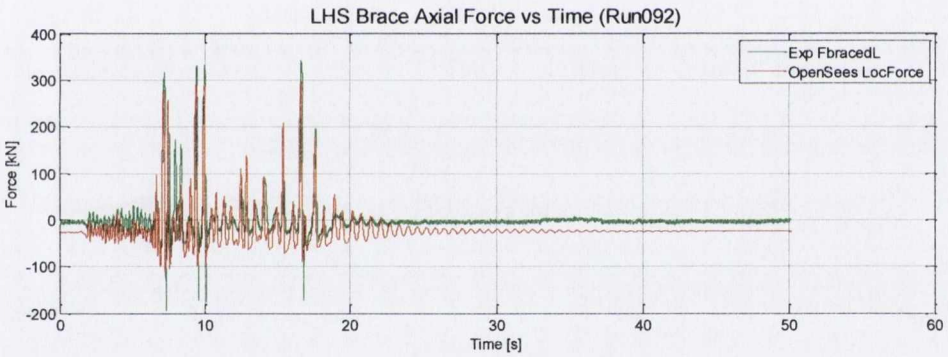

(c) Left brace axial force time history

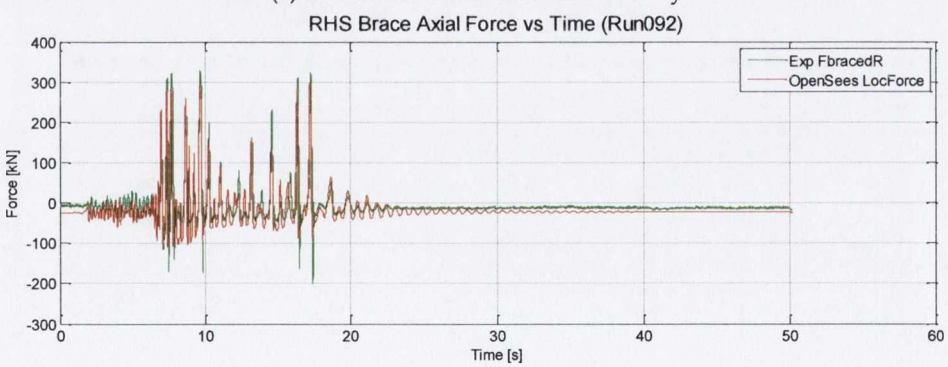

(d) Right brace axial force time history

Figure 10.7 – OpenSees response compared with recorded responses for 2%/50 level (Run092) Shake Table Test 6; S2-CA-G2.

10.3.7 Test 7: S3-CA-G2

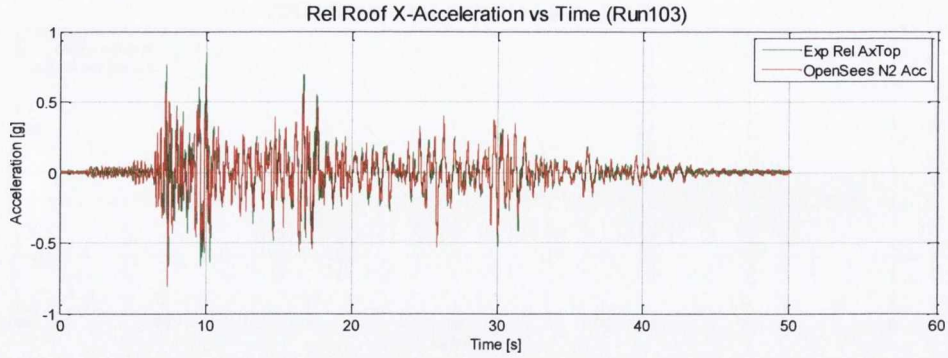

(a) Relative acceleration time history

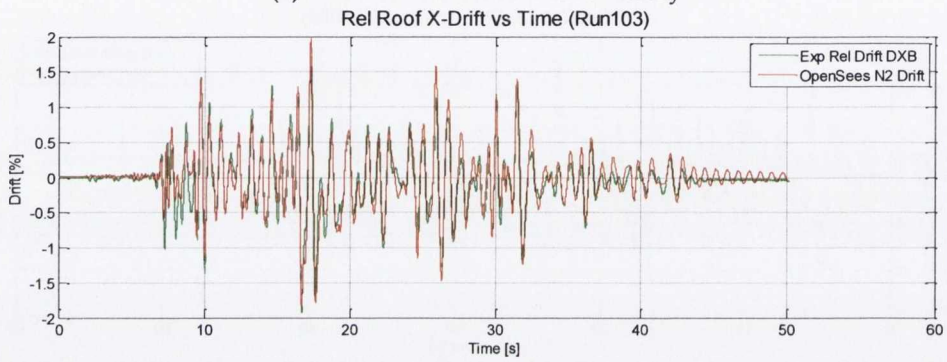

(b) Drift time history

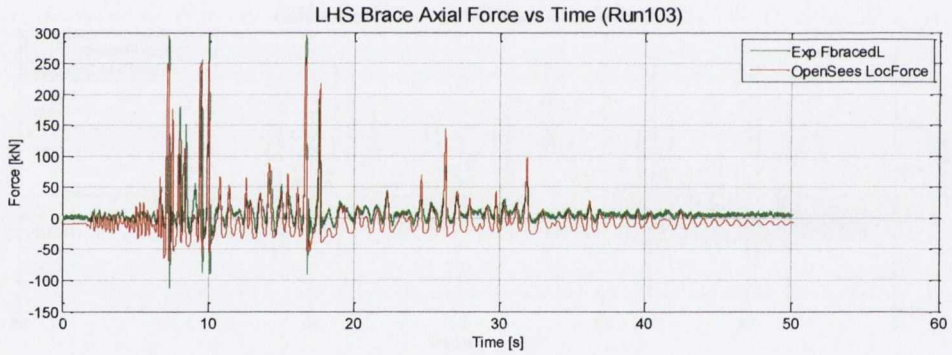

(c) Left brace axial force time history

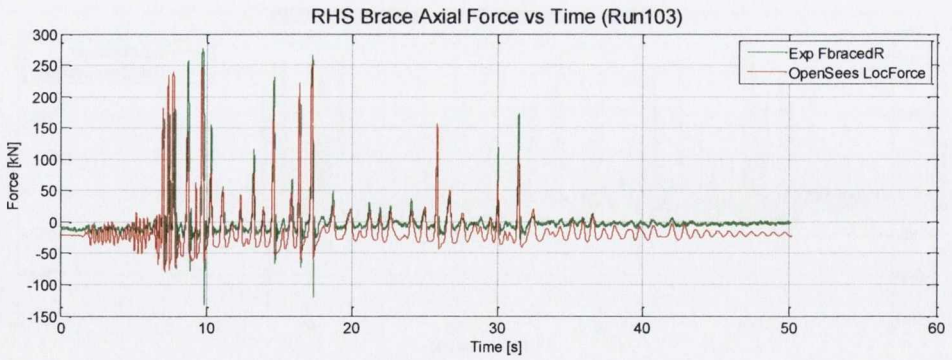

(d) Right brace axial force time history

Figure 10.8 – OpenSees response compared with recorded responses for 10%/50 level (Run103) Shake Table Test 7; S3-CA-G2.

10.3.8 Test 8: S1-CB-G1

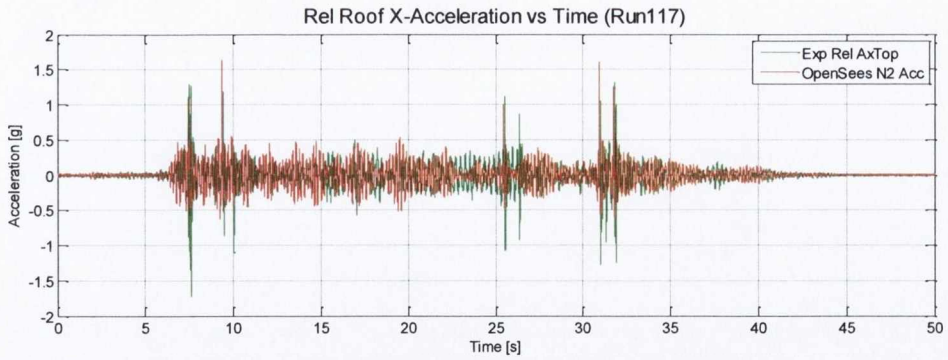

(a) Relative acceleration time history

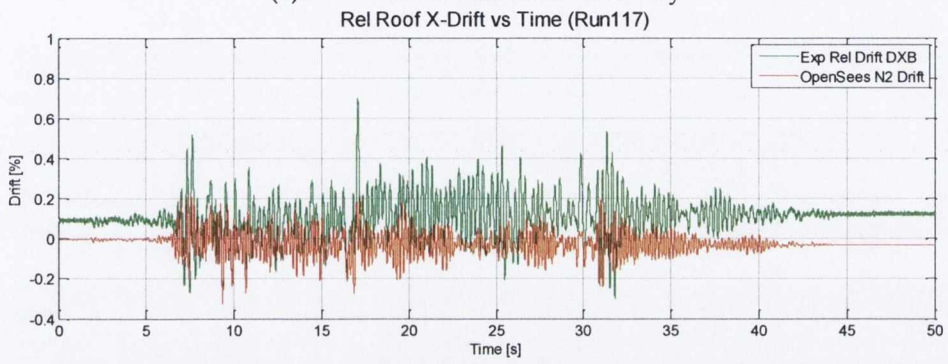

(b) Drift time history

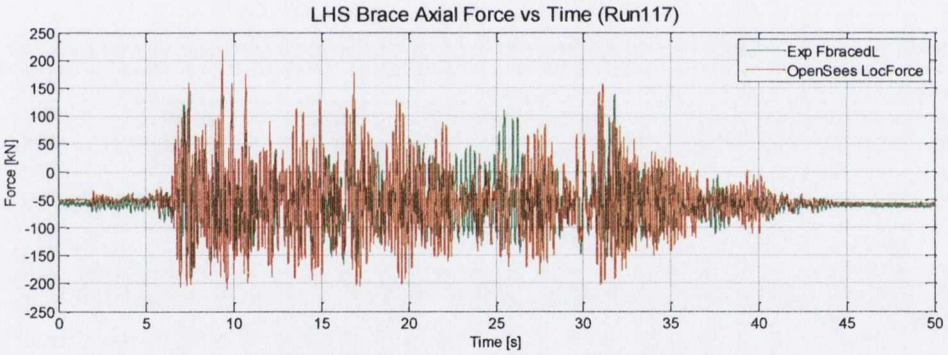

(c) Left brace axial force time history

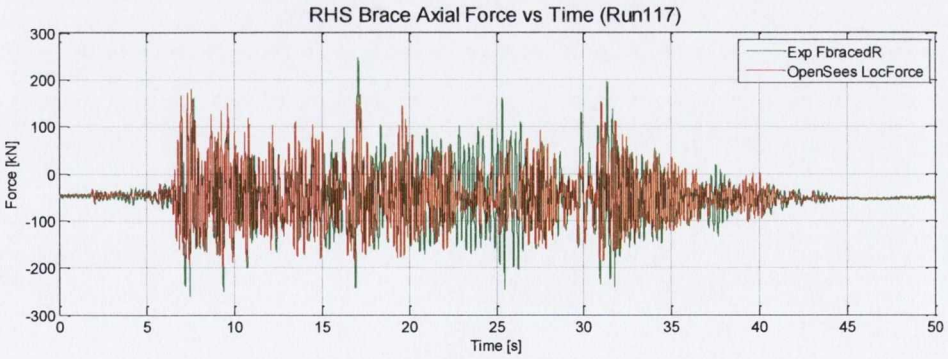

(d) Right brace axial force time history

Figure 10.9 – OpenSees response compared with recorded responses for 10%/50 level (Run117) Shake Table Test 8; S1-CB-G1.

10.3.9 Test 9: S2-CB-G1

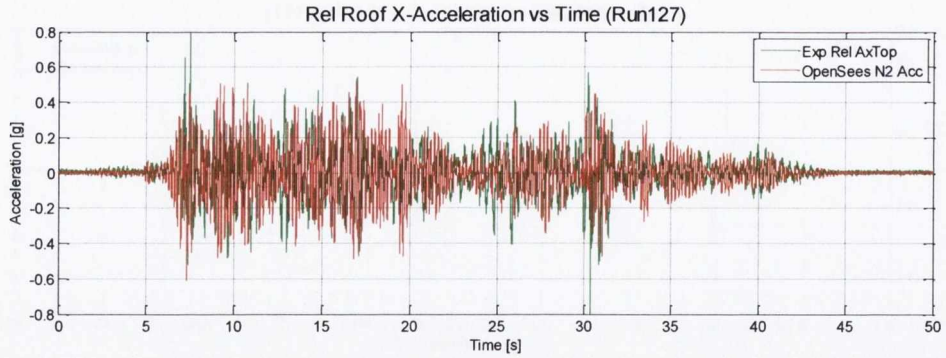

(a) Relative acceleration time history

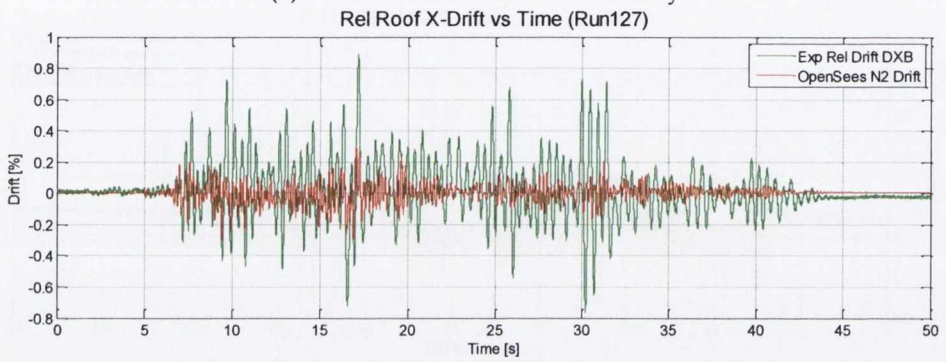

(b) Drift time history

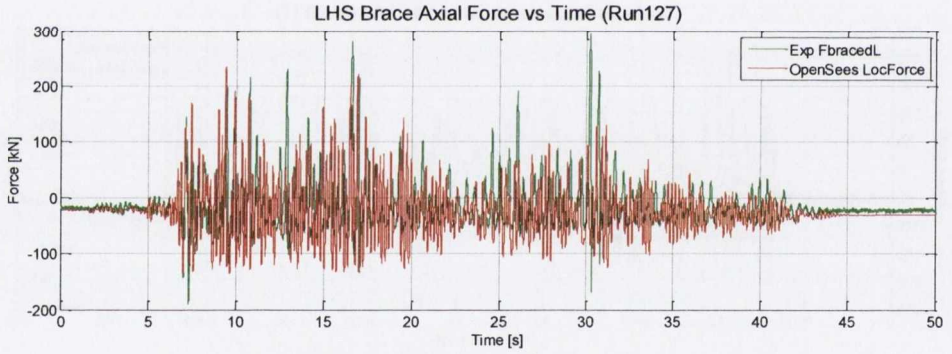

(c) Left brace axial force time history

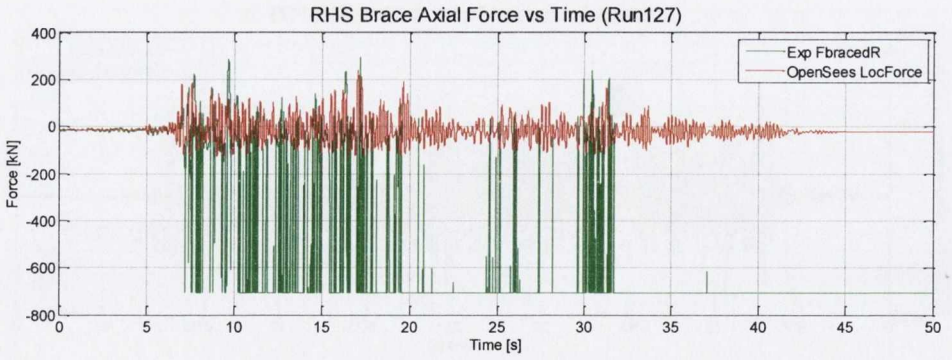

(d) Right brace axial force time history

Figure 10.10 – OpenSees response compared with recorded responses for 10%/50 level (Run127) Shake Table Test 9; S2-CB-G1.

10.3.10 Test 10: S4-CB-G2

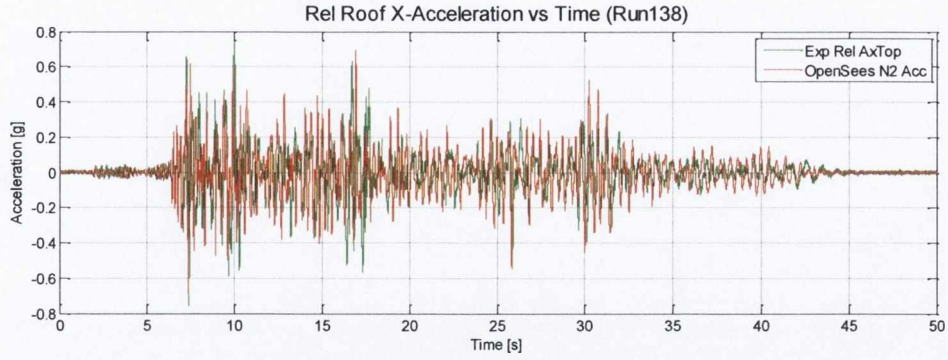

(a) Relative acceleration time history

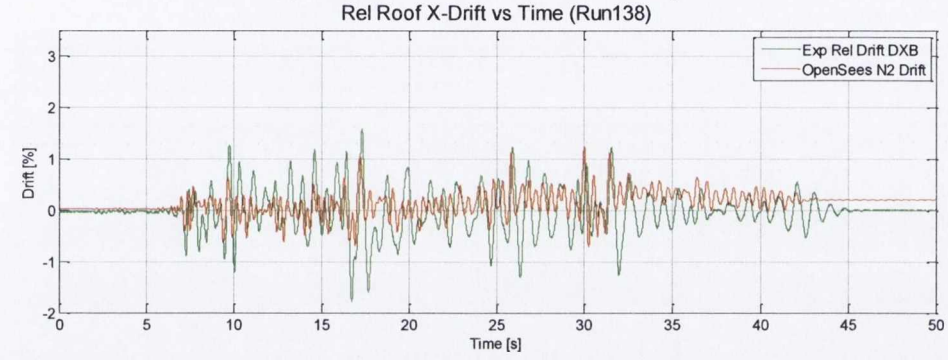

(b) Drift time history

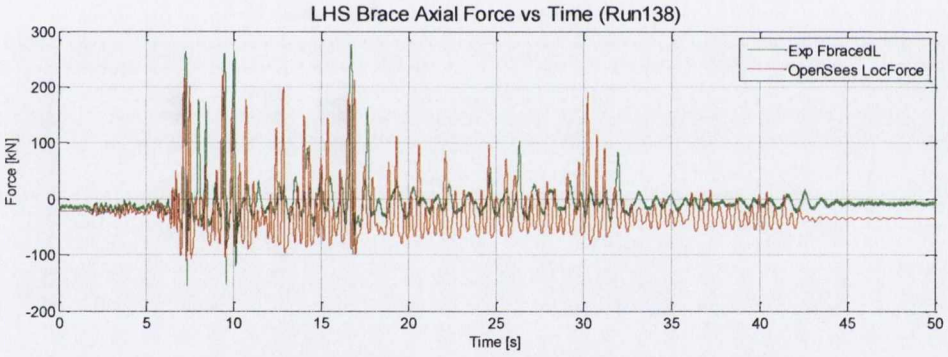

(c) Left brace axial force time history

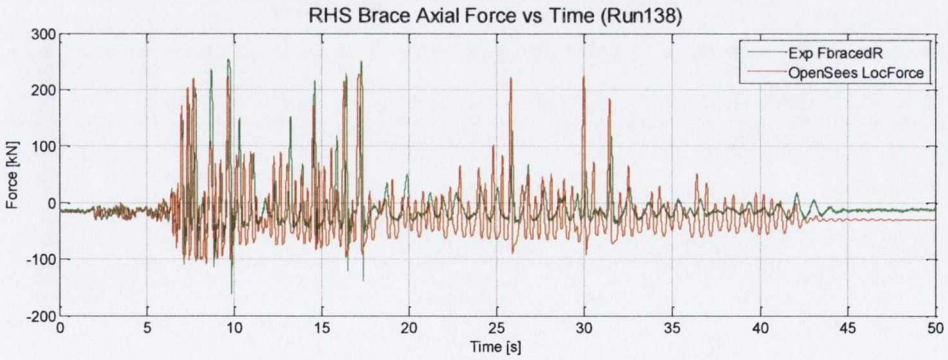

(d) Right brace axial force time history

Figure 10.11 – OpenSees response compared with recorded responses for 2%/50 level (Run138) Shake Table Test 10; S4-CB-G2.

10.3.11 Test 11: S2-CB-G2

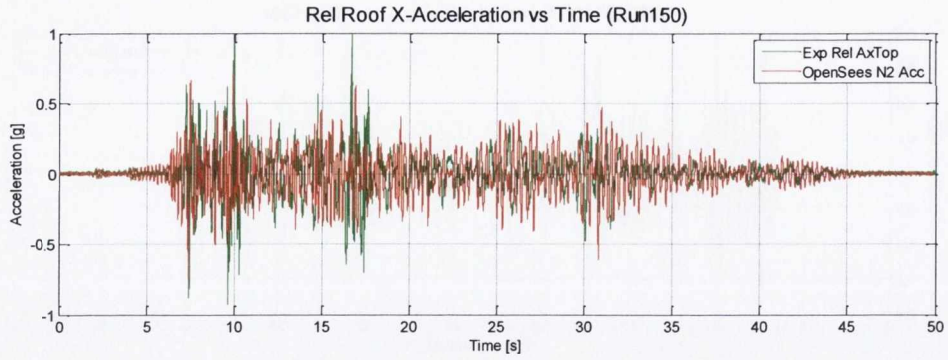

(a) Relative acceleration time history

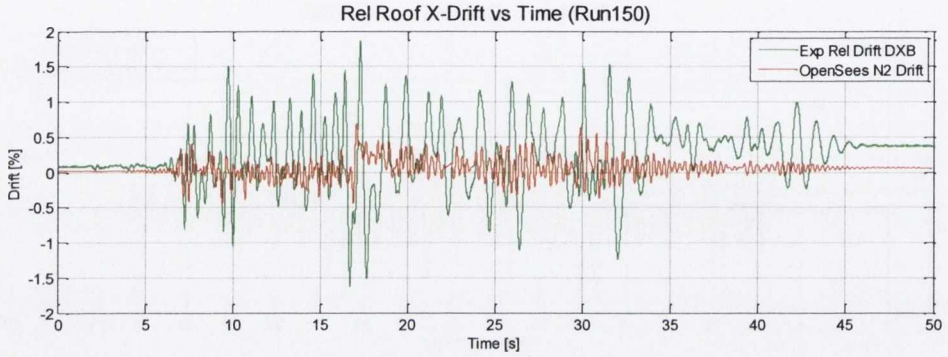

(b) Drift time history

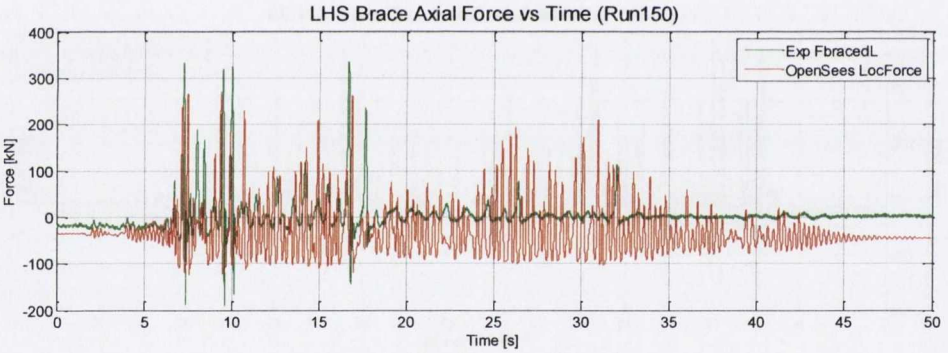

(c) Left brace axial force time history

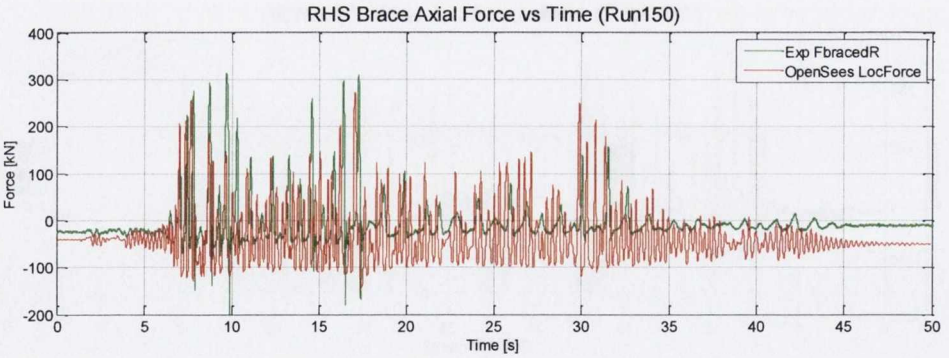

(d) Right brace axial force time history

Figure 10.12 – OpenSees response compared with recorded responses for 2%/50 level (Run150) Shake Table Test 11; S2-CB-G2.

10.3.12 Test 12: S3-CB-G2

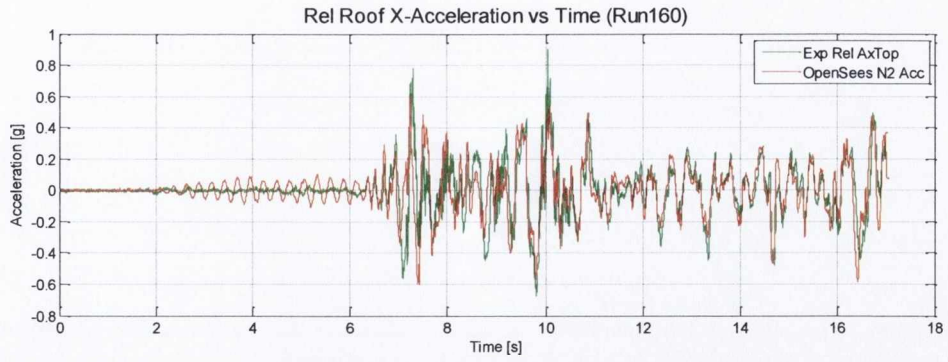

(a) Relative acceleration time history

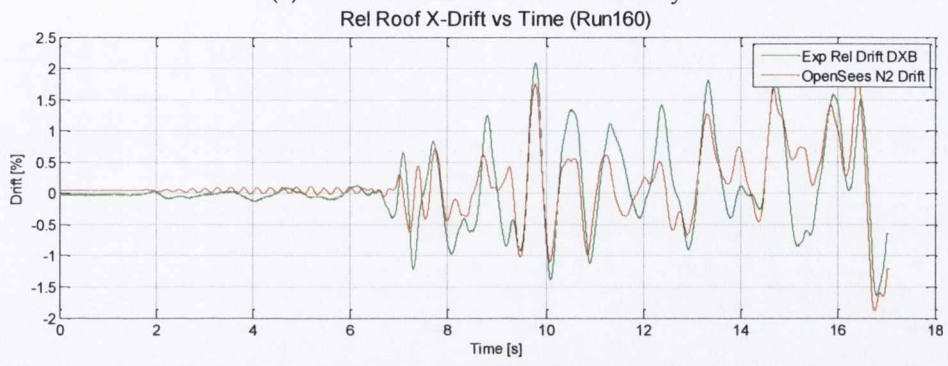

(b) Drift time history

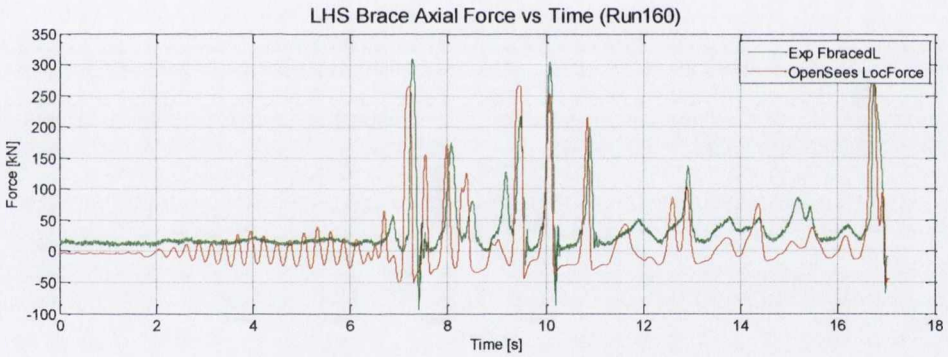

(c) Left brace axial force time history

(d) Right brace axial force time history

Figure 10.13 – OpenSees response compared with recorded responses for 2%/50 level (Run160) Shake Table Test 12; S3-CB-G2.

10.4 Swivel Boundary Conditions

In the previous section results for the Reference Model were presented and compared with the recorded measurements of each specimen configuration. In this section, further options for modelling the swivel boundary conditions are explored to advance the reference model towards more realistic model prediction.

In the Reference Model the swivel rotation was constrained about the Z-axis and free about the other two axes (1, 1, 1, 0, 0, 1). This was intended to approximate the actual swivel conditions based on the expected free rotation of the brace about the X and Y axes. When no rotational boundary constraints were applied (1, 1, 1, 0, 0, 0), drifts much larger than expected were predicted by the model for all specimens. This is examined here using two test results that demonstrated in one case reduced fidelity with the recorded responses (Test 10) and in another comparable test, very good prediction capabilities (Test 3).

In Figure 10.14, the acceleration and drift responses for Test 10 are compared using both boundary conditions. The comparisons are made within a short time window for easier identification and comparison purposes. Using the fully free rotational restraint option, the observed acceleration amplitudes are predicted more accurately Figure 10.14(a), which is particularly noticeable at the positive and negative peaks between 7 to 7.5 s. The most significant improvement is observable in the frequency of the acceleration response. Most of the OpenSees response peaks are synchronised with those displayed in the recorded response, suggesting that the structural response frequencies are closer to the actual frequencies of the structure.

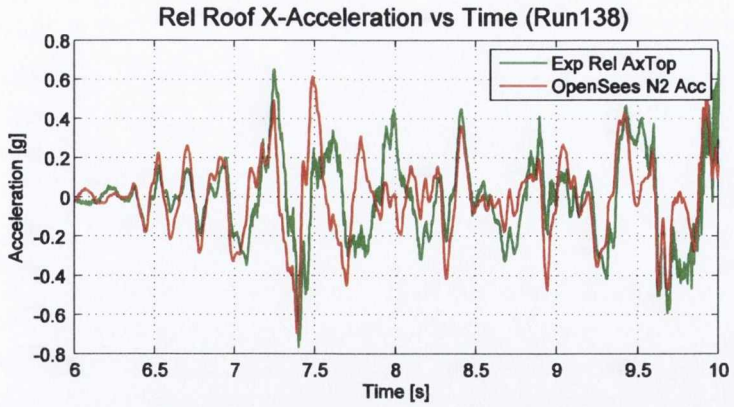

(1, 1, 1, 0, 0, 1)

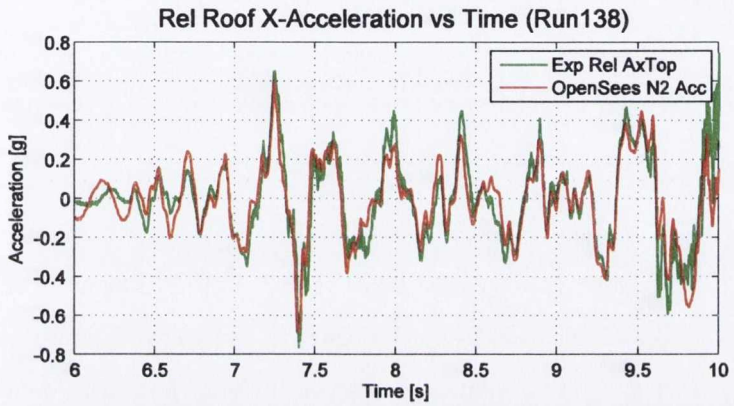

(1, 1, 1, 0, 0, 0)

(a) Acceleration responses for two boundary condition cases at nodes n18 and n20.

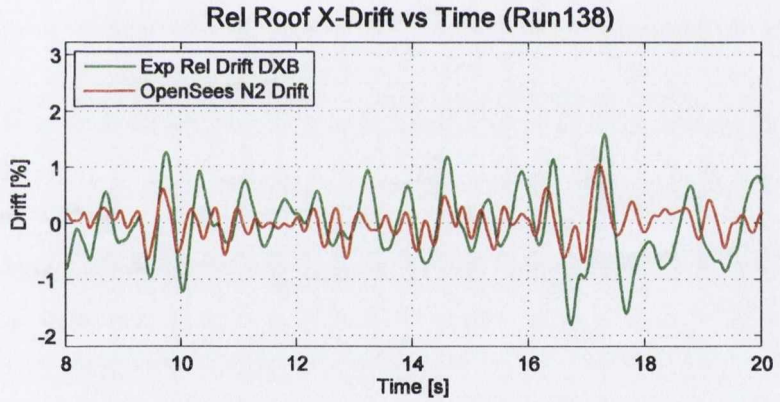

(1, 1, 1, 0, 0, 1)

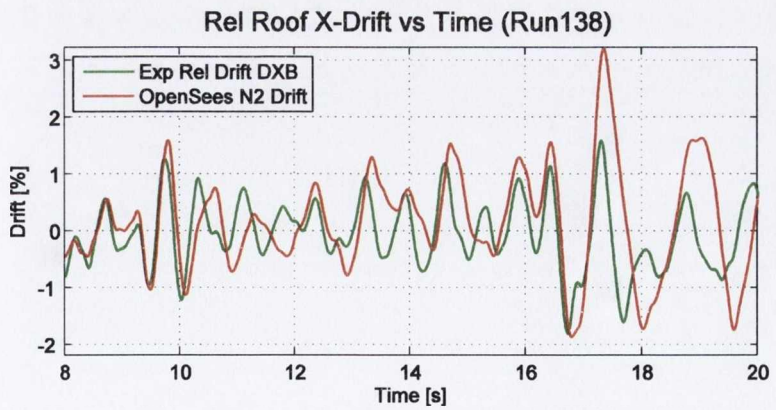

(1, 1, 1, 0, 0, 0)

(b) Drift responses for two boundary condition cases at nodes n18 and n20

Figure 10.14 – OpenSees responses compared for two boundary cases for Test 10; S4-CB-G2.

In Figure 10.14(b), the drift response predictions are also generally improved using the free rotation case. The use of the fully free modelled restraint changes the simulated drift response from an underprediction of the observed response to a slight overprediction. However, during the strong motion cycles at approximately 17 s, drift predictions exceed the recorded response by nearly 100%. In the reference case with $R_z = 1$, drifts are consistently underpredicted in the higher PGA runs.

The model output for Test 3 showed very accurate results that approached the actual experimental response. This is demonstrated for the acceleration response in Figure 10.15(a). Under the free rotation conditions near 7.5 s, accuracy was reduced in relation to amplitude, but most significantly, frequency content. Extreme overprediction of the drift response was also observed in Figure 10.15(b). As before, the numerical model has a longer structural period.

Overall, it is clear that the rotationally free boundary conditions help improve model accuracy for Test 10 with the CB connection configuration (beam only). This was also observable in other CB specimens (Test 8 – 12) to different degrees. As with Test 3, the opposite was observable for the CA (beam and column) specimens (Test 1 – 7). This indicates that the Reference Model boundary conditions, listed in Table 10.1 above, may produce a simulated frame stiffness that approaches the actual frame stiffness with the CA connection.

The improvement in OpenSees output for CB specimens due to this change in boundary conditions, is more pronounced for those CB specimens with G2 type gusset plates. This suggests that the out-of-plane stiffness of the gusset plate calculated using Equation 7.1 may provide an overly-stiff boundary condition for the thin G2 plates. Releasing the R_z component at the swivel end has the effect of counter-balancing this extra stiffness. This effect can be quantified by examining the change in structural period with boundary constraints, as displayed in Table 10.3. The comparison is illustrated in the plot in Figure 10.16. It is seen that the change in the G1 periods is not as significant with the alternative boundary conditions.

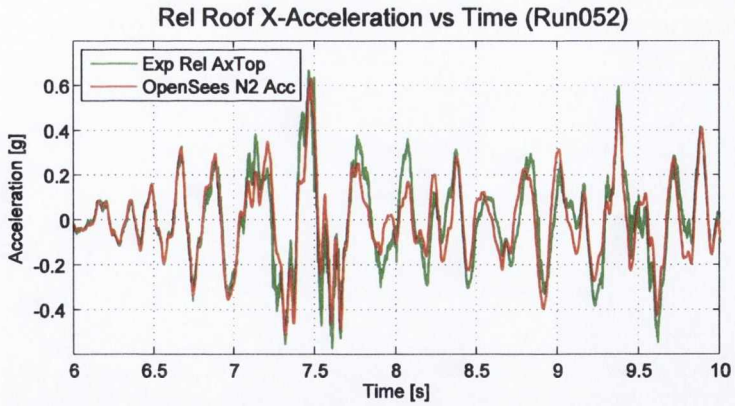

(1, 1, 1, 0, 0, 1)

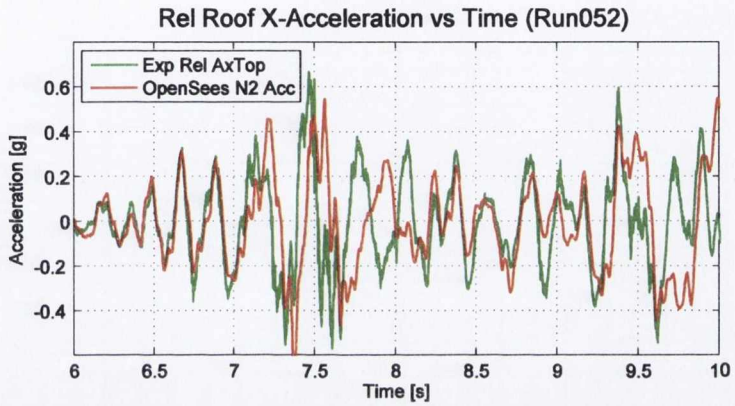

(1, 1, 1, 0, 0, 0)

(a) Acceleration responses for two boundary condition cases at nodes n18 and n20.

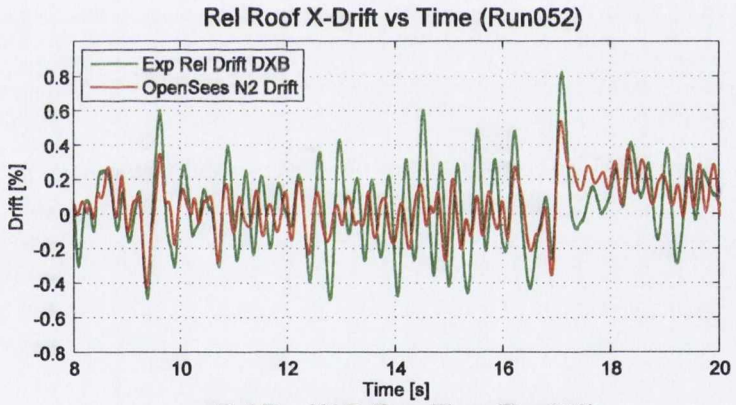

(1, 1, 1, 0, 0, 1)

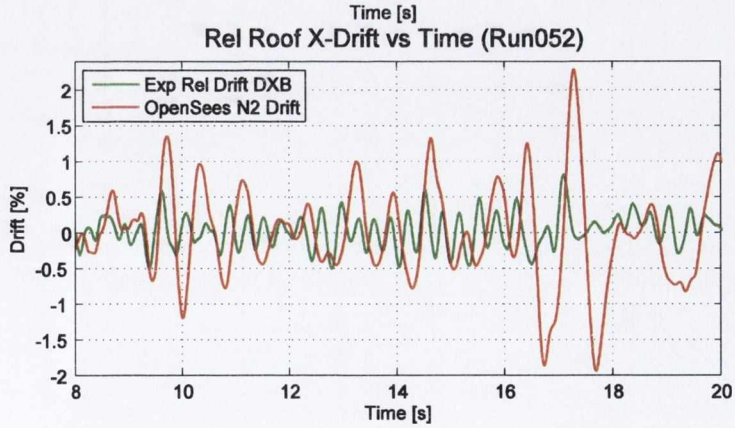

(1, 1, 1, 0, 0, 0)

(b) Drift responses for two boundary condition cases at nodes n18 and n20

Figure 10.15 – OpenSees responses compared for two boundary cases for Test 3; S4-CA-G1.

Table 10.3 – Change in structural period with alternative boundary conditions at n18, 20.

Test	Specimen	Natural Period, T_n (s)		
		Experimental	OpenSees, Ref. Model	OpenSees, Alt. Boundary Conditions
8	S1-CB-G1	0.226	0.188	0.19
9	S2-CB-G1	0.258	0.200	0.207
10	S4-CB-G2	0.242	0.225	0.235
11	S2-CB-G2	0.220	0.203	0.214
12	S3-CB-G2	0.246	0.239	0.262

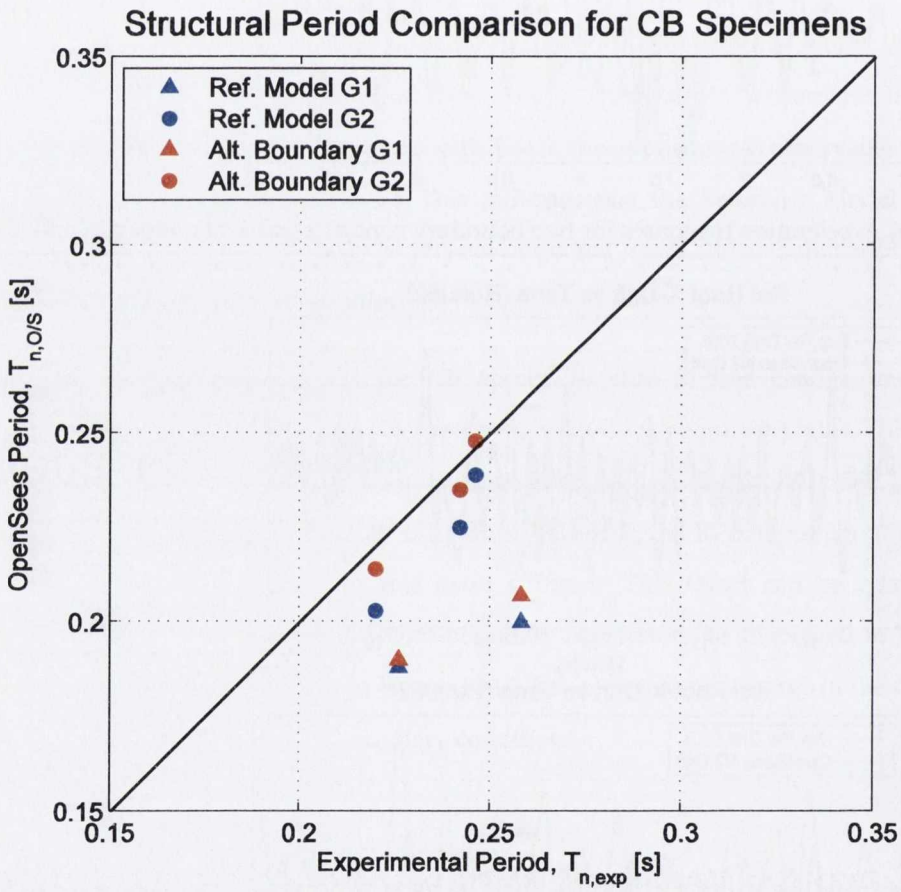

Figure 10.16 – Comparison plot showing the variation in structural period with boundary conditions at nodes n18, 20.

10.5 Modelling LCF and Fracture

In Chapter 4 fracture of brace members under LCF conditions was discussed. The fatigue model developed by (Uriz et al., 2008) for OpenSees was introduced. In this section the fatigue model is applied to the OpenSees model for calibration using Test 2 and Test 7. These tests were selected based on the agreement achieved between the modelled and experimental displacement responses in all earthquake runs. Each brace in the Reference Model consists of four elements with five integration points. The fatigue material is wrapped around the parent material used in the two elements at mid-length in each brace as this was the observed location of experimental fracture. As illustrated in Figure 10.1 these are the element pairs connected at n503 and n553 in the left and right braces respectively.

A number of fatigue model input parameters were tested for their suitability in modelling the BRACED earthquake tests. The parameter values are listed in Table 10.4 and are based on model calibrations in previous studies, including the correlation study in section 4.3.

Table 10.4 – Recommended values for the fatigue model input parameters.

	m	ε_0
Uriz and Mahin (2008)	-0.458	0.091
Santagati et al. (2012)	-0.458	0.120
Salawdeh (2012)	-0.5	0.190
Correlation Study	-0.458	0.165

The values recommended in Santagati (2012), Salawdeh (2012) and the correlation study did not lead to fracture predictions during the four earthquake tests of Test 2 and Test 7. However, Figure 10.17(a) and (c) show that using the parameters of Uriz and Mahin (2008), fracture is predicted to occur in the right-hand brace during Run041 at 131.4 s and during Run105 at 7.8s s. Both of the modelled fracture cases occur earlier than the experimental fracture. By varying the ε_0 parameter through an iterative procedure, the value $\varepsilon_0 = 0.106$ was found to extend the fatigue life of the braces and achieve a closer representation of the observed fracture initiation, as shown in Figure 10.17(b) and (d).

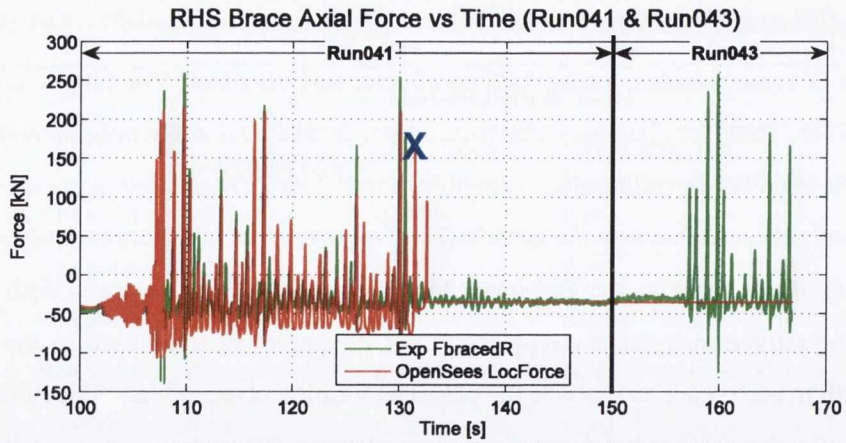

(a) Test 2, $\varepsilon_0 = 0.091$ (Uriz and Mahin 2008)

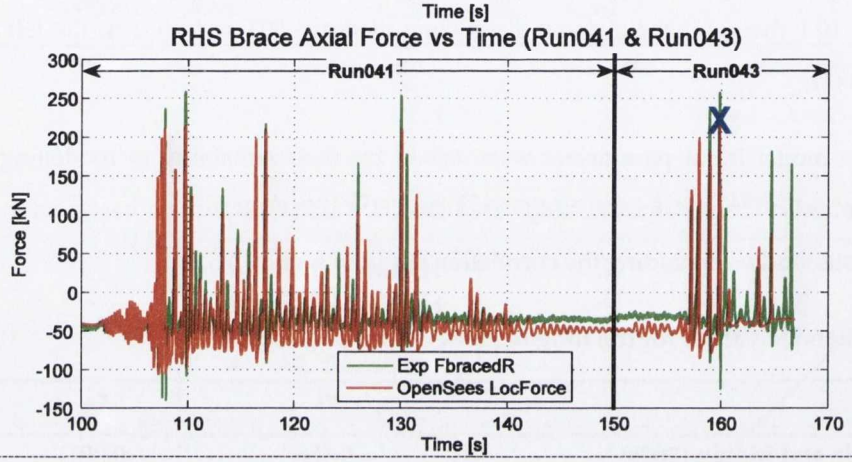

(b) Test 2, $\varepsilon_0 = 0.106$

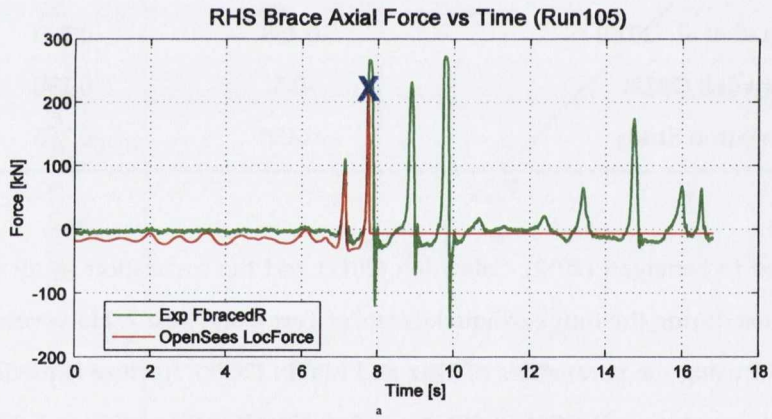

(c) Test 7, $\varepsilon_0 = 0.091$ (Uriz and Mahin 2008)

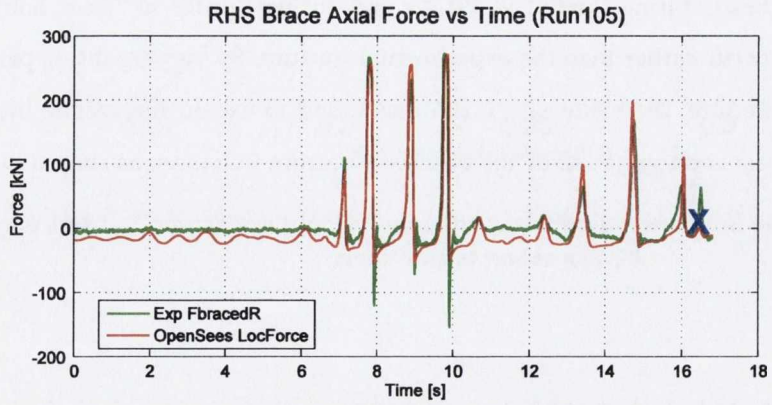

(d) Test 7, $\varepsilon_0 = 0.106$

Figure 10.17 – Fracture model implemented using (a) recommendations by Uriz and Mahin (2008) with $\varepsilon_0 = 0.091$ and (b) using $\varepsilon_0 = 0.106$. Predicted fracture point is indicated with 'X'.

Using the calibrated value of $\varepsilon_0 = 0.106$, the fatigue model was applied to the Reference Model for all tests. For the tests in which the simulated roof displacement was underpredicted, the corresponding elongation demand in the brace elements was insufficient to accumulate much damage in the element. Consequently, fibre removal was not triggered, and fracture was not initiated in those brace models. Table 10.5 identifies the five tests in which fracture was initiated in the model. Table 10.5 also shows, for all tests, the maximum brace elongation ΔL_{max}, measured yield strength R_{eH} (see Section 8.4), brace yield elongation ΔL_y and the simulated and experimental displacement ductility $\mu_{\Delta,OS}$ and $\mu_{\Delta,exp}$ respectively. For tests where no fracture was initiated, the maximum recorded brace elongation was used to calculate $\mu_{\Delta,OS}$.

In the OpenSees model simulations in which fracture was not detected, the ratio $\mu_{\Delta,OS}/\mu_{\Delta,exp}$ ranges from 1.16 to 3.78. These values reflect the underprediction of drift demand by OpenSees in these tests. For the five tests where fracture was detected there is a narrower range of 0.93 to 1.58, with one test overpredicting brace ductility capacity as illustrated in Figure 10.18. Figure 10.18 shows that fractured models display $\mu_{\Delta,OS}/\mu_{\Delta,exp}$ ratios close to 1.0. This is attributable to both the closer fidelity of simulated displacements to measured experimental roof displacements and the ability of the calibrated fatigue model to capture the point of fracture.

Table 10.5 – Predicted brace ductility capacity values using $\varepsilon_0 = 0.106$.

	Fracture Initiated?	ΔL_{max} (mm)	R_{eH} (MPa)	ΔL_y	$\mu_{\Delta,OS}$	$\mu_{\Delta,exp}$	$\mu_{\Delta,exp}/\mu_{\Delta,OS}$
Test 1	False	12.9	372.5	6.31	2.04	2.9	1.42
Test 2	True	42.3	384.3	6.51	6.49	8.3	1.28
Test 3	True	55.2	347.5	5.89	9.37	10.6	1.13
Test 4	False	15.6	341.5	5.79	2.69	6.3	2.34
Test 5	False	12.1	337.8	5.72	2.11	7	3.31
Test 6	True	35.6	341.7	5.79	6.15	9.7	1.58
Test 7	True	73.4	370.5	6.28	11.70	10.9	0.93
Test 8	False	9.5	336.5	5.70	1.67	6.3	3.78
Test 9	False	6.3	340.0	5.76	1.10	3.2	2.91
Test 10	True	54.5	347.5	5.89	9.25	12	1.30
Test 11	False	12.5	341.5	5.79	2.16	6.2	2.88
Test 12	False	33.6	370.5	6.28	5.35	6.2	1.16

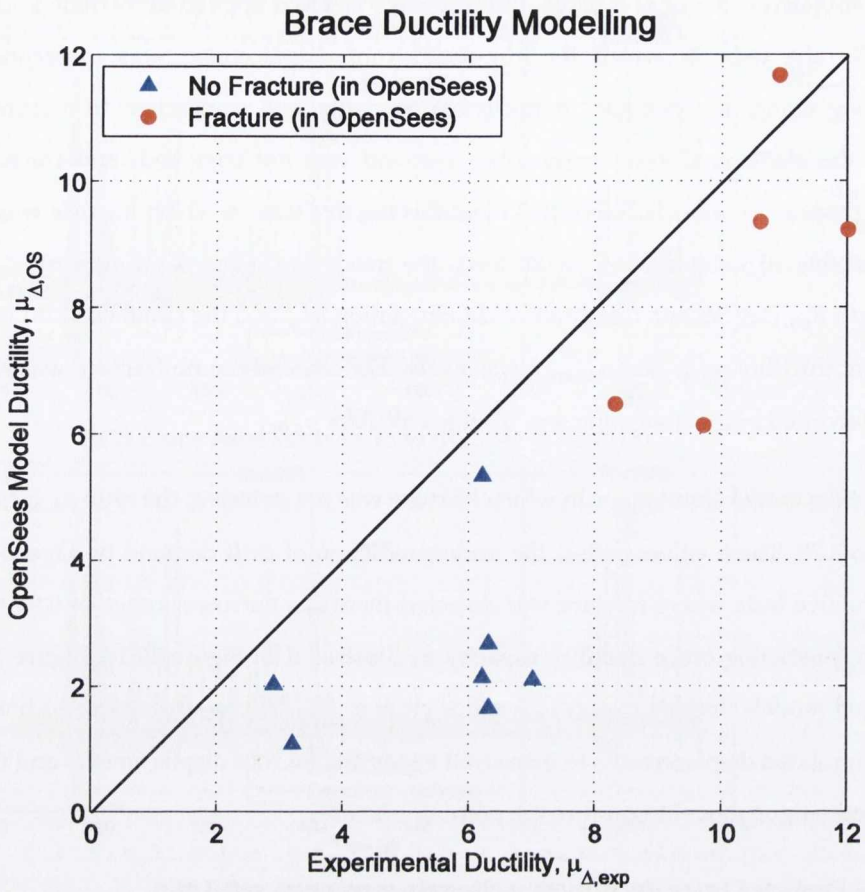

Figure 10.18 – Comparison of experimental and OpenSees brace ductility capacities/demands with and without fracture initiation.

10.6 CB Rotational Stiffness

In the Reference Model, the CA and CB style connections were modelled as continuous and pinned joints respectively. This section examines the effect of using a rotational spring to model joint rotation for the CB configuration in Tests 8 – 12. The rotational stiffness values employed were determined using the equivalent T-stub model and the recommendations of Thomson (2001) as described in Chapter 4.

As shown in Table 10.6, the effect of the prescribed stiffness slightly reduces the natural period of the OpenSees model compared to the pinned connection in the Reference Model. Effectively, the frame stiffness is increased, causing the modelled natural period to move slightly away from that observed during the shake table experiments.

Figure 10.19(a) compared the acceleration and drift responses of Test 8 obtained using the pinned and prescribed stiffness connections for a small response history window. Overall there is a negligible difference between the two responses, with no improvement in the OpenSees response prediction. The same behaviour is observed across the complete duration of these responses. Figure 10.19(b) illustrates different acceleration responses for Test 11. No distinctive pattern is observed, although the drift response shows a slight decrease in the peak drift response which is in line with the expected effect of implementing a non-zero connection stiffness.

Similar trivial changes were observed in the responses of all OpenSees models where the alternate connection stiffness was implemented.

Table 10.6 – Change in structural period with alternate CB connection stiffness.

Test	Specimen	Natural Period, T_n (s)		
		Experimental	OpenSees, Ref. Model (Pin)	OpenSees, w/ CB Stiffness
8	S1-CB-G1	0.226	0.188	0.186
9	S2-CB-G1	0.258	0.200	0.199
10	S4-CB-G2	0.242	0.225	0.223
11	S2-CB-G2	0.220	0.203	0.201
12	S3-CB-G2	0.246	0.239	0.236

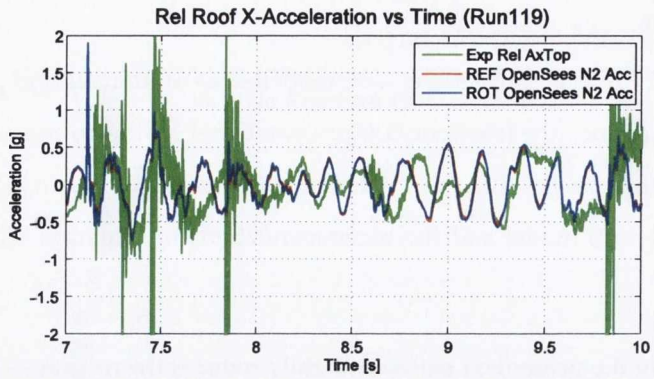

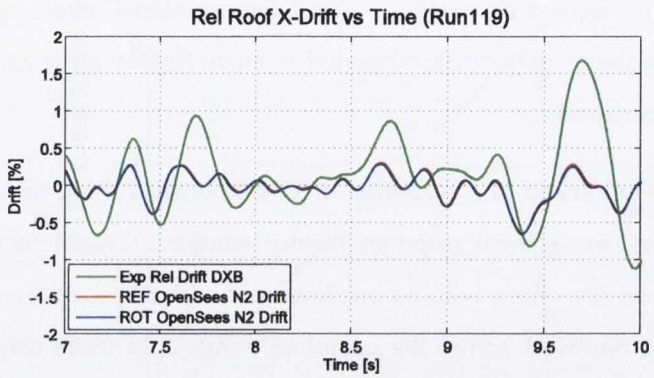

REF = Pinned Connection (Reference Model)
ROT = Prescribed Stiffness (Thomson, 2001)

(a) Acceleration and drift responses for Test 8.

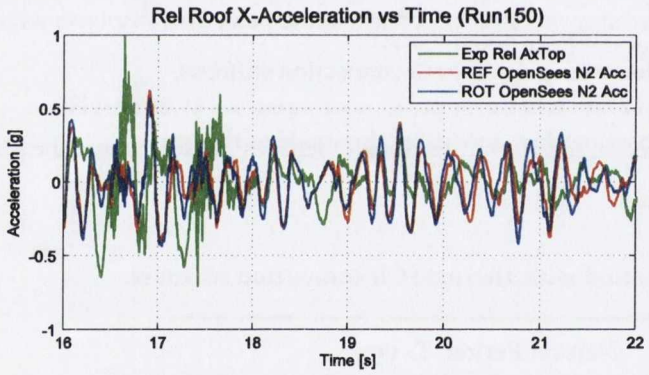

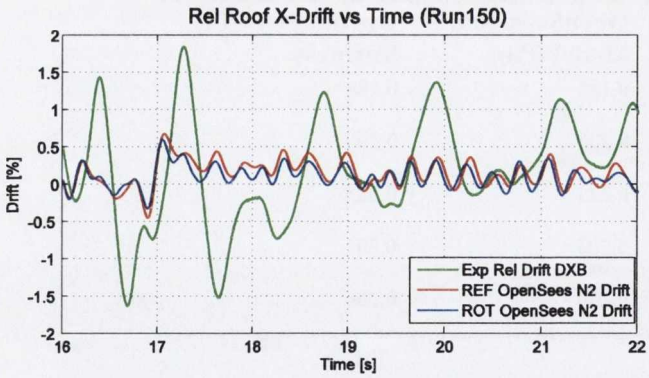

REF = Pinned Connection (Reference Model)
ROT = Prescribed Stiffness (Thomson, 2001)

(b) Drift responses of Test 11.

Figure 10.19 – OpenSees responses compared using pinned and prescribed stiffness connections for Tests 8 and 11.

10.7 Chapter Overview

In Chapter 4 important OpenSees modelling considerations were explored. At the beginning of this chapter, relevant modelling aspects were assembled to form the shake table Reference Model. The rationale behind many of the modelling decisions was explained leading to a generic model for all test specimens. Very good fidelity was shown for Tests 2, 3, 6 and 7 particularly in relation to matching modelled and observed response acceleration. Underestimation of the experimental roof displacements was consistent for most of the simulations. In the subsequent sections, more specific modelling options were explored, particularly in relation to their relevance for different specimen configurations. This included: changing the boundary conditions at the lower brace-swivel connections; implementing a fatigue model using recommended parameter values and suggesting parameter values that improve fatigue model accuracy; and investigating the influence of pinned and non-zero rotational stiffness values for CB style connections.

11 Conclusions

11.1 Summary

The overall aim of this work was to improve upon existing understanding of, and numerical modelling methods for, steel CBFs subjected to seismic loading; and to assess the implications for design methods and guidance. To achieve this pseudo-static and shake table tests of model CBFs were carried out with a range of realistic brace specimen and connection designs. The pseudo-static tests (Complementary Cyclic Tests) were performed at Trinity College Dublin to provide information on the strength and ductility of brace specimens under cyclic loading and assess the capabilities of proposed finite element models. This work helped in the preparation and development of the shake table tests, which were later performed as part of the BRACED project at CEA Saclay, France.

Prior to developing complete numerical simulation models of full CBFs, a tiered hierarchical approach was employed in which fundamental modelling aspects were investigated first, progressing to model optimisation using advanced models with greater detail. Firstly, different aspects of the available OpenSees modelling techniques were examined in a parametric study on simplified tube members. The optimum parameter properties were established and used in developing full-scale brace member models. Using these brace member models, a correlation study was carried out, using experimental results obtained by Goggins (2004), to demonstrate the capabilities and limitations of the OpenSees physical theory model when applied to hollow section bracing members. This lead the finer level of model development, where models of both the Complementary Cyclic Tests and BRACED project test frames and specimens were later used to predict their respective responses.

A total of six cyclic loading tests were performed on CBF models with a single diagonal brace member. The test parameters examined the following variables: two brace cross section sizes; conventional and recently-proposed gusset plate geometrical designs; and two gusset plate connection conditions. The brace slenderness range of 0.75 – 1.75 was similar to the range subsequently examined in the BRACED specimens (0.82 – 1.64). The results provided vital information on the response and failure mode of brace specimens, and indicated a significant dependency on the gusset plate connection boundary conditions at the beam-column connection. In addition, the influence of gusset plate geometrical design on maximum drift range and displacement ductility was presented. Finite element models in OpenSees were developed using

previously established modelling recommendations. Simulated and measured results were compared in a correlation study and good accuracy was demonstrated by the OpenSees models.

The BRACED project investigated the behaviour of concentrically braced frames (CBFs) under earthquake loading. While the primary focus of the project was the ultimate response of brace members during severe seismic events, frame and component behaviour under low-to-moderate earthquake loading was also examined. The research programme was designed to validate empirical models for the ductility capacity of hollow section bracing members and recent proposals for the improved detailing of gusset plate connections, to identify active yield mechanisms and failure modes in different brace member/connection configurations, and to provide essential data on the earthquake response of European CBFs.

The central element of the integrated experimental and numerical research programme was a series of shake table experiments on full-scale model single-storey CBFs designed to Eurocode 8 (CEN, 2004). Twelve separate experiments were performed on the AZALEE seismic testing facility at CEA Saclay. The properties of the brace members and gusset plate connections were varied between experiments to examine a range of feasible properties and to investigate the influence of conventional and improved design details on frame response. The large dimensions and capacity of the AZALEE table allowed realistically-sized brace members to be tested, with global and local slendernesses within the ranges allowed for dissipative CBFs designed to Eurocode 8. The improved gusset-plate designs incorporated two separate but linked approaches: the use of a balanced design approach that seeks to improve brace ductility by ensuring that gusset plate resistance is not considerably greater than brace resistance, and the detailing of an elliptical clearance plastic hinging zone that allows more compact gusset plate sizes.

Each experiment examined the response of the test frame and brace-gusset plate specimens to table excitations scaled to produce elastic response, brace buckling/yielding and brace fracture. The outputs of the research programme represent a unique set of data on the ultimate earthquake response of CBFs with realistic brace members and connections. The principal experimental outcomes included measurements of elastic frame stiffness and its evolution with brace damage, observations on brace failure mechanisms; measurements of the displacement ductility capacity of the brace specimens; an evaluation of the influence of brace connection configuration and gusset plate detailing on frame stiffness, damping and ductility; and observations on the contributions of brace and connection yielding to overall inelastic deformation of CBFs.

Numerical modelling of CBFs was discussed in the context of the model CBF from the BRACED project. A general, reference model was presented and its robustness was examined through

comparisons with test results of varying brace member specimens used in the BRACED project. Based on this, several modelling options were explored including: the influence of including different boundary conditions at the lower brace connection at the swivels; fatigue material input parameters; and moment-rotation stiffness at the beam-column connections.

11.2 Conclusions

The conclusions of the experimental and theoretical work undertaken within the scope of this research are presented within three main categories in the following sub-sections: complementary cyclic test results; BRACED project results and numerical modelling results.

11.2.1 Complementary Cyclic Test Results

Initial Brace Camber

- Prior to each test, the initial deformation of each brace member was measured in both the in-plane and out-of-plane directions. It was found that during all the cyclic tests, the initial measured out-of-plane camber dictated the direction of buckling of the brace member. The initial camber direction was applied to the OpenSees models but due to its small amplitude, using either direction had no measurable effect on the simulated results. It was observed that using initial cambers larger than measured values, reduced buckling resistances which is in agreement with the findings of Goggins (2004).

CA and CB connection configurations

- Comparison of measured and theoretical initial stiffnesses K_{fr} and K_{br}, showed that, in all tests, there existed sources of frame flexibility that were not considered by the theoretical formulation. With the exception of S40-CA-G1, larger K_{fr} values were observed for the CA connections compared to the CB connections.
- For all test specimens, the end conditions of the CB connection type exhibited a more 'pinched' hysteretic plot characteristic that is archetypal of CBF behaviour. This was not as prominent in the CA specimens because the extra rotational restraint of the connection reduces the brace effective length and increases the brace buckling load and post-buckling resistance. The post-buckling frame resistance was also supplemented by the frame joint rotation resistance provided by the connection of the gusset plate to both beam and column flanges.
- The yield and post-buckling lateral frame resistance offered by the beam-column connection decreased with subsequent testing. This was caused by local yielding in the right-hand connection due to an imposed history of large displacement amplitudes.

- The measured strain at the gusset plate boundaries approached or exceeded yield. For CA specimens the strains at both restrained edges (SG4 and SG6) were similar in magnitude. For CB specimens the strain at the restrained edge (SG6) was significantly larger than that the strain at the unrestrained edge (SG4).

G1 and G2 geometrical gusset designs

- Comparing Tests 3 and 4 (S40-CB-G1 and S40-CB-G2), a larger drift capacity and therefore larger ductility capacity was achieved with the G2 design. In Tests 5 and 6 (S60-CA-G1 and S60-CA-G2), the high cross-section slenderness dominated brace fracture behaviour leading to the same number of cycles to brace failure (N_f) and the same maximum drift values in both specimens. The high cross-section slenderness of these specimens resulted in significant localised strains at brace mid-length during early compression cycles.
- Comparison of strain measurements near the plastic hinge zones of the G1 and G2 geometrical designs showed that much higher strains were observed with G2 gusset plates in CA type connections, but not with CB type connections.
- An increase in total energy dissipated E_{tot} for G2 specimens was observed for all G2 specimens compared to corresponding G1 specimens.

Displacement ductility and energy dissipation

- Predictions of the displacement ductility capacity of each specimen made using the model proposed by Nip et al. (2010) were compared with the measured experimental values. For specimens with lower cross-section slenderness, the predicted values underestimate the measured ductility capacity. This may be attributable to influence of the gusset plate connections in the test specimens, which contrast with the fixed-end stiffened connections employed in the specimens tested by Nip et al. (2010). For specimens with high cross-section slenderness ratios, the predicted values overestimate the measured ductility capacity. The prediction methods of Tremblay (2002) and Goggins et al. (2006) overestimated the measured ductility capacities in all tests.
- Calculations for total energy dissipated E_{tot}, displayed a general increase in energy dissipation for larger β_{ww} values. Brace size was shown to significantly influence the energy dissipated in a single displacement cycle. S40 specimens showed greater E_{tot} values overall, particularly at higher β_{ww} values due to the more fully developed hysteretic loops.

11.2.2 BRACED Project Results

Frame Stiffness and Damping

- White noise excitation tests were conducted at the start of each set of tests on a pair of brace-gusset plate specimens, and again after each earthquake excitation test in which brace failure did not occur, to evaluate the initial elastic properties of the structure, and the evolution of these properties as the level of excitation applied to the structure increased. The obtained results displayed variations in initial frame stiffness and damping due to brace size, gusset plate design detail, and beam-to-column joint rotation stiffness due to different brace connection types. The results also quantified how the presence of residual global brace deformations following buckling is expected to lead to deterioration frame stiffness after each earthquake test.
- The initial natural frequency (and therefore stiffness) of the frame was directly influenced by brace specimen cross-section size and gusset plate connection configuration. The larger cross-sections (S1 and S2) tended to display shorter natural periods than the smaller ones (S3 and S4) which had longer periods. This was attributable the increased stiffness (higher frequencies) for larger brace cross-section areas. For a given cross-section size, the shortest natural period (highest frequency) tended to be displayed by specimens with the conventional CA-G1 connection configuration, but the lengthening of natural periods observed with other configurations was small.
- The initial damping values displayed by the test frame ranged from just below 2% to just over 4.5%. No definite trends are observable in the measured damping data, but frames with CB connections tended to have lower damping than frames with CA connections, and frames with G2 connections tended to have lower damping than frames with G1 connections.
- Response history, represented as the maximum drift experienced by the test frame, strongly influenced the stiffness and damping characteristics of the model CBF. Frame stiffness is observed to reduce, and damping is observed to increase, with the previous maximum drift experienced by the frame. Maximum frame drift, especially in the plastic range, was linked to the residual out-of-plane brace deformation at the end of an earthquake test run, and these effects were more pronounced with slender brace members.

Drift Demand

- The variation of test frame response with brace-gusset plate specimen properties was compared by examining the variation in maximum response quantities (drift, forces, etc.) between earthquake excitation runs in an individual test, and between different tests.
- When the larger brace cross sections (S1 and S2) were employed, the test frame displayed a mostly linear relationship between maximum drift demand and PGA, but with the smaller

cross sections (S3 and S4), increasing drift values were exhibited for higher PGA. This behaviour is expected in long period structures that are subjected to ground excitations substantially greater than those required for initial yield. While the experimental results indicated that maximum drift demand was sensitive to brace strength, they did not suggest that it was strongly influenced by connection configuration or design.

Brace Resistance

- The variation in maximum brace tension and compression forces with PGA was examined in terms of the characteristic plastic resistance, $N_{pl,meas}$, of the brace cross-section or the characteristic buckling strength, $N_{b,Rd}$, of the brace member.
- In all tests, the maximum tension forces experienced in the 50%/50 (low) level runs remained well below yield, typically in the range 0.3-0.6 $N_{pl,meas}$. Tensile yielding occurred in approximately half of the 10%/50 (intermediate) level runs and all but one of the 2%/50 (high) level runs. The maximum tension forces experienced in the different tests were in the range 1.0-1.25 $N_{pl,meas}$.
- The maximum measured brace compression forces were all significantly higher than characteristic buckling strength, $N_{b,meas}$, of the brace members, confirming that the actual effective lengths of the braces were less than the value of 1.0 used to calculate $N_{b,Rd}$. The maximum values generally lay in the range 1.5 to 2.0 $N_{b,Rd}$, which is consistent with an effective length factor of approximately 0.75. There was clearly substantial variation in these values between tests, which were influenced by the rotational restraint imposed by the different gusset plate connection types.
- The maximum brace compression forces observed in each test occurred at different excitation levels, but never in the first 50%/50 (low) level run, and confirmed that brace buckling occurred in all 10%/50 (intermediate) level runs.

Ultimate Response and Fracture

- The complementary cyclic tests carried out in support of the shaking table tests gave two important outcomes: they confirmed the feasibility of the test-set and the adequacy of the frame and test specimen design procedures; and they identified the form of ultimate failure to be expected in brace members with different types of gusset plate connections.
- A similar pattern of failure was displayed in all cyclic and shaking table tests: brace buckling in compression led to large out-of-plane brace bending and the formation of a plastic hinge close to brace mid-length. During large amplitude displacement cycles, local buckling occurred in these plastic hinges, and as the hinge rotation demand increased, a

small tear initiated at the peak of the local buckle. Upon subsequent reversal of the direction of frame response the brace experienced tension forces which caused these tears to propagate throughout the depth of the cross section causing brace fracture.

- Brace fracture was observed in all shaking table tests, either in the third or fourth earthquake excitation run. During the low level test excitations the frame remained elastic with no brace buckling. Brace buckling and yielding occurred in the intermediate level runs, sometimes with large out-of-plane brace buckling deformations, but always with limited plastic deformation demand. A fully inelastic response was observed in all high level excitation tests, usually causing fracture in one or both braces. In some tests, an additional failure level earthquake excitation run was added to cause brace fracture.
- In contrast, no gusset plate failures (plate fracture, plate buckling, weld or bolt failure) occurred in any test, validating the capacity design and overstrength procedures employed. This is an especially important result given that the experimental programmes included some less-common gusset plate connection features, such as the relatively thin gusset plates employed in the balanced design approach, brace connection to beam members only (as well as to beam and column), and bolted (rather than welded) connection of the gusset plate to the beam and column frame members. Both the SLC and EC gusset plate detailing models successfully provided the plastic hinge yield patterns required to accommodate large out-of-plane brace buckling deformations.

Frame Displacement Ductility

- The differences between the PGA values required to cause brace yield and brace fracture reflect the global dissipative capacity of the test frame. Overall these results suggested that the use of a G2 (balanced) gusset plate design instead of a G1 (conventional) design led to brace fracture at higher PGA values and higher maximum brace tension forces.
- The maximum frame drift and brace force measurements were also combined to give a high-level indication of the influence of brace-gusset plate specimen connection type on the global ductility capacity of the test frame. In each of the three pairs of tests which directly compared the application of the conventional and balanced design methods to CA-type connections, the balanced design specimens reached a larger drift before brace fracture. Across all tests, similar comparisons support the hypothesis that the use of the balanced gusset plate design method leads to a more ductile and dissipative response in CBFs without loss of brace resistance.

Measured Brace Ductility

- The displacement ductility capacities of the brace-gusset plate specimens were evaluated by normalizing the brace fracture elongation by the brace yield displacement. The brace fracture elongation value was taken as the maximum measured change in overall brace length in a fractured brace during the earthquake test run in which that brace fractured. The resulting measured brace displacement ductility capacities varied between 2.9 and 12.0, with a mean value of $\mu_\Delta = 7.5$. The variation between the values identified in each test was attributable to the main test specimen parameters: member slenderness, cross-section slenderness, connection type and gusset plate design method.
- Larger ductility capacities were displayed by specimens with smaller cross sections (S3 and S4), with ductility capacity increasing with increasing member slenderness, $\bar{\lambda}_{Rd}$, and reducing with increasing b/t ratio (cross-section slenderness). The use of the balanced gusset design approach (G2) led to larger brace ductility capacity than the conventional approach (G1). In the set of tests where a direct comparison of the two approaches can be made, the ductility capacity of the balanced design specimens was on average 80% greater than that of the conventionally-designed specimens. Displacement ductility capacity was observed to increase with gusset plate balance factor, β_{ww}.

Predicted Brace Ductility

- Previous experimental studies that examined the response of hollow section steel members under cyclic axial loading gave rise to empirical parametric prediction equations for brace displacement ductility capacity that account for the influence of member and section slenderness. The displacement ductility capacity values measured in the dynamic shaking table tests performed in this study were compared with predicted values given by these equations.
- None of the predicted data sets were observed to agree well with the measured values. The expression suggested by Tremblay (2002) overpredicted the measured values, while that suggested by Nip et al (2010) underpredicted the measured values for all but one test. While the trends of the data evident in these comparisons suggested that the parameterisation of these models is appropriate for the conditions considered in the experiments performed in this study, comparison with the expression suggested by Goggins (2006) emphasised the sensitivity of empirical models to the parameter range used in calibration.
- These comparisons also raised the difficulty in aligning ductility capacity measurements performed in the highly-controlled cyclic testing environment, with those obtained in dynamic shake table testing. In cyclic testing, specimen failure occurs in one of the largest

amplitude loading cycles and the corresponding ultimate deformation is readily identified. In contrast, during shake table testing with a highly variable displacement demand history, the maximum deformation may occur a number of cycles before final fracture. For asymmetric response such as is encountered with brace axial resistance, deformation in compression may also be treated differently to deformation in tension.

11.2.3 Numerical Modelling Results

Parametric Study

- Having examined the merits and disadvantages of Displacement Based Elements (DBE) and Force Based Elements (FBE), the FBE was utilised in the OpenSees models of the cyclic and shake table test frames. This was primarily because the accuracy of the FBE can be improved by increasing the number of integration points or the number of elements. Error can only be improved for the DBE by increasing the number of elements with larger computational effort required to achieve comparable accuracy to the FBE. This is especially important when calculating response time-histories using numerical integration, as was done for the shake table test correlative analysis.
- Due to the uncertainty associated with SHS buckling direction, prescribing an initial camber curvature in both buckling planes lead to the most realistic result.
- The order of magnitude of the initial camber strongly influences the initial buckling capacity, producing larger buckling loads with decreased camber magnitude. Conversely, reduced loads are observed with cambers approaching unrealistically large values. A value of 0.1% camber at brace mid-length was recommended to achieve buckling loads approaching those predicted by design standards.
- The effect of varying the number of elements was minimal when examining the monotonic compression and hysteretic performance of the test models. However, the optimum curvature response was observed when using at least four elements along the brace length.
- With regard to the balance between computation time and accuracy, a minimum of five integration points per element is recommended.

Complementary Cyclic Tests Correlation

- For modelling rigid zone elements at structural connections, rigid link elements provide more realistic behaviour than equal degree of freedom nodal constraints because they assume small rotations allowing the kinematic behaviour of the connection to be modelled.
- For connectivity at the beam-column connection, a continuous connection using rigid links is recommended for CA connections. For CB connections, a ZeroLength element with a

spring rotational stiffness calculated from design recommendations demonstrated reasonable accuracy. However, after subsequent testing and a history of large displacement amplitudes, the theoretical stiffness value became less relevant as the connection stiffness approached the conditions similar to a nominally pinned connection.

- To represent the out-of-plane stiffness of the gusset plate, very good fidelity was achieved by using a ZeroLength element spring with a stiffness calculated from gusset geometry, for standard thickness gusset plates using the SLC method (G1),. However, for thinner plates designed using the EC method, some overestimation of the true resistance provided by the brace boundary conditions was observed. This indicates that the stiffness formula becomes less applicable for very thin gusset plates.
- The fatigue model parameter $\varepsilon_0 = 0.165$ did not lead to fracture predictions in any of the cyclic tests. This was investigate more thoroughly in the BRACED project OpenSees models.

BRACED Project Correlation

- A numerical model of the shaking table test frame was created using guidance provided by earlier researchers and further developed using the results of the complementary cyclic tests performed in this study. In time-history analysis, the model proved capable of predicting the resistances of the brace members under dynamic loading conditions and of incorporating different brace member sizes and strengths, and different types of gusset plate connections, including the influence of this connection on the overall stiffness of the beam-to-column joint.
- For the high level earthquake excitation tests, the simulated response histories showed good agreement with the experimental acceleration response, which was closely influenced by the resistances of the brace members, but less good agreement with the experimental displacement response. The model also possesses the ability to predict brace fracture through a low-cycle fatigue approach, and this was demonstrated to be capable of accurately predicting brace fracture when global frame displacements are accurately modelled and particular values are used for the low-cycle fatigue model parameters. The value $\varepsilon_0 = 0.091$ recommended by (Uriz and Mahin, 2008) predicted fracture slightly before experimental fracture. Increasing this value to $\varepsilon_0 = 0.106$ achieved better representation of the observed experimental fractures.
- The OpenSees model was observed to be highly sensitive to a number of model parameters, with small changes in values leading to very different output, or to convergence failures. The modelled results were especially sensitive to the modelling of

boundary restraints at either end of the brace member, including the rotational restraint provided by the swivel bearing that connected the brace to the AZALEE shaking table. Specifically, it was observed that releasing a modelled rotational restraint at the swivel bearing improved model accuracy for CB specimens in terms of the dynamic properties and the response output. The inclusion of a calculated rotational stiffness in the beam-column connection, showed no notable improvement in model accuracy over the use of a fully pinned connection.

11.3 Future Work

The successful execution of the cyclic tests and the BRACED project has opened up further possibilities for research and the development of seismic design guidance for CBFs. Two types of additional research works can be identified: those that continue directly and employ outputs from the suite of experimental tests, and those that extend the scope of the work to other immediately relevant topics.

Experimental Analysis: The twelve shaking table tests performed within the BRACED project have produced a large amount of valuable experimental data on the seismic behaviour of CBFs and their brace members. These data have been presented and interpreted in this thesis, however in the time available it has not been possible to complete all associated experimental analysis. Amongst others, further analysis will examine the distribution of strains in the brace and gusset plates using recorded strain gauge and videometric data; apply signal processing techniques to the identification of short-term frame stiffness and damping, quantify the energy dissipation capabilities of the brace-gusset plate specimens, assess the influence of cycle number and amplitude on brace ductility, develop new ductility capacity prediction models relevant for seismic response histories, assess the utility of the balanced design approach for gusset plate connections, and compare the performance of the test CBF at different excitation and performance levels.

Numerical Modelling: The OpenSees reference model of the CBF test frame should be employed to widen the range of experimental parameters considered in the BRACED test programme. This should include different structural properties, including more combinations of brace sizes and gusset plate connection designs, and a wider range of earthquake excitations. The behaviour of the gusset plate connections should also be considered in detailed finite element analysis aimed at validating appropriate design ranges for key dimensional and strength parameters, considering the influence of this component on the brace member response, and the beam-to-column joint behaviour.

Further Shake Table Testing: The BRACED project sought to investigate the influence of structural parameters (e.g. brace size, gusset plate design) on overall CBF response and ductility. While all tests employed the same earthquake record, the test results indicated that system and element behaviour are response history dependent, and that seismic performance during strong seismic events is likely to be more sensitive than other structural forms to ground motion characteristics. A further set of shake table tests should be performed to assess this sensitivity by subjecting the test frame to table excitations from different earthquakes representing European seismic events of varying intensity. For consistency with the BRACED experimental results, the same test set-up, test frame, brace-gusset plate specimens, instrumentation and experimental methodology should be employed. These experiments should be supported by the numerical analysis described above, but results from the BRACED project suggest that analysis alone would not provide sufficiently reliable results.

CBF Design for Europe: The BRACED project was designed to investigate the ultimate response of bracing members and their connections in CBFs. This led to the completion of a set of tests in which brace fracture was successfully observed in each case. In addition, however, lower level earthquake excitation tests examined test frame performance during conditions where buckling, yielding and inelastic deformation demands were much more limited. These conditions are more likely to be encountered in earthquake-resistant CBF design throughout much of Europe, and the good seismic performance of the test frame during these test runs was apparent. There is a strong need for recent advances in the earthquake-resistant design of CBFs, developed for the case of highly-dissipative structures for regions of high seismicity, to be translated for the design of structures in regions of low-to-moderate seismicity and/or structures with low energy dissipation and deformation ductility demand.

Performance Based Design: CBFs offer efficient lateral strength and stiffness properties that are attractive for earthquake-resistant design. The benefits of these properties can be exploited in performance-based design that emphasizes the behavior of structures at limit states other than the ultimate limit state that was the principal focus of the BRACED project. Residual global and local structural deformations after a seismic event are an important performance parameter, and although braced frames are likely to perform well in this regard, current design on the topic is limited. There is need for further research to evaluate the probable magnitude of the residual deformations in CBFs taking into account variable ground motion characteristics and the properties of CBFs designed using various approaches (dissipative or non-dissipative; balanced or conventional). Further to this, supplementary methods, such as self-centring devices, for the

control of residual deformations for specific CBF typologies and performance requirements should be developed.

References

ABAQUS (2009). *Analysis User's Manual I-V. Version 6.9,* USA, ABAQUS Dassault Systems.

ABRAMOWITZ, M. & STEGUN, I. A. (1965). *Handbook of Mathematical Functions: With Formulas, Graphs, and Mathematical Tables*, Dover Publications.

AISC (2005a). ANSI/AISC 341-05, *Seismic Provisions for Structural Steel Buildings*. American Institute of Steel Construction, Chicago, Illinois.

AISC (2005b). ANSI/AISC 360-05, *Specification for Structural Steel Buildings*. American Institute of Steel Construction, Chicago, Illinois.

AISC (2005c). *Steel Construction Manual, 13th Edition,* Chicago, Illinois.

AISC (2010). ANSI/AISC 341-10, *Seismic Provisions for Structural Steel Buildings*. American Institute of Steel Construction, Chicago, Illinois.

AISI (2007). AISI S100-2007, *North American Specification for the Design of Cold-Formed Steel Structural Members*. American Iron and Steel Institute, Washington, DC.

ALGERMISSEN, S. & LEYENDECKER, E. A technique for uniform hazard spectra estimation in the US. Published Tenth World Conference on Earthquake Engineering, 1992. 391-397.

ARCHAMBAULT, M. H., TREMBLAY, R. & FILIATRAULT, A. (1995) Étude du comportement séismique des contreventements ductiles en X avec profiles tubulaires en acier. *EPM/GCS 1995-09*. Département de génie civil, École Polytechnique, Montréal, Canada.

ASCE (2010). SEI/ASCE 7-10, *Minimum Design Loads for Buildings and Other Structures*. American Society of Civil Engineers, Reston, Virginia.

ASTANEH-ASL, A. (1998) Seismic Behaviour and Design of Gusset Plates. University of California, Berkeley,

ASTANEH-ASL, A., CALL, S. M. & MCMULLIN, K. M. (1989). Design of single plate shear connections. *Engineering Journal,* First Quarter.

ASTANEH-ASL, A., GOEL, S. C. & HANSON, R. D. (1981). Behavior of Steel Diagonal Bracing. Published ASCE Conference, 1981 St. Louis, Missouri.

ASTM (2011). ASTM E1049 - 85, *Standard Practices for Cycle Counting in Fatigue Analysis*. American Society for Testing and Materials, West Conshohocken, PA.

BAKER, J. W., LIN, T. & SHAHI, S. K. (2011) New Ground Motion Selection Procedures and Selected Motions for the PEER Transportation Research Program. *PEER 2011/03*. Pacific Earthquake Engineering Center, University of California, Berkeley.

BALLIO, G. & CASTIGLIONI, C. A. (1995). A unified approach for the design of steel structures under low and/or high cycle fatigue. *Journal of Constructional Steel Research,* 34, 75-101.

BAUSCHINGER, J. (1886). On the change of the elastic limit and the strength of iron and steel, by drawing out, by heating and cooling, and by repetition of loading (summary). Published Minutes

of Proceedings of the Institution of Civil Engineers with Other Selected and Abstracted Papers, 1886. LXXXVII, 463.

BLACK, R. G., WENGER, W. A. B. & POPOV, E. P. (1980) Inelastic Buckling of Steel Struts Under Cyclic Load Reversals. *UCB/EERC-80/40*. Earthquake Engineering Research Center, University of California, Berkeley.

BOMMER, J. J. & PINHO, R. (2006). Adapting earthquake actions in Eurocode 8 for performance-based seismic design. *Earthquake Engineering & Structural Dynamics,* 35, 39-55.

BRODERICK, B. M., GOGGINS, J. M. & ELGHAZOULI, A. Y. (2005). Cyclic performance of steel and composite bracing members. *Journal of Constructional Steel Research,* 61, 493-514.

BRODERICK, B. M., GOGGINS, J. M., HUNT, A. D., MONGABURE, P., SALAWDEH, S., O'REILLY, G., BEG, D., MOZE, P., SINUR, F. & ELGHAZOULI, A. Y. (2013) BRACED - Brace Response and Assessment: Computation, Experiments and Design. *Project No.: 227887.* Trinity College, University of Dublin, Dublin.

BROWN , V. L. S. (1988). Stability of Gusseted Connections in Steel Structures. *Ph.D. Thesis*. University of Delaware,

BUCKLEY, S. N. & ENTWISTLE, K. M. (1956). The bauschinger effect in super-pure aluminum single crystals and polycrystals. *Acta Metallurgica,* 4, 352-361.

CEA. (2011). *Seismic Mechanic Studies Laboratory* [Online]. CEA Saclay: CEA. Available: http://www-tamaris.cea.fr/index_en.php [Accessed March 27 2013].

CEN (2004a). BS EN 1998-1:2004, *Eurocode 8: Design of structures for earthquake resistance - Part 1: General rules, seismic actions and rules for buildings*. European Committee for Standardization, Brussels, Belgium.

CEN (2004b). BS EN 10025-2:2004, *Hot rolled products of structural steels - Part 2: Technical delivery conditions for non-alloy structural steels*. European Committee for Standardization, Brussels, Belgium.

CEN (2004c). EN 10204:2004, *Metallic products - Types of inspection documents*. European Committee for Standardization, Brussels, Belgium.

CEN (2005a). BS EN 1993-1-1:2005, *Eurocode 3: Design of steel structures - Part 1-1: General rules and rules for buildings*. European Committee for Standardization, Brussels, Belgium.

CEN (2005b). BS EN 1993-1-8:2005, *Eurocode 3: Design of steel structures - Part 1-8: Design of joints*. European Committee for Standardization, Brussels, Belgium.

CEN (2006a). BS EN 10219-1:2006, *Cold formed welded structural hollow sections of non-alloy and fine grain steels - Part 1: Technical delivery conditions*. European Committee for Standardization, Brussels, Belgium.

CEN (2006b). BS EN 1993-1-3:2006, *Eurocode 3: Design of steel structures - Part 1-3: General rules - Supplementary rules for cold-formed members and sheeting*. European Committee for Standardization, Brussels, Belgium.

CEN (2008). BS EN 1090-2:2008, *Execution of steel structures and aluminium structures - Part 2: Technical requirements for steel structures*. European Committee for Standardization, Brussels, Belgium.

CEN (2009). BS EN ISO 6892-1:2009, *Metallic materials - Tensile testing - Part 1: Method of test at room temperature*. European Committee for Standardization, Brussels, Belgium.

CHEN, J. T. & YOU, D. W. (1997). Hysteretic damping revisited. *Advances in Engineering Software,* 28, 165-171.

CHEN, L. Y., CHEN, J. T., CHEN, C. H. & HONG, H. K. (1994). Free vibration of a SDOF system with hysteretic damping. *Mechanics Research Communications,* 21, 599-604.

CHOPRA, A. K. (2006). *Dynamics of Structures, 3rd,* New Jersey, Prentice Hall.

COCHRAN, M. L. Seismic Design and Steel Connection Detailing. Published NASCC 2003, 2003 Baltimore, MD.

COFFIN, L. F. (1954). A Study of the Effects of Cyclic Thermal Stresses on a Ductile Metal. *Transactions of the American Society of Mechanical Engineers,* 76, 931-950.

COOLEY, J. W. & TUKEY, J. W. (1965). An algorithm for the machine calculation of complex Fourier series. *Mathematics of computation,* 19, 297-301.

CSA (2009). CSA S16-09, *Design of Steel Structures*. Canadian Standards Association, Ontario, Canada.

DING, Y. (2000). Residual Stresses in Hot-rolled Solid Round Steel Bars and Their Effect on the Compressive Resistance of Members. *Master of Applied Science*. University of Winsdor, Winsdor, Ontario.

ECCS (1976). Committee 8 - Stability, *Manual on Stability of Steel Structures*. European Convention for Constructional Steelwork, Brussels, Belgium.

ECCS (1986). Technical Committee 1, Technical Working Group 1.3, *Recommended Testing Procedure for Assessing the Behaviour of Structural Steel Elements under Cyclic Loads*. European Convention for Constructional Steelwork, Brussels, Belgium.

ELGHAZOULI, A. Y. (2009). *Seismic Design of Buildings to Eurocode 8,* New York, Spon Press.

ENGLISH, J. P. & GOGGINS, J. M. (2012). Nonlinear Seismic Response of Concentrically Braced Frames using Finite Element Models. *15 WCEE.* Lisbon.

FACCIOLI, E., PAOLUCCI, R. & REY, J. (2004). Displacement spectra for long periods. *Earthquake Spectra,* 20, 347-376.

FARDIS, M., CARVALHO, E., ELNASHAI, A., FACCIOLI, E., PINTO, P. & PLUMIER, A. (2005). *Designers' Guide to EN 1998-1 and EN 1998-5 Eurocode 8: Design of Structures for Earthquake Resistance,* London, Thomas Telford Publishing.

FELL, B. V., MYERS, A. T., DEIERLEIN, G. G. & KANVINDE, A. M. Testing and simulation of ultra-low cycle fatigue and fracture in steel braces. Published Proceedings of the 8th

National Conference on Earthquake Engineering 2006, San Francisco, USA, April 18-22 2006 San Francisco, California.

GIONCU, V. (2000a). Framed structures. Ductility and seismic response: General Report. *Journal of Constructional Steel Research,* 55, 125-154.

GIONCU, V. Influence of strain-rate on the behaviour of steel members. Published In: *Proceedings of the Third International Conference.* STESSA 2000, MAZZOLANI, F. M. & TREMBLAY, R., eds. 2000b Montreal, Canada.

GODDEN, W. G. (1997). Structural Engineering Slide Library. *In:* LIBRARY, E. E. R. C. (ed.). University of California, Berkeley.

GOGGINS, J. M. (2004). Earthquake resistant hollow and filled steel braces. *Ph.D. Thesis*. Trinity College, University of Dublin, Ireland.

GOGGINS, J. M., BRODERICK, B. M., ELGHAZOULI, A. Y. & LUCAS, A. S. (2006). Behaviour of tubular steel members under cyclic axial loading. *Journal of Constructional Steel Research,* 62, 121-131.

GUGERLI, H. & GOEL, S. C. Large Scale Tests for The Hysteresis Behavior of Inclined Bracing Members. Published Proceedings of the Seventh World Conference on Earthquake Engineering, 1980 Istanbul,Turkey. 7.

HASELTON, C. B., GOULET, C. A., MITRANI-REISER, J., BECK, J. L., DEIERLEIN, G. G., PORTER, K. A., STEWART, J. P. & TACIROGLU, E. (2008) An Assessment to Benchmark the Seismic Performance of a Code-Conforming Reinforced Concrete Moment-Frame Building. *PEER 2007/12*. Pacific Earthquake Engineering Research Center, University of California, Berkeley.

HIGGINBOTHAM, A. B. & HANSON, R. D. (1976). Axial hysteretic behaviour of steel members. *Journal of the Structural Division,* 102, 1365-1381.

HJELMSTAD, K. D. & POPOV, E. P. (1984). Characteristics of Eccentrically Braced Frames. *Journal of Structural Engineering,* 110, 340-353.

HSIAO, P.-C., LEHMAN, D. E. & ROEDER, C. W. (2012). Improved analytical model for special concentrically braced frames. *Journal of Constructional Steel Research,* 73, 80-94.

HUNT, A. D. & BRODERICK, B. M. (2010). Modelling Earthquake Resistant Hollow and Filled Steel Braces. Published Bridge and Infrastructure Research in Ireland, NÍ NUALLÁIN, N.-Á., ed. September 2010 Cork, Ireland. 1, 465-472.

IBC (2009). IBC 09, *International Building Code*. International Code Council, Illinois.

IKEDA, K. & MAHIN, S. A. (1986). Cyclic response of steel braces. *Journal of Structural Engineering,* 112, 342-361.

IKEDA, K., MAHIN, S. A. & DERMITZAKIS, S. N. (1984) Phenomenological Modeling of Steel Braces under Cyclic Loading. *UCB/EERC-84/09*. Earthquake Engineering Research Center, University of California, Berkeley.

INSTITUTE, A. P. (1977). *Recommended practice for planning, designing and constructing fixed offshore platform, 8th,* Dallas, Texas.

JAIN, A. K., GOEL, S. C. & HANSON, R. D. (1977) Static and dynamic hysteresis behaviour of steel tubular members with welded gusset plates. *UMEE 77R3*. Dept. of Civil Engineering, The University of Michigan, Ann Arbor, Michigan.

JAIN, A. K., GOEL, S. C. & HANSON, R. D. (1978). Inelastic response of restrained steel tubes. *Journal of the Structural Division,* 104, 897-910.

JAIN, A. K., GOEL, S. C. & HANSON, R. D. (1980). Hysteretic Cycles of Axially Loaded Steel Members. *Journal of the Structural Division,* 106, 1777-1795.

JIN, J. & EL-TAWIL, S. (2003). Inelastic Cyclic Model for Steel Braces. *Journal of Engineering Mechanics,* 129, 548-557.

KAHN, L. F. & HANSON, R. D. (1976). Inelastic cycles of axially loaded steel members. *Journal of the Structural Division,* 102, 947-959.

KANVINDE, A. M. & DEIERLEIN, G. G. (2004) Micromechanical simulation of earthquake-induced fracture in steel structures. *TR145*. The John A. Blume Earthquake Engineering Center, Stanford University,

KHATIB, I. F., MAHIN, S. A. & PISTER, K. S. (1988) Seismic Behaviour of Concentrically Braced Steel Frames. *UCB/EERC-88/01*. Earthquake Engineering Research Center, University of California, Berkeley.

KRAWINKLER, H. Loading histories for cyclic tests in support of performance assessment of structural components. Published The 3rd International Conference on Advances in Experimental Structural Engineering, 2009. 15-16.

LEE, S. & GOEL, S. C. (1987) Seismic behaviour of hollow and concrete-filled square tubular bracing members. *UMCE 87-11*. Department of Civil Engineering, The University of Michigan, Ann Arbor.

LEHMAN, D. E., ROEDER, C. W., HERMAN, D., JOHNSON, S. & KOTULKA, B. (2008). Improved Seismic Performance of Gusset Plate Connections. *Journal of Structural Engineering,* 134, 890-901.

LIGNOS, D. G., E., K. & MARTIN, G. (2012). A Steel Database for Modeling Post-Buckling Behavior And Fracture of Concentrically Braced Frames Under Earthquakes. *15 WCEE.* Lisbon.

LIU, J. & ASTANEH-ASL, A. (2004). Moment–Rotation Parameters for Composite Shear Tab Connections. *Journal of Structural Engineering,* 130, 1371-1380.

LIU, Z. & GOEL, S. C. (1987) Investigation of concrete-filled steel tubular cyclic bending buckling members. *UMCE 87-3*. The University of Michigan, Ann Arbor, Michigan.

MAHIN, S. A. (1998). Lessons from damage to steel buildings during the Northridge earthquake. *Engineering Structures,* 20, 261-270.

MANJOINE, M. J. (1944). Influence of rate of strain and temperature on yield stresses of mild steel. *Journal of Applied Mechanics,* 66, 211-218.

MANSON, S. (1965). Fatigue: A complex subject—Some simple approximations. *Experimental Mechanics,* 5, 193-226.

MATSUISHI, M. & ENDO, T. (1968). Fatigue of metals subjected to varying stress. *Japan Society of Mechanical Engineers, Fukuoka, Japan*, 37-40.

MCCRUM, D. P. (2012). Seismic Analysis of Braced Plan Irregular Structures Using Hybrid Testing and Numerical Modelling. *Ph.D. Thesis*. Trinity College, University of Dublin, Ireland.

MCCRUM, D. P. & BRODERICK, B. M. (2010). Seismic analysis using real-time hybrid test method. *Joint Symposium on Bridge & Infrastructure Research in Ireland and Concrete Research in Ireland.* University College Cork & Cork Institute of Technology Ireland.

MCKENNA, F. (1997). Object orientated finite element programming frameworks for analysis, algorithms and parallel computing. *Ph.D. Thesis*. University of California, Berkeley.

MEDHEKAR, M. S. & KENNEDY, D. J. L. (2000). Displacement-based seismic design of buildings—application. *Engineering Structures,* 22, 210-221.

MENEGOTTO, M. & PINTO, P. (1973). Method of analysis for cyclically loaded reinforced concrete plane frames including changes in geometry and nonelastic behavior of elements under combined normal force and bending. Published Proceedings of IABSE Symposium on Resistance and Ultimate Deformability of Structures Acted on by Well Defined Repeated Loads, 1973.

NEHRP (2009). FEMA P-750, *Recommended Seismic Provisions for New Buildings and Other Structures*. Building Seismic Safety Council, Washington, D.C.

NEUENHOFER, A. & FILIPPOU, F. C. (1997). Evaluation of nonlinear frame finite-element models. *Journal of Structural Engineering,* 123, 958.

NIP, K. H., GARDNER, L. & ELGHAZOULI, A. Y. (2010). Cyclic testing and numerical modelling of carbon steel and stainless steel tubular bracing members. *Engineering Structures,* 32, 424-441.

NISEE. (2011). *The Earthquake Engineering Online Archive NISEE e-Library* [Online]. University of California, Berkeley. 2012].

O'MALLEY, J. & POPOV, E. P. (1984). Shear Links in Eccentrically Braced Frames. *Journal of Structural Engineering,* 110, 2275-2295.

OLMOS, B. A. & ROESSET, J. M. Analytical evaluation of the accuracy of the half-power bandwidth method to estimate damping ratios in a structure. Published 4th International Conference on Structural Health Monitoring on Intelligent Infrastructure (SHMII-4), 22-24 July 2009 Zurich, Switzerland.

PAPAGIANNOPOULOS, G. A. & HATZIGEORGIOU, G. D. (2011). On the use of the half-power bandwidth method to estimate damping in building structures. *Soil Dynamics and Earthquake Engineering,* 31, 1075-1079.

PEER. (2010). *PEER Ground Motion Database* [Online]. Available: http://peer.berkeley.edu/peer_ground_motion_database [Accessed 29/01/13.

POPOV, E. P., ZAYAS, V. A. & MAHIN, S. A. (1979). Cyclic Inelastic Buckling of Thin Tubular Columns. *Journal of the Structural Division,* 105, 2261-2277.

PRATHUANGSIT, D. (1976). Inelastic hysteresis behaviour of axially loaded steel members with rotational end restraints. *Ph.D. Ph.D.* The University of Michigan, Ann Arbor, Michigan.

PRIESTLEY, M. J. N. (1997). Displacement-Based Seismic Assessment of Reinforced Concrete Buildings. *Journal of Earthquake Engineering,* 1, 157-192.

PRIESTLEY, M. J. N., CALVI, G. M. & KOWALSKY, M. J. (2007). *Displacement-Based Seismic Design of Structures,* Pavia, Italy, IUSS Press.

ROEDER, C., LEHMAN, D. & YOO, J. (2004). Performance based seismic design of braced-frame connections. *International Journal of Steel Structures, submitted for publication.*

ROEDER, C. W. (2002). Connection Performance for Seismic Design of Steel Moment Frames. *Journal of Structural Engineering,* 128, 517.

ROEDER, C. W. & LEHMAN, D. E. (2008). Seismic Design and Behaviour of Concentrically Braced Steel Frames. *STRUCTURE.*

ROEDER, C. W., LEHMAN, D. E., CLARK, K., POWELL, J., YOO, J.-H., TSAI, K.-C., LIN, C.-H. & WEI, C.-Y. (2011a). Influence of gusset plate connections and braces on the seismic performance of X-braced frames. *Earthquake Engineering & Structural Dynamics,* 40, 355-374.

ROEDER, C. W., LEHMAN, D. E., JOHNSON, S., HERMAN, D. & HAN YOO, J. (2006). Seismic Performance of SCBF Braced Frame Gusset Plate Connections. Published 4th International Conference on Earthquake Engineering, October 12-13 2006 Taipei, Taiwan.

ROEDER, C. W., LEHMAN, D. E. & YOO, J. H. (2005). Improved Seismic Design of Steel Frame Connections. Published Conference of International Journal of Steel Structures, 2005 Seoul, Korea. 5, 141-53.

ROEDER, C. W., LUMPKIN, E. J. & LEHMAN, D. E. (2011b). A balanced design procedure for special concentrically braced frame connections. *Journal of Constructional Steel Research,* 67, 1760-1772.

ROEDER, C. W. & POPOV, E. P. (1977) Inelastic behaviour of eccentrically braced frames under cyclic loading. *UCB/EERC-77/18.* Earthquake Engineering Research Center, University of California, Berkeley.

RYCHLIK, I. (1987). A new definition of the rainflow cycle counting method. *International Journal of Fatigue,* 9, 119-121.

SALAWDEH, S. (2012). Seismic design of concentrically braced steel frames. *Ph.D. Thesis.* National University of Ireland, Galway, Ireland.

SANTAGATI, S., BOLOGNINI, D. & NASCIMBENE, R. (2012). Strain Life Analysis at Low-Cycle Fatigue on Concentrically Braced Steel Structures with RHS Shape Braces. *Journal of Earthquake Engineering,* 16, 107-137.

SAVITZKY, A. & GOLAY, M. J. E. (1964). Smoothing and Differentiation of Data by Simplified Least Squares Procedures. *Analytical Chemistry,* 36, 1627-1639.

SHABACK, B. & BROWN, T. (2003). Behaviour of square hollow structural steel braces with end connections under reversed cyclic axial loading. *Canadian Journal of Civil Engineering,* 30, 745-753.

SHENG, N., YAM, C. H. & IU, V. P. (2002). Analytical investigation and the design of the compressive strength of steel gusset plate connections. *Journal of Constructional Steel Research,* 58, 1473-1493.

SULLIVAN, T. J., PRIESTLEY, M. J. N. & CALVI, G. M. (2012). *A Model Code for the Displacement-Based Seismic Design of Structures,* Pavia, Italy, IUSS Press.

TANG, X. & GOEL, S. C. (1987) Seismic analysis and design considerations of concentrically braced steel structures. *UMCE 87-3*. Department of Civil Engineering, The University of Michigan, Ann Arbor.

THOMSON, A. W. (2001). The Earthquake-Resistance of Flush End-Plate Joints. *Ph.D. Thesis*. Trinity College, University of Dublin, Ireland.

THORNTON, W. (1984). Bracing connections for heavy construction. *Engineering Journal,* 3rd Quarter, 139-148.

THORNTON, W. (1991). On the analysis and design of bracing connections. Published AISC National Steel Construction Conference, 1991. 1, 26-1.

TREMBLAY, R. (2002). Inelastic seismic response of steel bracing members. *Journal of Constructional Steel Research,* 58, 665-701.

TREMBLAY, R., ARCHAMBAULT, M. H. & FILIATRAULT, A. (2003). Seismic Response of Concentrically Braced Steel Frames Made with Rectangular Hollow Bracing Members. *Journal of Structural Engineering,* 129, 1626-1636.

TREMBLAY, R. & FILIATRAULT, A. (1996). Seismic Impact Loading in Inelastic Tension-Only Concentrically Braced Steel Frames: Myth or Reality? *Earthquake Engineering & Structural Dynamics,* 25, 1373-1389.

UANG, C.-M. & BERTERO, V. V. (1986) Earthquake simulation tests and associated studies of a 0.3-scale model of a six-story concentrically braced steel structure. *EERC 86/10.*

URIZ, P., FILIPPOU, F. C. & MAHIN, S. A. (2008). Model for Cyclic Inelastic Buckling of Steel Braces. *Journal of Structural Engineering,* 134, 619-628.

URIZ, P. & MAHIN, S. A. (2004a). Seismic Performance Assessment of Concentrically Braced Steel Frames. *13th World Conference on Earthquake Engineering.* Vancouver, B.C., Canada.

URIZ, P. & MAHIN, S. A. (2004b). Seismic Vulnerability Assessment of Concentrically Braced Steel Frames. *Steel Structures,* 4, 239-248.

URIZ, P. & MAHIN, S. A. (2008) Toward Earthquake-Resistant Design of Concentrically Braced Steel-Frame Structures. *PEER 2008/08*. Pacific Earthquake Engineering Research Center, University of California, Berkeley.

USGS. (2013). *Seismic Hazard Maps and Data* [Online]. Available: http://earthquake.usgs.gov/hazards/ [Accessed 15/02/13.

UY, B. (1998). Local and post-local buckling of concrete filled steel welded box columns. *Journal of Constructional Steel Research,* 47, 47-72.

WANG, I. (2011). An Analysis of Higher Order Effects in the Half Power Method for Calculating Damping. *Journal of Applied Mechanics,* 78, 014501-3.

WELCH, P. (1967). The use of fast Fourier transform for the estimation of power spectra: a method based on time averaging over short, modified periodograms. *Audio and Electroacoustics, IEEE Transactions on,* 15, 70-73.

WHITMORE, R. E. (1950). Experimental Investigation of Stresses in Gusset Plates. University of Tennessee, Knoxville, Tennessee.

YAM, C. H. & CHENG, J. R. (1994) Analytical investigation of the compressive behaviour and strength of steel gusset plate connections. *Structural Engineering Report No.207*. University of Alberta, Alberta.

YANG, F. & MAHIN, S. A. (2005) Limiting net section fracture in slotted tube braces. Orinda, California.

YEE, Y. & MELCHERS, R. (1986). Moment-Rotation Curves for Bolted Connections. *Journal of Structural Engineering,* 112, 615-635.

YOO, J. H. (2006). Analytical investigation on the seismic performance of special concentrically braced frames. *Ph.D. Thesis*. University of Washington, Seattle.

Appendix A – Cyclic Test Drawings

A1 Frame Arrangement Drawings

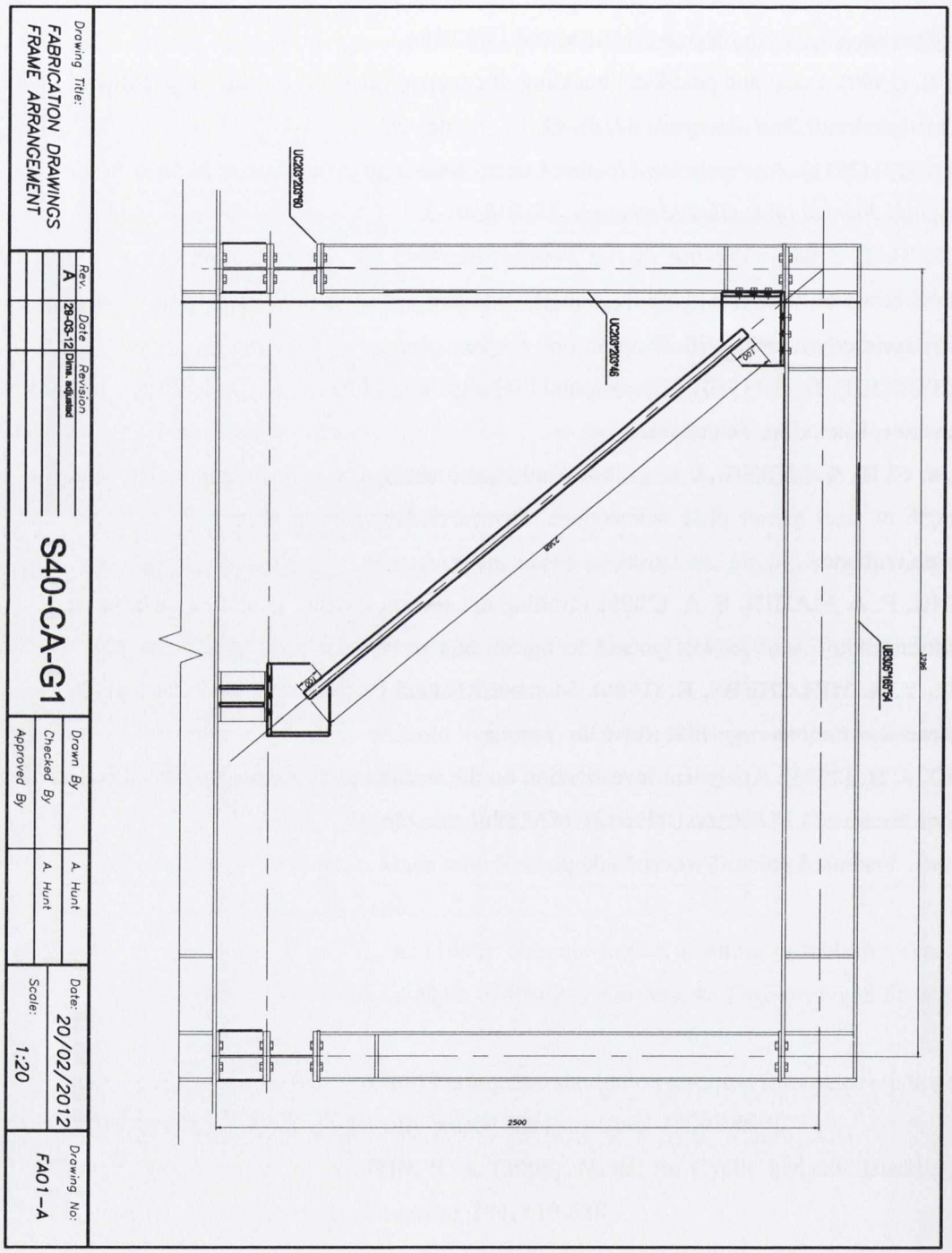

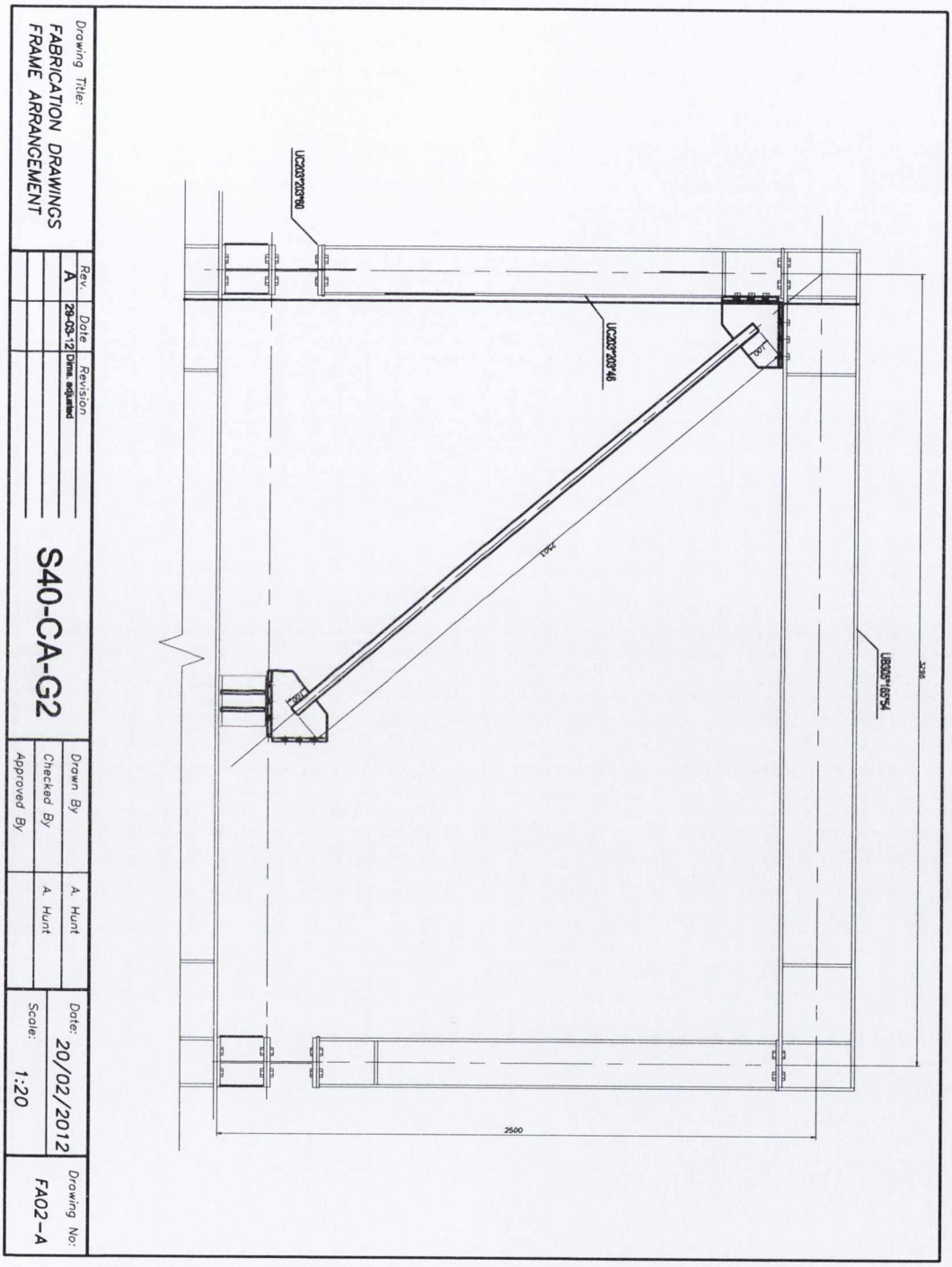
UC203*203*60
UC203*203*46
UB305*165*54
3296
2401
2500
Drawing Title:
FABRICATION DRAWINGS
FRAME ARRANGEMENT
Rev.
Date
Revision
A
28-03-12
Dims. adjusted
S40-CA-G2
Drawn By
A. Hunt
Checked By
A. Hunt
Approved By
Date:
20/02/2012
Scale:
1:20
Drawing No:
FA02-A

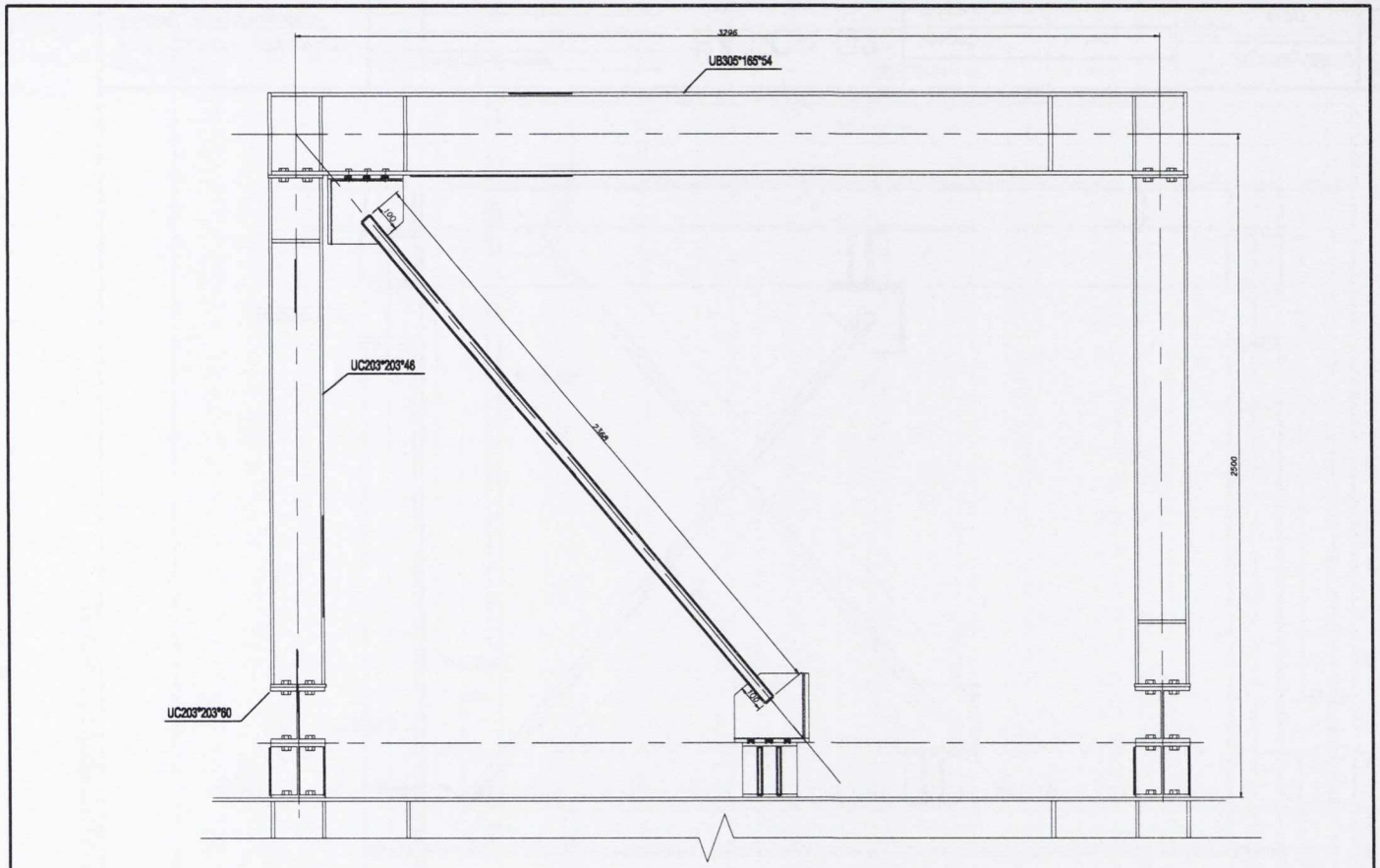

Drawing Title:	Rev.	Date	Revision					
FABRICATION DRAWINGS FRAME ARRANGEMENT	A	29-03-12	Dims. adjusted	S40-CB-G1	Drawn By	A. Hunt	Date: 20/02/2012	Drawing No:
					Checked By	A. Hunt	Scale: 1:20	FA03-A
					Approved By			

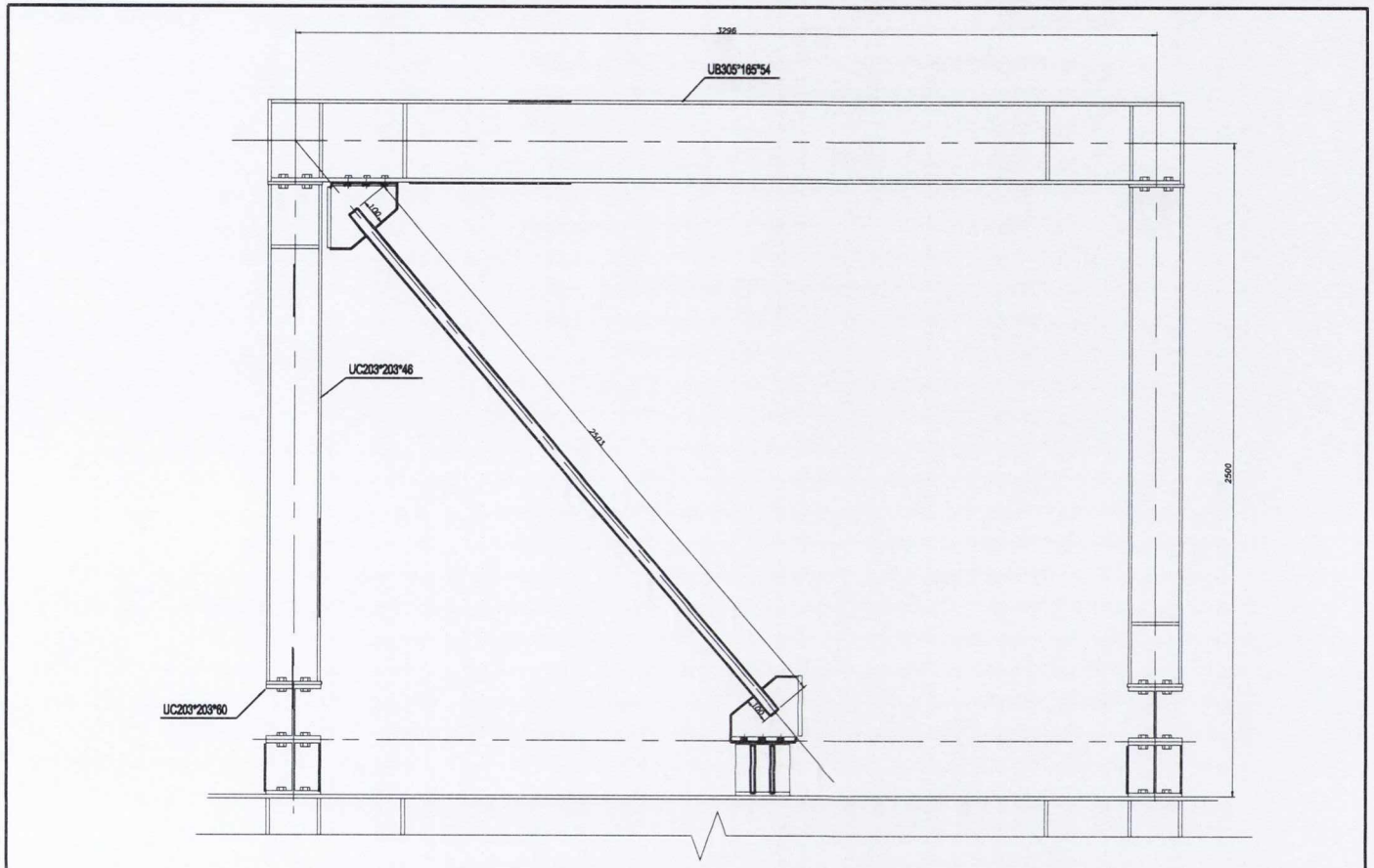

Drawing Title:	Rev.	Date	Revision					
FABRICATION DRAWINGS FRAME ARRANGEMENT	A	29-03-12	Dims. adjusted	S40-CB-G2	Drawn By	A. Hunt	Date: 20/02/2012	Drawing No: FA04-A
					Checked By	A. Hunt		
					Approved By		Scale: 1:20	

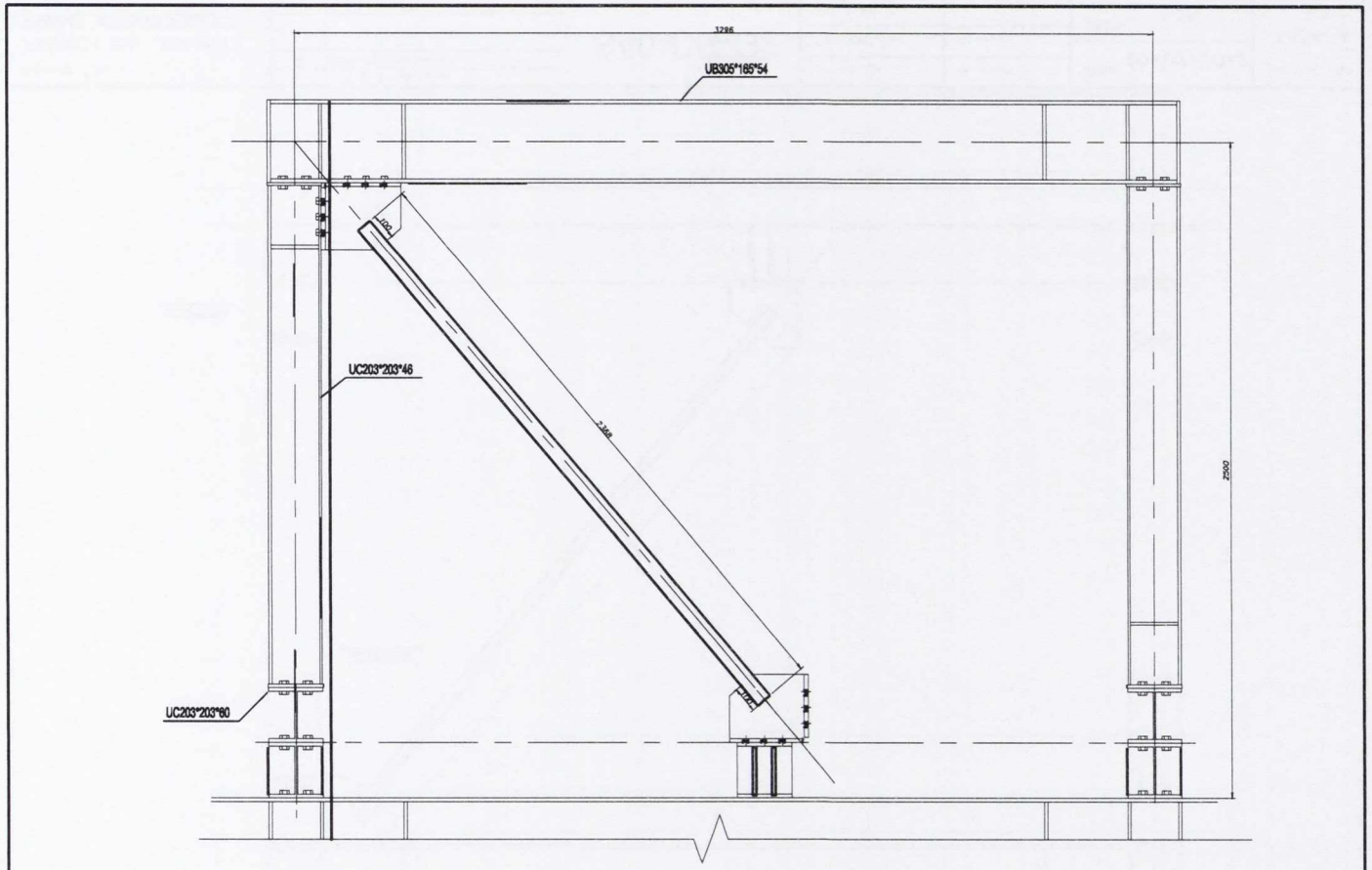

Drawing Title:	Rev.	Date	Revision					
FABRICATION DRAWINGS FRAME ARRANGEMENT	A	29-03-12	Dims. adjusted	S60-CA-G1	Drawn By	A. Hunt	Date: 20/02/2012	Drawing No: FA05–A
					Checked By	A. Hunt		
					Approved By		Scale: 1:20	

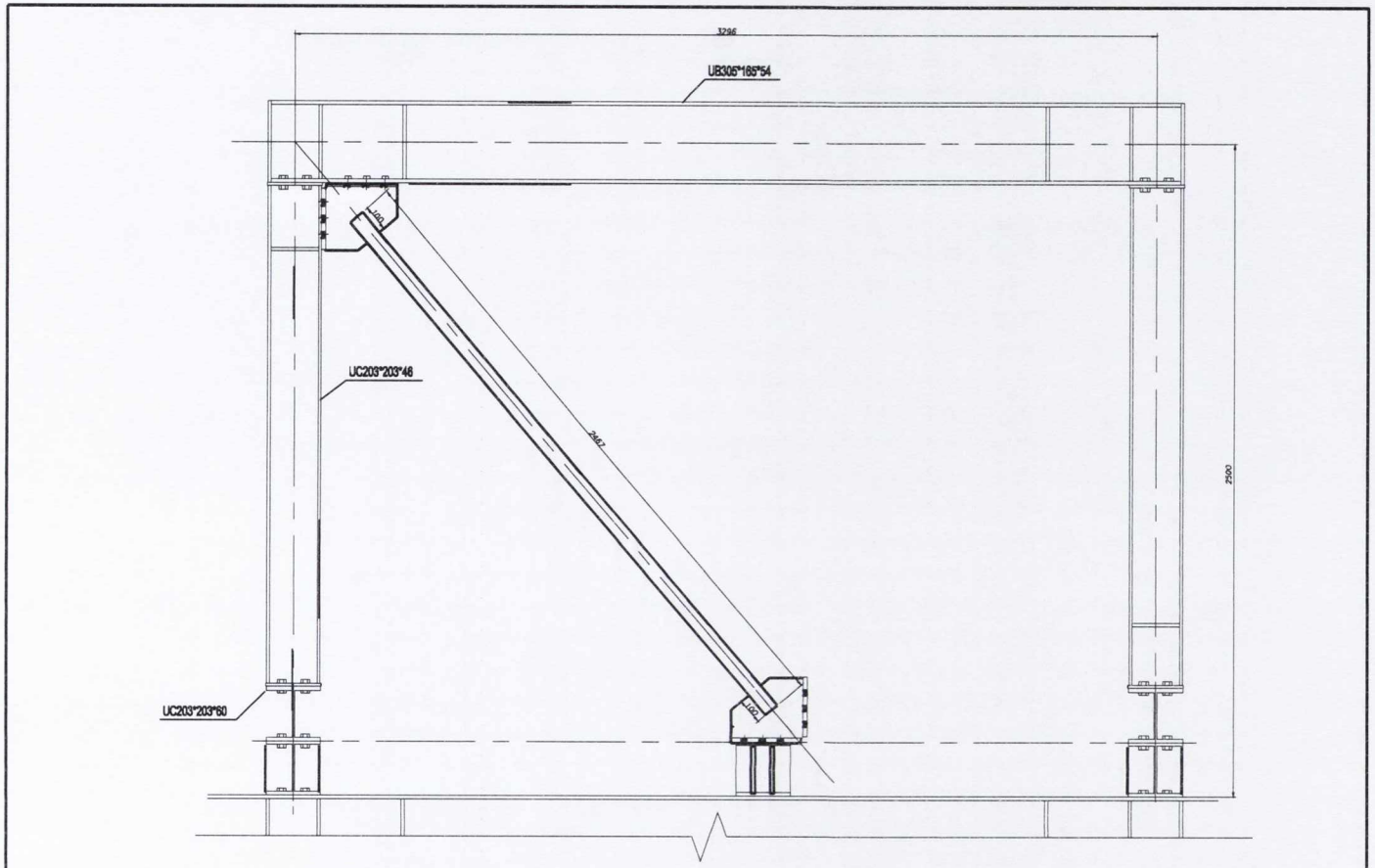

Drawing Title:	Rev.	Date	Revision					
FABRICATION DRAWINGS FRAME ARRANGEMENT	A	29-03-12	Dims. adjusted	S60-CA-G2	Drawn By	A. Hunt	Date: 20/02/2012	Drawing No: FA06-A
					Checked By	A. Hunt		
					Approved By		Scale: 1:20	

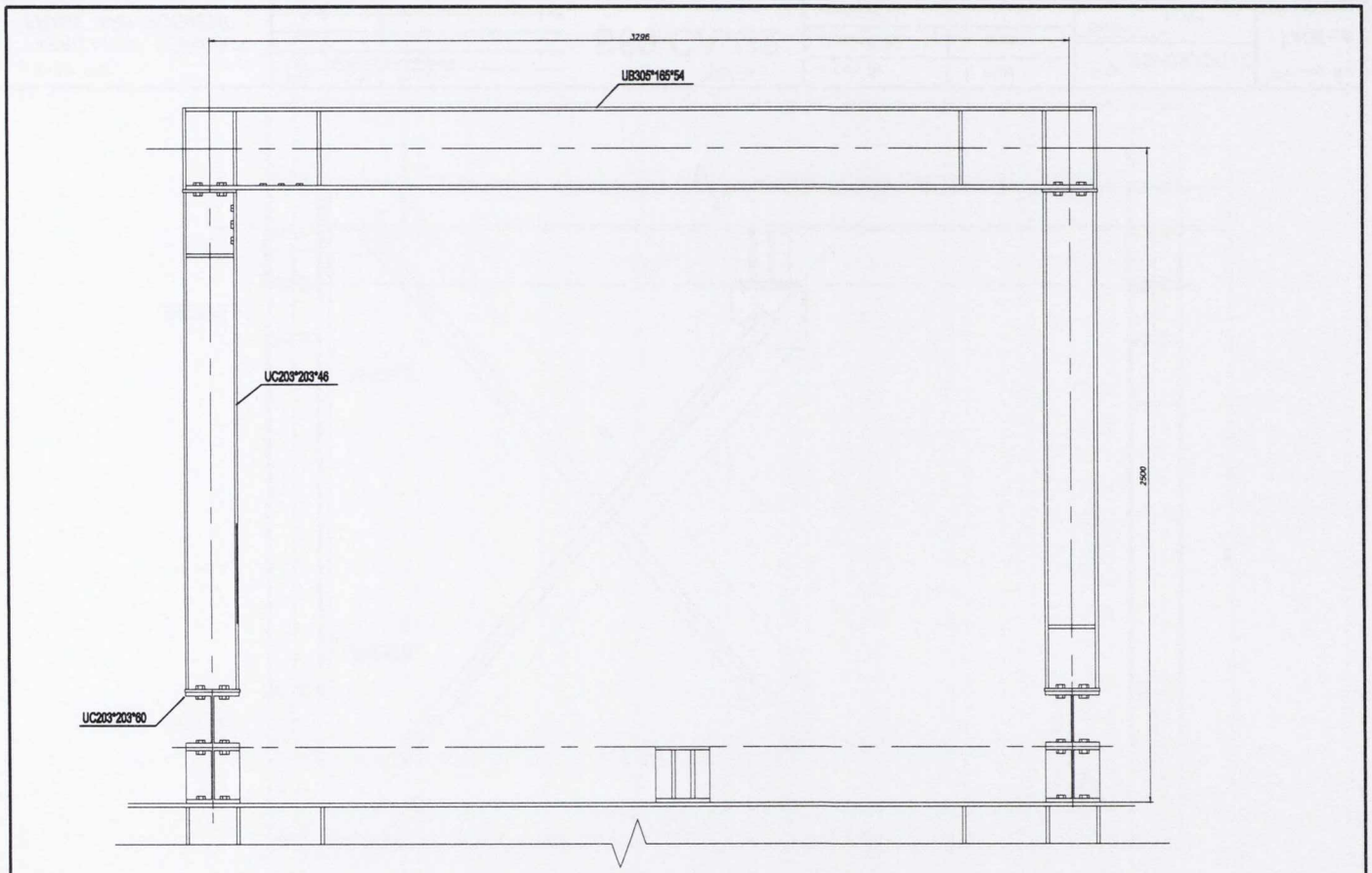

Drawing Title:	Rev.	Date	Revision					
FABRICATION DRAWINGS FRAME ARRANGEMENT	A	29-03-12	Dims. adjusted	UNBRACED	Drawn By	A. Hunt	Date: 20/02/2012	Drawing No: FA-UN-A
					Checked By	A. Hunt		
					Approved By	B. Broderick	Scale: 1:20	

A2 Specimen Detail Drawings

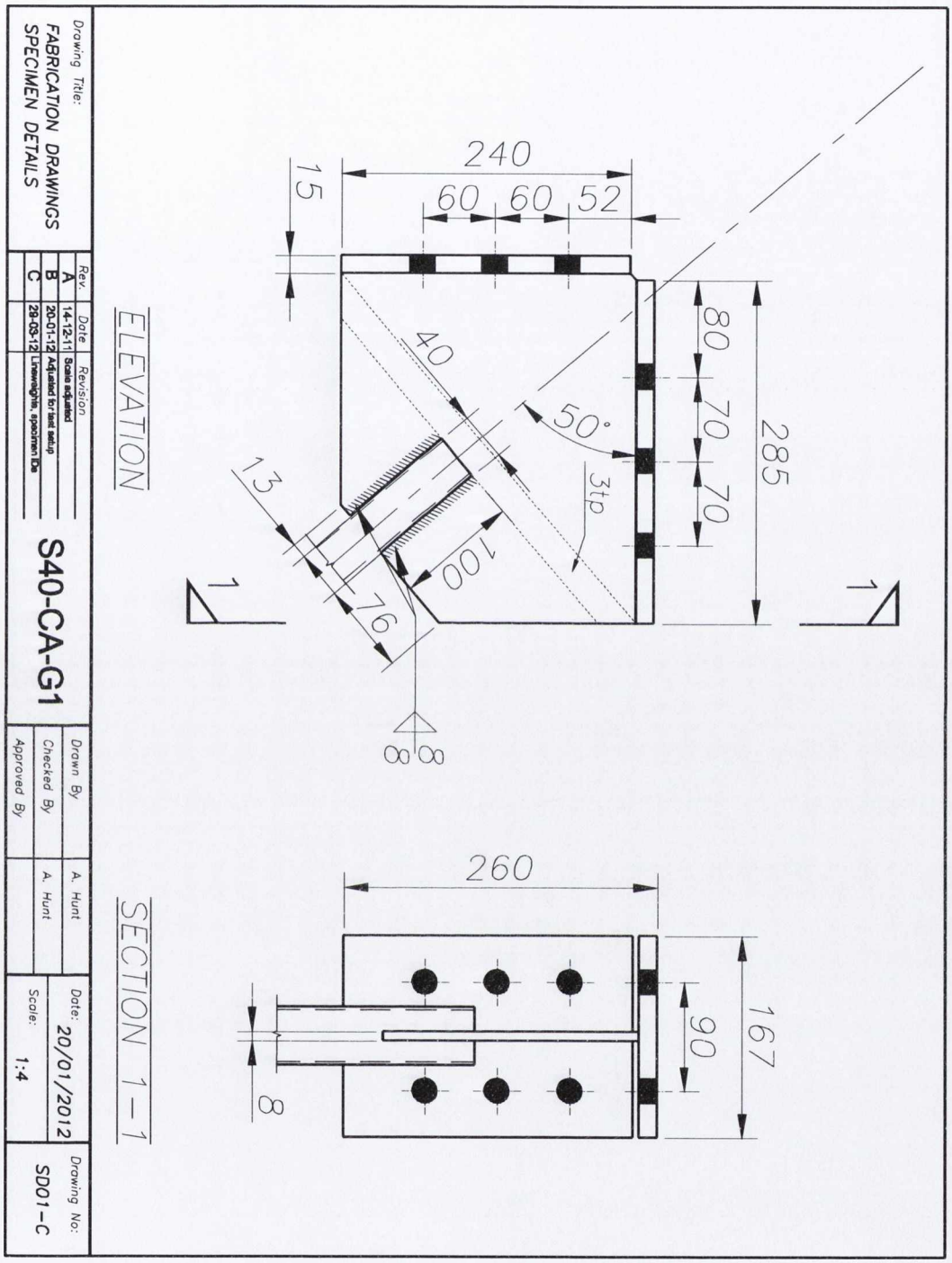

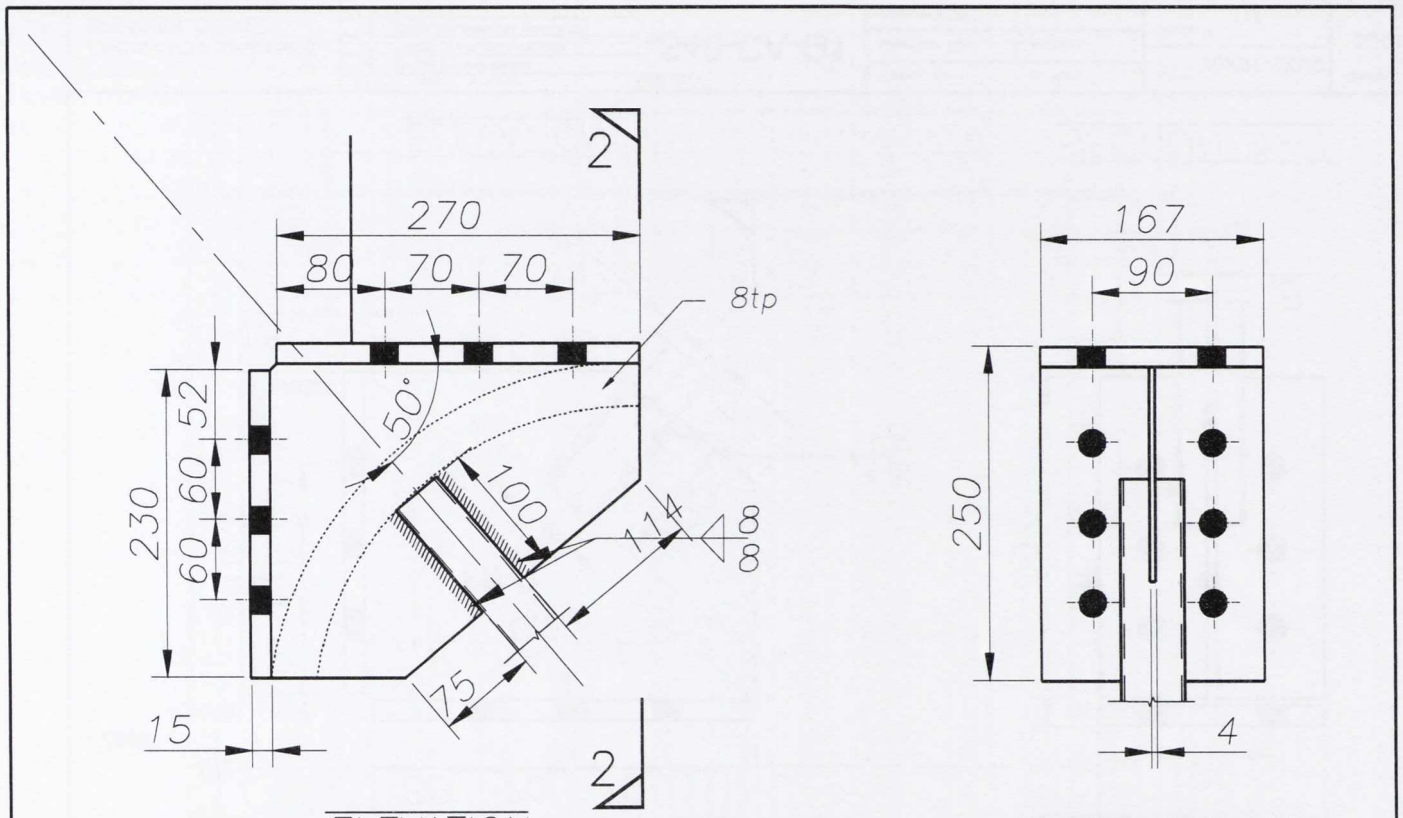

Drawing Title:	Rev.	Date	Revision					
FABRICATION DRAWINGS SPECIMEN DETAILS	A	14-12-11	Scale adjusted	S40-CA-G2	Drawn By	A. Hunt	Date: 12/12/2011	Drawing No:
	B	20-01-12	Adjusted for test setup		Checked By	A. Hunt		
	C	29-03-12	Lineweights, specimen IDs		Approved By		Scale: 1:4	SD02-C

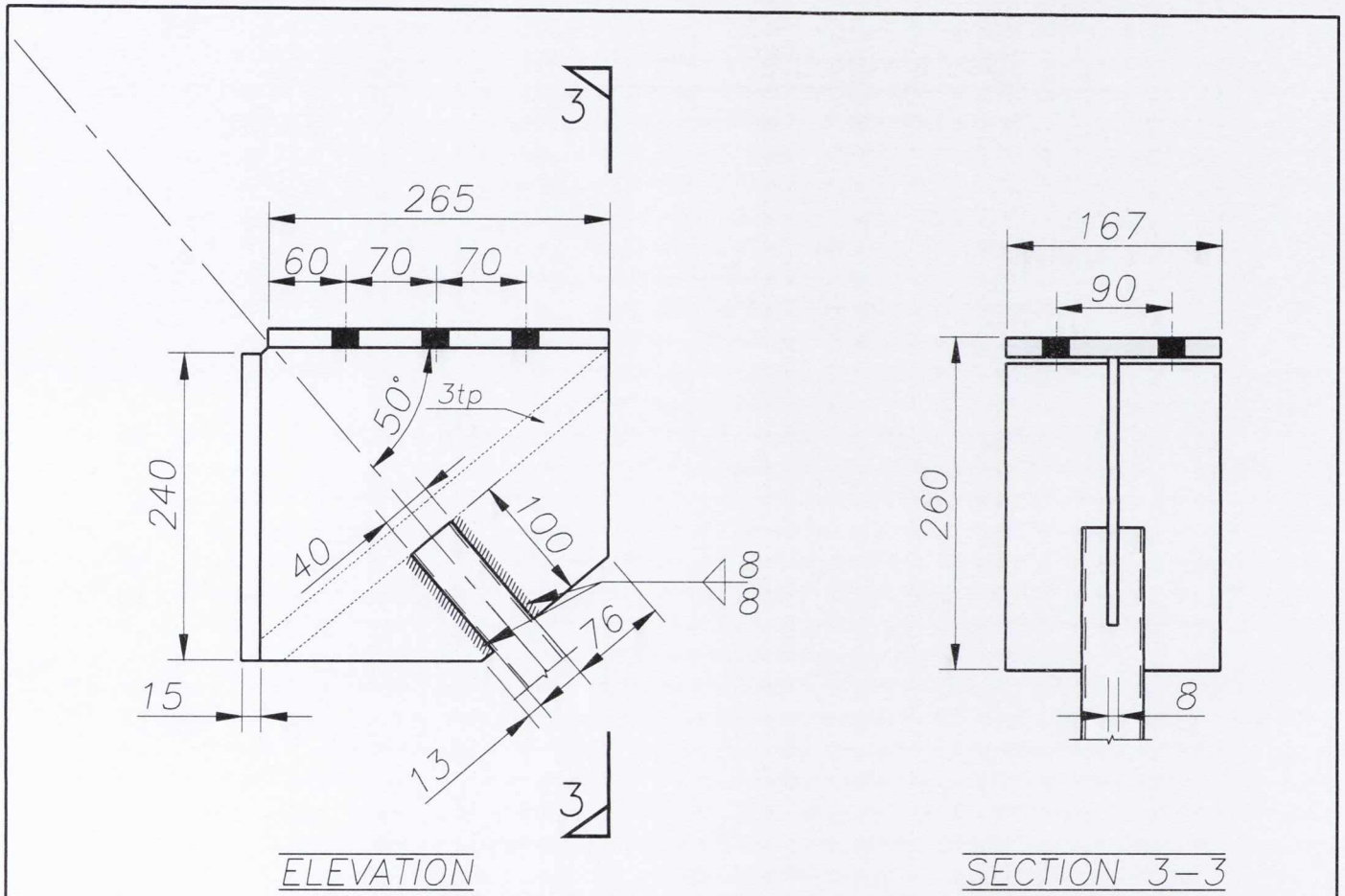

Drawing Title:	Rev.	Date	Revision					
FABRICATION DRAWINGS SPECIMEN DETAILS	A	14-12-11	Scale adjusted	S40-CB-G1	Drawn By	A. Hunt	Date: 12/12/2011	Drawing No:
	B	20-01-12	Adjusted for test setup		Checked By	A. Hunt		SD03–C
	C	29-03-12	Lineweights, specimen IDs		Approved By		Scale: 1:4	

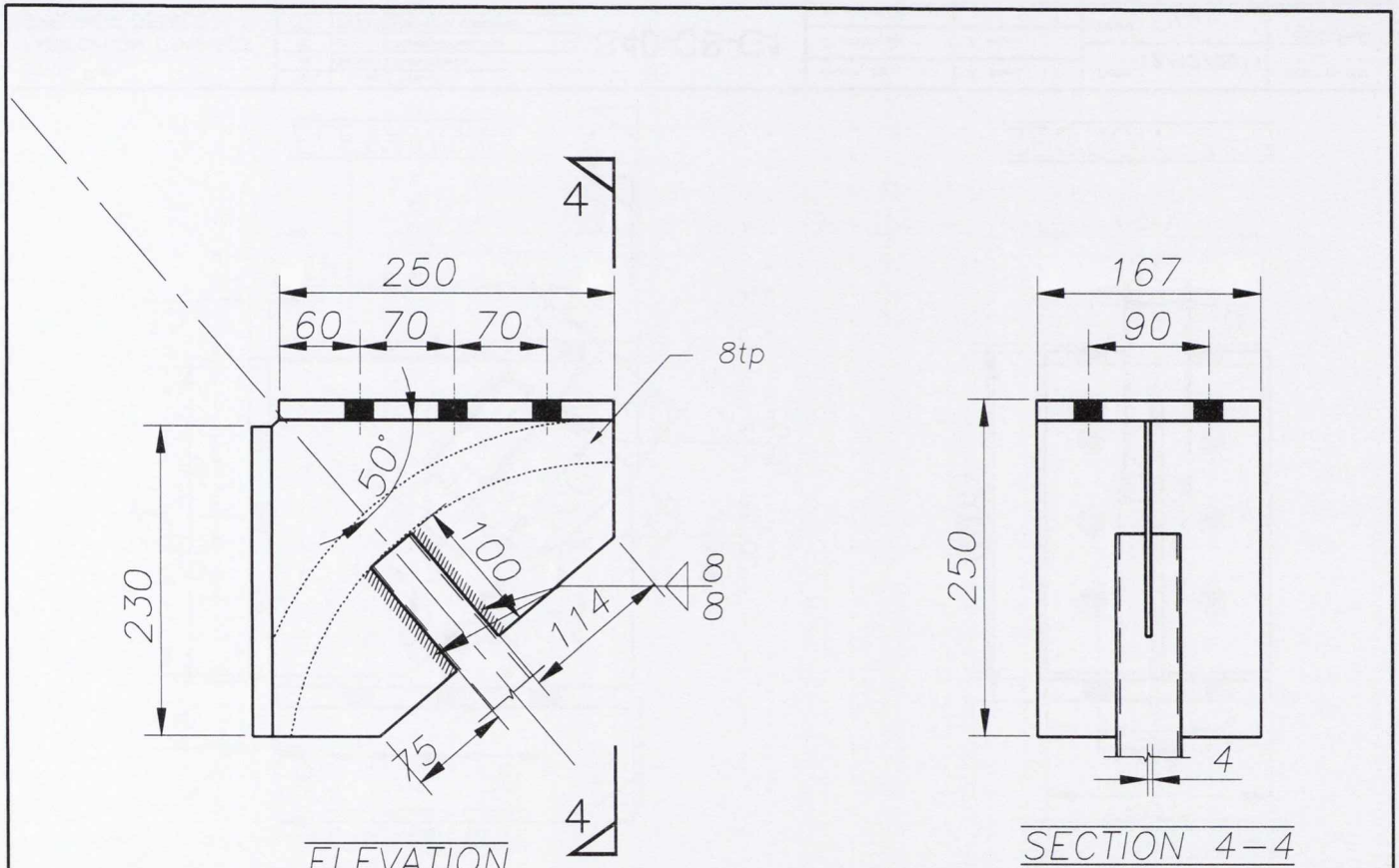

Drawing Title:	Rev.	Date	Revision					
FABRICATION DRAWINGS SPECIMEN DETAILS	A	14-12-11	Scale adjusted	S40-CB-G2	Drawn By	A. Hunt	Date: 12/12/2011	Drawing No: SD04–C
	B	20-01-12	Adjusted for test setup		Checked By	A. Hunt		
	C	29-03-12	Lineweights, specimen IDs		Approved By		Scale: 1:4	

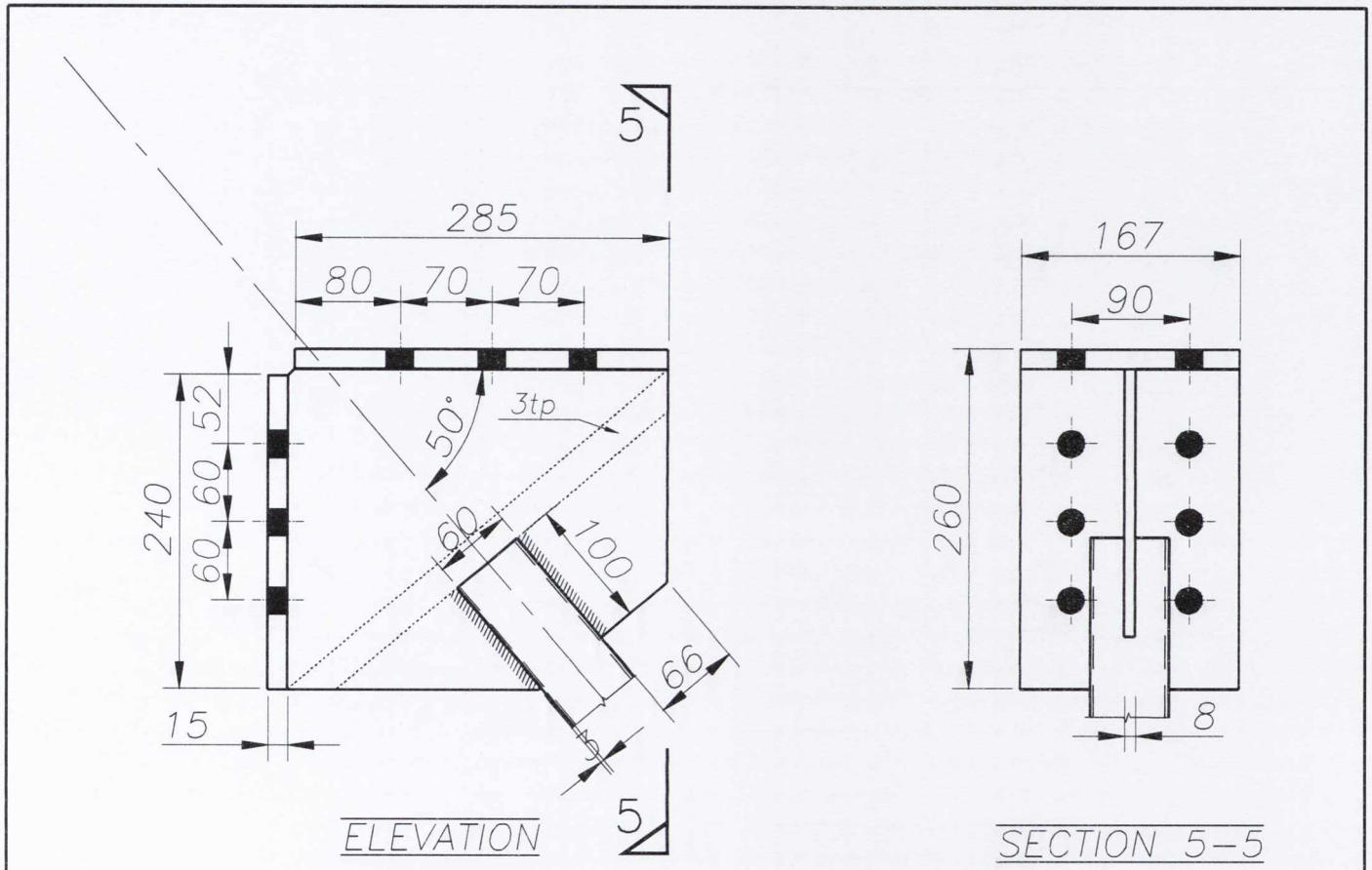

Drawing Title:	Rev.	Date	Revision					
FABRICATION DRAWINGS SPECIMEN DETAILS	A	14-12-11	Scale adjusted	S60-CA-G1	Drawn By	A. Hunt	Date: 12/12/2011	Drawing No:
	B	20-01-12	Adjusted for test setup		Checked By	A. Hunt		SD05-C
	C	29-03-12	Lineweights, specimen ID's		Approved By		Scale: 1:4	

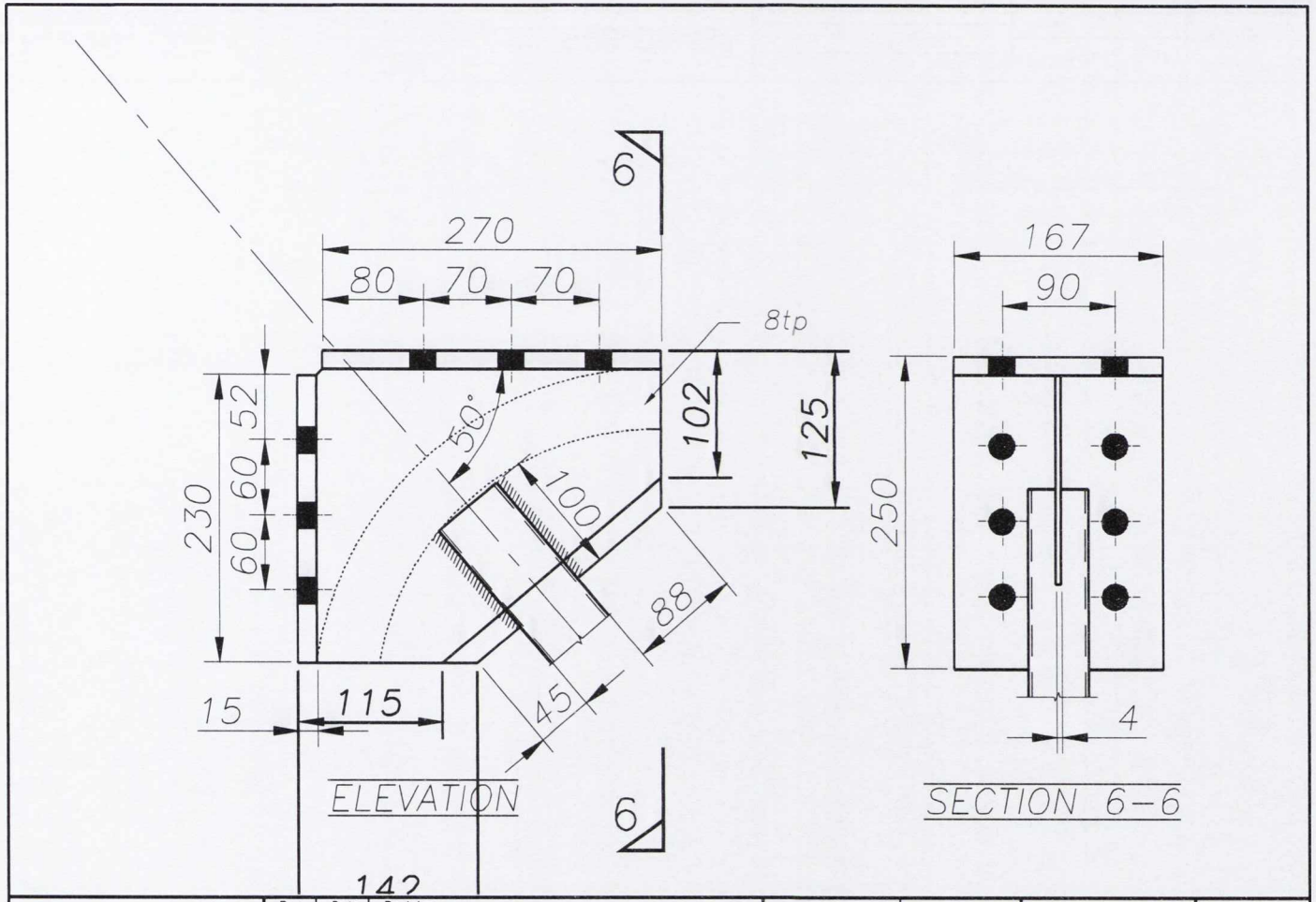

Drawing Title:	Rev.	Date	Revision					
FABRICATION DRAWINGS SPECIMEN DETAILS	A	14-12-11	Scale adjusted	S60-CA-G2	Drawn By	A. Hunt	Date: 12/12/2011	Drawing No:
	B	20-01-12	Adjusted for test setup		Checked By	A. Hunt		SD06-C
	C	29-03-12	Lineweights, specimen IDs		Approved By		Scale: 1:4	

A3 Instrumentation Drawings

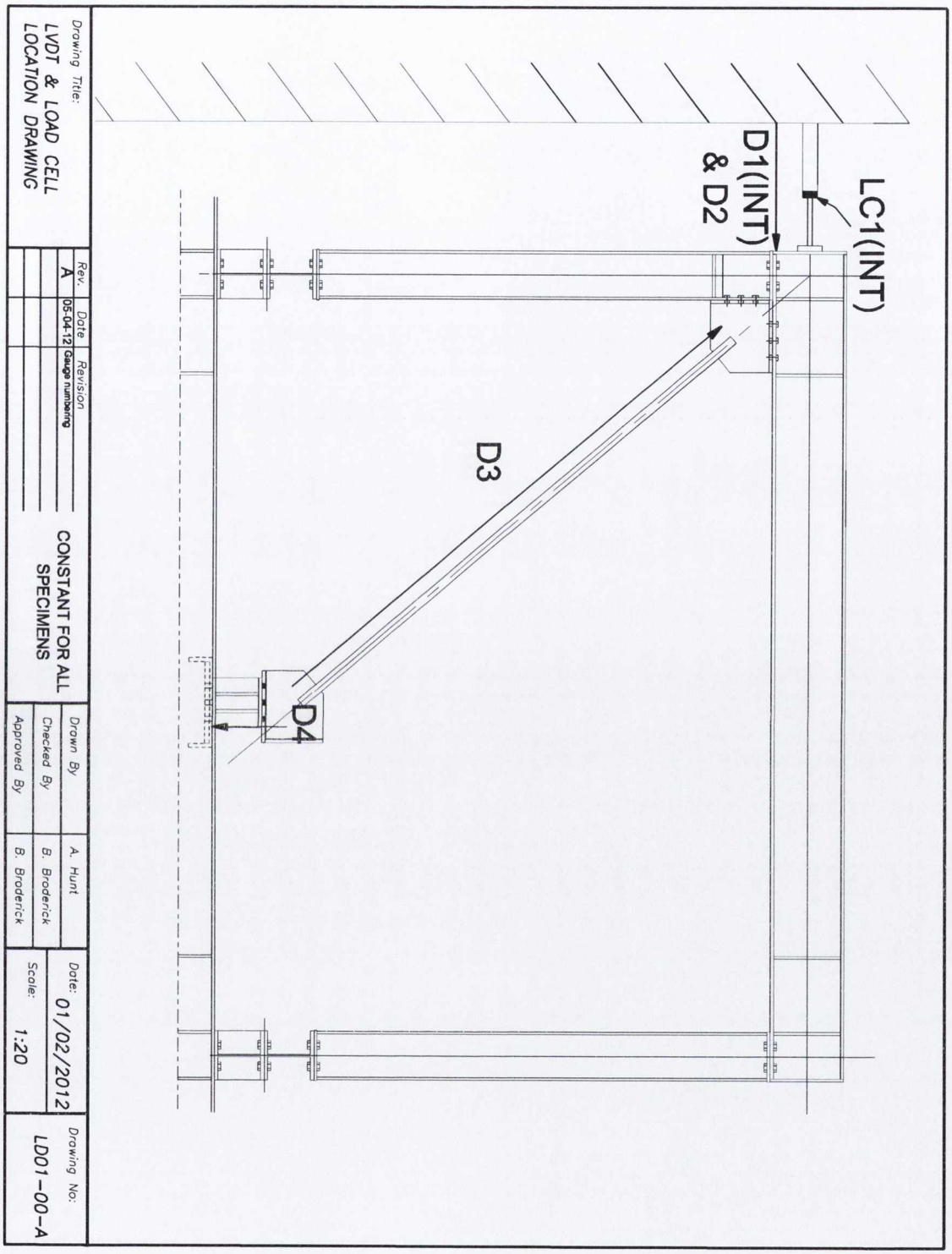

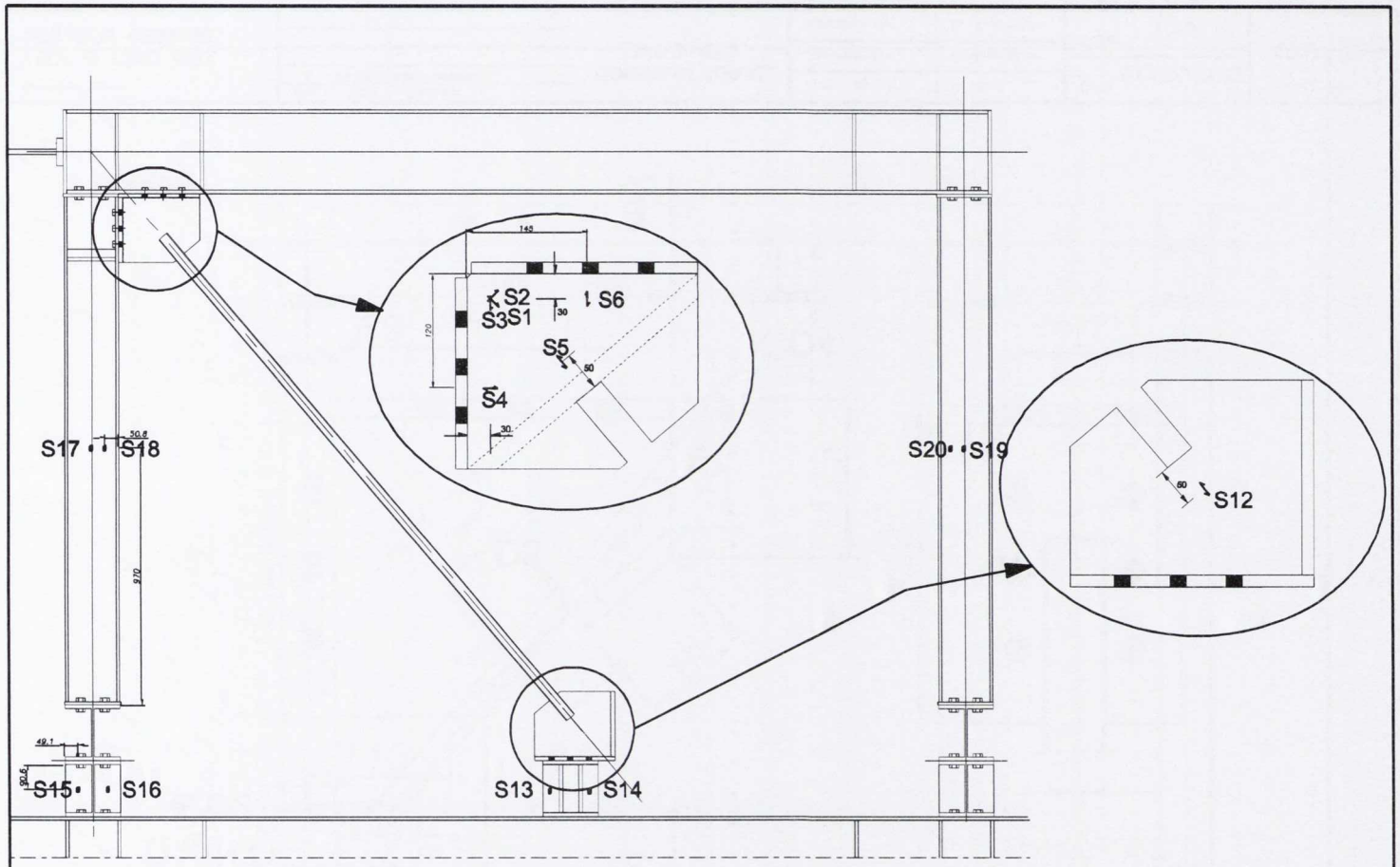

Drawing Title:	Rev.	Date	Revision					
STRAIN GAUGE LOCATION DRAWING	A	05-04-12	Gauge numbering	S40-CA-G1	Drawn By	A. Hunt	Date: 01/02/2012	Drawing No:
	B	09-05-12	S5 & S12 dims. changed	S1-S6, S12	Checked By	B. Broderick	Scale: 1:20	LD02-01-B
					Approved By	B. Broderick		

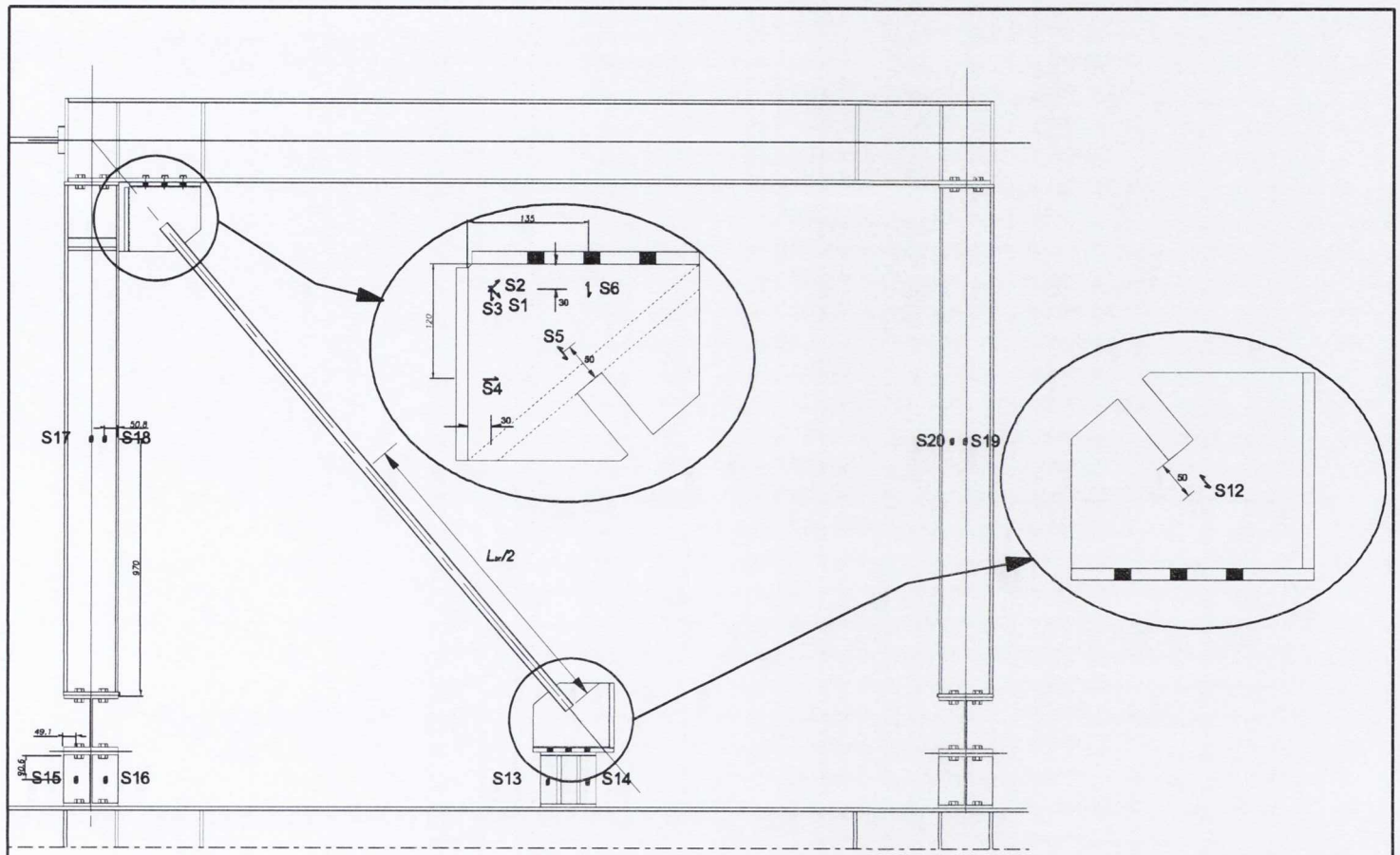

Drawing Title: STRAIN GAUGE LOCATION DRAWING	Rev.	Date	Revision	S40-CB-G1 S1-S6, S12	Drawn By	A. Hunt	Date: 01/02/2012
	A	05-04-12	Gauge numbering		Checked By	B. Broderick	Scale: 1:20
	B	09-05-12	S5 & S12 dims. changed		Approved By	B. Broderick	Drawing No: LD02-02-B

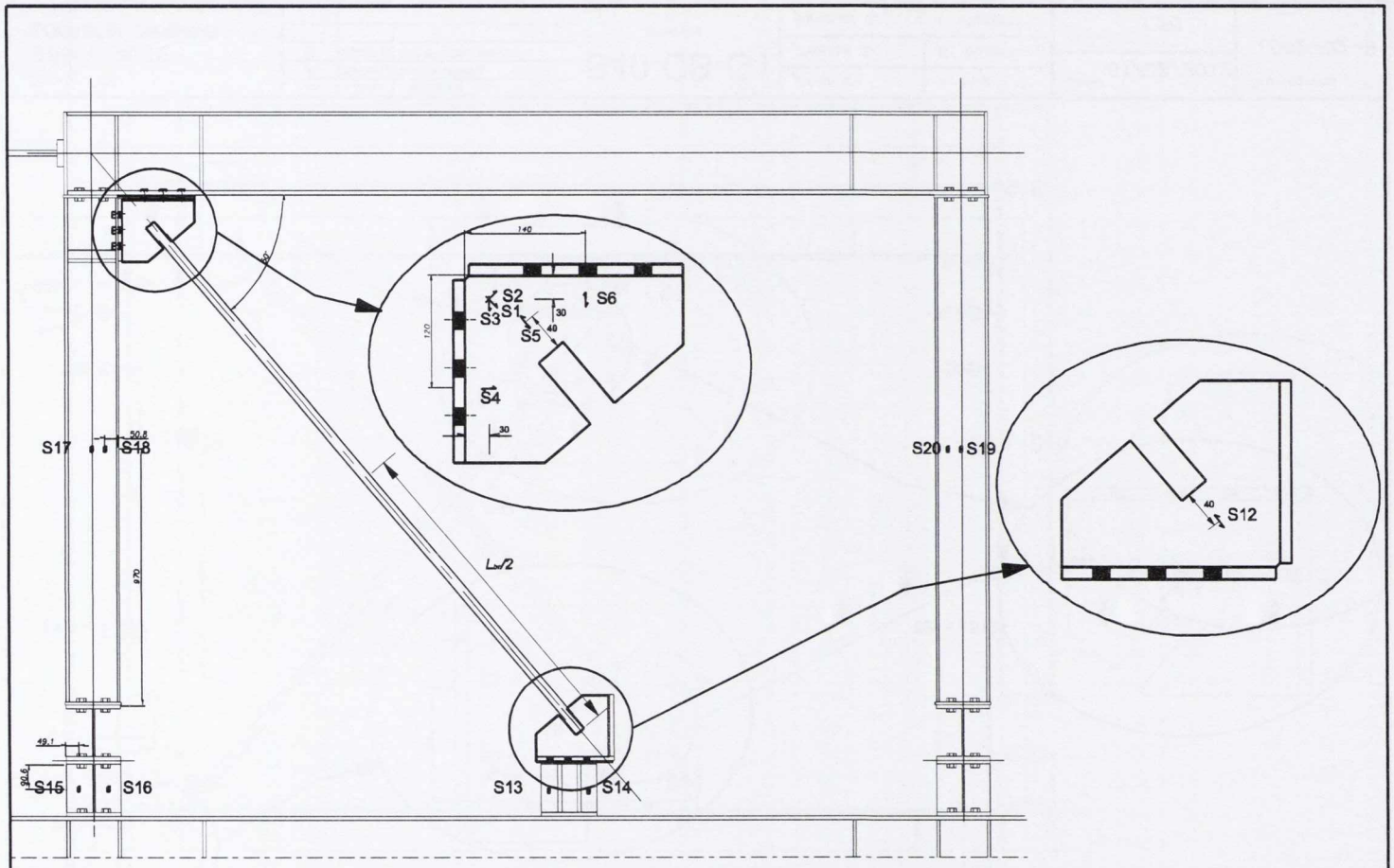

Drawing Title:	Rev.	Date	Revision					
STRAIN GAUGE LOCATION DRAWING	A	05-04-12	Gauge numbering	S40-CA-G2	Drawn By	A. Hunt	Date: 01/02/2012	Drawing No:
	B	09-05-12	S5 & S12 dims. changed	S1-S6, S12	Checked By	B. Broderick	Scale: 1:20	LD02-03-B
					Approved By	B. Broderick		

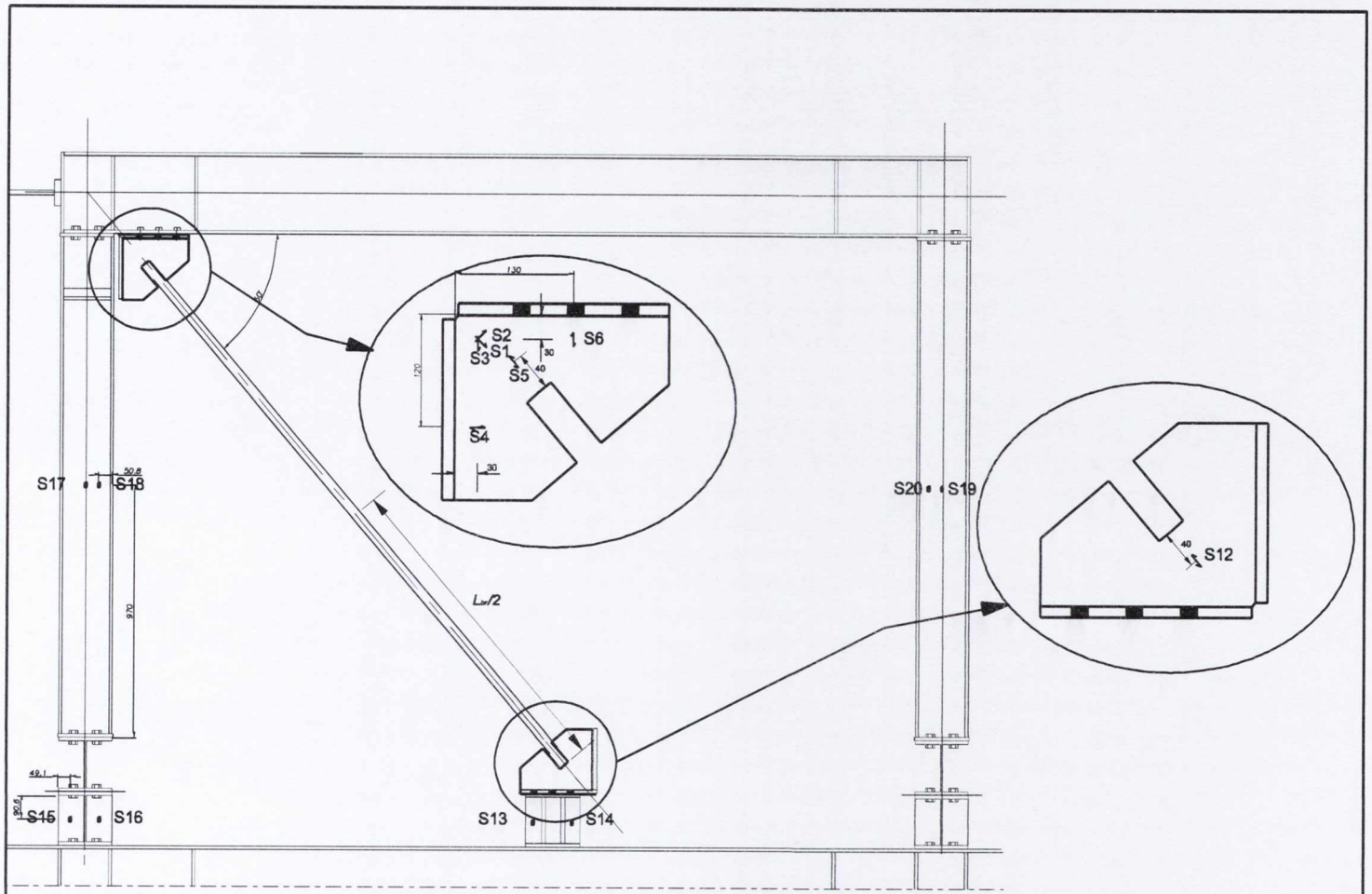

Drawing Title: STRAIN GAUGE LOCATION DRAWING	Rev.	Date	Revision	S40-CB-G2 S1-S6, S12	Drawn By	A. Hunt	Date: 01/02/2012
	A	05-04-12	Gauge numbering		Checked By	B. Broderick	Scale: 1:20
	B	09-05-12	S5 & S12 dims. changed		Approved By	B. Broderick	Drawing No: LD02-04-B

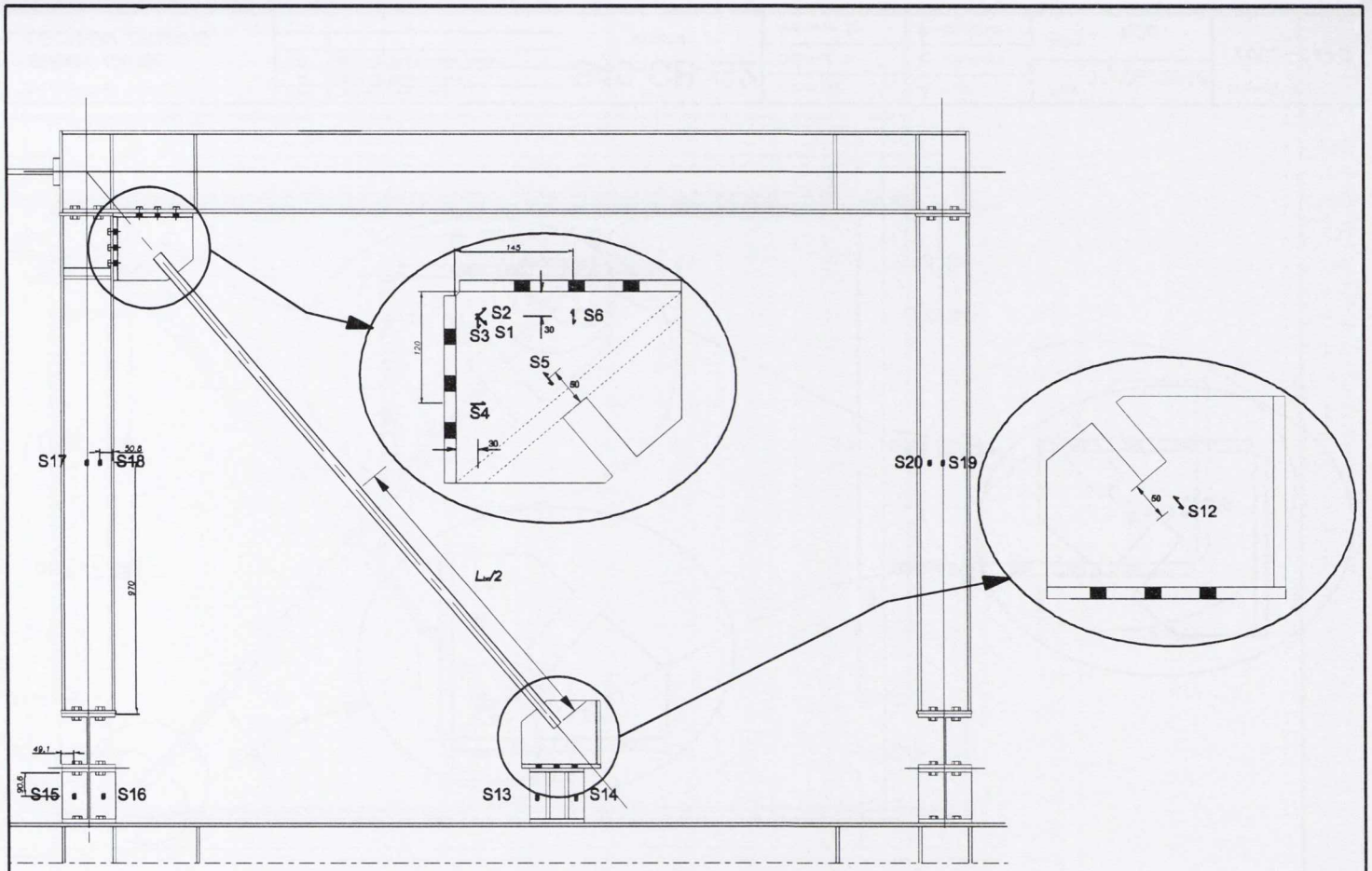

Drawing Title:	Rev.	Date	Revision		Drawn By	A. Hunt	Date:	Drawing No:
STRAIN GAUGE LOCATION DRAWING	A	05-04-12	Gauge numbering	S60-CA-G1	Checked By	B. Broderick	01/02/2012	LD02-05-B
	B	09-05-12	S5 & S12 dims. changed	S1-S6, S12	Approved By	B. Broderick	Scale: 1:20	

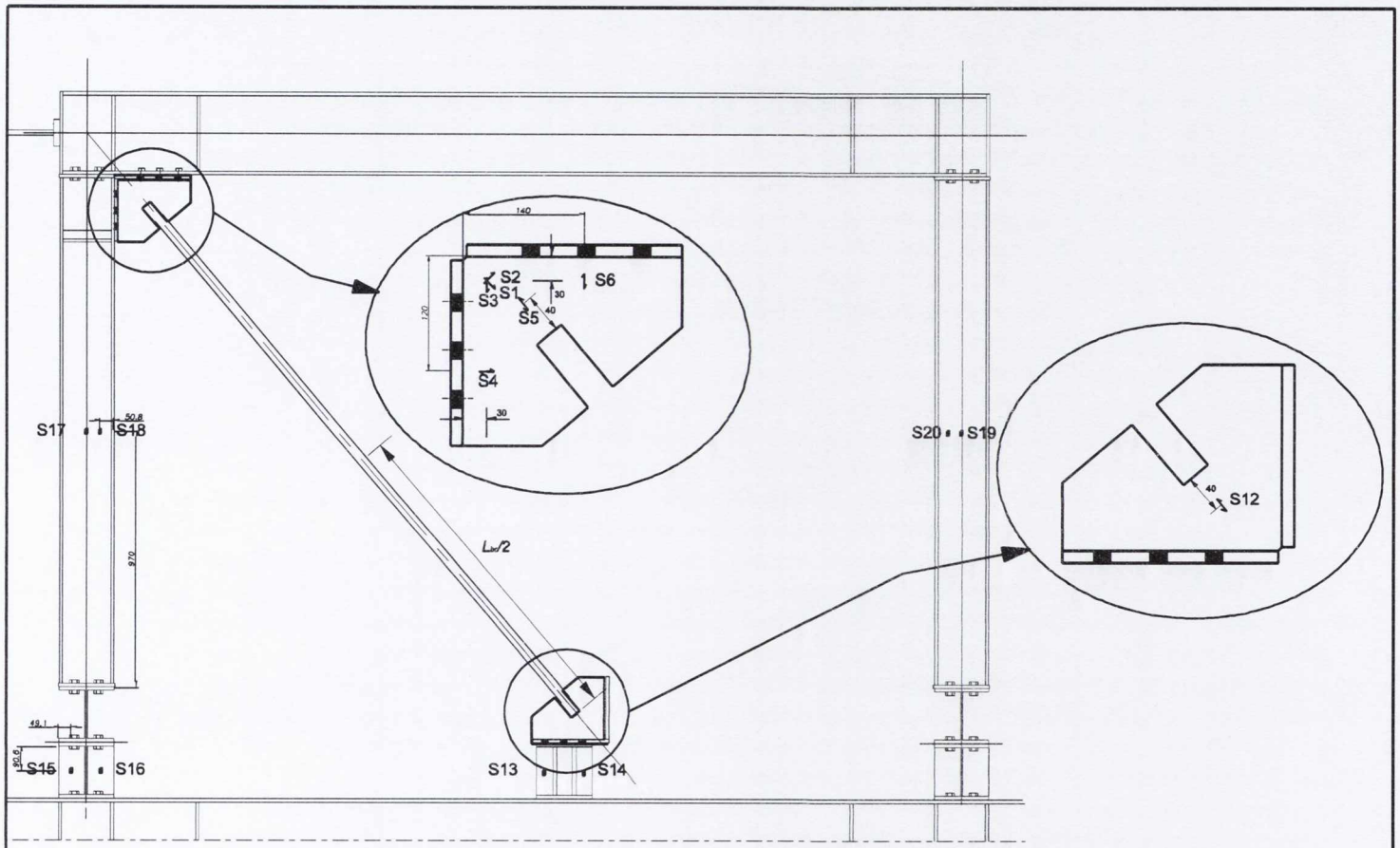

Drawing Title:	Rev.	Date	Revision					
STRAIN GAUGE LOCATION DRAWING	A	05-04-12	Gauge numbering	S60-CA-G2	Drawn By	A. Hunt	Date: 01/02/2012	Drawing No:
	B	09-05-12	S5 & S12 dims. changed	S1-S6, S12	Checked By	B. Broderick	Scale: 1:20	LD02-06-B
					Approved By	B. Broderick		

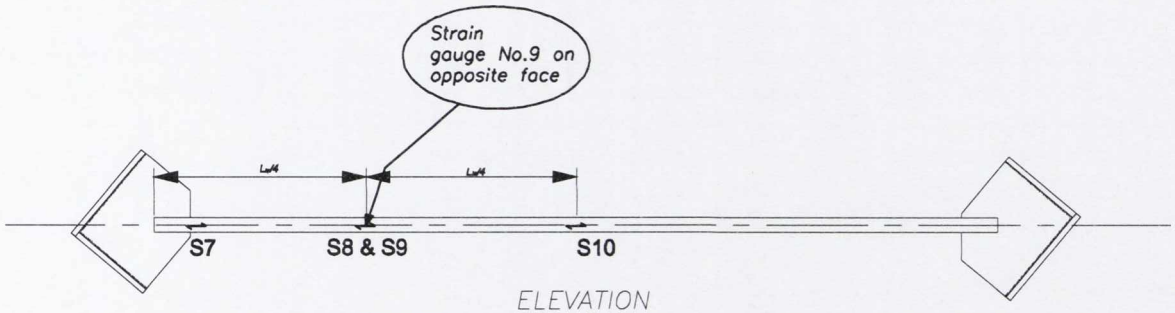

ELEVATION

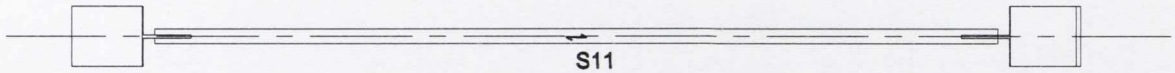

PLAN

Drawing Title:	Rev.	Date	Revision					
STRAIN GAUGE (LOCAL) LOCATION DRAWING	A	05-04-12	Gauge numbering	CONSTANT FOR ALL SPECIMENS S7-S11	Drawn By	A. Hunt	Date: 01/02/2012	Drawing No: LD03-00
					Checked By	B. Broderick	Scale: 1:15	
					Approved By	B. Broderick		

A4 Channel Section Modification Drawings

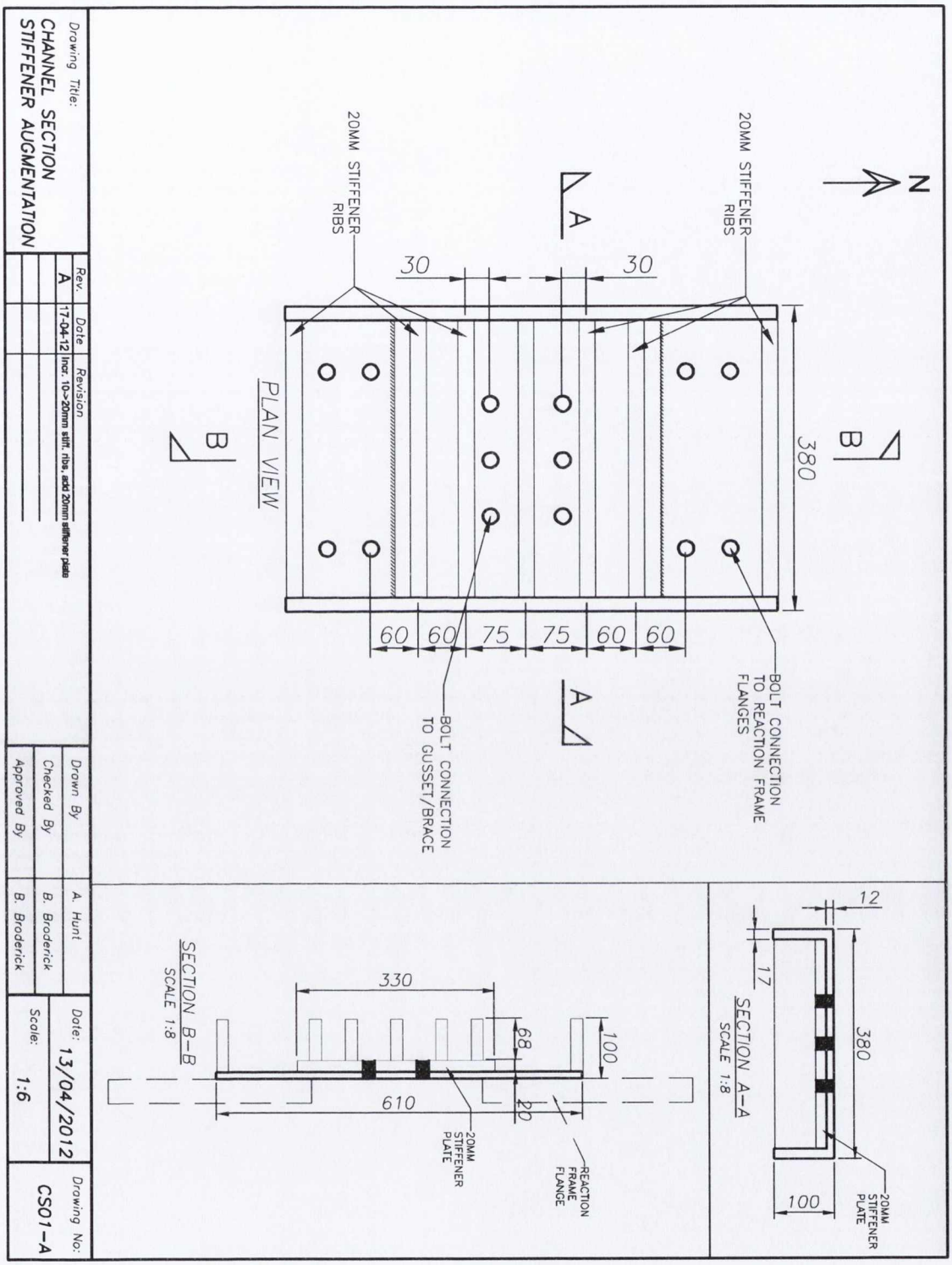

Appendix B – BRACED Project Results

B1 Table of Data Acquisition Channels

MTS Data Recorder					
Element	**Number**	**Measurement type**	**Name**	**Sensor Reference**	**Location**
	1	Synchronization signal	Synchro	MTS	-
Table	2	Displacement	DLongAct1	LVDT MTS	Actuator X1
	3	Displacement	DLongAct2	LVDT MTS	Actuator X4
	4	Displacement	DLatAct1	LVDT MTS	Actuator Y2
	5	Displacement	DLatAct2	LVDT MTS	Actuator Y3
	6	Displacement	DVertAct1	LVDT MTS	Actuator Z1
	7	Displacement	DVertAct2	LVDT MTS	Actuator Z2
	8	Displacement	DVertAct3	LVDT MTS	Actuator Z3
	9	Displacement	DVertAct4	LVDT MTS	Actuator Z4
Table	10	Acceleration	ALongAct1	PCB3711B1110G	Actuator X1
	11	Acceleration	ALongAct2	PCB3711B1110G	Actuator X4
	12	Acceleration	ALatAct1	PCB3711B1110G	Actuator Y2
	13	Acceleration	ALatAct2	PCB3711B1110G	Actuator Y3
	14	Acceleration	AVertAct1	PCB3711B1110G	Actuator Z1
	15	Acceleration	AVertAct2	PCB3711B1110G	Actuator Z2
	16	Acceleration	AVertAct3	PCB3711B1110G	Actuator Z3
	17	Acceleration	AVertAct4	PCB3711B1110G	Actuator Z4
Table	17	Load	FLongAct1	MTS	Actuator X1
	18	Load	FLongAct2	MTS	Actuator X4
	19	Load	FLatAct1	MTS	Actuator Y2
	20	Load	FLatAct2	MTS	Actuator Y3
	21	Load	FVertAct1	MTS	Actuator Z1
	22	Load	FVertAct2	MTS	Actuator Z2
	23	Load	FVertAct3	MTS	Actuator Z3
	24	Load	FVertAct4	MTS	Actuator Z4

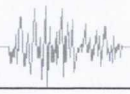

PACIFIC INSTRUMENTS System					
Element	**Number**	**Measurement type**	**Name**	**Sensor Reference**	**Location**
	1	Synchronization signal	Synchro	MTS	-
Table	2	Displacement	DLatMTS	MTS	Lat MTS / X
	3	Displacement	DLongMTS	MTS	Long MTS / Y
	4	Displacement	DVertMTS	MTS	Vert MTS / Z
	5	Displacement	DRollMTS	MTS	Roll MTS / X
	6	Displacement	DPitchMTS	MTS	Pitch MTS / Y
	7	Displacement	DYawMTS	MTS	Yaw MTS / Z
Frame	8	Displacement	Dx1	FGP (500 mm)	Top right X
	9	Displacement	Dx2	FGP (500 mm)	Top middle X
	10	Displacement	Dx3	FGP (500 mm)	Top left X
	11	Displacement	Dy1	FGP (500 mm)	Top left Y
	12	Displacement	Dy2	FGP (500 mm)	Top middle Y
	13	Displacement	Dy3	FGP (500 mm)	Top right Y
Braces	14	Displacement	DbraceR	FGP (500 mm)	Brace right
	15	Displacement	DbraceL	FGP (500 mm)	Brace left
Table	16	Acceleration	ALatMTS	MTS	Lat MTS / X
	17	Acceleration	ALongMTS	MTS	Long MTS / Y
	18	Acceleration	AVertMTS	MTS	Vert MTS / Z
	19	Acceleration	ARollMTS	MTS	Roll MTS / X
	20	Acceleration	APitchMTS	MTS	Pitch MTS / Y
	21	Acceleration	AYawMTS	MTS	Yaw MTS / Z
	22	Acceleration	Axtab	PCB3711B1110G	Table center / X
	23	Acceleration	Aytab	PCB3711B1110G	Table center / Y
	24	Acceleration	Aztab	PCB3711B1110G	Table center / Z
Frame	25	Acceleration	Axtop	PCB3711B1110G	Top plates center / X
	26	Acceleration	Aytop	PCB3711B1110G	Top plates center / Y
	27	Acceleration	Aztop	PCB3711B1110G	Top plates center / Z

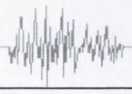

Brace	28	Strain gauges	SG1	CEA-00-125UW-120	Instrumented brace
	29	Strain gauges	SG2	CEA-00-125UW-120	Instrumented brace
	30	Strain gauges	SG3	CEA-00-125UW-120	Instrumented brace
	31	Strain gauges	SG4	CEA-00-125UW-120	Instrumented brace
	32	Strain gauges	SG5	CEA-00-125UW-120	Instrumented brace
	33	Strain gauges	SG6	CEA-00-125UW-120	Instrumented brace
	34	Strain gauges	SG7	CEA-00-125UW-120	Instrumented brace
	35	Strain gauges	SG8	CEA-00-125UW-120	Instrumented brace
	36	Strain gauges	SG9	CEA-00-125UW-120	Instrumented brace
	37	Strain gauges	SG10	CEA-00-125UW-120	Instrumented brace
	38	Strain gauges	SG11	CEA-00-125UW-120	Instrumented brace
	39	Strain gauges	SG12	CEA-00-125UW-120	Instrumented brace
	40	Strain gauges	SG13	CEA-00-125UW-120	Instrumented brace
	41	Strain gauges	SG14	CEA-00-125UW-120	Instrumented brace
	42	Strain gauges	SG15	CEA-00-125UW-120	Instrumented brace
	43	Strain gauges	SG16	CEA-00-125UW-120	Instrumented brace
Braces	44	Loadcell	FbraceL	MTS 661-23A-02	Brace left
	45	Loadcell	FbraceR	MTS 661-23B-02	Brace right
Frame	46	Strain gauges	SGF1	WFLA-6-11	Frame
	47	Strain gauges	SGF2	WFLA-6-11	Frame
	48	Strain gauges	SGF3	WFLA-6-11	Frame
	49	Strain gauges	SGF4	WFLA-6-11	Frame
	50	Strain gauges	SGF5	WFLA-6-11	Frame
	51	Strain gauges	SGF6	WFLA-6-11	Frame
	52	Strain gauges	SGF7	WFLA-6-11	Frame
	53	Strain gauges	SGF8	WFLA-6-11	Frame
	54	Strain gauges	SGF9	WFLA-6-11	Frame

	55	Strain gauges	SGF10	WFLA-6-11	Frame
	56	Strain gauges	SGF11	WFLA-6-11	Frame
	57	Strain gauges	SGF12	WFLA-6-11	Frame
	58	Strain gauges	SGF13	WFLA-6-11	Frame
	59	Strain gauges	SGF14	WFLA-6-11	Frame
	60	Strain gauges	SGF15	WFLA-6-11	Frame
	61	Strain gauges	SGF16	WFLA-6-11	Frame
	62	Strain gauges	SGF17	WFLA-6-11	Frame
	63	Strain gauges	SGF18	WFLA-6-11	Frame
	64	Strain gauges	SGF19	WFLA-6-11	Frame
	65	Strain gauges	SGF20	WFLA-6-11	Frame
	66	Strain gauges	SGF21	WFLA-6-11	Frame
	67	Strain gauges	SGF22	WFLA-6-11	Frame
	68	Strain gauges	SGF23	WFLA-6-11	Frame
	69	Strain gauges	SGF24	WFLA-6-11	Frame
	70	Strain gauges	SGF25	WFLA-6-11	Frame
	71	Strain gauges	SGF26	WFLA-6-11	Frame
Frame	72	Displacement	DzA	FGP	Gap under beam
	73	Displacement	DzB	FGP	Gap under beam
Braces	74	Voltage (loadcell)	Flex1	TEKSCAN	Top brace
	75	Voltage (loadcell)	Flex2	TEKSCAN	Top brace
	76	Voltage (loadcell)	Flex3	TEKSCAN	Top brace
	77	Voltage (loadcell)	Flex4	TEKSCAN	Top brace
	78	Voltage (loadcell)	Flex5	TEKSCAN	Top brace
	79	Voltage (loadcell)	Flex6	TEKSCAN	Top brace
	80	Voltage (loadcell)	Flex7	TEKSCAN	Top brace
	81	Voltage (loadcell)	Flex8	TEKSCAN	Top brace
	82	Voltage (loadcell)	Flex9	TEKSCAN	Top brace
	83	Voltage (loadcell)	Flex10	TEKSCAN	Top brace

B2 Table of Complete Experimental Campaign

Braces used	Run number	Test description (nominal acceleration)	Main results (achieved acceleration)
S1CAG1E1 No instrumentation	Run 001	AZALEE table driven in working position	
	Run 002	MTS white noise - Span 30%	
	Run 003	Seism -6 dB or 0.05 g	0,11 g
	Run 004	Seism 0 dB or 0.1 g	0,15 g
	Run 005	Seism +6 dB or 0.2 g	0,22 g
	Run 006	Seism +9.54 dB or 0.3 g	0,32 g → resonance
	Run 007	Seism 0 dB or 0.1 g	0,17 g → resonance
	Run 008	Seism 0 dB or 0.1 g	0,14 g
	Run 009	MTS white noise - Span 24%	
	Run 010	Seism 0 dB or 0.1 g	0,16 g
	Run 011	Seism +6 dB or 0.2 g	0,24 g
	Run 012	Seism +12 dB or 0.4 g	0,47 g
	Run 013	Seism +14 dB or 0.5 g	0,50 g
	Run 014	Seism +14 dB or 0.5 g	0.62 g → failure of right brace
S1CBG1E1 No instrumentation	Run 015	MTS white noise - Span 22%	
	Run 016	Seism 0 dB or 0.1 g	0,20 g → resonance
	Run 017	Seism 0 dB or 0.1 g	0,19 g
	Run 018	MTS white noise - Span 30%	
	Run 019	Seism +9.54 dB or 0.3 g	0,32 g
	Run 020	MTS white noise - Span 30%	
	Run 021	Seism +14 dB or 0.5 g	0.56 g → failure of right brace
S1CAG1E1-1-1 S1CAG1E1-2-1 (16 gauges)	Run 022	Tightening of braces bolts, acquisition 63 s	
	Run 023	MTS white noise - Span 30%	4.56 Hz
	Run 024	Seism 3.52 dB or 0.15 g	0,22 g→ resonance
	Run 025	Seism 0 dB or 0.1 g	0,14 g
	Run 026	Seism -6 dB or 0.05 g	0,08 g
	Run 027	Seism 0 dB or 0.1 g	0,13 g
	Run 028	Seism 3.52 dB or 0.15 g	0,19 g
	Run 029	MTS white noise - Span 30%	4.50 Hz
	Run 030	Seism 10.9 dB or 0.35 g	0.33 g
	Run 031	MTS white noise - Span 30%	4.62 Hz
	Run 032	Seism 15.56 dB or 0.6 g	0.62 g → failure of right brace

S3CAG1E1-3-2 S3CAG1E1-4-2 (7 gauges)	Run 033	Tightening of braces bolts	
	Run 034	MTS white noise - Span 30%	4.25 Hz
	Run 035	Seism -6 dB or 0.05 g	0,08 g
	Run 036	Seism -6 dB or 0.05 g	0,07 g
	Run 037	Seism 0.82 dB or 0.11 g	0,16 g
	Run 038	MTS white noise - Span 30%	4.25 Hz
	Run 039	Seism 7.95 dB or 0.25 g	0.38 g
	Run 040	MTS white noise - Span 30%	3.38 Hz
	Run 041	Seism 12.8 dB or 0.44 g	0.52 g
	Run 042	MTS white noise - Span 30%	1.75 Hz
	Run 043	Seism 14 dB or 0.5 g	0.67 g → failure of right brace
S4CAG1E1-1-1 S4CAG1E1-2-1 (7 gauges)	Run 044	Tightening of braces bolts	
	Run 045	MTS white noise - Span 30%	4.33 Hz
	Run 046	Seism -6 dB or 0.05 g	0,08
	Run 047	Seism -6 dB or 0.05 g	0,08
	Run 048	Seism 0 dB or 0.1 g	0,13
	Run 049	MTS white noise - Span 30%	4.32 Hz
	Run 050	Seism 7.23 dB or 0.23 g	0.25 g
	Run 051	MTS white noise - Span 30%	4.25 Hz
	Run 052	Seism 12.25 dB or 0.41 g	0.43 g
	Run 053	MTS white noise - Span 30%	2.69 Hz
	Run 054	Seism 14.8 dB or 0.5 g	0.72
	Run 055	MTS white noise - Span 30%	1.42 Hz
	Run 056	Seism 14.8 dB or 0.5 g	0.58 g → Failure of both braces after 15 s
S2CAG1E1 1-2 S2CAG1E1 2-2 (7 gauges)	Run 057	Tightening of braces bolts	
	Run 058	MTS white noise - Span 30%	4.50 Hz
	Run 059	Seism -6 dB or 0.05 g	0,08 g
	Run 060	Seism -6 dB or 0.05 g	0,08 g
	Run 061	Seism 2.92 dB or 0.14 g	0,18 g→ resonance
	Run 062	Seism 0 dB or 0.1 g	0,16 g→ resonance
	Run 063	Seism -6 dB or 0.05 g	0,09 g
	Run 064	Seism 0 dB or 0.1 g	0,13 g
	Run 065	Seism 2.92 dB or 0.14 g	0,21 g
	Run 066	MTS white - Span 30%	4.48 Hz
	Run 067	Seism 10.37 dB or 0.33 g	0.40 g
	Run 068	MTS white noise - Span 30%	3.96 Hz
	Run 069	Seism 15.12 dB or 0.57 g	0.64 g → Failure of both braces after 31 s

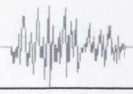

S1CAG2E1 1-3 S1CAG2E1 2-3 (16 gauges)	Run 070	Tightening of braces bolts	
	Run 071	MTS white noise - Span 30%	4.52 Hz
	Run 072	Seism -6 dB or 0.05 g	0,08 g
	Run 073	Seism -6 dB or 0.05 g	0,08 g
	Run 074	Seism 0 dB or 0.1 g	0,16 g → resonance
	Run 075	Seism -6 dB or 0.05 g	0,08 g
	Run 076	Seism -6 dB or 0.05 g	0,07 g
	Run 077	Seism 0 dB or 0.1 g	0,13 g
	Run 078	Seism 3.52 dB or 0.15 g	0,18 g
	Run 079	MTS white noise - Span 30%	4.40 Hz
	Run 080	Seism 10.8 dB or 0.35 g	0.35 g
	Run 081	MTS white noise - Span 30%	4.08 Hz
	Run 082	Seism 15.56 dB or 0.6 g	0.77 g → Failure of both braces after 31 s
S2CAG2E1 1-1 S2CAG2E1 2-1 (7gauges)	Run 083	Tightening of braces bolts	
	Run 084	MTS white noise - Span 30%	4.45 Hz
	Run 085	Seism -6 dB or 0.05 g	0,10 g
	Run 086	Seism -6 dB or 0.05 g	0,07 g
	Run 087	Seism 0 dB or 0.1 g	0,13 g
	Run 088	Seism 2.92 dB or 0.14 g	0,19 g
	Run 089	MTS white noise - Span 30%	4.39 Hz
	Run 090	Seism 10.37 dB or 0.33 g	0.36 g
	Run 091	MTS white noise - Span 30%	3.83 Hz
	Run 092	Seism 15.11 dB or 0.57 g	0.81 g
	Run 093	MTS white noise - Span 30%	1.57 Hz
	Run 094	Seism 15.11 dB or 0.57 g	0.72 g → Failure of left brace after 15 s
S3CAG2E1 1-1 S3CAG2E1 2-1 (7 gauges)	Run 095	Tightening of braces bolts	
	Run 096	MTS white noise - Span 30%	4.03 Hz
	Run 097	Seism -6 dB or 0.05 g	0,09 g
	Run 098	Seism -6 dB or 0.05 g	0,08 g
	Run 099	Seism 0.83 dB or 0.11 g	0,18 g
	Run 100	MTS white noise - Span 30%	3.78 Hz
	Run 101	Seism 7.95 dB or 0.25 g	0.39 g
	Run 102	MTS white noise - Span 30%	2.35 Hz
	Run 103	Seism 12.86 dB or 0.44 g	0.58 g
	Run 104	MTS white noise - Span 30%	1.43 Hz
	Run 105	Seism 15.56 dB or 0.6 g	0.59 g → Failure of right brace after 20 s

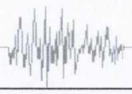

S1CBG1E1 3-3 S1CBG1E1 4-3 (7 gauges)	Run 106	Tightening of braces bolts	
	Run 107	MTS white noise - Span 25%	4.30 Hz
	Run 108	Seism -6 dB or 0.05 g	0,10 g → resonance
	Run 109	Seism -9.6 dB or 0.033 g	0,06 g
	Run 110	Seism -6 dB or 0.05 g	0,07 g
	Run 111	Seism -6 dB or 0.05 g	0,08 g
	Run 112	Seism 0 dB or 0.1 g	0,12 g
	Run 113	Seism 3.52 dB or 0.15 g	0,17 g→ resonance
	Run 114	MTS white noise - Span 30%	4.60 Hz
	Run 115	Seism 6 dB or 0.2 g	0.23 g
	Run 116	MTS white noise - Span 30%	4.29 Hz
	Run 117	Seism 10.88 dB or 0.35 g	0.43 g
	Run 118	MTS white noise - Span 30%	4.25 Hz
	Run 119	Seism 15.56 dB or 0.6 g	0.83 g → Failure of both braces after 18 s
S2CBG1E1 1-3 S2CBG1E1 2-3 (7 gauges)	Run 120	Tightening of braces bolts	
	Run 121	MTS white noise - Span 30%	3.87 Hz
	Run 122	Seism -6 dB or 0.05 g	0,10 g
	Run 123	Seism -6 dB or 0.05 g	0,08 g
	Run 124	Seism 0 dB or 0.1 g	0,17 g
	Run 125	Seism 2.92 dB or 0.14 g	0,19 g
	Run 126	MTS white noise - Span 20%	4.02 Hz
	Run 127	Seism 10.37 dB or 0.33 g	0.37 g
	Run 128	MTS white noise - Span 20%	2.32 Hz
	Run 129	Seism 13.06 dB or 0.45 g	0.42 g → Failure of left brace after 9 s
S4CBG2E2 1-1 S4CBG2E2 2-1 (16 gauges)	Run 130	Tightening of braces bolts	
	Run 131	MTS white noise - Span 20%	4.07 Hz
	Run 132	Seism -6 dB or 0.05 g	0,09 g
	Run 133	Seism -6 dB or 0.05 g	0,07 g
	Run 134	Seism 0 dB or 0.1 g	0,18 g→ resonance
	Run 135	MTS white noise - Span 20%	3.70 Hz
	Run 136	Seism 7.23 dB or 0.23 g	0.31 g
	Run 137	MTS white noise - Span 20%	3.09 Hz
	Run 138	Seism 12.26 dB or 0.41 g	0.50 g
	Run 139	MTS white noise - Span 20%	1.30 Hz
	Run 140	Seism 14.8 dB or 0.55 g	0.75 g → Failure of right brace after 17 s

S2CBG2E1 1-2 S2CBG2E1 2-2 (7 gauges)	Run 141	Tightening of braces bolts	
	Run 142	MTS white noise - Span 20	4.32 Hz
	Run 143	Seism -6 dB or 0.05 g	0,09 g
	Run 144	Seism -6 dB or 0.05 g	0,07 g
	Run 145	Seism 0 dB or 0.1 g	0,13 g
	Run 146	Seism 2.92 dB or 0.14 g	0,17 g→ resonance
	Run 147	MTS white noise - Span 20%	4.18 Hz
	Run 148	Seism 10.37 dB or 0.33 g	0.41 g
	Run 149	MTS white noise - Span 20%	2.59 Hz
	Run 150	Seism 13.06 dB or 0.45 g	0.68 g → no rupture
	Run 151	MTS white noise - Span 20%	1.08 Hz
S3CBG2E1 1-1 S3CBG2E1 2-1 (15 jauges)	Run 152	Tightening of braces bolts	
	Run 153	MTS white noise - Span 20%	4.06 Hz
	Run 154	Seism -6 dB or 0.05 g	0,11 g
	Run 155	Seism -6 dB or 0.05 g	0,07 g
	Run 156	Seism 0.83 dB or 0.11 g	0,15 g→ resonance
	Run 157	MTS white noise - Span 20%	3.81 Hz
	Run 158	Seism 7.96 dB or 0.25 g	0.35 g
	Run 159	MTS white noise - Span 20%	1.19 Hz
	Run 160	Seism 12.87 dB or 0.44 g	0.47 g → Failure of right brace after 21 s

B3 Earthquake Ground Motion Test Results

This sub-appendix includes supplementary data that was not included in Section 9.3. Primarily, the entire set of 50%/50 test results are shown with additional plots produced from the 10%/50 and 2%/50 tests.

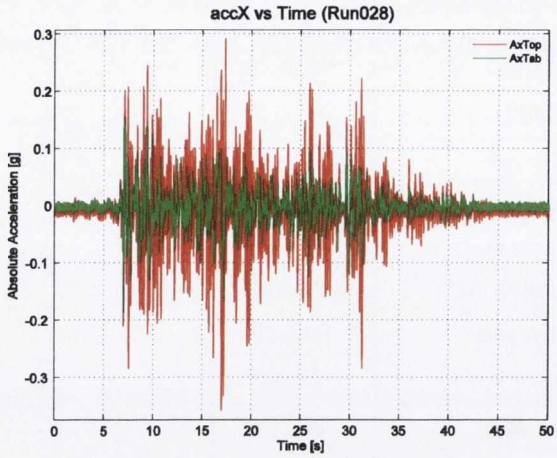

(a) Input (AxTab) and response (AxTop) absolute acceleration time history in x-direction

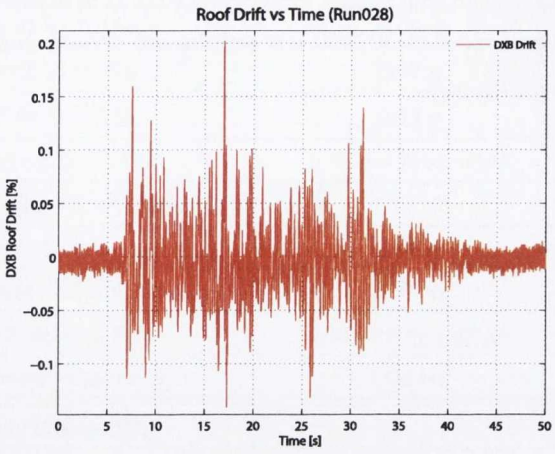

(b) Roof level drift (DXB Drift) time history in x-direction

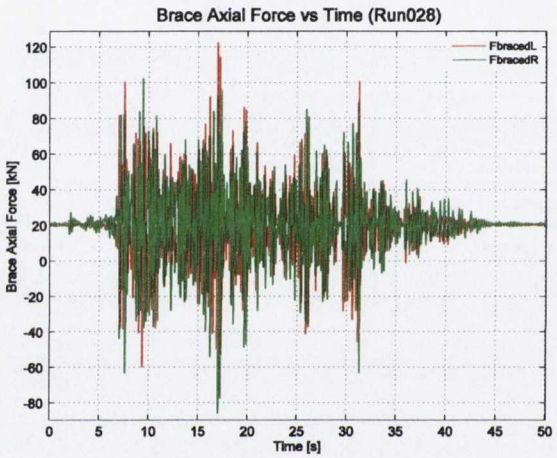

(c) Brace axial load time history for left (FbracedL) and right (FbracedR) braces

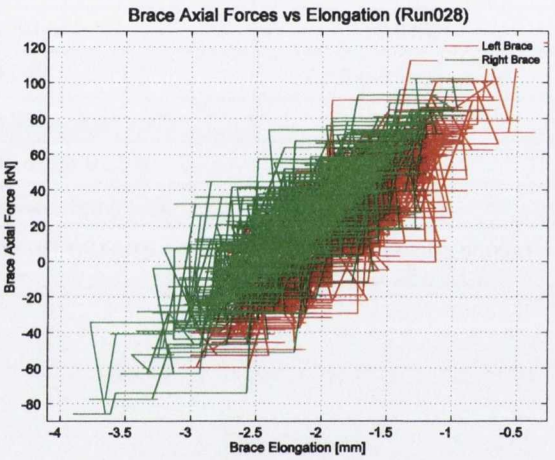

(d) Brace axial load hysteresis for left and right braces

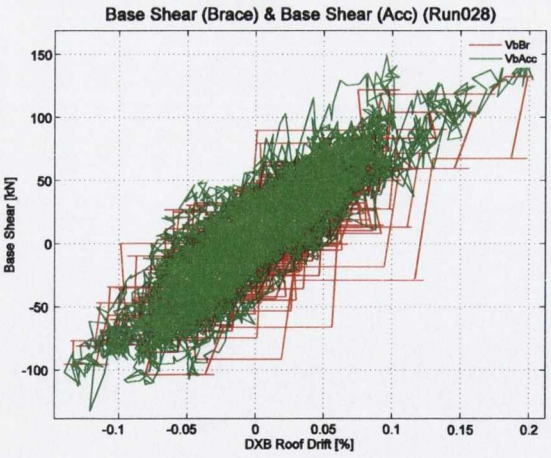

(e) Base shear from brace axial forces plotted against roof drift

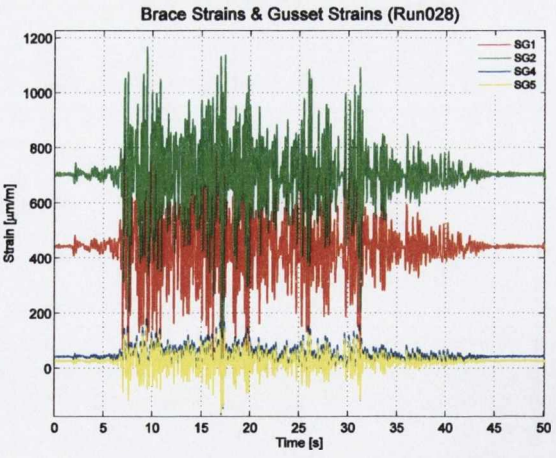

(f) Strain gauge measurements located on the right brace and gusset plate specimen

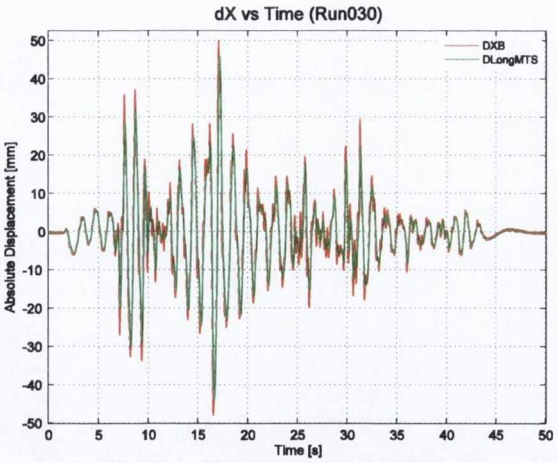

(g) Absolute displacements for table (DLongMTS) and roof level (DXB) time history

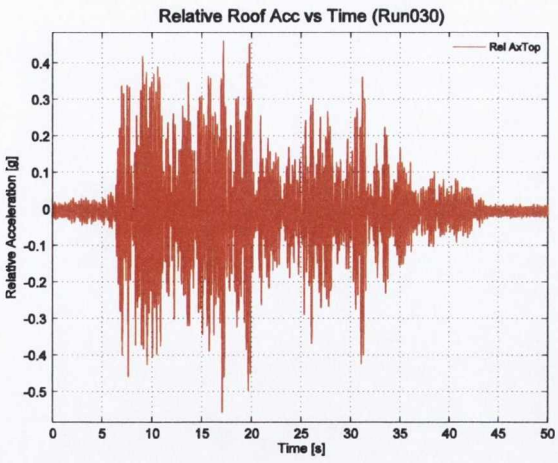

(h) Relative acceleration at roof level

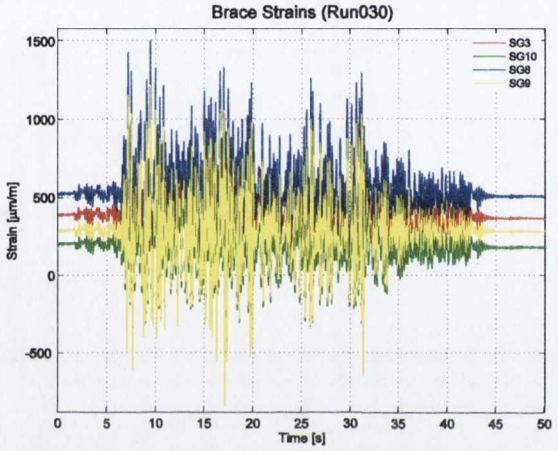

(i) Strain gauge measurements located on the right brace specimen

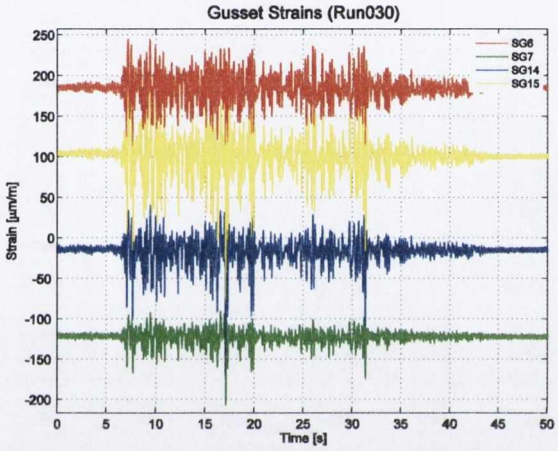

(j) Strain gauge measurements located on the right gusset specimen

10%/50 (Run030)

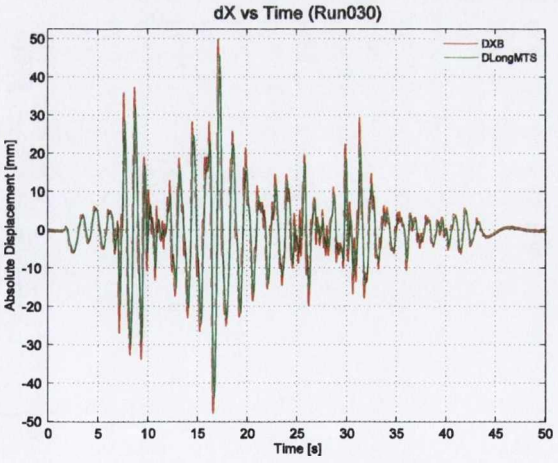

(a) Displacements for table (DLongMTS) and roof level (DXB)

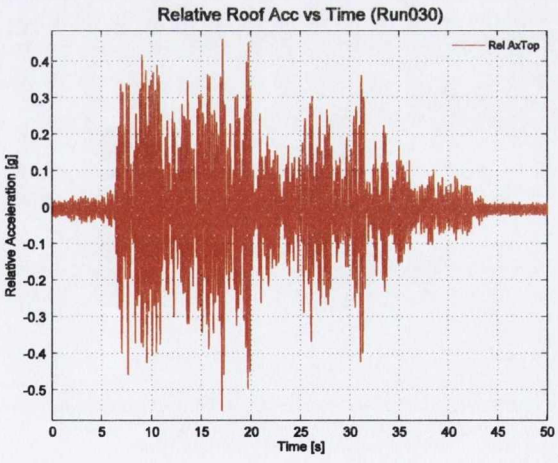

(b) Relative acceleration at roof level

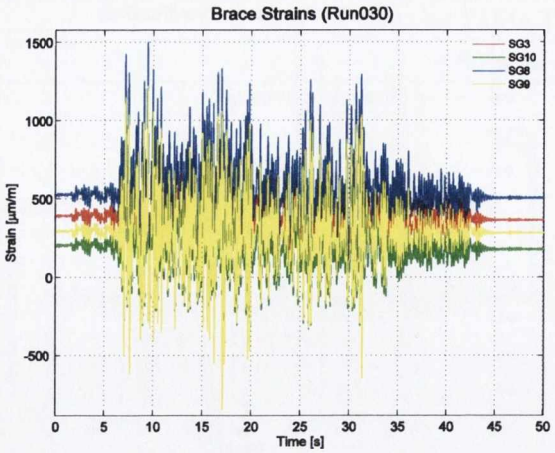

(c) Strain gauge measurements located on the right brace specimen

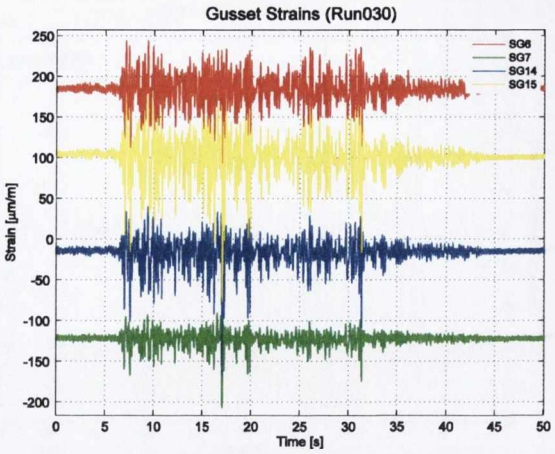

(d) Strain gauge measurements located on the right gusset specimen

2%/50 (Run032)

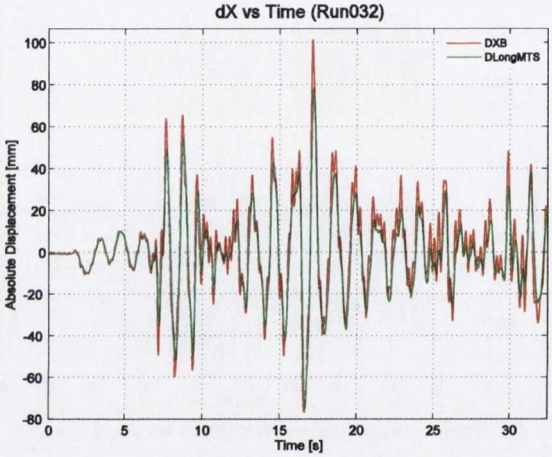

(a) Absolute displacements for table (DLongMTS) and roof level (DXB) time history

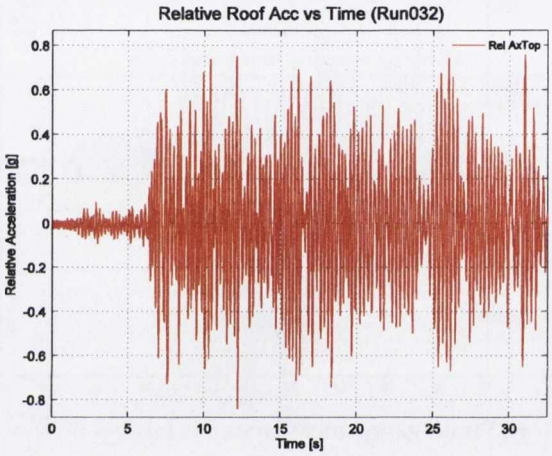

(b) Relative acceleration at roof level

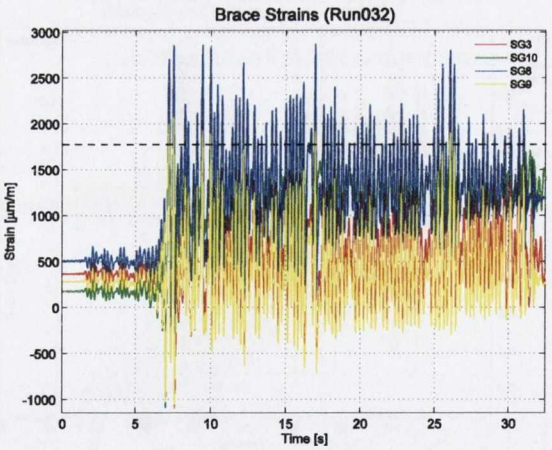

(c) Strain gauge measurements located on the right brace specimen

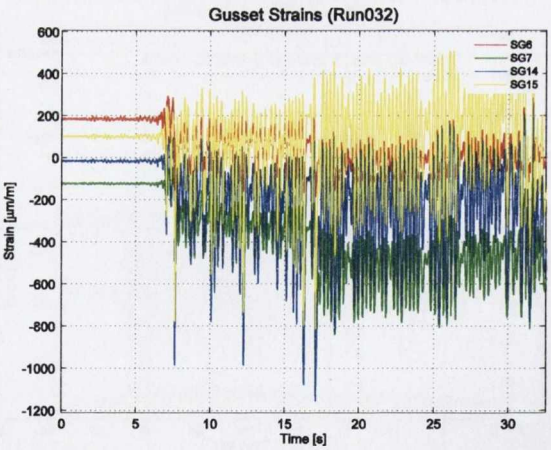

(d) Strain gauge measurements located on the right gusset specimen

Shake Table Test 2: S3-CA-G1

50%/50 (Run037)

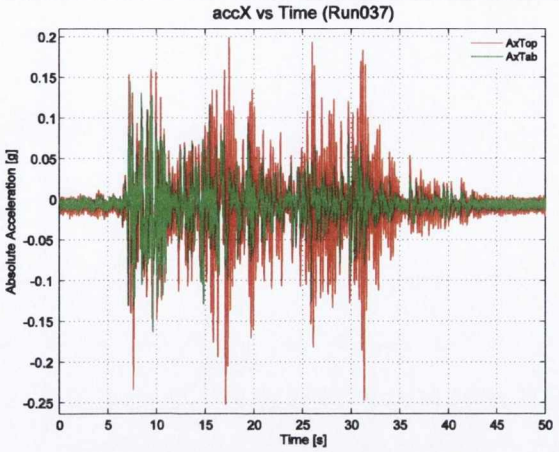

(a) Input (AxTab) and response (AxTop) absolute acceleration time history in x-direction

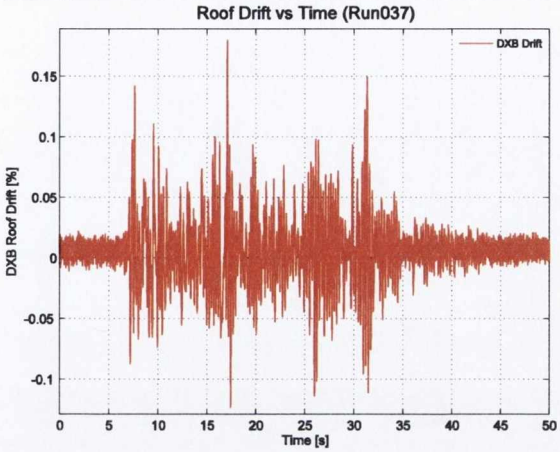

(b) Roof level drift (DXB Drift) time history in x-direction

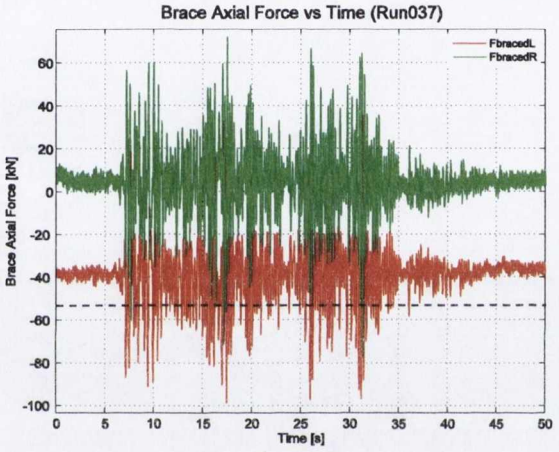

(c) Brace axial load time history for left (FbracedL) and right (FbracedR) braces

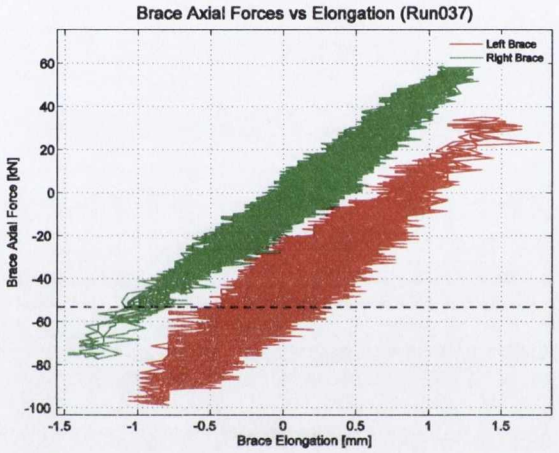

(d) Brace axial load hysteresis for left and right braces

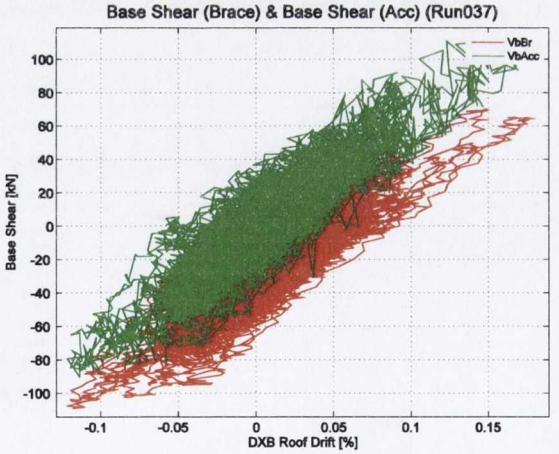

(e) Base shear from brace axial forces plotted against roof drift

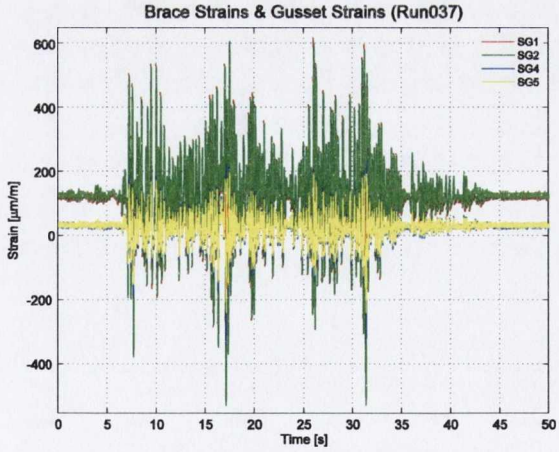

(f) Strain gauge measurements located on the right brace and gusset plate specimen

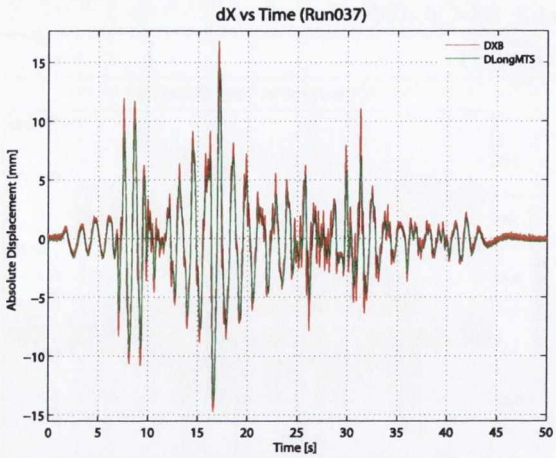

(g) Absolute displacements for table (DLongMTS) and roof level (DXB) time history

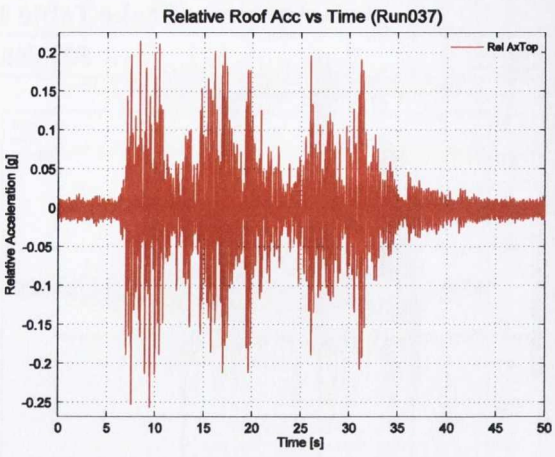

(h) Relative acceleration at roof level

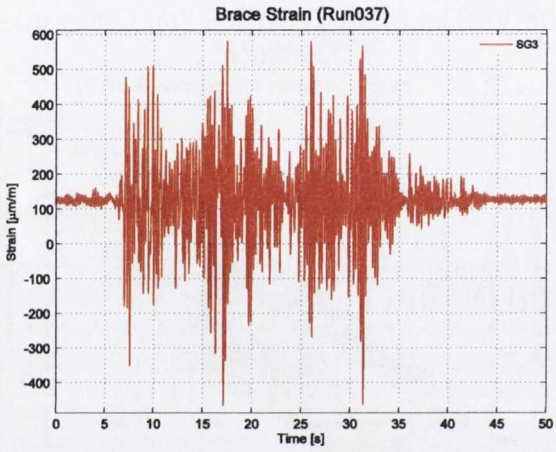

(i) Strain gauge measurements located on the right brace specimen

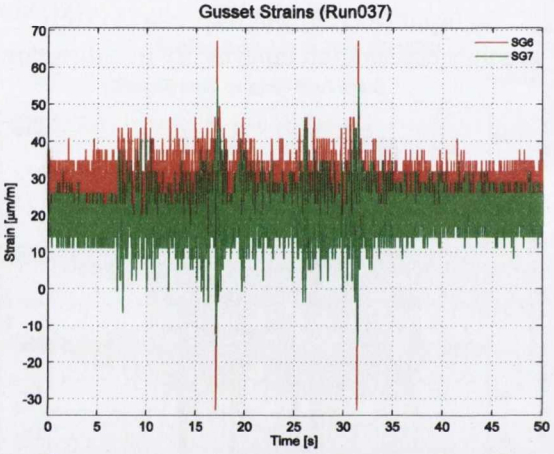

(j) Strain gauge measurements located on the right gusset specimen

2%/50 (Run041)

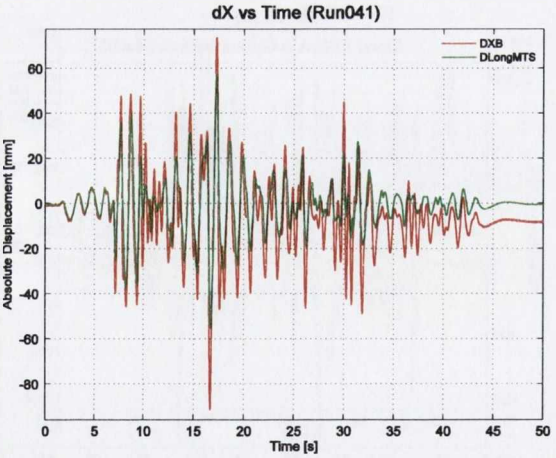

(a) Displacements for table (DLongMTS) and roof level (DXB)

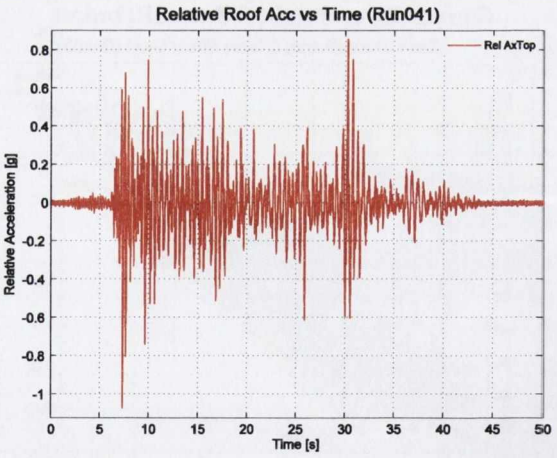

(b) Relative acceleration at roof level

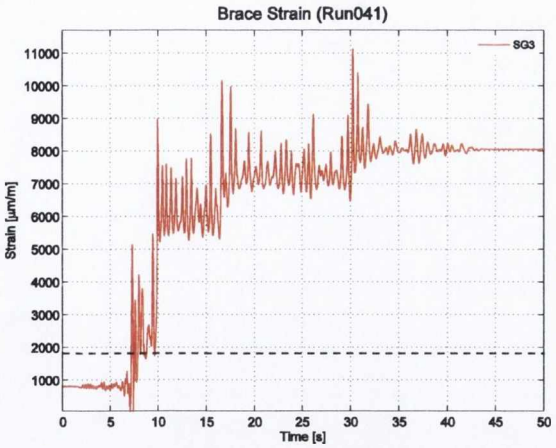

(c) Strain gauge measurements located on the right brace specimen

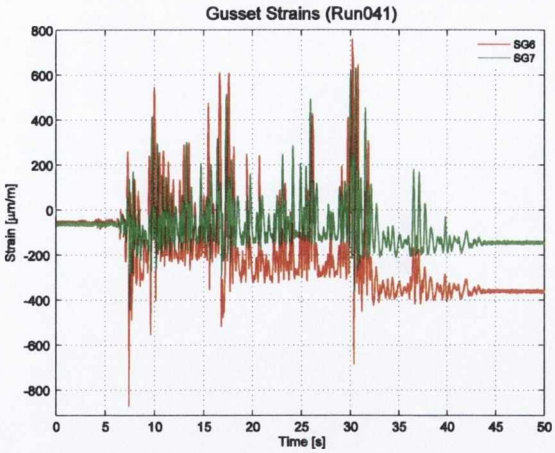

(d) Strain gauge measurements located on the right gusset specimen

Failure Level (Run043)

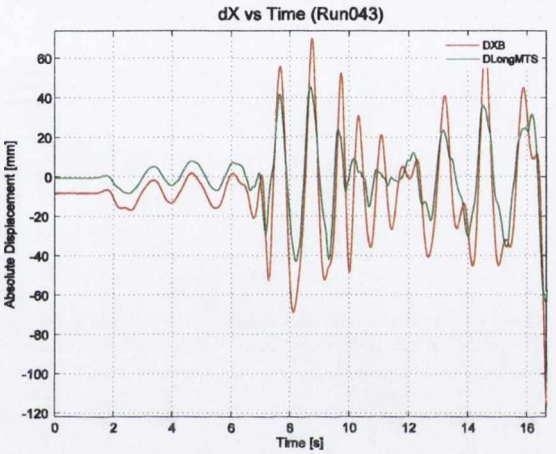

(a) Absolute displacements for table (DLongMTS) and roof level (DXB) time history

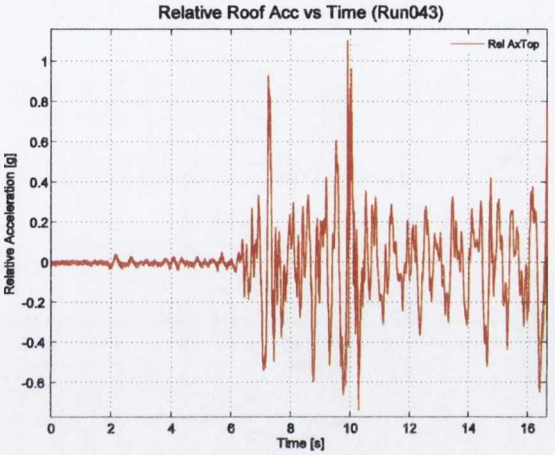

(b) Relative acceleration at roof level

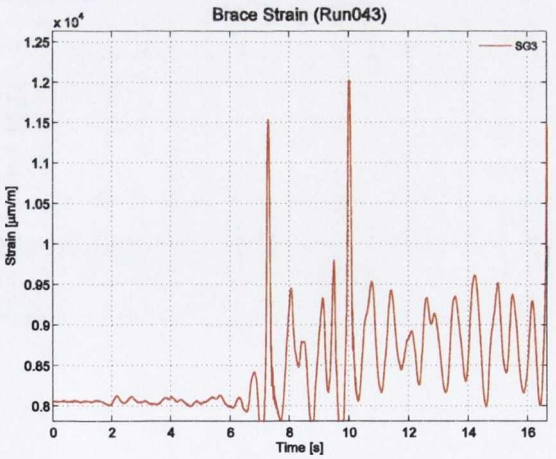

(c) Strain gauge measurements located on the right brace specimen

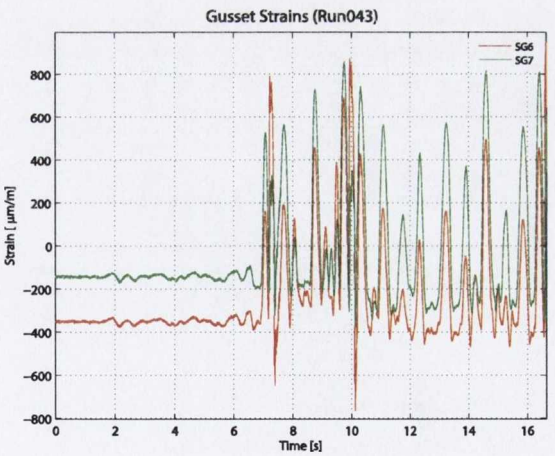

(d) Strain gauge measurements located on the right gusset specimen

Shake Table Test 3: S4-CA-G1

50%/50 (Run048)

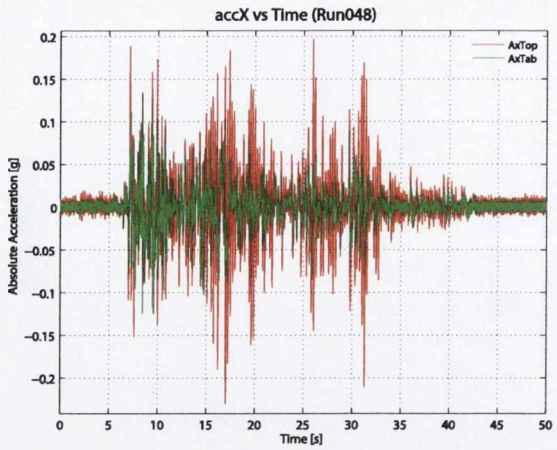

(a) Input (AxTab) and response (AxTop) absolute acceleration time history in x-direction

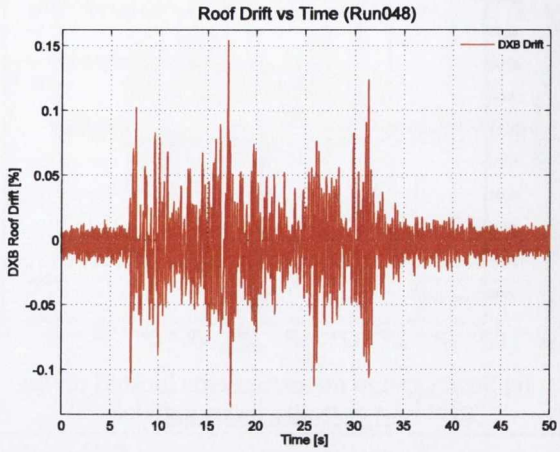

(b) Roof level drift (DXB Drift) time history in x-direction

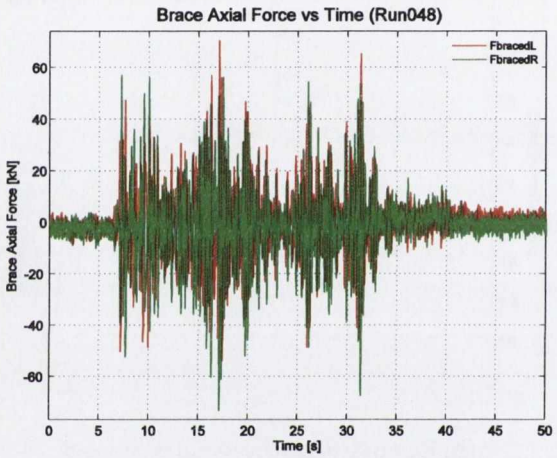

(c) Brace axial load time history for left (FbracedL) and right (FbracedR) braces

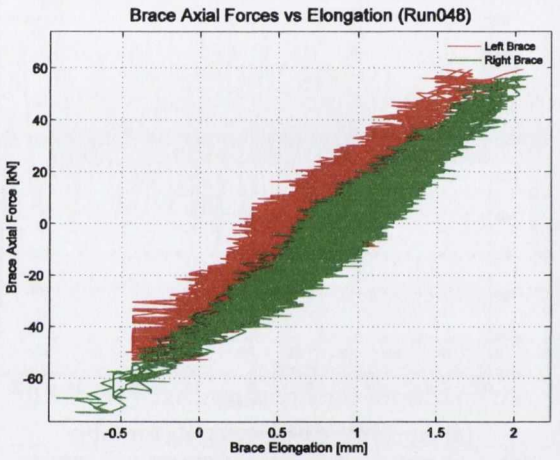

(d) Brace axial load hysteresis for left and right braces

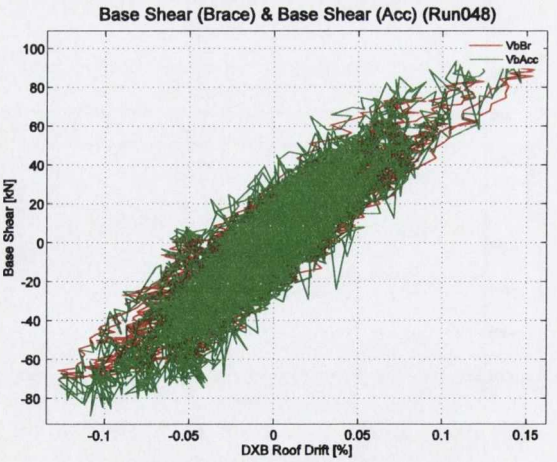

(e) Base shear from brace axial forces plotted against roof drift

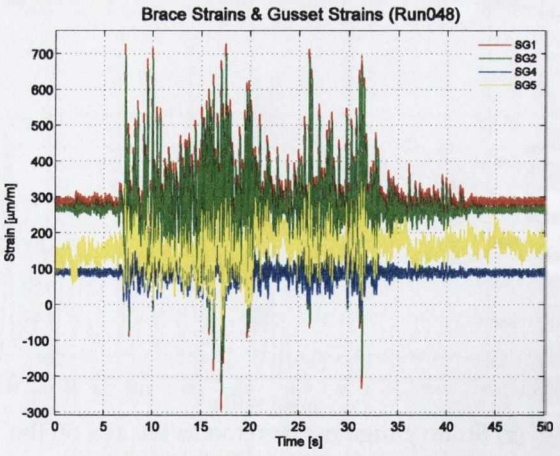

(f) Strain gauge measurements located on the right brace and gusset plate specimen

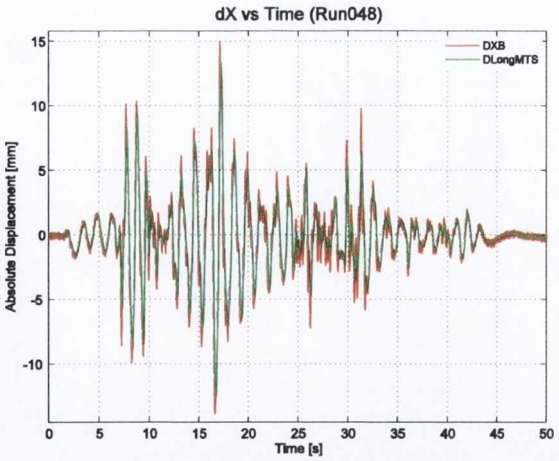

(g) Absolute displacements for table (DLongMTS) and roof level (DXB) time history

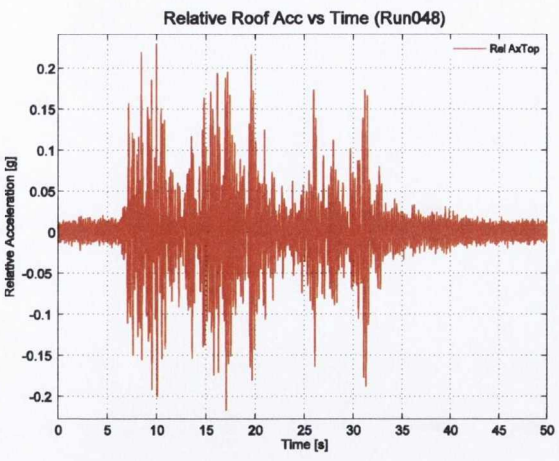

(h) Relative acceleration at roof level

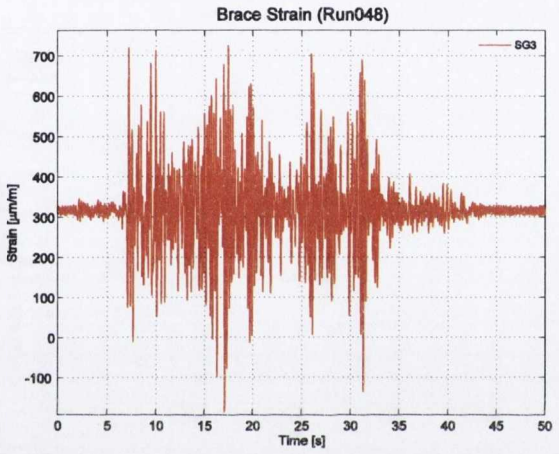

(i) Strain gauge measurements located on the right brace specimen

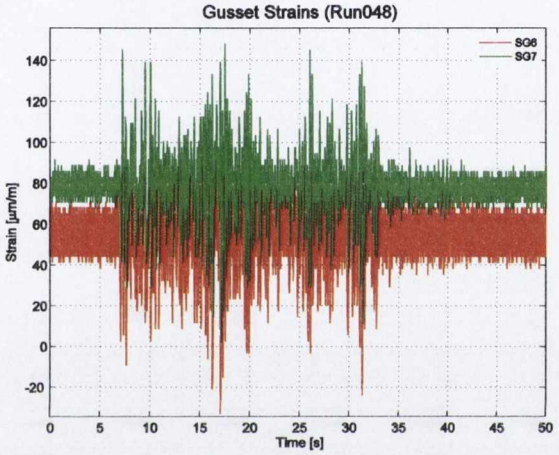

(j) Strain gauge measurements located on the right gusset specimen

2%/50 (Run052)

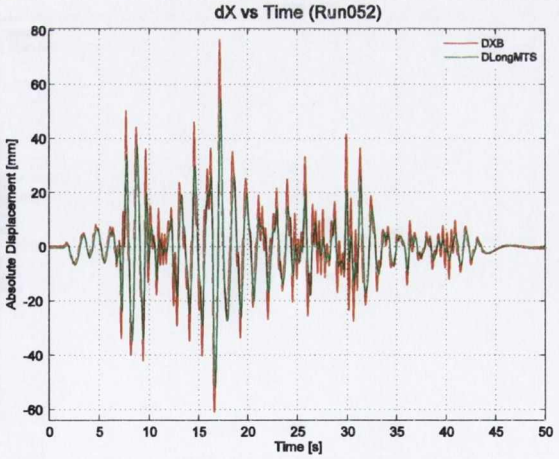

(a) Displacements for table (DLongMTS) and roof level (DXB)

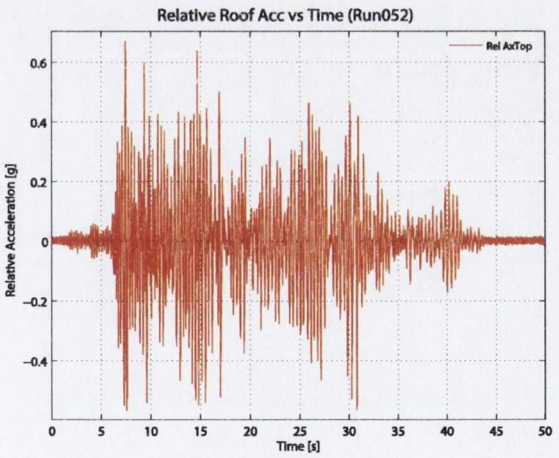

(b) Relative acceleration at roof level

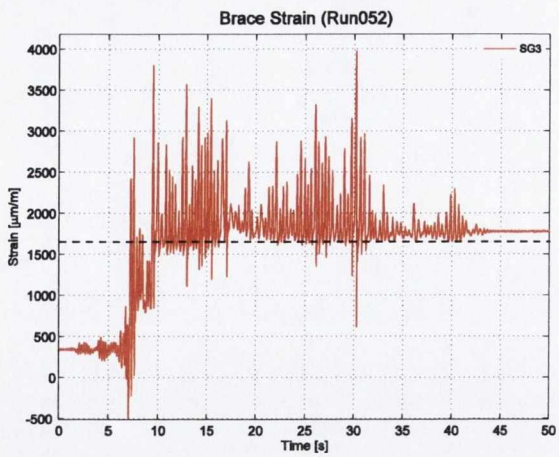

(c) Strain gauge measurements located on the right brace specimen

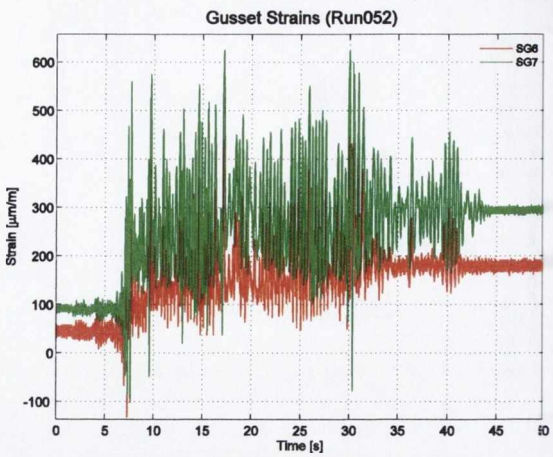

(d) Strain gauge measurements located on the right gusset specimen

Failure Level (Run054)

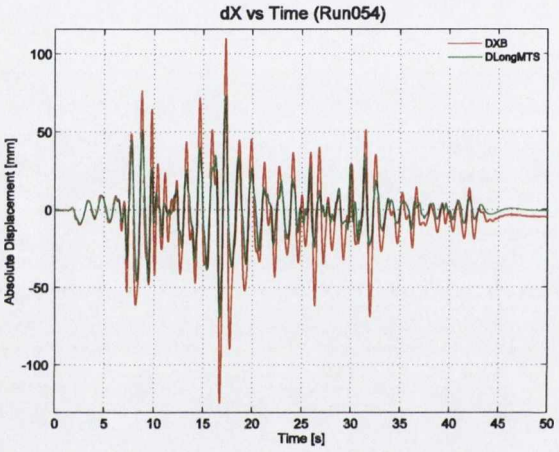

(a) Absolute displacements for table (DLongMTS) and roof level (DXB) time history

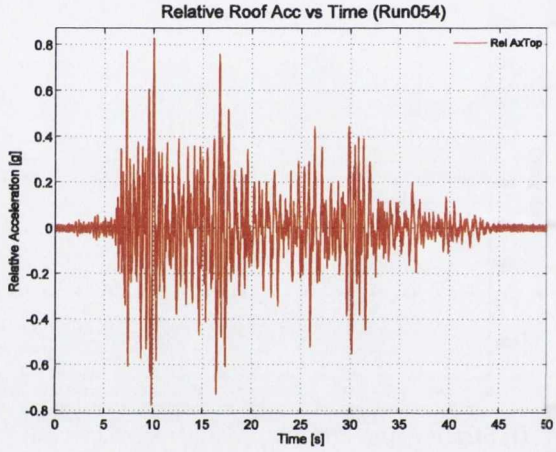

(b) Relative acceleration at roof level

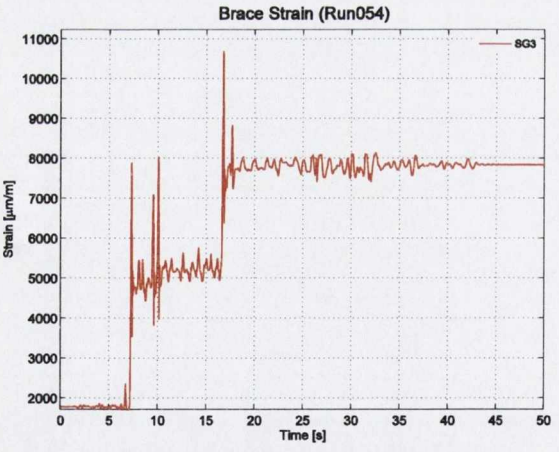

(c) Strain gauge measurements located on the right brace specimen

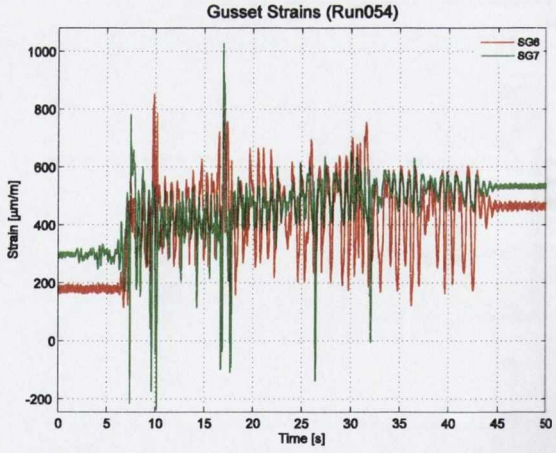

(d) Strain gauge measurements located on the right gusset specimen

Shake Table Test 4: S2-CA-G1

50%/50 (Run065)

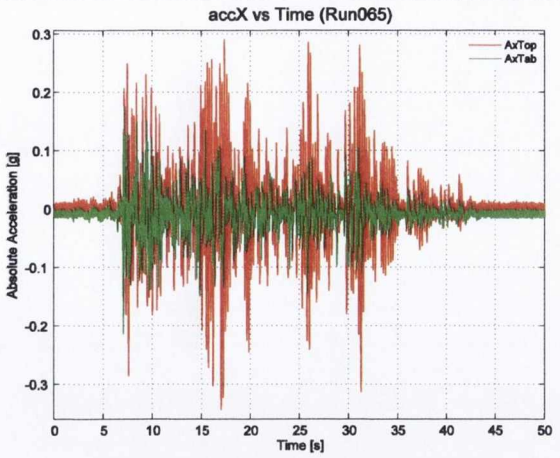

(a) Input (AxTab) and response (AxTop) absolute acceleration time history in x-direction

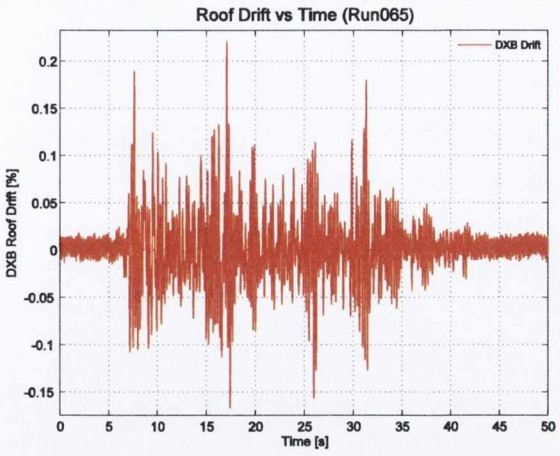

(b) Roof level drift (DXB Drift) time history in x-direction

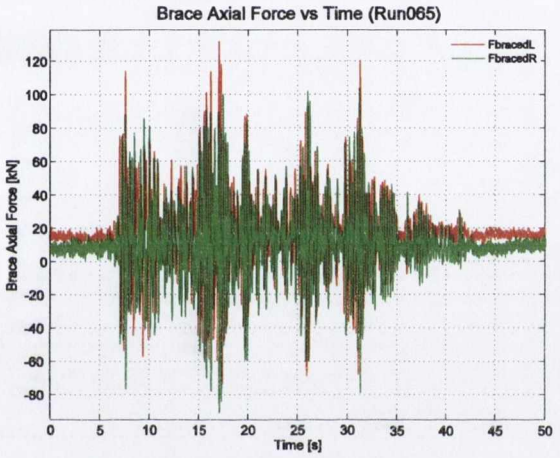

(c) Brace axial load time history for left (FbracedL) and right (FbracedR) braces

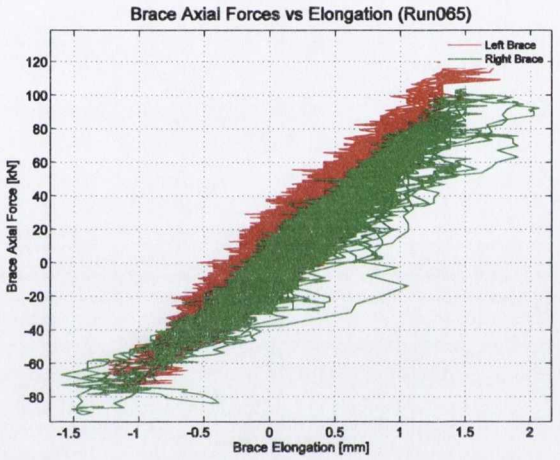

(d) Brace axial load hysteresis for left and right braces

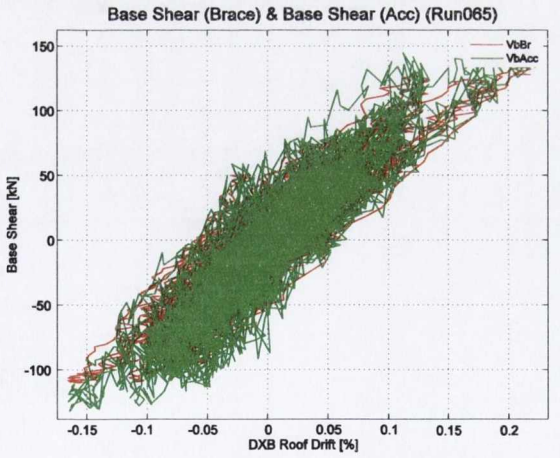

(e) Base shear from brace axial forces plotted against roof drift

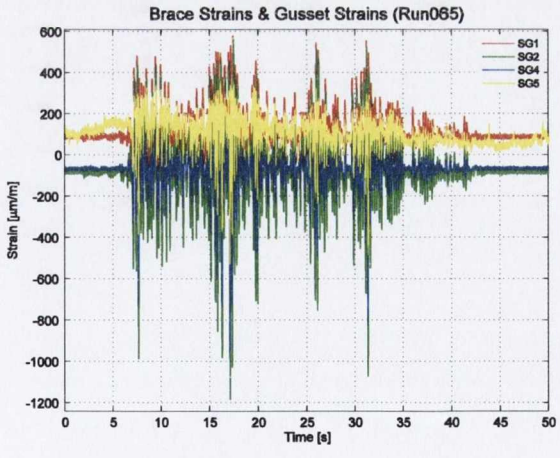

(f) Strain gauge measurements located on the right brace and gusset plate specimen

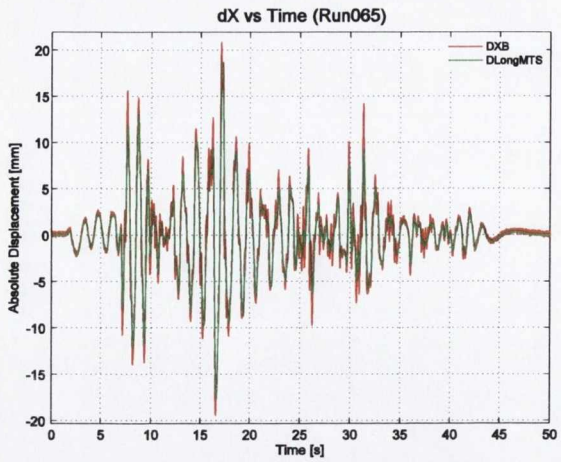

(g) Absolute displacements for table (DLongMTS) and roof level (DXB) time history

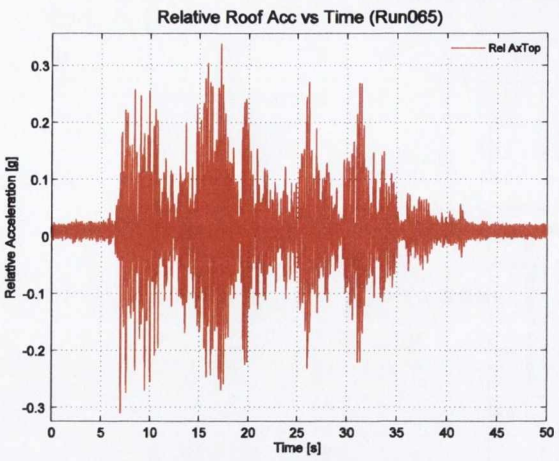

(h) Relative acceleration at roof level

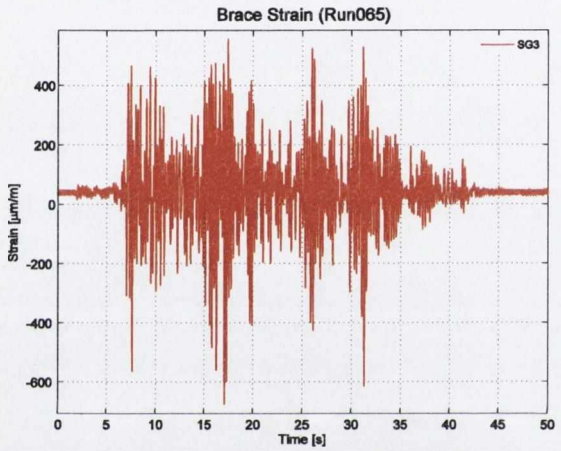

(i) Strain gauge measurements located on the right brace specimen

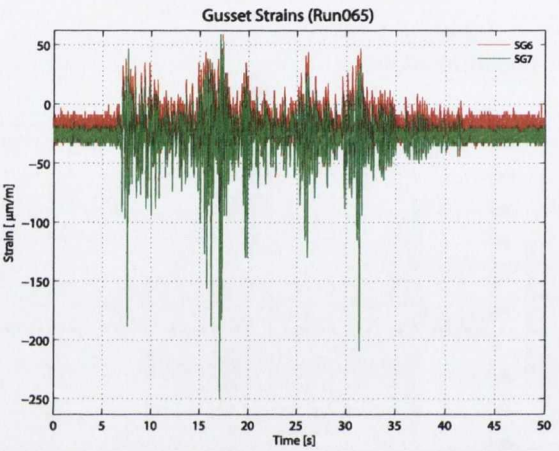

(j) Strain gauge measurements located on the right gusset specimen

10%/50 (Run067)

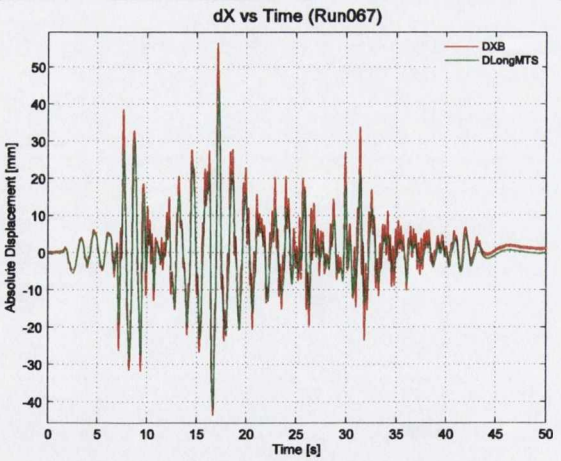

(a) Displacements for table (DLongMTS) and roof level (DXB)

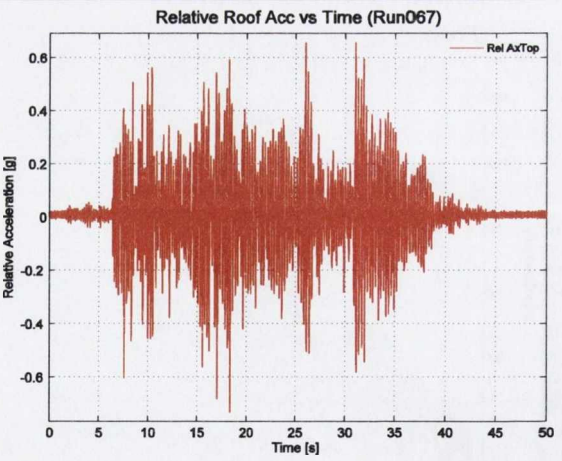

(b) Relative acceleration at roof level

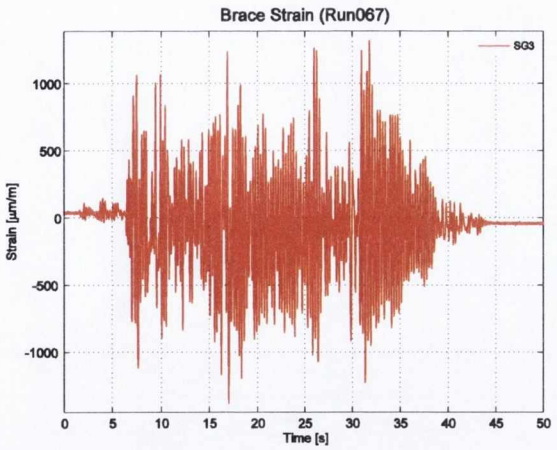

(c) Strain gauge measurements located on the right brace specimen

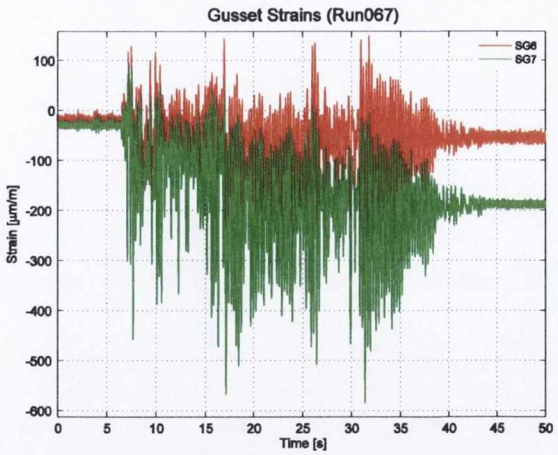

(d) Strain gauge measurements located on the right gusset specimen

2%/50 (Run069)

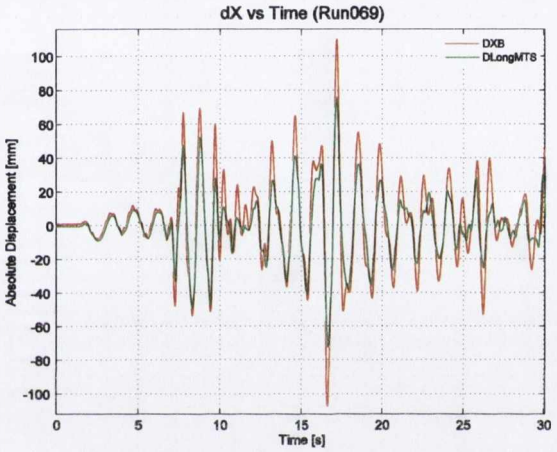

(a) Absolute displacements for table (DLongMTS) and roof level (DXB) time history

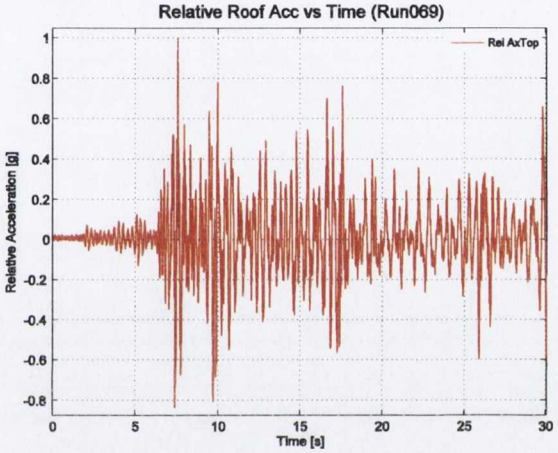

(b) Relative acceleration at roof level

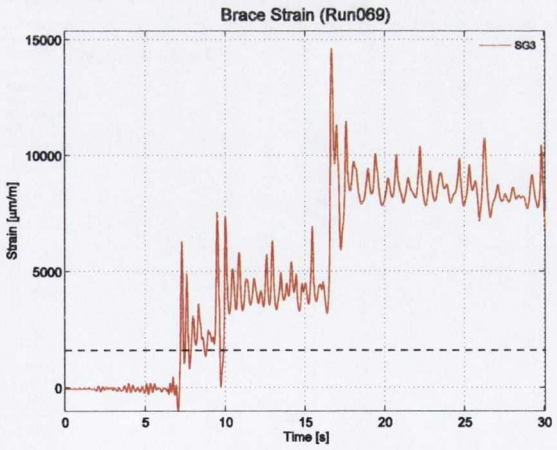

(c) Strain gauge measurements located on the right brace specimen

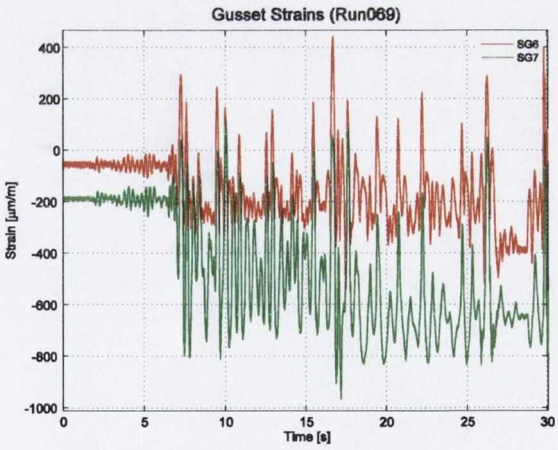

(d) Strain gauge measurements located on the right gusset specimen

Shake Table Test 5: S1-CA-G2

50%/50 (Run078)

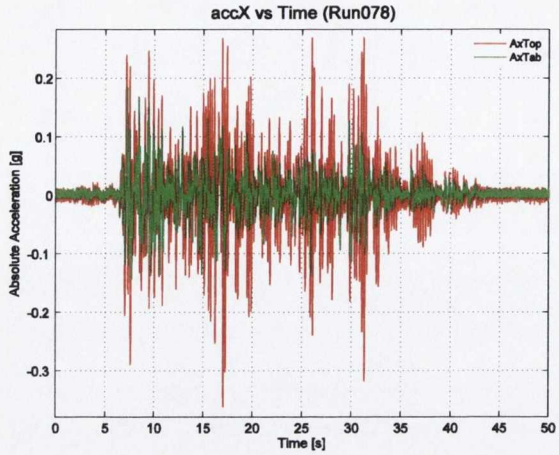

(a) Input (AxTab) and response (AxTop) absolute acceleration time history in x-direction

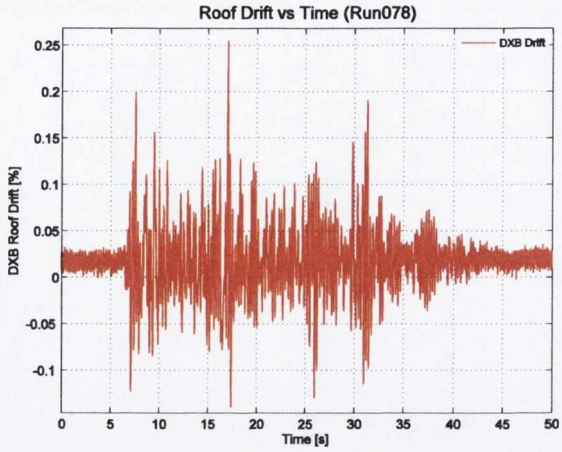

(b) Roof level drift (DXB Drift) time history in x-direction

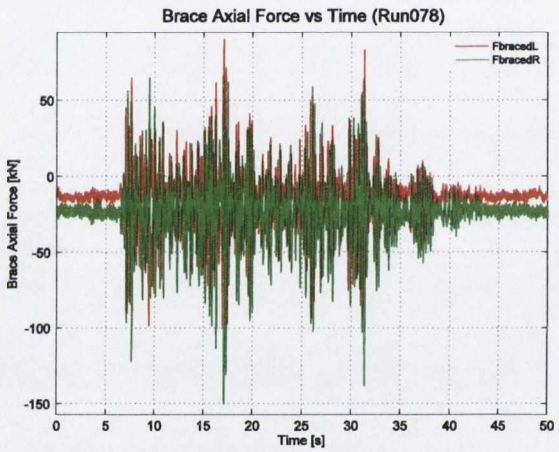

(c) Brace axial load time history for left (FbracedL) and right (FbracedR) braces

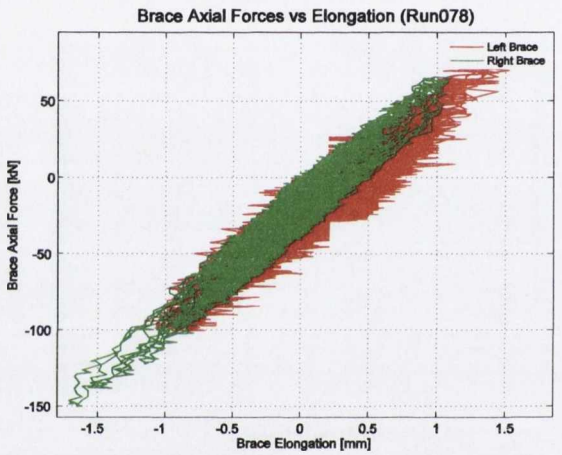

(d) Brace axial load hysteresis for left and right braces

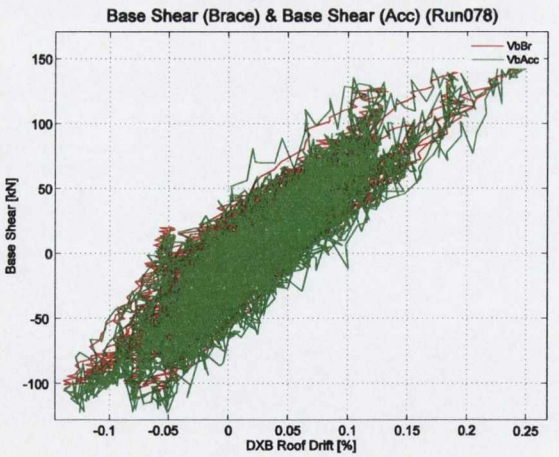

(e) Base shear from brace axial forces plotted against roof drift

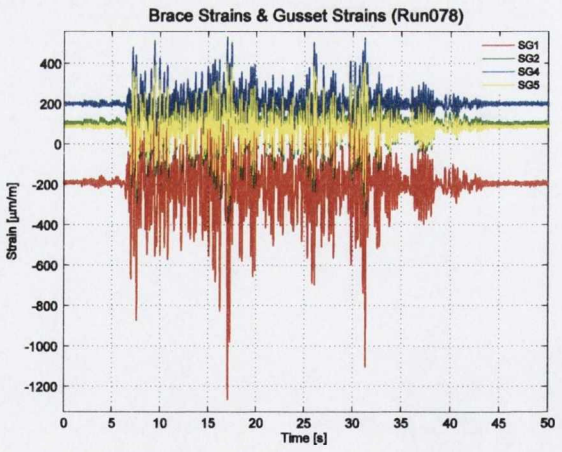

(f) Strain gauge measurements located on the right brace and gusset plate specimen

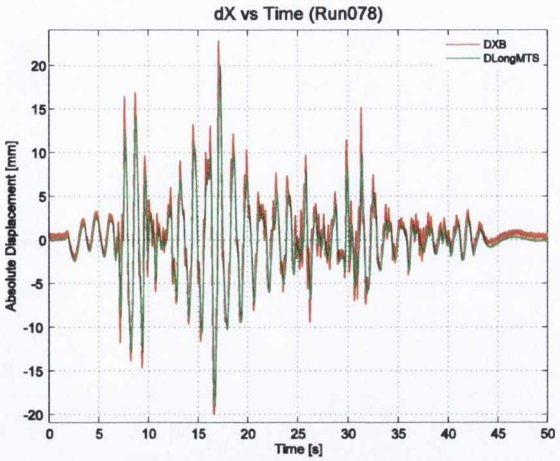

(g) Absolute displacements for table (DLongMTS) and roof level (DXB) time history

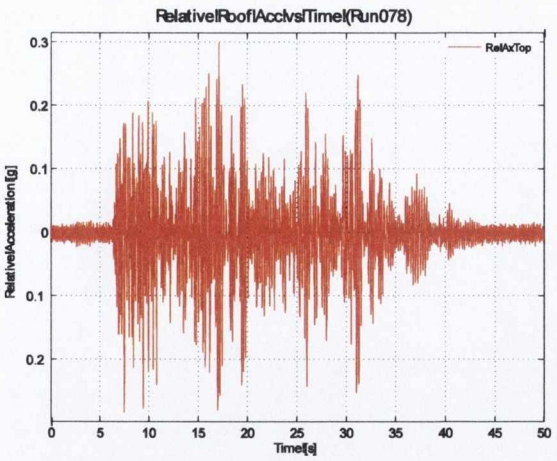

(h) Relative acceleration at roof level

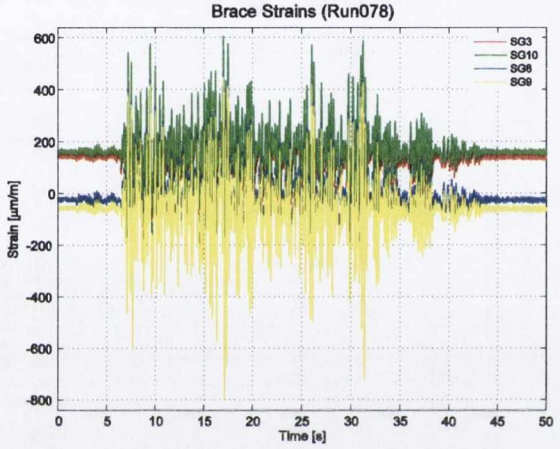

(i) Strain gauge measurements located on the right brace specimen

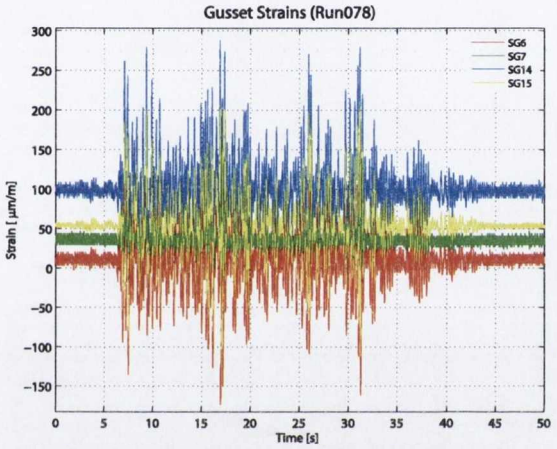

(j) Strain gauge measurements located on the right gusset specimen

10%/50 (Run080)

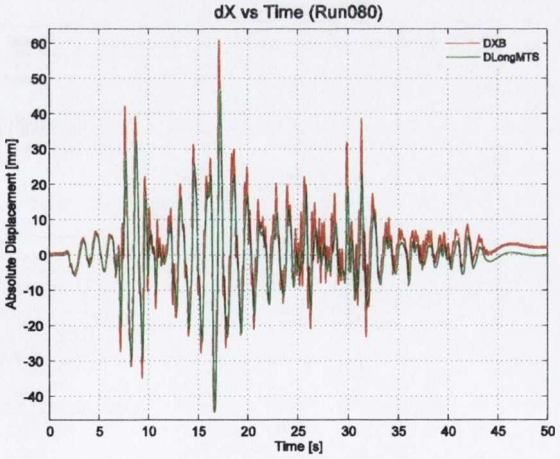

(a) Displacements for table (DLongMTS) and roof level (DXB)

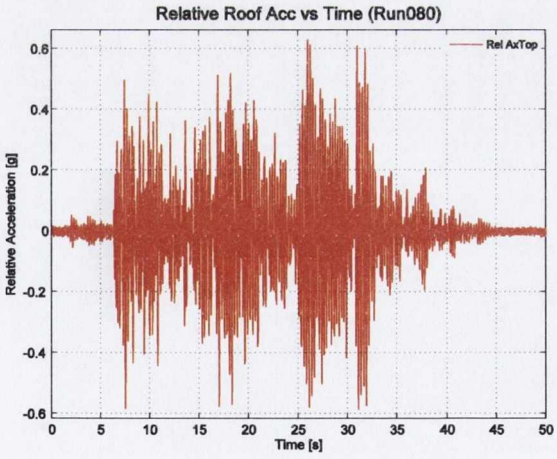

(b) Relative acceleration at roof level

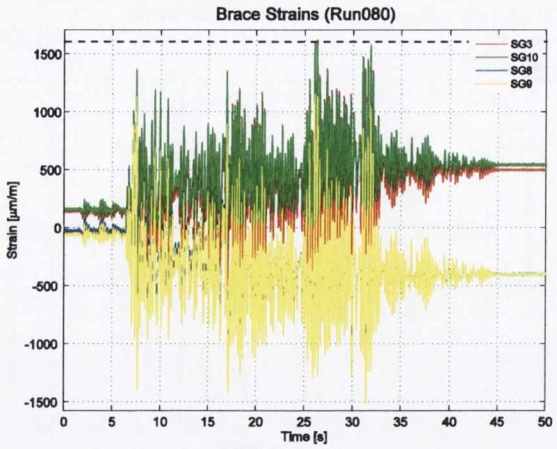

(c) Strain gauge measurements located on the right brace specimen

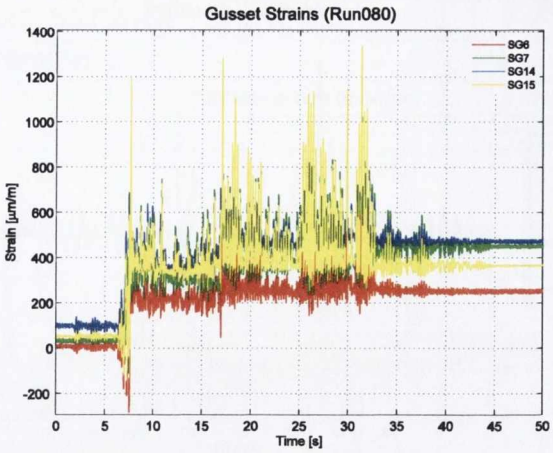

(d) Strain gauge measurements located on the right gusset specimen

2%/50 (Run082)

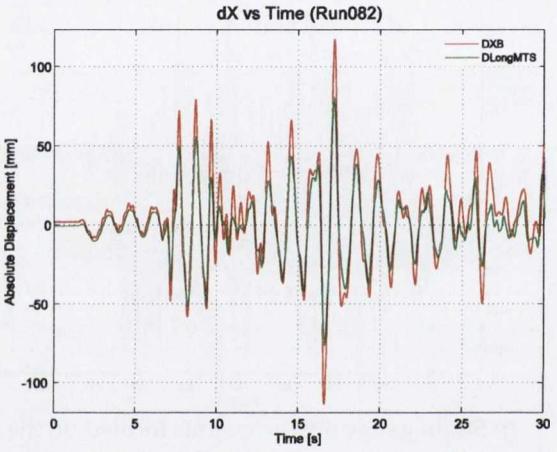

(a) Absolute displacements for table (DLongMTS) and roof level (DXB) time history

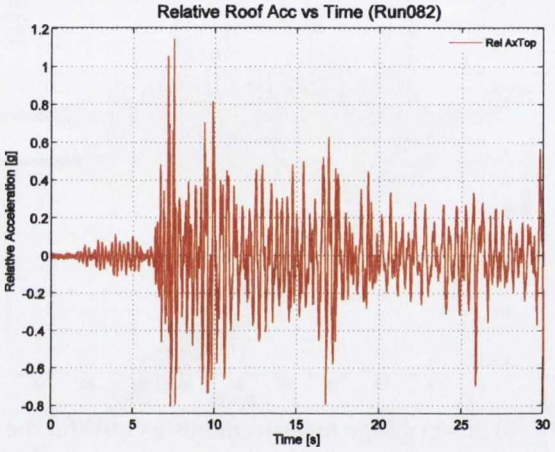

(b) Relative acceleration at roof level

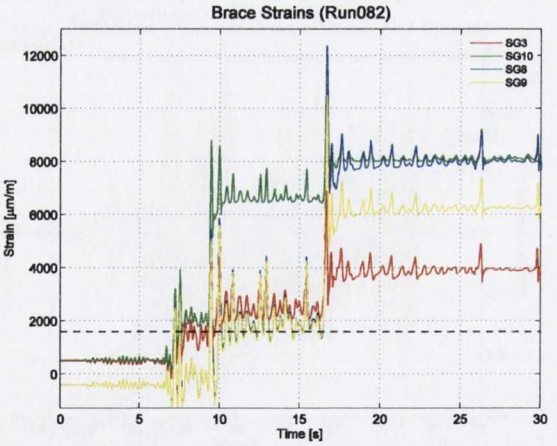

(c) Strain gauge measurements located on the right brace specimen

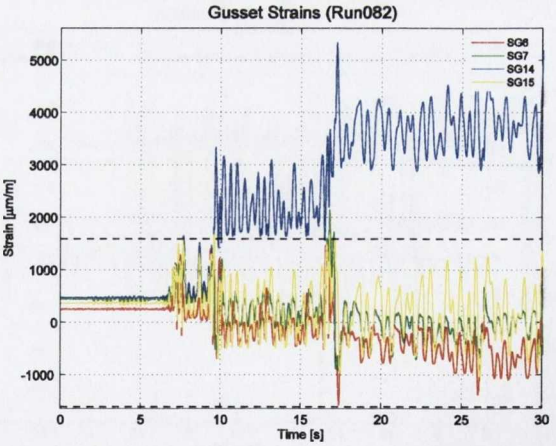

(d) Strain gauge measurements located on the right gusset specimen

Shake Table Test 6: S2-CA-G2

50%/50 (Run088)

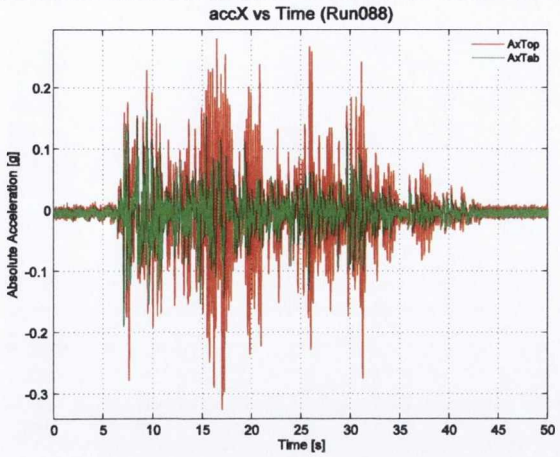

(a) Input (AxTab) and response (AxTop) absolute acceleration time history in x-direction

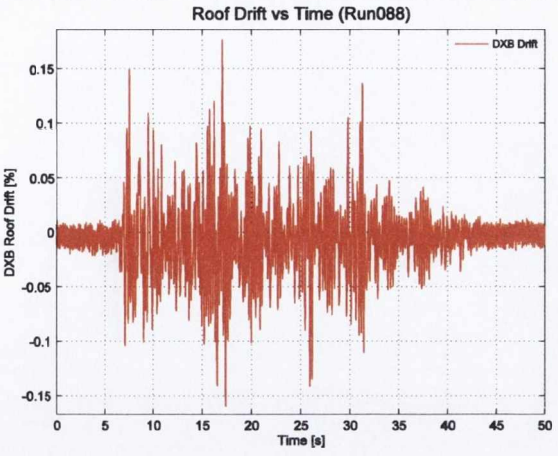

(b) Roof level drift (DXB Drift) time history in x-direction

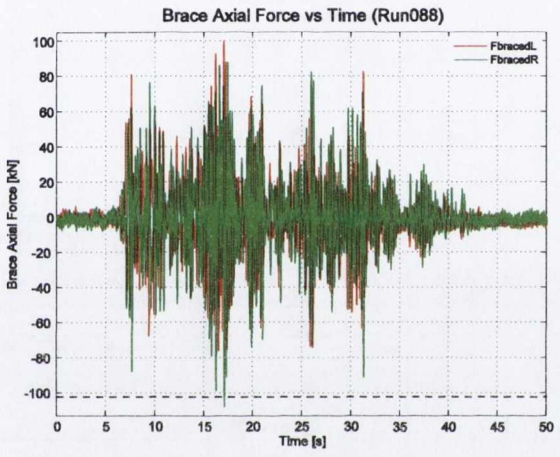

(c) Brace axial load time history for left (FbracedL) and right (FbracedR) braces

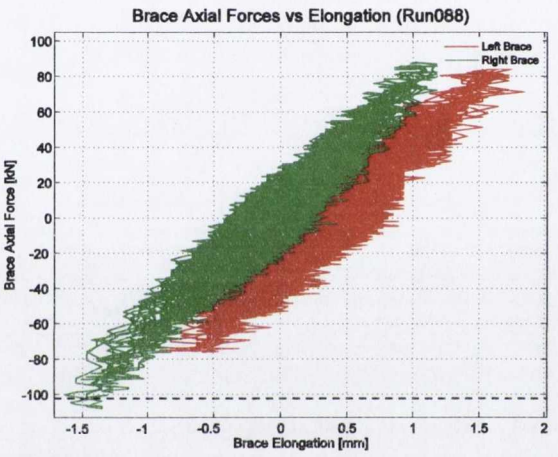

(d) Brace axial load hysteresis for left and right braces

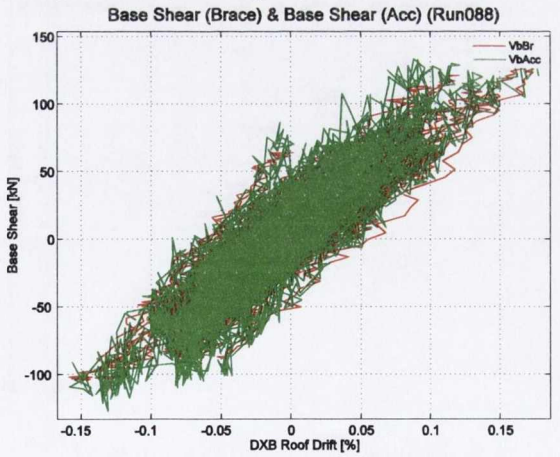

(e) Base shear from brace axial forces plotted against roof drift

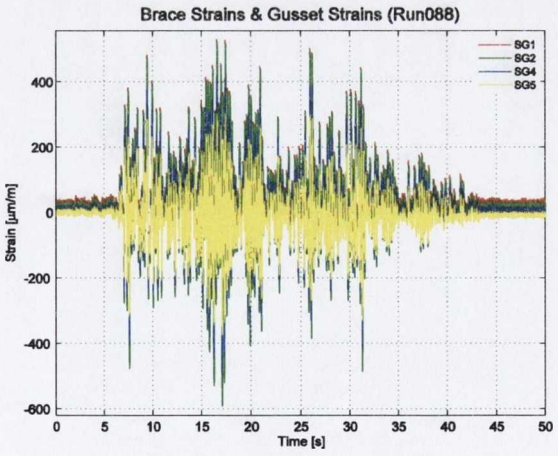

(f) Strain gauge measurements located on the right brace and gusset plate specimen

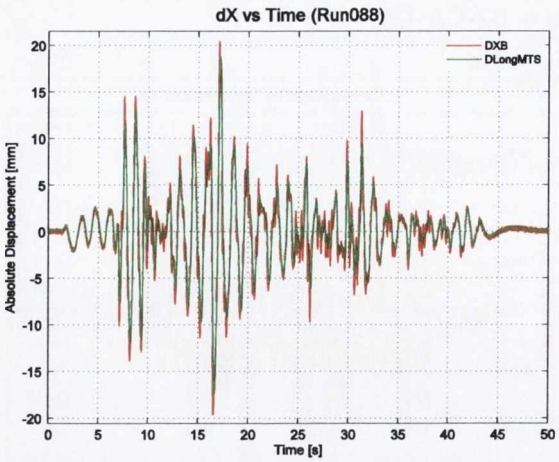

(g) Absolute displacements for table (DLongMTS) and roof level (DXB) time history

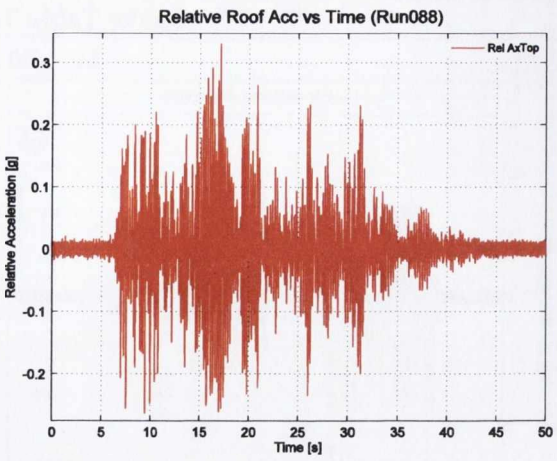

(h) Relative acceleration at roof level

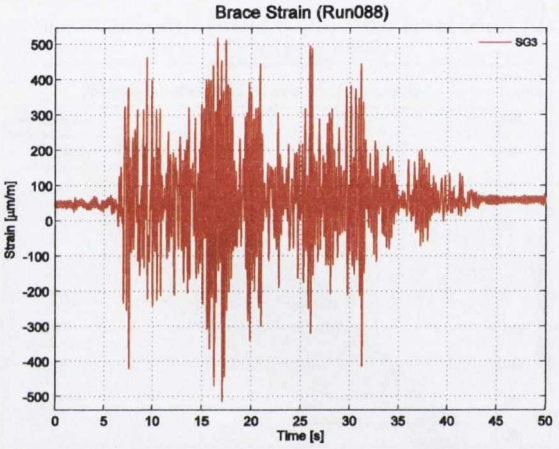

(i) Strain gauge measurements located on the right brace specimen

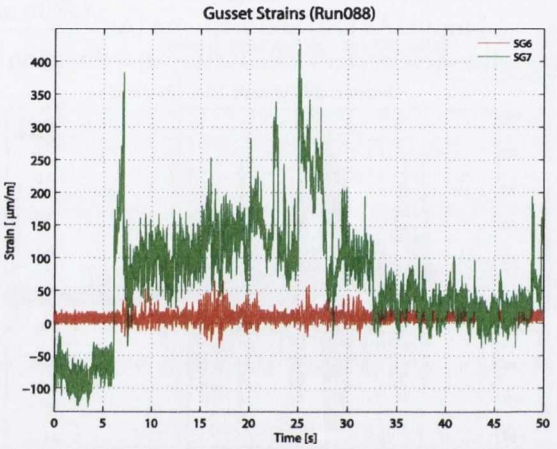

(j) Strain gauge measurements located on the right gusset specimen

10%/50 (Run090)

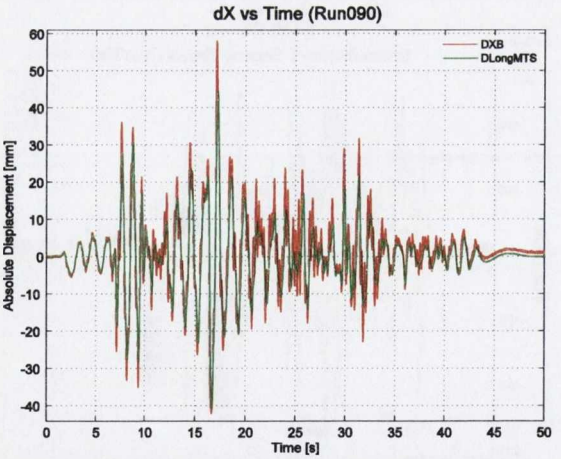

(a) Displacements for table (DLongMTS) and roof level (DXB)

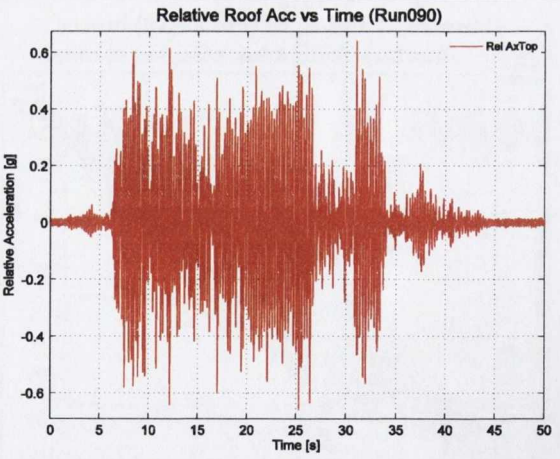

(b) Relative acceleration at roof level

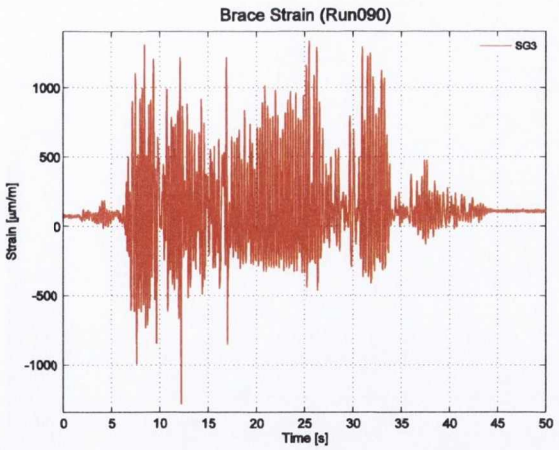

(c) Strain gauge measurements located on the right brace specimen

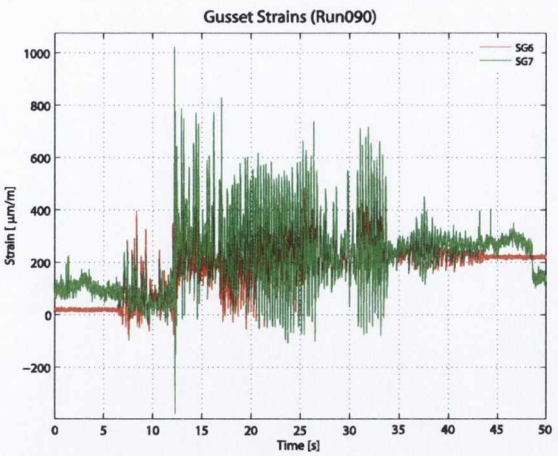

(d) Strain gauge measurements located on the right gusset specimen

2%/50 (Run092)

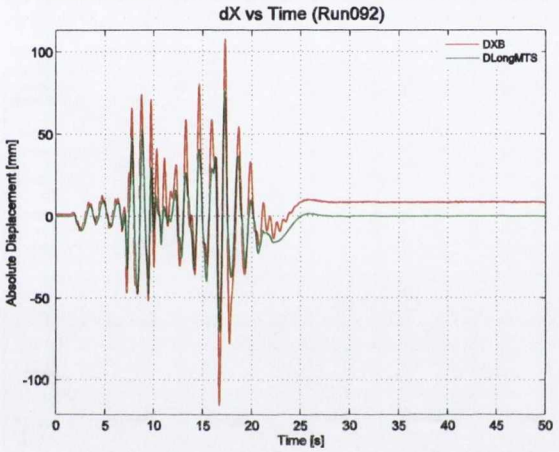

(a) Absolute displacements for table (DLongMTS) and roof level (DXB) time history

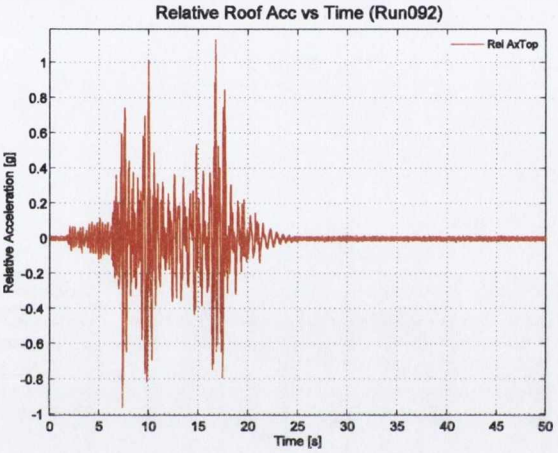

(b) Relative acceleration at roof level

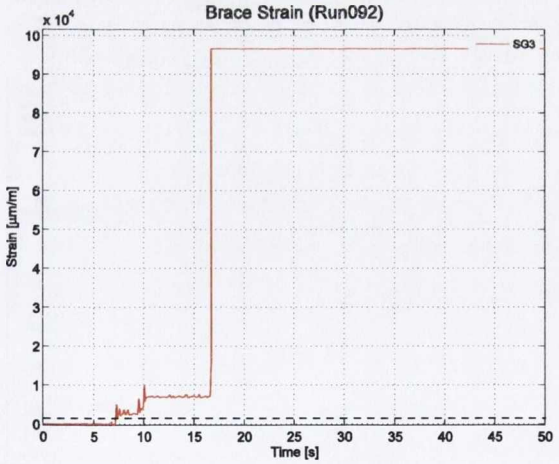

(c) Strain gauge measurements located on the right brace specimen

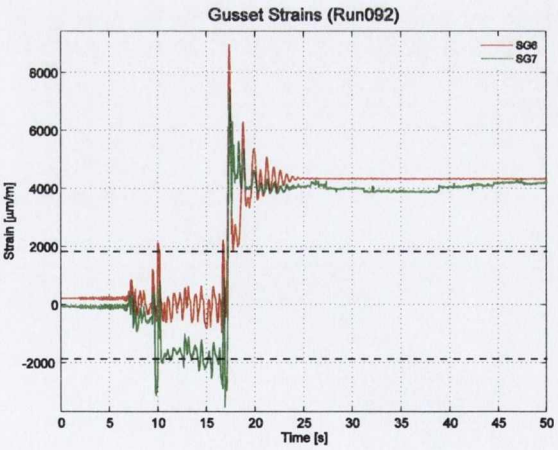

(d) Strain gauge measurements located on the right gusset specimen

Shake Table Test 7: S3-CA-G2

50%/50 (Run099)

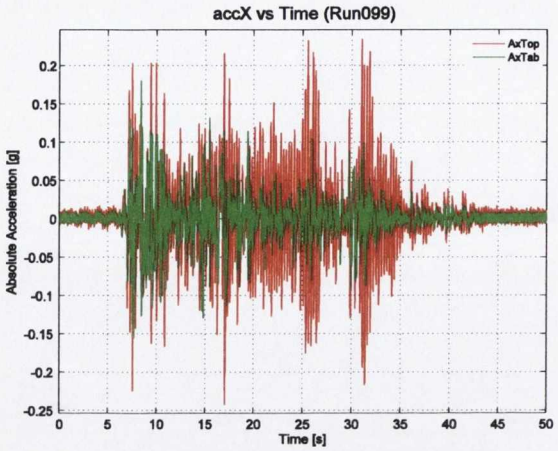

(a) Input (AxTab) and response (AxTop) absolute acceleration time history in x-direction

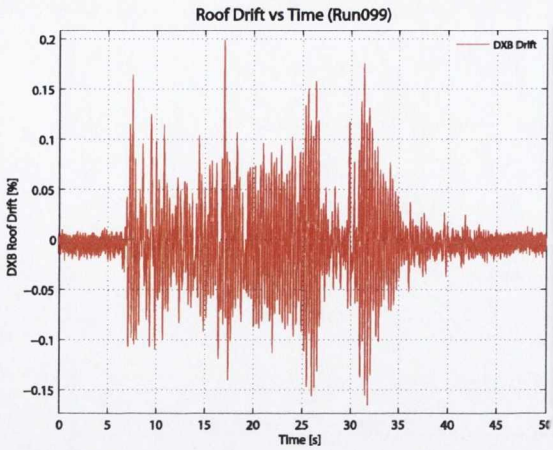

(b) Roof level drift (DXB Drift) time history in x-direction

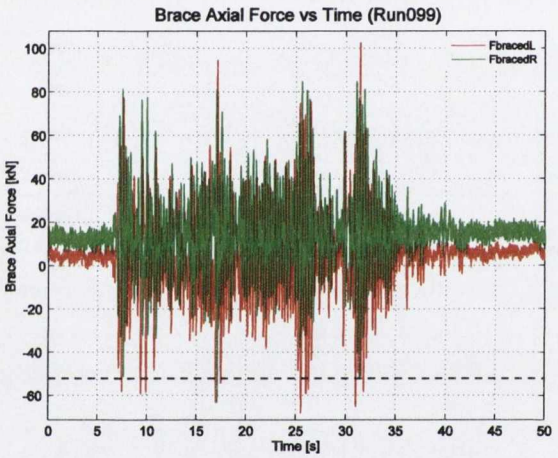

(c) Brace axial load time history for left (FbracedL) and right (FbracedR) braces

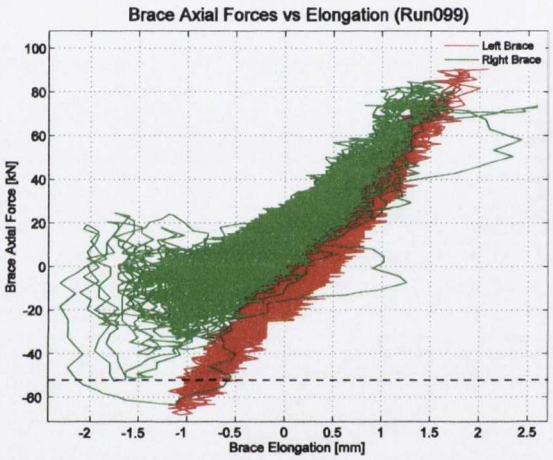

(d) Brace axial load hysteresis for left and right braces

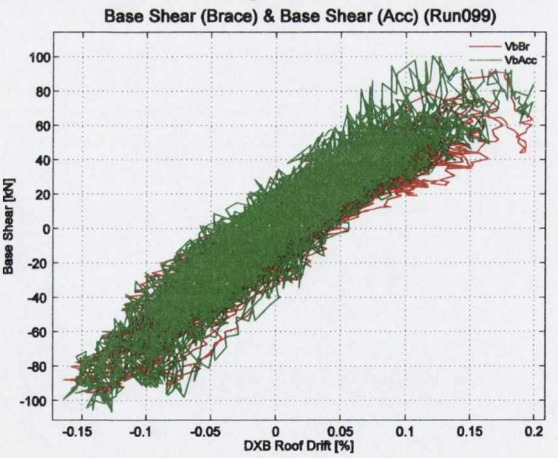

(e) Base shear from brace axial forces plotted against roof drift

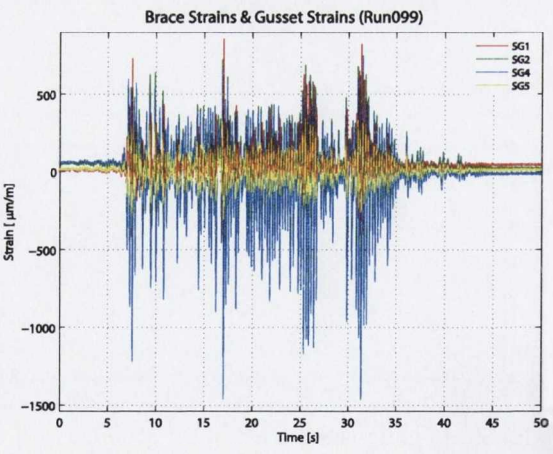

(f) Strain gauge measurements located on the right brace and gusset plate specimen

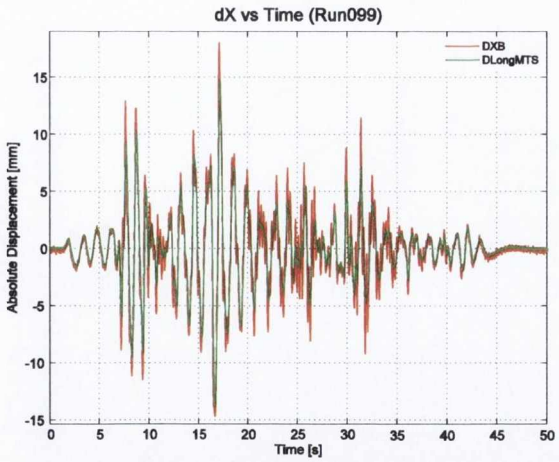

(g) Absolute displacements for table (DLongMTS) and roof level (DXB) time history

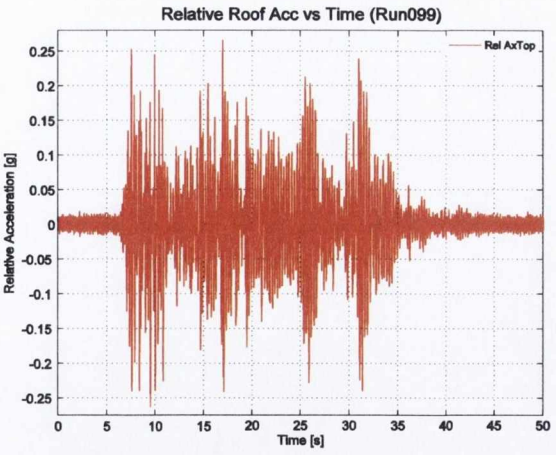

(h) Relative acceleration at roof level

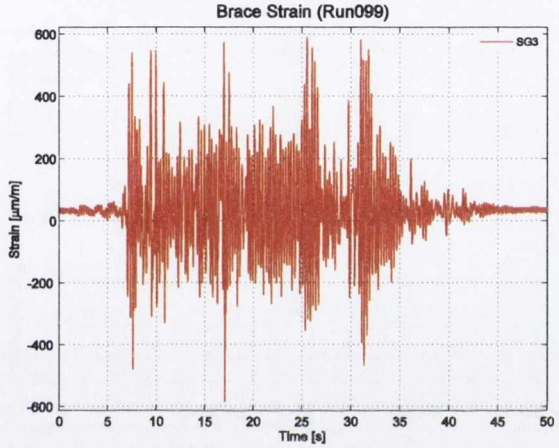

(i) Strain gauge measurements located on the right brace specimen

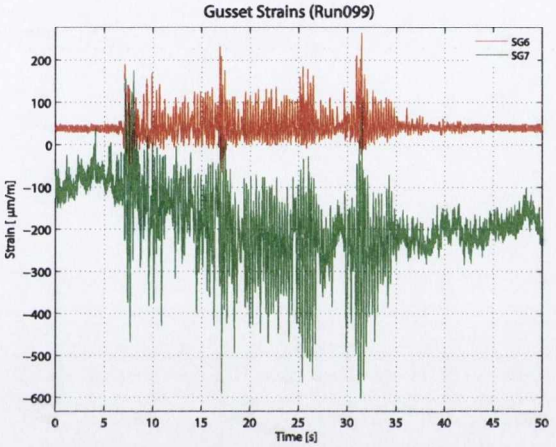

(j) Strain gauge measurements located on the right gusset specimen

10%/50 (Run101)

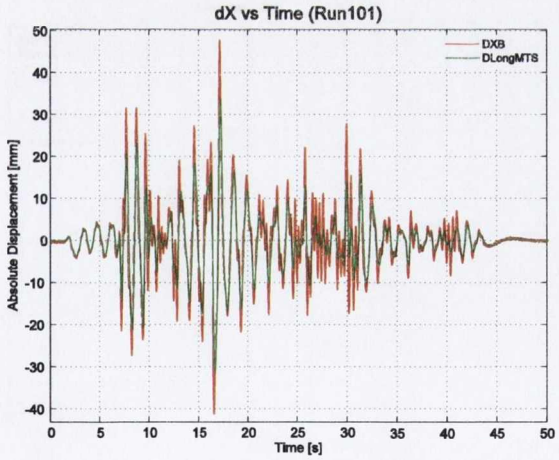

(a) Displacements for table (DLongMTS) and roof level (DXB)

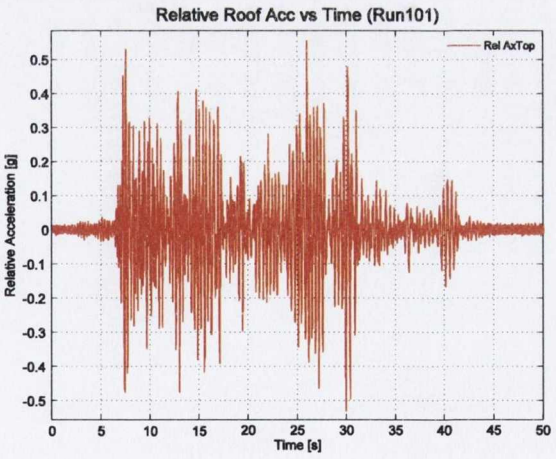

(b) Relative acceleration at roof level

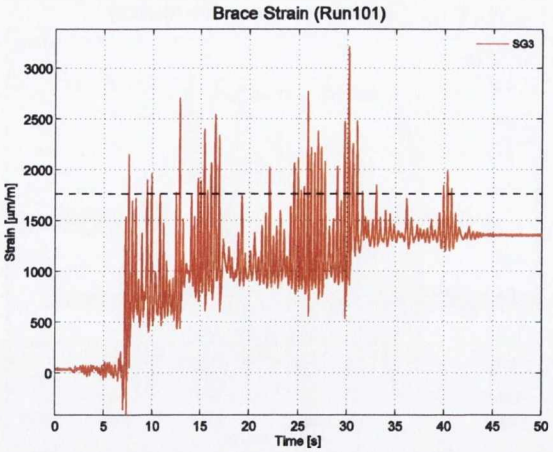

(c) Strain gauge measurements located on the right brace specimen

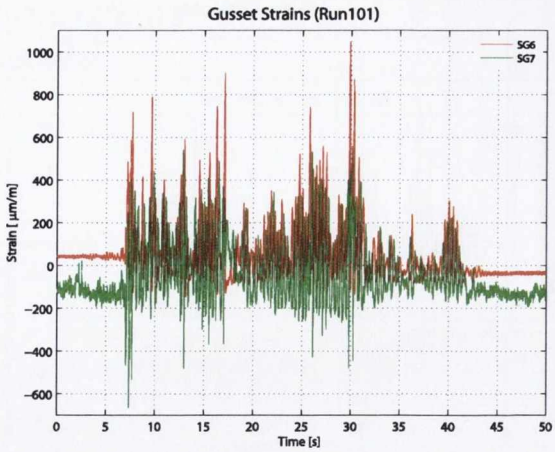

(d) Strain gauge measurements located on the right gusset specimen

2%/50 (Run103)

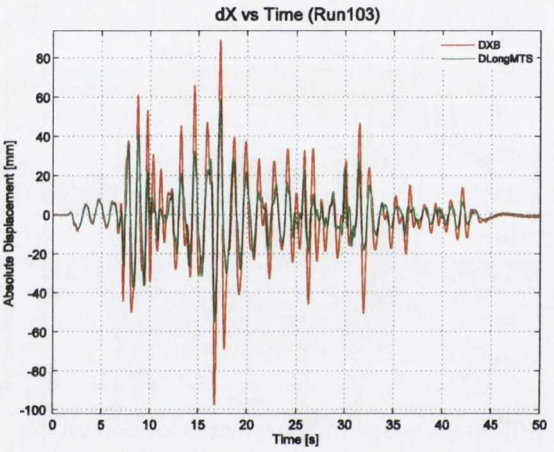

(a) Absolute displacements for table (DLongMTS) and roof level (DXB) time history

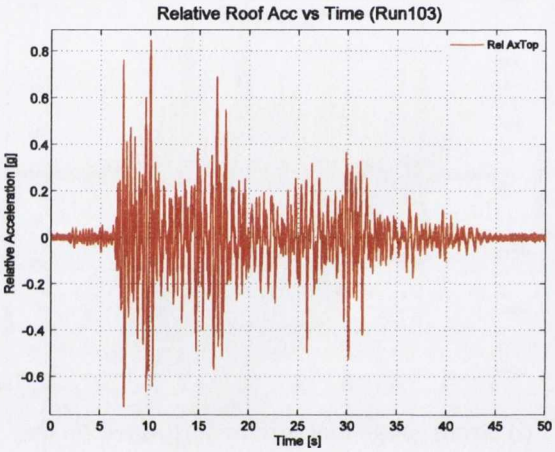

(b) Relative acceleration at roof level

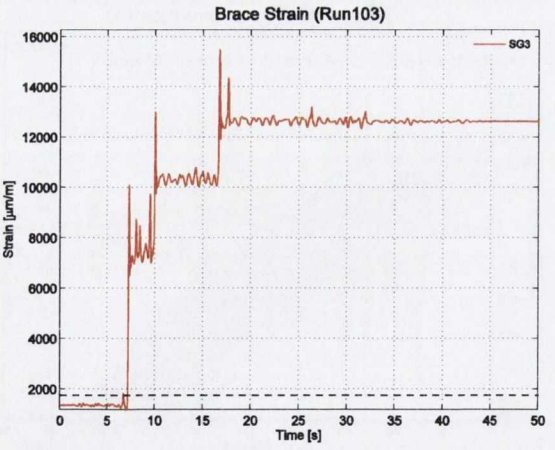

(c) Strain gauge measurements located on the right brace specimen

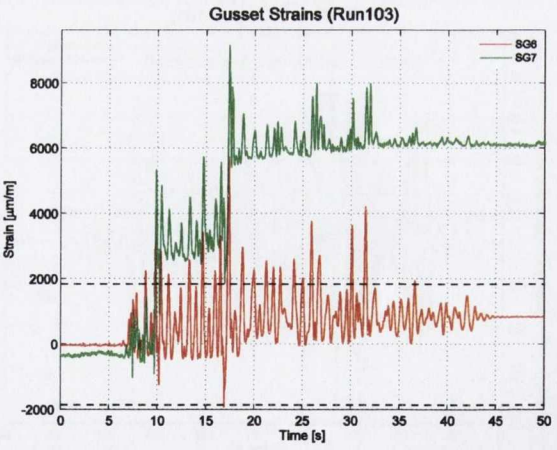

(d) Strain gauge measurements located on the right gusset specimen

Shake Table Test 8: S1-CB-G1

50%/50 (Run113)

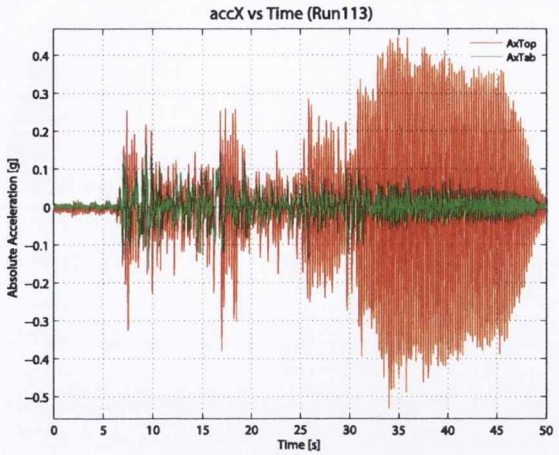

(a) Input (AxTab) and response (AxTop) absolute acceleration time history in x-direction

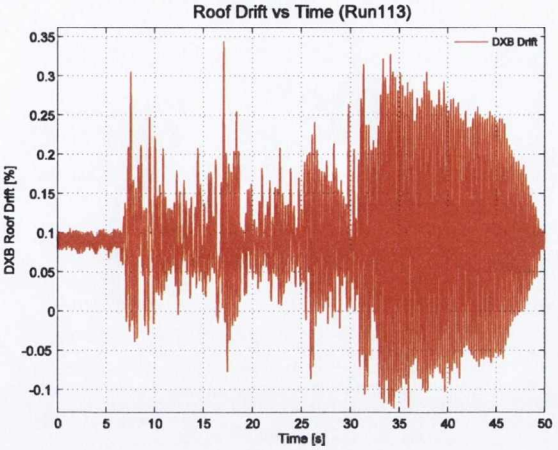

(b) Roof level drift (DXB Drift) time history in x-direction

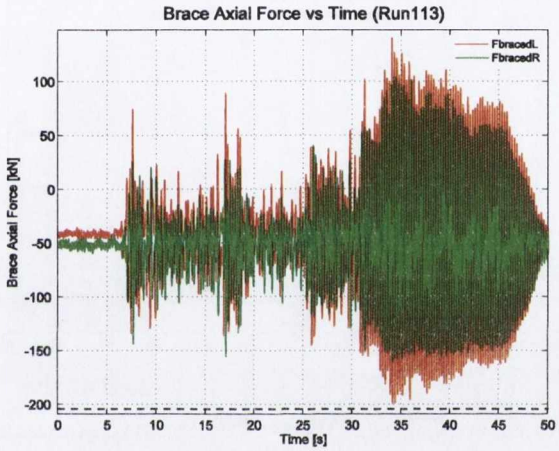

(c) Brace axial load time history for left (FbracedL) and right (FbracedR) braces

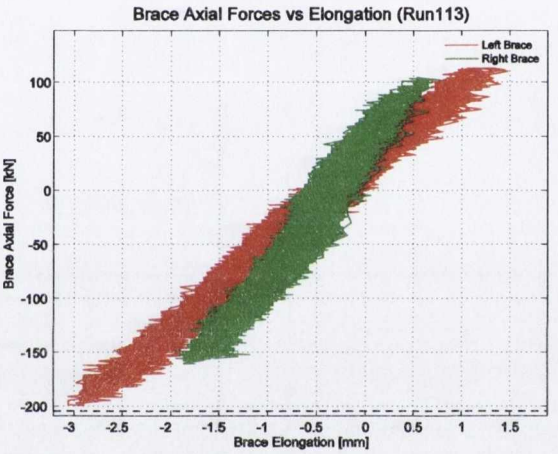

(d) Brace axial load hysteresis for left and right braces

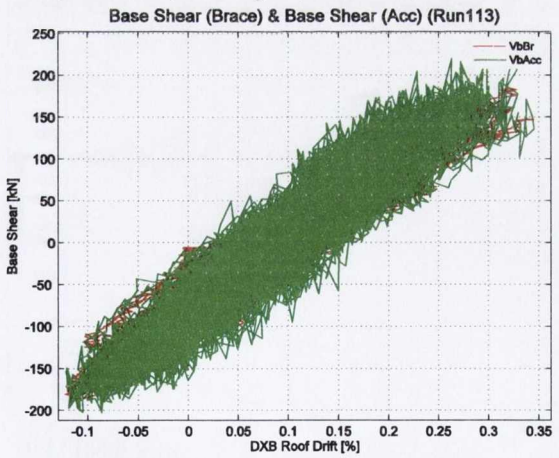

(e) Base shear from brace axial forces plotted against roof drift

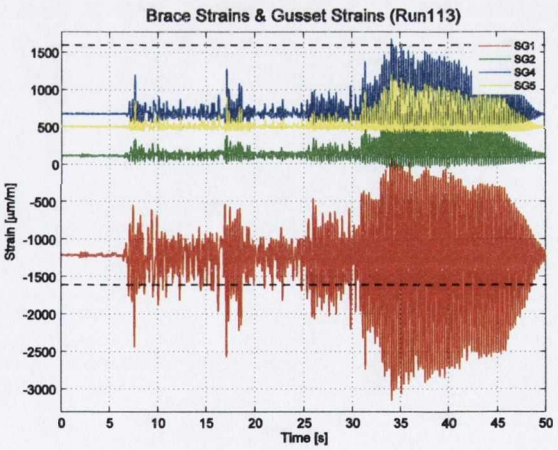

(f) Strain gauge measurements located on the right brace and gusset plate specimen

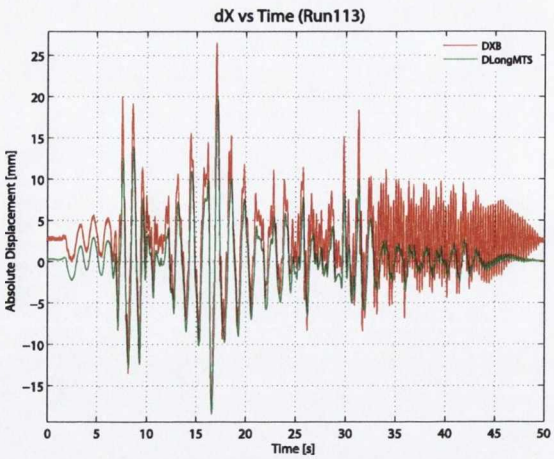

(g) Absolute displacements for table (DLongMTS) and roof level (DXB) time history

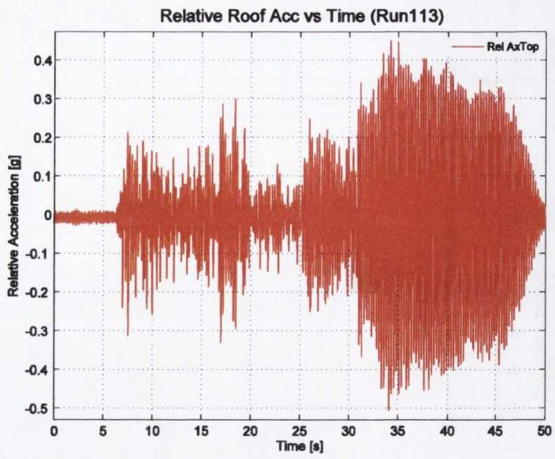

(h) Relative acceleration at roof level

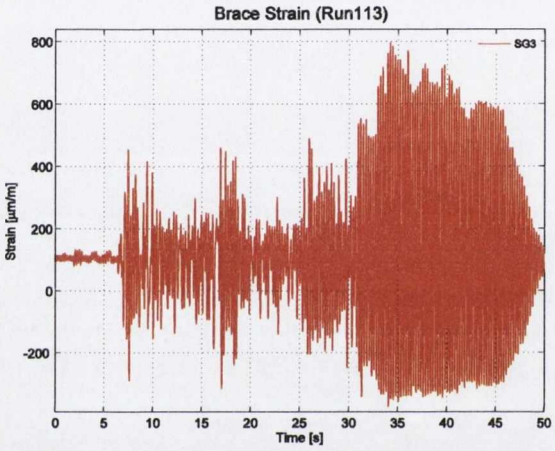

(i) Strain gauge measurements located on the right brace specimen

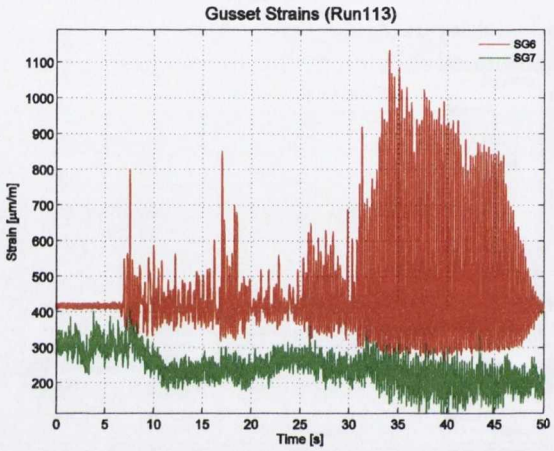

(j) Strain gauge measurements located on the right gusset specimen

10%/50 (Run117)

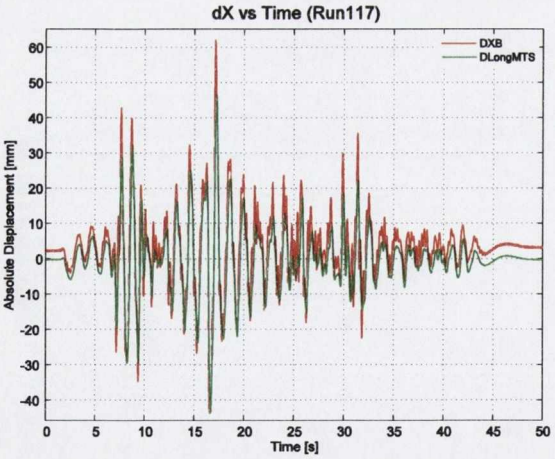

(a) Displacements for table (DLongMTS) and roof level (DXB)

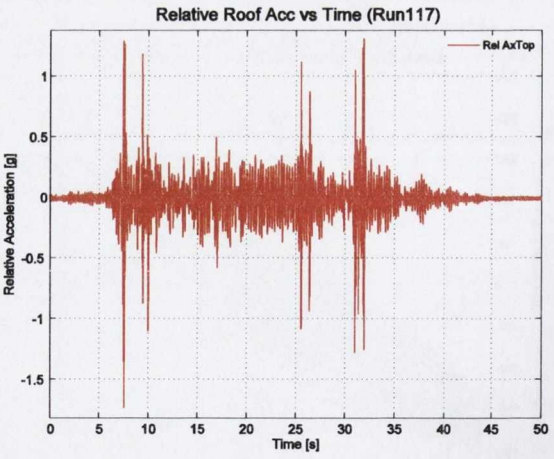

(b) Relative acceleration at roof level

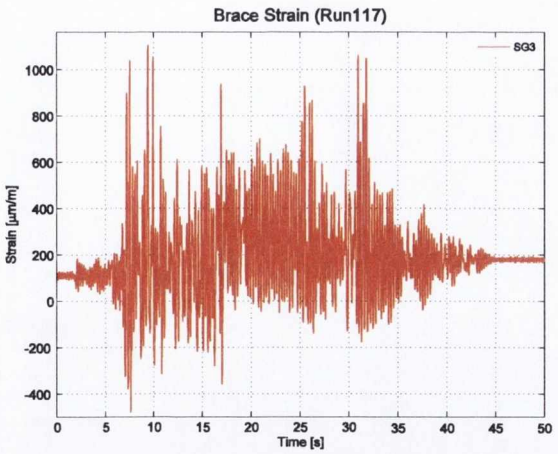

(c) Strain gauge measurements located on the right brace specimen

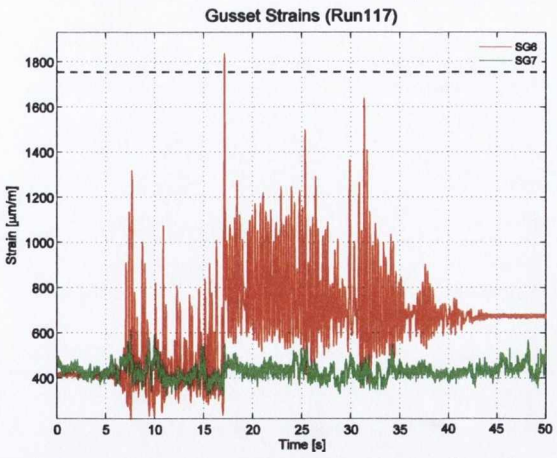

(d) Strain gauge measurements located on the right gusset specimen

2%/50 (Run119)

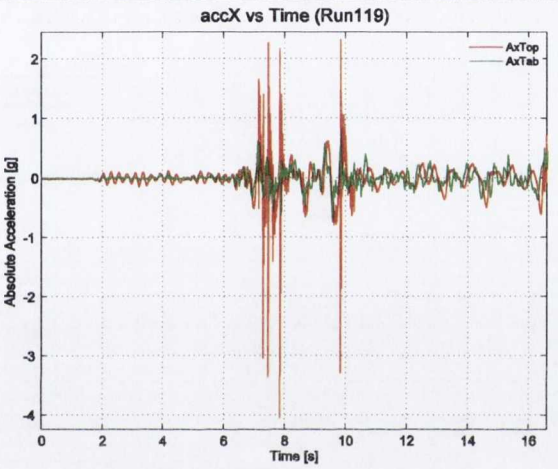

(a) Absolute displacements for table (DLongMTS) and roof level (DXB) time history

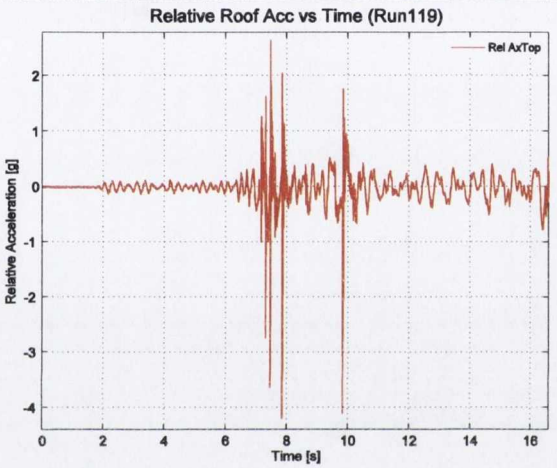

(b) Relative acceleration at roof level

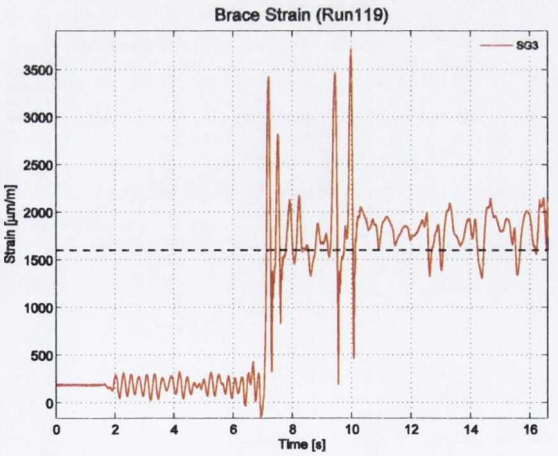

(c) Strain gauge measurements located on the right brace specimen

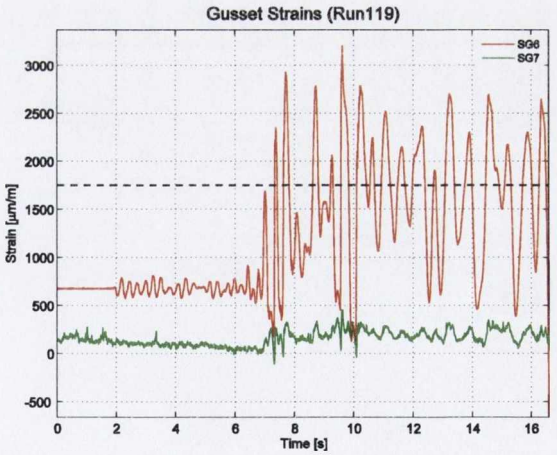

(d) Strain gauge measurements located on the right gusset specimen

Shake Table Test 9: S2-CB-G1

50%/50 (Run125)

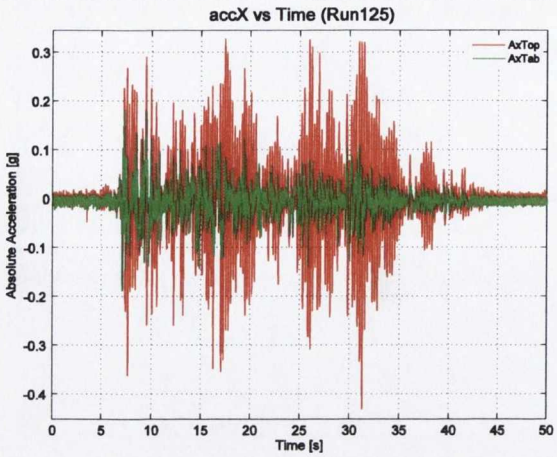

(a) Input (AxTab) and response (AxTop) absolute acceleration time history in x-direction

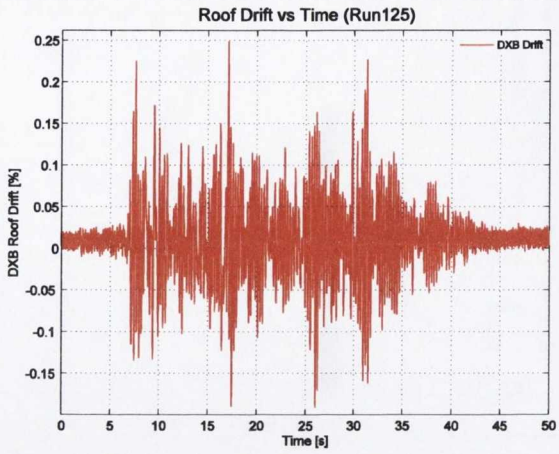

(b) Roof level drift (DXB Drift) time history in x-direction

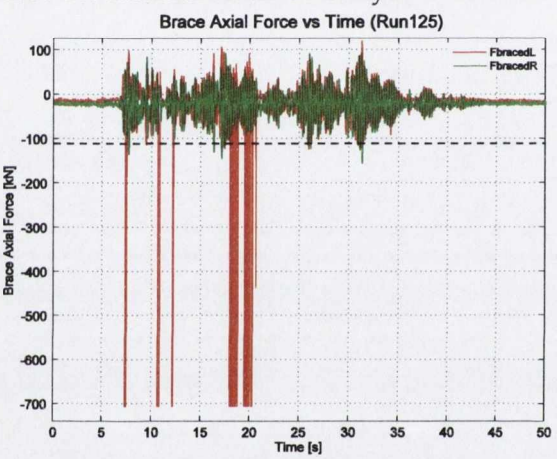

(c) Brace axial load time history for left (FbracedL) and right (FbracedR) braces

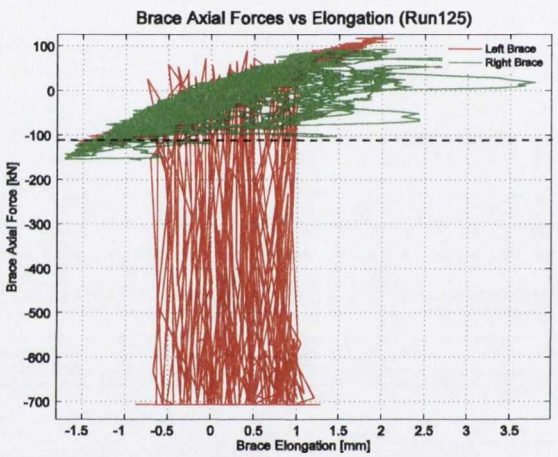

(d) Brace axial load hysteresis for left and right braces

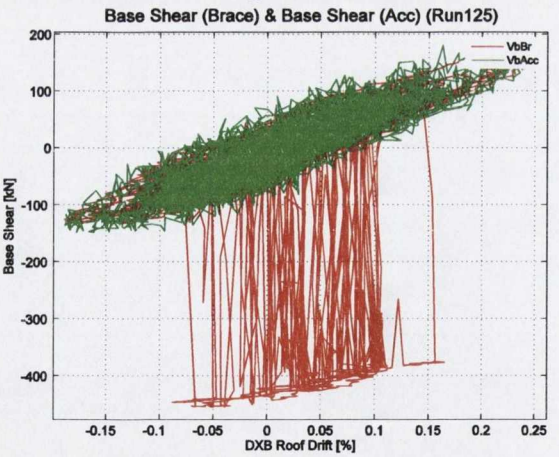

(e) Base shear from brace axial forces plotted against roof drift

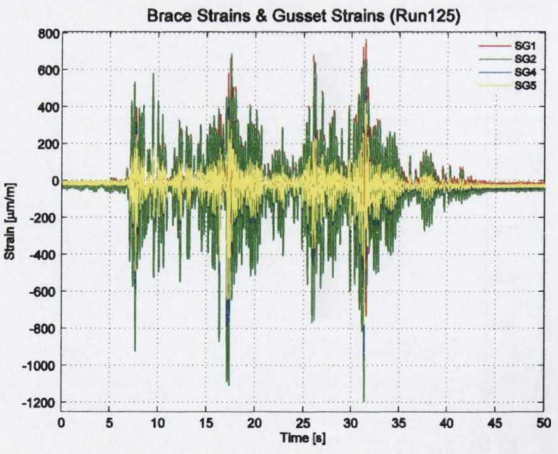

(f) Strain gauge measurements located on the right brace and gusset plate specimen

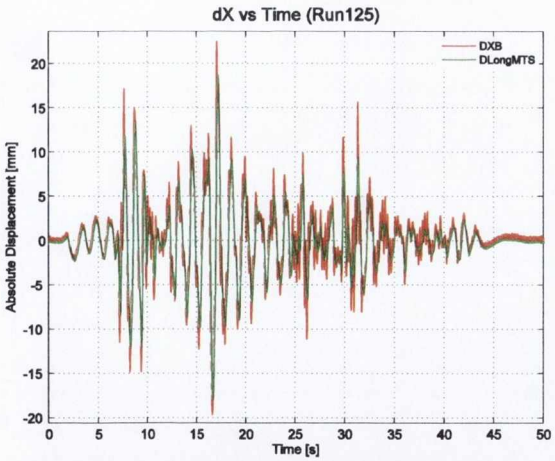

(g) Absolute displacements for table (DLongMTS) and roof level (DXB) time history

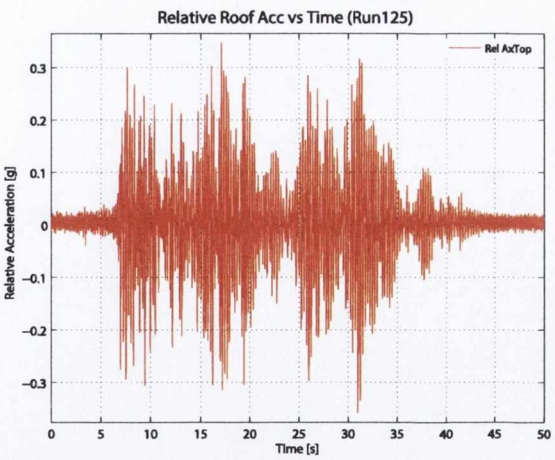

(h) Relative acceleration at roof level

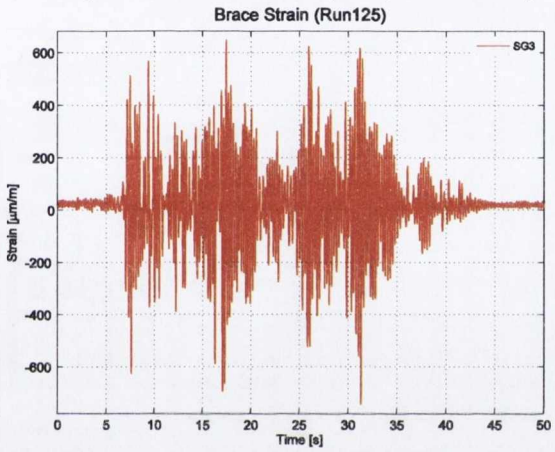

(i) Strain gauge measurements located on the right brace specimen

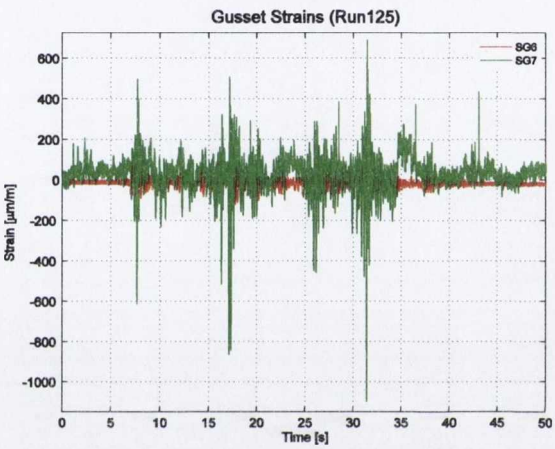

(j) Strain gauge measurements located on the right gusset specimen

10%/50 (Run127)

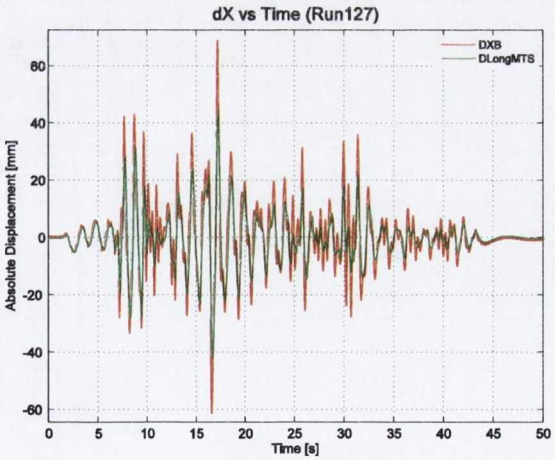

(a) Displacements for table (DLongMTS) and roof level (DXB)

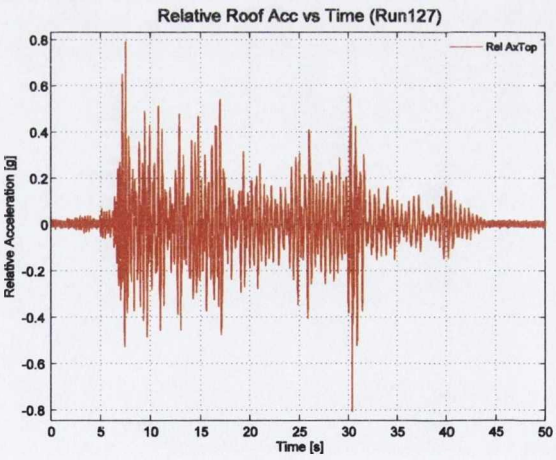

(b) Relative acceleration at roof level

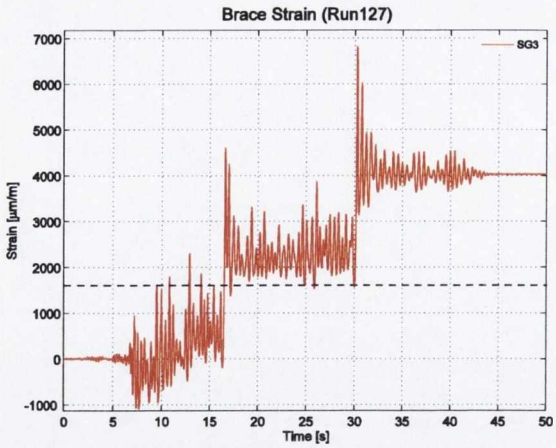

(c) Strain gauge measurements located on the right brace specimen

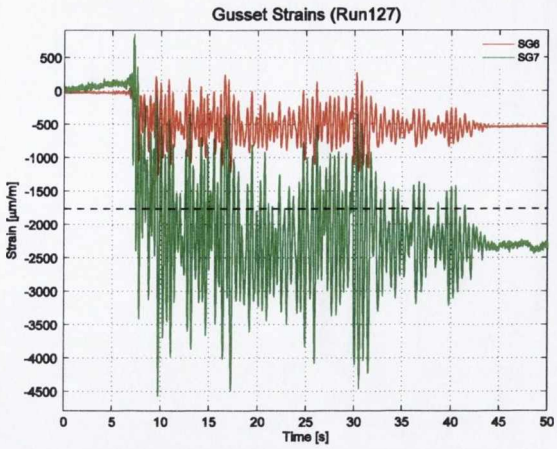

(d) Strain gauge measurements located on the right gusset specimen

2%/50 (Run129)

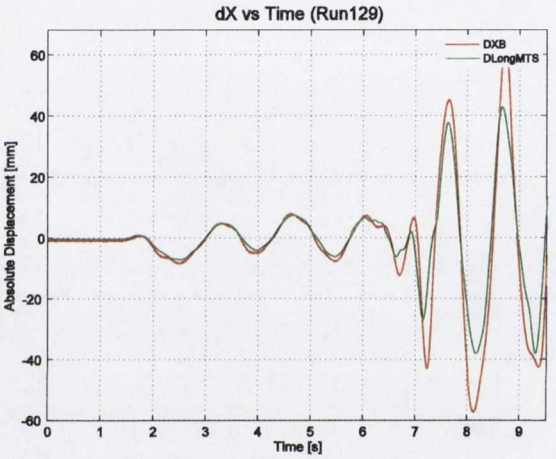

(a) Absolute displacements for table (DLongMTS) and roof level (DXB) time history

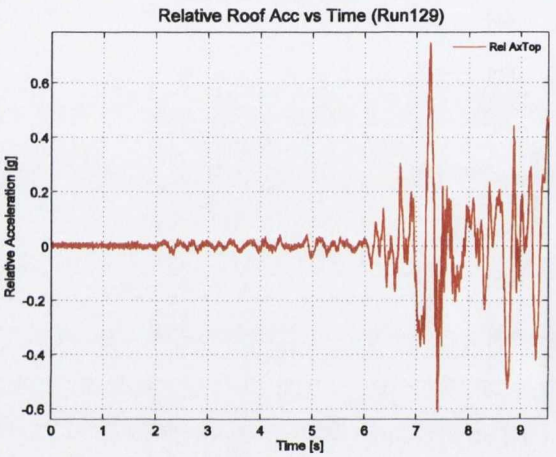

(b) Relative acceleration at roof level

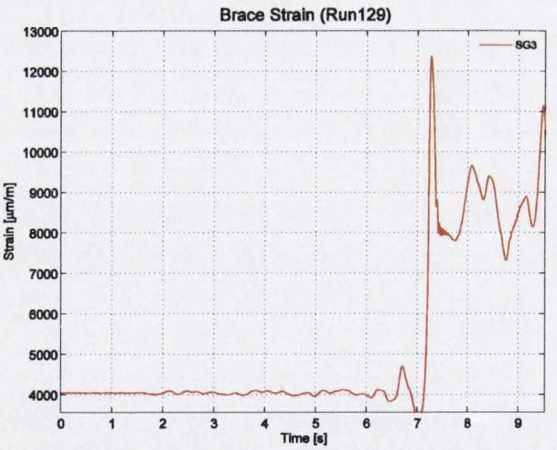

(c) Strain gauge measurements located on the right brace specimen

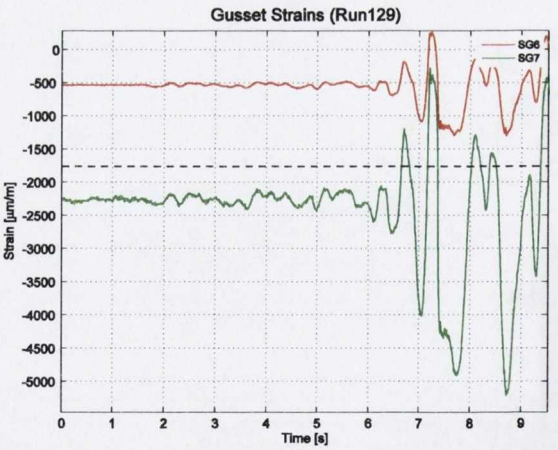

(d) Strain gauge measurements located on the right gusset specimen

Shake Table Test 10: S4-CB-G2

50%/50 (Run134)

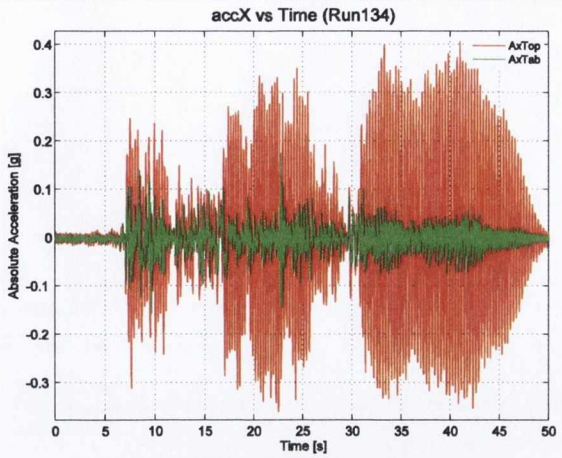

(a) Input (AxTab) and response (AxTop) absolute acceleration time history in x-direction

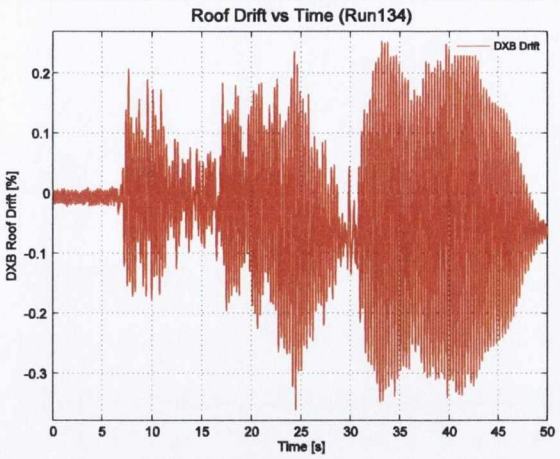

(b) Roof level drift (DXB Drift) time history in x-direction

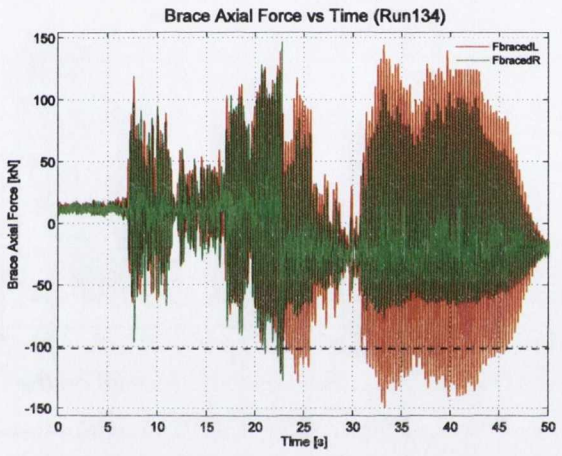

(c) Brace axial load time history for left (FbracedL) and right (FbracedR) braces

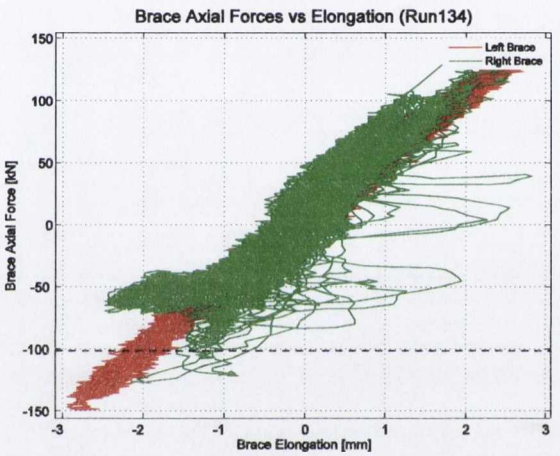

(d) Brace axial load hysteresis for left and right braces

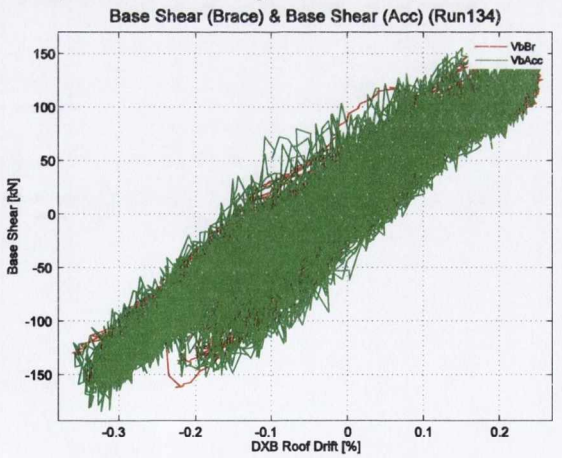

(e) Base shear from brace axial forces plotted against roof drift

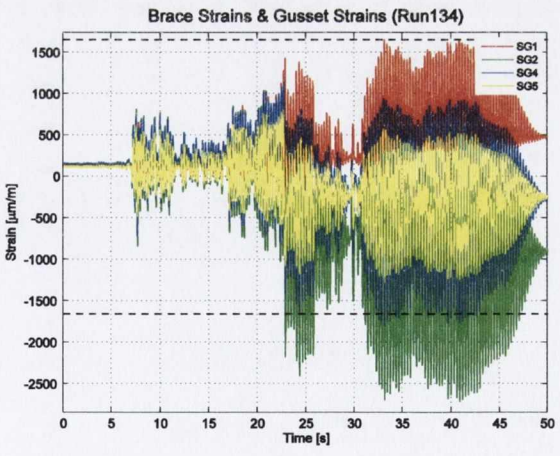

(f) Strain gauge measurements located on the right brace and gusset plate specimen

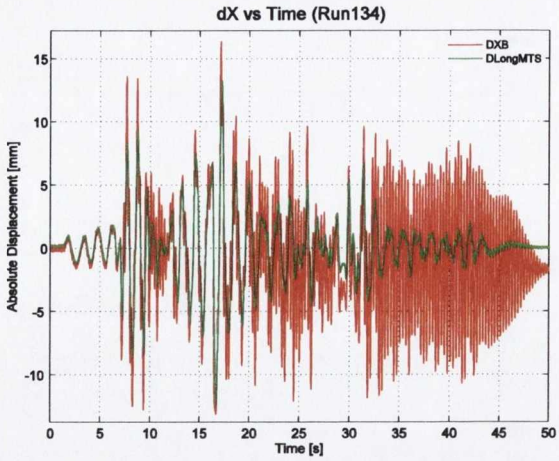

(g) Absolute displacements for table (DLongMTS) and roof level (DXB) time history

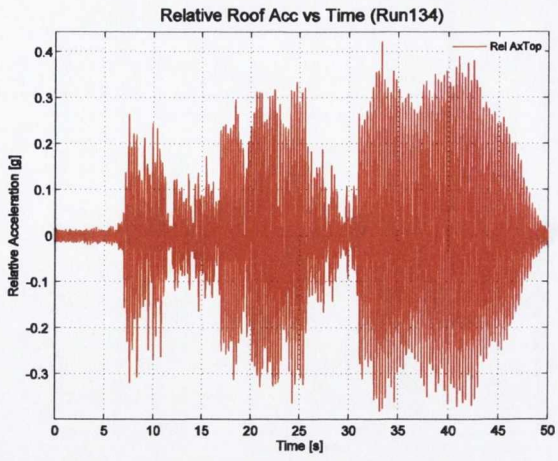

(h) Relative acceleration at roof level

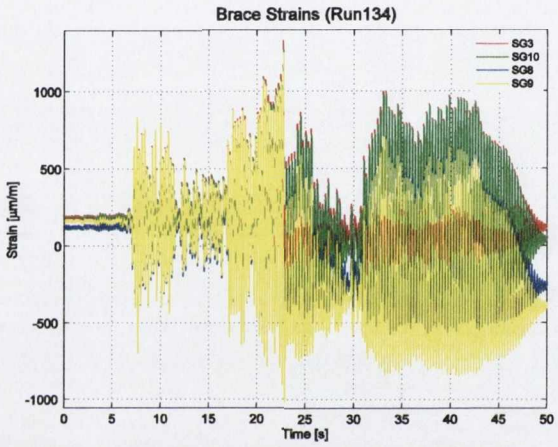

(i) Strain gauge measurements located on the right brace specimen

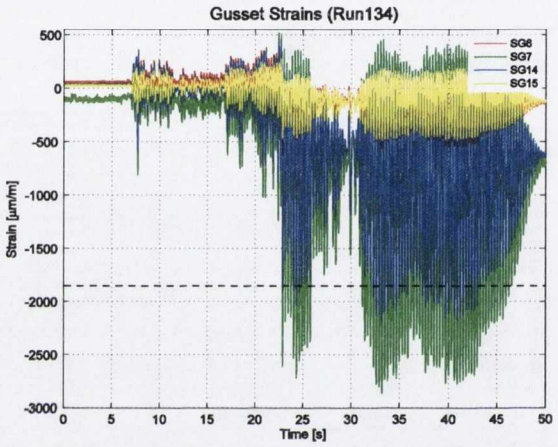

(j) Strain gauge measurements located on the right gusset specimen

10%/50 (Run136)

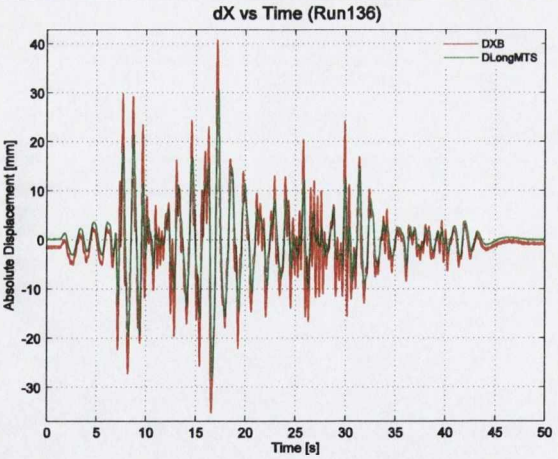

(a) Displacements for table (DLongMTS) and roof level (DXB)

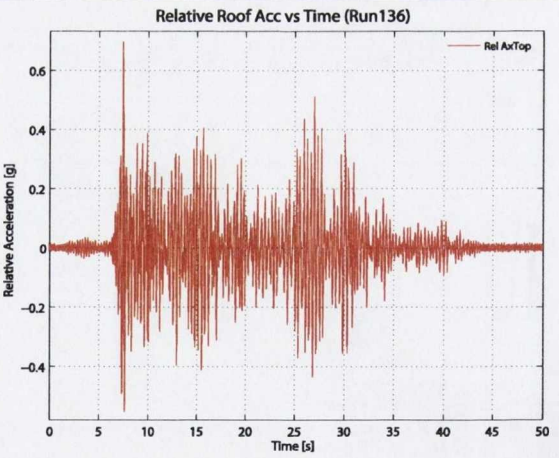

(b) Relative acceleration at roof level

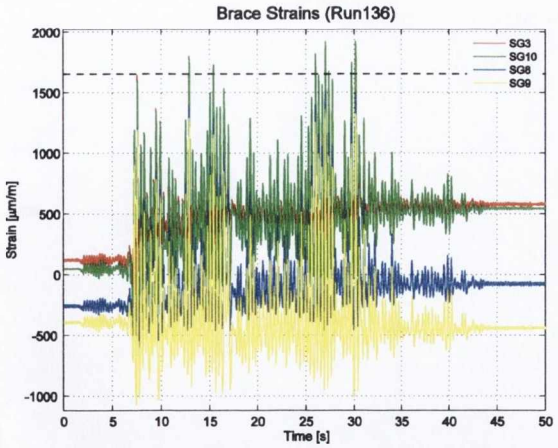

(c) Strain gauge measurements located on the right brace specimen

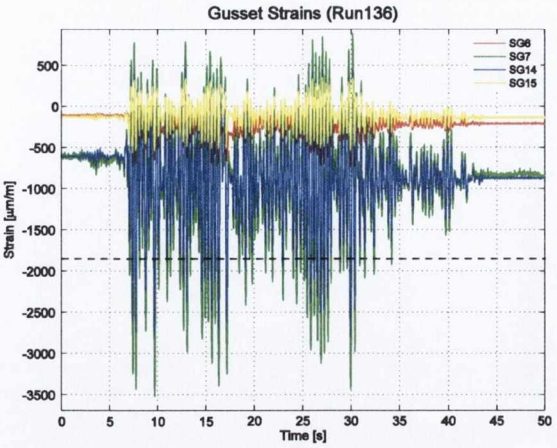

(d) Strain gauge measurements located on the right gusset specimen

2%/50 (Run138)

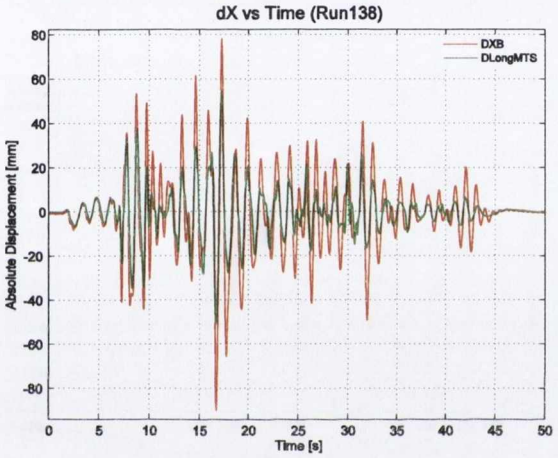

(a) Absolute displacements for table (DLongMTS) and roof level (DXB) time history

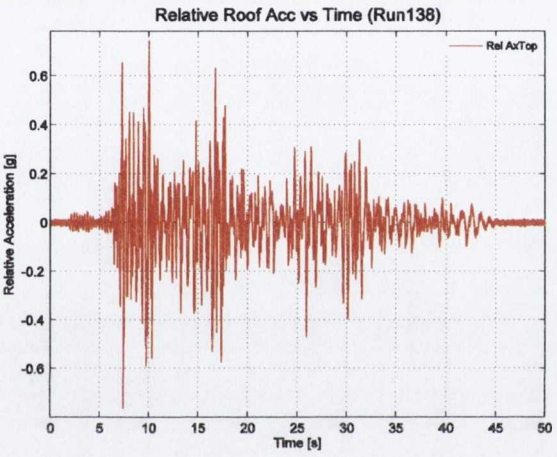

(b) Relative acceleration at roof level

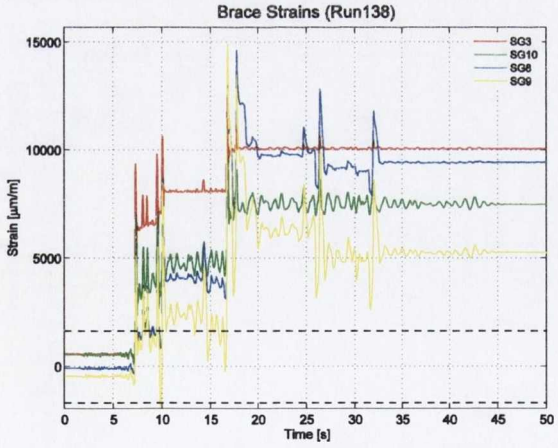

(c) Strain gauge measurements located on the right brace specimen

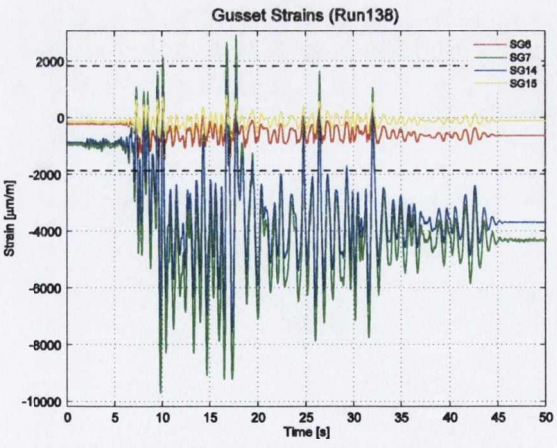

(d) Strain gauge measurements located on the right gusset specimen

Shake Table Test 11: S2-CB-G2

50%/50 (Run146)

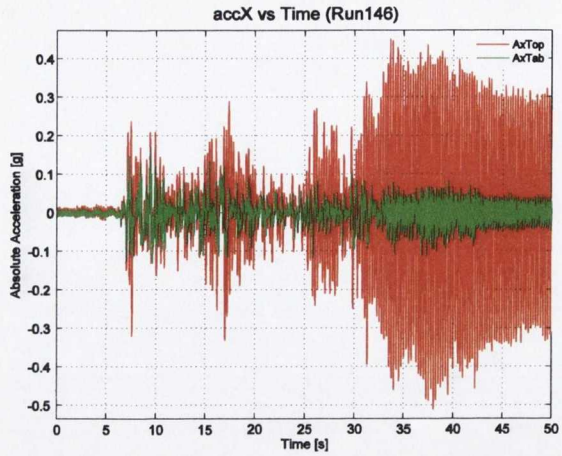

(a) Input (AxTab) and response (AxTop) absolute acceleration time history in x-direction

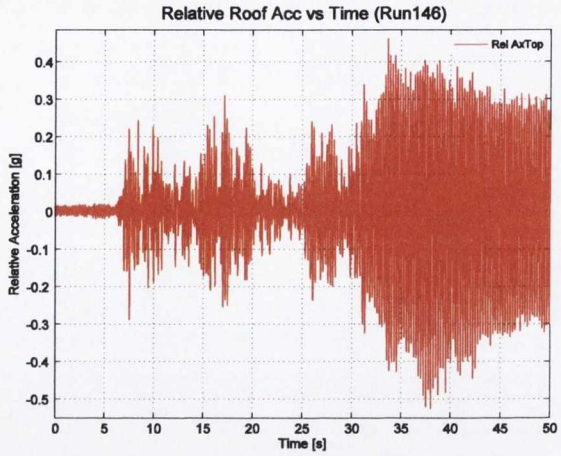

(b) Roof level drift (DXB Drift) time history in x-direction

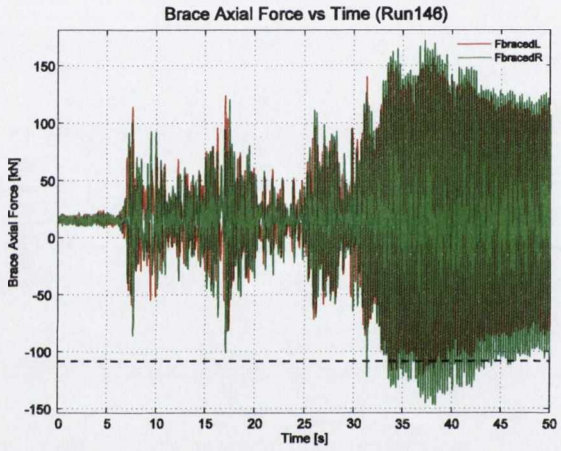

(c) Brace axial load time history for left (FbracedL) and right (FbracedR) braces

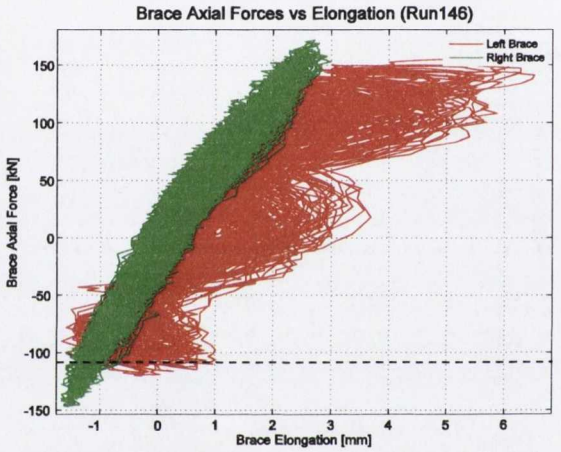

(d) Brace axial load hysteresis for left and right braces

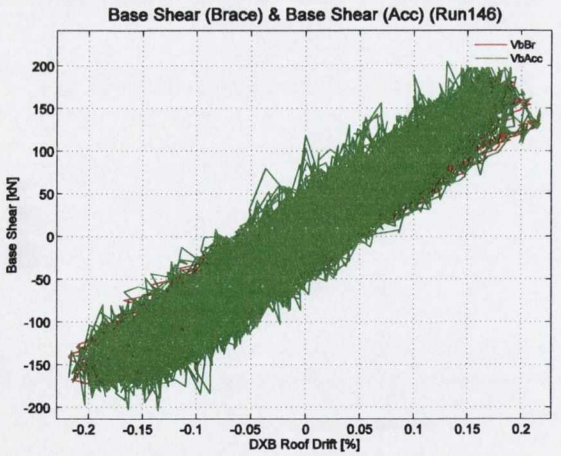

(e) Base shear from brace axial forces plotted against roof drift

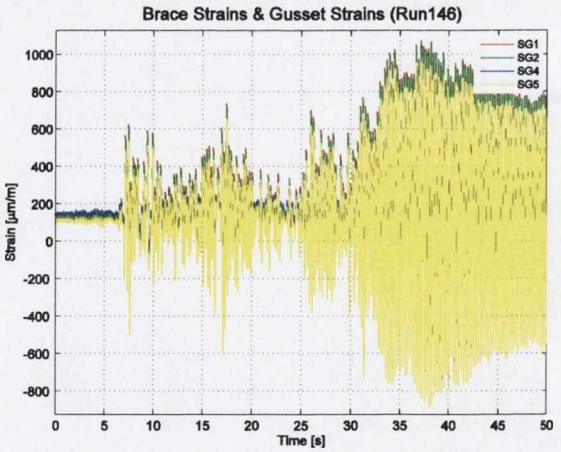

(f) Strain gauge measurements located on the right brace and gusset plate specimen

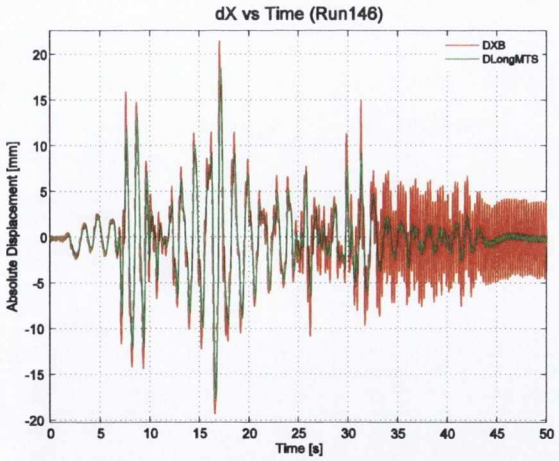

(g) Absolute displacements for table (DLongMTS) and roof level (DXB) time history

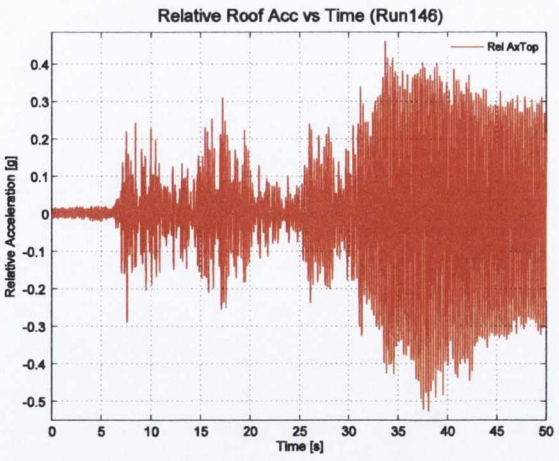

(h) Relative acceleration at roof level

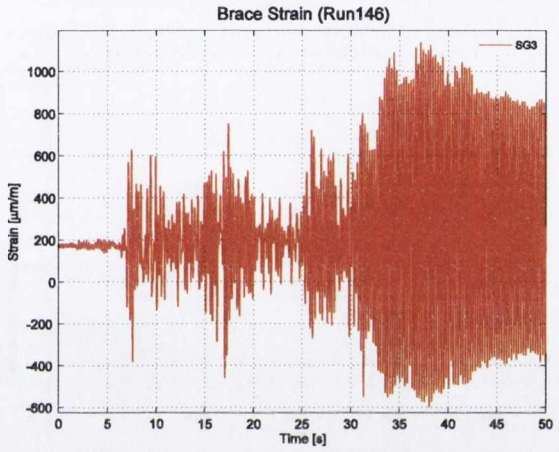

(i) Strain gauge measurements located on the right brace specimen

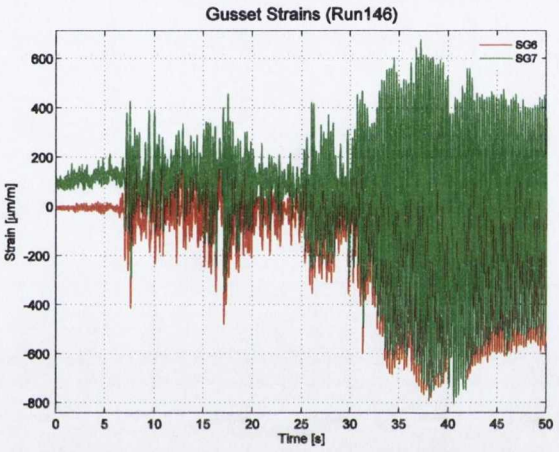

(j) Strain gauge measurements located on the right gusset specimen

10%/50 (Run148)

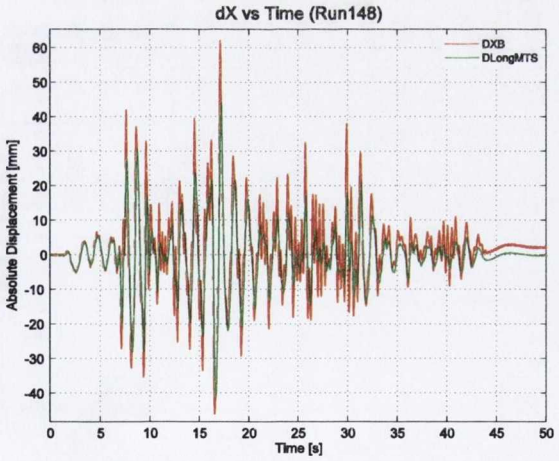

(a) Displacements for table (DLongMTS) and roof level (DXB)

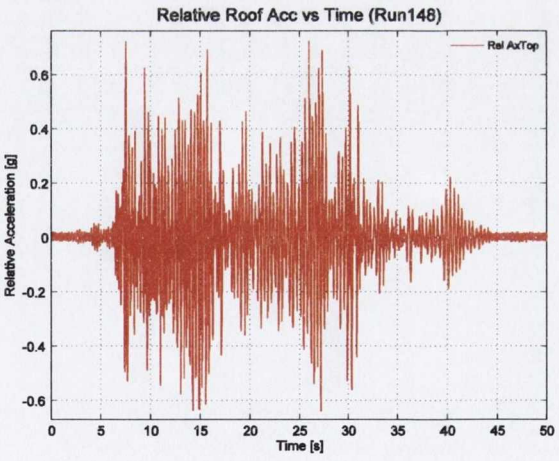

(b) Relative acceleration at roof level

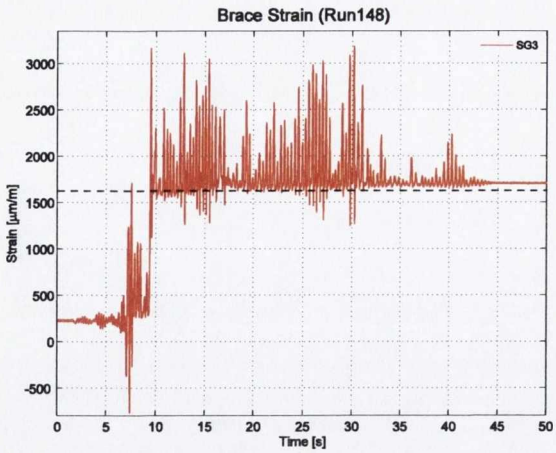

(c) Strain gauge measurements located on the right brace specimen

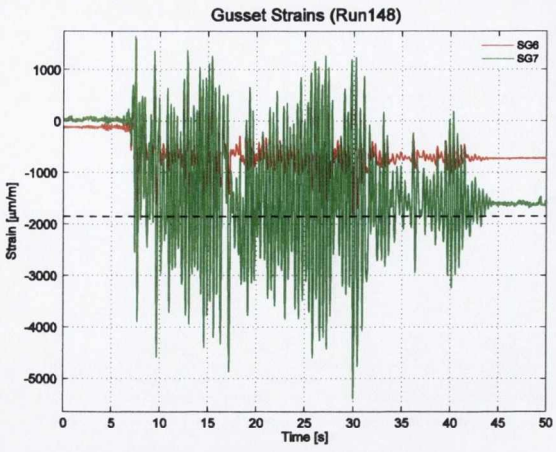

(d) Strain gauge measurements located on the right gusset specimen

2%/50 (Run150)

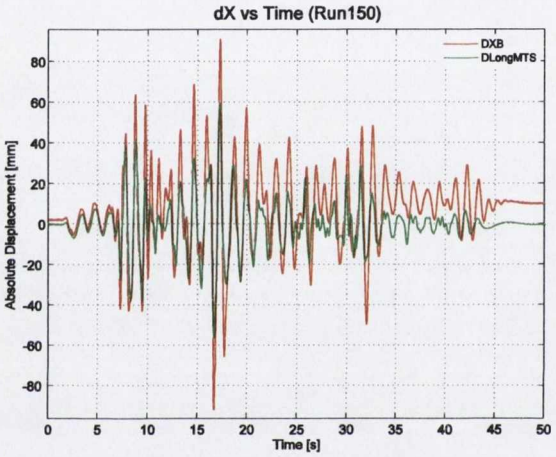

(a) Absolute displacements for table (DLongMTS) and roof level (DXB) time history

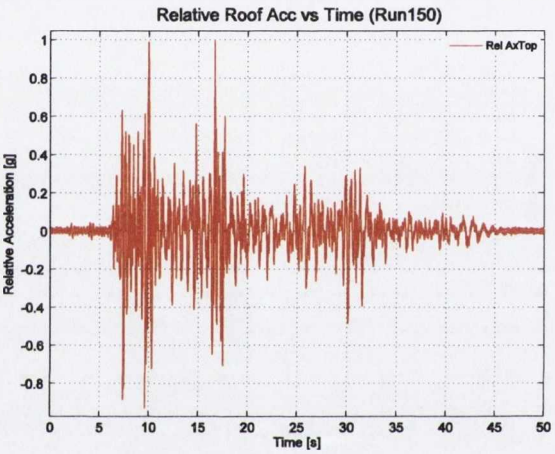

(b) Relative acceleration at roof level

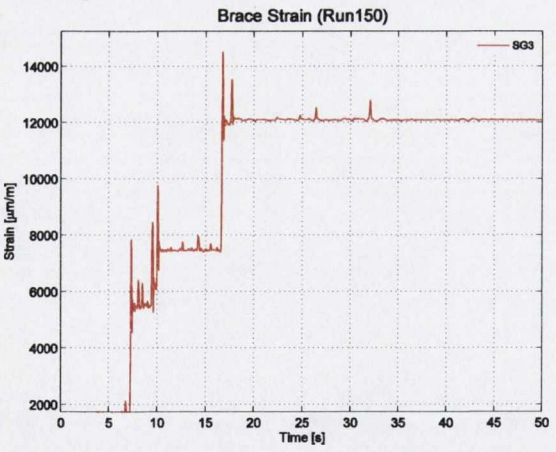

(c) Strain gauge measurements located on the right brace specimen

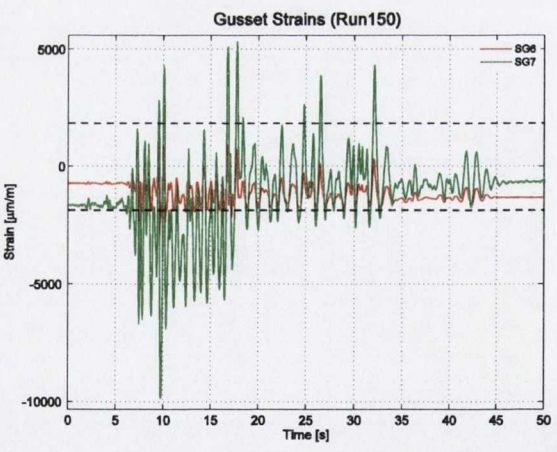

(d) Strain gauge measurements located on the right gusset specimen

Shake Table Test 12: S3-CB-G2

50%/50 (Run156)

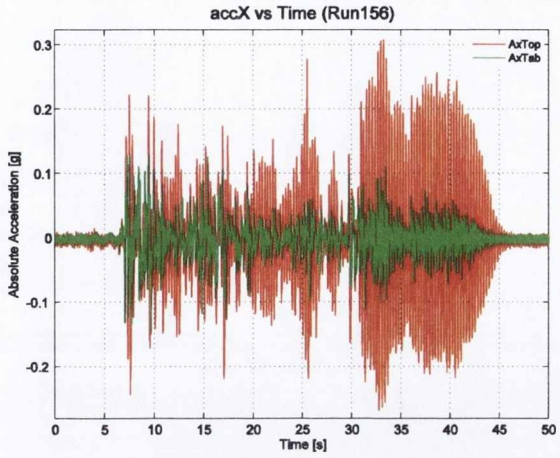

(a) Input (AxTab) and response (AxTop) absolute acceleration time history in x-direction

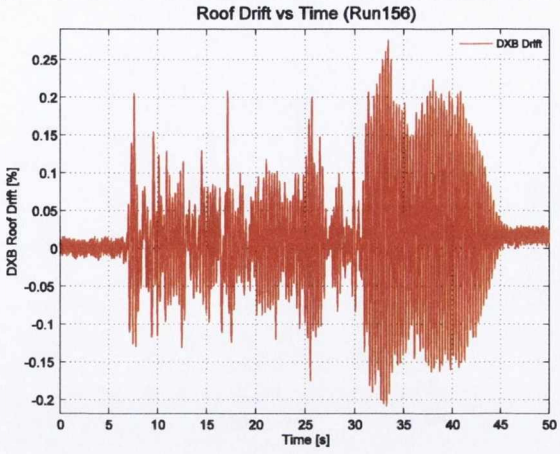

(b) Roof level drift (DXB Drift) time history in x-direction

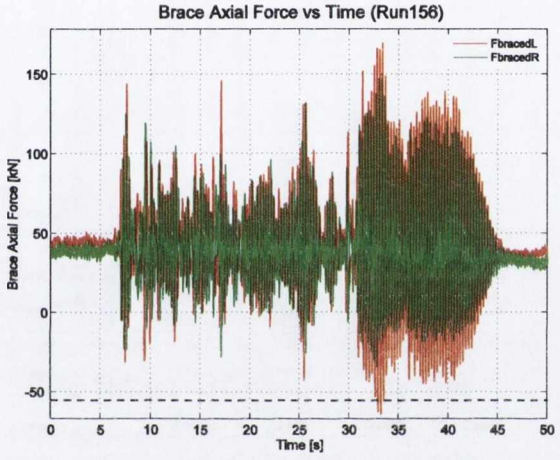

(c) Brace axial load time history for left (FbracedL) and right (FbracedR) braces

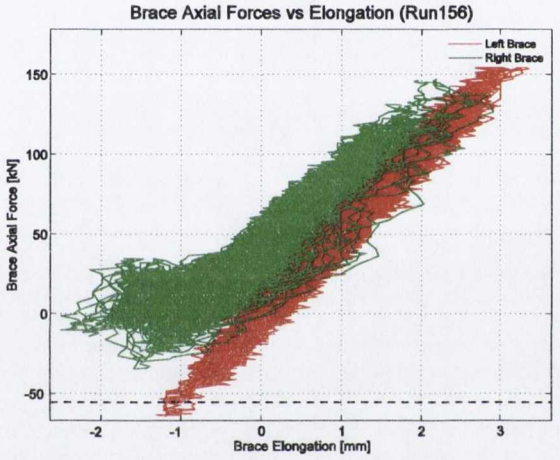

(d) Brace axial load hysteresis for left and right braces

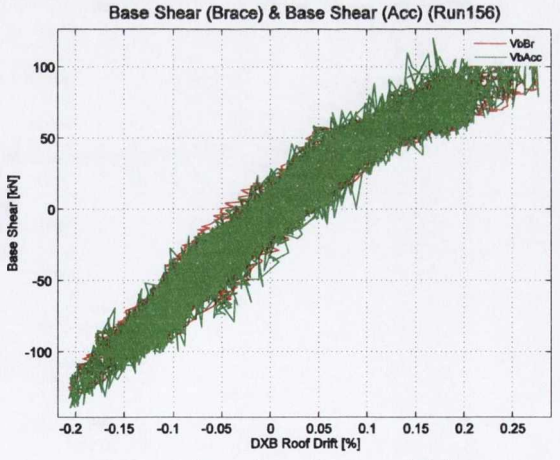

(e) Base shear from brace axial forces plotted against roof drift

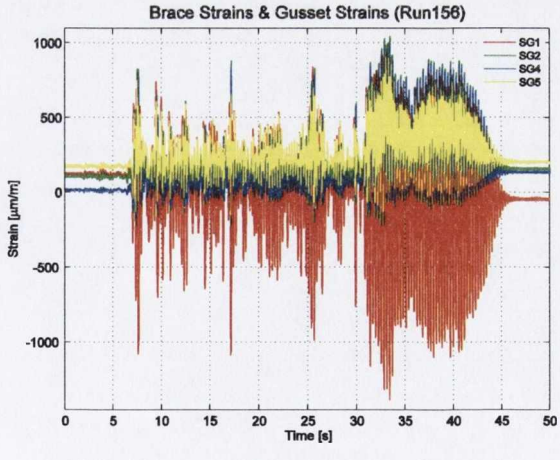

(f) Strain gauge measurements located on the right brace and gusset plate specimen

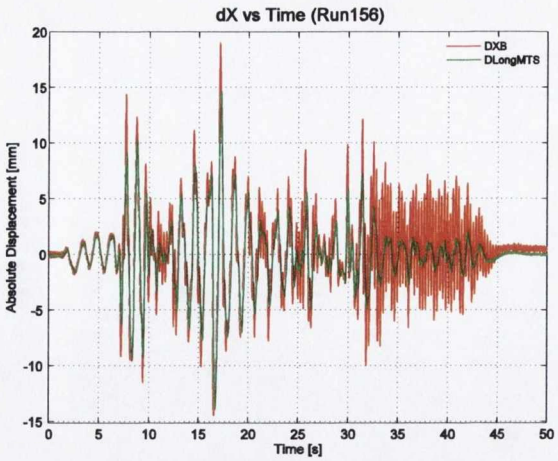

(g) Absolute displacements for table (DLongMTS) and roof level (DXB) time history

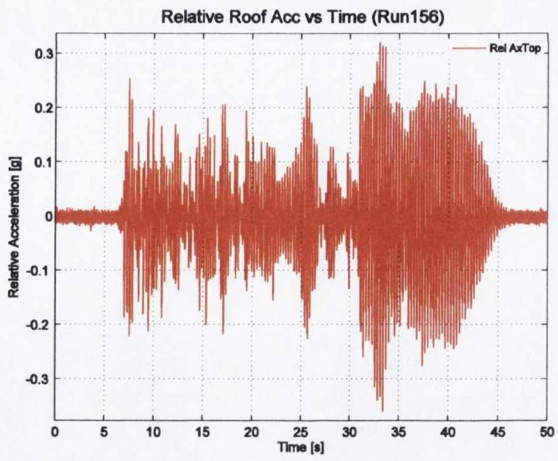

(h) Relative acceleration at roof level

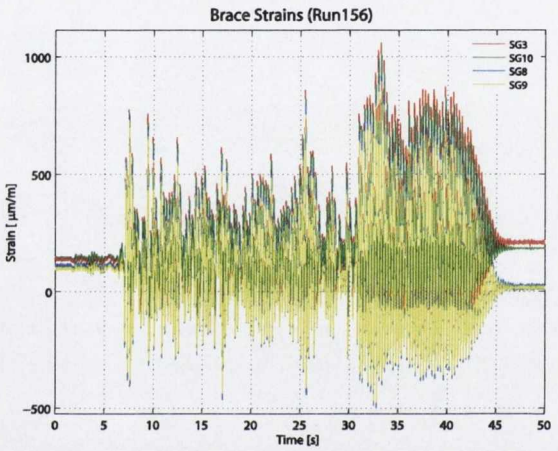

(i) Strain gauge measurements located on the right brace specimen

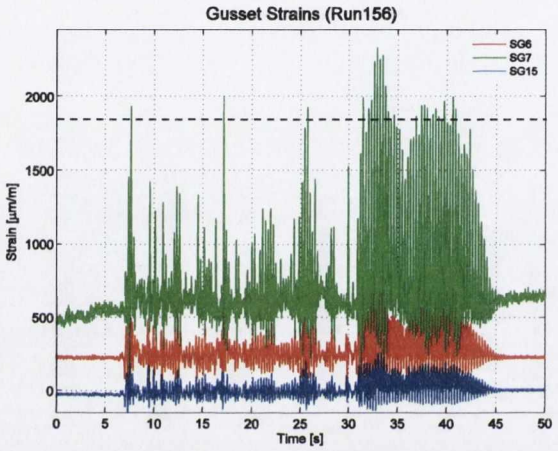

(j) Strain gauge measurements located on the right gusset specimen

10%/50 (Run158)

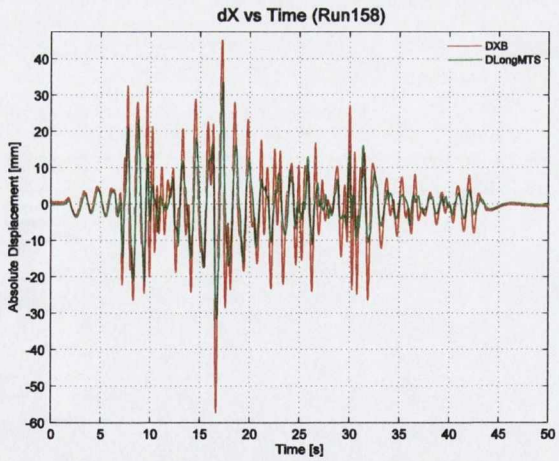

(a) Displacements for table (DLongMTS) and roof level (DXB)

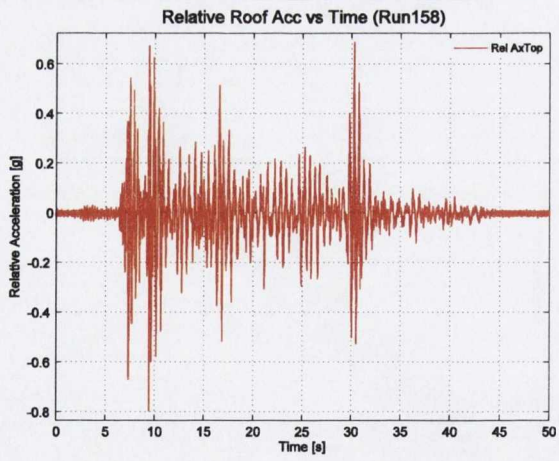

(b) Relative acceleration at roof level

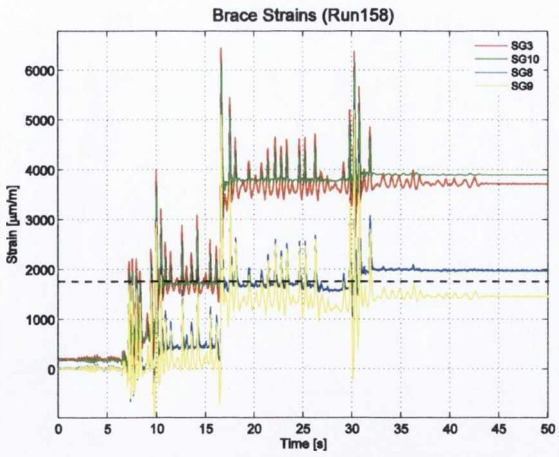

(c) Strain gauge measurements located on the right brace specimen

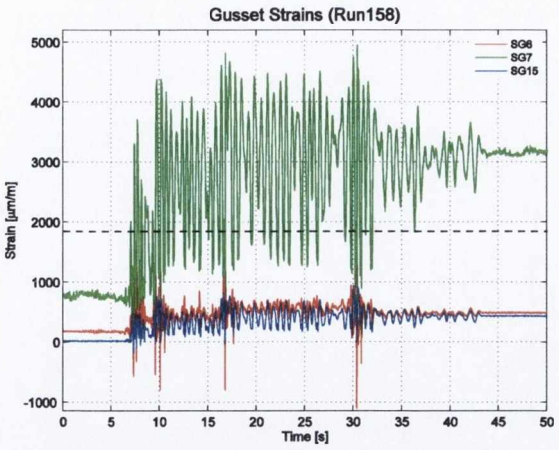

(d) Strain gauge measurements located on the right gusset specimen

2%/50 (Run160)

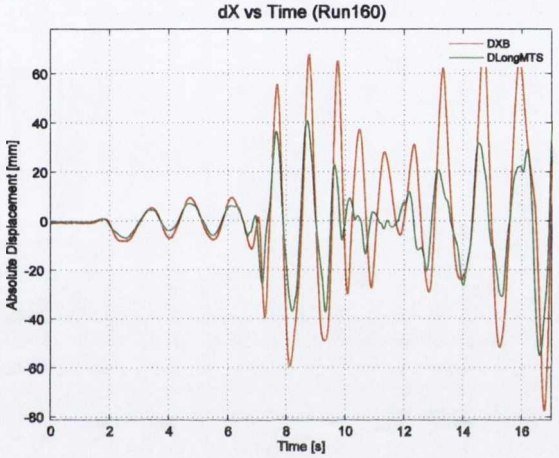

(a) Absolute displacements for table (DLongMTS) and roof level (DXB) time history

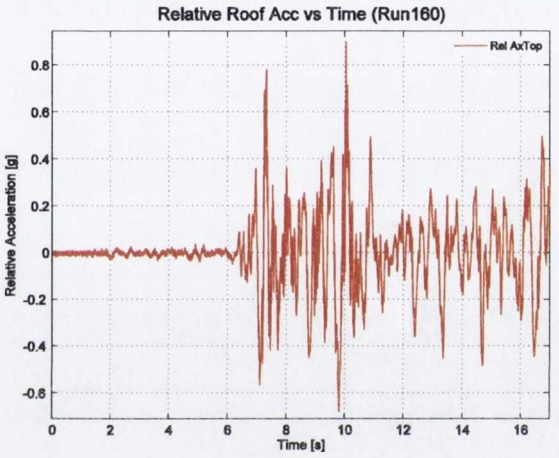

(b) Relative acceleration at roof level

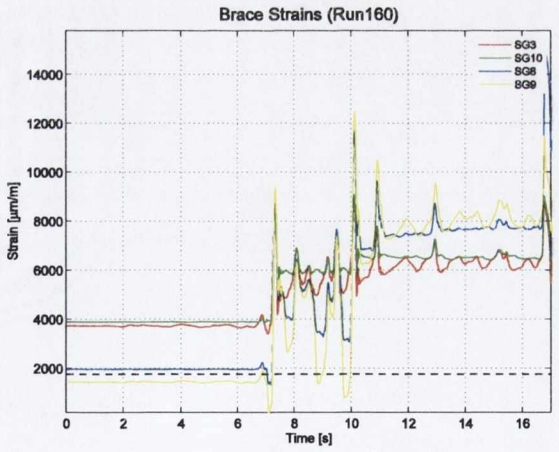

(c) Strain gauge measurements located on the right brace specimen

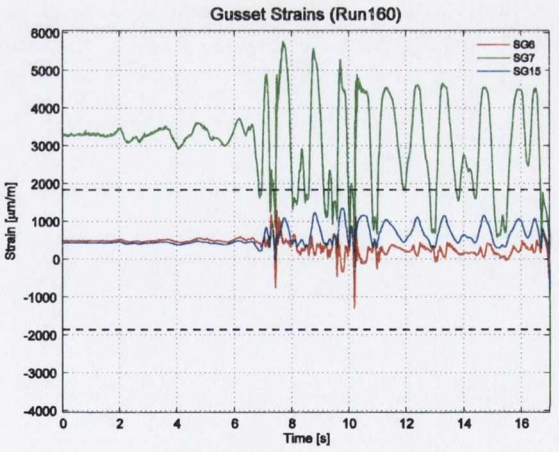

(d) Strain gauge measurements located on the right gusset specimen

B4 Ground Motion Acceleration and Displacement Response Spectra

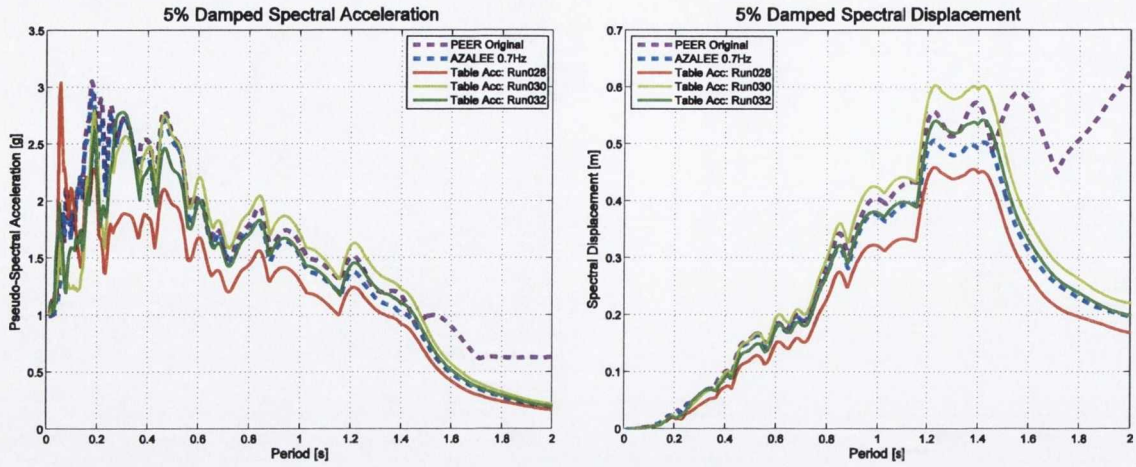

(a) Test 1; S1-CA-G1

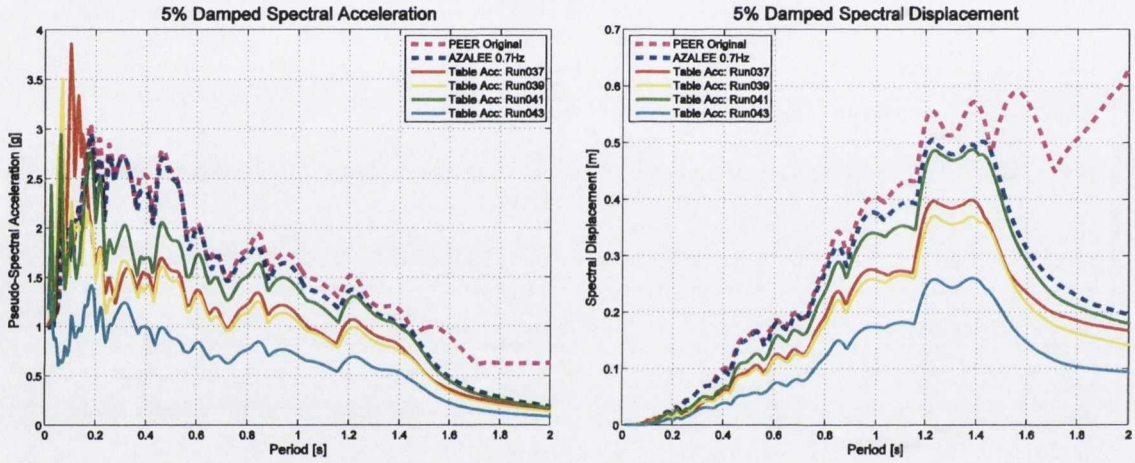

(b) Test 2; S3-CA-G1

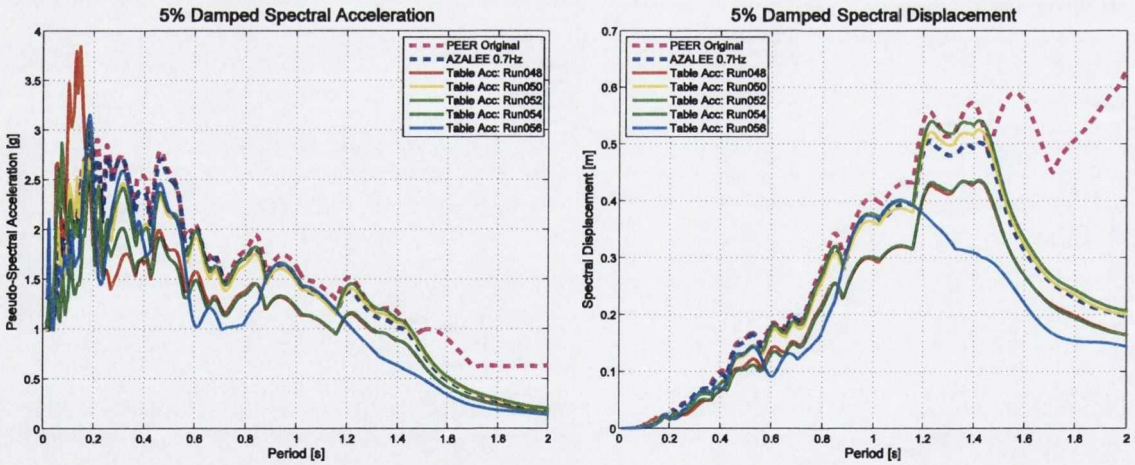

(c) Test 3; S4-CA-G1

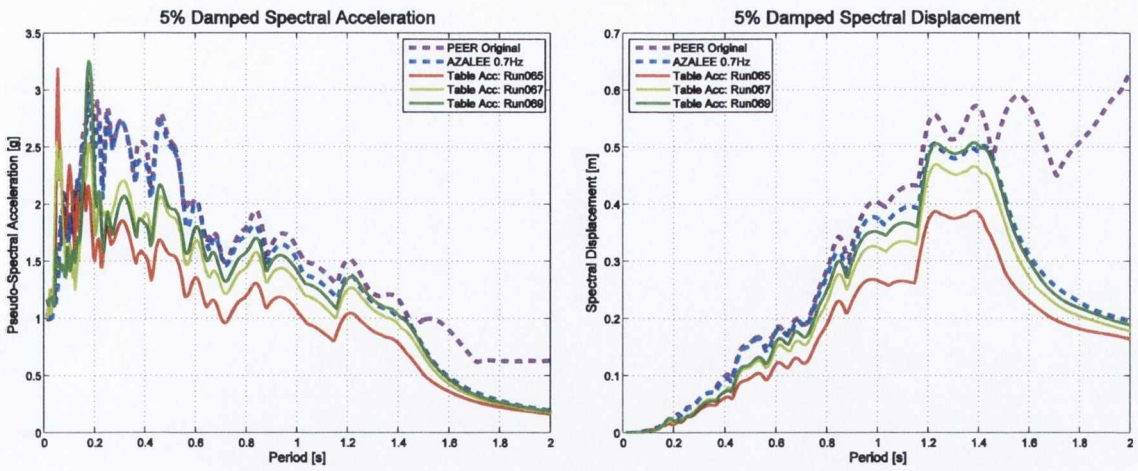

(d) Test 4; S2-CA-G1

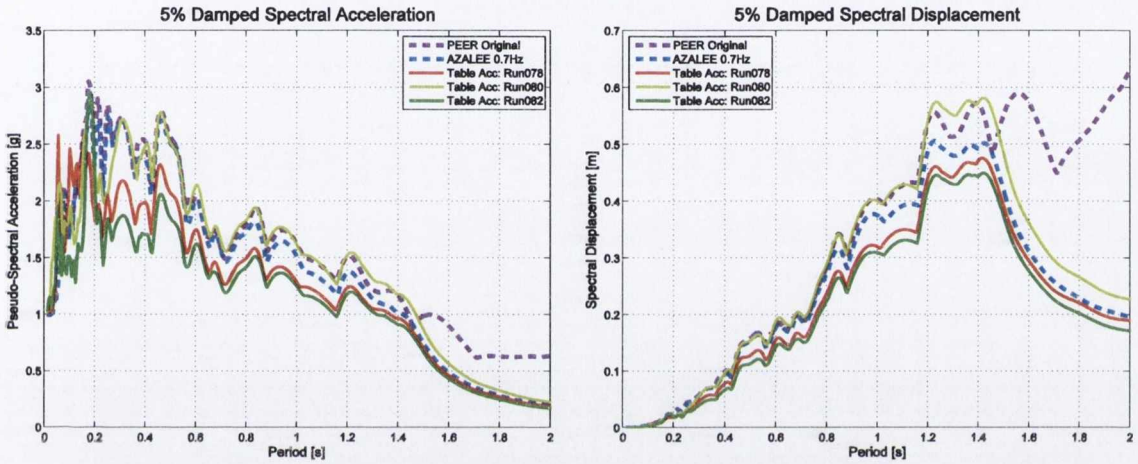

(e) Test 5; S1-CA-G2

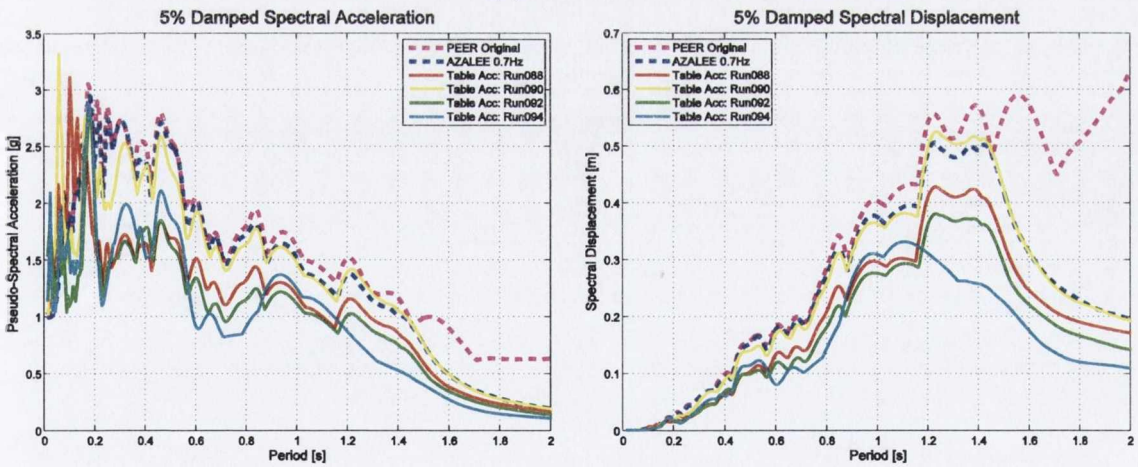

(f) Test 6; S2-CA-G2

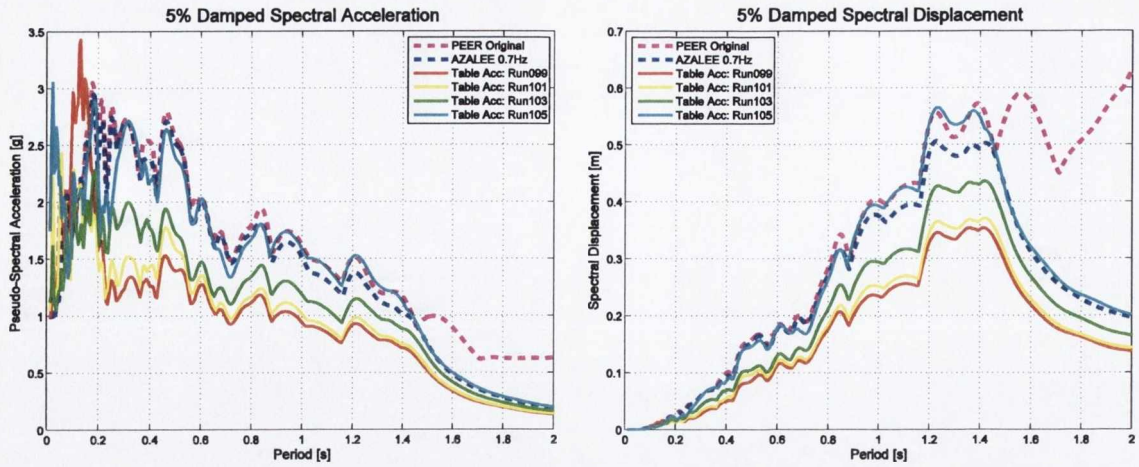

(g) Test 7; S3-CA-G2

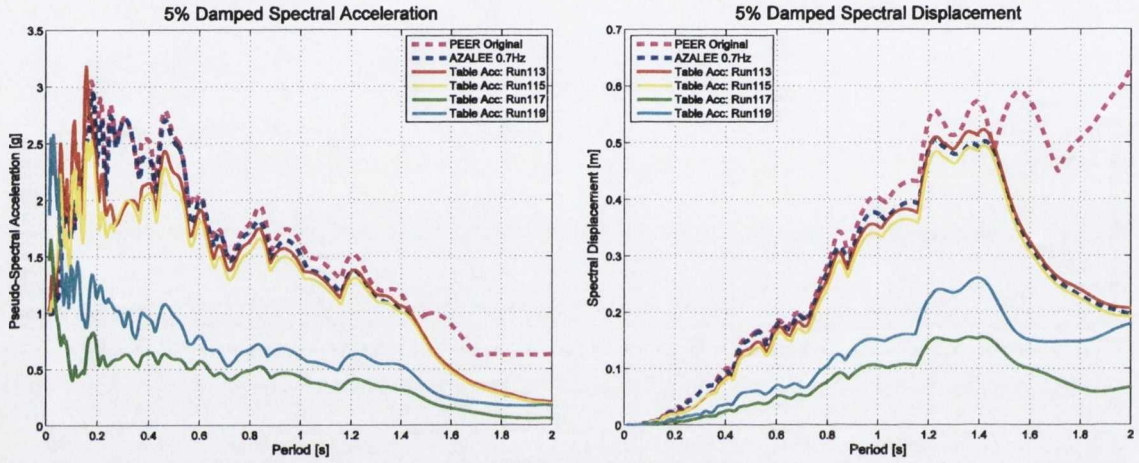

(h) Test 8; S1-CB-G1

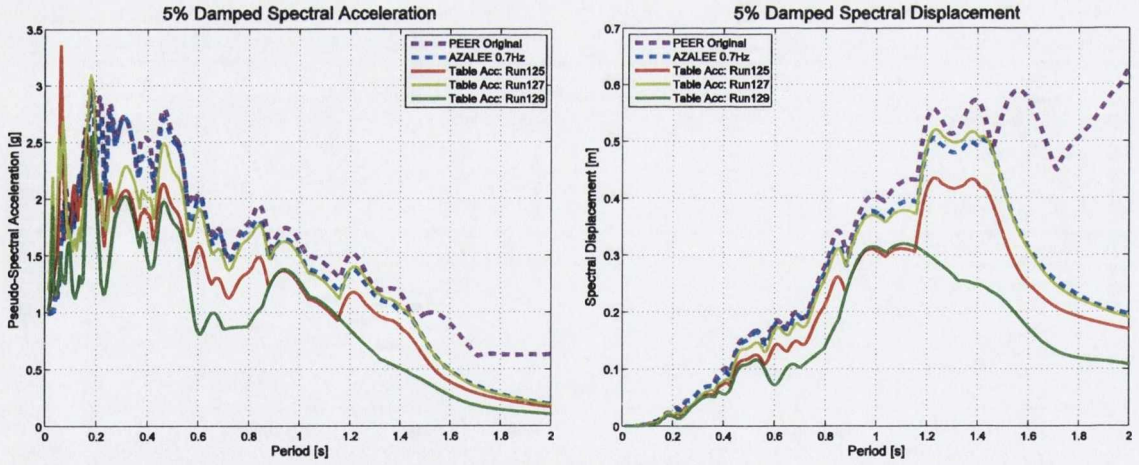

(i) Test 9; S2-CB-G1

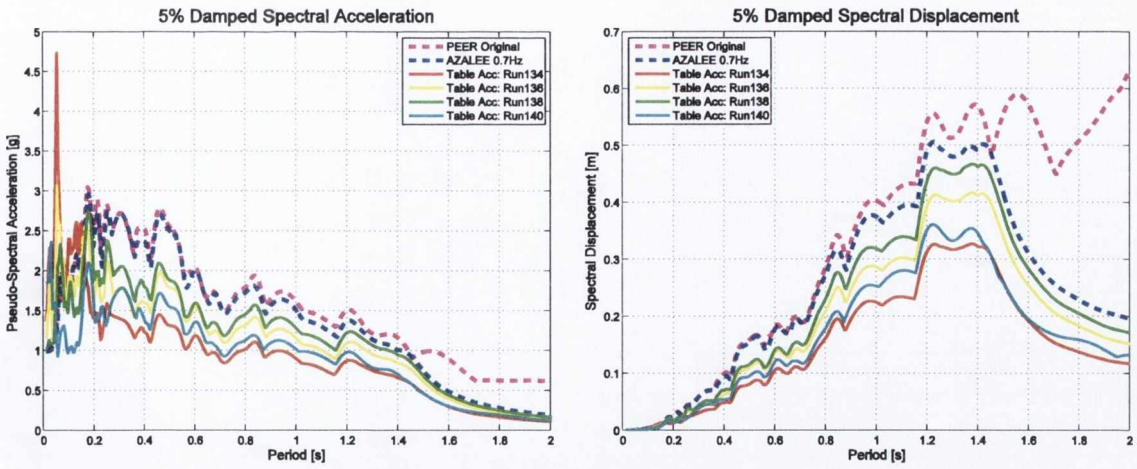

(j) Test 10; S4-CB-G2

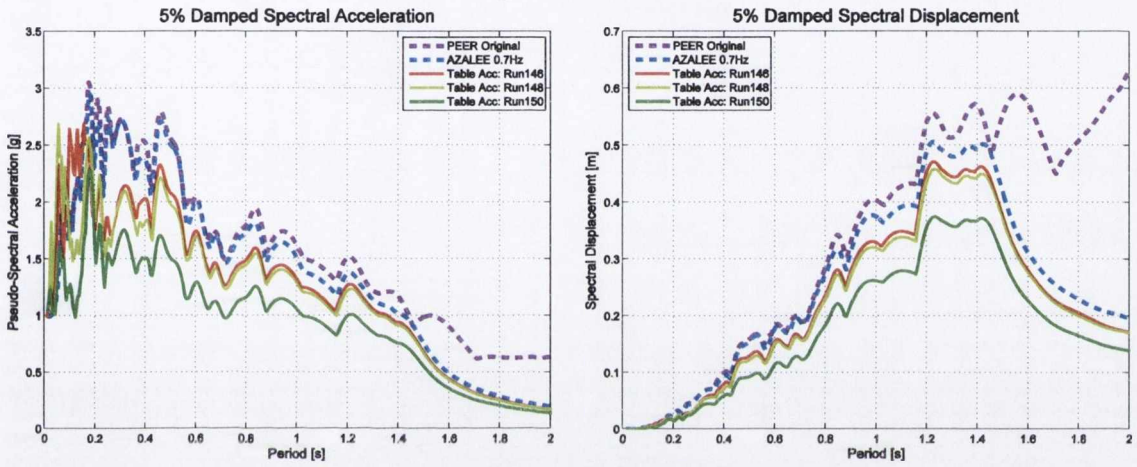

(k) Test 11; S2-CB-G2

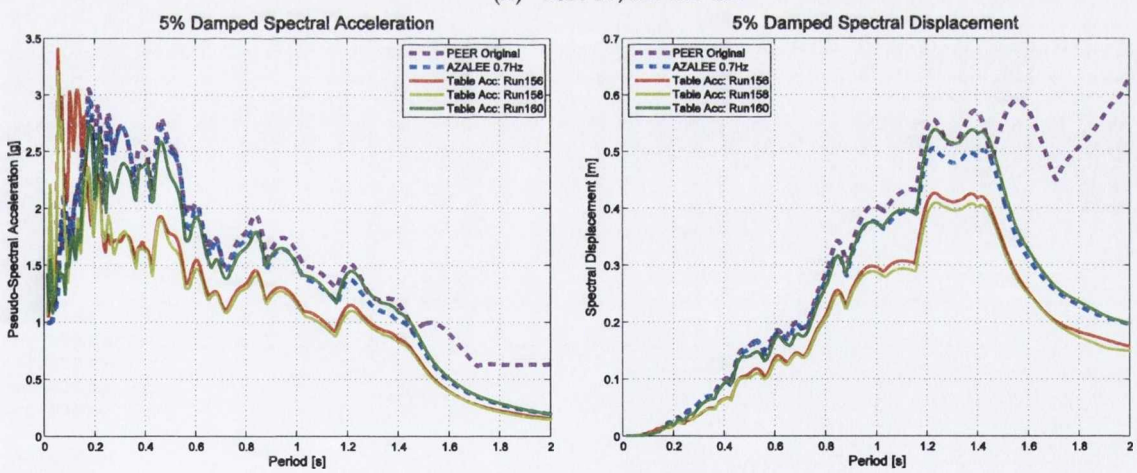

(l) Test 12; S3-CB-G2

Appendix C – OpenSees Model Results

C1 Reference Model (Sample OpenSees Script for Test 10)

```
#       File Name:      T10.2DZ.build.tcl
#       Author:         Alan Hunt
#       Email:          ahunt@tcd.ie
#       Info:           Assembles a 3D model of specimen 10.S4-CB-G2-E1 for BRACED project
#       Units:          N, m

#       GLOBAL COORDINATE SYSTEM:
#                ^ Y axis "out-of-plane"
#          ^ Z  /
#          |   /
#          |------>X

wipe;
file mkdir Data;                                        # Create directory for data
# Define 3 dimensions and 6 DoFs/node
model BasicBuilder -ndm 3 -ndf 6

# Source section definition files
source ../../../../Opensees/SourceFiles/HEsection.tcl;
source ../../../../Opensees/SourceFiles/HSSsection3DNoTor.tcl

# ------------------------------------
# Test Specific Variables
# ------------------------------------

set Fygu                388e6;          # Gusset N/m2
set Fybr                348e6;          # Brace tube N/m2
set t_gp                0.004;          # Gusset plate thickness
set Ww                  0.233;          # Whitmore Width
set Krot_gp             2.46E+03;       # OOP gusset stiffness as per Hsaio et al. [2012]
set Krot_gp_IP          8.35E+06;       # IP gusset stiffness

# # Brace section size
# 60 x 60 x 3.0 SHS
set d_br 0.060;
set b_br 0.060;
set t_br 0.00294;                       # from mean measured value

# ------------------------------------
# Define Geometry
# ------------------------------------

set Lbeam       4.900;          # main beam length
set IPE400d     0.404;          # main beam depth
set Lcol        2.553;          # main column length
set LHgusset 0.270;             # horizontal length of gusset plate
set LVgusset 0.340;             # vertical length of gusset plate
set coldepth 0.220;             # main column depth

set numBraceEle 4;              # no. of brace elements
set braceCamber 1;              # in %

set swiv_h      0.469;          # verical height of swivel
set h8          0.395;
set b5          0.311;
set swiv_w      0.376;          # horizontal length of swivel
set b7          2.254;
set b8          2.254;
set H           [expr $Lcol+$IPE400d/2];        # Total Frame Height (table to beam CL)

# Columns
# -----------------
#               nodeTag         X               Y               Z
# Left
node    1                       0               0               0
node    601                     0               0               [expr $Lcol-$LVgusset]
node    602                     0               0               $Lcol
node    6020                    0               0               $Lcol
```

```
node    2                       0               0               $H
# Right
node    3                       $Lbeam          0               0
node    603                     $Lbeam          0               [expr $Lcol-$LVgusset]
node    604                     $Lbeam          0               $Lcol
node    6040                    $Lbeam          0               $Lcol
node    4                       $Lbeam          0               $H

# Beams
# -----------------
#       nodeTag X                                               Y                       Z
node    402     [expr ($LHgusset*0.75)+($coldepth/2)]           0                       $H
node    403     [expr $Lbeam/2]                                 0                       $H
node    404     [expr $Lbeam-(($LHgusset*0.75)+($coldepth/2))] 0                        $H

# Braces
# -----------------
#       nodeTag X                                       Y               Z
node    80      $b5                                     0.0             [expr $H-$h8]
node    120     [expr $Lbeam-$b5]                       0.0             [expr $H-$h8]
node    18      $b7                                     0.0             0.0
node    19      [expr $b7-$swiv_w]                      0.0             $swiv_h
node    20      [expr $Lbeam-$b8]                       0.0             0.0
node    21      [expr $Lbeam-$b8+$swiv_w]               0.0             $swiv_h

# Define brace node parameters
set node1x_1 [nodeCoord 19 1]; # Find the x-coord of first bottom node of left brace
set node1y_1 [nodeCoord 19 2]; # Find the y-coord of first bottom node of left brace
set node1z_1 [nodeCoord 19 3]; # Find the z-coord of first bottom node of left brace
set node2x_1 [nodeCoord 80 1]; # Find the x-coord of second top node of left brace
set node2y_1 [nodeCoord 80 2]; # Find the y-coord of second top node of left brace
set node2z_1 [nodeCoord 80 3]; # Find the z-coord of second top node of left brace

set node1x_2 [nodeCoord 21 1]; # Find the x-coord of first bottom node of right brace
set node1y_2 [nodeCoord 21 2]; # Find the y-coord of first bottom node of right brace
set node1z_2 [nodeCoord 21 3]; # Find the z-coord of first bottom node of right brace
set node2x_2 [nodeCoord 120 1];# Find the x-coord of second top node of right brace
set node2y_2 [nodeCoord 120 2];# Find the y-coord of second top node of right brace
set node2z_2 [nodeCoord 120 3];# Find the z-coord of second top node of right brace

set dX1 [expr $node1x_1-$node2x_1];
set dY1 [expr $node2y_1-$node1y_1];
set dZ1 [expr $node2z_1-$node1z_1];
set dX2 [expr $node2x_2-$node1x_2];
set dY2 [expr $node2y_2-$node1y_2];
set dZ2 [expr $node2z_2-$node1z_2];
set dx1 [expr $dX1/$numBraceEle];
set dz1 [expr $dZ1/$numBraceEle];
set dx2 [expr $dX2/$numBraceEle];
set dz2 [expr $dZ2/$numBraceEle];

set     Lbrace1 [expr sqrt($dX1*$dX1+$dZ1*$dZ1)];
set     Lbrace2 [expr sqrt($dX2*$dX2+$dZ2*$dZ2)];
set     mpCamber1 [expr 0.01*$braceCamber*$Lbrace1]; # Camber at midpoint of brace 1(in m)
set     mpCamber2 [expr 0.01*$braceCamber*$Lbrace2]; # Camber at midpoint of brace 2(in m)

# Define brace nodes start and end nodes
set b1Start             501
set b2Start             551
set b1End [expr $b1Start+$numBraceEle];
set b2End [expr $b2Start+$numBraceEle];

set dXY1        [expr ($Lbrace1/cos(atan($dX1/$dZ1)))-$dZ1];
set dXY2        [expr ($Lbrace2/cos(atan($dX2/$dZ2)))-$dZ2];

if {$numBraceEle == 4
} {
        #               X                       Y                                               Z
        node    501     $node1x_1               [expr 0*$mpCamber1/1.0/$numBraceEle]
        $node1z_1
        node    502     [expr $node1x_1-1*$dx1] [expr 2*$mpCamber1/1.0/$numBraceEle]
        [expr $node1z_1+1*$dz1]
        node    503     [expr $node1x_1-2*$dx1] [expr 4*$mpCamber1/1.0/$numBraceEle]
        [expr $node1z_1+2*$dz1]
        node    504     [expr $node1x_1-3*$dx1] [expr 2*$mpCamber1/1.0/$numBraceEle]
        [expr $node1z_1+3*$dz1]
        node    505     [expr $node1x_1-4*$dx1] [expr 0*$mpCamber1/1.0/$numBraceEle]
        [expr $node1z_1+4*$dz1]
```

```
        node    551     $node1x_2               [expr 0*$mpCamber2/1.0/$numBraceEle]
$node1z_2
        node    552     [expr $node1x_2+1*$dx2] [expr 2*$mpCamber2/1.0/$numBraceEle]
        [expr $node1z_2+1*$dz2]
        node    553     [expr $node1x_2+2*$dx2] [expr 4*$mpCamber2/1.0/$numBraceEle]
        [expr $node1z_2+2*$dz2]
        node    554     [expr $node1x_2+3*$dx2] [expr 2*$mpCamber2/1.0/$numBraceEle]
        [expr $node1z_2+3*$dz2]
        node    555     [expr $node1x_2+4*$dx2] [expr 0*$mpCamber2/1.0/$numBraceEle]
        [expr $node1z_2+4*$dz2]
}

# -------------------------------------
# Boundary Conditions
# -------------------------------------

#       nodeTag         DX      DY      DZ      RX      RY      RZ
fix     1               1       1       1       1       0       1
fix     3               1       1       1       1       0       1
fix     2               0       1       0       1       0       1
fix     4               0       1       0       1       0       1
fix     18              1       1       1       0       0       1
fix     20              1       1       1       0       0       1

# -------------------------------------
# Nodal Masses & Weights
# -------------------------------------

set g 9.81;
                # m/s2
set MassBeam    [expr (75.7*$Lbeam)];                   # Mass of main beam in kg
set MassCol     [expr (71.5*$Lcol)];                    # Mass of columns in kg
set BeamW13     [expr $MassBeam*$g];                    # m/s2 * kg = N
set ColW1               [expr $MassCol*$g];             # N
set TestmassM   44000;                                  # kg
set TestmassW   [expr $TestmassM*$g];                   # N

# Nodal Weights (used in loading pattern)
set TotalW2     [expr ($BeamW13/2) + $ColW1 + ($TestmassW/2)];       # N
set TotalW4     [expr ($BeamW13/2) + $ColW1 + ($TestmassW/2)];       # N

# Nodal Masses see below (for modal analysis)
set TotalM2     [expr $TotalW2/$g];                                 # kg
set TotalM4     [expr $TotalW4/$g];                                 # kg

puts "Total mass at node 2 (kg) = $TotalM2";        # check mass at node 2
puts "Total mass at node 4 (kg) = $TotalM4";        # check mass at node 4

# Assignment of masses in X (in kg)
mass 2 $TotalM2 0 0 0 0 0
mass 4 $TotalM4 0 0 0 0 0

# -------------------------------------
# Material Properties
# -------------------------------------

# General NL FRAME steel mat
# ------------------
set matID 1;
set Fyfr 323e6;                 # Beam-Col N/m2 (stays constant)
set E0 210000e6;                # N/m2
set b1 0.008;                   # Inelastic Hardening Ratio of Brace
set R0 18.5
set cR1 0.925
set cR2 0.15
set v 0.3;                      # Poisson's ratio steel
set G [expr $E0/(2*(1+$v))];  # Shear Modulus
        uniaxialMaterial Steel02 $matID $Fyfr $E0 $b1       $R0 $cR1 $cR2

# BRACE steel mat
# ------------------
set matIDbrace 2;
# Use the commented below for fatigue material
        # Use the parameters derived in Santagati [2012] for 4ele, 5intpts
        # set Enull 0.12
        # set m -0.458
        # Use the parameters derived in Uriz and Mahin [2008]
```

```
        # set Enull 0.091;
        # set m -0.458;
        # Use the parameters derived in Thesis (from Goggins cyclic results)
        # set Enull 0.163;
        # set m -0.458;
        # Use the parameters derived in Salawdeh [2012] for 2ele, 10intpts
        # set Enull 0.19
        # set m -0.5

set matIDfatBrace 3;
        uniaxialMaterial Steel02      $matIDbrace           $Fybr   $E0 $b1        $R0 $cR1
$cR2
        # uniaxialMaterial Fatigue $matIDfatBrace $matIDbrace -E0 $Enull -m $m

# Spring Materials for ZeroLengths
# -----------------
# Rigid DOF elastic material
set matIDelasticDOF 60;
set E2 1e15;
        uniaxialMaterial Elastic $matIDelasticDOF $E2

#  Pin DOF elastic material
set matIDpin 61;
set E3 200;
        uniaxialMaterial Elastic $matIDpin $E3

# GUSSET OOP stiffness based on calcd gusset stiffness
set matIDgusOOP 62;
set E0  $E2;                          # Youngs modulus of gusset plate
set b1 0.008;                         # Inelastic Hardening Ratio of Brace
set R0 18.5
set cR1 0.925
set cR2 0.15
set My_gp       [expr $Ww*$t_gp*$t_gp*$Fygu/6];
# Steel                       mTag            fy      E               b       R0  cR1  cR2
uniaxialMaterial Steel02      $matIDgusOOP    $My_gp  $Krot_gp        0.01    $R0 $cR1 $cR2

# GUSSET IP stiffness based on calcd gusset stiffness
set matIDgusIP 63;
set My_gp       [expr $Ww*$t_gp*$t_gp*$Fygu/6];
# Steel                       mTag            fy      E               b       R0  cR1  cR2
uniaxialMaterial Steel02      $matIDgusIP     $My_gp  $Krot_gp_IP     0.01    $R0 $cR1 $cR2

# -----------------------------------
# Define Section Properties
# -----------------------------------

# Columns
# ----------------
# Braced frame central columns HE220B
set BracedColSecID 2;
set d 0.220;   # section depth
set b 0.220;   # section width
set t 0.0095;  # web thickness
set T 0.016;   # flange thickness
set dw [expr $d - 2*$T];
set subdivFlw 10;
set subdivFlh 5;
set subdivWbw 10;
set subdivWbh 5;
HEsection $BracedColSecID $matID $d $b $dw $t $subdivFlw $subdivFlh $subdivWbw $subdivWbh
# Torsion
set BracedColSecIDT 12;
set J 77e-8;          # m4 Torsional Moment of Inertia
set GJ 1e6;    # Torsional Rigidity
uniaxialMaterial Elastic $BracedColSecIDT $GJ;
set BracedColSecIDTor 22;
section Aggregator $BracedColSecIDTor $BracedColSecIDT T -section $BracedColSecID;

# Beam
# ----------------
# Main beam IPE400 O
set BeamASecID 4;
set d 0.404;   # section depth
set b 0.182;   # section width
set t 0.0097;  # web thickness
set T 0.0155;  # flange thickness
set dw [expr $d - 2*$T];
```

```
set subdivFlw 6;
set subdivFlh 3;
set subdivWbw 6;
set subdivWbh 3;
HEsection $BeamASecID $matID $d $b $dw $t $subdivFlw $subdivFlh $subdivWbw $subdivWbh
# Torsion
set BeamASecIDT 14;
set J 73.3e-8;          # Torsional Moment of Inertia
set GJ 1e6;     # Torsional Rigidity
uniaxialMaterial Elastic $BeamASecIDT $GJ;
set BeamASecIDTor 24;
section Aggregator $BeamASecIDTor $BeamASecIDT T -section $BeamASecID;

# Braces
# ----------------
set BraceSecID 30;
set subdivShl 5;
set subdivSht 5;
set subdivLol 5;
set subdivLot 5;
HSSsection3DNoTor $BraceSecID $matIDbrace $d_br $b_br $t_br 5 5 5 5
# Torsion
set BraceSecIDT 15;
set GJ 1e6;     # Torsional Rigidity
uniaxialMaterial Elastic $BraceSecIDT $GJ;
set BraceSecIDTor 25;
section Aggregator $BraceSecIDTor $BraceSecIDT T -section $BraceSecID;

# ------------------------------------
# Transform Coordinates
# ------------------------------------

set transfTag_C         1;
set transfTag_Brace     2;
set transfTag_B         3;

# 3D Transformation
geomTransf PDelta               $transfTag_C            0 1 0;
geomTransf Corotational         $transfTag_Brace        0 1 0;
geomTransf PDelta               $transfTag_B            0 1 0;

# ------------------------------------
# Connectivity
# ------------------------------------

set ColIntegPts                 7;
set BeamFrameCnxIntegPts        7;
set BeamFrameIntegPts           7;
set BraceIntegPts               7;

# Columns
# -----------------
# Left Col
element nonlinearBeamColumn 100 1 601 $ColIntegPts $BracedColSecIDTor $transfTag_C
element zeroLength 102 602 6020 -mat $matIDelasticDOF $matIDelasticDOF $matIDelasticDOF
$matIDelasticDOF $matIDelasticDOF $matIDpin -dir 1 2 3 4 5 6 -orient 0 0 1 -1 0 0;

# Right Col
element nonlinearBeamColumn 104 3 603 $ColIntegPts $BracedColSecIDTor $transfTag_C
element zeroLength 106 604 6040 -mat $matIDelasticDOF $matIDelasticDOF $matIDelasticDOF
$matIDelasticDOF $matIDelasticDOF $matIDpin -dir 1 2 3 4 5 6 -orient 0 0 1 -1 0 0;

# Beams
# -----------------
# Frame Beams
element nonlinearBeamColumn 300 402 403 $BeamFrameIntegPts $BeamASecIDTor $transfTag_B
element nonlinearBeamColumn 301 403 404 $BeamFrameIntegPts $BeamASecIDTor $transfTag_B

# Braces
# -----------------
# Column sections for swivel length (non-brace section)
element nonlinearBeamColumn 5 18 19  $ColIntegPts $BracedColSecIDTor $transfTag_C
element nonlinearBeamColumn 6 20 21  $ColIntegPts $BracedColSecIDTor $transfTag_C

# Zerolengths at swivel-brace connection
element zeroLength     7              $b1Start 19     -mat $matIDelasticDOF $matIDelasticDOF
$matIDelasticDOF $matIDelasticDOF $matIDelasticDOF $matIDelasticDOF -dir 1 2 3 4 5 6 -
orient  -$dX1 $dY1 $dZ1 -$dX1 $dY1 -$dXY1
```

```
element zeroLength     8              $b2Start 21    -mat $matIDelasticDOF $matIDelasticDOF
$matIDelasticDOF $matIDelasticDOF $matIDelasticDOF $matIDelasticDOF -dir 1 2 3 4 5 6 -
orient $dX2 $dY2 $dZ2 -$dX2 $dY2  $dXY2

# LHS
element nonlinearBeamColumn 401 501 502 $BraceIntegPts $BraceSecIDTor $transfTag_Brace
element nonlinearBeamColumn 402 502 503 $BraceIntegPts $BraceSecIDTor $transfTag_Brace
element nonlinearBeamColumn 403 503 504 $BraceIntegPts $BraceSecIDTor $transfTag_Brace
element nonlinearBeamColumn 404 504 505 $BraceIntegPts $BraceSecIDTor $transfTag_Brace

# RHS
element nonlinearBeamColumn 601 551 552 $BraceIntegPts $BraceSecIDTor $transfTag_Brace
element nonlinearBeamColumn 602 552 553 $BraceIntegPts $BraceSecIDTor $transfTag_Brace
element nonlinearBeamColumn 603 553 554 $BraceIntegPts $BraceSecIDTor $transfTag_Brace
element nonlinearBeamColumn 604 554 555 $BraceIntegPts $BraceSecIDTor $transfTag_Brace

# Zerolengths at gusset-brace connection (TOP)
element zeroLength     9              $b1End 80              -mat $matIDelasticDOF
$matIDelasticDOF $matIDelasticDOF $matIDelasticDOF $matIDgusOOP $matIDelasticDOF  -dir 1 2
3 4 5 6 -orient -$dX1 $dY1 $dZ1 -$dX1 $dY1 -$dXY1
element zeroLength     10             $b2End 120             -mat $matIDelasticDOF
$matIDelasticDOF $matIDelasticDOF $matIDelasticDOF $matIDgusOOP $matIDelasticDOF  -dir 1 2
3 4 5 6 -orient $dX2 $dY2 $dZ2 -$dX2 $dY2  $dXY2

# Rigid Zones - Beam, Col
# -----------------
rigidLink beam 602     601
rigidLink beam 2       6020
rigidLink beam 604     603
rigidLink beam 4       6040
rigidLink beam 2       402
rigidLink beam 4       404

# Rigid Zones - Gussets
# -----------------
rigidLink beam 80  2
rigidLink beam 120 4

# ------------------------------------
# Recorders
# ------------------------------------

# Check disp and accel at roof level
recorder Node -file Data/RoofDisp_n2.out     -time -node 2 -dof 1 disp;            # Node 2
DX
recorder Node -file Data/RoofAccel_n2.out    -time -node 2 -dof 1 accel;
recorder Node -file Data/RoofDisp_n4.out     -time -node 4 -dof 1 disp;            # Node 4
DX
recorder Node -file Data/RoofAccel_n4.out    -time -node 4 -dof 1 accel;

# Brace forces
# Left
recorder Element -time -file Data/ele401sec1Force.out -ele 401 section 1 force;
recorder Element -file Data/ele401local.out -time -ele 401 localForce;
# Right
recorder Element -time -file Data/ele601sec1Force.out -ele 601 section 1 force;
recorder Element -file Data/ele601local.out -time -ele 601 localForce;

# Base Shear
recorder Node -file Data/BaseShear1.out -time -node 1 3 18 20 -dof 1 reaction;

# ------------------------------------
# Dead Loads
# ------------------------------------

pattern Plain 1 Linear {
        # Assignment of loads in X & Z
        load 2 0 0 -$TotalW2 0 0 0
        load 4 0 0 -$TotalW4 0 0 0
        }

# ------------------------------------
# Gravity Analysis
# ------------------------------------

constraints Transformation;
set NumIter 10;               # Set the number of iterations for convergence
set Tol 1.0e-6;               # convergence tolerance for test
```

```
test NormDispIncr $Tol $NumIter;
numberer RCM ;
system BandGeneral ;
algorithm Newton ;
set LoadSteps 10;
set LoadIncr [expr 1.0/$LoadSteps];
integrator LoadControl $LoadIncr;
analysis Static ;
analyze $LoadSteps ;  # applying gravity
# maintain constant gravity loads and reset time to zero
loadConst -time 0.0

# ------------------------------------
# Dynamic Analysis Definition
# ------------------------------------

# set up ground-motion-analysis parameters
set iGMfile "T10_all_runs.txt";              # input time history
set iGMdirection "1";                        # ground-motion directions
set iGMfact "9.81";                                 # define g
puts "Input GM file = $iGMfile";      # output filename to screen
set DtAnalysis 0.001953;                     # select suitable time-step Dt for analysis
(512 Hz)
set TmaxAnalysis 200.06532;                  # maximum duration of ground-motion analysis
(for 4 runs)
# set TmaxAnalysis 50.01633;          # maximum duration of ground-motion analysis (for 1
run)

set alphaSP 1e15 ;
set alphaMP 1e15 ;
constraints Penalty $alphaSP $alphaMP;
numberer RCM ;
system UmfPack ;
set Tol 1.e-5;
set maxNumIter 100;
test NormDispIncr $Tol $maxNumIter;
algorithm KrylovNewton ;
set gamma 0.8;
integrator HHT $gamma
analysis Transient

# ------------------------------------
# Rayleigh Damping
# ------------------------------------

set xDamp 0.03;
set lambda [eigen generalized 1];
set omega [expr pow($lambda,0.5)];
set Tperiod [expr 2*3.141592654/$omega];
puts "Structural Period (s) = $Tperiod";
set alphaM 0;                # stiffness-prop. RAYLEIGH damping parameter; D = alphaM*M
set betaK 0;           # stiffness proportional damping; +beatK*KCurrent
set betaKcomm [expr 2*$xDamp/($omega)]; # mass-prop. RAYLEIGH damping parameter;
+betaKcomm*KlastCommitt
set betaKinit 0;       # initial-stiffness proportional damping +beatKinit*Kini
rayleigh $alphaM $betaK $betaKinit $betaKcomm;       # RAYLEIGH damping

# ------------------------------------
# Perform Dynamic Analysis
# ------------------------------------

set IDloadTag 400;     # for uniformSupport excitation
# Uniform EXCITATION: acceleration input
foreach GMdirection $iGMdirection GMfile $iGMfile GMfact $iGMfact {
       incr IDloadTag;
       set AccelSeries "Series -dt $DtAnalysis  -filePath $iGMfile -factor  $iGMfact";
       # time series information
       pattern UniformExcitation  $IDloadTag  1 -accel  $AccelSeries  ;    # create Uniform
excitation
}
set startT [clock seconds];                                                    # tic
set Nsteps [expr int($TmaxAnalysis/$DtAnalysis)];
set ok [analyze $Nsteps $DtAnalysis];                              # actually perform
analysis; returns ok=0 if analysis was successful
set endT [clock seconds];                                                      # toc
puts "Execution time: [expr $endT-$startT] seconds.";       # tic-toc to screen

if {$ok != 0
```

```
} {    ;
       # if analysis was not successful,
       # change some analysis parameters to achieve convergence
       # performance is slower inside this loop
       #    Time-controlled analysis
       set ok 0;
       set controlTime [getTime];
       while {$controlTime < $TmaxAnalysis && $ok == 0
} {
              set controlTime [getTime]
              set ok [analyze 1 $DtAnalysis]
              if {$ok != 0
} {
                     puts "Trying Newton with Initial Tangent .."
                     test NormDispIncr   $Tol 1000  0
                     algorithm Newton -initial
                     set ok [analyze 1 $DtAnalysis]
                     test $testTypeDynamic $TolDynamic $maxNumIterDynamic  0
                     algorithm $algorithmTypeDynamic
              }
              if {$ok != 0
} {
                     puts "Trying Broyden .."
                     algorithm Broyden 8
                     set ok [analyze 1 $DtAnalysis]
                     algorithm $algorithmTypeDynamic
              }
              if {$ok != 0
} {
                     puts "Trying NewtonWithLineSearch .."
                     algorithm NewtonLineSearch .8
                     set ok [analyze 1 $DtAnalysis]
                     algorithm $algorithmTypeDynamic
              }
       }
};      # end if ok !0

puts "Ground Motion Done. End Time: [getTime]"
set fmt1 "%s Analysis Result: CtrlNode %.2i, dof %.1i, Disp=%.4f %s";

# ------------------------------
# Final Output to Screen Info
# ------------------------------

set LunitTXT "m";
set IDctrlNode 2;
set IDctrlDOF 1;

if {$ok != 0
 } {
       puts [format $fmt1 "PROBLEM WITH DYNAMIC ANALYSIS" $IDctrlNode $IDctrlDOF [nodeDisp
$IDctrlNode $IDctrlDOF] $LunitTXT]
} else {
       puts [format $fmt1 "DYNAMIC ANALYSIS COMPLETE:"  $IDctrlNode $IDctrlDOF [nodeDisp
$IDctrlNode $IDctrlDOF] $LunitTXT]
}
puts "\a";     # beep
```